frontiers | Research Topics

The relationship between petroleum accumulation and mineralization in sedimentary basins

Edited by
Dongming Zhi, Deyu Gong, Leon Bagas and Hao Zou

Published in
Frontiers in Earth Science

ISSN 1664-8714
ISBN 978-2-83251-745-1
DOI 10.3389/978-2-83251-745-1

About Frontiers

Frontiers is more than just an open access publisher of scholarly articles: it is a pioneering approach to the world of academia, radically improving the way scholarly research is managed. The grand vision of Frontiers is a world where all people have an equal opportunity to seek, share and generate knowledge. Frontiers provides immediate and permanent online open access to all its publications, but this alone is not enough to realize our grand goals.

Frontiers journal series

The Frontiers journal series is a multi-tier and interdisciplinary set of open-access, online journals, promising a paradigm shift from the current review, selection and dissemination processes in academic publishing. All Frontiers journals are driven by researchers for researchers; therefore, they constitute a service to the scholarly community. At the same time, the *Frontiers journal series* operates on a revolutionary invention, the tiered publishing system, initially addressing specific communities of scholars, and gradually climbing up to broader public understanding, thus serving the interests of the lay society, too.

Dedication to quality

Each Frontiers article is a landmark of the highest quality, thanks to genuinely collaborative interactions between authors and review editors, who include some of the world's best academicians. Research must be certified by peers before entering a stream of knowledge that may eventually reach the public - and shape society; therefore, Frontiers only applies the most rigorous and unbiased reviews. Frontiers revolutionizes research publishing by freely delivering the most outstanding research, evaluated with no bias from both the academic and social point of view. By applying the most advanced information technologies, Frontiers is catapulting scholarly publishing into a new generation.

What are Frontiers Research Topics?

Frontiers Research Topics are very popular trademarks of the *Frontiers journals series*: they are collections of at least ten articles, all centered on a particular subject. With their unique mix of varied contributions from Original Research to Review Articles, Frontiers Research Topics unify the most influential researchers, the latest key findings and historical advances in a hot research area.

Find out more on how to host your own Frontiers Research Topic or contribute to one as an author by contacting the Frontiers editorial office: frontiersin.org/about/contact

The relationship between petroleum accumulation and mineralization in sedimentary basins

Topic editors

Dongming Zhi — Turpan-Hami oil company, PetroChina, China
Deyu Gong — Research Institute of Petroleum Exploration and Development (RIPED), China
Leon Bagas — China Geological Survey, China
Hao Zou — Chengdu University of Technology, China

Citation

Zhi, D., Gong, D., Bagas, L., Zou, H., eds. (2023). *The relationship between petroleum accumulation and mineralization in sedimentary basins*. Lausanne: Frontiers Media SA. doi: 10.3389/978-2-83251-745-1

Table of contents

frontiers | Frontiers in Earth Science

TYPE Editorial
PUBLISHED 08 February 2023
DOI 10.3389/feart.2023.1116440

OPEN ACCESS

EDITED AND REVIEWED BY
Valerio Acocella,
Roma Tre University, Italy

*CORRESPONDENCE
Deyu Gong,
deyugong@126.com

SPECIALTY SECTION
This article was submitted to Economic Geology,
a section of the journal
Frontiers in Earth Science

RECEIVED 05 December 2022
ACCEPTED 01 February 2023
PUBLISHED 08 February 2023

CITATION
Zhi D, Gong D, Bagas L and Zou H (2023), Editorial: The relationship between petroleum accumulation and mineralization in sedimentary basins. *Front. Earth Sci.* 11:1116440. doi: 10.3389/feart.2023.1116440

Editorial: The relationship between petroleum accumulation and mineralization in sedimentary basins

Dongming Zhi[1,2], Deyu Gong[3]*, Leon Bagas[4] and Hao Zou[4,5]

[1]Xinjiang Oilfield Company, PetroChina, Karamay, China, [2]Turpan-Hami Oilfield Company, PetroChina, Hami, China, [3]Research Institute of Petroleum Exploration and Development, PetroChina, Beijing, China, [4]Key Laboratory of Tectonic Controls on Mineralization and Hydrocarbon Accumulation of Ministry of Land and Resources, Chengdu University of Technology, Chengdu, China, [5]State Key Laboratory of Oil and Gas Reservoir Geology and Exploitation, Chengdu University of Technology, Chengdu, China

KEYWORDS

sedimentary basin, petroleum accumulation, ore deposits, coupling, fluid

Editorial on the Research Topic
The relationship between petroleum accumulation and mineralization in sedimentary basins

Introduction

Sedimentary basins are critical geological units that can host fossil fuel (oil, natural gas, and coal) as well as metallic and non-metallic mineral deposits (i.g., Pb, Zn, Cu, NaCl, and Li brines) (Carpenter et al., 1974; Kyser, 2000). Mineral deposits are often closely related to petroleum reservoirs in sedimentary basins (Oliver, 1986; Chen et al., 2001). Several low-to-medium-temperature hydrothermal ore deposits in sedimentary basins often have a coupling relationship of homology with hydrocarbon reservoirs (Williams-Jones and Migdisov, 2006). With economic development and population growth, the global demand for fossil fuels as well as metallic and non-metallic mineral deposits is increasing. Basinal fluids related to metallization and petroleum accumulation include hydrocarbon-rich organic, metal-rich aqueous, and hydrocarbon- and mineral-rich ore-forming fluids. The evolution of these fluids may determine the nature of coupled mineralization and petroleum accumulation in a basin (Sverjensky, 1984; Parnell, 1994; Hulen and Collister, 1999; Zhuang et al., 2000).

Several examples of global sedimentary basins show close symbiosis or association among minerals, oil, and gas reservoirs in space as well as striking similarities in material composition (Liu et al., 2006; Gu et al., 2010). There are three possible scenarios between mineralization and petroleum accumulation: 1) petroleum accumulation precedes mineralization, 2) petroleum accumulation and mineralization co-occur, and 3) petroleum accumulation occurs after mineralization (Liu et al., 2006; Gu et al., 2010). The first two reflect the close relationship between petroleum accumulation and mineralization. In the scenario 1), hydrocarbons and organic matter provide sulfur sources and reducing agents for mineralization. In the scenario 2), hydrocarbon accumulation and mineralization tend to be characterized by fluid homologation, co-transportation, and homogenization.

Owing to the relatively independent exploration, development, and utilization of solid minerals and petroleum in the industrial sector, the academic community has not paid much attention to the comprehensive interdisciplinary research of various resources (fossil fuels, metallic and non-metallic mineral deposits) for a long time. Thus, the synergistic exploration and integrated evaluation of multiple resources coexisting with sedimentary basins has not been achieved; this delays the discovery of related resources and increases the cost of scientific research, exploration, and development. Systematic theoretical and technical research is necessary to clarify the spatiotemporal relationships between mineral deposits and petroleum reservoirs in sedimentary basins.

In this report, we present a Research Topic on the relationship between petroleum accumulation and mineralization in sedimentary basins. A total of 18 papers are included in the Research Topic, mainly divided into two categories: the mineralization process (Wang et al.) and controlling factors for petroleum accumulation. The latter can be subcategorized into three: (1) source rock and oil-source correlation (Qin et al.; Gong et al.; Zhai et al.; Zhang et al.; (b) reservoir evaluation (Qin et al.; Wang et al.; Dan et al.; He et al.; Ning et al.; Wan et al.; Xu et al.; Zhao et al.; Zhi et al.); and (c) petroleum accumulation process (Ablimiti et al.; Kang et al.; Xiao et al.; Xue et al).

Mineralization process

Quartz is an abundant mineral on the Earth's crust and the most common gangue mineral in various hydrothermal deposits. Quartz commonly crystallizes at a wide range of temperatures (50°C–750°C) from fluids with diverse origins and compositions (Rusk and Reed, 2002; Rusk et al., 2008; Thomas et al., 2010; Götte et al., 2011). Recent advances in the use of LA–ICP–MS have allowed for the *in situ* analyses of numerous trace elements in quartz, such as Ti, Al, Li, Na, K, Fe, Ca, P, Mg, Mn, Cu, and Ge, at increasingly low detection limits. Wang et al. presented the petrographic description and trace element geochemistry of quartz in the Hongniu–Hongshan Cu skarn deposit in southwestern China, illustrating the genesis of their trace element tenures, quartz crystallization, and resorption of quartz phenocrysts. In addition, they discussed whether the igneous host rock at the deposit underwent magmatic mixing or recharge. Finally, quartz trace element data from 14 deposits were compiled to demonstrate the difference between magmatic and hydrothermal quartz.

Controlling factors for petroleum accumulation

Source rock and oil-source correlation

Source rocks refer to rocks rich in organic matter and capable of generating and discharging large quantities of oil and gas (Tissot and Welte, 1984); they are the material basis of petroleum formation. Therefore, accurate source rock evaluation is critical to clarify the exploration potential of petroliferous basins.

By analyzing organic geochemistry, organic petrology, and basin modeling, Gong et al. systematically evaluated a set of marine–terrigenous transitional source rocks developed in the Lower Carboniferous Bashan Formation in the Jimuar Sag, northwestern China, and revealed a potential giant petroleum system.

Previous studies have shown that several intervals of high-quality source rocks generally contain varying volcanic ash layers (Liu et al., 2019a,b). Extensive studies have been conducted on the impact of these volcanic ash layers on the development of high-quality source rocks (Duggen et al., 2007; Lee et al., 2018). However, these studies mainly focused on the development of hydrocarbon-forming organisms and the preservation of organic matter but rarely considered the differential development of hydrocarbon-forming organisms between multiple volcanic ash layers (Liu et al., 2019a,b). The Permian Dalong Formation in the northwestern Sichuan Basin, China, is a set of high-quality source rocks with multiple volcanic sedimentary layers. Considering the marine source rocks in the Permian Dalong Formation, southwestern China, as the research objects, Zhang et al. analyzed the types of hydrocarbon-generating materials of high-quality source rocks and the reasons volcanic activities affected the growth of hydrocarbon-forming organisms. They also explored the impact of volcanic activity on the development of different types of hydrocarbon-forming organisms.

Diamondoid, named considering its diamond-like structure, is highly resistant to thermal degradation and biodegradation. Thus, it is preserved and enriched during the long and complex geological process and carries geological information. Therefore, diamondoid has broad applications in petroleum geochemistry, such as oil maturity ascertainment (Chen et al., 1996), oil cracking extent assessment (Dahl et al., 1999), lithofacies discernment (Schulz et al., 2001), secondary change assessment (Jiang et al., 2020), thermochemical sulfate reduction (Wei et al., 2011), and oil spill source identification in an accident (Stout and Douglas, 2004; Wang et al., 2006) in marine strata. However, its application in coal measures and related petroleum systems is in its infancy. Based on gold tube thermal simulation experiments on the soluble components (extracts) and insoluble components of coal-measure mudstones, Zhai et al. quantitatively analyzed diamondoid compounds in the pyrolysis products as well as showed that diamondoid compounds in the extracts and extracted coal-measure mudstones formed and decomposed during thermal evolution. In addition, the evolution characteristics and some diamondoid maturity parameters in the extracts and extracted coal-measure mudstones showed a good linear relationship. However, the specific characteristics differed, which may enable the identification of the kerogen and secondary cracking of crude oil.

Oil (gas)-source correlation is an effort to determine the genetic relationship between oil and source rocks based on geological and geochemical evidence (Volkman, 1986; Dai et al., 1992; Peters et al., 2005). This Research Topic includes the correlation between oil (gas) and source rock as well as between oil and gas in different reservoirs. Consequently, the direction and distance of oil and gas migration and the secondary alterations of oil and gas can be judged by the comparative study to further delineate reliable oil-source areas, determine exploration targets, and effectively guide oil and gas exploration and development (Volkman, 1986; Dai et al., 1992; Peters et al., 2005). Qin et al. conducted a detailed geochemical anatomy of 18 oil samples collected from key oil-bearing structural units of the southern thrust belt of Junggar, northwestern China. Based on the characteristics of light hydrocarbons, adamantanes,

biomarkers, and stable carbon isotopic composition of the bulk oil ($\delta^{13}C_{bulk}$), the geochemical classification and potential secondary alterations, such as biodegradation, thermal cracking, and evaporative fractionation, were discussed, thereby providing a classic case to bolster the understanding of the origin and accumulation process of oil and gas in a complex structural zone (Qin et al).

Reservoir evaluation

Reservoir evaluation is a comprehensive subject that applies various data to study and explain the sedimentary environment, diagenesis, and formation mechanism of petroleum reservoirs. By analyzing and determining reservoirs' geological information, oil and gas exploration and development efficiency will be improved significantly. Reservoir evaluation extensively uses geological, seismic, well logging, well testing, and other data and various reservoir testing methods. The research objects are mainly divided into carbonate and clastic rocks.

The sedimentary environment is the determinant factor controlling reservoir macroscopic distribution. Zhi et al. employed core observation, logging curve, and seismic data to determine the stratigraphic characteristics and sedimentary-filling process for the Lower Permian Fengcheng Formation in the Junggar Basin, northwestern China—the oldest alkali lake in the world. Storm deposits are helpful indicators for sedimentary facies and palaeogeographic analysis (Aigner and Reineck., 1982; Aigner., 1985a; Aigner., 1985b; Myrow et al., 2008; Immenhauser, 2009). In addition, tempestites are essential reservoirs for stratigraphic traps (Aigner, 1985a,b; Mohseni and Al-Aasm, 2004). He et al. discussed an unrecognized phenomenon known as storm deposition and tempestite in the Cretaceous Qingshankou Formation of the Songliao Basin, the largest proliferous basin in China. This work is significant for elucidating the formation environment and diagenetic process of the Qingshankou shale reservoir, providing a reference for oil and gas exploration and development.

Diagenesis is a key factor controlling reservoir quality. The diagenesis of carbonate and clastic rocks differs significantly. In sedimentary petrology, the identification of geologic fluids and the related fluid–rock interactions during diagenesis has attracted considerable attention. Authigenic calcite potentially provides a record of geologic fluids and it occurs heterogeneously in the Upper Permian Wuerhe Formation in the Shawan Sag, Junggar Basin, northwestern China, which has a complex history of geologic fluid activity. Xu et al. conducted petrological and mineralogical studies of the Wuerhe Formation and used the *in situ* major element, trace element, and carbon and oxygen isotopic compositions of calcite formed at different stages to reveal the possible composition of geologic fluids present as well as the fluid–rock interactions and alteration of the reservoir that occurred during diagenesis. In addition, considering the Wuerhe sandstone reservoir as the research object, Qin et al. employed rock-cast thin section, scanning electron microscopy, fluid inclusions, piezometric mercury analysis, and porosity–permeability analysis to illustrate the characteristics and genesis mechanism of the Wuerhe clastic reservoir and provided a basis for the preferential selection of promising targets and sweet-spot areas. The Qiangtang Mesozoic marine sedimentary basin is the least explored oil-bearing basin in China. In recent years, dolostone paleo-reservoirs were discovered in the Middle Jurassic Buqu Formation in the southern Qiangtang depression of Tibet, providing a new direction for oil and gas exploration in the basin (Chen et al., 2018; Wang and Fu, 2018; Sun et al., 2020; Wang et al., 2020; Yi and Xia, 2022). Wan et al. investigated the petrography, geochemistry, and origin of various types of dolomites collected from the boreholes using various methods, such as core description; petrographic observation, cathodoluminescence imaging, and carbon, oxygen, and strontium isotope analyses. Combined with fluid inclusion measurements and salinity analysis, they revealed the genetic mechanism of the dolostone in the Buqu Formation and provided a geological basis for evaluating the dolostone reservoir. Using the inclusions in the calcite of fracture caves in the Yingshan Formation of Central Tarim Basin, northwestern China, Dan et al. provided relevant evidence to judge the nature of the paleokarst fluid and karst environment as well as established a paleokarst reservoir prediction model for oil and gas exploration. Proven to be closely related to hydrocarbon accumulation, strike-slip faults are important hydrocarbon accumulation zones. To clarify the controlling effects of strike-slip faults on reservoirs, the characteristics of two types of carbonate reservoirs in the central Tarim Basin, northwestern China—strike-slip fault-controlled fracture caverns and strike-slip fault-dissolved fracture caverns—were delineated through detailed analyses of seismic data, tectonic evolution, and observations of the core and thin sections (Ning et al).

Reservoir prediction is a process of predicting the longitudinal and transverse distribution characteristics and reservoir physical properties of reservoirs using various technical means in geophysical and geological aspects (including sedimentary facies analysis, small bed correlation, seismic data inversion, and attribute analysis) under the guidance and control of sequence stratigraphy and sedimentology to provide the geological basis for well location deployment and development program. Zhao et al. presented a case study of deep-water submarine fans in the Albacora Leste oilfield in Brazil and systematically established a sedimentary microfacies distribution model for each reservoir based on a detailed stratigraphic framework with a well-seismic joint characterization method and various data types (e.g., geological, well-log, and seismic data). Wang et al. predicted fractured reservoirs using coherence cubes and linearly enhanced attributes as well as identified fractured cave reservoirs with single-frequency attribute bodies in the Bongor Basin, southwestern Chad. In addition, they summarized a set of granitic buried hill reservoir prediction techniques for intensely-inverted rift basins in the Central African Rift System.

Petroleum accumulation process

Petroleum accumulation refers to the geological process in which oil and gas are generated in a sedimentary basin, migrated in the carrier layer, finally filled into the trap, and accumulated to form oil and gas reservoirs. Petroleum accumulation is the comprehensive result of various geological factors and is a temporary equilibrium state of oil and gas in the

crust. Xue et al. proposed a model of natural gas enrichment and accumulation in a lacustrine basin. The model indicated that rapid subsidence and high gas-generating intensity during the highly-mature stages were the main contributors to the natural gas field formation. Archean metamorphic buried hill reservoirs and thick overpressured mudstone with the strong vertical sealing ability provide favorable storage space and preservation. Using the model, an integrated Archaean metamorphic buried hill condensate gas reservoir—Bozhong 19–6—was discovered in the Bohai Bay Basin, eastern China, with proven gas reserves of approximately 450 × 10^9 m^3. Based on research on the chemical composition of natural gas, carbon isotope features of source rock and natural gas, and geological feature differences between different regions in the northwestern Sichuan Basin, Xiao et al. determined the origins of natural gas, clarified the petroleum accumulation process, and fixed the main factors controlling natural gas accumulation. This work provided a favorable case study for petroleum exploration in the basin-mountain transition regions.

With the increasing difficulty in conventional oil and gas exploration, various countries and oil companies have paid considerable attention to unconventional oil and gas, such as volcanic reservoirs, coal bed methane (CBM), shale oil, and shale gas. To date, the CBM development targets are mostly undersaturated shallow coals in China and other countries (Kuuskraa and Wyman, 1993; Johnson and Flores, 1998). Kang et al. explained the reason for gas oversaturation in deep coals in the Ordos Basin, central China, and proposed that in most large tectonically compressed coal basins, there is a critical depth beyond which the oversaturation areas could occur, presenting opportunities and challenges for CBM development. As an unconventional petroleum reservoir, the volcanic reservoir is essential to find large-scale oil and gas reserves in deep sedimentary basins. Based on analog modeling of reservoir formation, including reservoir properties, hydrocarbon fluid phases, migration pathways, and source rock evolution history, Ablimiti et al. systematically illustrated the potential deep-buried volcanic petroleum system.

Author contributions

All authors listed have made a substantial, direct, and intellectual contribution to the work and approved it for publication.

Acknowledgments

We are grateful to all of the authors who responded to our call to participate in the compilation of this Research Topic. Our gratitude is also extended to all reviewers who kindly reviewed one or more of the manuscripts submitted to this Research Topic and provided valuable comments and recommendations. Special thanks are extended to Associate Editor Valerio Acocella who reviewed this manuscript and whose suggestions significantly improved the clarity and quality of this Editorial article.

Conflict of interest

Author DZ was employed by Xinjiang Oilfield Company, PetroChina, and Turpan-Hami Oilfield Company, PetroChina. Author DG was employed by Research Institute of Petroleum Exploration and Development, PetroChina.

The remaining authors declare that the research was conducted in the absence of any commercial or financial relationships that could be construed as a potential conflict of interest.

Publisher's note

References

Aigner, T. A., and Reineck, H. E. (1982). Proximality trends in modern storm sands from the Helgoland Bight (North Sea) and their implications for basin analysis. *Senckenberg Marítima* 14, 83.

Aigner, T. A. (1985b). Storm depositional systems: Dynamic stratigraphy in modern and ancient shallow-marine sequences: Berlin. Lect. *Notes Earth Sci.* 3, 174.

Aigner, T. (1985a). *Storm depositional systems*. Berlin: Springer-Verlag.

Carpenter, A. B., Trout, M. L., and Pickett, E. E. (1974). Preliminary report on the origin and chemical evolution of lead-and zinc-rich oil field brines in Central Mississippi. *Econ. Geol.* 69, 1191–1206. doi:10.2113/gsecongeo.69.8.1191

Chen, H., Chen, M., Sun, W., and Wang, Y. K. (2018). Sedimentary facies and paleogeography of the middle Jurassic Buqu formation in the longeni - esimaancient oil reservoirs zone, Qiangtang basin, northern Xizang. *Geol. Tethyan Geol.* 38 (2), 74–81. (in Chinese with English abstract).

Chen, J. H., Fu, J. M., Sheng, G. Y., Liu, D. H., and Zhang, J. J. (1996). Diamondoid hydrocarbon ratios: Novel maturity indices for highly mature crude oils. *Org. Geochem.* 25, 179–190. doi:10.1016/s0146-6380(96)00125-8

Chen, Y. J., Zhang, J., Liu, C. Q., and He, S. D. (2001). The lateral source of the oil and gas of China: Extension and application of the CPMF model. *Geol. Rev.* 47 (3), 261–271. (in Chinese).

Dahl, J. E., Moldowan, J. M., Peters, K. E., Claypool, G. E., Rooney, M. A., Michael, G. E., et al. (1999). Diamondoid hydrocarbons as indicators of natural oil cracking. *Nature* 399, 54–57. doi:10.1038/19953

Dai, J. X., Pei, X. G., and Qi, H. F. (1992). *Natural gas Geology of China*. Beijing: Petroleum Industry Press.

Duggen, S., Croot, P., Schacht, U., and Hoffmann, L. (2007). Subduction zone volcanic ash can fertilize the surface ocean and stimulate phytoplankton growth: Evidence from biogeochemical experiments and satellite data. *Geophys. Res. Lett.* 34, L01612–1612. doi:10.1029/2006gl027522

Götte, T., Pettke, T., Ramseyer, K., Koch-Muller, M., and Mullis, J. (2011). Cathodoluminescence properties and trace element signature of hydrothermal quartz: A fingerprint of growth dynamics. *Am. Mineral.* 96, 802–813. doi:10.2138/am.2011.3639

Gu, X. X., Zhang, Y. M., Li, B. H., Xue, C. J., Dong, S. Y., Fu, S. H., et al. (2010). The coupling relationship between metallization and hydrocarbon accumulation in sedimentary basins. *Earth Sci. Front.* 17 (2), 83–105.

Hulen, J. B., and Collister, J. W. (1999). The oil-bearing, Carlin-type gold deposits of Yankee Basin, Alligator Ridge district, Nevada. *Econ. Geol.* 94, 1029–1049. doi:10.2113/gsecongeo.94.7.1029

Immenhauser, A. (2009). Estimating palaeo-water depth from the physical rock record. *Earth. Sci. Rev.* 96, 107–139. doi:10.1016/j.earscirev.2009.06.003

Jiang, W. M., Li, Y., and Xiong, Y. Q. (2020). Reservoir alteration of crude oils in the Junggar Basin, northwest China: Insights from diamondoid indices. *Mar. Pet. Geol.* 119, 104451. doi:10.1016/j.marpetgeo.2020.104451

Johnson, R. C., and Flores, R. M. (1998). Developmental geology of coalbed methane from shallow to deep in Rocky Mountain basins and in Cook Inlet–Matanuska basin, Alaska, U.S.A. and Canada. *Int. J. Coal Geol.* 35, 241–282. doi:10.1016/s0166-5162(97)00016-5

Kuuskraa, V. A., and Wyman, R. E. (1993). "Deep coal seams: An overlooked source for long-term natural gas supplie," in *The SPE gas technology symposium* (Calgary, Alberta: Onepetro).

Kyser, K. (2000). Fluids and Basin Evolution. *Short. Course Ser.* 28, 1–18.

Lee, C.-T. A., Jiang, H., Ronay, E., Minisini, D., Stiles, J., and Neal, M. (2018). Volcanic Ash as a Driver of Enhanced Organic Carbon Burial in the Cretaceous. *Sci. Rep.* 8, 4197. doi:10.1038/s41598-018-22576-3

Liu, C. Y., Zhao, H. G., Tan, X. Q., and Wang, J. Q. (2006). Occurrence of multiple energy mineral deposits and mineralization-reservoiring system in the basin. *Oil Gas Geol.* 27 (2), 131–141. (in Chinese).

Liu, Q., Zhu, D., Jin, Z., Meng, Q., and Li, S. (2019a). Influence of Volcanic Activities on Redox Chemistry Changes Linked to the Enhancement of the Ancient Sinian Source Rocks in the Yangtze Craton. *Precambrian Res.* 327, 1–13. doi:10.1016/j.precamres.2019.02.017

Liu, Q., Zhu, D., Meng, Q., Liu, J., Wu, X., Zhou, B., et al. (2019b). The Scientific Connotation of Oil and Gas Formations under Deep Fluids and Organic-Inorganic Interaction. *Sci. China Earth Sci.* 62, 507–528. doi:10.1007/s11430-018-9281-2

Mohseni, H., and Al-Aasm, I. S. (2004). Tempestite deposits on a storminfluenced carbonate ramp: An example from the pabded formation (Paleogene), Zagros basin, swirl. *J. Pet. Geol.* 27, 163–178. doi:10.1111/j.1747-5457.2004.tb00051.x

Myrow, P. M., Lukens, C., Lamb, M. P., Houck, K., and Strauss, J. (2008). Dynamics of a transgressive prodeltaic system: Implications for geography and climate within a Pennsylvanian intracratonic basin, Colorado, U.S.A. *J. Sediment. Res.* 78, 512–528. doi:10.2110/jsr.2008.061

Oliver, J. (1986). Fluids expelled tectonically from orogenic belts: Their role in hydrocarbon migration and other geologic phenomena. *Geology* 14, 99–102. doi:10.1130/0091-7613(1986)14<99:fetfob>2.0.co;2

Parnell, J. (1994). *Geofluids: Origin, migration and evolution of fluids in sedimentary basins*. London: Geological Society Special Publication.

Peters, K. E., Walters, C. C., and Moldowan, J. M. (2005). *The biomarker guide [M]*. Cambridge: Cambridge University Press.

Rusk, B. G., Lowers, H. A., and Reed, M. H. (2008). Trace Elements in Hydrothermal Quartz: Relationships to Cathodoluminescent Textures and Insights into Vein Formation. *Geol* 36, 547–550. doi:10.1130/g24580a.1

Rusk, B., and Reed, M. (2002). Scanning Electron Microscope-Cathodoluminescence Analysis of Quartz Reveals Complex Growth Histories in Veins from the Butte Porphyry Copper deposit, Montana. *Geol* 30, 727–730. doi:10.1130/0091-7613(2002)030<0727:semcao>2.0.co;2

Schulz, L. K., Wilhelms, A., Rein, E., and Steen, A. S. (2001). Application of diamondoids to distinguish source rock facies. *Org. Geochem.* 32, 365–375. doi:10.1016/s0146-6380(01)00003-1

Stout, S. A., and Douglas, G. S. (2004). Diamondoid hydrocarbons – application in the chemical fingerprinting of natural gas condensate and gasoline. *Environ. Forensics* 5, 225–235. doi:10.1080/15275920490886734

Sun, W., Chen, M., Wan, Y. L., He, J. L., Lan, Y. F., Wei, H. W., et al. (2020). Closed-system dolomitization process and the significance for petroleum geology, an example from dolostone in the Middle Jurassic Buqu Formation in southern Qiangtang Depression. *Geol. Rev.* 66 (5), 1218–1230. (in Chinese with English abstract).

Sverjensky, D. A. (1984). Oil field brines as ore-forming solutions. *Econ. Geol.* 79, 23–37. doi:10.2113/gsecongeo.79.1.23

Thomas, J. B., Bruce Watson, E., Spear, F. S., Shemella, P. T., Nayak, S. K., and Lanzirotti, A. (2010). TitaniQ under Pressure: the Effect of Pressure and Temperature on the Solubility of Ti in Quartz. *Contrib. Mineral. Pet.* 160, 743–759. doi:10.1007/s00410-010-0505-3

Tissot, B. P., and Welte, D. H. (1984). *Petroleum Formation and occurrence[M]*. New York: Springer.

Volkman, J. K. (1986). A Review of Sterol Markers for marine and Terrigenous Organic Matter. *Org. Geochem.* 9, 83–99. doi:10.1016/0146-6380(86)90089-6

Wang, J., and Fu, X. G. (2018). Sedimentary evolution of the Qiangtang basin. *Geol. China* 45 (2), 237–259. (in Chinese with English abstract).

Wang, J., Fu, X. G., Shen, L. J., Tan, F. W., Song, C. Y., and Chen, W. B. (2020). Prospect of the potential of oil and gas resources in Qiangtang basin, Xizang (Tibet). *Geol. Rev.* 66 (5), 1091–1113. (in Chinese with English abstract).

Wang, Z. D., Yang, C., Hollebone, B., and Fingas, M. (2006). Forensic fingerprinting of diamondoids for correlation and differentiation of spilled oil and petroleum products. *Environ. Sci. Technol.* 40, 5636–5646. doi:10.1021/es060675n

Wei, Z. B., Mankiewicz, P., Walters, C., Qian, K. N., Phan, N. T., Madincea, M. E., et al. (2011). Natural occurrence of higher thiadiamondoids and diamondoidthiols in a deep petroleum reservoir in the Mobile Bay gas field. *Org. Geochem.* 42, 121–133. doi:10.1016/j.orggeochem.2010.12.002

Williams-Jones, A. E., and Migdisov, A. A. (2006). An experimental study of the solubility of gold in crude oil: Implications for ore Genesis. *Geochimica Cosmochimica Acta* 70 (18), A703. doi:10.1016/j.gca.2006.06.1526

Yi, H. S., and Xia, G. Q. (2022). Stratigraphic position of higher quality source rocks and distribution of oil-bearing dolomites in the Qiangtang Basin. *Sediment. Geol. ethyan Geol.* 42 (3), 455–464 (in Chinese with English abstract). doi:10.19826/j.cnki.1009-3850.2022.04005

Zhuang, H. P., Lu, J. L., Fu, J. M., and Liu, D. H. (2000). Organic petrological study on solid organic matter in two Carlin-type gold deposits in Southwest Guizhou, China. *Sci. Geol. Sin.* 35 (1), 83–90. (in Chinese).

frontiers | Frontiers in Earth Science

ORIGINAL RESEARCH
published: 13 April 2022
doi: 10.3389/feart.2022.879712

The Hydrocarbon Potential of Carboniferous Reservoirs in the Jimsar Sag, Northwest China: Implications for a Giant Volcanic-Petroleum Reserves

Deyu Gong[1], Yong Song[2], Miao Peng[2], Chaowei Liu[2], Ruiju Wang[1] and Wei'an Wu[1]*

[1]Research Institute of Petroleum Exploration and Development, Beijing, China, [2]Xinjiang Oil Company, PetroChina, Karamay, China

As an unconventional petroleum reservoir, the volcanic reservoir is essential for finding large-scale oil and gas reserves in deep sedimentary basins. Based on basin modeling, organic geochemistry, and organic petrology, this study evaluates the exploration potential of the Carboniferous volcanic-petroleum system in the Jimsar Sag of the southeastern Junggar Basin. The Carboniferous source rocks in the study area were developed in the Lower Carboniferous Songkharsu Formation, a set of marine–terrigenous transitional source rocks, lithologically composed of carbonaceous mudstone, mudstone, and coal. The kerogen is characterized by type II_2–III, indicating a gas-prone source rock. Carbonaceous mudstones, mudstone, and coal are classified as medium–good, medium, and poor source rocks, respectively. The hydrocarbon-generating potential is close to that of the Kelameili gas field. The Carboniferous-reservoir oil in well J15 is characterized by ^{13}C-enriched stable carbon isotopes, relatively high $\Sigma C_{31-35}/C_{30}$ and Pr/Ph ratios, relatively low density, gammacerane index, regular C_{29}-sterane content, and undetected β-carotene, indicating a Songkharsu origin. The Carboniferous-reservoired gas from well J3301 has stable carbon isotope composition enriched in ^{13}C, similar to the gas from the Kelameili gas field, and should be from the Songkharsu source rock. This set of source rocks is widely distributed in the Jimsar Sag with considerable thickness, among which thickness >100 m reaches 580 km^2, accounting for 38.7% of the whole sag. The Songkharsu source rocks entered the main oil-generating window at the end of the Early Jurassic. The area of Songkharsu source rocks in the Jimsar Sag with gas-generating intensity greater than 20 × 10^8 m^3/km^2 reaches 1,015 km^2, whereas that with oil-generating intensity greater than 500 × 10^4 t/km^2 reaches 1,146 km^2. However, 13 Carboniferous volcanic lithological traps were found in the sag, covering an area of 230 km^2. The Carboniferous volcanic-petroleum system in the Jimsar Sag has the resource potential to form large and medium oil and gas fields, which could become a critical replacement field for volcanic oil and gas exploration in the Junggar Basin after the Klameili gas field.

Keywords: Junggar basin, Jimsar Sag, Carboniferous, volcanic rocks, hydrocarbon-generating potential, oil and gas sources, exploration domain

OPEN ACCESS

Edited by:
Guanglong Sheng,
Yangtze University, China

Reviewed by:
Shu Tao,
China University of Geosciences, China
Bin Cheng,
China University of Petroleum, China

****Correspondence:***
Deyu Gong
deyugong@petrochina.com.cn

Specialty section:
This article was submitted to Economic Geology, a section of the journal Frontiers in Earth Science

Received: *20 February 2022*
Accepted: *17 March 2022*
Published: *13 April 2022*

Citation:
Gong D, Song Y, Peng M, Liu C, Wang R and Wu W (2022) The Hydrocarbon Potential of Carboniferous Reservoirs in the Jimsar Sag, Northwest China: Implications for a Giant Volcanic-Petroleum Reserves. Front. Earth Sci. 10:879712. doi: 10.3389/feart.2022.879712

1 INTRODUCTION

Volcanic reservoirs are unconventional petroleum reservoirs whose physical properties are not constrained by depth (Zou et al., 2008) and are important for finding large-scale oil and gas reserves in deep sedimentary basins. Since the first discovery of volcanic reservoirs in the San Joaquin Basin, California, United States, in 1887 (Petford and Mccaffrey, 2003), there has been a history of volcanic oil and gas exploration for more than 130 years. Volcanic reservoirs, such as Scott Reef (Australia), Jatibarang (Indonesia), Kudu (Namibia), Lake Kivu (Congo), Ben Khalala (Algeria), Samgori (Georgia), Urucu (Brazil), Yaraktin (Russia), and Ragusa (Italy) have been discovered globally (Petford and Mccaffrey, 2003).

Volcanic rocks are in and around sedimentary basins in China, and the exploration of volcanic reservoirs has been conducted for more than 60 years. Currently, China has made a series of significant breakthroughs in oil and gas exploration for volcanic reservoirs in the Junggar, Songliao, Erlian, Tarim, Santanghu, and Sichuan basins; volcanic oil and gas resources have been developed (Zou et al., 2008; Dai et al., 2021). Among them, the Junggar Basin has the highest degree of exploration for volcanic-petroleum reservoirs, and several large and medium volcanic reservoirs have been discovered in the northwest margin (Cao et al., 2010; Chang et al., 2019), hinterland (Chen et al., 2017; Zhi et al., 2022), and east (Yu et al., 2014; Sun et al., 2016; Guo et al., 2020) of the basin. In 2006, the Kelameili gas field was discovered in the northeastern part of the basin (**Figure 1A**), with proven reserves of $1{,}033 \times 10^8$ m^3, the largest volcanic gas reservoir discovered in China (Gong et al., 2019,2021).

The Jimsar Sag is approximately 120 km southeast of the Kelameili gas field (**Figure 1A**). Its shale reservoir in the Permian Lucaogou Formation (P_2l) has a billion-ton resource scale, which has become an important shale oil production base in China (Bai et al., 2017; Hu et al., 2018). The Kelameili gas field and the Jimsar Sag share a similar geotectonic setting during the Carboniferous; they are both parts of the remnant ocean basin formed after the closure of the Paleo-Asian Ocean (Carroll et al., 1995; Xiao W. J. et al., 2008). In 2001, well J15 in the Jimsar Sag obtained an industrial oil flow of 5.1 t/d in the Carboniferous system. In 2019, well J3301 obtained an excellent oil and gas in the Carboniferous system (**Figure 1B**). In addition, wells JT1 and J20 drilled in the Carboniferous encountered huge thick volcanic reservoirs (**Figure 1B**). The information shows that the Carboniferous petroleum system of this sag has excellent exploration prospects.

However, in the past 20 years, efforts have focused on exploring and developing P_2l shale oil in this area. Thus, the source rock quality, oil/gas source, and hydrocarbon accumulation conditions of the Carboniferous petroleum system have not been studied. By analyzing organic geochemistry, organic petrology, and basin modeling, this study evaluates the exploration potential of the Carboniferous volcanic reservoirs in the Jimsar Sag and reveals a potential giant volcanic-petroleum system. The research results have important implications for domestic and international exploration of volcanic reservoirs.

2 GEOLOGICAL BACKGROUND

The Junggar Basin, located in northwest China (**Figure 1A**), is an intraland superimposed basin that developed from the Early Carboniferous to the Quaternary (Xiao W. J. et al., 2008). It is at the intersection of Kazakhstan, Siberian, and Tarim Paleoplates (Xiao W. J. et al., 2008; He et al., 2018). Based on the Permian tectonic pattern, the basin can be divided into six first-order tectonic units (Central Depression, Wulungu Depression, Luliang Uplift, Western Uplift, Eastern Uplift, and North Tianshan Piedmont Thrust Belt). These first-order tectonic units can be further subdivided into 44 second-order tectonic units (**Figure 1A**) (He et al., 2018).

The Jimsar Sag is a "dustpan-shaped" sag developed on a Carboniferous folded basement. It is a second-order tectonic unit of the Eastern Uplift covering approximately 1,500 km^2 (**Figures 1A,B**) (Bai et al., 2017). During the Late Carboniferous, the Shaqi Salient to the north and the Gusi Salient to the east of the sag were uplifted under the influence of the Hercynian movement (Xiao W. J. et al., 2008; He et al., 2018). The water in the Jimsar Sag was connected to that of the Bogda Mountain Front Sag and the Fukang Sag simultaneously (Li et al., 2015a,b; Zhang L. et al., 2020). During the early Middle Permian, the study area subsided dramatically and became a relatively independent sedimentary unit (Li et al., 2015a,b; Zhang L. et al., 2020). At the end of the Triassic, the Shaqi Salient was strongly uplifted by the Indochinese movement, and the Permian and Triassic strata of the east slope of the Jimsar Sag suffered different denudation (Novikov, 2013; Li et al., 2015a,b; Zhang L. et al., 2020). During the Late Jurassic–Cretaceous, the southeast corner of the sag uplifted, and the study area denudated under the influence of Acts II and III of the Yanshan Movement (He et al., 2013; Novikov, 2013). During the Himalayan period, the sag was uplifted from east to west, and the strata were thinned to the east, forming the present-day tectonic pattern (He et al., 2013; Li et al., 2015a,b).

The Jimsar Sag is developed with Carboniferous–Quaternary strata from the bottom up, with five regional unconformities (i.e., top Carboniferous, top Middle Permian, top Triassic, top Jurassic, and top Cretaceous) (**Figure 1C**). P_2l is the most crucial source rock formation in the study area (Carroll, 1998; Wang et al., 2013). It was formed in a saline lacustrine environment after the closure of the residual sea, with high organic matter abundance, and is an excellent oil-prone source rock (Bai et al., 2017; Hu et al., 2018). The Carboniferous in the study area contains the Lower Carboniferous Songkharsu Formation (C_1s) and Upper Carboniferous Bashan Formation (C_2b) (Du, 2010; Yu et al., 2014) (**Figure 1C**). These two sets of strata are coastal–offshore deposits, comprising volcanic clastic rocks with a maximum cumulative thickness of more than 4 km (Du, 2010; Yu et al., 2014). Medium and acidic volcanic lavas and tuffaceous volcanic clastic rocks dominate the lower section of the Songkharsu Formation (C_1s^a) (Du, 2010; Gong et al., 2019). The upper section (C_1s^b) is a clastic rock deposited during the lull volcanic activity, locally interbedded with thin coal seams (**Figure 1C**), which is the primary source-rock-bearing section of the Carboniferous system in the eastern Junggar Basin (Du, 2010; Gong et al., 2019). C_2b is dominated by medium-basic volcanic

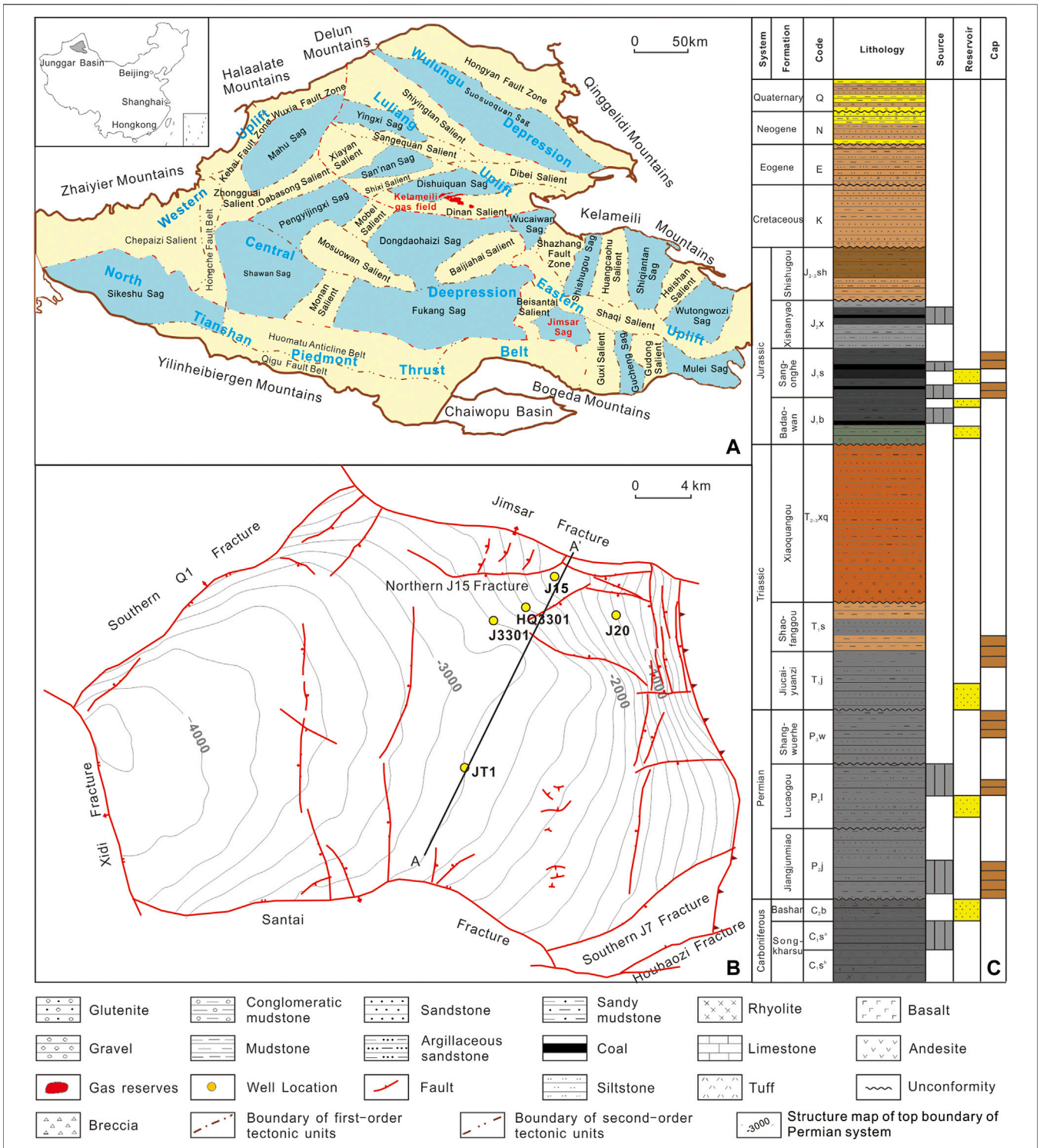

FIGURE 1 | Geological background of Jimsar Sag in the southeastern Junggar Basin. **(A)**: The geological setting of Junggar Basin; **(B)**: The geological setting of Jimsar Sag; **(C)**: The stratigraphic column in the Jimsar Sag.

lava interspersed with tuffaceous volcanic clastic rocks (**Figure 1C**).

Four sets of the reservoir–caprock assemblages are developed in the Jimsar Sag: 1) a reservoir–caprock with volcanic breccia and volcanic clastic rocks at the top of the Carboniferous as reservoirs and mudstones in the lower part of the Middle Permian Jiangjunmiao Formation (P_2j) as caprocks; 2) a reservoir–caprock assemblage with sandstones in the lower part of the P_2l and Upper

TABLE 1 | The maceral characteristics of C_1s^b source rocks in the Jimsar Basin.

Well	Formation	Depth (m)	Lithology	Whole Rock Components (%)			Organic Maceral Content (%)			
				Total Organic Matter	Pyrite	Other Minerals	Sapropelite	Exinite	Vitrinite	Inertinite
J15	C_1s^b	2,860	Coal	60.7	1.5	37.8	4.3	12.6	54.9	28.2
J3301	C_1s^b	4,135	Carbonaceous mudstone	15.3	1.3	83.4	1.2	3.5	88.9	6.4
J3301	C_1s^b	4,441	Mudstone	2.1	2.9	92.1	4.3	18.0	71.5	6.2

Permian Shangwuerhe Formation (P_3w) as reservoirs and mudstones in the middle and upper part of P_3w as caprocks; 3) a reservoir–caprock assemblage with sandstones in the Lower Triassic Jiucaiyuanzi (T_1j) and Shaofanggou (T_1s) Formations as reservoirs and thick mudstones developed in their upper part as caprocks; 4) reservoir–caprock assemblages formed by the sand and gravels developed at the bottom of Jurassic groups as reservoirs and mudstones developed in the interior or middle and upper parts as caprocks (Bai et al., 2017; Hu et al., 2018; Zhang S. et al., 2020) (**Figure 1C**).

3 SAMPLES AND EXPERIMENTAL METHODS

3.1 Sampling

In this study, 137 source rock samples (21 from Jimsar Sag and 116 from Kelameili gas field), 36 oil samples (1 from Carboniferous reservoir and 35 from P_2l reservoir in the Jimsar Sag), and 21 gas samples (1 from Jimsar Sag and 20 from Kelameili gas field) were discussed, with part of the well locations shown in **Figure 1B**. Natural gas was collected at the wellheads and stored in 1-L gas-tight cylinders. Oil and condensates were collected at the wellheads under ambient pressure and stored in 5-ml glass containers with screw-on Teflon-lined caps. The samples were refrigerated to below –6°C.

3.2 Analytical Processes

3.2.1 Total Organic Carbon (TOC) and Rock-Eval Analysis

The analyses were conducted at the China University of Petroleum (Beijing). First, the 146 rock samples were crushed to powder for TOC analysis (**Table 1**). In addition, the powdered samples were split into 200-mg subsamples and treated using HCl at 60°C to remove the carbonates and then washed using distilled water to remove the HCl. Finally, the washed subsamples were dried overnight at 50°C, and their carbon contents were determined using LECO CS–230 analyzers.

For rock-eval pyrolysis, 100 g of each crushed rock sample was placed in the vessel of an OGE-II instrument. These samples were heated from 300 to 600°C in a helium atmosphere at a heating rate of 50°C/min, and their Rock-Eval parameters (S_1, S_2, and T_{max}) were measured. In this study, S_1 is the amount of free hydrocarbon that can be volatilized from the rock sample (mg HC/g rock); S_2 is the amount of hydrocarbon produced by the cracking of organic matter (mg HC/g rock). T_{max} (°C) is the temperature at which the S_2 yield is maximized, which estimates the thermal maturity of the sediment (Peters, 1986).

3.2.1 Organic Petrology Analysis and Measurement of Vitrinite Reflectance

Optical microscopy analyses were conducted on thin rock sections at the China University of Geoscience (Beijing) (**Table 2**). Before being embedded in a homogeneous mixture of Buehler's epoxy resin and hardener (ratio 5:1), 11 core samples from eight wells were sectioned perpendicular to the bedding. The preparations involve drying and polishing, as described by Taylor et al. (1998) and Amijaya and Littke (2006). The thin rock sections were examined at different magnifications and under different light conditions (incident white- and blue-light excitation) to characterize the organic matter features of C_1s^b source rock. The optical instrument was a Nikon LV 100 microscope.

The vitrinite reflectances (R_o) of 46 samples were measured at the China University of Geoscience (Beijing) (**Table 1**), using a Zeiss Scope A1 incident light microscope at a wavelength (λ) of 546 nm. The reflectances of samples, rich in vitrinite or solid bitumen particles, were measured at least 50 times.

3.2.2 GC and GC–MS Analysis

Mass spectrometry (MS) and gas chromatography MS (GC–MS) analyses were performed at the China University of Petroleum (Beijing). Soxhlet apparatus was used to extract 30 samples using $CHCl_3$ for 72 h. The resulting extracts were fractionated using open silica gel column chromatography with *n*-hexane. The resulting saturated hydrocarbons were analyzed using GC and GC–MS.

The GC analysis was performed in an Agilent 7890A gas chromatograph fitted with a 60 m × 0.25 mm × 0.25 μm capillary column with nitrogen (99.999%) as the carrier gas. The GC oven temperature was at 40°C for 10 min, and then, it ramped from 40 to 70°C at 4°C/min and 300°C at 8°C/min, and finally held at 300°C for 40 min.

The GC–MS analysis was performed in an Agilent 7890–5975C using the same column type as in the GC analysis but with helium (99.999%) as the carrier gas. During the GC–MS analysis, the GC oven temperature was held at 50°C for 1 min before it ramped to 120°C at 20°C/min, from 120 to 250°C at 4°C/min, and from 250 to 310°C at 3°C/min. Finally, it was held at 310°C for 30 min.

3.2.3 Geochemical Analysis of Natural Gas

The geochemical analysis of the natural gas was conducted at the Experimental and Testing Institute of PetroChina Xinjiang Oilfield Company and Northwest Institute of Eco-Environment

TABLE 2 | The hydrocarbon generating potential of C_1s^b source rocks in the Jimsar Basin.

Lithology	Formation	Location	Statistics	S_1 (mg HC/g Rock)	S_2 (mg HC/g Rock)	T_{max} (°C)	S_1+S_2 (mg HC/g Rock)	TOC (%)	PI	HI (mg HC/g TOC)	PC (%)	D (%)	Sample Number
Mudstone	C_1s^b	Jimusar Sag	min	0.15	0.64	436	0.88	0.57	0.07	32	0.07	3.70	9
			max	0.77	9.60	447	10.37	5.89	0.42	216	0.86	22.90	
			mean	0.45	2.41	442	2.87	1.96	0.22	140	0.24	14.60	
	C_1s^b	Kelameili gas	min	0.04	0.24	432	0.39	0.50	0.05	38	0.03	3.52	97
		Field	mean	2.06	14.52	480	16.58	5.85	0.49	248	1.38	26.35	
			max	0.54	2.33	459	2.87	2.04	0.21	106	0.24	11.14	
Carbonaceous mudstone	C_1s^b	Jimusar Sag	min	0.24	22.27	431	23.47	13.60	0.01	97	1.95	8.12	7
			max	5.11	53.28	433	55.60	29.32	0.12	214	4.61	18.57	
			mean	2.28	43.03	432	45.31	24.03	0.05	180	3.76	15.76	
	C_1s^b	Kelameili gas	min	0.76	20.41	442	24.08	11.35	0.02	129	2.00	12.54	10
		Field	mean	9.75	88.12	457	96.85	32.87	0.22	288	8.04	26.78	
			max	5.18	45.57	450	50.75	20.59	0.10	215	4.21	19.99	
Coal	C_1s^b	Jimusar Sag	min	0.67	35.82	431	36.49	39.60	0.02	87	3.03	7.35	4
			max	15.84	93.36	441	109.20	57.75	0.15	182	9.06	16.60	
			mean	7.87	70.11	437	77.99	45.83	0.09	152	6.47	13.95	
	C_1s^b	Kelameili gas	min	1.18	52.54	437	53.93	42.92	0.02	101	4.48	8.63	10
		Field	mean	1.95	87.61	447	88.95	58.15	0.03	204	7.38	17.20	
			max	1.57	72.87	441	74.45	48.77	0.02	151	6.18	12.82	

and Resources, Chinese Academy of Sciences. A Hewlett–Packard 6890 II gas chromatograph (GC) analyzed the natural gas components. The hydrocarbon gas component was separated using capillary columns (Plot Al_2O_3 50 m × 0.53 mm). The furnace temperature of the GC was first set to be 30°C and held for 10 min. Then, the temperature was ramped up to 180°C at a rate of 10°C/min. Stable carbon isotope analysis of alkane gas (C_1–C_4) was conducted using a Finnigan Mat Delta S mass spectrometer interfaced with an HP 6890II gas chromatograph. The alkane gas components (C_1–C_4) and CO_2 were separated using a chromatographic column (Plot Q 30 m × 0.32 mm). The column heating process was as follows: the heating rate was 8°C/min at 35–80°C; the temperature was then increased to 260°C at a heating rate of 5°C/min. The final temperature was held for 10 min. Each sample was analyzed three times with an accuracy of ± 0.3‰ (VPDB).

3.2.4 Basin Modeling

The burial and thermal histories of the source rocks in the study area were reconstructed using PetroMod software. The current heat flow and thermal conductivity values of the source rocks were adopted from previous studies (Wang et al., 2000a,b; Qiu et al., 2000,2001; Qiu, 2002). The R_o values were calculated using the Easy%Ro model proposed by (Sweeney and Burnham, 1990; Ren et al., 2020). This model can be applied R_o ranging of 0.3–4.6%.

4 RESULTS AND DISCUSSION

4.1 Source Rock Evaluation

4.1.1 Types of Organic Matter

The type of organic matter determines the hydrocarbon-generating capacity and product type in a source rock (Tissot et al., 1984; Bordenave, 1993). Therefore, the organic macerals of source rocks and their assemblage characteristics can be studied to characterize the types of organic types (Tissot et al., 1984; Bordenave, 1993; Taylor et al., 1998; Suárez et al., 2012). In this study, the whole-rock maceral contents of C_1s^b source rocks with three different lithologies (coal, carbonaceous mudstone, and mudstone) in the Jimsar Sag were analyzed based on thin section, oil immersion, and fluorescence observations (**Figure 2**; **Table 1**). Organic macerals can be classified into four major groups: sapropelite, exinite, vitrinite, and inertinite (Tissot et al., 1984; Bordenave, 1993; Taylor et al., 1998; Suárez et al., 2012). The hydrocarbon generation capacity of the four macerals decreases sequentially, with their products transiting from liquid hydrocarbons to natural gas. The inert maceral group has almost no hydrocarbon-generating capacity.

The original matrices of the sapropelite maceral are primarily lower organisms (i.e., algal and bacteria) and zooplankton (Taylor et al., 1998; Suárez et al., 2012). This study is characterized by mineral bituminous exhibiting weak fluorescence (**Figure 2**). In addition, sporadically distributed alginate was found in the mudstone samples (**Figures 2G,H**). The primitive matrices of the exinite group are mainly the plant's reproductive organs and the *epidermis* and secretions of branches, leaves, and roots (Tissot et al., 1984; Bordenave, 1993; Taylor et al., 1998; Suárez et al., 2012). The exinite maceral group in the C_1s^b source rocks of the Jimsar Sag mainly include microsporinite, liptodetrinite, cutinite, and resinite (**Figure 2**). Some dark striped vertical fractures are filled with sphaltenite (**Figures 2D,E**). The parent material of both the vitrinite and inertinite groups is the xylem of higher plants. The former formed in a reducing–semi-oxidizing environment and the latter in a semi-oxidizing–oxidizing environment (Tissot et al., 1984; Bordenave, 1993; Taylor et al., 1998; Suárez et al., 2012). In this study, the vitrinite maceral

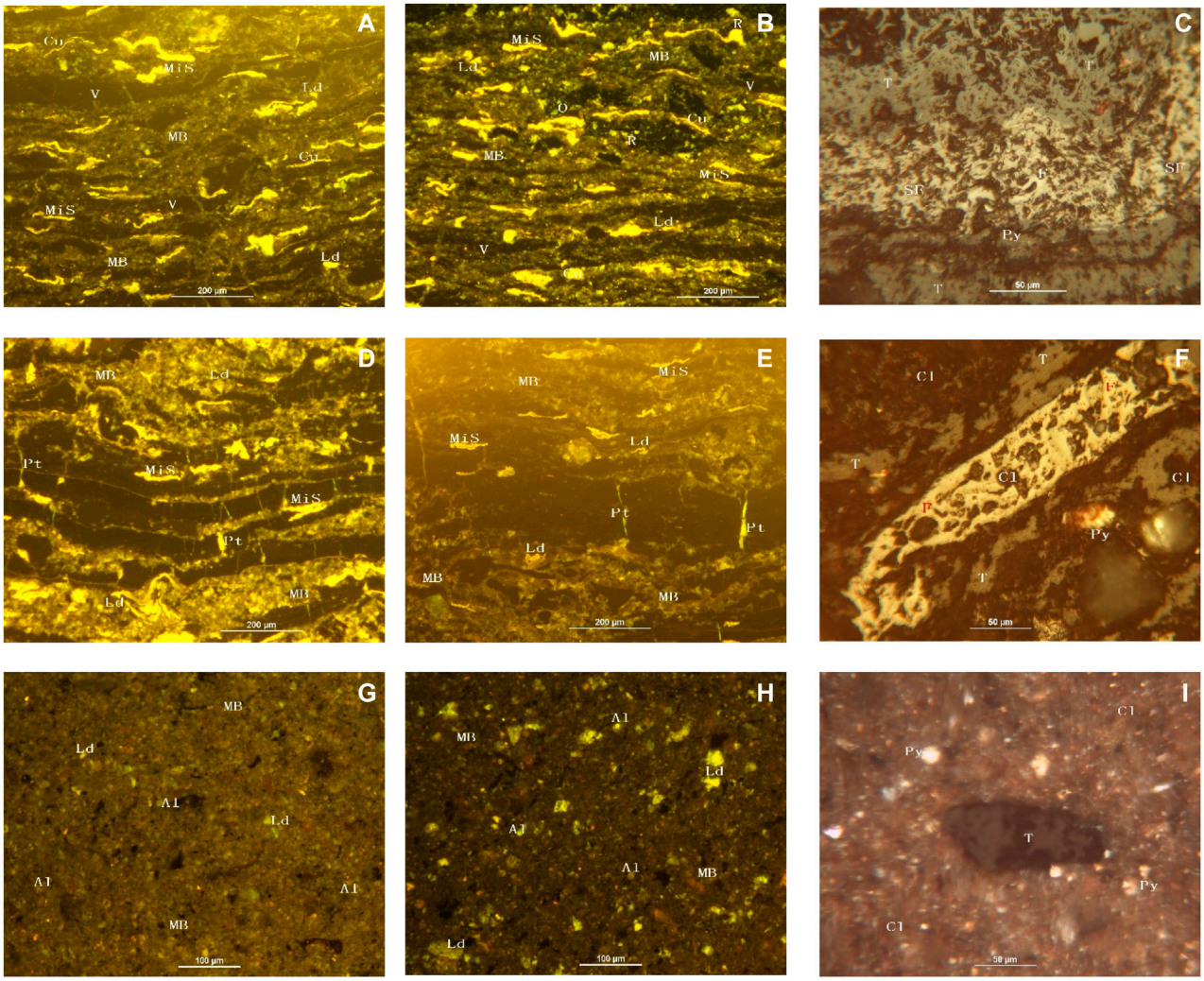

FIGURE 2 | Photomicrographs of macerals for C_1s^b source rock in the southeastern Junggar; Note:clay minerals (Cl); mineral bituminous (MB); microsporinite (Mis); vtrinite (V); liptodetrinite (Ld); cutinite (Cu); resinite (R); oil satins (O); telinite (T); semi-fusinite (SF); fusinite (F); Pyrite (Py); asphaltenite (Pt); alginate (Al). **(A–C)** demonstrate the coal sample from well J15 (2,860 m, core). **(D–F)** demonstrate the carbonaceous mudstone sample from well J3301 (4,135 m, cuttings). **(G–I)** demonstrate the carbonaceous mudstone sample from well J3301 (4441 m, core). **(A,B,D,E,G,H)** are inspired by blue light (reflected fluorescence). **(C,F,I)** are inspired by reflected light (oil immersion).

consists of telinite, collinite, semi-fusinite, and fusinite (**Figure 2**). Fragments of broken fusinite were visible in the center of some semifusinite (**Figure 2C**). Most of them preserved the woody cell structure, indicating that they underwent different degrees of cell wall swelling (**Figure 2C**). Various components can be seen in a parallel arrangement under the microscope, reflecting the hydrostatic sedimentary microenvironment (**Figure 2B**), confirmed by the widespread pyrite observed in C_1s^b source rocks (**Figure 2**).

The maceral components of the C_1s^b source rocks, with different lithologies in the Jimsar Sag, are dominated by the vitrinite group (>50%), reflecting their gas-prone characteristics (**Figure 2**; **Table 1**). The oil-prone maceral content (the sum of the sapropelite and exinite groups) of the mudstone and carbonaceous mudstone reached 22.3 and 16.9%, respectively (**Table 1**), showing a bit oil-generating potential (**Figure 2**; **Table 1**). The "oil stains" identified through fluorescence observation are evidence (**Figure 2B**).

The Rock-Eval hydrogen index [$HI = (100 \times S_2)/TOC$] is a fast and economical method to distinguish organic matter types of the source rocks (Tissot et al., 1984; Bordenave, 1993). Based on the HI values of 600, 300–600, 200–300, 50–200, and less than 50 mg HC/g TOC, the organic matter can be classified into five types: Type I (extremely oil-prone), Type II (oil-prone), Type II/III (oil-prone/gas-prone), Type III (gas-prone) and Type IV (barren source rock) (Tissot et al., 1984; Bordenave, 1993). Among the C_1s^b source rocks of the Jimsar Sag, the HI values of mudstone, carbonaceous mudstone, and coal ranged from 32 to 216 mg HC/g TOC (average 140 mg HC/g TOC), 97–214 mg HC/g TOC (average 180 mg HC/g TOC), and 87–183 mg HC/g TOC

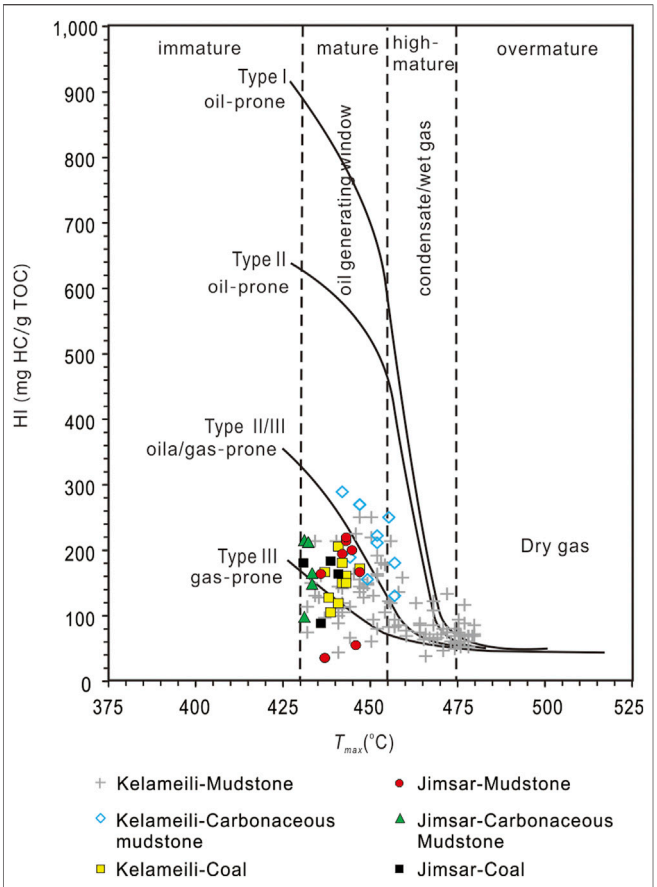

FIGURE 3 | The T_{max} vs hydrogen index (HI) plot of the C_1s^b source rock in the Jimsar Sag and Kelameili gas field.

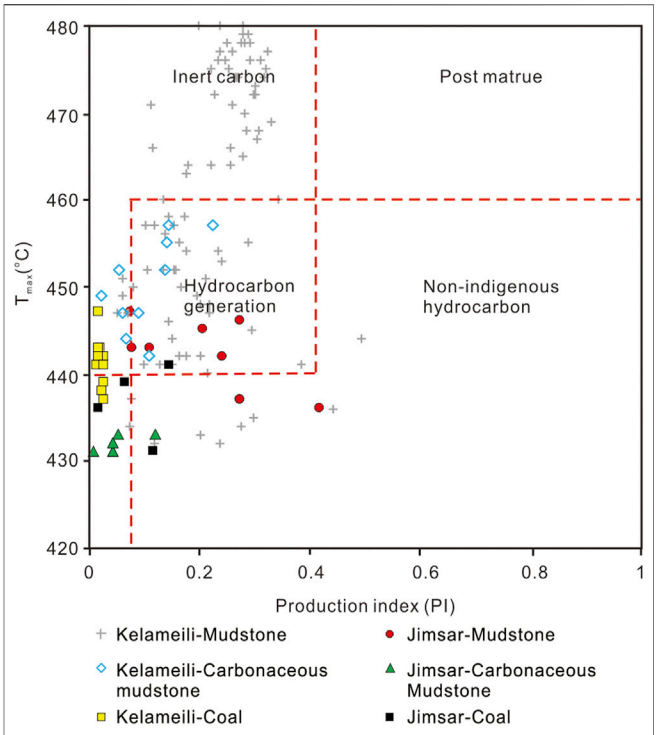

FIGURE 4 | The PI vs T_{max} plot of C_1s^b source rocks in the Jimsar Sag and Kelameili gas field.

(average 152 mg HC/g TOC), respectively (**Figure 3**; **Table 2**). The C_1s^b source rocks were dominated by kerogen type III. Carbonaceous mudstone is more oil-prone than coal, and mudstone has the poorest oil-generating capacity (**Figure 3**; **Table 2**). Some of the carbonaceous mudstone samples have high HI values (>200 mg HC/g TOC) and show some oil-generating capacities (**Figure 3**; **Table 2**). Among the C_1s^b source rocks in the Kelameili gas field, the average HI ratios for mudstone, carbonaceous mudstone, and coal are 106, 215, and 151 mg HC/g TOC, respectively, and the overall characteristics are close to those of the Jimsar Sag (**Figure 3**; **Table 2**).

4.1.2 Source Rock Maturity

In this study, R_o data were obtained for three C_1s^b source rock samples from the Jimsar Sag. The R_o value of the sample from well J15 (2860 m) is 0.65%, and the R_o values of the two samples from well J3301 (4,441 and 4,445 m) are 1.38 and 1.41%, respectively. Well J15 is in the eastern margin of the Jimsar Sag (**Figure 1B**) and has a lower maturity. According to the Ro values of well J3301, the C_1s^b source rocks have recently entered at least the main oil-generating window in the depression area. The Rock-Eval maturity indicators of C_1s^b source rocks in the study area and the Kelameili gas field are similar. Their hydrocarbon production indices [PI = $S_1/(S_1+S_2)$] and T_{max} are distributed between 0.8 and 1.0 and 440 and 460°C, respectively, in the main oil-generating window and samples with low PI and T_{max} values are in the immature stage (**Figure 4**; **Table 2**). A few samples with a poor correlation between PI and T_{max} may have suffered from the contamination of nonindigenous hydrocarbons (**Figure 4**). Some of the C_1s^b mudstone samples from the Kelameili gas field fall within the "inert carbon" (**Figure 4**), suggesting that those mudstone samples with low HI in **Figure 3** have a poor initial hydrocarbon-generating capacity, in addition to the effect of thermal maturation.

Based on the R_o and T_{max} data of C_1s^b source rock samples from the Jimsar Sag and previous studies on the R_o-depth relationship in the eastern Junggar Basin (Gong et al., 2021), and combined with the tectonic map of the C_1s^b bottom boundary of the sag, the R_o contour map of the study area was plotted (**Figure 5A**). The area of the C_1s^b source rocks in the Jimsar Sag entering the main oil-generating window (R_o > 0.7%) and condensate-generating stage (R_o = 1.3–2.0%) reaches 980 and 490 km^2, respectively (**Figure 5A**). Considering that the humic source rocks produce large amounts of natural gas at the main oil-generating window (Dai et al., 1992; Petersen, 2002; Petersen and Nytoft, 2006; Petersen et al., 2011), the Jimsar Sag favor large- and medium-gas field formation.

In this study, a two-dimensional seismic profile, running longitudinally through the Jimsar Sag in a nearly north-south direction, was selected to recover the burial and thermal evolution history of the C_1s^b source rocks. At the end of the Carboniferous

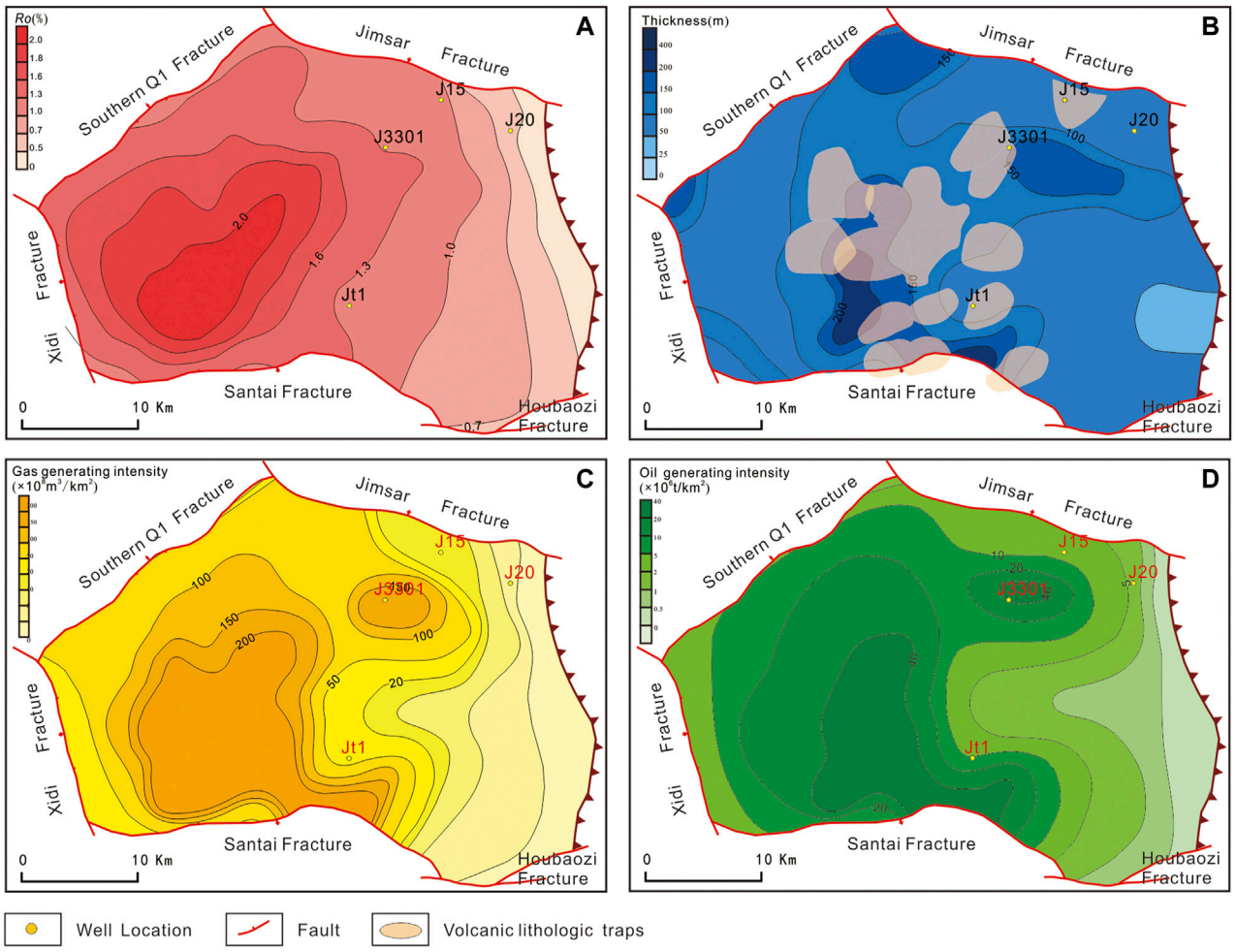

FIGURE 5 | The contour map of **(A)** R_o, **(B)** thickness, **(C)** gas-generating potential, and **(D)** oil generating potential for C_1s^b source rocks in the Jimsar Sag.

(~305 Ma), the C_1s^b source rocks were in the immature–low maturity stage (R_o < 0.7%) and had not reached the main oil-generating window (**Figure 6A**). After that, the C_1s^b source rocks slowly subsided, and by the end of the Early Jurassic (~182 Ma), they entered the early stage of the oil-generating window (R_o = 0.7–1.0%) (**Figure 6B**). Subsequently, the subsidence rate accelerated, and the C_1s^b source rocks entered the late stage of the oil-generating window (R_o = 1.0–1.3%) and the condensate/wet gas-generating window (R_o = 1.3–2.0%) stages in the Cretaceous (~100 Ma). The R_o of the deepest part of the sag reached 1.7% (**Figure 6C**). In addition, regional tectonic uplift occurred in the study area, and the hydrocarbon-generating process of C_1s^b source rocks was temporarily stalled (**Figure 6D**). With further deep burial, the maturity of C_1s^b source rocks continues to increase. Recently, the deep C_1s^b source rocks in the Jimsar Sag have entered the massive condensate generation stage. In contrast, the maturity of source rocks at the edge of the sag is low, and a few of them enter the main oil-generating window (**Figure 6E**).

4.1.3 Hydrocarbon-Generating Potential

Humic source rocks form in fresh marsh-phase environments (oxidizing–semi-oxidizing), whereas lacustrine/marine source rocks form in reducing–semi-reducing environments (Tissot et al., 1984; Bordenave, 1993; Gong et al., 2019). Thus, there are differences in hydrocarbon-generating mechanisms and product types between the two. Their evaluation criteria should be more demanding than those for lacustrine/marine source rocks. The coaly source rocks are rich in aromatic functional groups and poor in lipid functional groups (carbon-rich and hydrogen-poor) and have high inert carbon content (Chen et al., 1997; Petersen, 2002; Petersen and Nytoft, 2006; Petersen et al., 2011). Based on thousands of Rock-Eval data of terrigenous source rocks of different lithologies in the major proliferous basins in northwest China, Chen et al. (1997) proposed a scheme to evaluate the hydrocarbon-generating potential of coaly (humic) source rocks using lithologies (mudstone, carbonaceous mudstone, and coal). This scheme has been well tested in the practice of evaluating terrigenous

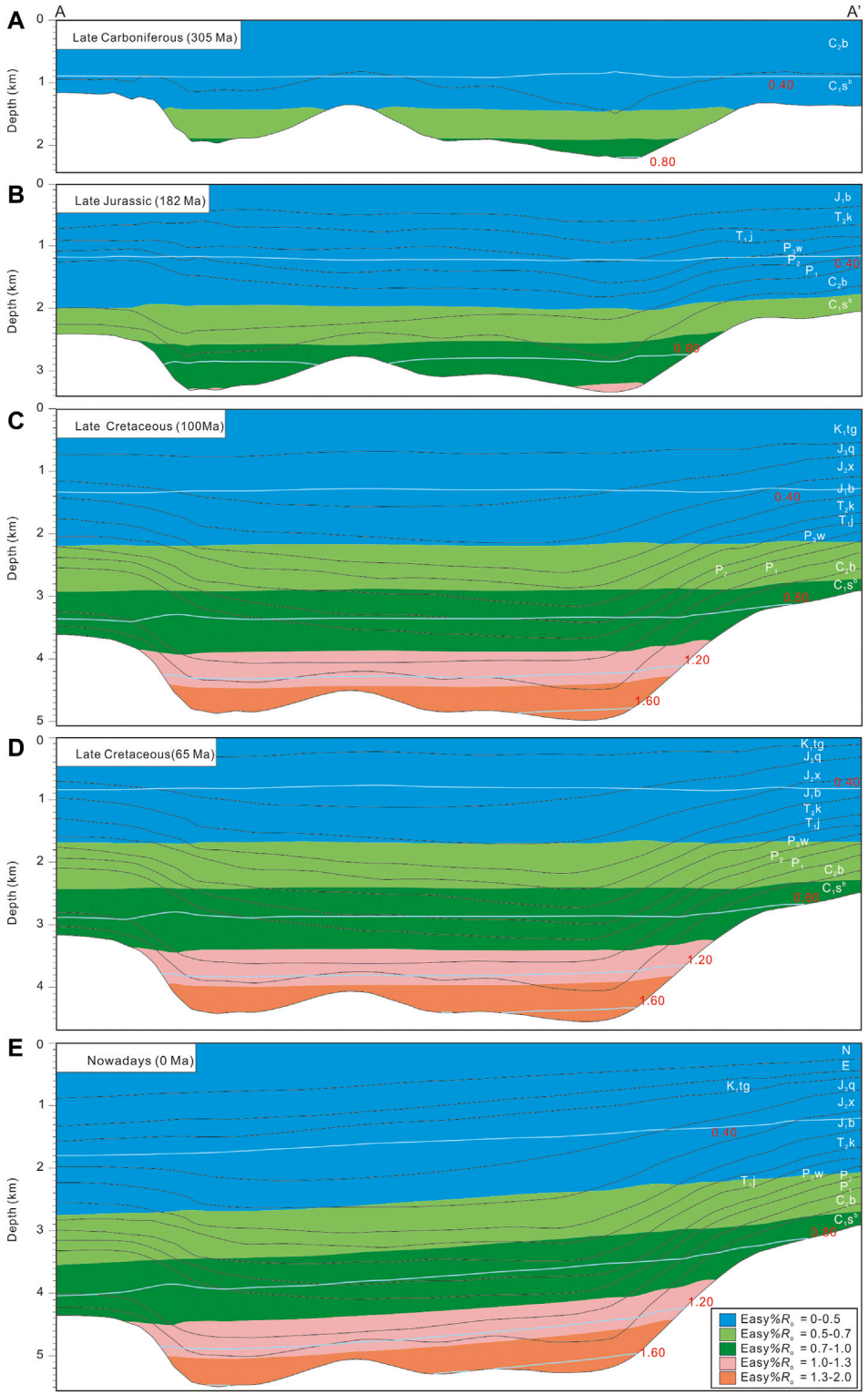

FIGURE 6 | The hydrocarbon generating profile for C_1s^b source rocks in the Jimsar Sag. **(A)**: The thermal evolution history in the Late Carboniferous (305 Ma). **(B)**: The thermal evolution history in the Late Jurassic (182 Ma); **(C)**: The thermal evolution history in the Late Cretaceous (100 Ma); **(D)**: The thermal evolution history in the Late Cretaceous (65 Ma); **(E)**: The thermal evolution history in nowadays (0 Ma);

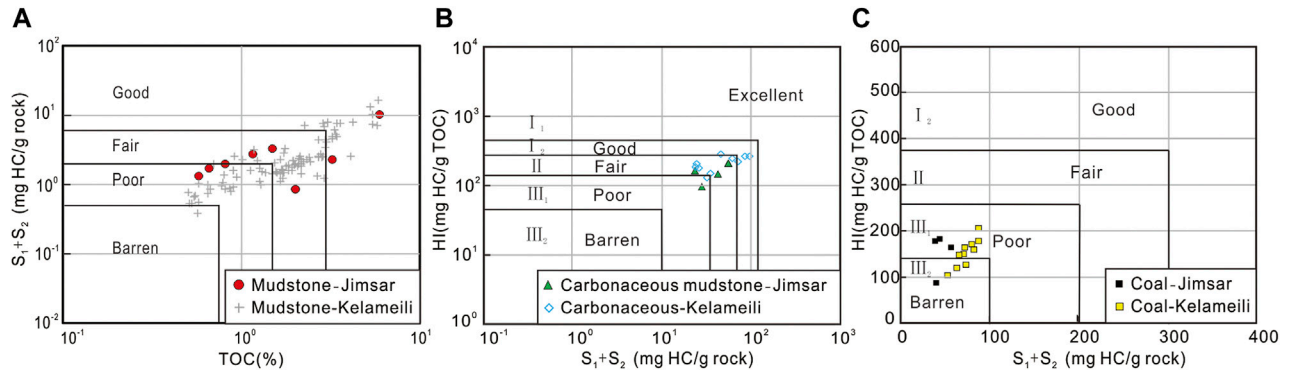

FIGURE 7 | The abundance of organic matters for C_1s^b **(A)** mudstones, **(B)** carbonaceous mudstones, and **(C)** coals in the Jimsar Sag and Kelameili gas field (Plot after Chen et al., 1997).

source rocks in China. This study evaluates the hydrocarbon-generating capacity of C1sb source rocks in Jimsar Sag based on this scheme.

The TOC of C_1s^b mudstone in the study area ranged from 0.57 to 5.89%, with an average of 1.96%; the hydrocarbon-generating potential (S_1+S_2) ranged from 0.88 to 10.37 mg HC/g rock, with an average of 2.87 mg HC/g rock. Thus, the C_1s^b mudstone belonged to medium–good source rocks (**Figure 7A**; **Table 2**). Chen et al. (1997) found that for carbonaceous mudstones and coal, the correlation between S_1+S_2 and HI is better than that between S_1+S_2 and TOC, and it is more suitable as an index for evaluating organic matter abundance. The C_1s^b carbonaceous mudstone is dominated by medium source rocks, with their S_1+S_2 and HI ratios being 23.47–55.60 mg HC/g rock (average 45.31 mg HC/g rock) and 97–214 mg HC/g TOC (average 180 mg HC/g TOC), respectively (**Figure 7B**; **Table 2**). The average S_1+S_2 and HI values of coal were 77.99 mg HC/g rock and 152 mg HC/g TOC, respectively, indicating a poor source rock (**Figure 7C**; **Table 2**). The hydrocarbon-generating capacity of C_1s^b source rocks in the Jimsar Sag and Kelameili gas fields is similar (**Figure 7**; **Table 2**).

4.2 Oil and Gas Sources

4.2.1 Ga Source Correlation

One gas sample from the Carboniferous reservoir has been obtained in the Jimsar Sag (from well J3301). The methane content of the natural gas is 78.79%, and the drying factor ($C_1/\sum C_{1-4}$) is 0.89, indicating a wet gas ($C_1/\sum C_{1-4}$ < 0.95). The methane content of the natural gas from the Kelameili gas field ranged from 84.90 to 93.56%, with an average of 88.80%. The natural gases have their $C_1/\sum C_{1-4}$ ratios ranging from 0.89 to 0.96 (average 0.92), and wet gas accounted for 85.9% of the total samples. The $C_1/\sum C_{1-4}$ ratios of the gas from the Kelameili gas field are higher than those of the Jimsar Sag, reflecting a relatively higher thermal maturity.

The stable carbon isotope compositions of methane (δ^{13}C-CH_4), ethane (δ^{13}C-C_2H_6) and propane (δ^{13}C-C_3H_8) in well J3301 are −33.8‰, −28.6‰, and −26.8‰, respectively (**Figure 8**). The δ^{13}C-CH_4, δ^{13}C-C_2H_6, and δ^{13}C-C_3H_8 of natural gas from Kelameili gas field are −32.3‰ ~ −29.2‰ (average −30.5‰), −28.9‰ ~ −25.6‰ (average −27.1‰), and −26.8‰ ~ −23.1‰ (average −24.7‰), respectively, which are more enriched in ^{13}C than those of the gas from well J3301 (**Figure 8**). Considering similar carbon isotopic compositions of kerogen ($\delta^{13}C_{kerogen}$) in the C_1s^b source rocks of the Jimsar Sag and Kelameili gas field (Gong et al., 2019,2021), the difference in the stable carbon isotopic compositions of the two types of gas reflects the higher maturity of the gas in the Kelameili gas field, consistent with that in $C_1/\sum C_{1-4}$ ratios. The humic source rocks are characterized by kerogen types III and II_2, composed of aromatic structures relatively enriched in ^{13}C isotopes (Barry and Fang., 2014; Dai et al., 2014; Liu et al., 2008; Liu et al., 2019; Yao et al., 2020). In contrast, the sapropelic source rocks are characterized by kerogen types I and II_1, composed of aliphatic structures enriched in ^{12}C isotopes (Barry and Fang., 2014; Dai et al., 2014; Liu et al., 2019; Wu et al., 2020). Therefore, when humic and sapropelic source rocks generate natural gas at similar maturity, the former generates natural gas (coal-type gas) with a more enriched ^{13}C carbon isotope composition than the latter (oil-type gas).

Previous studies have confirmed that natural gas from the Kelameili gas field is derived from C_1s^b source rocks (Dai et al., 2016; Sun et al., 2016), which exhibit the characteristics of coal-type gas in the δ^{13}C-CH_4–δ^{13}C-C_2H_6–δ^{13}C-C_3H_8 diagram proposed by (Dai et al., 2014) (**Figure 8**). The natural gas from well J3301 has ^{13}C-CH_4, δ^{13}C-C_2H_6, and δ^{13}C-C_3H_8 values similar to those from the Kelameili gas field (**Figure 8**), demonstrating the gas was derived from C_1s^b source rocks. Although influenced by maturity, the δ^{13}C-C_2H_6 values are more reflective of the original parent material and can distinguish coal-type gas from oil-type gas (Dai et al., 2005; Liu et al., 2016; Wu et al., 2021). Previous studies have shown that the limit of δ^{13}C-C_2H_6 value for both is around −29.0‰ (Fu et al., 1990; Gang et al., 1997; Liu et al., 2004; Dai et al., 2005, 2014; Xiao Z. H. et al., 2008; Liang et al., 2013; Liu et al., 2016; Wu et al., 2021). The δ^{13}C-C_2H_6 value of gas from well J3301 is −28.6‰, which shows the characteristics of coal-type gas (**Figure 8**).

Oil-type gas is drier than coal-type gas at the same thermal evolutionary stages (Bernard et al., 1978; Whiticar, 1999; Liu et al., 2019; Ci et al., 2020). In the δ^{13}C-CH_4–C_1/C_{2+3} gas genetic

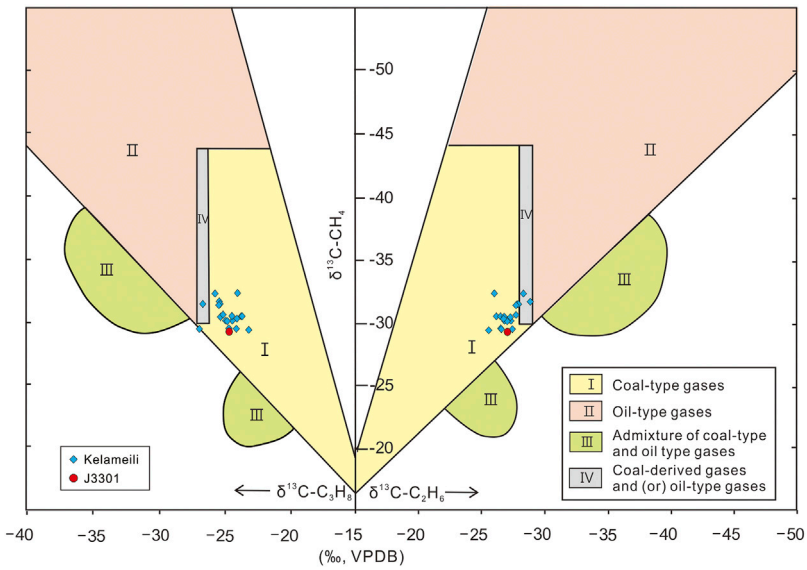

FIGURE 8 | Using the $\delta^{13}C\text{-}CH_4$–$\delta^{13}C\text{-}C_2H_6$–$\delta^{13}C\text{-}C_3H_8$ plot to identify the genetic types of natural gases in the Jimsar Sag (Plot after Dai et al., 1992, 2014).

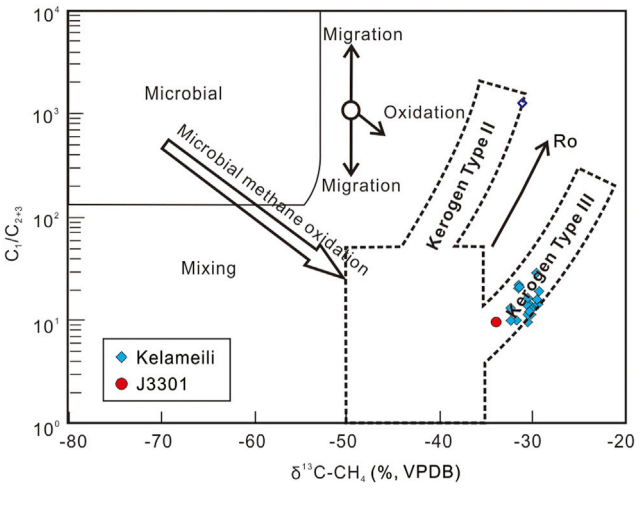

FIGURE 9 | Using the C_1/C_{2+3} vs $\delta^{13}C\text{-}CH_4$ plot to identify the genetic types of natural gases in the Jimsar Sag (Plot after Bernard et al., 1978; Whiticar, 1999).

identification plate, gases from the J3301 well and Kelameili field gas fall in the evolution trend line of coal-type gas (**Figure 9**), reflecting their origin from C_1s^b source rocks. **Figure 9** reflects the lower maturity of gas from well J3301 than gas from the Kelameili gas field.

4.2.2 Oil–Source Correlation

Two sets of effective source rocks, i.e., P_2l and C_1s^b, were developed in the Jimsar Sag (the Middle and Lower Jurassic source rocks are immature). Previous studies showed that the P_2l source rocks are brackish lacustrine source rocks deposited in a reducing environment (Bai et al., 2017; Hu et al., 2018). The oil from the Jimsar billion-ton shale oil field is derived from this set of source rocks (Bai et al., 2017; Hu et al., 2018). The C_1s^b source rocks are a set of marine–terrigenous transitional deposits in an oxidizing environment with a predominantly terrestrial higher plant input (Gong et al., 2019,2021). A tiny amount of oil has been obtained in the Jimsar Sag from the Carboniferous weathered crust reservoir in well J15. This study compared the physical properties, biomarker fingerprints, and carbon-isotope characteristics of oil samples from well J15 with oil from the P_2l reservoirs in the Jimsar Sag.

As discussed in **Section 4.2.1**, sapropelic source rocks (P_2l) have more ^{13}C-depleted $\delta^{13}C_{kerogen}$ values than the humic source rocks (C_1s^b) when their maturity is close. In addition, the carbon isotopic composition of global Carboniferous sediments is enriched in ^{13}C (Wang et al., 2013). Therefore, the carbon isotopes of oil derived from C_1s^b source rock should be more ^{13}C-enriched than those from P_2l source rocks. The stable carbon isotopic compositions of saturated ($\delta^{13}C_{saturated}$) and aromatic ($\delta^{13}C_{aromatic}$) fractions of oil from well J15 are –26.7‰ and –25.9‰, respectively. The $\delta^{13}C_{saturated}$ and $\delta^{13}C_{aromatic}$ values of P_2l reservoired oil in the study area are –33.4‰ to –29.8‰ (average –31.9‰) and –31.4‰ to –27.6‰ (average –30.4‰), respectively, which are lower than those in the J15 well. Therefore, the J15 oil should be derived from C_1s^b source rock.

The β-carotene is associated with anoxic/saline environments (Jiang and Fowler, 1986; Peters et al., 2005). The prevalence of β-carotene is a characteristic of Permian-sourced oils in the Junggar Basin (Wang et al., 2013; Cao et al., 2020). In this study, β-carotene was undetected in the oil from well J15 (**Figure 11A**), whereas some amount of β-carotene was detected in the P_2l reservoired oil (**Figure 11D**), reflecting the different genetic sources of the two.

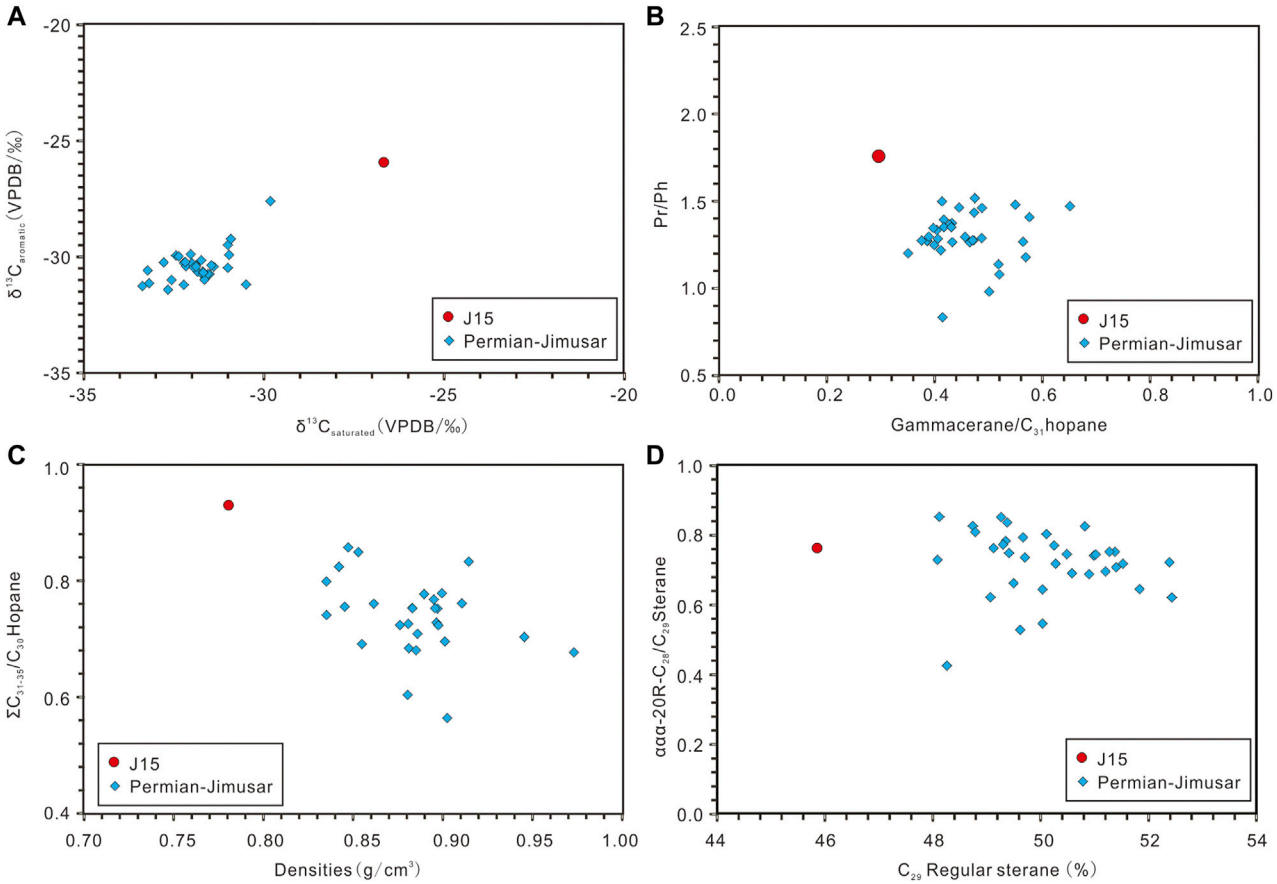

FIGURE 10 | The geochemical characteristics of biomarker fingerprints for oils with different types in the Jimsar Sag. **(A)**: The $\delta^{13}C_{aromatic}$ vs $\delta^{13}C_{saturated}$ plot; **(B)**: The Pr/Ph vs gammacerane index plot; **(C)**: The Pr/Ph vs gammacerane index plot; **(B)**: The $\Sigma C_{31-35}/C_{30}$ hopane ratio vs density plot; **(D)**: The ααα-20R-C_{28}/C_{29} sterane ratio vs C_{29} regular steranes rato plot.

The main precursors of pristane (Pr) and phytane (Ph) are chlorophylls of photosynthetic organisms, and their abundance is related to the sedimentary environment (Powell, 1988; Peters et al., 2005). The high Pr/Ph value of 1.76 for oil from well J15 (**Figure 10B**, **Figure 11A**) indicates an oxidizing environment with abundant terrigenous organic matter input Powell, corresponding to the C_1s^b source rock. In contrast, Pr/Ph values for oil from the P_2l reservoir are lower, ranging from 0.83 to 1.52, with an average of 1.30 (**Figure 10B**, **Figure 11D**), reflecting that the source rocks were deposited in a reducing–oxidizing transitional environment dominated by algal and bacterial inputs, with some input from the terrigenous higher plant (Powell, 1988; Peters et al., 2005).

Note:1) n-C_{17}; 2) Pr; 3) n-C_{18}; 4) Ph; 5) β-carotene; 6) C_{19} tricyclic terpane; 7) C_{20} tricyclic terpane; 8) C_{21} tricyclic terpane; 9) C_{30} hopane (10) gammacerane 11) C_{31} hopane20S 12) pregnanes 13) ααα-C_{28}20S-regular sterane 14) αββ-C_{28}20R-regular sterane 15) αββ-C_{28}20S-regular sterane 16) ααα-C_{28}20R-regular sterane 17) ααα-C_{29}20S-regular sterane 18) αββ-C_{29}20R-regular sterane 19) αββ-C_{29}20S-regular sterane (20)ααα-C_{29}20R-regular sterane.

The gammacerane reflects the stratified water in the depositional environments in which different source rocks were developed (Peters et al., 2005). The stratified water is due to the longitudinal salinity gradients (Sinninghe et al., 1995; Vu et al., 2009). An increase in water salinity increases the gammacerane index [gammacerane/(gammacerane + C_{31} hopane)] and decreases the Pr/Ph values (Sinninghe et al., 1995; Vu et al., 2009). The P_2l reservoired oils have a higher gammacerane index of 0.35–0.65 (average 0.46), showing that they were derived from a set of saline and reducing source rock (**Figure 10B**, **Figure 11E**). In contrast, the gammacerane index of oil from well J15 is lower at 0.30 (**Figure 10B**, **Figure 11B**), indicating a set of fresh source rock (Sinninghe et al., 1995; Vu et al., 2009), corresponding to the C_1s^b source rocks.

The oil density from well J15 is 0.7898 g/cm^3, approximately 0.1 g/cm^3 lower than that of the P_2l reservoired oil (0.8352–0.9732 g/cm^3, average 0.8809 g/cm^3), indicating that they may have different genetic sources (**Figure 10C**). A higher abundance of C_{31-35} hopane is a feature of the marine environment (Peters et al., 2005). The $\Sigma C_{31-35}/C_{30}$ hopane ratio of the P_2l reservoired oil is low, ranging from 0.56 to 0.86

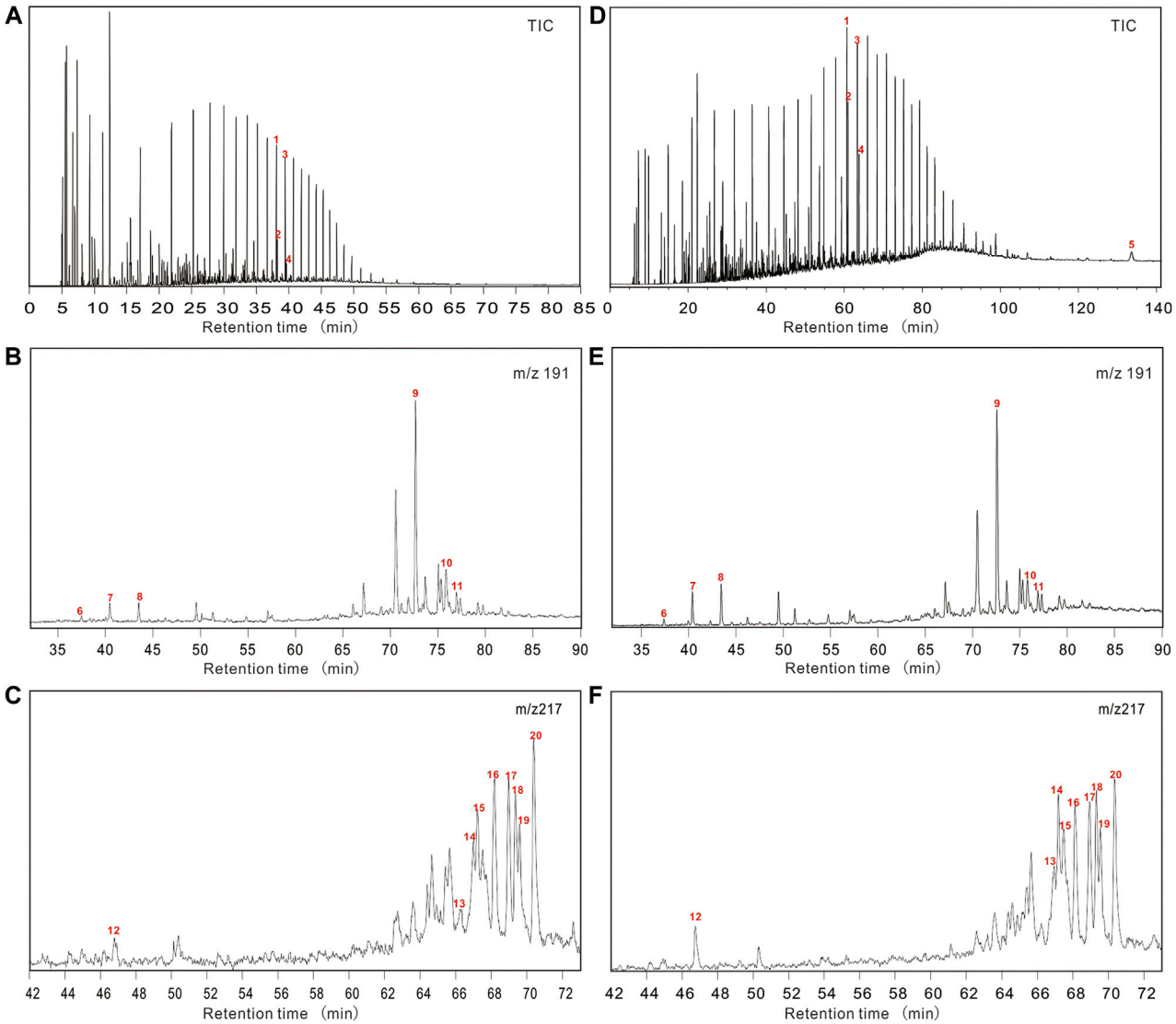

FIGURE 11 | The biomarker spectrograms of oils with different origins in the Jimsar Sag. **(A,D)**: TIC chromatograms of oils from wells J15 (Carboniferous reservoir) and J251–H (P_2l reservoir); **(B,E)**: m/z 191 chromatograms of oils from wells J15 (Carboniferous reservoir) and J251–H (P_2l reservoir); **(C,F)**: m/z 217 chromatograms of oils from wells J15 (Carboniferous reservoir) and J251–H (P_2l reservoir). Note: (1) n-C_{17}; (2) Pr; (3) n-C_{18}; (4) Ph; (5) β-carotene; (6) C_{19} tricyclic terpane; (7) C_{20} tricyclic terpane; (8) C_{21} tricyclic terpane; (9) C_{30} hopane; (10) gammacerane; (11) C_{31} hopane20S; (12) pregnanes; (13) αααα-C_{28}20S-regular sterane; (14) αββ-C_{28}20R-regular sterane; (15) αββ-C_{28}20S-regular sterane; (16) αααα-C_{28}20R-regular sterane; (17) αααα-C_{29}20S-regular sterane; (18) αββ-C_{29}20R-regular sterane; (19) αββ-C_{29}20S-regular sterane; (20) αααα-C_{29}20R-regular sterane.

(average 0.74) (**Figure 10C**). In contrast, the $\Sigma C_{31-35}/C_{30}$ hopane ratio of oil from well J15 is higher, 0.96 (**Figure 10C**), corresponding to the depositional environment of C_1s^b source rock whose sediment environment was affected by seawater (Du, 2010).

From the αααα-20R-C_{28}/C_{29} sterane ratio, the difference between the oil from well J15 and P_2l reservoir is negligible (**Figure 10D**, **Figures 11C,F**). However, the relative content of C_{29} regular steranes in oil from well J15 was low at 45.86% compared to 48.08–52.43% (average 50.12%) for the P_2l reservoired oil (**Figure 10D**, **Figures 11C,F**). High levels of C_{29} steranes indicate significant plant biomass input, reflecting a poor organic matter type (Volkman, 1986; Schwark and Empt., 2006), which seems to be the opposite of the situation in the study area. In previous studies, abundance C_{29}-regular steranes appeared in some algae, such as diatoms and green algae (Orcutt and Patterson, 1975; Grantham, 1986; Volkman, 1986). However, the abundance of C_{29} steranes in oil does not signify that most organic matter comes from vascular plants. One possible explanation is that the C_{29}-regular steranes in P_2l reservoired oil may come from specific zooplankton that feeds on algae and bacteria. Similar situations have appeared in Paleozoic oils in Oman and the Tarim Basin in China (Grantham, 1986; Zhang and Cheng, 2021).

4.3 Oil and Gas Exploration Potential

It is confirmed that a set of C_1s^b marine–terrigenous transitional source rocks was developed in the Jimsar Sag and that oil and natural gas derived from this set of source rocks have been identified. A planar tracing based on 2D and 3D seismic data evaluated the scale of this source rock. The results show that C_1s^b source rocks are distributed in the Jimsar Sag with considerable thickness, among which the range of thickness >100 m reaches 580 km^2, accounting for 38.7% of the whole sag; the range of thickness >50 m reaches 220 km^2 (**Figure 5B**). Three subdepositional centers developed in the sag (**Figure 5B**).

The lithology of C_1s^b source rocks in Jimsar Sag is dominated by carbonaceous mudstone, followed by mudstone, and a few thin coal seams are developed. Therefore, kinetic simulation of hydrocarbon generated from C_1s^b carbonaceous mudstone and mudstone was conducted in a closed system (golden tubes), adopting Tang et al. (2000) and Xiong et al. (2004) experimental method (the details will be discussed in another manuscript). The experimental results showed that the maximum gas yield of the mudstone and carbonaceous mudstone is 213.69 and 250.16 mg HC/g TOC, respectively, at a heating rate of 2°C/h. Their maximum oil yield was 26.22 and 162.46 mg HC/g TOC, respectively. Based on the obtained parameters, such as pre-exponential factor and activation energy, according to the Arrhenius formula, and the characteristics of thermal evolution and hydrocarbon generation histories of source rocks (**Figure 6**), this study sketched the planar contour maps of the gas- (**Figure 5C**) and oil- (**Figure 5D**) generating intensities of C_1s^b source rocks in the Jimsar Sag.

The relationship between the distribution of large and medium gas fields and the gas-generating intensity of source rocks in China shows that large gas fields (proven geological reserves $>300 \times 10^8$ m^3) in China are distributed in areas with gas-generating intensity $>20 \times 10^8$ m^3/km^2 (Dai et al., 1996,1999,2000; Li et al., 2020; Wei et al., 2020). The area of C_1s^b source rocks in the Jimsar Sag with gas-generating intensity $>20 \times 10^8$ m^3/km^2 reaches 1,015 km^2 (**Figure 5C**), accounting for 67.7% of the study area. Approximately one-third of the sag has gas-generating intensity $>100 \times 10^8$ m^3/km^2 (**Figure 5C**). The area of C_1s^b source rocks with the oil-generating intensity $>500 \times 10^4$ and $1{,}000 \times 10^4$ t/km^2 are 1,146 and 702 km^2 (**Figure 5D**), respectively, showing a favorable oil-generating potential.

Seismic, gravitational, and magnetic data identified 13 Carboniferous volcanic lithologic traps (buried hills), covering 230 km^2, in the Jimsar Sag (**Figure 5**). These traps are distributed in areas with high gas and oil-generating intensities, and source rocks have entered the main oil-generating window (**Figure 5**), conducive for forming self-generated and -stored petroleum reservoirs. In summary, the Jimsar Sag has the resource potential to form large and medium oil/gas fields and is an alternative for petroleum exploration in the Junggar Basin after the Kelameili gas field.

5 CONCLUSION

1) In the Jimsar Sag (in the southeastern part of Junggar Basin), a set of marine–terrigenous transitional source rocks were developed in the Lower Carboniferous Songkharsu Formation, comprising carbonaceous mudstone and mudstone. They belong to medium–good source rocks that are characterized by kerogen types II2–III and are primarily gas-prone, with some oil-generating ability. The quality of C_1s^b source rocks in the Jimsar Sag is close to that in the Kelameili gas field. At the end of the Early Jurassic, C_1s^b source rocks reached the oil-generating peak in the Jimsar Sag. Recently, most of them have reached the highly-mature stage.

2) The Carboniferous-reservoired oil in well J15 has more ^{13}C-enriched $\delta^{13}C_{saturated}$ and $\delta^{13}C_{aromatic}$ values and higher $\Sigma C_{31-35}/C_{30}$ hopane and Pr/Ph values (0.96 and 1.76) than the P_2l-reservoired oil. The density, gammacerane index, and C_{29} regular sterane content of the J15 oil are 0.7898 g/cm^3, 0.39, and 45.86%, respectively, which were lower than those of the oil from the P_2l reservoir. The β-carotene was undetected in the J15 oil. Therefore, J15 oil should be derived from C_1s^b source rock.

3) The $\delta^{13}C$-CH_4, $\delta^{13}C$-C_2H_6, and $\delta^{13}C$-C_3H_8 values of gas from well J3301 are –33.8‰, –28.6‰ and –26.8‰, respectively, which are similar to carbon isotope values from the Kelameili gas field and show the characteristics of coal-type gas, indicating a C_1s^b origin.

4) The C_1s^b source rocks are distributed in the Jimsar Sag with considerable thickness, among which the area with thickness >100 m reaches 580 km^2, accounting for 38.7% of the study area. In addition, 13 Carboniferous volcanic lithological traps have been identified in the Jimsar Sag, covering 230 km^2. The Carboniferous petroleum system of the Jimsar Sag can form large and medium oil and gas fields, which would be an alternative oil and gas exploration in volcanic reservoirs in the Junggar Basin after the Kelameili gas field.

DATA AVAILABILITY STATEMENT

The original contributions presented in the study are included in the article/Supplementary Material, further inquiries can be directed to the corresponding author.

AUTHOR CONTRIBUTIONS

DG: Conceptualization, Writing Review; Editing, Supervision; YS: Writing Original Draft, Formal analysis; MP: Formal analysis, Methodology; CL: Investigation, Data Curation; RW: Investigation, Data Curation; WW: Geophysical research.

FUNDING

This study received funding from the Chinese National Natural Science Foundation (No. 41802177), the Prospective and Fundamental Project of PetroChina (2021DJ0206), and the Fund for Basic Science Research of PetroChina (2020D–5008–04). The funder was not involved in the study design, collection, analysis, interpretation of data, the writing of this article, or the decision to submit it for publication.

REFERENCES

Amijaya, H., and Littke, R. (2006). Properties of Thermally Metamorphosed Coal from Tanjung Enim Area, South Sumatra Basin, Indonesia with Special Reference to the Coalification Path of Macerals. *Int. J. Coal Geology*. 66, 271–295. doi:10.1016/j.coal.2005.07.008

Bai, H., Pang, X., Kuang, L., Pang, H., Wang, X., Jia, X., et al. (2017). Hydrocarbon Expulsion Potential of Source Rocks and its Influence on the Distribution of Lacustrine Tight Oil Reservoir, Middle Permian Lucaogou Formation, Jimsar Sag, Junggar Basin, Northwest China. *J. Pet. Sci. Eng.* 149, 740–755. doi:10.1016/j.petrol.2016.09.053

Barry, K., and Fang, L. (2014). Lacustrine basin Unconventional Resource Plays: Key Differences [J]. *Mar. Pet. Geology*. 56, 255–265. doi:10.1016/j.marpetgeo.2014.02.013

Bernard, B. B., Brooks, J. M., and Sackett, W. M. (1978). Light Hydrocarbons in Recent Texas continental Shelf and Slope Sediments. *J. Geophys. Res.* 83, 4053–4061. doi:10.1029/jc083ic08p04053

Bordenave, M. L. (1993). *Applied Petroleum Geochemistry[M]*. Paris: Technip.

Cao, J., Jin, Z., Hu, W., Zhang, Y., Yao, S., Wang, X., et al. (2010). Improved Understanding of Petroleum Migration History in the Hongche Fault Zone, Northwestern Junggar Basin (Northwest China): Constrained by Vein-Calcite Fluid Inclusions and Trace Elements. *Mar. Pet. Geology*. 27, 61–68. doi:10.1016/j.marpetgeo.2009.08.014

Cao, J., Xia, L., Wang, T., Zhi, D., Tang, Y., and Li, W. (2020). An Alkaline lake in the Late Paleozoic Ice Age (LPIA): A Review and New Insights into Paleoenvironment and Petroleum Geology. *Earth-Science Rev.* 202, 103091. doi:10.1016/j.earscirev.2020.103091

Carroll, A. R., Graham, S. A., Hendrix, M. S., Ying, D., and Zhou, D. (1995). Late Paleozoic Tectonic Amalgamation of Northwestern China: Sedimentary Record of the Northern Tarim, Northwestern Turpan, and Southern Junggar Basins. *Geol. Soc. America Bull.* 107 (5), 571–594. doi:10.1130/0016-7606(1995)107<0571:lptaon>2.3.co;2

Carroll, A. R. (1998). Upper Permian Lacustrine Organic Facies Evolution, Southern Junggar Basin, NW China. *Org. Geochem.* 28, 649–667. doi:10.1016/s0146-6380(98)00040-0

Chang, X., Wang, Y., Shi, B., and Xu, Y. (2019). Charging of Carboniferous Volcanic Reservoirs in the Eastern Chepaizi Uplift, Junggar Basin (Northwestern China) Constrained by Oil Geochemistry and Fluid Inclusion. *Bulletin* 103 (7), 1625–1652. doi:10.1306/12171818041

Chen, J. P., Zhao, C. Y., and He, Z. H. (1997). Criteria for Evaluating the Hydrocarbon Generating Potential of Organic Matter in Coal Measures. *Pet. Exploration Develop.* 24, 1–5. (in Chinese with English abstract).

Chen, Z., Wang, X., Wang, X., Zhang, Y., Yang, D., and Tang, Y. (2017). Characteristics and Petroleum Origin of the Carboniferous Volcanic Rock Reservoirs in the Shixi Bulge of Junggar Basin, Western China. *Mar. Pet. Geology*. 80, 517–537. doi:10.1016/j.marpetgeo.2016.12.028

Ci, X., Zhang, H., Niu, Q., Zhu, D., Kang, S., Hu, J., et al. (2020). Analysis of Tight Oil and Gas Charging Characteristics by the Carbon Isotope On-Site Detection Technology: A Case Study of the Northern Slope of the Minfeng Subsag in the Bohai Bay Basin. *Nat. Gas Industry B* 7 (3), 197–204. doi:10.1016/j.ngib.2019.11.002

Dai, J., Gong, D., Ni, Y., Huang, S., and Wu, W. (2014). Stable Carbon Isotopes of Coal-Derived Gases Sourced from the Mesozoic Coal Measures in China. *Org. Geochem.* 74, 123–142. doi:10.1016/j.orggeochem.2014.04.002

Dai, J., Li, J., Luo, X., Zhang, W., Hu, G., Ma, C., et al. (2005). Stable Carbon Isotope Compositions and Source Rock Geochemistry of the Giant Gas Accumulations in the Ordos Basin, China. *Org. Geochem.* 36, 1617–1635. doi:10.1016/j.orggeochem.2005.08.017

Dai, J., Ni, Y., Dong, D., Qin, S., Zhu, G., Huang, S., et al. (2021). 2021-2025 Is a Period of Great Development of China's Natural Gas Industry: Suggestions on the Exploration and Development of Natural Gas during the 14th Five-Year Plan in China. *J. Nat. Gas Geosci.* 6 (4), 183–197. doi:10.1016/j.jnggs.2021.08.001

Dai, J. X., Pei, X. G., and Qi, H. F. (1992). *Natural Gas Geology of China*, 1. Beijing: Petroleum Industry Press, 46–50. (in Chinese with English abstract).

Dai, J. X., Song, Y., and Zhang, H. F. (1996). Main Controlling Factors of Large and Middle Sized Gas fields in China[J]. *Sci. China: Ser. D.* 26 (6), 481–487.

Dai, J. X., Xia, X. Y., Hong, F., Zhao, L., Sun, D. M., and Shi, X. (1999). Main Controlling Factors of Large and Middle Sized Coal-Formed Gas fields in China [J]. *Chin. Sci. Bull.* 44 (22), 2455–2464.

Dai, J. X., Zhong, N. N., Liu, D. H., Xia, X. Y., Yang, J. Y., and Tang, D. Z. (2000). *Geologic Bases and Major Controlling Factors of Large and Medium Humic Gas Fields in China[M]*. Beijing: Petroleum Industry Press. (in Chinese).

Dai, J. X., Zou, C. N., Li, W., and Hu, G. Y. (2016). *Giant Coal-Derived Gas Fields and Their Gas Sources in China*. New York: Academic Press.

Du, J. H. (2010). *Petroleum Exploration for Volcanic Reservoirs in the Northern Xinjiang[M]*. Beijing: Petroleum Industry Press. (in Chinese).

Fu, J. M., Liu, D. H., and Sheng, G. Y. (1990). *Geochemistry of Coal-Derived Hydrocarbons*. Beijing: Science Press, 103–113. 31–32(in Chinese).37–76

Gang, W. Z., Gao, G., Hao, S. S., Huang, Z. L., and Zhu, L. (1997). Carbon Isotope of Ethane Applied in the Analyses of Genetic Types of Natural Gas. *Pet. Geology. Exp.* 19 (2), 164–167. (in Chinese with English abstract).

Gong, D., Song, Y., Wei, Y., Liu, C., Wu, Y., Zhang, L., et al. (2019). Geochemical Characteristics of Carboniferous Coaly Source Rocks and Natural Gases in the Southeastern Junggar Basin, NW China: Implications for New Hydrocarbon Explorations. *Int. J. Coal Geology*. 202, 171–189. doi:10.1016/j.coal.2018.12.006

Gong, D. Y., Wang, X. L., Zhou, C. M., Zheng, M. L., Jiang, W. L., and Wu, W. A. (2021). Discovery of Large-Scale Carboniferous Source Rocks and Natural Gas Exploration Potential in the Southeast of Junggar Basin. *Acta Petrolei Sinica* 42, 836–852. (in Chinese with English abstract). doi:10.7623/syxb202107002

Grantham, P. J. (1986). The Occurence of Unusual C27 and C29 Sterane Predominances in Two Types of Oman Crude Oil. *Org. Geochem.* 9 (1), 1–10. doi:10.1016/0146-6380(86)90077-x

Guo, J. M., Fan, H. L., Zhang, S. Y., Liu, X., Wu, T., Ma, W. Y., et al. (2020). Petrological, He-Ne-Ar and Sr-Nd-Pb Geochemical of Volcanic Rocks Constraint on Tectonic Settings and Geodynamic Process of the Carboniferous, East Junggar. *J. Nat. Gas Geosci.* 5 (1), 91–104. doi:10.1016/j.jnggs.2020.02.002

He, D.-F., Li, D., Fan, C., and Yang, X.-F. (2013). Geochronology, Geochemistry and Tectonostratigraphy of Carboniferous Strata of the Deepest Well Moshen-1 in the Junggar Basin, Northwest China: Insights into the continental Growth of Central Asia. *Gondwana Res.* 24 (2), 560–577. doi:10.1016/j.gr.2012.10.015

He, D. F., Zhang, L., Wu, S. T., Li, D., and Zhen, Y. (2018). Tectonic Evolution Stages and Features of the Junggar Basin. *Oil Gas Geology*. 39, 845–861. (in Chinese with English abstract). doi:10.11743/ogg20180501

Hu, T., Pang, X. Q., and Jiang, S. (2018). *Oil Content Evaluation of Lacustrine Organic-Rich Shale with strong Heterogeneity: A Case Study of the Middle Permian Lucaogou Formation in Jimusaer Sag, Junggar Basin, NW China [J]*. Fuel, 221.

Jiang, Z. S., and Fowler, M. G. (1986). Carotenoid-derived Alkanes in Oils from Northwestern China. *Org. Geochem.* 10, 831–839. doi:10.1016/s0146-6380(86)80020-1

Li, D., He, D., Santosh, M., Ma, D., and Tang, J. (2015a). Tectonic Framework of the Northern Junggar Basin Part I: The Eastern Luliang Uplift and its Link with the East Junggar Terrane. *Gondwana Res.* 27 (3), 1089–1109. doi:10.1016/j.gr.2014.08.015

Li, D., He, D., Santosh, M., Ma, D., and Tang, J. Y. (2015b). Tectonic Framework of the Northern Junggar Basin Part II: The Island Arc basin System of the Western Luliang Uplift and its Link with the West Junggar Terrane. *Gondwana Res.* 27 (3), 1110–1130. doi:10.1016/j.gr.2014.08.019

Li, W., Yu, Z., Wang, X., Yu, Z., Lu, X., and Feng, Q. (2020). Formation Mechanisms of Deep and Ultra-deep over Pressure Caprocks and Their Relationships with Super-large Gas fields in the Petroliferous Basins of China. *Nat. Gas Industry B* 7 (5), 443–452. doi:10.1016/j.ngib.2020.09.002

Liang, D. G., Zhang, S. C., Chen, J. P., Wang, F. Y., and Wang, P. R. (2013). Organic Geochemistry of Oil and Gas in the Kuqa Depression, Tarim Basin, NW China. *Org. Geochem.* 34, 873–888.

Liu, Q., Dai, J., Jin, Z., Li, J., Wu, X., Meng, Q., et al. (2016). Abnormal Carbon and Hydrogen Isotopes of Alkane Gases from the Qingshen Gas Field, Songliao Basin, China, Suggesting Abiogenic Alkanes? *J. Asian Earth Sci.* 115, 285–297. doi:10.1016/j.jseaes.2015.10.005

Liu, Q., Qin, S., Li, J., Liu, W., Zhang, D., Zhou, Q., et al. (2008). Natural Gas Geochemistry and its Origins in Kuqa Depression. *Sci. China Ser. D-earth Sci.* 51, 174–182. doi:10.1007/s11430-008-5003-3

Liu, Q., Wu, X., Wang, X., Jin, Z., Zhu, D., Meng, Q., et al. (2019). Carbon and Hydrogen Isotopes of Methane, Ethane, and Propane: A Review of Genetic

Identification of Natural Gas. *Earth-Science Rev.* 190, 247–272. doi:10.1016/j.earscirev.2018.11.017

Liu, W. H., Zhang, D. W., Wang, X. F., and Nan, Q. (2004). Geochemistry Study on Gas Source Correlation of Natural Gas. *Acta Sedimentologica Sinica* 22 (Suppl. l), 27–32. (in Chinese with English abstract).

Novikov, I. S. (2013). Reconstructing the Stages of Orogeny Around the Junggar basin from the Lithostratigraphy of Late Paleozoic, Mesozoic, and Cenozoic Sediments. *Russ. Geology. Geophys.* 54 (2), 138–152. doi:10.1016/j.rgg.2013.01.002

Orcutt, D. M., and Patterson, G. W. (1975). Sterol, Fatty Acid and Elemental Composition of Diatoms Grown in Chemically Defined media. *Comp. Biochem. Physiol. B: Comp. Biochem.* 50 (4), 579–583. doi:10.1016/0305-0491(75)90093-0

Peters, K. E. (1986). Guidelines for Evaluating Petroleum Source Rock Using Programmed Pyrolysis. *AAPG Bull.* 70, 318–329. doi:10.1306/94885688-1704-11d7-8645000102c1865d

Peters, K. E., Walters, C. C., and Moldowan, J. M. (2005). *The Biomarker Guide [M]*. second edition. Cambridge: Cambridge University Press.

Petersen, H. I. (2002). A Re-consideration of the "Oil Window" for Humic Coal and Kerogen Type Iii Source Rocks. *J. Pet. Geol* 25, 407–432. doi:10.1111/j.1747-5457.2002.tb00093.x

Petersen, H. I., Holme, A. C., Thomsen, E., Whitaker, M. F., Brekke, T., Bojesen-Koefoed, J. A., et al. (2011). Hydrocarbon Potential of Middle Jurassic Coaly and Lacustrine and Upper Jurassic - Lowermost Cretaceous Marine Source Rocks in the Søgne Basin, North Sea. *J. Pet. Geology*. 34, 277–304. doi:10.1111/j.1747-5457.2011.00506.x

Petersen, H. I., and Nytoft, H. P. (2006). Oil Generation Capacity of Coals as a Function of Coal Age and Aliphatic Structure. *Org. Geochem.* 37, 558–583. doi:10.1016/j.orggeochem.2005.12.012

Petford, N., and Mccaffrey, K. J. W. (2003). *Hydrocarbons in Crystalline Rocks [M]*. London: The Geological Society of London.

Powell, T. G. (1988). Pristane/phytane Ratio as Environmental Indicator. *Nature* 333, 604. doi:10.1038/333604a0

Qiu, N. S. (2002). Characters of thermal Conductivity and Radiogenic Heat Production Rate in Basins of Northwest China. *Chin. J. Geology*. 37, 196–206. (in Chinese with English abstract).

Qiu, N. S., Wang, X. L., Yang, H. B., and Xiang, Y. (2001). The Characteristics of Temperature Distribution in the Junggar Basin. *Chin. J. Geology*. 36, 350–358. (in Chinese with English abstract).

Qiu, N. S., Zha, M., and Wang, X. L. (2000). Simulation of Geothermal Evolution History in Junggar Basin. *Xinjiang Pet. Geology*. 21, 39–41. (in Chinese with English abstract).

Ren, Z., Cui, J., Qi, K., Yang, G., Chen, Z., Yang, P., et al. (2020). Control Effects of Temperature and thermal Evolution History of Deep and Ultra-deep Layers on Hydrocarbon Phase State and Hydrocarbon Generation History. *Nat. Gas Industry B* 7 (5), 453–461. doi:10.1016/j.ngib.2020.09.003

Schwark, L., and Empt, P. (2006). Sterane Biomarkers as Indicators of Palaeozoic Algal Evolution and Extinction Events. *Palaeogeogr. Palaeoclimatol. Palaeoecol.* 240, 225–236. doi:10.1016/j.palaeo.2006.03.050

Sinninghe, J. S., Kenig, F., Koopmans, M. P., Köster, J., Schouten, S., Hayes, J. M., et al. (1995). Evidence for Gammacerane as an Indicator of Water Column Stratification. *Geochimica et Cosmochimica Acta* 59, 1895–1900. doi:10.1016/0016-7037(95)00073-9

Suárez-Ruiz, I., Flores, D., Mendonça Filho, J. G., Hackley, P. C., and Hackley, P. C. (2012). Review and Update of the Applications of Organic Petrology: Part 1, Geological Applications. *Int. J. Coal Geology*. 99, 54–112. doi:10.1016/j.coal.2012.02.004

Sun, P. A., Wang, Y., Leng, K., Li, H., Ma, W., and Cao, J. (2016). Geochemistry and Origin of Natural Gas in the Eastern Junggar Basin, NW China. *Mar. Pet. Geology*. 75, 240–251. doi:10.1016/j.marpetgeo.2016.04.018

Sweeney, J. J., and Burnham, A. K. (1990). Evaluation of a Simple Model of Vitrinite Reflectance Based on Chemical Kinetics. *AAPG Bull.* 74, 1559–1570. doi:10.1306/0c9b251f-1710-11d7-8645000102c1865d

Tang, Y., Perry, J. K., Jenden, P. D., and Schoell, M. (2000). Mathematical Modeling of Stable Carbon Isotope Ratios in Natural Gases. *Geochimica et Cosmochimica Acta* 64 (15), 2673–2687. doi:10.1016/s0016-7037(00)00377-x

Taylor, G. H., Teichmüller, M., Davis, A., Diessel, C. F. K., and Robert, P. (1998). *Organic Petrology[M]*. Berlin-Stuttgart: Borntraeger.

Tissot, B. P., and Welte, D. H. (1984). *Petroleum Formation and Occurrence[M]*. New York: Springer.

Volkman, J. K. (1986). A Review of Sterol Markers for marine and Terrigenous Organic Matter. *Org. Geochem.* 9, 83–99. doi:10.1016/0146-6380(86)90089-6

Vu, T. T. A., Zink, K.-G., Mangelsdorf, K., Sykes, R., Wilkes, H., and Horsfield, B. (2009). Changes in Bulk Properties and Molecular Compositions within New Zealand Coal Band Solvent Extracts from Early Diagenetic to Catagenetic Maturity Levels. *Org. Geochem.* 40, 963–977. doi:10.1016/j.orggeochem.2009.06.002

Wang, S., Hu, S., Li, T., Wang, J., and Zhao, W. (2000b). Terrestrial Heat Flow in Junggar Basin, Northwest China. *Chin.Sci.Bull.* 45, 1808–1813. doi:10.1007/bf02886273

Wang, S. J., Hu, S. B., and Wang, J. Y. (2000a). The Characteristics of Heat Flow and Geothermal fields in Junggar Basin. *Chin. J. Geophys.* 43, 771–779. (in Chinese with English abstract). doi:10.1002/cjg2.98

Wang, X. L., Zhi, D. M., Wang, Y. T., Chen, J. P., and Qin, Z. J. (2013). *Organic Geochemistry of Source Rocks and Hydrocarbons in the Junggar Basin*. Beijing: Petroleum Industry Press. (*in Chinese*).

Wei, G., Yang, W., Liu, M., Xie, W., Jin, H., Wu, S., et al. (2020). Distribution Rules, Main Controlling Factors and Exploration Directions of Giant Gas fields in the Sichuan Basin. *Nat. Gas Industry B* 7 (1), 1–12. doi:10.1016/j.ngib.2020.01.001

Whiticar, M. J. (1999). Carbon and Hydrogen Isotope Systematics of Bacterial Formation and Oxidation of Methane [J]. *Chem. Geology*. 161 (1-3), 291–314. doi:10.1016/s0009-2541(99)00092-3

Wu, X., Chen, Y., Wang, Y., Zeng, H., Jiang, X., and Hu, Y. (2021). Geochemical Characteristics of Natural Gas in Tight sandstone of the Chengdu Large Gas Field, Western Sichuan Depression, Sichuan Basin, China. *J. Nat. Gas Geosci.* 6 (5), 279–287. doi:10.1016/j.jnggs.2021.09.003

Wu, X., Chen, Y., Zhai, C., Zhou, X., Liu, W., Yang, J., et al. (2020). Gas Source and Exploration Direction of the Middle Triassic Leikoupo Formation in the Sichuan Basin, China. *J. Nat. Gas Geosci.* 5 (6), 317–326. doi:10.1016/j.jnggs.2020.10.001

Xiao, W. J., Han, C. M., Yuan, C., Sun, M., Lin, S. F., Chen, H. L., et al. (2008a). Middle Cambrian to Permian Subduction Related Accretionary Orogenesis of Northern Xinjiang, NW China: Implications for the Tectonic Evolution of Central Asia[J]. *J. Asian Earth Sci.* 32 (2–4), 102–117. doi:10.1016/j.jseaes.2007.10.008

Xiao, Z. H., Xie, Z. Y., Li, Z. S., Ma, C. H., and Sun, Q. W. (2008b). Geochemical Characteristics of Natural Gas of Xujiahe Formation in Southern and Middle Sichuan. *J. Southwest Pet. Univ. (Science Tech. Edition)* 30 (4), 27–30. (in Chinese with English abstract).

Xiong, Y., Geng, A., and Liu, J. (2004). Kinetic-simulating experiment Combined with GC-IRMS Analysis: Application to Identification and Assessment of Coal-Derived Methane from Zhongba Gas Field (Sichuan Basin, China). *Chem. Geology*. 213 (4), 325–338. doi:10.1016/j.chemgeo.2004.07.007

Yao, W., Xu, J., Xia, W., Wang, Q., Rao, D., and Chen, Q. (2020). A Characteristic Analysis between Acidolysis Gas and Absorbed Gas and its Application to Gas Source Correlation in Mao 1 Member, Fuling Area, Sichuan Basin. *Nat. Gas Industry B* 7 (1), 24–29. doi:10.1016/j.ngib.2019.06.001

Yu, S., Wang, X., Xiang, B., Liao, J., Wang, J., Li, E., et al. (2014). Organic Geochemistry of Carboniferous Source Rocks and Their Generated Oils from the Eastern Junggar Basin, NW China. *Org. Geochem.* 77, 72–88. doi:10.1016/j.orggeochem.2014.09.011

Zhang, L., He, D., Yi, Z., and Li, D. (2020a). Tectonic Relationship between the Kelameili Range and the Dajing Depression: Insights into the Carboniferous Tectonic-Sedimentary Framework. *Pet. Exploration Develop.* 47 (1), 30–45. doi:10.1016/s1876-3804(20)60003-9

Zhang, M., and Cheng, Q. S. (2021). Distribution and Significance of High Abundance C_{29} Regular Sterane in the Crude Oil of Lower Paleozoic in Tarim Basin. *J. Yangtze Univ. (Natural Sci. Edition)* 18 (1), 11–19.

Zhang, S., Zhang, S., Fang, L., Lu, X., Guo, H., and Shi, J. a. (2020b). Petrological and Geochemical Constraints on Tectonic Settings of the Late Carboniferous-Early Permian, Central Junggar, China. *J. Nat. Gas Geosci.* 5 (1), 1–10. doi:10.1016/j.jnggs.2019.12.002

Zhi, D., Wang, X., and Qin, Z. (2022). Geneses, Sources and Accumulation Process of Natural Gases in the Hinterland of the Junggar Basin. *Front. Earth Sci.* 10. doi:10.3389/feart.2022.843245

Zou, C. N., Zhao, W. Z., Jia, C. Z., Zhu, R. K., Zhang, G. Y., Zhao, X., et al. (2008). Formation and Distribution of Volcanic Hydrocarbon Reservoirs in

Sedimentary Basins of China. *Pet. Exploration Develop.* 35, 257–271. (in Chinese with English abstract).

Conflict of Interest: YS, MP, and CL were employed by Xinjiang Oil Company.

The remaining authors declare that the research was conducted in the absence of any commercial or financial relationships that could be construed as a potential conflict of interest.

Publisher's Note: All claims expressed in this article are solely those of the authors and do not necessarily represent those of their affiliated organizations, or those of the publisher, the editors, and the reviewers. Any product that may be evaluated in this article, or claim that may be made by its manufacturer, is not guaranteed or endorsed by the publisher.

frontiers | Frontiers in Earth Science

ORIGINAL RESEARCH
published: 19 April 2022
doi: 10.3389/feart.2022.879297

Inclusion Characteristics of the Fracture-Cave Calcite of Ordovician Yingshan Formation and Its Indication to the Formation of Paleokarst Reservoir in the Northern Slope of Tarim Basin Center Area, China

Yong Dan[1,2], *Junjie Ba*[1,2]*, *Bin Liang*[1,2], *Qingyu Zhang*[1,2], *Jingrui Li*[1,2] *and Guoquan Nie*[1,2]

[1]*Institute of Karst Geology, Chinese Academy of Geological Sciences/Karst Dynamics Laboratory, Guilin, China,* [2]*International Research Center on Karst Under the Auspices of UNESCO, Guilin, China*

OPEN ACCESS

Edited by:
Hao Zou,
Chengdu University of Technology, China

Reviewed by:
Guoqing Xiong,
Chengdu Geological Survey Center, China
Bo Peng,
Chinese Academy of Geological Sciences (CAGS), China

***Correspondence:**
Junjie Ba
bajunjie@karst.ac.cn

Specialty section:
This article was submitted to Economic Geology, a section of the journal Frontiers in Earth Science

Received: *19 February 2022*
Accepted: *07 March 2022*
Published: *19 April 2022*

Citation:
Dan Y, Ba J, Liang B, Zhang Q, Li J and Nie G (2022) Inclusion Characteristics of the Fracture-Cave Calcite of Ordovician Yingshan Formation and Its Indication to the Formation of Paleokarst Reservoir in the Northern Slope of Tarim Basin Center Area, China. Front. Earth Sci. 10:879297. doi: 10.3389/feart.2022.879297

A karst fracture-cavity was developed in the Ordovician Yingshan Formation in the northern slope of the Tarim Basin center area (Tazhong area); however, the area experienced multistage karst and diagenesis in the later period, and the reservoir was heavily reformed, characterized by complex distribution. Based on the testing of the inclusions in the karst fractures and fracture-cave calcite, this study summarizes the physical and chemical characteristics of the inclusions in the northern slope of Tazhong. The major inclusions were liquid and gas–liquid phases, while the minor ones were hydrocarbon phases. Based on the salinity–homogenization temperature diagram, the gas–liquid inclusions could be divided into seven types: low-temperature low-salinity inclusions (the lowest salinity was 0.88%, which is lower than that of present sea water; the lowest temperature of the inclusions was 49°C); low-temperature high-salinity inclusions; medium-temperature low-salinity inclusions; medium-temperature medium-salinity inclusions; medium-temperature high-salinity inclusions; high-temperature medium-salinity inclusions; and high-temperature high-salinity inclusions. The development of inclusions was characterized by high temperature and high salinity or low temperature and low salinity. In addition, the low-temperature and low-salinity inclusions near the unconformity surface were well-developed. The high-temperature and higher-salinity inclusions far from the unconformity surface were also well-developed. A burial history analysis showed three stages of karstification or filling in the area: exposed karstification in the Middle Caledonian, shallow burial filling in the Middle Hercynian, and burial filling in the Late Hercynian. By determining the inclusions in calcite associated with mud in the karst caves and combined with previous studies, the Middle Caledonian was found to be the period associated with the eogenetic karstification of meteoric water and seawater. This is the key factor in the formation of karst reservoirs in the Tazhong area. The large-scale calcite growth in the Middle Hercynian and Late Hercynian burial periods led to further filling of the early karst reservoir, reduced reservoir space, and enhanced reservoir heterogeneity.

Keywords: inclusion, fracture-cavity reservoir, Yingshan formation, buried karst, homogenization temperature, burial history, eogenetic karstification

1 INTRODUCTION

Since the 1990s, the Ordovician carbonate fracture-cavity oil and gas field located in the Tarim Basin has been continuously explored and developed. It has been the most important oil and gas exploration field in China and continues to have significant exploration potential (Yang et al., 2011). Previous studies have shown that the long-term exposure of meteoric water karst in the Caledonian–Hercynian period led to development of karst caves in the Ordovician in the northern Tarim Basin (Yan et al., 2002; Yan et al., 2005; He et al., 2007; Dan et al., 2012). Since 2006, several karst hole–type oil and gas reservoirs have been discovered in the Middle and Lower Ordovician Yingshan Formations in the Tazhong area (Yang et al., 2011). Unlike the karst in the northern region (which has an exposure time of more than 200 Ma) (Chen et al., 2004; Zhu et al., 2009; Zhao et al., 2013), the top of the Yingshan Formation in Tazhong has few lacunas, and the exposure time is generally short (approximately in the range of 7–11 Ma). The karst holes in the Yingshan Formation are small but many, and they contain vast inclusions (Yang et al., 2011; Ni et al., 2013; Pang et al., 2013; Dan et al., 2015). Regarding the origin of these types of karst holes, previous studies have suggested that they are similar to those formed in the north of the Tarim Basin in the early stage—the development of the holes was mainly controlled by the meteoric water in the Caledonian period and then by the buried karst in the later stage (Yang et al., 2011; Ni et al., 2013; Pang et al., 2013). In recent years, scholars have conducted in-depth studies on the characteristics of fracture-cavity karst morphology, distribution law, and inclusion geochemistry (carbon and oxygen isotopes; major, trace, and rare earth elements); eogenetic karstification was proven to be the origin of the karst in this area. Larger caves were more likely to develop in mixed-water karst zones controlled by sea level (Dan et al., 2015; Chen et al., 2016; Zhang et al., 2016; Dan et al., 2018; Dan et al., 2019; Dan et al., 2021). Nonetheless, the above mentioned studies did not provide direct evidence of karst fluid salinity, temperature, etc.

Fluid inclusions are diagenetic fluids trapped in crystal defects during mineral crystallization, which record the information of diagenetic fluids. They are widely used in the study of petroleum geology as a technical tool, such as the morphology, composition, and homogenization temperature characteristics of the inclusions in fractures and caves. They directly reflect the fluid characteristics and environmental conditions at the time of their formation (Lu, 1990). The dissolution and inclusion growth in carbonate rocks occurs simultaneously. The fluid inclusions developed during the growth of calcite from fracture-caves can reflect the information of karst fluids to some extent and are also a good indicator of the paleokarst environment and stages (Lu, 1990; Liu, 1991; Chen et al., 2003; Chen et al., 2004; Xia and Tang, 2004; Xia et al., 2006; Liu et al., 2007; Cai et al., 2009; Wu et al., 2010; Dan et al., 2015). Analyzing the inclusions has become an important tool in the study of paleokarstification.

Given the lack of clear data on the karst stages and karst fluid environment of the Yingshan Formation in the Tazhong area, the inclusions in calcite were sampled from the fracture-caves in drilling cores and then tested to obtain relevant parameters. The results provide relevant evidence to judge the nature of the paleokarst fluid and karst environment formed in the fracture-cave of the Yingshan Formation. They can promote the study of the genetic mechanism of fracture-cavity reservoirs in the Yingshan Formation in the northern slope of the Tazhong area and can provide a basis for establishing paleokarst reservoir prediction models and guiding oil and gas exploration in the Tazhong area.

2 GEOLOGICAL SETTING

The Tazhong Uplift is oriented NW–SE, with the Bachu fault uplifted to the west, lower Tadong bulging to the east, Manjiaer Sag located to the north, and Tongguzabasi Depression to the south (Shu et al., 2008) (**Figure 1A**). It is divided into three subtectonic belts from north to south: northern slope, central fault horst, and southern slope (Lan et al., 2014). The study area is located in the northern slope between the central-faulted horst belt and Tazhong No. I fault zone (**Figure 1A**). During the Early Ordovician–Middle Ordovician period, the Tazhong area was in a relatively stable tectonic setting, and the Yingshan Formation comprised a set of calcarenite and micrite of carbonate platform facies (Pang et al., 2013).

The northern slope of Tazhong has experienced four main tectonic movements (Quan, 2020): Cambrian Early Ordovician extensional environment and development of extensional faults; under the influence of Caledonian tectonic movement in the middle and late Ordovician, the study area was subjected to NE–SW compression; a large-scaled thrust system of trending NWW, such as the Tazhong No. I fault zone, was formed due to the influence of the tectonic movement of Caledonian I. In addition, Middle–Lower Ordovician carbonate rocks were entirely uplifted as a result of regional compression. The carbonate platform was exposed and underwent intense erosion and karstification, leading to formation of the unconformity surface of the Yingshan Formation (**Figure 1**) (Yu et al., 2011; Chen et al., 2016). In the high part of the uplift, the Middle Ordovician Yijianfang Formation and Upper Ordovician Tumuxiuke Formation were missing due to severe denudation. The Middle–Lower Ordovician Yingshan Formation also underwent denudation. From Silurian to Devonian, strike slip faults were developed under continuous compression from northeast to southwest. In the Permian, due to subduction, a large number of volcanic activities developed tensile fractures. In the Cambrian Early Ordovician tectonic activity stage, the Ordovician Yingshan Formation was not deposited and had no direct impact on the formation of the target reservoir (Quan, 2020).

Currently, the Ordovician formation can be divided (from top to bottom) into the following formations: Sangtamu, Lianglitage, Yingshan, and Penglaiba (**Figures 1B,C**). The depositional break between the Yingshan and Lianglitage Formations lasted for approximately 12–15 Ma (Yu et al., 2011; Chen et al., 2016). The exposed karstification of the Yingshan Formation lasted for 7–11 Ma. The Yingshan Formation in the northern slope of

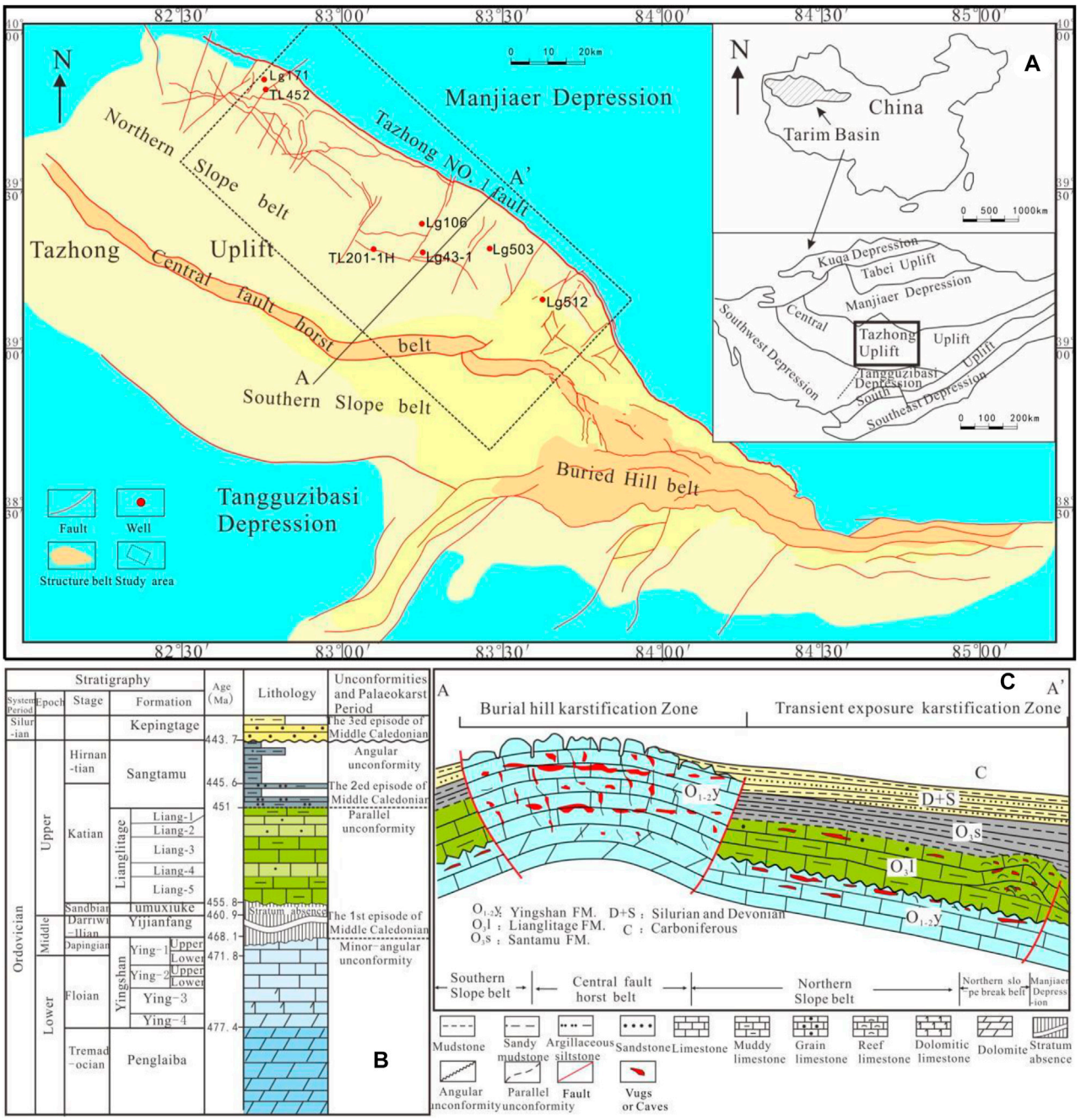

FIGURE 1 | Sketch of the structural features in the Tazhong area. **(A)** Tectonic division of the Tazhong Uplift and location of the study area; **(B)** Generalized stratigraphy and associated reservoir intervals (northern slope belt) of the Yingshan Formation in the study area. **(C)** Karstification division of the Tazhong Uplift and location of the northern slope belt.

Tazhong can be divided into four members (**Figure 1B**) based on the well-logging electrical properties (**Figure 1B**). Ying-1 and Ying-2 members comprise pure limestone with a thickness of approximately 300 m, whereas Ying-3 and Ying-4 members comprise dolomitic limestone and dolomite.

The unconformity exposed strata comprise limestone from the Ying-1 and Ying-2 members, which are noneffective reservoirs having low porosity and low permeability, with an average porosity of 0.91% and a permeability of 3.76×10^{-3} μm^2 (Yang et al., 2011). The present reservoir is mainly the secondary fracture-cave reservoir formed under the impact of the karstification and tectonic movement at the late stage, and it is an important oil and gas reservoir in the Tarim Basin. Its effective reservoir space consists of mainly karst holes, caves, and fractures

(Feng et al., 2014). These fractures and caves are distributed within 300 m below the unconformity surface and often filled with calcite, clay, and organic matter (Dan et al., 2018). The large karst caves are considered the main reservoir space and are mostly filled with clay, limestone breccias, and calcite (Dan et al., 2018). A total of 107 karst caves (with a height of more than 0.3 m) have been discovered in 90 wells in the study area, among which 62 karst caves are filled, accounting for 57.94% (Dan et al., 2018). The currently unfilled reservoirs are mainly developed in the lower part of the filled section (Dan et al., 2018). To understand the formation mechanism of most fracture-cavities of the Yingshan Formation, the formation and filling environment of the karst caves should be determined by sampling and analyzing the inclusions in the caves.

3 SAMPLING AND TESTING

3.1 Sample Collection of Calcite From the Fracture Cave at Different Stages

The samples were mainly taken from the carbonate strata of the Ordovician Yingshan Formation on the northern slope of the Tazhong area. In addition to the calcite taken from the karst cave, calcite was also taken from the cracks. As for the fracture stages, the fracture stages in the Tazhong area have been studied by conducting acoustic emission experiments. Three stages of fractures have been considered to mainly develop in the study area: calcite-filled structural fractures formed in the Silurian Devonian and Late Hercynian; it was formed in the unfilled structural fracture of the Himalayan period (Xu et al., 2012). On this basis, the geometric shape and cutting relationship of the fractures in the rock core were determined. The results showed the development of multistage fractures in the study area, and the sequence of fracture development was as follows: 1) Horizontal suture (mainly filled with organic matter and black argillaceous matter); 2) High-angle suture; 3) Dissolution fractures (holes) are formed by dissolution expansion and filled with grayish–green mud with different occurrences; 4) High-angle shear joints filled with white calcite or translucent, with local joints also having the characteristics of solution expansion; 5) White calcite-filled horizontal structural fine joints; 6) Horizontal opening seam; and 7) High-angle opening seam. Quan (2020) considered the formation of stages 1 horizontal suture and 2 a high-angle suture between the Middle and Late Ordovician and Silurian. Stage 3 is the dissolution fracture formed during the exposure period of the Middle–Late Ordovician by the dissolution expansion along the early suture and the fractures in the same period during the exposure period; it is filled with terrigenous argillaceous material. The white or translucent calcite-filled shear fractures or solution fractures were formed in the Middle–Late Ordovician and Silurian Devonian. 5) The origin of the white-calcite-filled horizontal structural fine fracture is unclear; it was formed after the formation of the Silurian Devonian shear fracture. The open joints of the stages 6 and 7 were formed in the Himalayan tectonic stage. Megacryst calcite precipitates (>2 cm) were found in seven of the 40 rock cores, with mainly argillaceous inclusions in the fractures and caves. The collected samples are mainly from the 3) and 4) stages, and the types include coarse-grained calcite filled in the 4) stage high-angle solution fracture and coarse-grained calcite filled in the 4) stage high-angle structural fracture. In addition, to study the karst fluid properties of the karst cave filled with mud during the exposure period in the northern slope of the Tazhong area, a microscope and cathodoluminescence instrument are specially used to select the calcite filled with mud from the 3) stage fracture and cave. The interlayer joints were filled with calcite in calcareous mudstone (**Figure 2**). There were eight samples mainly located 0–210 m below the unconformity surface at the top of the Yingshan Formation, obtained from six wells (**Table 1**).

3.2 Test Method

Petrographic and cathodoluminescence (CL) analyses were conducted on five thin sections of the samples. A cold cathode luminescence microscope was used with a beam voltage of 17 kV and a beam current of 500 μA on all the samples. The CL8200 MK5 cathode luminescence analyzer (CITL, United Kingdom, in conjunction with a Leica polarizing microscope) was used for the cathode luminescence analysis. The inclusion slices from the samples were grinded and then tested using the THMSG600 heating/freezing stage (Linkam Company, United Kingdom). The inclusion test was conducted in the Analysis and Testing Research Center of Beijing Institute of Geology, China Nuclear Industry Geological Bureau.

4 RESULTS

4.1 Physical Characteristics of Inclusions

Lu (1990) considered that the inclusions contained in calcite are mainly primary inclusions; the test results showed that they were primary inclusions and were not divided into primary and secondary. The inclusions were mainly liquid inclusions at room temperature, including some hydrocarbon inclusions. The liquid inclusions mainly existed in the liquid phase, while a few existed in the gas–liquid phase (**Table 1**). The liquid-phase inclusions were mainly round and oval, colorless, and transparent under the microscope, with a size range of 2–15 μm (some of 50 μm). The liquid-phase inclusions were generally smaller than the gas–liquid inclusions and were distributed in groups or strips along the microfractures in the calcite crystals (**Figure 3A**). The gas–liquid phase inclusions were mainly round, rectangular or polygonal, colorless, and transparent under the microscope, with a size range of 3–20 μm (some had a size of 80 μm). They were distributed in groups, uniformly, or in strips in the calcite (**Figure 3B**). **Table 1** shows that except for sample no. 6, the liquid-phase inclusions in the other samples account for more than 35–40% of the total inclusions. Moreover, all the samples contained more or less hydrocarbon inclusions, indicating the abundance of oil and gas in the northern slope of the Tazhong area.

FIGURE 2 | Calcite development in the fractures and caves of the Yingshan Formation in the northern slope of the Tazhong area. **(A)** Calcite filled in period 4 fractures, LG106, 2 (44/58), 6,074.4 m. **(B)** Calcite filled in high-angle fractures in period 4, LG503, 1 (23/53), 5,942.4 m. **(C)** Calcite filled in period 4) fractures, LG171, 4 (23/74), 6,493 m. **(D)** Calcite filled in period 4 fractures. The opening joints of periods 6 and 7, LG512, 4 (4/70), 5,582.5 m. **(E)** Calcite filled in high-angle fractures, where the suture can be seen in period 1, TL452, 3 (22/43), 6,461 m. **(F)** Calcite filled in period 4 structural fractures, LG512, 4 (49/70), 5,587.6 m. **(G)** Calcite filled in a 40-cm-long cave, which is completely filled with calcareous argillaceous (limestone gravel and grayish–green calcareous clay) fillings; it is the stage 3 of exposed karst formation, TL201-1H, 4 (46/62), 5,460.6–6,461 m. **(H)** Calcite filled in period 3 inter-formational fractures with grayish-green calcareous mudstone, LG512, 3 (36/58), 5,484.3 m. **(I)** Micrograph at the white circle in **(G)**, containing dissolved and dissociated limestone debris particles (Gr), clay (Cl), and calcite (Cal), TL201-1H, 4 (46/62), 5,460.7 m **(J)** cathodoluminescence image of **(I)**, in which the sandy sparite limestone is weak–moderately luminous, with luminous bands at the edges, while calcite is not luminous.

TABLE 1 | Outcomes of calcite samples and physical characteristics of inclusions in the northern slope of the Tazhong area.

No.	Sampling well	Distance[a]	Calcite occurrence	Inclusions				
				Phase state	Proportion (%)	Size (μm)	Shape	Inclusion distribution
1	LG106 2 (44/58)	0	In fracture	Gaseous hydrocarbons	10	3–5	Round, oval	Group/strip distribution along the micro fractures
				Liquid hydrocarbons	15	2–20	Irregular, rectangle	Group/strip distribution along the micro fractures
				Liquid	45	2–20	Round, square	Group, uniform/strip distribution
				Gas–liquid	30	3–25	Round, polygon	Group, uniform/strip distribution
2	LG503 1 (23/53)	3	In high-angle fracture	Gaseous hydrocarbons	10	4–10	Round, oval	Group/strip distribution along the microfractures
				Liquid hydrocarbons	1	4–10	Irregular, rectangle	Line distribution along the microfractures
				Gas–liquid hydrocarbons	4	3–15	Irregular, square	Group/strip distribution along the microfractures
				Liquid	40	2–20	Round, polygon	Group, uniform/strip distribution
				Gas–liquid	45	2–40	Round, polygon	Group, uniform/strip distribution
3	TL201-1H 4 (46/62)	18	In cavity with mud	Gaseous hydrocarbons	10	3–8	Round, oval	Group/strip distribution along the microfractures
				Liquid hydrocarbons	15	2–10	Irregular, rectangle	Group/strip distribution along the microfractures
				Liquid	55	2–10	Round, oval	Group, uniform/strip distribution
				Gas–liquid	20	3–15	Round, polygon	Group, uniform/strip distribution
4	TL452 3 (22/43)	100	In fracture	Gaseous hydrocarbons	8	3–6	Round, oval	Group/strip distribution along the microfractures
				Liquid hydrocarbons	15	2–20	Irregular, rectangle	Group/strip distribution along the microfractures
				Liquid	45	2–20	Round, square	Group, uniform/strip distribution
				Gas–liquid	32	3–15	Round, polygon	Group, uniform/strip distribution
5	LG512 3 (36/58)	104	In interlayer fracture with calcareous Mudstone	Gaseous hydrocarbons	10	4–10	Round, oval	Group/strip distribution along the microfractures
				Liquid hydrocarbons	3	3–10	Irregular, rectangle	Line distribution along the microfractures
				Gas–liquid hydrocarbons	5	2–10	Irregular, square	Group/strip distribution along the microfractures
				Liquid	32	3–50	Round, polygon	Group, uniform/strip distribution
				Gas–liquid	50	2–80	Round, polygon	Group, uniform/strip distribution
6	LG171 4 (23/74)	108	In fracture	Gaseous hydrocarbons	15	2–10	Round, oval	Group, uniform/strip distribution
				Liquid hydrocarbons	20	2–10	Irregular, rectangle	Group, uniform/strip distribution
				Liquid	25	2–20	Round, square	Group, uniform/strip distribution
				Gas–liquid	40	3–20	Round, polygon	Group, uniform/strip distribution
7	LG512 4 (4/70)	207	In fracture	Gaseous hydrocarbons	8	4–15	Round, oval	Group/strip distribution along the microfractures
				Liquid hydrocarbons	12	3–10	Irregular, rectangle	Line distribution along the microfractures
					10	2–10		

(Continued on following page)

TABLE 1 | (*Continued*) Outcomes of calcite samples and physical characteristics of inclusions in the northern slope of the Tazhong area.

No.	Sampling well	Distance[a]	Calcite occurrence	Inclusions				
				Phase state	Proportion (%)	Size (μm)	Shape	Inclusion distribution
				Gas–liquid hydrocarbons			Irregular, square	Group/strip distribution along the microfractures
				Multiphase hydrocarbon	3	2–15	Irregular, square	Group/strip distribution along the microfractures
				Liquid	37	3–40	Round, polygon	Group, uniform/strip distribution
				Gas–liquid	30	2–50	Round, polygon	Group, uniform/strip distribution
8	LG512 4 (49/70)	210	In structural fracture	Gaseous hydrocarbons	15	4–10	Round, oval	Group/strip distribution along the microfractures
				Liquid hydrocarbons	2	3–10	Irregular, rectangle	Line distribution along the microfractures
				Gas–liquid hydrocarbons	8	2–15	Irregular, square	Group/strip distribution along the microfractures
				Liquid	40	3–30	Round, polygon	Group, uniform/strip distribution
				Gas–liquid	40	2–40	Round, polygon	Group, uniform/strip distribution

[a]*Distance to the top of the Yingshan Formation.*

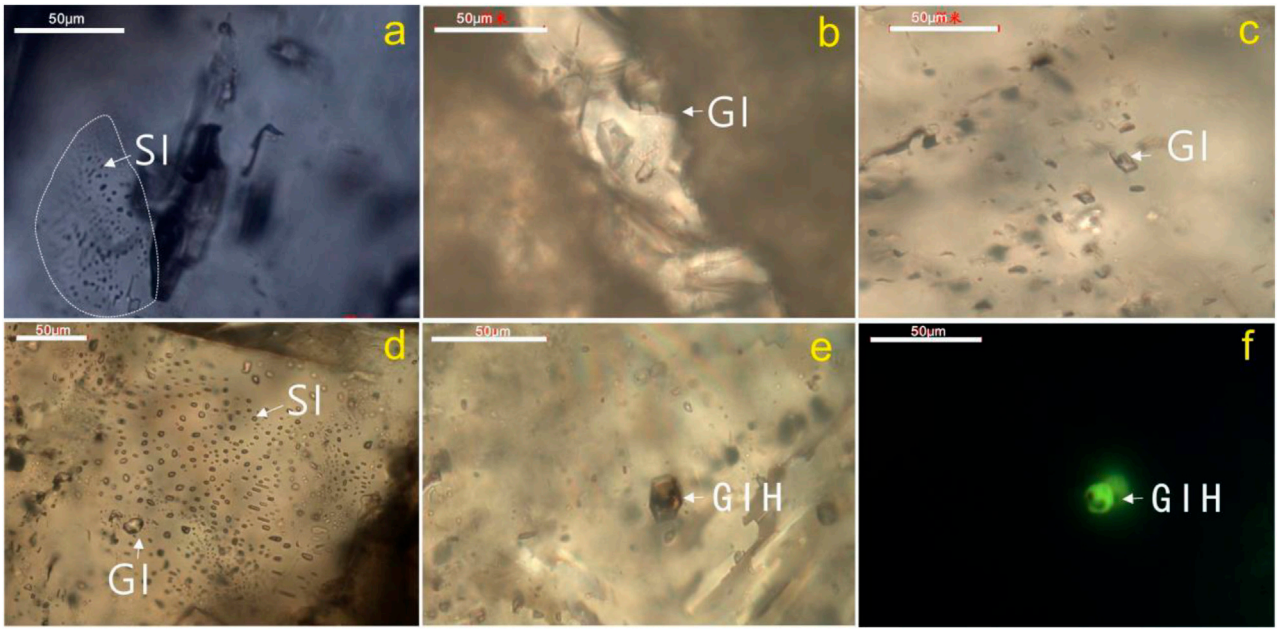

FIGURE 3 | Shapes and distribution characteristics of inclusions. **(A)** Group-distributed liquid inclusions (SI) in calcite of period 3 karst cave, TL201-1H; **(B)** gas–liquid (GI) distributed inclusions in calcite, TL452; **(C)** group-distributed inclusions in calcite of period 4) crack, LG106; **(D)** inclusions distributed along the microfractures of period 4) crack, LG512 **(E,F)** inclusions distributed in the gas–liquid–hydrocarbon (GIH) phase of period 4 cracked calcite, while the liquid hydrocarbon phase is yellow-green under UV fluorescence excitation.

4.2 Chemical Characteristics of Gas–Liquid Phase Inclusions

In this study, 273 gas–liquid phase inclusions were selected from eight samples to measure the freezing point temperature, initial dissolving temperature, and homogenization temperature. The salinity was calculated on the basis of the conversion relationship between the freezing point temperature and NaCl salinity, which was proposed by Bodnar (1992). **Table 2** presents the results.

TABLE 2 | Chemical characteristics of the gas–liquid phase inclusions in Ordovician calcite from the northern slope of the Tazhong area.

No.	Sampling well	Depth (m)	Distance[a] (m)	Calcite formation	Phase	Freezing point T (°C)	Homogenization T (°C)	w (NaCl)%	Initial dissolving T (°C)	Water-salt system
1	LG106 2 (44/58)	6,074.4	0	In fracture	Gas–liquid1	−4.8to−0.8	78–105	1.4–7.59	−23.2to−22.4	NaCl-KCl-H_2O
					Gas–liquid2	−20.1to−18.4	66–90	21.26–22.38	−35.5to−34.4	NaCl-H_2O-$MgCl_2$
2	LG503 1 (23/53)	5,942.4	3	In high-angle fracture, coarse crystals	Gas–liquid	−20 to −19.4	63–111	21.96–22.38	−54.1 to −52.5	$CaCl_2$-NaCl-H_2O
3	TL201-1H 4 (46/62)	5,460.7	18	In cavity with mud	Gas–liquid	−14.1 to −1.5	49–116	2.57–17.87	−23.0 to −22.2	NaCl-KCl-H_2O
4	TL452 3 (22/43)	6,461	100	In fracture	Gas–liquid	−11 to −1.1	79–119	1.91–14.97	−35.0 to −34.4	NaCl-H_2O-$MgCl_2$
5	LG512 3 (36/58)	5,484.3	104	In interlayer fracture with Calcareous Mudstone	Gas–liquid1	−20 to −6.8	78–128	10.24–22.38	−34.8 to −32.2	NaCl-H_2O-$MgCl_2$
6	LG171 4 (23/74)	6,493	108	In fracture	Gas–liquid	−20 to −0.5	56–106	0.88–22.38	−49.0 to −47.5	$CaCl_2$-NaCl-H_2O
7	LG512 4 (4/70)	5,582.5	207	In fracture	Gas–liquid	−20 to −16	68–100	19.53–22.38	−35.3 to −33.8	NaCl-H_2O-$MgCl_2$
8	LG512 4 (49/70)	5,587.6	210	In structural fracture	Gas–liquid1	−20 to −12.4	75–113	16.34–22.38	−35.6 to −34.5	NaCl-H_2O-$MgCl_2$

[a]*Depth to the top of the Yingshan Formation.*

4.2.1 Salinity Characteristics of Gas–Liquid Phase Inclusions

Based on the salinity distribution chart of each sample (**Figure 4**), the salinity span was found to be relatively wide in the northern slope of the Tazhong area. The NaCl mass fraction salinity (w (NaCl)%) was in the range of 0.88–22.38%. In addition, the closer the calcite sample was to unconformity, the more likely that it contained low-salinity inclusions. However, the salinity of the same well, such as LG106, was also significantly different. The salinity of LG106 was in the range of 1.4–7.59% in the gas–liquid phase 1, whereas that of w (NaCl) % was in the range of 21.26–22.38% in gas–liquid phase 2. This also shows that the area was affected by karst fluids with different salinities.

Based on the salinity analysis results, the inclusions can be divided into three types: 1) Low-salinity inclusions, w (NaCl)% 0.88–5%, which were found in LG106, TL201-1H, TL452, and LG171; the sampling point was 0–108 m below the unconformity surface; belonging to the NaCl–KCl–H_2O system; 2) Medium-salinity inclusions, w (NaCl)% 5–15%, which were found in TL201-1H, TL452, LG512, and LG171; the sampling point was 18–108 m below the nonconformity surface; with freezing point temperatures ranging from −12.0 to −5.0°C, belonging to $CaCL_2$–H_2O, NaCl–$CaCl_2$–H_2O, and NaCl–$MgCl_2$–H_2O systems.

According to Boni (1986), the change in the water–salt system is related to the change in the ions in the system, which indicates that Ca (Mg) ions are important components in this type of inclusion fluid. 3) High-salinity inclusions, w (NaCl)% 15–23%. Except for TL452, all the other samples contained high-salinity inclusions. The sampling point was 0–210 m below the unconformity surface, which belongs to $CaCl_2$–H_2O and NaCl–$CaCl_2$–H_2O systems. This also indicates that the Ca ion is an important component in this type of inclusion fluid, and high-salinity inclusions are common in the study area. In addition, there were some extremely low-salinity inclusions, for example, LG106 and LG171, with a minimum w (NaCl)% of 0.88% (**Table 2**), which is much lower than the current seawater salinity of 3.5%.

4.2.2 Homogenization Temperature Characteristics of Gas–liquid Phase Inclusions

The temperature of 273 gas–liquid inclusions was tested in the range of 49–128°C, and the temperatures of Ordovician inclusions in different drilling wells were different (see **Table 2**). There were also differences between different gas–liquid phase inclusions in the same well. For example, the homogenization temperatures of the LG106 gas–liquid phase 1 and gas–liquid phase 2 inclusions were in the ranges of 66–90°C and 78–105°C, respectively (**Table 2**). Overall, the highest temperature in the measured samples was 128°C (**Table 2**, **Figure 5**), the number of such inclusions was small, and there were no extremely high-temperature inclusions (>140°C). This may be related to the small number of samples and the sampling location. According to previous studies, the maximum homogenization temperature of the two-phase gas–liquid brine

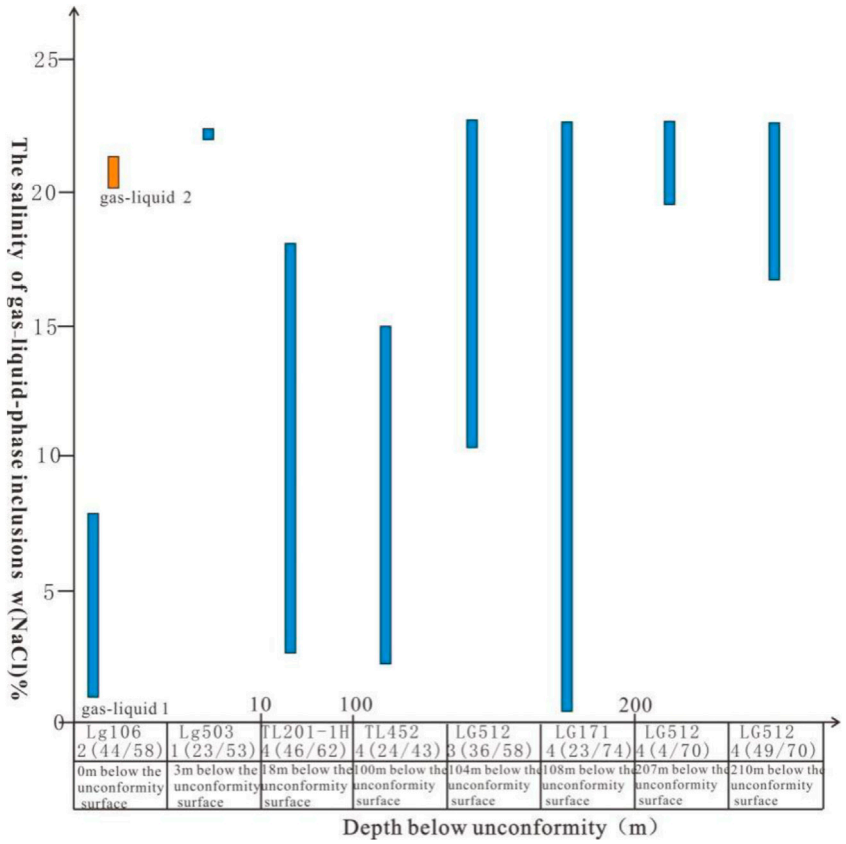

FIGURE 4 | Salinity distribution of gas–liquid inclusions in the northern slope of the Tazhong area.

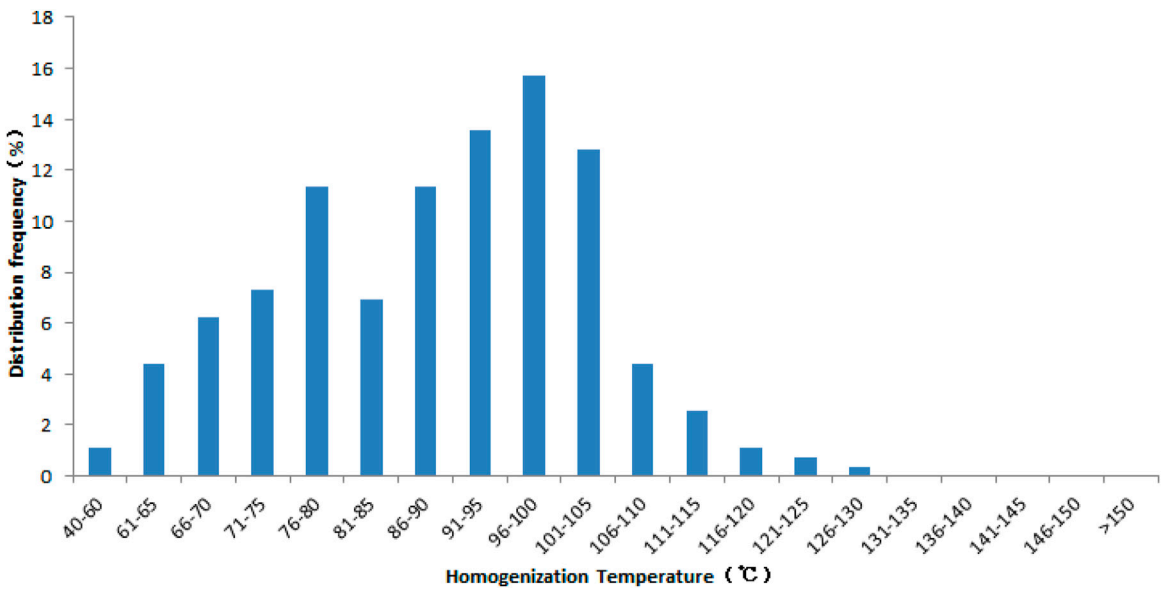

FIGURE 5 | Homogenization temperature distribution of inclusions in calcite from the northern slope of the Tazhong area.

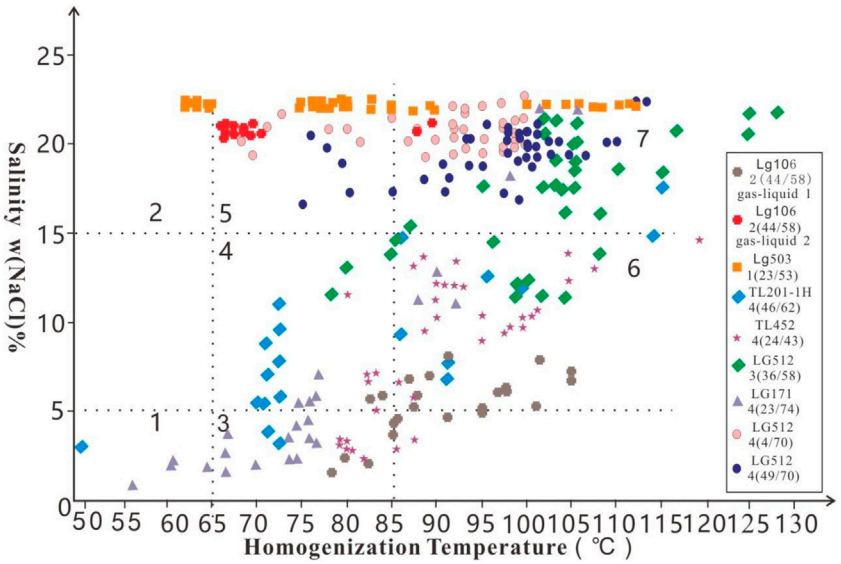

FIGURE 6 | Salinity–homogenization temperature intersection diagram of the two-phase gas–liquid brine inclusions in the northern slope of the Tazhong area, 1-low temperature and low-salinity inclusions; 2-low-temperature and high-salinity inclusions; 3-medium-temperature and low-salinity inclusions; 4-medium-temperature and medium-salinity inclusions; 5-medium-temperature and high-salinity inclusions; 6-high temperature and medium–salinity inclusions; and 7-high-temperature and high-salinity inclusions.

inclusions in the northern slope of the Tazhong area can reach 200°C (Quan, 2020). This shows that there may be an abnormal high-temperature fluid in this area; however, the scope of action is limited. No corresponding samples were obtained this time. On the other hand, low-temperature inclusions were visible (<65°C), and some inclusions had a temperature of only 49°C, for example, in samples close to the unconformity surface such as wells tl201-1h, lg171, and lg503.

Based on the statistical distribution proportion, the main homogenization temperatures of the inclusion formation were found to be in the ranges of 65–85°C and 85–110°C (**Figure 5**). 1) 65–85°C section: The main peak temperature of the inclusion formation was in the range of 75–80°C, which was the main period for the formation of inclusions and karst fillings. 2) 85–110°C section: The main peak temperature of the inclusion formation was in the range of 95–100°C, which was the main period for the formation of inclusions and karst fillings.

4.2.3 Corresponding Characteristics of Homogenization Temperature and Salinity

Based on the salinity–homogenization temperature diagram (intersecting part) (**Figure 6**), 273 samples of eight samples were found to have generally increased temperature, increased salinity, low temperature, and low salinity; these can be divided into seven types of fluid genetic inclusions with different properties: 1) Low-temperature and low-salinity inclusions, 2) Low-temperature and high-salinity inclusions: the homogenization temperature of the two types of inclusions was less than 65°C, the salinity of the low-salinity inclusions was in the range of 0.88–5%, and the salinity of the high-salinity inclusions was in the range of 15–23%; 3) Medium-temperature and low-salinity inclusions, 4) Medium-temperature and medium-salinity inclusions, 5) Medium-temperature and high-salinity inclusions: the homogenization temperature of the above mentioned three types of genetic inclusions was in the range of 65–85°C; however, the salinity value gradually changed from 0.88–5% to 15–23%; 6) High-temperature and medium-salinity inclusions, and 7) High-temperature and high-salinity inclusions. The formation temperature of the above mentioned two types of inclusions was in the range of 85–110°C or even higher, and the salinity was in the range of 5–22%.

Through the analysis of the homogenization temperature and salinity of a single well (**Figure 7**), it is found that the closer to the unconformity surface, the greater the development of the low-temperature and low-salinity inclusions will be; in comparison, the farther away from the unconformity surface, the greater the development of the high-temperature and high-salinity inclusions will be. In addition, the single-well analysis shows that multistage fluid inclusions are recorded in the calcite contained in the sample, and there are more stages near the unconformity. The LG106 2 (44/58) sample was taken from the fracture-cavity calcite near the weathering surface (**Figure 7C**). Gas–liquid phase 1 had a low-medium salinity (some parts had lower and some parts had higher salinity than seawater), with the peak homogenization temperature in the range of 60–70°C. Therefore, the inclusions were of medium temperature and low salinity (**Figure 7C**), with the lowest salinity <3.5%. Similar medium-temperature and low-salinity inclusions also existed in the sample taken from TL452 3 (22/43) (**Figure 7B**). However, the inclusions in the sample taken

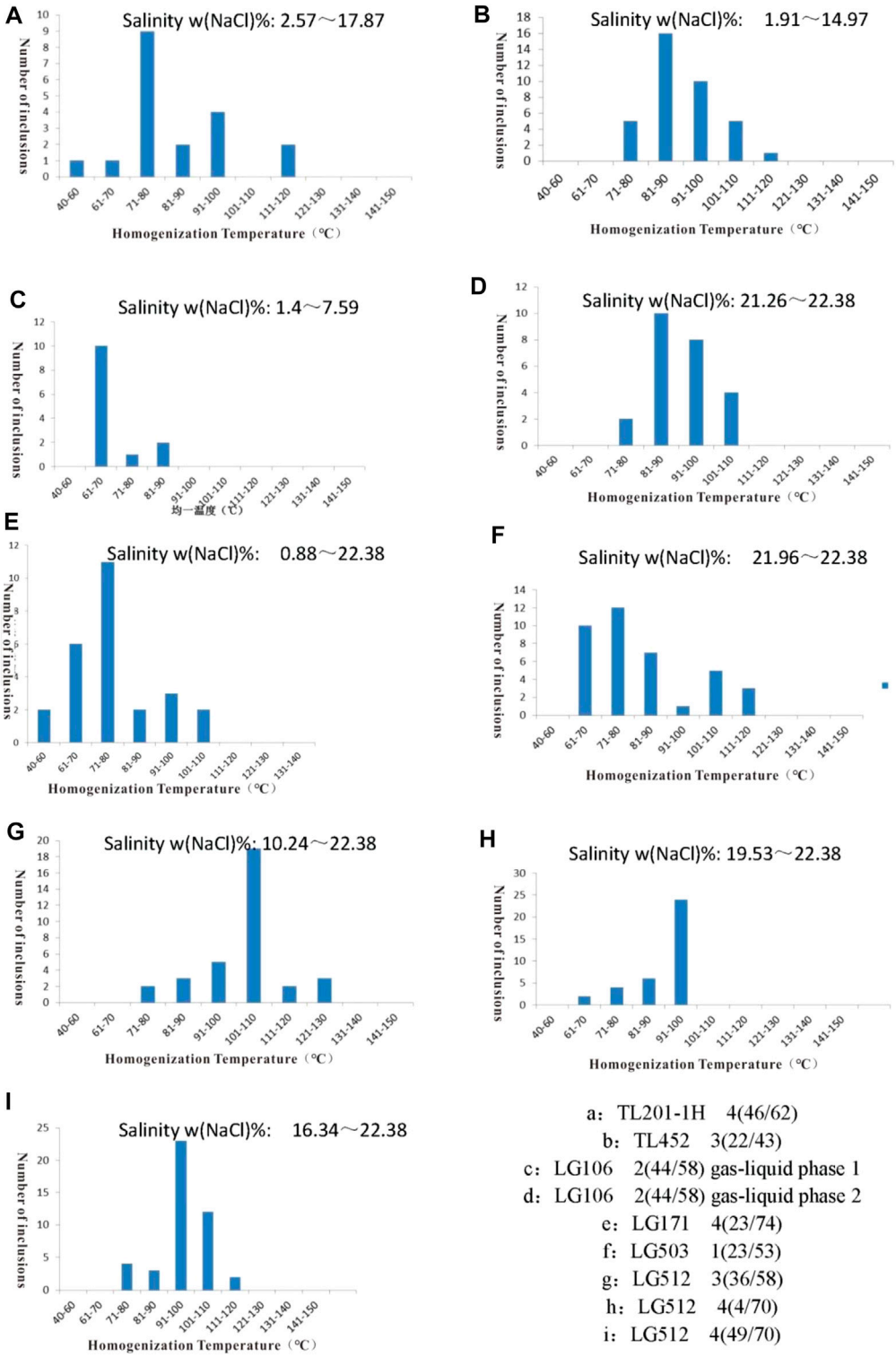

FIGURE 7 | Corresponding relationship between the homogenization temperature and salinity of the inclusions in the northern slope of the Tazhong area. **(A)** Samples taken from TL201-1H 4 (46/62); **(B)** TL452 3 (22/43); **(C)** LG106 2 (44/58), gas–liquid phase 1; **(D)** LG106 2 (44/58), gas–liquid phase 2; **(E)** LG171 4 (23/74); **(F)** LG503 1 (23/53); **(G)** LG512 3 (36/58); **(H)** LG512 4 (4/70); and **(I)** LG512 4 (49/70).

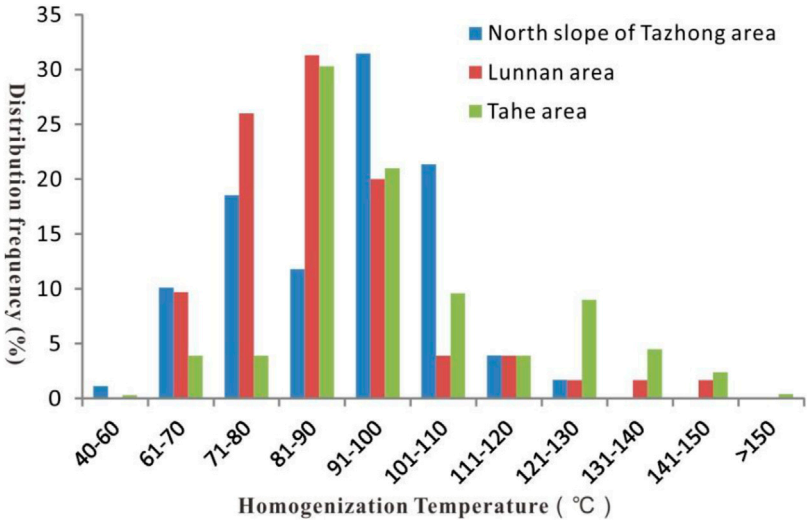

FIGURE 8 | Homogenization temperature distribution of inclusions in Tahe and Lunnan areas, northern Tarim Basin (Dan et al., 2015).

from LG106 2 (44/58) were of high salinity, filled in gas–liquid phase 2, and formed by another period of fluid activity (**Figure 7D**). **Figure 6A** shows the result of the sample taken from TL201-1H 4 (46/62). It was taken from the calcite associated with mud in a cave 18 m below the weathering crust surface. The salinity and homogenization temperature were widely distributed, with the lowest temperatures <65°C. Therefore, the conditions made it possible for the low-temperature and low-salinity and low-temperature and medium-salinity inclusions. In addition, medium-temperature (70–80°C) and high-temperature (110–120°C) inclusions can be seen. The sample LG171 4 (23/74) was taken from the calcite in the dissolved fracture, which was 108 m below the unconformity surface, with a salinity range of 0.88–22.38% and a temperature range of 40–110°C. All types of inclusions existed in this sample, showing the characteristics of continuous fluid activity in multiple periods (**Figure 7E**). Three LG512 samples were taken from the calcite in the dissolution fractures 104, 207, and 210 m below the unconformity surface. The inclusions were mainly of high-temperature and medium–high salinity, with no occurrence of low-temperature and low-salinity inclusions (**Figures 7G–I**).

5 DISCUSSION

5.1 Fluid Activities on Calcite Formation in the Tazhong Area

Dan et al. (2015) found that the peak homogenization temperatures of inclusions in Tahe and Lunnan Oilfields in the Tarim Basin were in the ranges of 85–95°C and 80–90°C, respectively. The inclusions were formed in the similar temperature range in Tahe and Lunnan areas (**Figure 8**). Evidently, the peak homogenization temperature (90–100°C) of most inclusions in the Tazhong area was higher than that in the previously mentioned two areas. This indicates that the tectonic settings of Tahe and Lunnan were similar and that the diagenetic fluid activity was the same during the burial diagenetic period, while it was different in the Tazhong area. In addition, high-temperature (>140°C) inclusions were found in the Tahe and Lunnan Oilfields, indicating the influence of hydrothermal activity. However, no such high-temperature inclusions were found in the samples taken from the Tazhong area. The formation of karst fractures and caves in the Yingshan Formation in this area might be less affected by abnormally high-temperature hydrothermal fluid activities, but predominantly by the fluid activities during the normal burial period. Moreover, there were low-temperature (<65°C) inclusions in the three areas, indicating that they were all influenced by the low-temperature fluid activities during the exposure period.

5.2 Karst and Filling Stages and Fluid Properties in the Tazhong Area

Based on the tectonic background and division of fracture stages in the core, the Tazhong area is found to have experienced multistage tectonic movement, resulting in fluid activity, fracture, karst, and filling of carbonate rocks. In the Middle–Late Ordovician exposure period, the mud in the fracture cave was filled with calcite, and in the Middle–Late Ordovician and Silurian Devonian, the filling was fracture calcite. The inclusion test showed two stages of fluid activity after the formation of the fracture cave and fracture. The homogenization temperatures of the inclusions were analyzed from the burial history map of the area. The two homogenization temperature ranges of the inclusions were just in the two burial periods of Middle Hercynian and Late Hercynian (**Figure 9**). In the Caledonian period, the dissolution fracture cave formed by karst and the fracture formed by Silurian Devonian tectonic activity were exposed, and two large-scale fillings occurred in the Middle Hercynian and Late Hercynian periods.

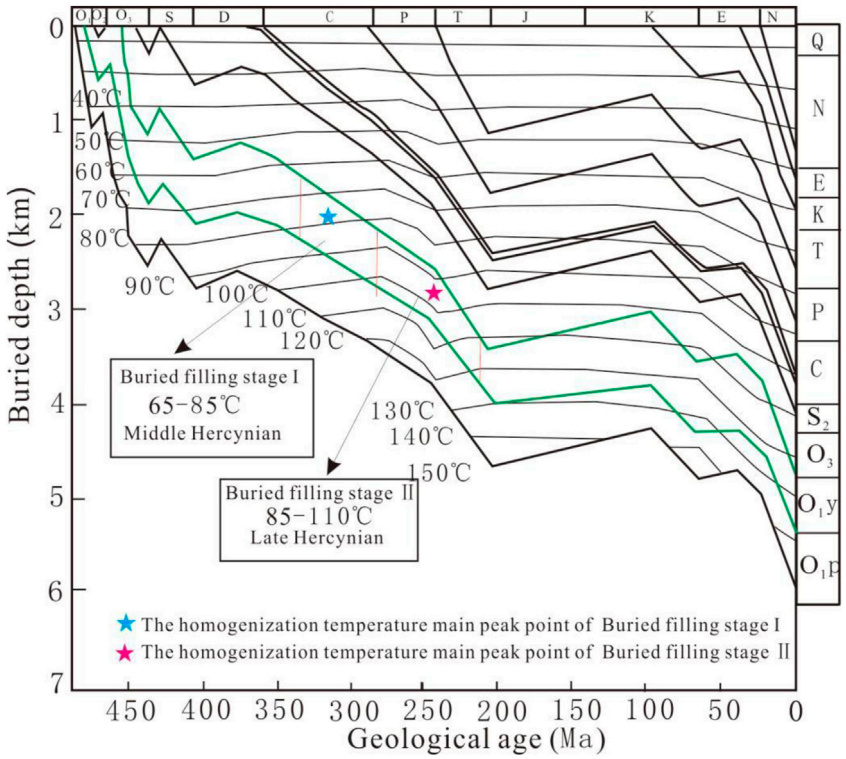

FIGURE 9 | Burial history map of the Ordovician Karst stage from Well TL162 in the Tazhong area (Base Map Burial History Map by (Zhao et al., 2007).

In addition, many evidences point to low-temperature low-salinity karsts in the Yingshan Formation exposure period in this area, and many types of fluids were identified:

1) A large number of irregularly distributed liquid-phase inclusions were formed in the calcite crystals (**Table 1**). The liquid-phase inclusions might have been formed by the leakage of multiphase inclusions due to the late tectonic action or by the formation of inclusions in an environment where the temperature is lower than 50°C (Wu et al., 2010). This low-temperature environment did not produce gas-phase inclusions. Therefore, it can be inferred that part of the liquid-phase inclusions was formed in the normal-temperature environment, that is, these inclusions were formed on the surface or near the surface in the Middle Caledonian period.
2) The homogenization temperature of the inclusions was lower than 65°C, and the lowest temperature was 49°C. Wu et al. (2010) also considered that 50–65°C can be classified as the temperature range near the surface subsurface flow zone. Based on the analysis of the burial history map, these inclusions were also exposed to the surface or near the surface in the Middle Caledonian (**Figure 9**). The salinity analysis showed that the low-temperature inclusions were of low or high salinity, reflecting the existence of freshwater or seawater karst environment, while the surface was exposed in the Middle Caledonian period.
3) Some medium-temperature inclusions (65–85°C) had extremely low salinity (**Figures 7B,C**), which was lower than that of seawater. Liu et al. (2008) found that the existence of freshwater salinity indicated the formation of calcite in the low-temperature environment of surface karst. Moreover, the freshwater salinity indicated that the inclusions were affected by the rebalancing effect, which caused an increase in the homogenization temperature. However, the fluid in some inclusions did not exchange heat with the outside environment, and the salinity of the fluid remained the same.

Through the above mentioned analysis, it can be found that there were three main stages of karst or filling development in the Yingshan Formation in the Tazhong area: Middle Caledonian exposed karst, Middle Hercynian buried filling, and Late Hercynian buried filling. The calcite formed by Middle Caledonian exposed karst mainly comprised three types of liquid-phase inclusions: low-temperature low salinity, medium-temperature low salinity, and low-temperature high-salinity inclusions. The calcite inclusions formed in the Middle Hercynian buried filling were dominated by medium-temperature medium-salinity inclusions and medium-temperature high-salinity inclusions. The calcite inclusions formed in the Late Hercynian buried karst were dominated by high-temperature medium-salinity inclusions and high-temperature high-salinity inclusions.

TABLE 3 | Types of inclusions and paleokarst environment in the northern slope of Tazhong area.

Inclusion type		Homogenization T (°C)	Karst system	Paleo environment	Formation period
Liquid Phase	Normal	Freshwater/seawater	Exposed freshwater/seawater karst	Middle Caledonian	
Gas–liquid phase	LTLS[a]	<65	Salinity 0.88–5%	Exposed freshwater karst	
	MTLS[a]	65–85	NaCl-KCl-H_2O system		
	LTMS[a]	<65	Salinity 5–15%, NaCl-$CaCl_2$-H_2O or NaCl-$MgCl_2$-H_2O system	Exposed seawater karst	
	MTMS[a]	65–85	Salinity 5–15%, NaCl-$CaCl_2$-H_2O or NaCl-$MgCl_2$-H_2O system	Buried filling stage I	Middle Hercynian
	MTHS[a]		Salinity 15–22.38%, $CaCl_2$-H_2O or NaCl-$CaCl_2$-H_2O system		
	HTMS[a]	85–110	Salinity 5–15%, $CaCl_2$-H_2O-$MgCl_2$ or NaCl-$MgCl_2$-H_2O system	Buried filling stage II	Late Hercynian
	HTHS[a]		Salinity 15–22.38%, $CaCl_2$-H_2O-$MgCl_2$ or NaCl-$MgCl_2$-H_2O system		

[a]*LTLS: low-temperature low-salinity; MTMS: medium-temperature medium-salinity; LTMS: low-temperature medium-salinity; MTMS: medium-temperature medium-salinity; MTHS: medium-temperature high-salinity; HTMS: high-temperature medium-salinity; HTHS: high-temperature high-salinity.*

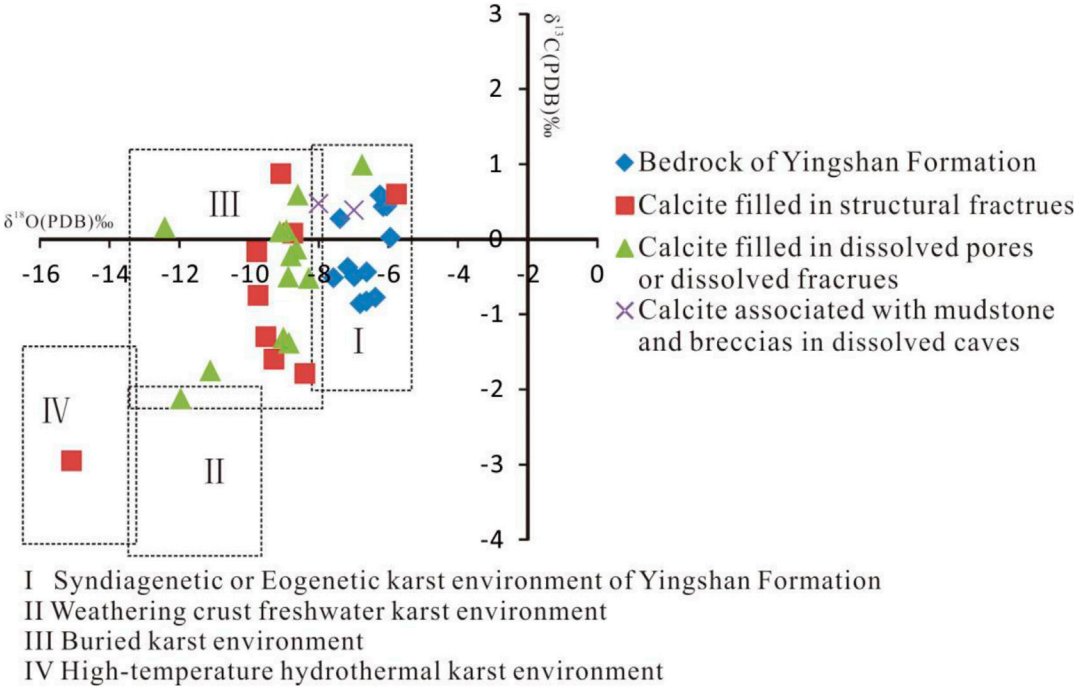

FIGURE 10 | Carbon and oxygen isotopic characteristics of fracture-cave calcite in the northern slope area of Tazhong (Dan et al., 2019).

Table 3 shows the specific stages and fluid parameters of each stage.

Dan et al. (2019) found that calcite was mainly formed in the Middle Caledonian syndiagenetic or eogenetic karst environment and burial environment, and small amounts of calcite were formed in the buried high-temperature environment and Middle Caledonian weathering crust karst environment (**Figure 10**). A large number of structural fractures and solution fracture calcite were formed during burial, and the cave was filled with mud. Calcite was developed in the exposure environment of early diagenetic mixed water, consistent with the inclusion data.

5.3 Indication of Paleokarst Reservoir Development

Most of the fracture-cavity reservoirs in the northern slope of the Tazhong area were filled with mud, which had a significant

influence on reservoir development. Through the testing of calcite inclusions associated with mud in the TL201-1H karst cave, the main karst fluids formed in this area can be accurately determined. Furthermore, when testing the TL201-1H sample, low-temperature low-salinity inclusions and low-temperature medium-salinity inclusions were found (**Figure 6A**), proving the existence of freshwater and seawater fluids in these fractures and caves. These results correspond to the results of cathodoluminescence analysis. Limestone grain edges and cements in the TL201-1h inclusions showed bright luminescence, reflecting the influence of meteoric water. The associated calcite cathodoluminescence was dark, reflecting the influence of seawater (**Figure 2J**). In addition, Dan et al. (2019) found the presence of carbon and oxygen isotopes of calcite associated with mud in another well, showing similar results of bedrock and also reflecting the characteristics of early karst environment (**Figure 10**). The above mentioned results showed that eogenetic karstification may be the key factor in the formation of reservoirs in the Tazhong area.

After the formation of the early diagenetic karst fracture cave reservoir in central Caledonia and the formation of the structural fracture reservoir caused by Silurian Devonian strike slip, the large-scale calcite growth in the middle Hercynian and Late Hercynian burial periods reflected by the inclusions was studied, as discussed in **Section 5.2**. The results point to further filling of the early fracture cave reservoir, reduction in reservoir space, and enhancement in reservoir heterogeneity.

6 CONCLUSION

A test was conducted on calcite inclusions in the fracture cave of the northern slope of the Tazhong area. The results showed that most of the inclusions were single-liquid phase and gas–liquid two-phase inclusions, while some of them contained gas-phase or liquid-phase hydrocarbons. The inclusions assumed various shapes, mainly in free form, small groups, and distributed along microfractures in the crystal. The number of single liquid-phase inclusions was more than that of two-phase gas–liquid inclusions. The two-phase gas–liquid inclusions in the study area could be divided into seven types: low-temperature low-salinity; low-temperature high-salinity; medium-temperature low-salinity; medium-temperature medium-salinity; medium-temperature high-salinity; high-temperature medium-salinity; and high-temperature high-salinity inclusions. They have the characteristics of positive correlation between high temperature and high salinity and low temperature and low salinity. The closer to the unconformity surface, the greater the development of low-temperature and low-salinity inclusions will be; the further away from the unconformity surface, the greater the development of high-temperature and high-salinity inclusions will be. Based on a comprehensive analysis of the burial history, three stages of fluid action were judged in the northern slope of the Tazhong area: Middle Caledonian exposed karst stage, Middle Hercynian buried filling stage I, and Late Hercynian buried filling stage II. By testing the calcite inclusions associated with mud in the karst cave and combining with previous research, it is judged that the Middle Caledonian period is associated with early diagenetic atmospheric fresh water and seawater karstification, which is key to the formation of karst reservoirs in this area. Two instances of burial filling in the Middle and Late Hercynian periods destroyed the reservoir and led to enhanced reservoir heterogeneity.

DATA AVAILABILITY STATEMENT

The original contributions presented in the study are included in the article/Supplementary Material, further inquiries can be directed to the corresponding author.

AUTHOR CONTRIBUTIONS

Conceptualization: YD and GN; methodology: YD; formal analysis: YD; investigation: BL, QZ and GN; writing—original draft preparation: YD; writing—review and editing: JB and YD; project administration: BL; All the co-authors performed a critical revision of the intellectual content of the study.

FUNDING

This research was funded by the Natural Science Foundation of Guangxi, China (2020GXNSFAA297095, 2021AB29005, 2020AB22013), the National Key R&D Program of China (No. 2018YFC0604301, 41902261), the Nonprofit Industry Research Program of the Chinese Academy of Geological Sciences (YYWF201723), the Geological Survey Program of the China Geological Survey (DD20190723, DD20221658), the basic research program of Institute of Karst Geology, Chinese Academy of Geological Sciences (2020012, 2020018).

ACKNOWLEDGMENTS

Prof. Pan Wen-Qing and Senior Engineer Zhang Zheng-Hong of the Research Institute of Exploration and Development at Tarim Oilfield Company of Petro China have been of great assistance during the core observations and sample collection processes.

REFERENCES

Bodnar, R. J. (1992). *Revised Equation and Table for Freezing point Depressions of H2O-Salt Fluid Inclusions*. Program and Abstracts. Lake Arrowhead, CA: Geoarabia Journal of the Middle East Petroleum Geosciences. 14, 15.

Boni, M. (1986). The Permo-Triassic Vein and Paleokarst Ores in Southwest Sardinia: Contribution of Fluid Inclusion Studies to Their Genesis and Paleoenvironment. *Mineralium Deposita* 21 (1), 53–62. doi:10.1007/BF00204362

Cai, C. F., Li, K. K., Cal, L. L., Li, B., and Jiang, L. (2009). Geochemical Characteristics and Origins of Fracture-And Vug-Fillings of the Ordovician in Tahe Oilfield, Tarim Basin. *Acta Petrologica Sinica* 25 (10), 2399–2404.

Chen, H. H., Li, C. Q., and Zhang, X. M. (2003). The Use of Fluid Inclusions to Determine Tahe Oil and Gas Accumulation Periods and the Main Accumulation Period. *Earth Sci. Front.* 10 (1), 265–270.

Chen, H. H., Wu, Y., and Zhu, H. T. (2016). Eogenetic Karstification and Reservoir Formation Model of the Middle-Lower Ordovician in the Northeast Slope of Tazhong Uplift (In Chinese with English Abstract), Tarim Basin. *Acta Petrolei Sinica*, 1231–1246. doi:10.7623/syxb201610003

Chen, X. S., Yi, W. X., and Lu, W. Z. (2004). The Paleokarst Reservoirs of Oil/Gas Fields in China. *Acta Sedimentologica Sinica* 22 (2), 243–252.

Dan, Y., Liang, B., and Cao, J. W. (2012). Geochemical Features and Environmental Significances of Deposits in Ordovician Karstic Fractures and Caves, Lunnan Area, Tarim Basin. *Pet. Geology. Exp.* 34 (6), 623–628. doi:10.11781/sysydz201206624

Dan, Y., Liang, B., Cao, J. W., Zhang, Q. Y., and Hao, Y. Z. (2015). Eogenetic Karstification in Carbonatite and its Significance for Hydrocarbon Geology. *Carsologica Sinica* 34, 126. doi:10.11932/karst20150205

Dan, Y., Lin, L., Liang, B., Zhang, Q., Cao, J., and Li, J. (2019). Geochemistry of the Fracture-Cave Calcite of the Ordovician Yingshan Formation and its Paleokarst Environment in the Tazhong Area, Tarim Basin, China. *Carbonates Evaporites* 34, 1511–1524. doi:10.1007/s13146-019-00500-8

Dan, Y., Lin, L., Liang, B., Zhang, Q., Yu, Y., Cao, J., et al. (2018). Eogenetic Karst Control of Carbonate Reservoirs During a Transient Exposure: a Case Study of the Ordovician Yingshan Formation in the Northern Slope of the Tazhong Uplift, Tarim Basin, China. *Minerals* 8 (8), 345. doi:10.3390/min8080345

Dan, Y., Nie, G., Liang, B., Zhang, Q., Li, J., Dong, H., et al. (2021). The Source of Fracture-Cave Mud Fillings of the Ordovician Yingshan Formation and its Paleokarst Environment in the Northern Slope of the Tazhong Uplift, Tarim Basin, China: Based on Petrology and Geochemical Analysis. *Minerals* 11 (12), 1329. doi:10.3390/min11121329

Feng, R., Ouyang, C., Pang, Y., Li, Z., Luo, X., Zhang, Q., et al. (2014). Evolution Modes of Interbedded Weathering Crust Karst: A Case Study of the 1 St and 2 Nd Members of Ordovician Yingshan Formation in EPCC Block, Tazhong, Tarim Basin. *Pet. Exploration Dev.* 41, 49–59. doi:10.1016/s1876-3804(14)60005-7

He, J., Han, J. F., and Pan, W. Q. (2007). Hydrocarbon Accumulation Mechanism in the Giant Buried Hill of Ordovician in Lunnan Paleohigh of Tarim Basin. *Acta Petroleo Sinica* 28 (2), 44–48. doi:10.1016/S1872-5813(07)60034-6

Lan, X., Lü, X., Zhu, Y., Yu, H., Zhou, J., and Zhu, F. (2014). Characteristics and Differential Accumulation of Oil/Gas in Lower Paleozoic Marine Carbonate on Northern Slope of Tazhong Low Rise, Tarim Basin, NW China: a Case Study of Lower Ordovician Yingshan Formation. *Arab J. Geosci.* 7, 4487–4498. doi:10.1007/s12517-013-1091-2

Liu, C. G., Zhang, Y., and Lu, H. T. (2008). Genesis and Evolution of Gigantic Calcites in Paleokarstic Caves of Middle-Lower Ordovician in Tahe Oilfield. *Geol. Sci. Tech. Inf.* 27 (4), 33–38.

Liu, D. H., Lu, H. Z., and Xiao, X. M. (2007). *The Application of Fluid Inclusions in Oil and Gas Exploration Research [M]*. Guangzhou: Guangdong Science and Technology Press, 9–19.

Liu, X. (1991). Carbonate Rock and mineral Inclusions in Logistics the Main Body of Research Method and its Application. *Exp. Pet. Geology* 13 (4), 399–401. doi:10.11781/sysydz199104399

Lu, H. Z. (1990). *Fluid Inclusion Geochemistry*. Beijing: Geological Publishing House, 6–53.

Ni, X. F., Shen, A., and Pan, W. Q. (2013). Geological Modeling of Excellent Fractured-Vuggy Carbonate Reservoirs: A Case Study of the Ordovician in the Northern Slope of Tazhong Palaeouplift and the Southern Area of Tabei Slope, Tarim Basin. *Pet. Exploration Dev.* 40, 414–422. doi:10.1016/s1876-3804(13)60056-7

Pang, H., Chen, J., Pang, X., Liu, L., Liu, K., and Xiang, C. (2013). Key Factors Controlling Hydrocarbon Accumulations in Ordovician Carbonate Reservoirs in the Tazhong Area, Tarim Basin, Western China. *Mar. Pet. Geology* 43, 88–101. doi:10.1016/j.marpetgeo.2013.03.002

Quan, H. (2020). *Fluid Environment and Geological Model of Ordovician Reservoir in Northern Slope of Central Tarim Basin*. Beijing: China University of Petroleum.

Shu, Z. G., Zhu, Z. D., and He, X. P. (2008). Reservoir Characteristics of Palaeokarsts in the Tazhong Uplift. *Xinjiang Geology* 26 (3), 274–278. doi:10.3969/j.issn.1000-8845.2008.03.012

Wu, M., Zeng, C. B., and Huang, S. J. (2010). Fluid Inclusion Study of the Ordovician Carbonate Rock Reservoir in the Tahe Oilfield. *Geology China* 37 (5), 1360–1373. doi:10.3724/SP.J.1011.2010.01081

Xia, R. Y., Tang, J. S., and Zou, S. Z. (2006). The Northern Margin of the Tarim Basin Paleokarst Filling Characteristics of Fluid Inclusions. *Carsologica Sinica* 25 (3), 246–249.

Xia, R. Y., and Tang, J. S. (2004). Indication of Mineral Inclusion Characteristics to Palaeokarst Actions. *Acta Geosci. Sinica* 25 (3), 373–377. doi:10.1007/BF02911033

Xu, K., Liu, S., and Yu, B. S. (2012). Fracture Development Characteristics and Logging Responses of Ordovician Carbonate Reservoirs in the Tazhong Area of the Tarim Basin. *Chin. Foreign Energ.* 17 (9), 45–50.

Yan, X. B., Han, Z. H., and Li, Y. H. (2002). Reservoir Characteristics and Formation Mechanisms of the Ordovician Carbonate Pools in the Tahe Oilfield. *Geol. Rev.* 48, 619–626. doi:10.1080/12265080208422884

Yan, X. B., Li, T. J., and Zhang, T. (2005). Differences Between Formation Conditions of Ordovician Karstic Reservoirs in Tazhong and Tahe Areas. *Oil Gas Geology* 26 (2), 202–209. doi:10.3321/j.issn:0253-9985.2005.02.013

Yang, H. J., Han, J. F., and Sun, C. H. (2011). A Development Model and Petroleum Exploration of Karst Reservoirs of Ordovician Yingshan Formation in the Northern Slope of Tazhong Palaeouplift. *ActaPetrolei Sinica* 32, 199–205. doi:10.1007/s12182-011-0123-3

Yu, H. F., Bai, Z. K., and Deng, L. P. (2011). Determination and Geologic Significance of Yingshan Unconformity of Lower Ordovician in Tazhong Area, Tarim Basin. *Xinjiang Pet. Geology* 32, 231–234. doi:10.1007/s12182-011-0123-3

Zhang, Q. Y., Liang, B., and Qin, F. R. (2016). Environmental and Geochemical Significance of Carbon and Oxygen Isotopes of Ordovician Carbonate Paleokarst in Lunnan, Tarim Basin. *Environ. Earth Sci.* 75, 1074–1079. doi:10.1007/s12665-016-5882-0

Zhao, W. Z., Shen, A. J., Pan, W. Q., Zhang, B. M., Qiao, Z. F., and Zheng, J. F. (2013). A Research on Carbonate Karst Reservoirs Classification and its Implication on Hydrocarbon Exploration: Cases Studies from Tarim Basin. *Acta Petroleo Sinica* 29, 3213–3222. doi:10.1086/671395

Zhao, Z. J., Wang, Z. M., Wu, X. N., and Chen, X. S. (2007). Genetic Types and Distribution Forecast of Available Carbonate Reservoirs in Ordovician in the Central Area of Tarim Basin. *Pet. Geology. Exp.* 29 (1), 40–46. doi:10.1016/S1872-5813(07)60034-6

Zhu, G. Y., Zhang, S. C., Wang, H. H., Yang, H. J., Meng, S. C., and Gu, Q. Y. (2009). The Formation and Distribution of Deep Weathering Crust in North Tarim Basin. *Acta Petrologica Sinica* 25, 2384–2398. doi:10.1016/S1874-8651(10)60080-4

Conflict of Interest: The authors declare that the research was conducted in the absence of any commercial or financial relationships that could be construed as a potential conflict of interest.

frontiers | Frontiers in Earth Science

ORIGINAL RESEARCH
published: 27 April 2022
doi: 10.3389/feart.2022.892902

Characterization of Deep-Water Submarine Fan Reservoir Architecture: AB120 Reservoir in the Campos Basin

Chen Zhao[1], *Xiuquan Hu*[1,2]*, *Jianghan Li*[1], *Chi Yi*[1], *Jieyi Li*[1] *and Zhipeng Niu*[1]

[1]College of Energy Resources, Chengdu University of Technology, Chengdu, China, [2]State Key Laboratory of Oil and Gas Reservoir Geology and Exploitation, Chengdu University of Technology, Chengdu, China

OPEN ACCESS

Edited by:
Dongming Zhi,
PetroChina, China

Reviewed by:
Yong Dan,
Chinese Academy of Geological Sciences, China
Fei Ning,
SINOPEC Petroleum Exploration and Production Research Institute, China

***Correspondence:**
Xiuquan Hu
huxiuquan15@cdut.edu.cn

Specialty section:
This article was submitted to Economic Geology, a section of the journal Frontiers in Earth Science

Received: *09 March 2022*
Accepted: *11 April 2022*
Published: *27 April 2022*

Citation:
Zhao C, Hu X, Li J, Yi C, Li J and Niu Z (2022) Characterization of Deep-Water Submarine Fan Reservoir Architecture: AB120 Reservoir in the Campos Basin. Front. Earth Sci. 10:892902. doi: 10.3389/feart.2022.892902

The exploration of deep-water submarine fan reservoirs has become a prominent research area for hydrocarbon discovery and recovery. However, the high operational costs render efficient exploration of this type of reservoir crucial, and the pivotal foundation lies in studying reservoir architectures. A case study of deep-water submarine fans in the Albacora Leste oilfield in Brazil is presented along with a characterization of the underground reservoir architecture based on well-log and seismic model fitting. A sedimentary microfacies distribution model is systematically established for each reservoir based on a detailed stratigraphic framework with a well-seismic joint characterization method and various types of data (e.g., geological, well-log, and seismic data). The results are as follows: the sedimentary microfacies of the deep-water submarine fans in the study area can be subdivided into tongue-shaped-lobe, muddy-channel, sandy-channel, and contourite deposits. Owing to data abundance and quality constraints, the architecture of the target layer in the study area was characterized based on Level 4 architectural elements. The AB120 Reservoir consisted of three complex channels (I, II, and III) and two tongue-shaped complex lobes (I and II). Complex channels I and III were the first and last to be deposited, respectively, and complex lobe I was deposited earlier than complex lobe II. Complex channels II and III supply complex lobes I and II, respectively. Vertically, complex lobe II was composed of three single lobes formed at different stages, the youngest of which was distributed over the largest area. Complex lobe II has already been drilled and is currently under development. However, complex lobe I has not yet been developed. This study has great practical significance for the effective development of deep-water submarine-fan reservoirs in this area and is of considerable theoretical significance for the advancement of deep-water sedimentology.

Keywords: deep-water sedimentation, tongue-shaped lobes, Albacora Leste oilfield, sedimentary microfacies, architectural characterization

1 INTRODUCTION

Deep-water submarine fans are rich in oil and gas resources. High exploration and development costs and immature processing techniques prevented previous deep-water exploration efforts from receiving serious attention. As a result, global deep-water oil and gas resource development levels are low, and the potential amount of resources available is huge. Statistical data show that untapped oil and natural gas resources worldwide exceed 300×10^8 tons and 34×10^{12} m^3, respectively, demonstrating immense potential for discovery and recovery (Walker, 1978; Weimer and Link, 1991; Fetter et al., 2008; Yin, 2018; Liu et al., 2020; Wang L. et al., 2020; Gu et al., 2021; Li et al., 2021). Continual advancement in deep-water sandy oil and gas exploration theories and technologies, such as high-resolution three-dimensional (3D) seismic analysis and deep-sea drilling platforms, has allowed deep-water sedimentological research to attract growing attention worldwide (Gervais et al., 2006; Mann et al., 2007; Bhuiyan and Hossain, 2020; Gao et al., 2020; Sun et al., 2020; Wang W. et al., 2020; Tang et al., 2021; Zhao et al., 2021). Currently, deep-water submarine fans constitute an important area for hydrocarbon exploration and development.

The genetic mechanism of deep-water submarine fan deposition is very complex, including the transport process of turbidity currents, debris flows, and sliding-collapse blocks. These mechanisms form complex and diverse submarine fan deposition types e.g., turbidity fans which are a type of deep-water submarine fan (Zhang and Wu, 2019; Sajid et al., 2020). Romans et al. (2010) conducted an in-depth investigation on the evolution of the deep-water stratigraphic architecture in the Magallanes Basin in Chile and analyzed the relationship between architectural changes and intrinsic tectonic evolution. Zhao et al. (2012) introduced a technique to characterize deep-water turbidite channel reservoir architectures based on integrated well-log and seismic data. Following an investigation of a particular architectural model of turbidite channel systems, Liu et al. (2013) identified and subsequently established corresponding architectural models for different types of channel systems and analyzed their control factors, evaluation criteria, and spatial distribution patterns. Lin et al. (2014) examined the distribution patterns of composite sand bodies in the turbidite channels. Zhang et al. (2015) discussed variations in the physical properties of reservoirs in sinuous deep-water channel systems and their relevant control mechanisms. They identified rock texture, lithofacies, and channel architecture as the primary controlling factors responsible for variations in reservoir quality in sinuous deep-water channel systems. According to the water depth measurement data, Reimchen et al. (2016) determined the statistical relationship between the cross-sectional asymmetry and the plane shape of the bent curved channel, and determined the relationship between the geometric shape and the plane shape of the submarine channel. Using unsupervised neural network (UANN) to integrate artificial intelligence (AI) and fluid identification of seismic attributes, Obafemi et al. (2020) studied the structural characteristics of deep-water turbidite channels and submarine fan lobes of deep-water oil and gas reservoirs in Frem Oilfield, Niger Delta. Recent published research has focused primarily on turbidite channels and provides an in-depth examination of their architectural characteristics, structural models, and control factors. In contrast, attention to turbidite lobes remains inadequate, with the investigation of the architectural characteristics of their reservoirs still in its incipient stages. In this study, guided by a detailed stratigraphic framework, a sedimentary microfacies distribution model was systematically established for each reservoir in the study area through characterization based on integrated data (e.g., geological, well-log, and seismic data). With a focus on both turbidite channels and turbidite lobes, reservoir architectures are characterized in detail based on well-log and seismic model fitting.

2 GEOLOGICAL SETTING

The Campos Basin is located 120 km off the coast of Rio de Janeiro in southeast Brazil, and the basin is distributed both onshore and offshore, is approximately 500 km long and 150 km wide, and is the most prolific oil- and gas-producing basin in the country. Basement heights perpendicular to the continental margin separate the Campos Basin from its adjoining basins. Specifically, the Campos Basin is separated from the Espirito Santo Basin by the Victoria High in the north, and from the Santos Basin by the Cabo Frio High in the south (**Figure 1**). The tectonic evolution of the Campos Basin has undergone four stages: the pre-rift, rift, transitional, and drift stages. The Campos Basin is a typical Atlantic passive continental margin basin formed by the separation of South America from Africa. Sediments are deposited in the South Atlantic crust and become thicker eastward, forming a sedimentary wedge. (Bybee, 2006; Ma et al., 2011; Kang et al., 2018; Lima and De Ros., 2019; Pandolpho et al., 2021).

Three main sedimentary sequences have developed in the Campos Basin: the continental sequence of the rift stage, the rock-salt sequence of the transitional stage, and the marine sequence of the drift stage. There are three Oligocene-Miocene formations in the study area, which, from the bottom up, are CRT, Marlim, and Albacora. Albacora Formation was examined in the present study, and for simplicity, it was divided into six layers: Sq-AB250, Sq-AB210, Sq-AB140, Sq-AB120, Sq-AB110, and Mio400. Sq-AB120 is considered a primary example for illustration purposes and was further subdivided into three stratigraphic units: Sq-AB120-1, Sq-AB120-2, and Sq-AB120-3. In the western part of the study area, the stratum thickness of the target layer tends to become thinner from north to south; in the eastern part of the study area, the stratum thickness tends to become thicker from north to south; in the northern part of the study area, the stratum thickness changes in equal proportions from west to east, and there is a thinning trend. In the southern part of the study area, the stratum thickness varies unevenly from west to east. Overall, from southwest to northeast, the target layer appears to be thicker in the central region and thins out at both ends.

3 METHODS OF ANALYSIS

Based on a detailed stratigraphic framework, this study thoroughly characterized the single-well, sectional, and planar

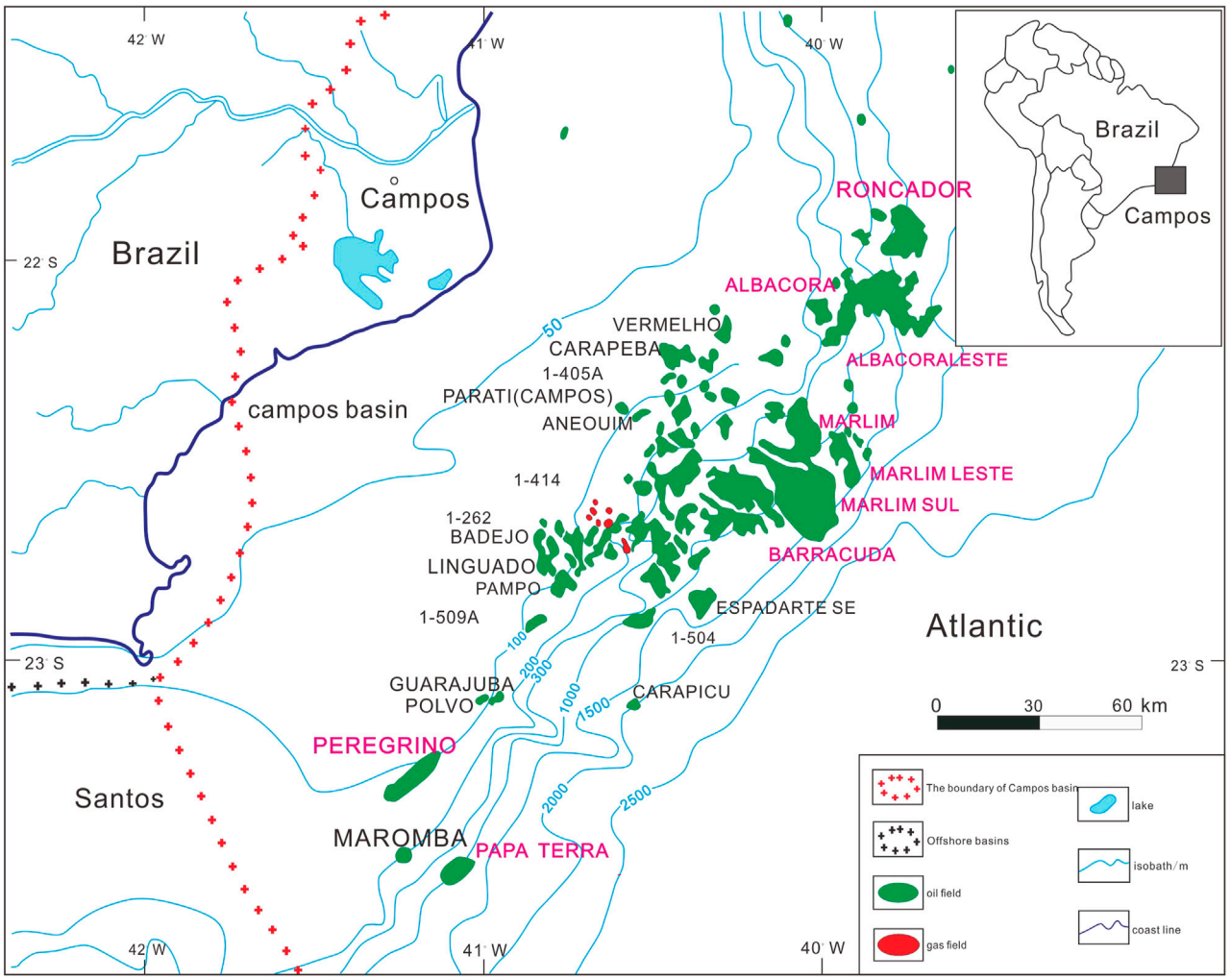

FIGURE 1 | Location of the Campos Basin and the distribution of the main oil and gas fields.

perspectives of the reservoir by analyzing the sedimentary microfacies types and their spatial distribution patterns using well-seismic technical methods and different types of data (e.g., geological, well-log, and seismic data). The types and characteristics of the sedimentary microfacies were identified with detailed analysis methods including: core description results, rock-electricity calibration, well-seismic calibration, determining the single-well interpretation and the sectional distribution patterns through integrated well-log and seismic sections along different directions, selecting the limit values of the seismic attribute corresponding to the sandstone facies, and estimating the macroscopic morphology of the sedimentary bodies with a truncation procedure. The results facilitate architectural characterization using a hierarchical system based on the abundance and quality of the data for the study area. Subsequently, a sedimentary model was used to characterize the single-well and sectional architecture of different sedimentary microfacies by identifying the boundaries of the architectural elements. Finally, the architectural elements were connected according to their geometrical relationships, and the detailed two-dimensional (2D) depiction of the architectural elements was completed.

The study area was 19 km^2. A detailed core description was provided for seven coring wells in the study area. A comprehensive histogram was plotted using the coring well combined with logging data, and a rock-electric model was established. A single-well phase interpretation was conducted for the remaining 53 uncoring wells. The study area was fully covered with 3D seismic data with good volume quality. The imaging of the target layer was good, and the signal-to-noise ratio was high, which can adequately fulfil the requirements of this reservoir architecture study. The fine seismic interpretation and tracking of three small layers of the AB120 Formation was conducted, with the interpretation accuracy reaching 10*10.

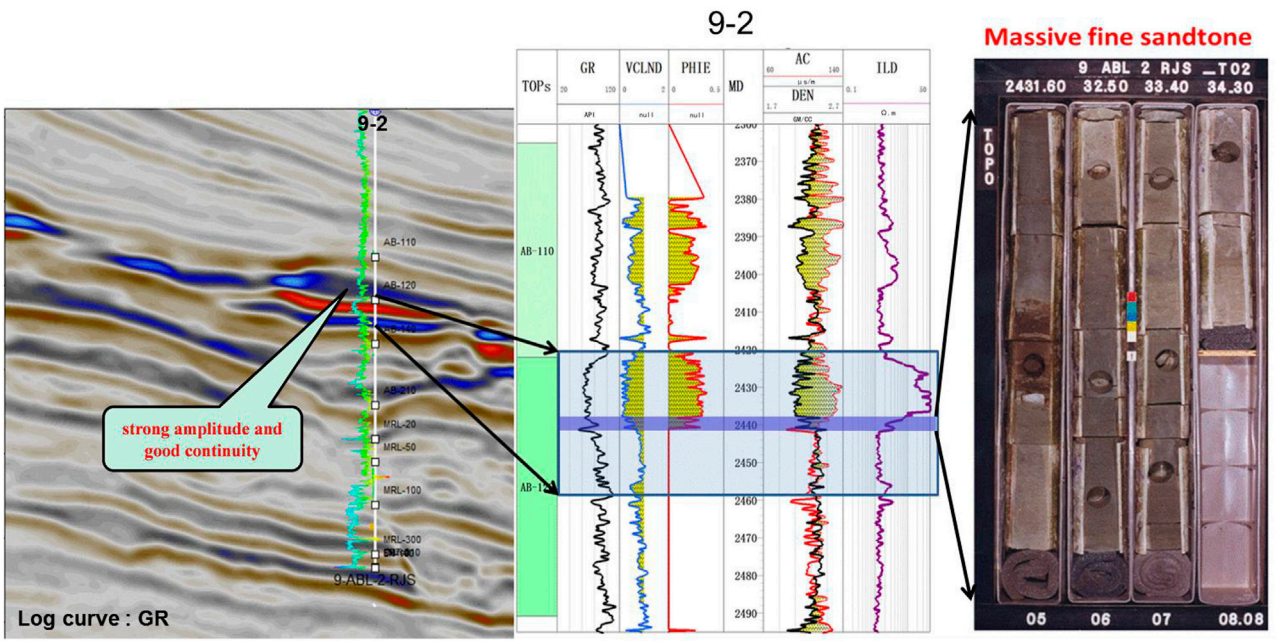

FIGURE 2 | Seismic response, logging and lithologic characteristics of the tongue-shaped lobes in AB120 reservoir.

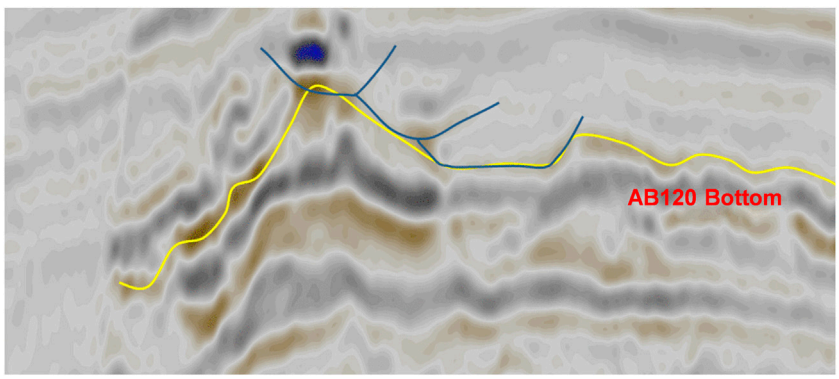

FIGURE 3 | Seismic response characteristics of the muddy channels.

Various seismic attributes were extracted including amplitude, coherence, and impedance. The correlation between mudstone thickness, sandstone thickness, sand-ground ratio, and other parameters and seismic attributes was calculated, and the corresponding limit value were determined for the sandstone facies. The sedimentary facies plan of the AB120 Formation was drawn based on well-seismic combination. The hierarchy of architecture characterization of the whole area was determined according to the number of coring wells, logging data and seismic data quality. Based on the detailed characterization of seismic profiles, single-well Level 3 architecture was characterized through lateral transformation features, seismic amplitude changes, sand body thickness changes. The architecture unit boundaries were identified according to the geometric relationships between each unit.

4 RESULTS AND DISCUSSION

4.1 Sedimentary Microfacies Analysis

Sedimentary environments and conditions govern sand bodies in terms of their level of development, spatial distribution, and internal structure. Sand bodies that formed in different sedimentary environments have different reservoir qualities. Sedimentary microfacies analysis can unequivocally reveal the macroscopic distribution of sand bodies.

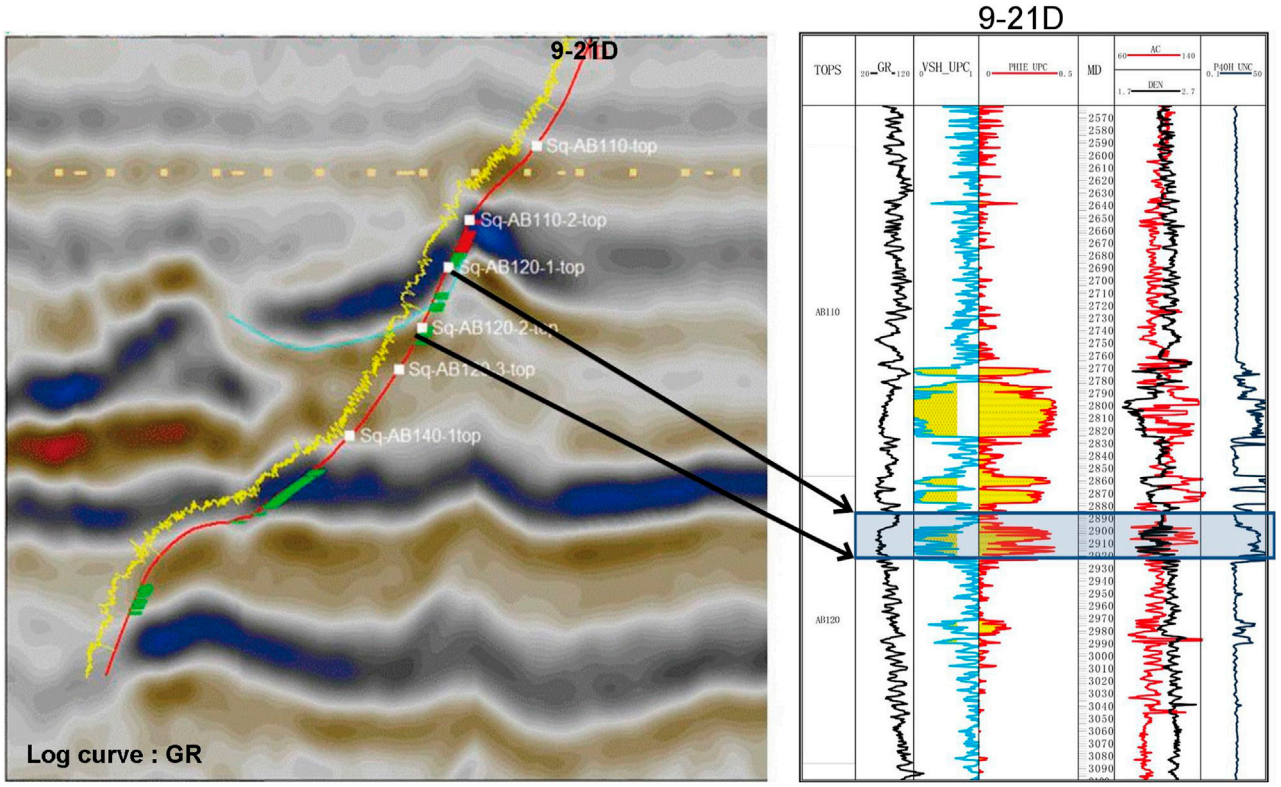

FIGURE 4 | Well-log and seismic response characteristics of the sandy channels.

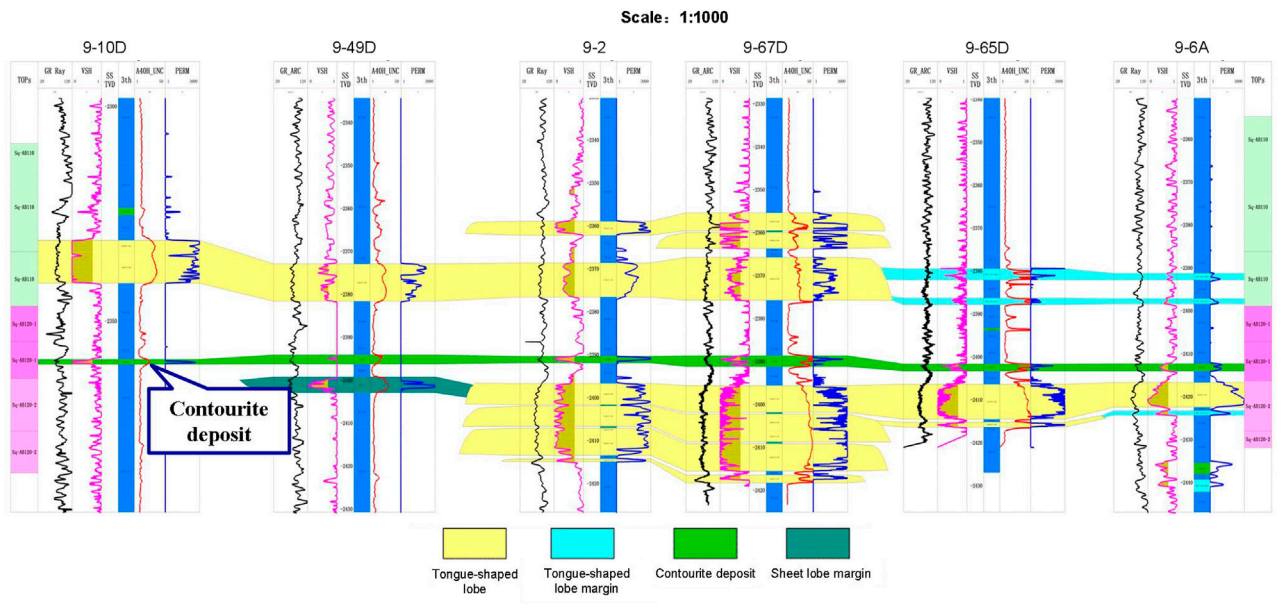

FIGURE 5 | Contourite deposits at the top of the AB120 reservoir.

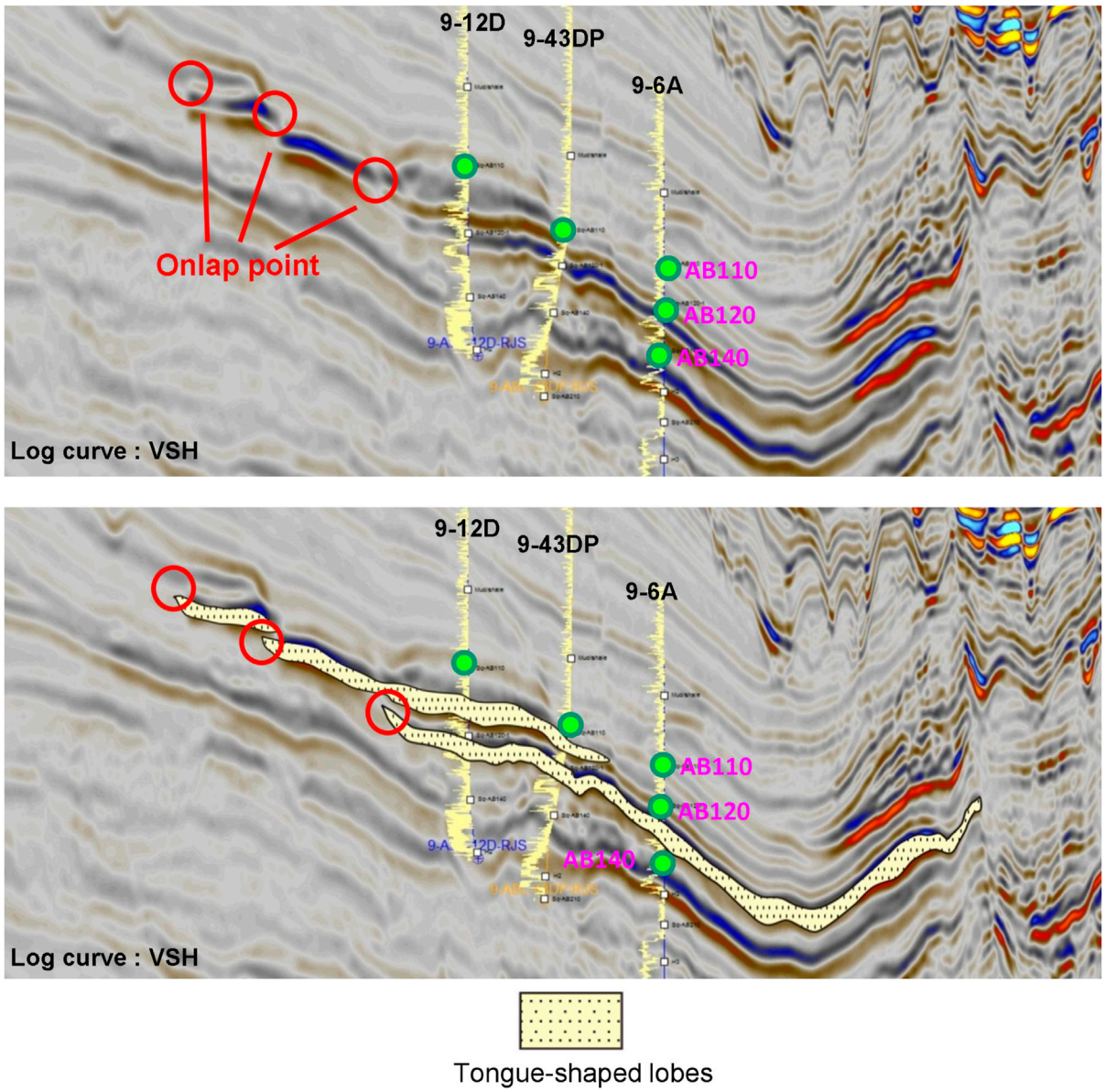

FIGURE 6 | Well seismic profile along the source direction of AB110—AB120 reservoir.

Provenance is an important tool for judging the distribution of sedimentary facies and sand body dispersion systems. The provenance of deep-water submarine fans can be roughly determined using channel direction (Li C. et al., 2017). The downcutting energy of the channel was strong in the western part of the study area, and the channel was distributed in a northwestern direction. In the central part of the study area, the downcutting capacity is weak to non-existent, and the channel is distributed in a northeastern direction. Constructing seismic profiles is also an important means to study provenance, and regression and overpass can indicate source direction (Pu et al., 2003; Liang et al., 2019). The overlapping points on the seismic profile of the combined well (**Figure 6**) show that the sand body receded in a northwestern direction, and the longitudinal extension scale of the sand body gradually decreased from bottom to top. Therefore, the provenance was from the northwest part of the study area. This agrees with the findings of Kang et al. (2018).

4.1.1 Sedimentary Microfacies Types

The AB120 Reservoir contains various types of sedimentary microfacies. In-depth analysis of the core, well-log, and seismic data revealed the presence of four main sedimentary microfacies in this reservoir: tongue-shaped lobes, muddy channels, sandy channels, and contourite deposits.

4.1.1.1Tongue-Shaped Lobes

The tongue-shaped lobes display a reverse rhythm, with a composition that transitions upward from thinly interbedded

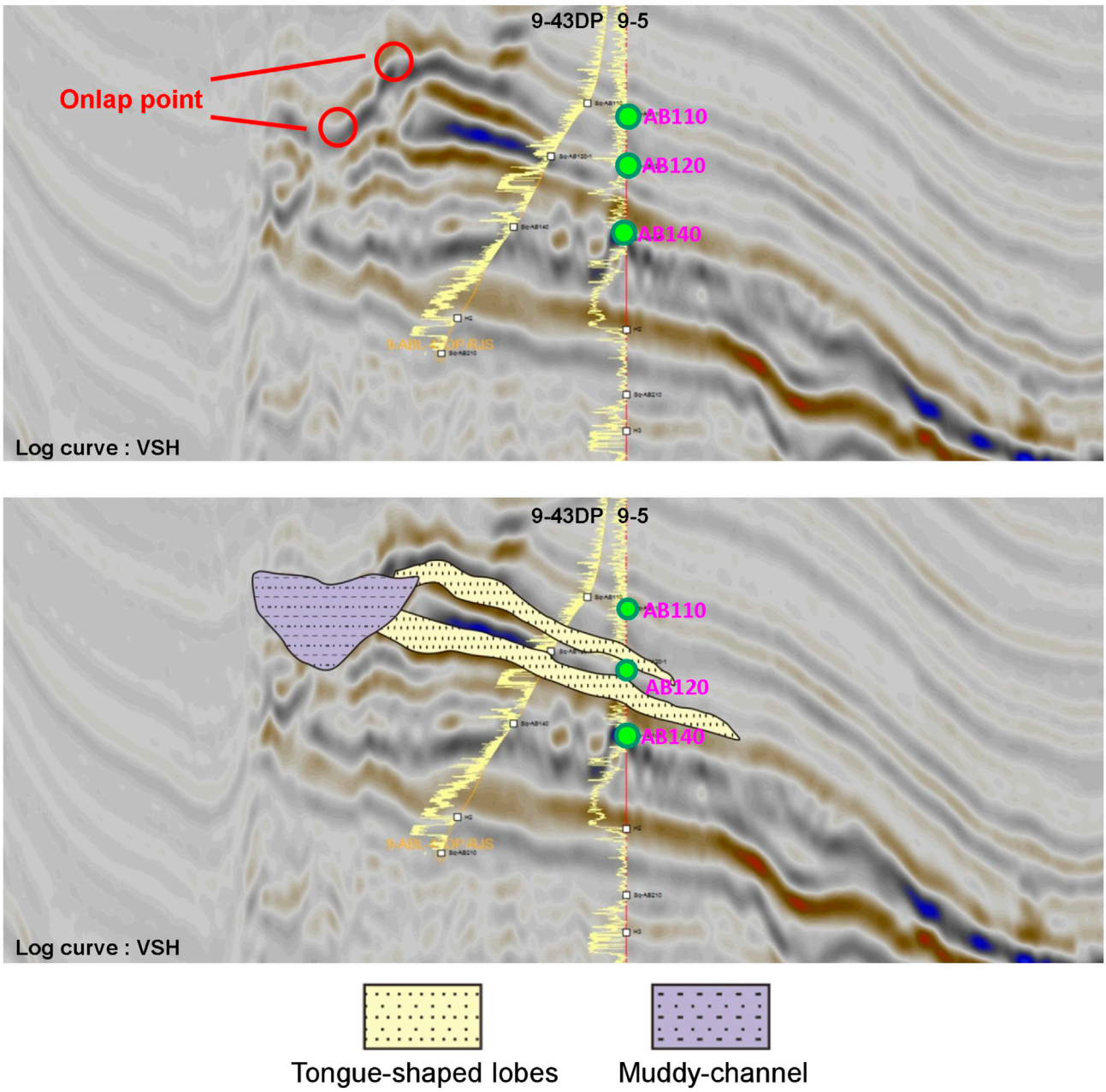

FIGURE 7 | Well seismic profile in the direction perpendicular to material source supply from AB110 to AB120 reservoir — near source end.

sandstone and mudstone to massive fine sandstone. Observation of the well-logs shows a typical funnel-shaped natural gamma ray (GR) pattern, low density, large arrival-time difference, and high electrical resistance in the reservoir segment, suggesting good reservoir quality. The seismic response of the tongue-shaped bodies was characterized by distinctly high-amplitude and continuous reflections (**Figure 2**).

4.1.1.2 Muddy Channels

No cores were retrieved from the muddy channels in the study area. Analysis of the extracted 3D root-mean-square (RMS) amplitude map for the AB120 Formation revealed distinct connections between the channels and tongue-shaped lobes in the western part of the study area, corresponding to low-amplitude reflections. This suggests that the channels were filled with muddy sediment. A section perpendicular to the source direction was taken at the suspected location where the channels had developed to confirm this. An analysis of this section of the AB120 Formation reveals a vertical low-amplitude, imbricate reflection structure, which is characteristic of a typical cut, and a stacked muddy channel complex (**Figure 3**).

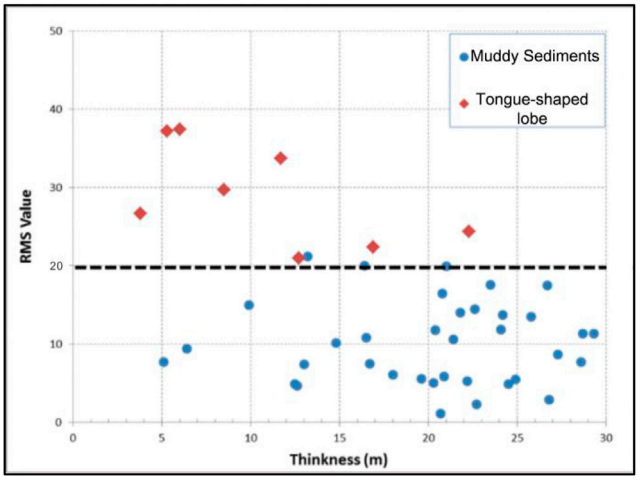

FIGURE 8 | Relationship between thickness and RMS amplitude of different microfacies in AB120 reservoir.

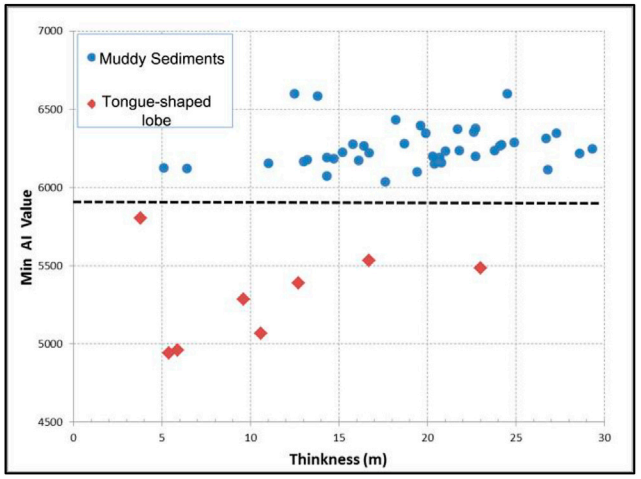

FIGURE 9 | Relationship between thickness and minimum impedance of different microfacies in AB120 reservoir.

4.1.1.3 Sandy Channels

The sandy channels primarily consist of massive fine sandstone and display a positive rhythm. Specifically, from the bottom up, they are composed of mass-transport deposits, massive fine sandstone, fine sandstone intercalated with thinly interbedded sandstone and mudstone, and finally thinly interbedded silty sandstone and mudstone. The sandy channels were density-flow deposits. Observation of the well-logs showed a typical bell-shaped natural GR pattern, low density, large arrival-time difference, and high electrical resistance in the reservoir layer, suggesting good reservoir quality. In the seismic section, the sandy channels appear U- or V-shaped, with short axes and wavy reflectors filled with moderate-to high-amplitude seismic facies (**Figure 4**).

4.1.1.4 Contourite Deposits

The core data for the AB120 Reservoir revealed the presence of numerous thinly interbedded sandstone and mudstone. The sandstone lithology is mainly silty fine sandstone and is likely a product of frequent contourite activity. The cross-well section in **Figure 6** shows the presence of contourite deposits at the top of AB120 Reservoir. This reservoir layer is approximately 2 m thick and is distributed transversely in a stable manner (**Figure 5**). Examination of the reservoir parameters interpreted from the well-logs shows that the contourite deposits are inferior to the tongue-shaped lobes in terms of their physical properties.

4.1.2 Sectional Facies Analysis

Following the determination of the sedimentary microfacies types, a sectional facies analysis of the AB120 Reservoir was done using integrated well-log and seismic data.

Marked retrogression is evident along the source direction, which is associated with a rise in the relative sea level and a decrease in supply from the source. Analysis of the well-log-calibrated seismic data revealed that high-amplitude continuous reflections characterized the AB110 and AB120 Reservoirs. On the side close to the source, onlap points are recognizable during seismic events. In addition, the vertical thickness of the sand bodies gradually decreased from the bottom of the units to the top. These findings suggest a rapid rise in relative sea level and a rapid decrease in supply from the source during the corresponding period (**Figure 6**).

In the direction perpendicular to the source direction, moving from the proximal end of the tongue-shaped lobes to their distal end, the sand bodies in the AB110 and AB120 Reservoirs varied in their origin and scale. Within the AB110 and AB120 Formation, at the proximal end of the tongue-shaped lobes, two moderate-to high-amplitude continuous reflection events are visible on the seismic section corresponding to their oil-bearing sand bodies. In addition, the seismic section shows marked erosional truncation points and a U-shaped reflection structure filled with low-amplitude seismic facies, which indicate muddy channel deposits (**Figure 7**). At the distal end of the tongue-shaped lobes, there remains only one moderate-to high-amplitude continuous reflection event within the target layer, which, as revealed by the well-log-calibrated seismic data, corresponds to the AB120 oil-bearing sand body. This suggests the disappearance of the AB110 oil-bearing sand body at this location due to a rapid rise in sea level and the decrease in supply from the source. Moreover, the U-shaped reflection structure in the AB120 Formation on the seismic section was inconspicuous, indicating a weakened downcutting capacity of the channels on the distal side from the source.

4.1.3 Planar Facies Analysis

Based on the stratigraphic framework and seismic horizon interpretations, the planar seismic attributes (e.g., RMS amplitude, maximum amplitude, minimum amplitude, coherent attribute, minimum impedance, maximum impedance, and average impedance) of the AB120 Reservoir were extracted. These attributes and their correlations with parameters such as sandstone and mudstone thicknesses and

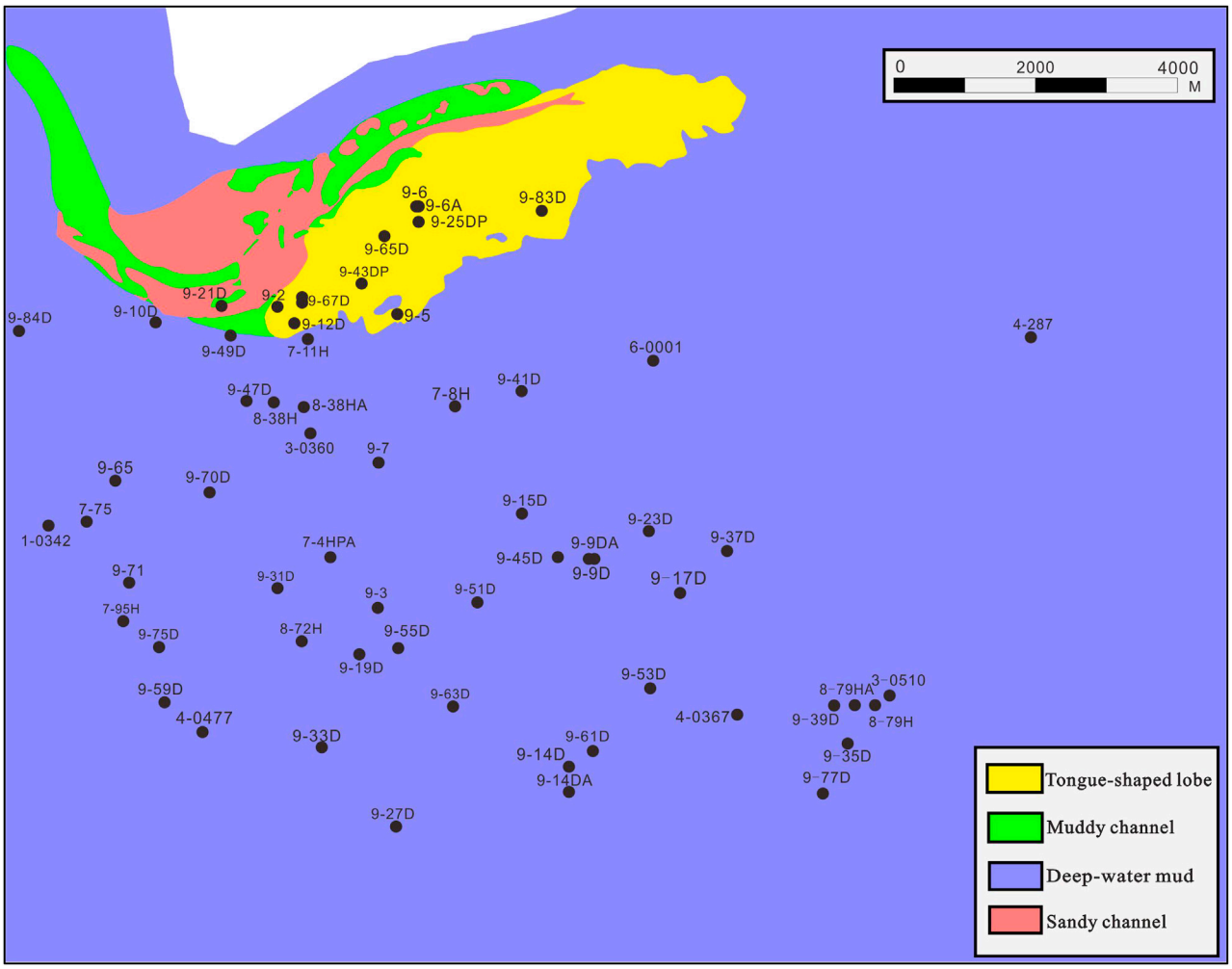

FIGURE 10 | Sedimentary microfacies distribution model for the AB120 Formation based on the integrated well-log and seismic data.

the sandstone–formation thickness ratio were analyzed. The RMS and wave impedance attributes were identified as the most sensitive and were selected for further analysis. The limit values corresponding to the sandstone facies were subsequently determined. The lower-limit RMS amplitude and upper-limit minimum impedance of the sandstone facies in the AB120 Reservoir are 20 and 5,850, respectively (**Figures 8**, **9**).

The minimum impedance was selected to interpret the sandstone facies based on the determined limit values of its seismic attributes. Through the minimum impedance analysis of single-well facies in a superimposed AB120 Formation, the sandstone facies was identified as the dominant facies in the low value area. The dominant facies in the high value area was the mudstone facies, and the sandstone-mudstone transition facies was in the central numerical area. A sedimentary microfacies distribution model for the AB120 Reservoir was produced through an integration of the single-well facies analysis, cross-well sectional facies analysis, and sensitive attributes. Tongue-shaped lobes were present in the main body of the AB120 Reservoir, and their roots were connected to muddy and sandy channels (**Figure 10**).

4.2 Architectural Characterization

The architecture of a reservoir refers to the morphology, scale, and direction of its constituent elements at varying levels, including how they are stacked (Allen, 1977; Allen, 1978). This concept reflects the spatial arrangement of the reservoir storage elements of varying origins and levels and seepage barriers, as well as the difference between the distribution patterns of these elements. Characterizing reservoir architectures is vital for the evaluation and development of oil and gas reservoirs.

4.2.1 Characterization Level of Architectural Bounding Surface

The hierarchical structure of a sedimentary body is the result of multiple levels and rates of sedimentary environments. Generally, a sedimentary body is hierarchically divided based on its

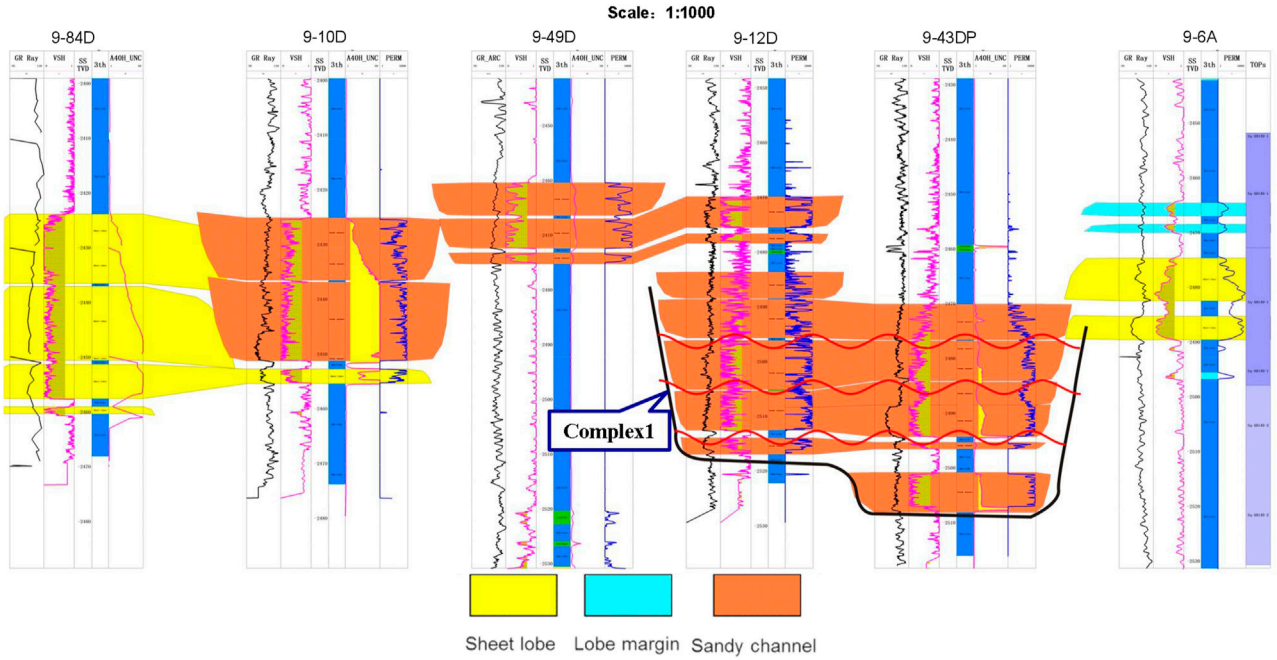

FIGURE 11 | Architecture boundary characteristics with lateral phase change in ABL oil field.

architectural bounding surfaces (ABSs), which are hierarchically sequential contact surfaces between the rock layers. A stratum can be split into genetically linked stratigraphic blocks based on its ABSs (Miall, 1985).

4.2.1.1 Architectural Bounding Surface Classification in the Albacora Leste Oilfield

Based on prior understanding of ABS systems, the deep-water sedimentary ABSs in the Albacora Leste (ABL) oilfield are categorized into seven levels (1–7), with levels 1 and 7 being the lowest and highest levels, respectively, using deep-water sedimentary architectures and characteristics of the ABL oilfield as reflected by its geological, well-log, and seismic data.

Level 7 is a complex fan, which corresponds to layers AB250-110 and contains a complete stratigraphic formation. This level can be traced throughout the basin. Level 6 consists of single fans and includes sequence stratigraphic elements in the target layer (i.e., AB120). Level 5 is composed of channelized-lobe systems, including deposits in multiple sedimentary environments and flow types. Level 4 comprises complex lobes or complex lobe systems that are deposits formed by the same sedimentation mechanism but at different stages. The particle size, thickness, and spatial trends of the sedimentary rock displayed patterns. Level 3 consists of single lobes that are deposits formed by the same sedimentation mechanism and stage. They were similar in terms of particle size, thickness, and spatial trends. Level 2 is composed of rock facies sequences with single sedimentary elements. Level 1 comprises single rock facies that are further breakdowns of individual sedimentary elements, such as single sections in the Bouma sequence that are similar in particle sizes and sedimentary structures.

4.2.1.2 Levels Suitable for Architectural Characterization

First, to characterize a specific reservoir requires the selection of appropriate levels. If the levels are too low, the results cannot meet the development and production needs, whereas if the levels are too high, the results are inadequate to allow for good predictions. The determination of the levels suitable for characterization depends on the data abundance and quality. The following section outlines the selection of suitable levels for the architectural characterization of the ABL oilfield through site-specific data.

Levels 3 and 2 ABSs had distinctly identifiable features in the core data of the study area. Further meticulous observation and description of the core data revealed Level 1 ABSs with extremely high vertical resolution. However, because of operating expenditure constraints, there are only a limited number of coring wells in the study area, which presents a tremendous challenge to transverse tracing of ABSs and comparing low-level ABSs based on cores retrieved from different wells is a daunting task.

Observation of the well-logs obtained for the study area revealed notable well-log responses for Level 3 ABSs likely due to the abundance of calcareous layers present at these locations. Therefore, Level 3 ABSs can be identified from the well-log data in the vertical direction. However, the

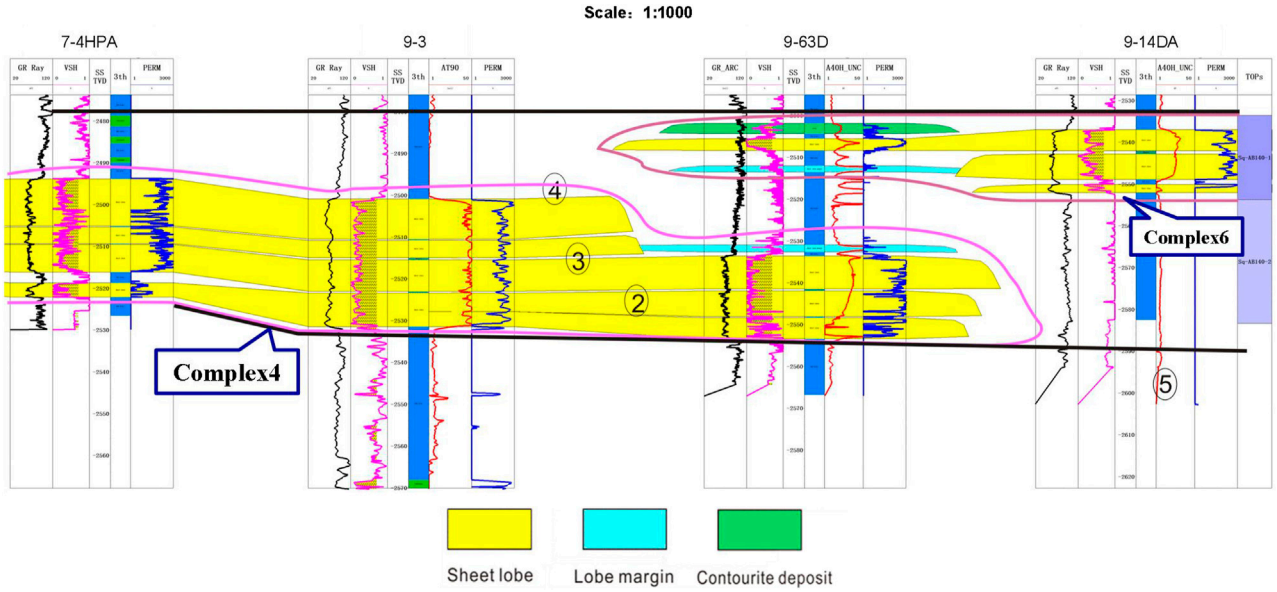

FIGURE 12 | Architecture boundary characteristics of sand bodies with elevation difference in ABL oil field.

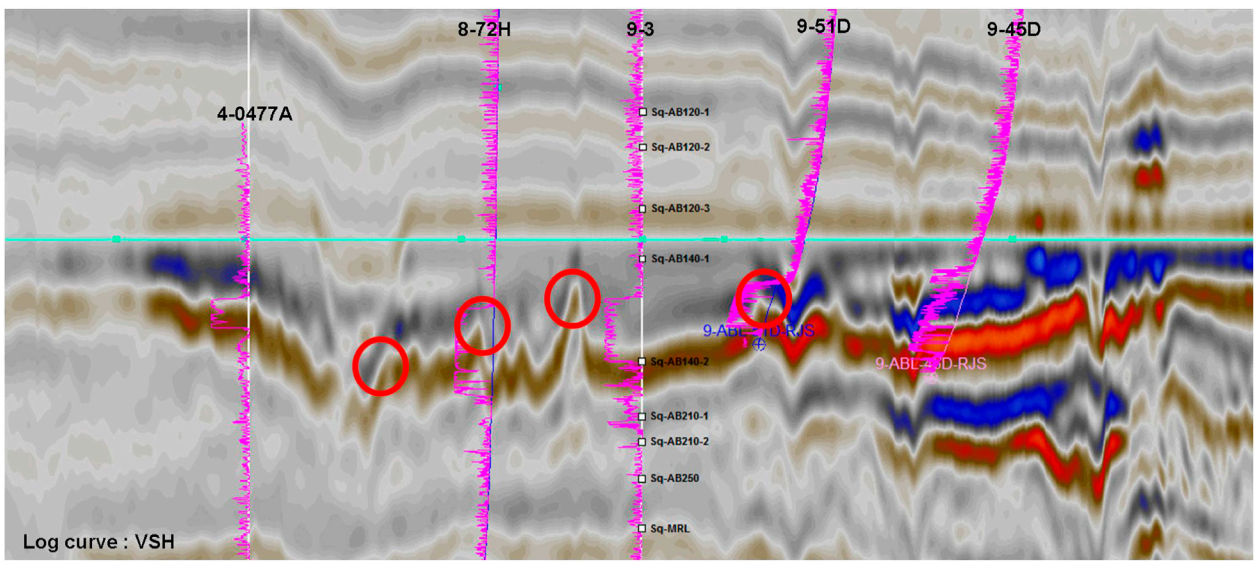

FIGURE 13 | Seismic amplitude change of architecture boundary characteristics for sand body in ABL oil field.

large distances between the deep-water drilling wells in the study area present an obstacle to the transverse tracing of Level 3 ABSs. In contrast, the lobe deposits exhibit good transverse continuity. Therefore, transversely tracing lobe deposits is more likely to succeed than in tracing channel deposits. However, channelization in the study area results in ambiguity for the transverse tracing of the Level 3 ABSs between single lobes based on the well-log data.

The available seismic data cover the entire study area. An analysis of the well-log-calibrated seismic data for the target layer in the ABL oilfield identifies Level 4 ABSs (i.e., intercomplex ABSs) and, in some areas, Level 3 ABSs (i.e., ABSs between single-origin elements).

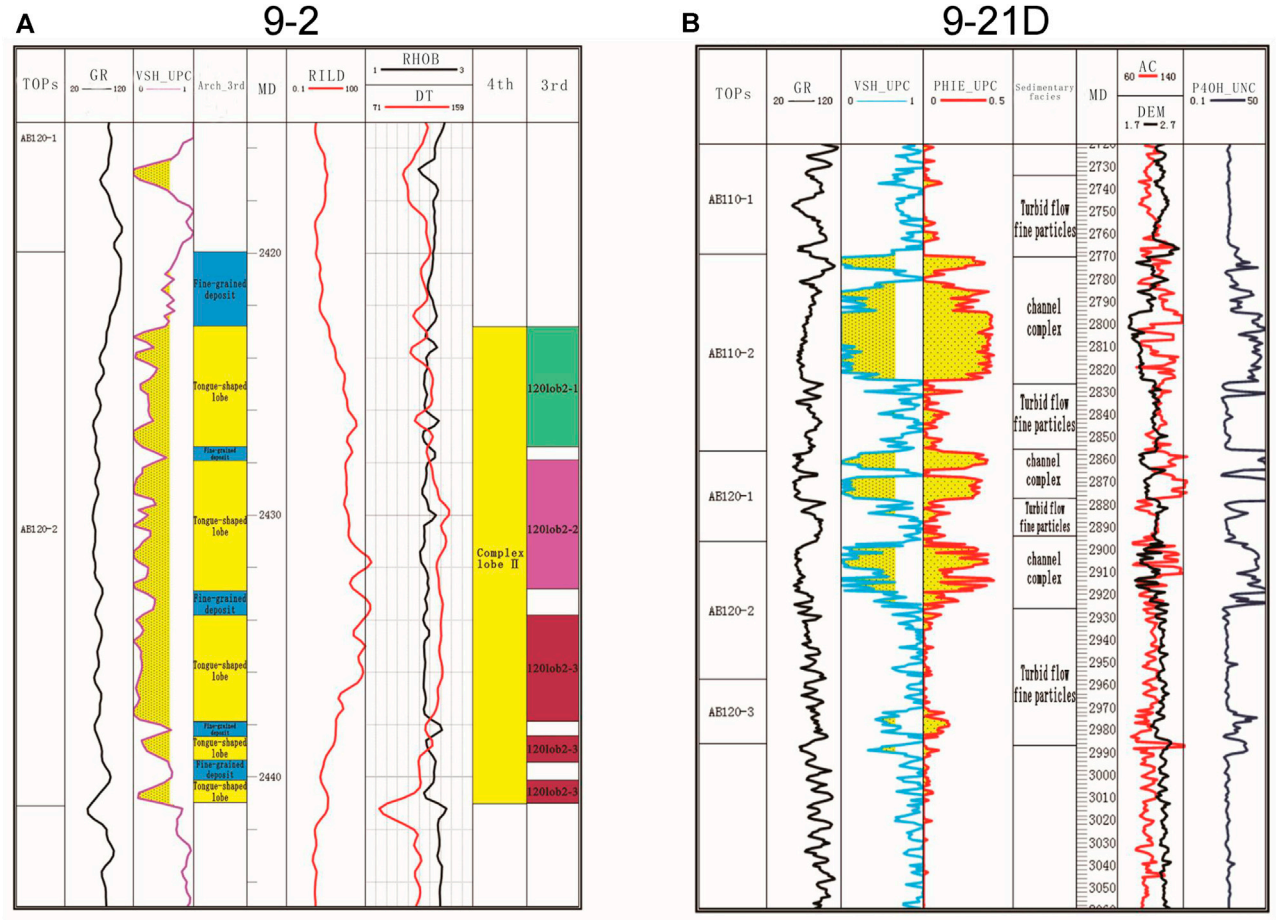

FIGURE 14 | Architectural characterization of single well. [**(A)** Architectural characterization of the complex lobes in Well 9–2; **(B)** Architectural characterization of the complex channels in Well 9–21D).

Based on the above comprehensive abundance and quality analysis of the data for the study area, Level 4 architectural elements were selected to facilitate architectural characterization of the target layer in the ABL oilfield.

4.2.2 Identification of the Architectural Element Boundaries

The identification of architectural element boundaries is a key step in architectural characterization. The following four characteristics were used in this study as markers for identifying the boundaries of architectural elements:

4.2.2.1 Lateral Changes in the Facies

Sedimentary microfacies analyses revealed the presence of two primary sedimentary microfacies in the study area: complex channels and lobes. These products were formed in different sedimentary environments and constitute architectural elements of different types and levels. There is often a seepage barrier or change at the boundaries of these microfacies, resulting in disconnection or poor connection between the sand bodies. Therefore, each boundary displaying a change in lateral facies is an architecture boundary (**Figure 11**).

4.2.2.2 Elevation Difference Between Sand Bodies

Elements which formed at different stages and have different origins differ in terms of their period of development. Therefore, corresponding sand bodies have different relative elevation of their top horizons and the marker bed which is the formation boundary. In practice, the measured elevation difference must be combined with the curve patterns, scale and extension of the sand bodies to determine the boundaries of the architectural elements accurately (**Figure 12**).

4.2.2.3 Changes in Seismic Amplitude

Changes in the shale content, extent of erosion, and cross-cutting and stacking relationships at the boundaries of the sedimentary bodies of different stages lead to marked changes

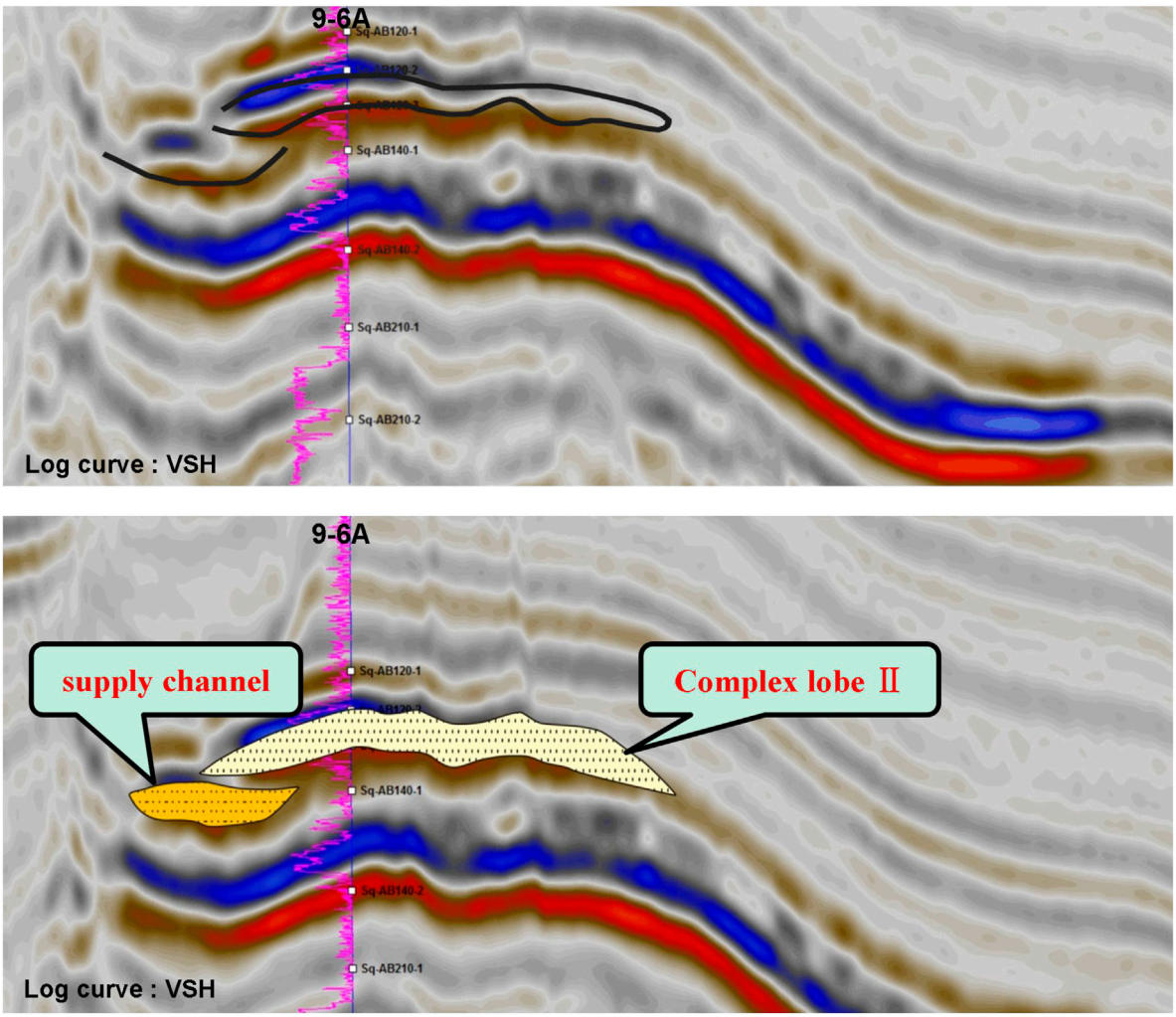

FIGURE 15 | Well-log and seismic responses of the AB120 reservoir in the direction perpendicular to the source direction.

in the seismic response characteristics. This is primarily reflected by phenomena such as the appearance of erosional truncation points and changes in the amplitude (**Figure 13**).

4.2.2.4 Changes in Sand Body Thickness

A lobe is characterized by a flat bottom and a convex top. The sand body deposits are thicker along the central flow line of a single lobe and gradually thin out towards its edges. Therefore, the sand body thickness may first decrease and then increase, moving from one single lobe to another. At the macroscopic level, the boundaries of the architectural elements can be approximated based on the thickness contours of the sedimentary body.

4.2.3 Architectural Characterization of the AB120 Reservoir

An earlier sedimentary microfacies analysis revealed that the AB120 Reservoir formed in a deep-water submarine-fan sedimentary environment and contained tongue-shaped, sandy channel, muddy channel, and contourite deposits. Contourite deposits are difficult to distinguish on the seismic sections owing to their small thickness (approximately 2 m) which inhibits their detailed characterization in this study. The following section presents an architectural characterization and analysis of the AB120 Reservoir based on complex lobe and channel elements.

4.2.3.1 Characterization of Complex Lobes

4.2.3.1.1 Single-Well Architectural Characterization. A previous analysis of the deep-water submarine-fan sedimentary facies in the study area revealed that tongue-shaped lobes primarily consist of massive fine sandstone sediments. Well-log observations revealed a low GR value, low density, large arrival-time difference, and high electrical resistance in the reservoir layer, suggesting good reservoir quality (**Figure 14A**). It has been reported that a complex-lobe sedimentary body was found in the study area during the drilling of 12 wells, most of which were clustered in the western tongue-shaped lobe.

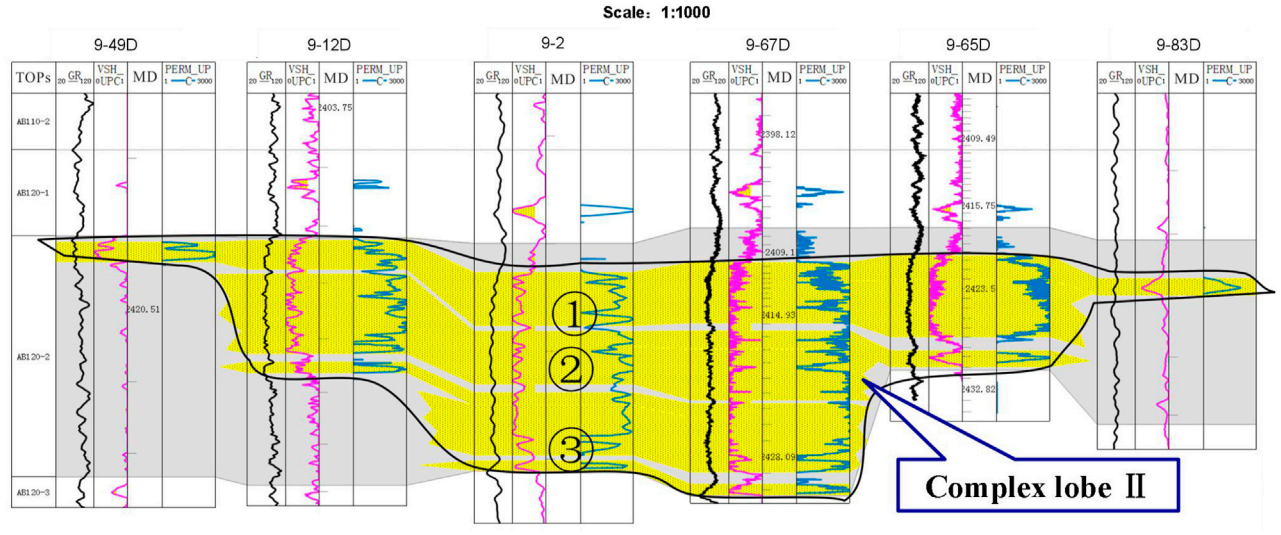

FIGURE 16 | Cross-well section of the AB120 reservoir.

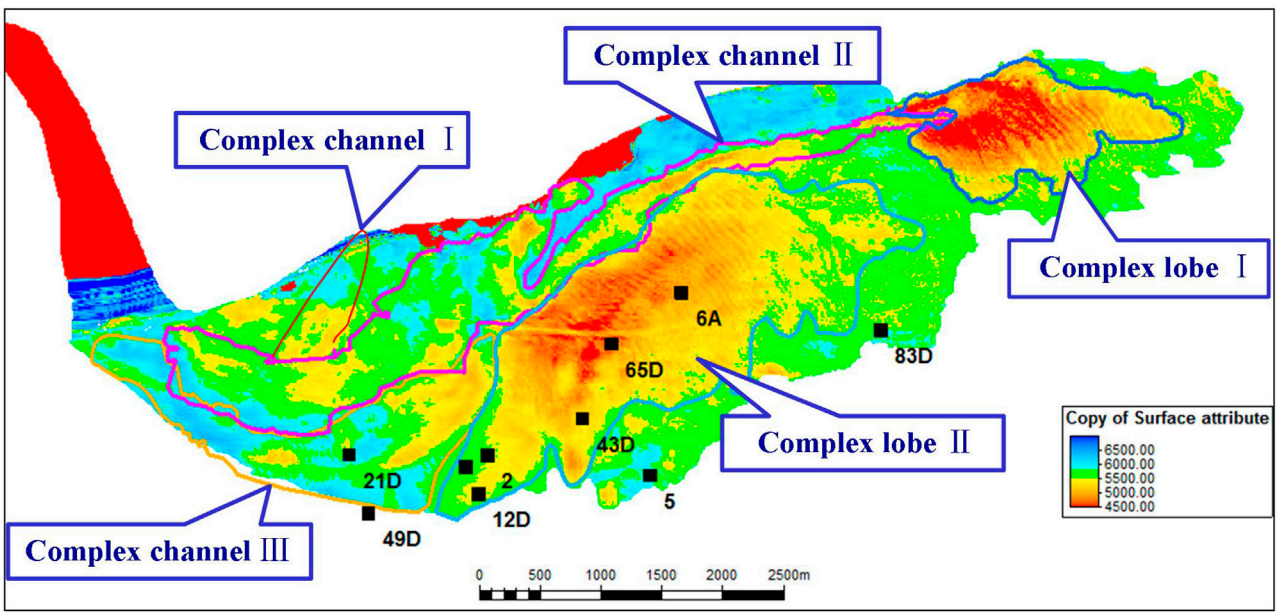

FIGURE 17 | AB120 reservoir plane attribute map (minimum impedance distribution).

Because of factors such as shale content and basal lag deposits, single lobes formed at different stages may differ in terms of their vertical well-log patterns, and their contact interfaces may be associated with high GR values. On this basis, single-well data can be used to distinguish between single lobes. Three single lobes of different stages were present in the AB120 Reservoir (**Figure 14A**).

4.2.3.1.2 Sectional Architectural Characterization. Integrated well-log and seismic data revealed the presence of two complex lobes formed at different stages in the AB120 Reservoir based on sectional architectural analysis. The complex lobes in the eastern undrilled area and western drilled area are denoted by I and II, respectively. Marked well-logs and seismic responses can also be observed for complex lobe II.

Along the source direction, the AB120 Formation was characterized by continuous high-amplitude reflections, which suggest an overall dominance of tongue-shaped lobe deposits. There is a significant decrease in the amplitude of seismic

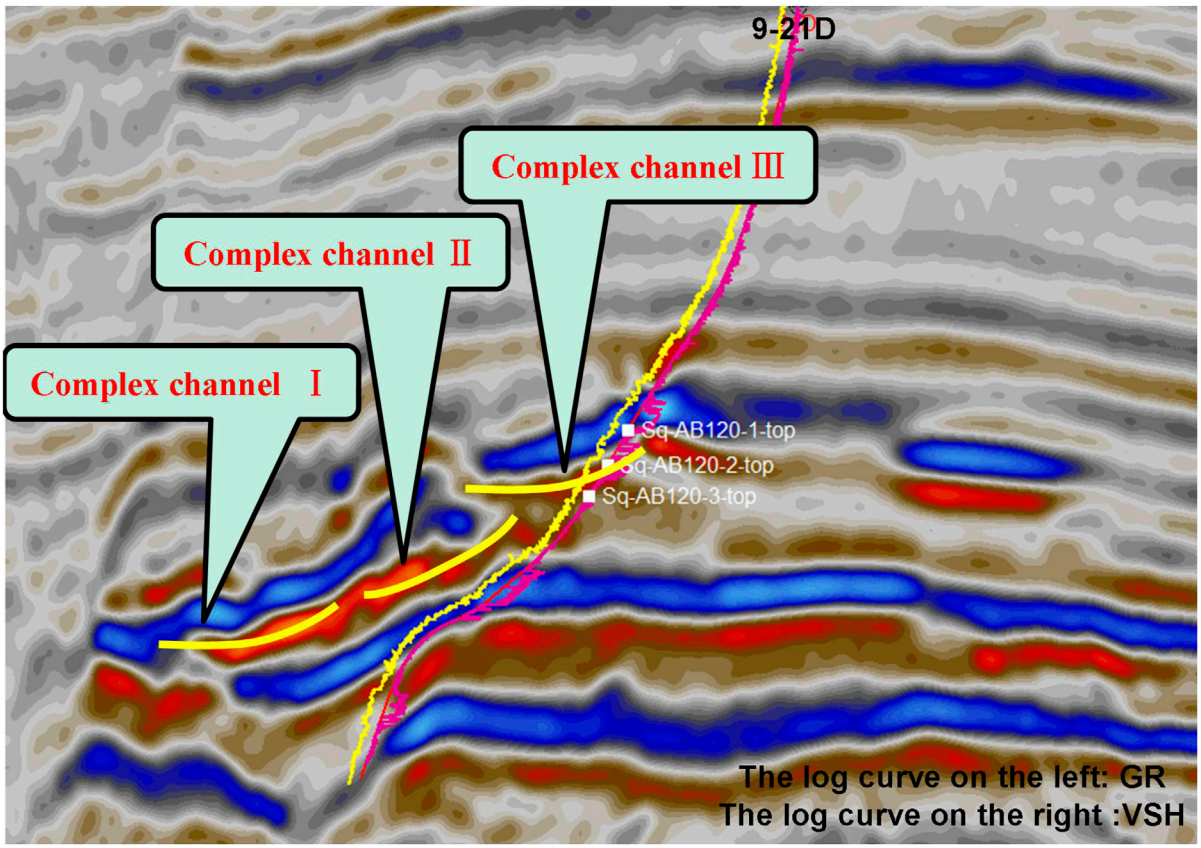

FIGURE 18 | Seismic section of the AB120 reservoir perpendicular to the source direction and through well 9–21D.

reflections at the lowest part of the architecture. This location represented the boundary between the complex lobes. In the section perpendicular to the source direction shown in **Figure 15**, the geological body is characterized by a continuous, high-amplitude reflection structure. Well-log-calibrated seismic data revealed that these structures were tongue-shaped deposits.

Each complex lobe also has a complex internal structure which is difficult to characterize in undrilled areas. This study focused on investigating the complex lobe in the drilled area (i.e., complex lobe II) based on Level 3 architectural elements (e.g., single lobes). Based on single-well architectural characterization, single lobes were identified. A cross-well comparison revealed the presence of three single lobes in complex lobe II which formed at different development stages of the AB120 Reservoir in the vertical direction. The youngest lobe was distributed over the largest area (**Figure 16**). The three single lobes are difficult to identify and characterize using seismic profiles owing to the thinness (2–20 m) of complex lobe II and the low vertical resolution of the seismic data.

4.2.3.1.3 Planar Architectural Characterization. In the plane, there were two regions in the study area with a low minimum impedance. One is located along the line connecting Wells 9–2, 9–65D, and 9-6A in the work area, whereas the other is situated in the northern part of the study area where no drilling has been conducted to date. Differences in shale content, as well as sandstone and mudstone conditions, can lead to changes in seismic attributes near the boundaries or junctions of different sedimentary bodies. In the study area, impedance may first increase and then decrease at the boundaries or junctions of different sedimentary bodies. This distribution pattern was observed in the minimum impedance of the AB120 Reservoir, which supports the earlier finding that two complex lobes exist in this reservoir (**Figure 17**).

The boundaries of the architectural elements were characterized based on well-log and seismic data and guided by the sedimentation model obtained from the microfacies analysis. Interactive single-well, sectional, and planar characterizations were performed using integrated well-log and seismic data. A detailed 2D depiction (or "planar division") of architectural elements was subsequently completed through the connection of their boundaries based on their geometrical relationships. An analysis of the reservoir architecture based on integrated well-log and seismic data revealed the presence

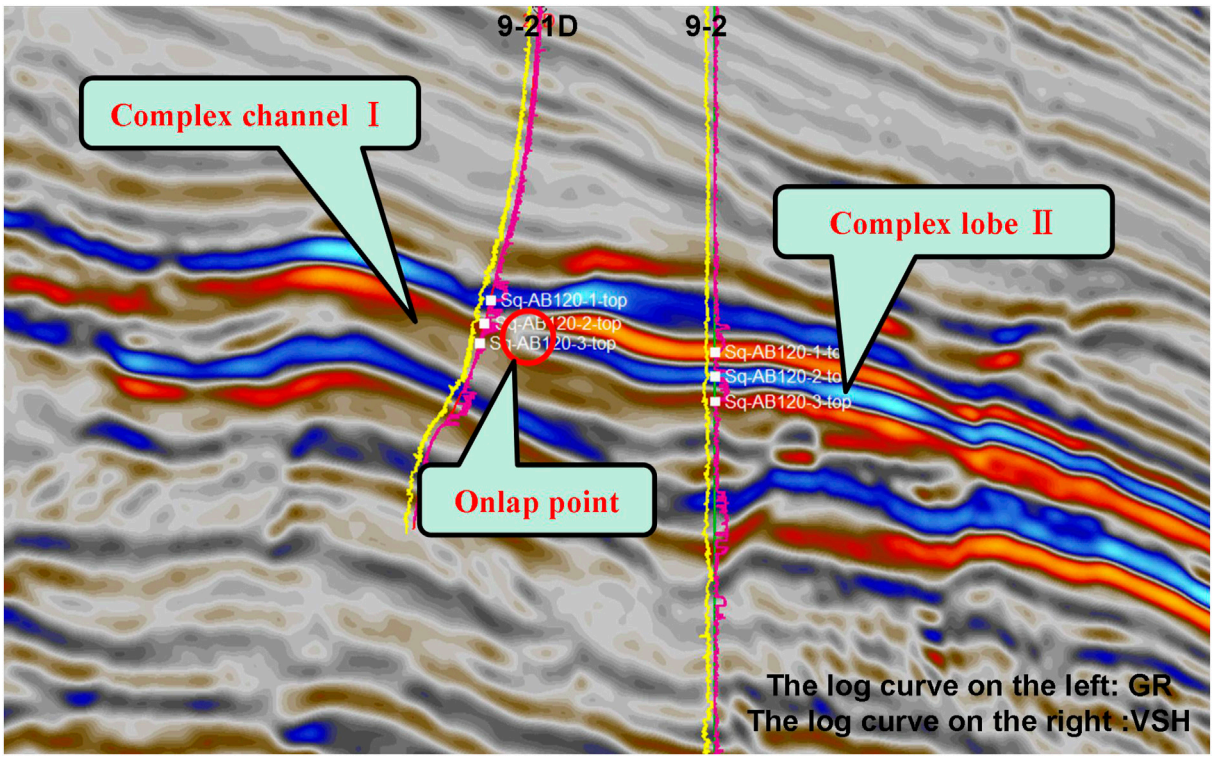

FIGURE 19 | Seismic section of the AB120 reservoir along the source direction and through wells 9–21D and 9-2

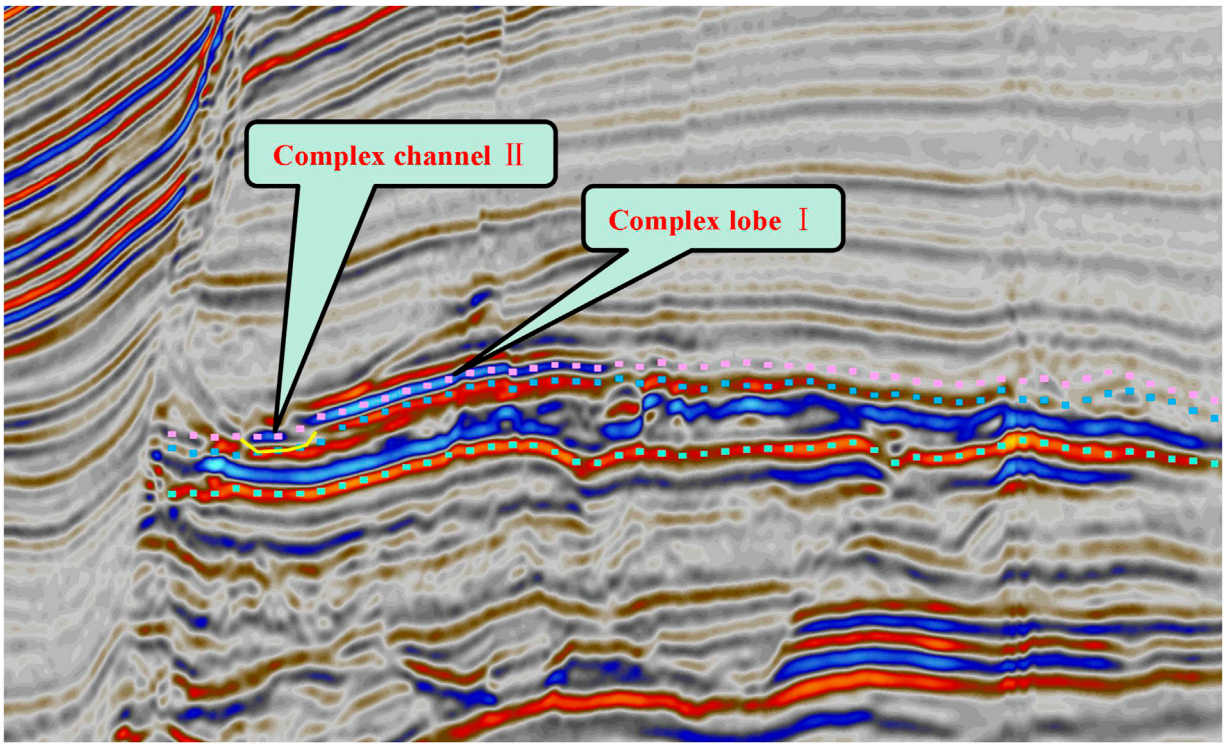

FIGURE 20 | Seismic section of the AB120 reservoir perpendicular to the source direction (remote source end).

of two complex lobes formed at different stages (I and II) in the AB120 Reservoir (**Figure 17**).

4.2.3.2 Architectural Characterization of Complex Channels
4.2.3.2.1 Single-Well Architectural Characterization. Deep-water submarine-fan channels can be categorized as follows based on paleo-geomorphological features: restricted, semi-restricted, and unrestricted channels (Clark and Pickering, 1996; Deptuck et al., 2003). Characterized by marked U- and V-shaped reflections on the seismic sections, restricted channels have notable downcut surfaces, and their boundaries show large, incised river valleys. In comparison, while semi-restricted channel systems have distinct downcutting surfaces, large-scale natural levee deposits are present at their edges and appear as seagull-shaped features in the seismic sections. The principal characteristic of unrestricted channels is the lack of notable incised river valleys at their boundary. In the study area, complex channel deposits were only encountered in the AB120 Formation during drilling of Well 9–21D. An analysis revealed that this channel is a restricted, enveloped, and complex channel, which is characterized by distinct U- and V-shaped reflections on seismic sections and has distinct downcutting surfaces. At present no vertical contact has occurred between sand bodies in complex channels. A stable interlayer composed of fine-grained sediments separated the sand bodies and corresponded to notable returns on the well-log (**Figure 14B**).

4.2.3.2.2 Sectional Architectural Characterization. Within the AB120 Formation a seismic section perpendicular to the source direction and through Well 9–21D revealed distinctly discontinuous seismic events and multiple U-shaped reflection structures filled with high-amplitude seismic facies. These characteristics correspond to three sandy complex channels (denoted as I, II, and III). The stacking of these three complex channels on the seismic section suggests that complex channels I and III are the first and last to be deposited, respectively. The well-log-calibrated seismic data revealed that complex channel III was encountered during the drilling of well 9–21D (**Figure 18**).

Observation of a seismic section along the source direction and through Wells 9–21D and 9-2 showed that the AB120 Formation is characterized by marked continuous, high-amplitude reflections. In addition, onlap points were visible at the seismic events on the side close to the source. The well-log-calibrated seismic data indicated the formation of a channel (i.e., complex channel III) near the source (**Figure 19**).

Notable discontinuous seismic events are visible within the AB120 Formation on the side furthest from the source and in the direction perpendicular to the source direction. In addition, there was a U-shaped reflection structure filled with high-amplitude seismic facies, which was inferred to be a complex channel (i.e., complex channel II) (**Figure 20**).

4.2.3.2.3 Planar Architectural Characterization. Changes in the shale content, extent of erosion, and cutting and stacking relationships at the boundaries of sedimentary bodies formed at different stages of reservoir development can cause considerable changes in the seismic response characteristics at the boundaries of architectural elements (e.g., changes in the seismic amplitude). The analysis of the extracted minimum impedance of the AB120 Reservoir agrees with previous findings that three complex channels (I, II, and III) may exist in the AB120 Reservoir (**Figure 17**). As the oldest of the three complex channels, complex channel I has been severely cut by younger complex channels and is distributed over a limited area in the northwestern part of the study area. The low quality of relevant seismic data due to the presence of large faults presents a challenge for obtaining a detailed description of complex channel I.

Based on the spatial relationship of the reflection structure in the seismic profile and the distribution characteristics of the wave impedance plane figure, it is considered that complex channels III and II are the supply channels for complex lobes II and I, respectively. The stacking of complex lobe II onto the supply channel for complex lobe I on the seismic sections, suggests that complex lobe I was deposited earlier than complex lobe II (**Figures 15**, **17**, **19**, **20**).

5 CONCLUSION

(1) The AB120 Reservoir contains four primary sedimentary microfacies: tongue-shaped, muddy channel, sand channel, and contourite deposits. Thinly interbedded sandstone and mudstone form the bottom of each tongue-shaped lobe and transition upwards into massive fine sandstone. Tongue-shaped lobes are characterized by a typical funnel-shaped pattern on natural GR logs and high-amplitude, continuous reflections on the seismic sections. Vertically, the muddy channels are characterized in the seismic sections by a low-amplitude, imbricate reflection structure. The sandy channels are primarily composed of massive fine sandstone, display a positive rhythm and are characterized by a typical bell-shaped pattern on the natural GR logs and U- or V-shaped short-axis wavy reflections filled with moderate-to high-amplitude seismic facies in the seismic sections. Consisting of thinly interbedded sandstone (mainly silty fine sandstone) and mudstone, the contourite deposits have a thickness of approximately 2 m and are transversely distributed in a stable manner.

(2) A seven-level classification scheme was adopted for the deep-water submarine-fan ABS system in the study area. Because of data abundance and quality constraints, the configuration characterization of the study area can only identify up to Level 4 ABSs. Changes in the lateral facies, seismic amplitude, sand body thickness, and sand body elevation differences typically delineate the boundaries of architectural elements.

(3) The AB120 Reservoir consists of three complex channels (I, II, and III) and two tongue-shaped complex lobes (I and II). Complex channels I and III are the first and last to be deposited, respectively. Complex lobe I was deposited before complex lobe II. Complex channels II and III

supply complex lobes I and II, respectively. Vertically, complex lobe II (located to the west) is composed of three single lobes formed at different stages, the youngest of which is distributed over the largest area.

DATA AVAILABILITY STATEMENT

The original contributions presented in the study are included in the article/Supplementary Material, further inquiries can be directed to the corresponding author.

AUTHOR CONTRIBUTIONS

CZ, XH, JL, and CY contributed to the conception and design of the study. JL wrote the first draft of this manuscript. ZN conducted the investigation and data collation. All authors contributed to manuscript revision, and have read and approved the final submitted version.

FUNDING

This study was financially supported by the National Natural Science Foundation of China (grant no. 42172175).

ACKNOWLEDGMENTS

We would like to thank the SINOPEC Shanghai Offshore Petroleum Branch for providing the data and allowing the publication of this article.

REFERENCES

Allen, J. R. L. (1978). Studies in Fluviatile Sedimentation: an Exploratory Quantitative Model for the Architecture of Avulsion-Controlled Alluvial Suites. *Sediment. Geology.* 21, 129–147. doi:10.1016/0037-0738(78)90002-7

Allen, J. R. L. (1977). The Plan Shape of Current Ripples in Relation to Flow Conditions. *Sedimentology* 24 (1), 53–62. doi:10.1111/j.1365-3091.1977.tb00119.x

Bhuiyan, A. H., and Hossain, S. (2020). Petrographic Characterization and Diagenetic Evaluation of Reservoir Sandstones from Smørbukk and Heidrun fields, Offshore Norway. *J. Nat. Gas Geosci.* 5 (1), 11–20. doi:10.1016/j.jnggs.2019.12.001

Bybee, K. (2006). Albacora Leste Field - Subsea Production- System Development. *J. Journal Pet. Technol.* 58 (08), 59–60. doi:10.2118/0806-0059-JPT

Clark, J. D., and Pickering, K. T. (1996). *Submarine Channels:Processes and Architecture*. London: Vallis Press.

Deptuck, M. E., Steffens, G. S., and Barton, M. (2003). Architecture and Evolution of Upper Fan Channel-Belts on the Niger Delta Slope and in the Arabian Sea. *Mar. Pet. Geology.* 20 (6- 8), 649–676. doi:10.1016/j.marpetgeo.2003.01.004

Fetter, M., De Ros, L. F., Bruhn, C. H. L., Carlos, H., and Bruhn, L. (2009). Petrographic and Seismic Evidence for the Depositional Setting of Giant Turbidite Reservoirs and the Paleogeographic Evolution of Campos Basin, Offshore Brazil. *Mar. Pet. Geology.* 26 (6), 824–853. doi:10.1016/j.marpetgeo.2008.07.008

Gao, S., Liu, H., Ye, L., Wen, Z., Zhu, W., and Zhang, C. (2020). A New Method for Well Pattern Density Optimization and Recovery Efficiency Evaluation of Tight sandstone Gas Reservoirs. *Nat. Gas Industry B* 7 (2), 133–140. doi:10.1016/j.ngib.2019.08.003

Gervais, A., Mulder, T., Gonthier, E., and Savoye, B. (2006). Sandy Modern Turbidite Lobes:A New Insight from High Resolution Seismic Data. *J. Mar. Pet. Geology.* 23 (4). doi:10.1016/j.marpetgeo.2005.10.006

Gu, C., Li, Q., Ma, R., Lin, Y., Li, X., Li, Y., et al. (2021). Propagation Characteristics of Doppler Ultrasonic Wave in Gas-Liquid Two-phase Flow in an Offshore deepwater Riser. *Nat. Gas Industry B* 8 (6), 615–621. doi:10.1016/j.ngib.2021.11.009

Kang, H., Meng, J., Cheng, T., Jia, H., Bai, B., and Li, M. (2018). Characteristics of Deep Water Depositional System in Campos basin, Brazil. *J. Petroleum Exploration Develop.* 45 (01), 93–104. doi:10.11698/PED.2018.01.0910.1016/s1876-3804(18)30009-0

Li, C., Chen, G., Zhang, G., Lv, C., Yang, H., Ma, M., et al. (2017). Developmental Characteristics and Provenances of the Submarine Fans Developed During the Middle Miocene in the Eastern Deepwater Area of the Qiongdongnan Basin. *J. Natural Gas Geoscience* 28 (10), 1555–1564. doi:10.11764/j.issn.1672-1926.2017.08.009

Li, P., Zhou, S., Ji, B., Liu, X., Li, J., Zhang, X., et al. (2021). Water-soluble Organic Acids in Sedimentary Rocks: Compositions and Influencing Factors. *J. Nat. Gas Geosci.* 6 (3), 173–181. doi:10.1016/J.JNGGS.2021.06.003

Liang, J., Huang, X., Cai, W., Wang, Y., Chen, L., Zhang, Y., et al. (2019). Source-to-Sink System and Exploration Prospects of the Wilcox Formation in Perdido Fold Belt, Burgos Basin. *Mexico. J. Acta Petrolei Sinica.* 40 (12), 1439–1450. doi:10.7623/syxb201912003

Lima, B. E. M., and De Ros, L. F. (2019). Deposition, Diagenetic and Hydrothermal Processes in the Aptian Pre-salt Lacustrine Carbonate Reservoirs of the Northern Campos Basin, Offshore Brazil. *Sediment. Geology.* 383, 55–81. doi:10.1016/j.sedgeo.2019.01.006

Lin, Y., Wu, S., Wang, X., Ling, Y., Lu, Y., Zhang, J., et al. (2014). Composite Sand Bodies Architecture of Deep-Water Turbidite Channels in the Niger Delta Basin. *J. Acta Geologicasinica(englishedition).* 88 (06), 1822–1834. doi:10.1111/1755-6724.12348

Liu, L., Zhang, T., Zhao, X., Wu, S., Hu, J., Wang, X., et al. (2013). Sedimentary Architecture Models of deepwater Turbidite Channel Systems in the Niger Delta continental Slope, West Africa. *Pet. Sci.* 10 (02), 139–148. doi:10.1007/s12182-013-0261-x

Liu, Y., Wang, H., Meng, W., Zhang, C., Zhi, J., and Shen, A. (2020). Stimulation experiment of Horizontal wells Filled with Permeable and Water-Blocking Gravel in Deepsea Bottom-Water Gas Reservoirs. *Nat. Gas Industry B* 7 (4), 390–396. doi:10.1016/j.ngib.2020.01.006

Ma, Z., Xie, Y., Geng, C., and Zhang, F. (2011). Petroleum Geology and Favorable Exploration Targets of Campos Basin,Brazil. *J.Journal Jilin University:Earth Sci. Edition* 41 (05), 1389–1396. doi:10.13278/j.cnki.jjuese.2011.05.021

Mann, P., Horn, M., and Crossl (2007). *Tectonic Setting of 79 Giant Oil and Gas Fields Discovered from 2000-2007:Implications for Future Discovery Trends*. Long Beach, California: AAPG,Annual Convention.

Miall, A. D. (1985). Architectural-element Analysis: A New Method of Facies Analysis Applied to Fluvial Deposits. *Earth-Science Rev.* 22, 261–308. doi:10.1016/0012-8252(85)90001-7

Obafemi, S., Oyedele, K. F., Omeru, T., and Bankole, S. I. (2020). Characterization of Deep Water Turbidite Channels and Submarine Fan Lobes Using Artificial Intelligence; Case Study of Frem Field Deep Offshore Niger Delta. *J. Afr. Earth Sci.* 167, 103852. doi:10.1016/j.jafrearsci.2020.103852

Pandolpho, B. T., da Fontoura Klein, A. H., Dutra, I., Mahiques, M. M., Viana, A. R., Bueno, G. V., et al. (2021). Seismic Record of a Cyclic Turbidite-Contourite System in the Northern Campos Basin, SE Brazil. *Mar. Geology.* 434, 106422. doi:10.1016/J.MARGEO.2021.106422

Pu, R., Du, J., Cui, Y., and Shen, J. (2003). Some Examples of Lacustrine Retrogradation Reflection. *J. Oil Geophysical Prospecting.* 67–71+117-118+112. doi:10.13810/j.cnki.issn.1000-7210.2003.01.016

Reimchen, A. P., Hubbard, S. M., Stright, L., and Romans, B. W. (2016). Using Sea-Floor Morphometrics to Constrain Stratigraphic Models of Sinuous Submarine Channel Systems. *Mar. Pet. Geology.* 77, 92–115. doi:10.1016/j.marpetgeo.2016.06.003

Romans, B. W., Fildani, A., Hubbard, S. M., Covault, J. A., Fosdick, J. C., and Graham, S. A. (2011). Evolution of Deep-Water Stratigraphic Architecture, Magallanes Basin, Chile. *Mar. Pet. Geology.* 28 (3), 612–628. doi:10.1016/j.marpetgeo.2010.05.002

Sajid, Z., Ismail, M. S., Tsegab, H., Hanif, T., and Ahmed, N. (2020). Sedimentary Geology and Geochemical Approach to Determine Depositional Environment

of the Triassic Turbidites Bearing Semanggol Formation, NW Peninsular Malaysia. *J. Nat. Gas Geosci.* 5 (4), 207–226. doi:10.1016/j.jnggs.2020.07.001

Sun, G., Wang, Y., Jiang, Y., Pan, S., Zhang, S., and Zhang, M. (2020). Provenance and Tectonic Setting of Paleogene sandstone in the center of the Northern Qaidam Basin, China. *J. Nat. Gas Geosci.* 5 (5), 273–284. doi:10.1016/j.jnggs.2020.09.002

Tang, H., Tang, H., He, J., Zhao, F., Zhang, L., Liao, J., et al. (2021). Damage Mechanism of Water-Based Fracturing Fluid to Tight sandstone Gas Reservoirs: Improvement of the Evaluation Measurement for Properties of Water-Based Fracturing Fluid: SY/T 5107-2016. *Nat. Gas Industry B* 8 (2), 2021163–2021172. doi:10.1016/j.ngib.2020.09.016

Walker, R. G. (1978). Deep—water sandstone Facies and Ancient Submarine Fans: Models for Exploration for Stratigraphic Traps. *J. AAPG Bull.* 62 (6), 932–966. doi:10.1306/c1ea4f77-16c9-11d7-8645000102c1865d

Wang, L., Pan, J., and Yang, L. (2020). Present Conditions and Prospect of Global Deepwater Oil and Gas Exploration and Development. *J. Oil Forum.* 39 (02), 31–37. doi:10.3969/j.issn.1002-302x.2020.02.005

Wang, W., Zhu, Y., Yu, C., Zhao, L., and Chen, D. (2020). Pore Size Distribution in the Tight sandstone Reservoir of the Ordos Basin, China and Their Differential Origin. *J. Nat. Gas Geosci.* 5 (2), 45–55. doi:10.1016/j.jnggs.2020.02.001

Weimer, P., and Link, M. H. (1991). *Global Petroleum Occurrences in Submarine Fans and Turbidite Systems.Seismic Facies and Sedimentary Processes of Submarine Fans and Turbidite Systems*. New York: Springer, 9–67. doi:10.1007/978-1-4684-8276-8_2

Yin, S. (2018). *The Global Distribution of Oil and Gas Resourses in Deep Waters*. Beijing, China: China university of petroleum. doi:10.27643/d.cnki.gsybu.2018.001084

Zhang, J., and Wu, S. (2019). Research Progress on the Depositional Architecture of Submarine-Fan Lobes. *J.China Offshore Oil and Gas* 31 (5), 88–106. doi:10.11935/j.issn.1673-1506.2019.05.010

Zhang, J., Wu, S., Wang, X., Lin, Y., Fan, H., Jiang, L., et al. (2015). Reservoir Quality Variations within a Sinuous Deep Water Channel System in the Niger Delta Basin, Offshore West Africa. *J.Marine Pet. Geology*. 63. doi:10.1016/j.marpetgeo.2015.02.041

Zhao, X., Wu, S., and Liu, L. (2012). Characterization of Reservoir Architectures for Neogene deepwater Turbidity Channels of Akpo Oilfield,Niger Delta Basin. *J. Acta Petrolei Sinica.* 33 (06), 1049–1058.

Zhao, Y., Liu, X., Zhang, L., Tang, H., Xiong, Y., Guo, J., et al. (2021). Laws of Gas and Water Flow and Mechanism of Reservoir Drying in Tight sandstone Gas Reservoirs. *Nat. Gas Industry B* 8 (2), 195–204. doi:10.1016/j.ngib.2020.09.018

Conflict of Interest: The authors declare that the research was conducted in the absence of any commercial or financial relationships that could be construed as a potential conflict of interest.

Publisher's Note: All claims expressed in this article are solely those of the authors and do not necessarily represent those of their affiliated organizations, or those of the publisher, the editors and the reviewers. Any product that may be evaluated in this article, or claim that may be made by its manufacturer, is not guaranteed or endorsed by the publisher.

frontiers | Frontiers in Earth Science

ORIGINAL RESEARCH
published: 11 May 2022
doi: 10.3389/feart.2022.864118

Trace Element Composition and Cathodoluminescence of Quartz in the Hongniu–Hongshan Skarn Deposit in Yunnan Province, Southwest China

Shi-ling Wang, Hui-juan Peng, Tian-rui Wang, Hao Zou, Qi Zhou, Dong-jie Yang, Ce Sun and Xue Tian*

Key Laboratory of Tectonic Controls on Mineralization and Hydrocarbon Accumulation, Ministry of Natural Resources of the People's Republic of China, College of Earth Sciences, Chengdu University of Technology, Chengdu, China

The Hongniu–Hongshan Cu skarn deposit is located in the central part of the Zhongdian porphyry and skarn Cu belt in southwestern China. Various elements, including Al, Ti, Li, K, Na, Ca, Fe, and Ge, have been completed by using scanning electron microscopy–cathodoluminescence (SEM-CL) and laser ablation inductively coupled plasma-mass spectrometry (LA-ICP-MS) on quartz phenocrysts from the Hongniu–Hongshan porphyry and skarn Cu deposit. Three quartz generations were identified in the porphyritic granite based on the CL textures and trace element signatures. Samples of the first-generation quartz (Qtz1) contain dark gray luminescent cores assaying 22–85 ppm Ti, 58–129 ppm Al, 4–18 ppm Li, and 0.43–40 ppm Fe. The Ti-in quartz geothermometer indicates crystallization temperatures of 593–664°C for Qtz1. Samples of the second-generation quartz (Qtz2) are characterized by clear bright gray oscillatory overgrowths with medium Ti concentrations of 51–70 ppm with elevated and variable amounts of Al, Li, and Fe, and low K. The Ti-in quartz geothermometer indicates crystallization temperatures of 672–706°C. Samples of the third-generation quartz (Qtz3) contain narrow light gray rims assaying 56–93 ppm Ti, 80–101 ppm Al, 11–19 ppm Li, 1.42–17 ppm K, and 2–25 ppm Fe. The Qtz3 crystallised crystallized at higher temperatures of 706–799°C. Our study indicates that the quartz phenocryst in the Hongniu–Hongshan porphyry may have undergone two mixing episodes involving a second hotter magma. Before the first resorption, average Ti concentration in the quartz phenocryst cores was 24 ppm, and Ti of the bright band halo at the edge of the crystal core is 56 ppm; the maximum temperature difference is 109°C higher than that of the pre-resorption. Furthermore, the Ti concentration is 75 ppm at the edge of the quartz phenocryst before resorption. After resorption, the average Ti increased to 81 ppm at maximum temperature difference of 54°C higher than that of pre-resorption. Moreover, on the basis of quartz composition collected from 14 different deposits and our new dataset, we propose that covariations of Ge/Al ratio can be used to effectively discriminate magmatic quartz and hydrothermal quartz. Magmatic quartz has a Ge/Al ratio of <0.013, and the hydrothermal quartz has a ratio of >0.013.

Keywords: Hongniu–Hongshan deposit, quartz, cathodoluminescence, trace elements, skarn

OPEN ACCESS

Edited by:
Leon Bagas,
China Geological Survey, China

Reviewed by:
Qihai Shu,
China University of Geosciences, China
Lin Hou,
Chengdu Geological Survey Center, China

****Correspondence:***
Hui-juan Peng
346665401@qq.com

Specialty section:
This article was submitted to Economic Geology, a section of the journal Frontiers in Earth Science

Received: *28 January 2022*
Accepted: *29 March 2022*
Published: *11 May 2022*

Citation:
Wang S-l, Peng H-j, Wang T-r, Zou H, Zhou Q, Yang D-j, Sun C and Tian X (2022) Trace Element Composition and Cathodoluminescence of Quartz in the Hongniu–Hongshan Skarn Deposit in Yunnan Province, Southwest China. Front. Earth Sci. 10:864118. doi: 10.3389/feart.2022.864118

1. INTRODUCTION

Quartz is not only one of the most abundant minerals in the crust but is also the most common gangue mineral in various hydrothermal deposits. Quartz commonly crystallizes at a wide range of temperature between 50° and 750°C from fluids with diverse origins and compositions (Rusk and Reed, 2002; Rusk et al., 2008; Thomas et al., 2010; Götte et al., 2011). Quartz is almost 100% SiO_2 with amounts of mineral impurities assaying at the ppm levels.

Recent advances in the use of LA–ICP–MS have allowed for *in situ* analyses of numerous trace elements in quartz, such as Ti, Al, Li, Na, K, Fe, Ca, P, Mg, Mn, Cu, and Ge, at increasingly lower detection limits. The trace element concentrations in quartz is generally related to the abundance in melts or hydrothermal fluids, partitioning between the co-genetic minerals, pressure, temperature, and growth rate (Smith and Stenstrom, 1965; Andersson and Eklund, 1994; Gurbanov et al., 1999; Pagel and Orberger, 2000; Larsen et al., 2000; Götze et al., 2001; Takahashi et al., 2002; Larsen et al., 2004; Landtwing and Pettke, 2005; Wark and Watson, 2006; Jacamon and Larsen, 2009; Thomas et al., 2010; Rusk et al., 2011; Lehmann et al., 2011; Liang et al., 2014; Fu and Yan, 2020). Given that quartz is less prone to retrograde alteration and weathering than most hydrothermal minerals, its

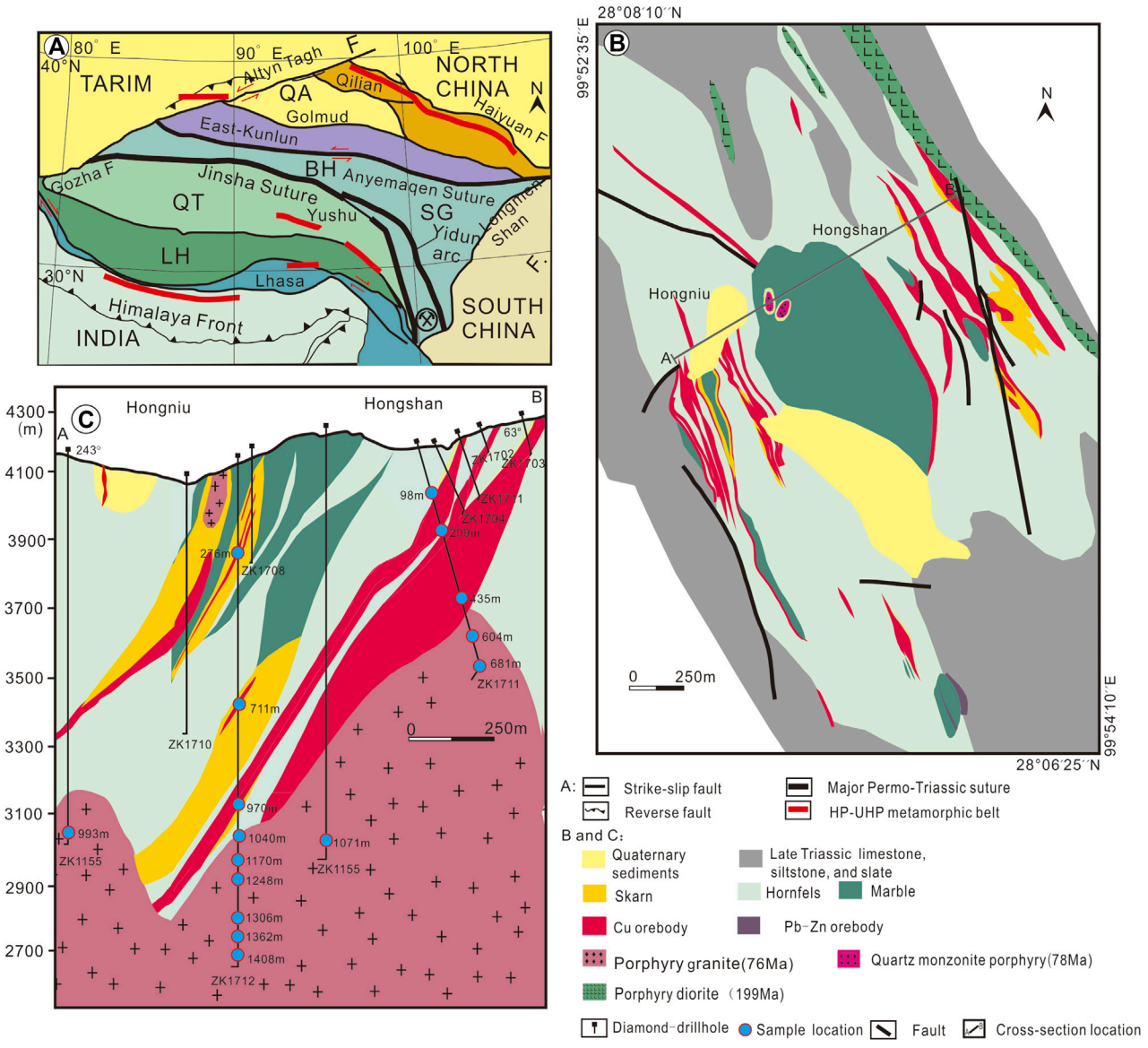

FIGURE 1 | Geological maps showing **(A)** the tectonic setting of the Yidun Arc and Hongniu–Hongshan copper deposit (Xiong et al., 2014), **(B)** the Hongniu–Hongshan Cu deposit (Peng et al., 2021), and **(C)** simplified cross sections through the Hongniu–Hongshan Cu deposit, showing the spatial relationship between the different rock types and ore bodies. The locations of the cross sections are shown in panel B. The samples analyzed in this study were all collected from cross sections A–B. LH = Lhasa Block; QT = Qiangtang Block; BH = Bayan Har terrane; QA = Qaidam Basin; S = Suture; F = Fault.

trace element composition can indicate its point of crystallization, which can be used to better understand the genesis of various types of deposits (Monecke et al., 2002; n; Wark and Watson, 2006; Rusk et al., 2008; Lehmann et al., 2009; Thomas et al., 2010; Agangi et al., 2011; Rusk, 2012; Wertich et al., 2018; Zhang et al., 2019; Fu and Yan, 2020). In addition, the trace element geochemistry of quartz and its cathodoluminescence (CL) reflectivity response have also been studied by various researchers (c.f. Marshall, 1988; Ramseyer and Müllis, 1990; Remond et al., 1992; Perny et al., 1992; Penniston-Dorland, 2001; Peppard et al., 2001; Götze et al., 2005; Rusk et al., 2006; Coulson et al., 2007; Rusk et al., 2008; Müller et al., 2010; Peng et al., 2010a; Peng et al., 2010b; Peng et al., 2010c; Götte et al., 2011; Rusk, 2012; Breiter et al., 2017a; Breiter et al., 2017b; Fu and Yan, 2020). These studies suggest that the trace element geochemistry of quartz is an indicator of its growth dynamics, physicochemical conditions during crystallization, and evolution (Monecke et al., 2002; Yang et al., 2008; Chen and Zhang, 2011; Götte et al., 2011). Furthermore, magmatic and hydrothermal quartz can be distinguished by their Ge/Al and Li/Al ratios (Müller et al., 2018).

The Hongniu–Hongshan skarn Cu deposit is located in the Zhongdian area of the Shangri-La County, Yunnan Province, China (**Figure 1**). The deposit includes two ore blocks known as the Hongshan and Hongniu blocks. The Hongshan block is relatively located to the northeast and has been mined since 1971, and the recently discovered Hongniu block is located to the southwest. In the past decade, the deposit has been regarded as skarn deposits (Hou et al., 2004; Song et al., 2006; Wang et al., 2011; Meng et al., 2013; Peng et al., 2014; Wang et al., 2016), and has been studied in detail, including isotopic ratio, fluid inclusion studies (Peng et al., 2016; Wang et al., 2016), mineralogy (Song et al., 2006; Wang et al., 2008; Peng et al., 2021; Tian et al., 2019), and geochronology (Wang et al., 2011; Huang et al., 2012; Meng et al., 2013; Peng et al., 2014).

A porphyritic granite has recently been identified in diamind-drillhole core from the northeastern part of the deposit (**Figures 1A,B**). The intrusion hosts quartz–pyrite–chalcopyrite–molybdenite veins, and sub-economic porphyry-type Cu–Mo mineralization at the Hongniu–Hongshan deposit. In this contribution, we present the petrographic description and trace element geochemistry of quartz aiming to understand the genesis of their trace element tenures, quartz crystallization, and resorption of quartz phenocrysts. We discuss whether the igneous host rock at the deposit underwent magmatic mixing or recharge. Additionally, quartz trace element data from 14 deposits were compiled to study the difference between magmatic and hydrothermal quartz.

2. GEOLOGICAL SETTING

2.1 Regional Geology

The Hongniu–Hongshan Cu deposit is located in the Zhongdian area in the southern part of the Yidun Arc. The area is in the eastern part of the Paleo-Tethyan Orogen in South Asia (**Figure 1A**; Sengor and Natal, 1996; Hou et al., 2007; Qu et al., 2010; Xu et al., 2012; Xu et al., 2018). The Yidun Arc is bounded by the Jinshajiang Suture to the west and the Garze–Litang Suture to the east. It is connected to the western margin of the Yangtze Block and extends for over 500 km from Gaogong in Sichuan Province in the north to Zhongdian in Yunnan Province in the south (**Figures 1A,B**). The Zhongdian polymetallic belt is situated in the southern segment of the Yidun Arc and is considered one of the most important non-ferrous metallic belts in China. It is characterized by Late Triassic porphyry skarn Cu(-Mo) deposits, such as Xuejiping and Pulang (Leng et al., 2008; Wang et al., 2008; Hou et al., 2010; Li et al., 2011; Mao et al., 2014; Ting et al., 2018). Recent geochronological studies indicate that some intrusions and associated porphyry-skarn deposits in the belt formed in the Late Cretaceous, such as the Hongniu–Hongshan Cu and Tongchanggou Mo deposits (Li et al., 2012; Li et al., 2013; Meng et al., 2013; Peng et al., 2014).

2.2 Hongniu–Hongshan Deposit

The Hongniu–Hongshan deposit is located in the Shangri-La County (Zhongdian) of Yunnan Province. It covers an area of ~24 km^2 at an elevation of 4,060–4,460 m above sea level (**Figures 1B,C**). The country rocks include gray slate, quartzite, and limestone of the Late Triassic Qugasi Formation. The formation metamorphosed to biotite hornfels, calc–silicate hornfels, and marble near the porphyritic granite (**Figure 1B**). The country rocks are cut by NW- and NE-trending faults, with the NW-trending faults hosting the mineralization at the Hongniu–Hongshan deposit subparallel to the strike of the Qugasi Formation, and the NE-trending faults dipping SE (**Figure 1B**).

The Hongniu–Hongshan granite is subdivided into a ca. 199 Ma porphyritic diorite located in the northeastern part of the Hongshan ore block (Peng et al., 2014), ca. 78 Ma porphyritic quartz monzonite and ca. 76 Ma porphyritic granite (Huang et al., 2012). The younger igneous phases are thought to be genetically associated with the skarn and mineralization (Peng et al., 2016).

The porphyritic quartz monzonite is located in the central part of the deposit and is often in direct contact with marble (**Figure 1B**). It is light grayish to white with phenocrysts of plagioclase (25–35%), K-feldspar (5–10%), biotite (5–10%), and quartz (3–5%). The quartz monzonite hosts endoskarn and exoskarn zones. The endoskarn consists of reddish grossular garnet, diopside, vesuvianite, and epidote (Peng et al., 2016).

The porphyritic granite is present below a depth of ~600 m at the deposit (**Figure 1C**), where it comprises 20- to 100-mm-long phenocrysts of pinkish K-feldspar and zoned gray plagioclase in a coarse- to fine-grained groundmass of the quartz, plagioclase, K-feldspar, biotite, and hornblende (**Figures 2A–F**), with accessory chalcopyrite, pyrite, sphene, and apatite. The porphyritic granite has an early K-alteration characterized by secondary biotite- and quartz- K-feldspar veins. This is overprinted by argillic and sericitic alteration in the upper part of the granite. Both alterations are overprinted by weak propylitic

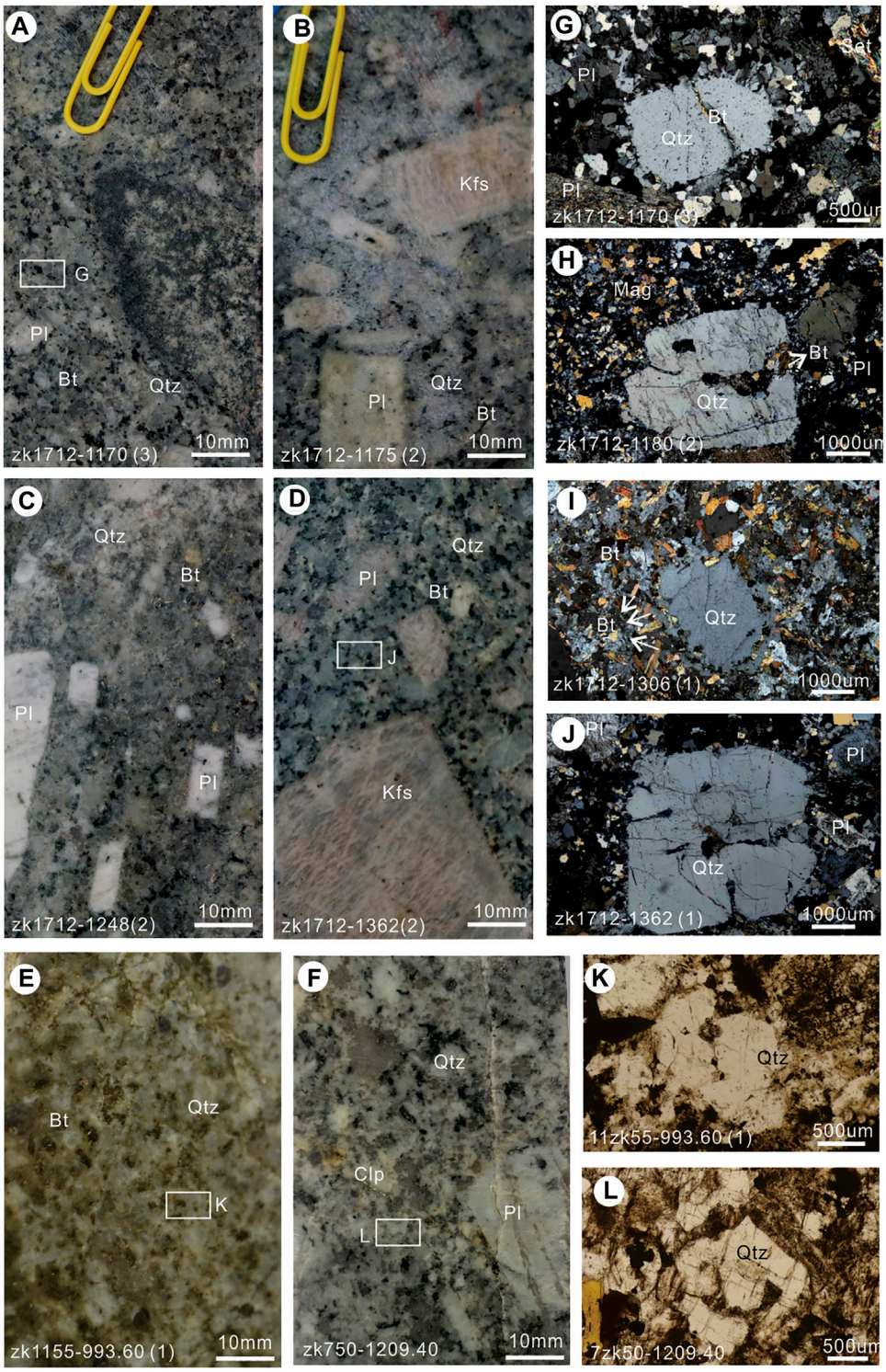

FIGURE 2 | Photomicrographs of representative mineral assemblages from the Hongniu–Hongshan Cu deposit. The quartz forms phenocryst and is in the matrix in the porphyritic granite at the Hongniu–Hongshan deposit Panels **(2A–F)**. Quartz coexists with K-feldspar, plagioclase, amphibole, and biotite. Quartz phenocryst is subhedral–euhedral and 4–6 mm in diameter, and some of them show rounded or embay surfaces (Panels **2G–L**). The quartz matrix is allotriomorphic and 0.5–1 mm in size. Amp = amphibole; Bt = biotite; Kfs = K-feldspar; Pl = plagioclase; Qtz = quartz (after Kretz, 1983).

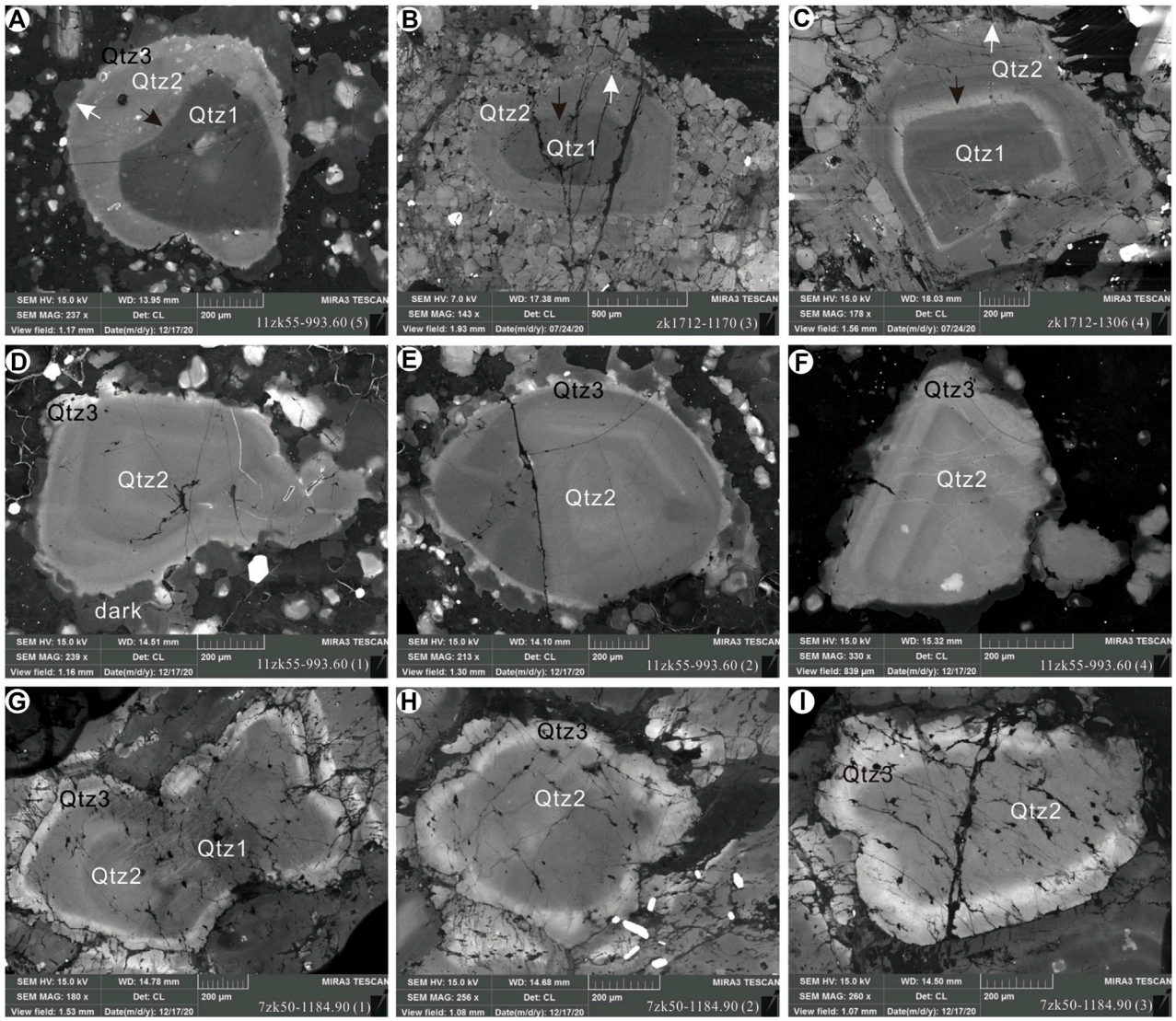

FIGURE 3 | SEM-CL image of quartz from the Hongniu-Hongshan deposit. The quartz from the first generation of quartz (Qtz1) contains a strong dark grey luminescent core (in SEM-CL) with an average diameter of 0.4-0.6 mm (**Figures 3A-C**).The second generation of quartz (Qtz2) has a clear bright grey oscillatory overgrowth zonation with layers averaging 0.2 mm thick (**Figures 3D-F**). The third generation of quartz (Qtz3) typically has a narrow light grey rim on the SEM-CL images, with have an average thickness of 0.04 mm (**Figures 3G-I**). The black arrow show the resorption surfaces.

alteration characterized by chlorite and epidote, replacing biotite in the upper part of the deposit.

The prograde metamorphism at the Hongniu–Hongshan deposit includes garnet, pyroxene, and wollastonite. This assemblage is overprinted by an intense retrograde metamorphism characterized by epidote, tremolite, magnetite, and chlorite (Peng et al., 2021). The bulk of the mineralization is hosted by skarn and calc–silicate hornfels.

3. SAMPLES AND ANALYTICAL METHODS

Twenty-one samples of drill cores were analysed from the porphyritic granite. Polished thin sections were used to petrologically study all of the samples, with emphasis on the occurrence, morphology, and texture of quartz. Seven samples were collected for scanning electron microscopy cathodoluminescence (SEM-CL) imaging and LA-ICP-MS analysis.

3.1 SEM-CL

SEM-CL images were obtained using a Tescan MIRA3 LM instrument set at an acceleration voltage of 15 kV and current of 15–20 nA/mm at Nanjing Hongchuang Geological Exploration Technology Service Co., Ltd., Nanjing, China. The bialkali tube had a CL response ranging from 300 nm (violet) to 650 nm (red), and it peaked in the violet spectrum at ~400 nm. The CL images were collected from one scan with a 60-s photo speed and a processing resolution of 1,024 × 768 pixels. The brightness and

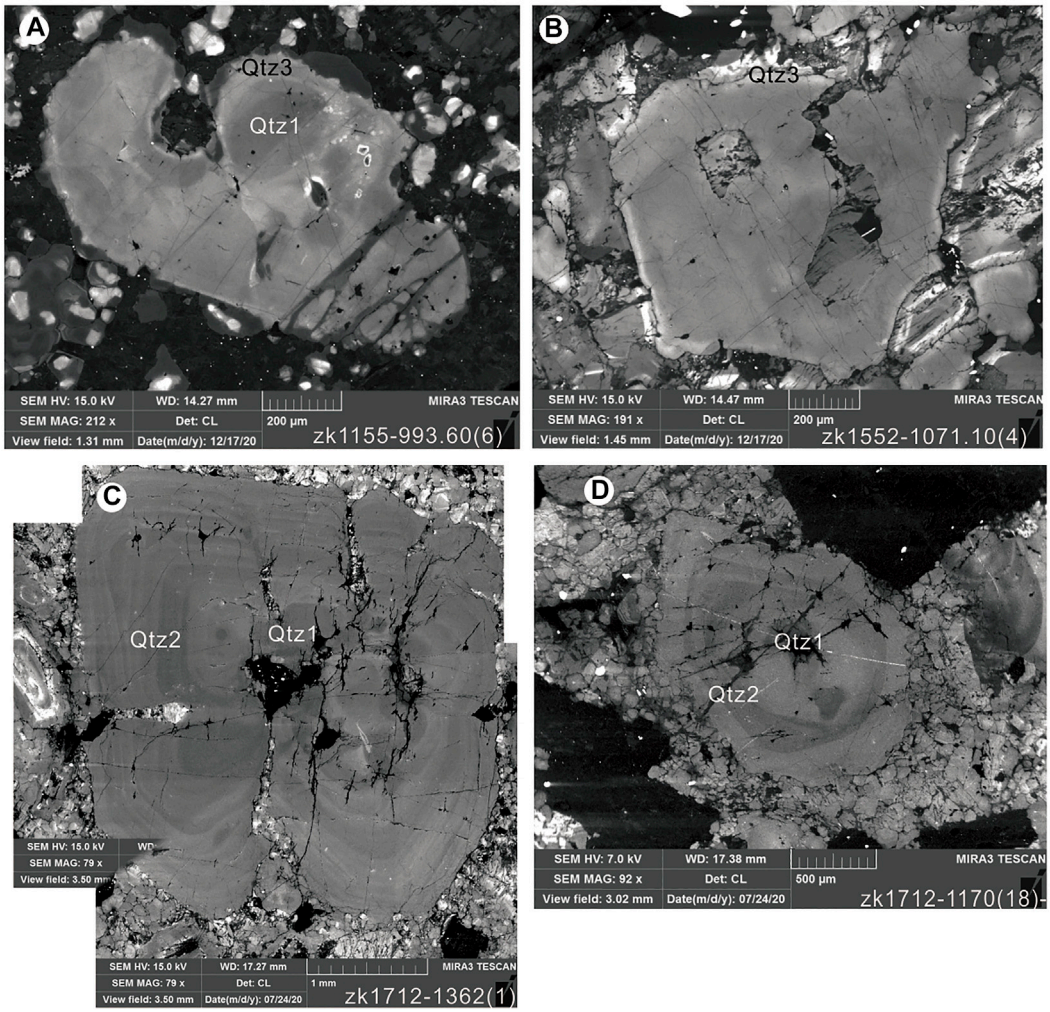

FIGURE 4 | SEM-CL image of quartz from the Hongniu–Hongshan deposit (for explanations of symbols, see **Figure 3**).

contrast of the collected CL images were improved using Adobe Photoshop software.

3.2 LA-ICP-MS

Trace element concentrations of quartz was analyzed using an Agilent 7900 ICP-MS equipped with a GeoLasPro 193 nm ArFexcimer laser at the State Key Laboratory of Ore Deposit Geochemistry, Institute of Geochemistry, Chinese Academy of Sciences, Guiyang, China. The laser repetition was set at 10 Hz with an energy density of 12 J/cm2 and a spot size of 44 μm. The NIST SRM610 and GSD-1G standards were analyzed as external standards. The standards were run before and after each set of 10–15 spots on the analyzed samples. The analysis time for each spot was set at 90 s, comprising a 30-s background measurement time with the laser off, followed by 60 s with the laser on. An internal standard-independent calibration strategy, based on the normalization of the sum of all metal oxides to 100 wt%, was applied to the calibrations (Liu et al., 2008). The NIST SRM612 and GSD-1G standards were analyzed to monitor the accuracy of the results, which showed that the uncertainties of most elements (Li, Na, Mg, Al, K, Ca, Sc, Ti, Sb, Ge, Rb, and Sr) were <6%, with detection limits ranging from ppb to a few ppm. More details on the analytical procedures can be found in Lan et al. (2017).

4. RESULTS

4.1 Quartz Petrography and Micro-Textures

The phenocrysts of porphyritic granite samples are composed of plagioclase (5-10 vol%), K-feldspar (5 vol%), quartz (<5 vol %), and amphibole (<5 vol%). Its matrix is mainly composed of feldspar, quartz, amphibole, and biotite. The quartz phenocrysts are subhedral to euhedral, 4–6 mm in diameter, and some are rounded or embayed (**Figures 2G-**

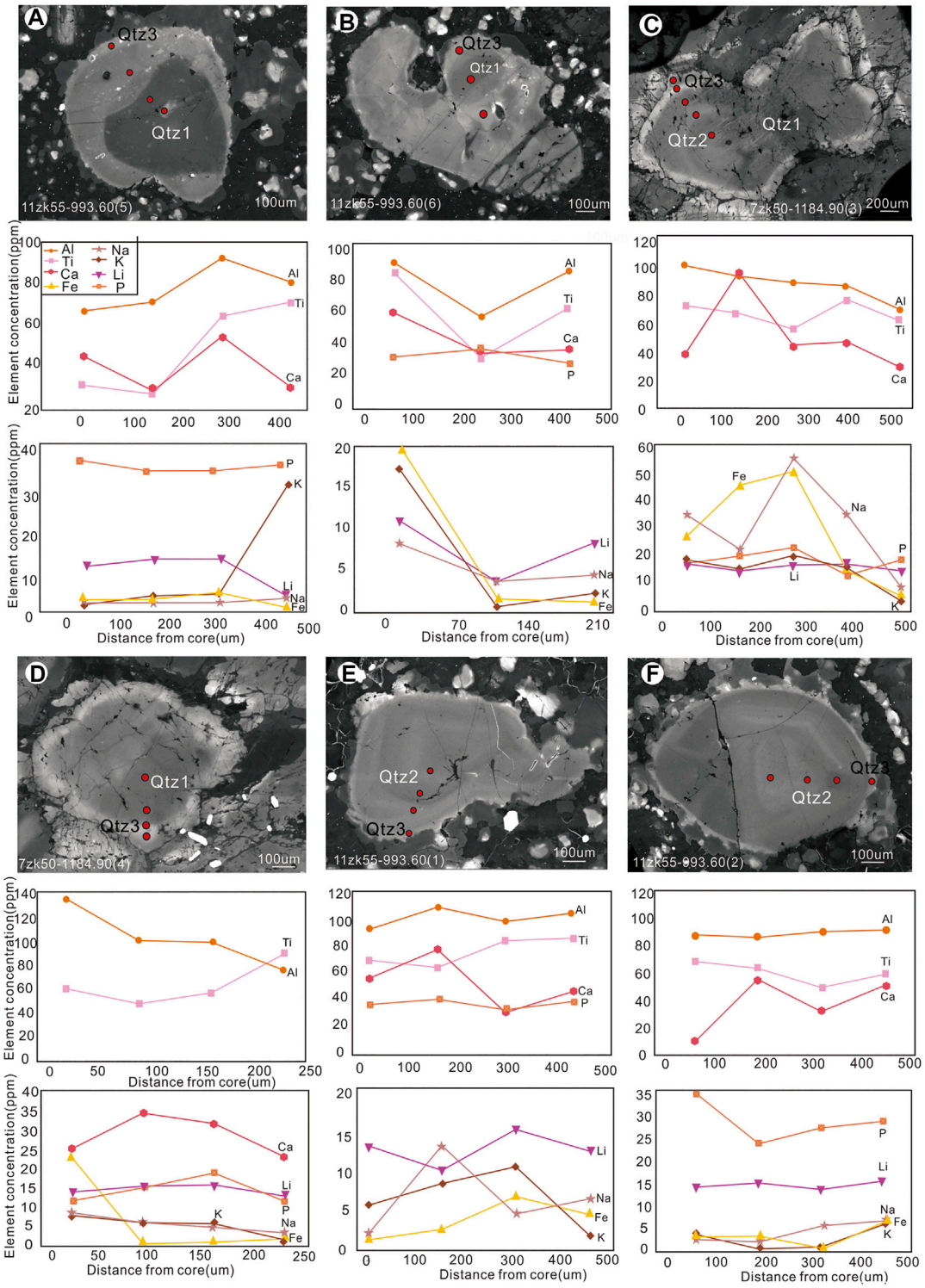

FIGURE 5 | Concentrations of trace elements in single quartz phenocrysts from their core to rim determined using LA-ICP-MS.

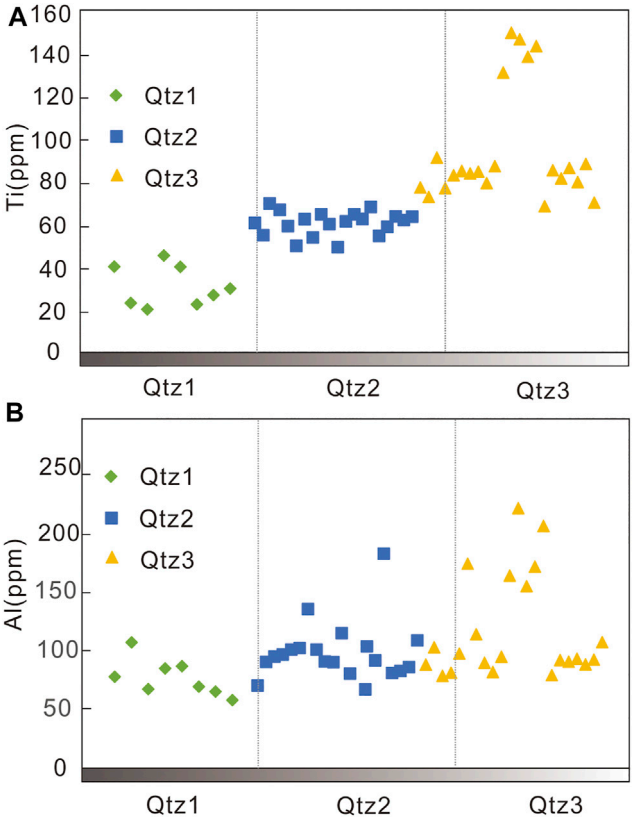

FIGURE 6 | Content of Al and Ti contents in the three quartz generations from the Hongniu–Hongshan deposit.

L). The quartz in the matrix is allotriomorphic and 0.5–1 mm across. The euhedral quartz phenocrysts were selected for the CL structural analysis. Three generations of quartz phenocrysts (Qtz1–3) were identified (**Figure 3**).

The first generation of quartz (Qtz1) is the most voluminous (Müller et al., 2010), and contains dark gray luminescent and rounded cores with an average diameter of 0.4–0.6 mm (**Figures 3A,B**). Some include slight oscillatory zones (**Figure 3C**). The second generation of quartz (Qtz2) has clear bright grey oscillatory zonation (**Figures 3D–F**). The average width of the growth is 0.2 mm. The zonation is commonly bright on the CL images and has been nucleated on weakly luminescent homogenous cores (dark in CL) (**Figures 3**, **4A-D**). The third-generation quartz (Qtz3) crystals are represented by narrow light-gray rims, with an average width of 0.04 mm (**Figures 3D–I**). The crystal surfaces were wavy and probably developed shortly before crystallization (**Figures 3A,D,E**). The average crystal size of the matrix quartz is 0.02–0.04 mm, with weak contrasting growth zones (gray in CL).

4.2 Trace Element Compositions of Quartz Phenocryst

The samples were analyzed for Al, Ti, K, Fe, Ca, Na, Li, and P using LA-ICP-MS along transecting different quartz generations (**Figure 5**). The concentrations of these elements vary considerably between different quartz generations (**Supplementary Table S1**). The Al and Ti assays are relatively high in the three quartz generations of quartz, whereas Sb, Li, Ba, Sr, Ge, and As are common elements at lower concentrations (**Figure 5**). The concentrations of Zr, Nb, Gd, Hf, Ta, and U are below the detection limit in some analyzed spots.

The dark luminescent crystal cores in the Qtz1 phenocrysts have the lowest concentrations of Ti (22–47 ppm) among the three generations. The Qtz2 quartz with oscillatory zonation has medium Ti concentrations (51–70 ppm). The bright gray luminescent rim in the Qtz3 quartz is enriched in titanium, assaying 70–151 ppm Ti. The CL reflectivity always correlated positively with the Ti concentration in all the three generations of the quartz (**Figure 6A**).

Aluminum is the most common and abundant trace element in all of the three generations of the quartz, with a wide range in concentration. The Qtz1 quartz assays 58–129 ppm Al, Qtz2 assays 82–188 ppm Al, and Qtz3 assays 80–101 ppm (**Figure 6B**).

All of the quartz grains have relatively low Li assaying 4–18 ppm Li for Qtz1, 8–23 ppm Li for Qtz2, and 11–19 ppm Li for Qtz3. (**Figure 5**). The Qtz1 quartz assays 0.43–40 ppm FeT, Qtz2 assays 0.24–88 ppm, and Qtz3 assays 0.11–56 ppm FeT (**Figure 5C**). The Qtz1 and Qtz2 quartz samples have consistently low concentrations of K averaging 15 ppm K, but the Qtz3 quartz samples have a higher average value of 32 ppm K (**Figure 5A**). Phosphorus ranges from 13 to 47 ppm in all the three quartz generations, and in one crystal, P is evenly spread and does not correlate with any other element. Calcium is irregularly distributed among the three generations of quartz, with assays varying between 9 and 62 ppm. The Ca content of the Qtz3 samples, however, decreases significantly (**Figures 5A,D**). The Na content is variable among the three generations of quartz, ranging between 0.57 and 61 ppm. The Ge concentrations varied from 0.39 to 0.92 ppm in the three quartz generations, which corresponds to the range described from other magmatic systems (e.g., Jacamon and Larsen, 2009; Müller, 2018).

5. DISCUSSION

5.1 Occurrence of Trace Elements in Quartz

The chemical structure of quartz consists of Si–O bonds with limited spaces, making it difficult for other elements to be incorporated in its structure (Jourdan et al., 2009). Previous geochemical studies of quartz have revealed significant occurrence of trace elements, such as Al, B, Ca, Cr, Cu, Fe, Ge, K, Li, Mg, Mn, Na, P, Rb, Pb, Ti, and U (Flem et al., 2002; Müller et al., 2003; Landtwing and Pettke, 2005; Müller and Koch-Müller, 2009). The LA-ICP-MS assays of Al, Na, K, Mg, Li, Mn, Fe, Ge, and Ti for most of the studied quartz phenocrysts were flat and stable (**Figures 7A,B**). This indicates that they are homogeneously distributed in the quartz crystal lattice, or are

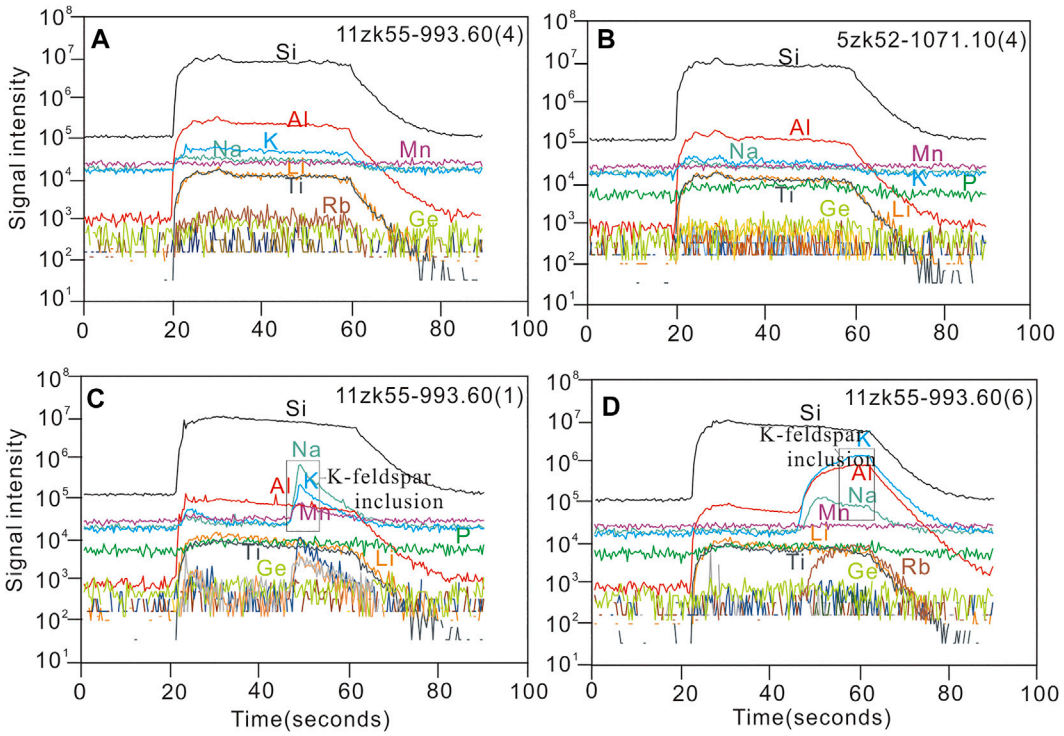

FIGURE 7 | Time-resolved analysis (TRA) of elements across quartz grains.

present as nanoparticles in the quartz (Genna and Gaboury, 2015; Dehnavi et al., 2018). However, significant differences between individual spots and irregular depth profiles for Ca, Sc, Ba, and As imply that these elements may be present in both the solid solution and as micro-inclusions in the quartz (Ciobanu et al., 2013; **Figures 7C,D**).

Mono-, tri-, tetra-, and even pentavalent cations can be incorporated into the interstitial or tetrahedral sites of quartz to form crystal point defects (Götte and Ramseyer, 2012). Ge^{4+} and Ti^{4+} are similar in size to Si4+ and can substitute for it in the quartz crystal lattice (Chen et al., 2011; Rusk, 2012). Furthermore, pentavalent P^{5+} and trivalent Al^{3+} can combine to substitute for $2Si^{4+}$ (e.g., Chen et al., 2011). Trivalent Al^{3+} and Fe^{3+} can also enter quartz substituting for Si^{4+}, which requires monovalent alkali metals (Li^+, Na^+, K^+, and Rb^+) or trivalent (Ca^{2+} and Sr^{2+}) cations as charge compensators (Müller et al., 2003; Rusk et al., 2008; Götte and Ramseyer, 2012; Rusk, 2012). The quartz phenocrysts of the Hongniu–Hongshan deposit are significantly negatively correlated with Si and Ti (**Figure 8B**), which indicates that Ti^{4+} could enter quartz to substitute for Si^{4+} (**Figure 9**). In addition, Al negatively correlates with Si and positively correlates with alkali metals (**Figures 8D–F**). These elemental substitutions can be summarized by the equation Al^{3+} + Li^+ (Na^+, K^+, and/or H^+) → $Si4^+$. Furthermore, a lack of clear positive correlation between Si and Ge and positive correlation between Al and Ge shown in **Figures 8A,H** indicates that Ge^{4+} has been substituted for Si^{4+} and Ge^{2+} acted as a charge compensator for the substitution of Si^{4+} by Al^{3+} (Götte and Ramseyer, 2012) (**Figure 9**).

5.2 Metallogenic Implications of the Hongniu–Hongshan Deposit

5.2.1 The Condition of the Quartz Phenocryst Crystallization

A significant correlation exists between Ti concentration and quartz precipitation temperature, especially at temperatures over 600°C (Wark and Watson, 2006; Wark et al., 2007; Götze, 2009; Thomas et al., 2010). The Ti concentration of the hydrothermal quartz formed at <350°C is < 10 ppm, and that formed at temperatures over 400°C is > 10 ppm (Rusk et al., 2008; Rusk, 2012). The Ti in the quartz samples from the study area assays 21–158 ppm indicative of relatively high crystallization over 400°C (Wark and Watson, 2006).

The crystallization temperature of the quartz is also affected by the pressure and Ti activity (αTiO_2) of the melt or fluid (Wark and Watson, 2006; Huang and Audétat, 2012). The TitaniQ thermobarometer of Thomas (2015) is defined by the equation logTi = −0.27943 × 104/T−(−660.53 × P0.35/T) + 5.6459, which helps in determining the quartz crystallization temperature using pressure. Peng et al. (2016) used fluid inclusion micro-thermobarometry to determine the formation temperatures of quartz phenocrysts in the

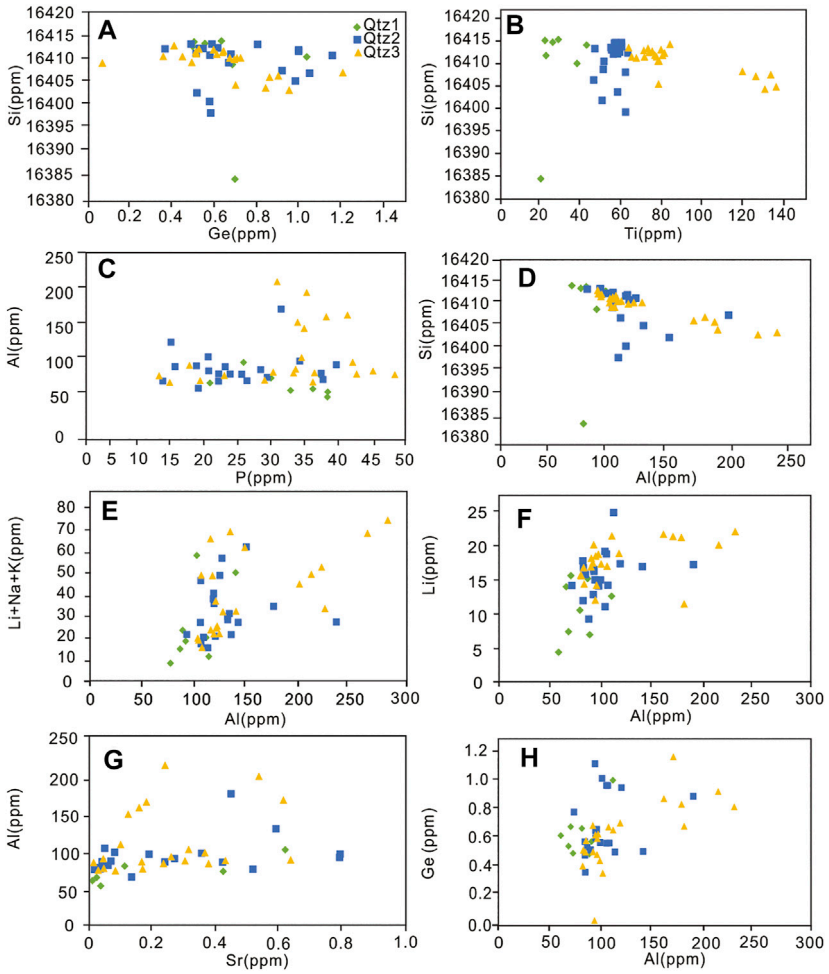

FIGURE 8 | Plots of minor and trace elements in quartz from the Hongniu-Hongshan deposit.

Hongniu–Hongshan porphyritic granite, which ranged from ~410° to 720°C at pressures of 680–940 bar. Owing to the relatively wide range of pressure, the crystallization temperature of quartz was calculated using the TitaniQ thermobarometer of Wark and Watson (2006) defined by the equation T(°C) = (−3,765/(log(Xqtz Ti/ αTiO_2)−5.69)−273. The TiO2 activity is difficult to determine; however, rutile is common in the samples of the porphyritic granite, which indicates that TiO_2 is saturated (i.e.,αTiO_2 = 1) (Hayden and Mathewes, 2005; Wark et al., 2007). From the TitaniQ thermobarometer, the crystallization temperature of Qtz1 was 593–664°C, and the gray oscillating rim of Qtz2 crystallized at 672–706°C. These temperatures are consistent with the temperatures measured by micro-thermometry of fluid inclusions. However, the Qtz3 crystallized at a temperature of 706–800°C, which is higher than the micro-thermometry temperatures. This is probably due to the small size of Qtz3, which resulted in a lack of melt/fluid inclusions.

The factors influencing Al concentrations in quartz are still under debate (Rusk, 2012)The high Al content in quartz indicate that it precipitated from a pH-dependent magma-derived hydrothermal fluid (Rusk et al., 2008; Müller et al., 2010; Götte, 2016). Breiter and Müller (2009) documented that there is no correlation between the Al content of igneous quartz and the Al content and peraluminosity of the parental melt. The relatively low average Al and K in Qtz1 presumably indicates that Al and K complexes in the magma preferentially precipitated as K-feldspar in the wall rock, incorporating Al and K that might have otherwise entered the quartz lattice. The higher average and variable Al content in Qtz2 of 71–187 ppm may reflect a relatively late-magmatic origin (Müller et al., 2000). The high Al content in Qtz3 of 79.5–227 ppm probably indicates that it precipitated from a magma-derived hydrothermal fluid. Acidic pH is commonly observed at this evolutionary stage of porphyry systems (Heinrich et al., 2005), providing the H+ necessary for the ionization of Al; however, Qtz3 shows the highest crystallization temperature among the three quartz generations pointing to a different origin.

5.2.2 Resorption of Quartz Phenocrysts

According to Müller et al. (2005, 2006, 2009), the processes that may form a resorption structure in quartz are 1) a semi-

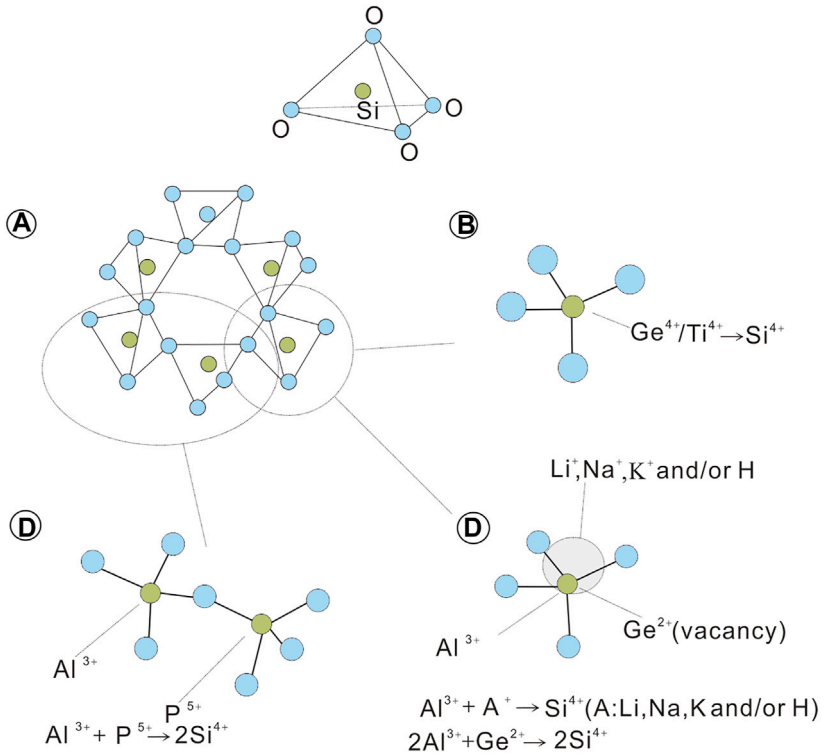

FIGURE 9 | The substitution of trace elements in quartz from the Hongniu-Hongshan deposit (after Larsen et al., 2004).

adiabatic magma ascent, 2) metasomatism by magma-derived hydrothermal fluids, and 3) magma mixing. The Ti-in quartz geothermometer provides the quartz crystallization temperature prior to and after a major phenocryst resorption episode. If resorption is caused by semi-adiabatic magma ascent, or the quartz grains were replaced by the magmatic fluid, the Ti-in quartz would not increase after resorption.

Supplementary Table S2 presents the changes in the minimum temperature after a major resorption episode. The resorbed cores and marginal resorption surfaces are overgrown by more luminescent quartz. Before resorption, the average concentration of Ti in the quartz phenocryst cores was 24 ppm at a crystallization temperature of ~600°C. After resorption, the average concentration of Ti in the bright band halo at the edge of the crystal core was 56 ppm (**Figure 10**, white arrows). This was at a crystallization temperature of 683°C, being 83°C higher than that of pre-resorption, and a maximum temperature difference was 109°C. Furthermore, the Ti concentration was 75 ppm at the edge of the pre-resorption quartz phenocryst with a crystallization temperature of 714°C. During post-resorption, the average Ti increased to 81 ppm, with a crystallisation temperature of 72°C, and a maximum temperature difference of 54°C. Assuming that the concentration of trace elements in the solid phase is controlled by the concentration of the elements in the melt, the high Ti content in quartz indicates that the crystals became part of a more Ti-rich melt after resorption. This indicates that the quartz phenocrysts at the Hongniu–Hongshan have experienced two mixing episodes involving a high-temperature magma. However, the injection of hotter magma at the deeper levels of a magma reservoir may lead to higher gas pressures and trigger magma ascent (e.g., Blake and Pincus, 1996; Smith et al., 2004). This indicates that magma mixing and adiabatic magma ascent are normally simultaneous during magma evolution.

5.3 Implications on Ore Deposit Type

The Al and Ti contents of epithermal, orogenic gold, and porphyry gold deposits differ from each other (**Figures 11**, **12**, **Supplementary Table S3**). The Ti content of quartz from orogenic gold deposits is higher than that of typical epithermal deposits with values < 3 ppm and lower than that of quartz from typical porphyry deposits assaying 1–200 ppm at >400°C (Rusk et al., 2008; Rusk, 2012).

The concentration of Al in quartz reflects its solubility in hydrothermal fluids, which is closely related to the fluid's pH. Thus, the Al concentration in quartz reflects the flow at a certain

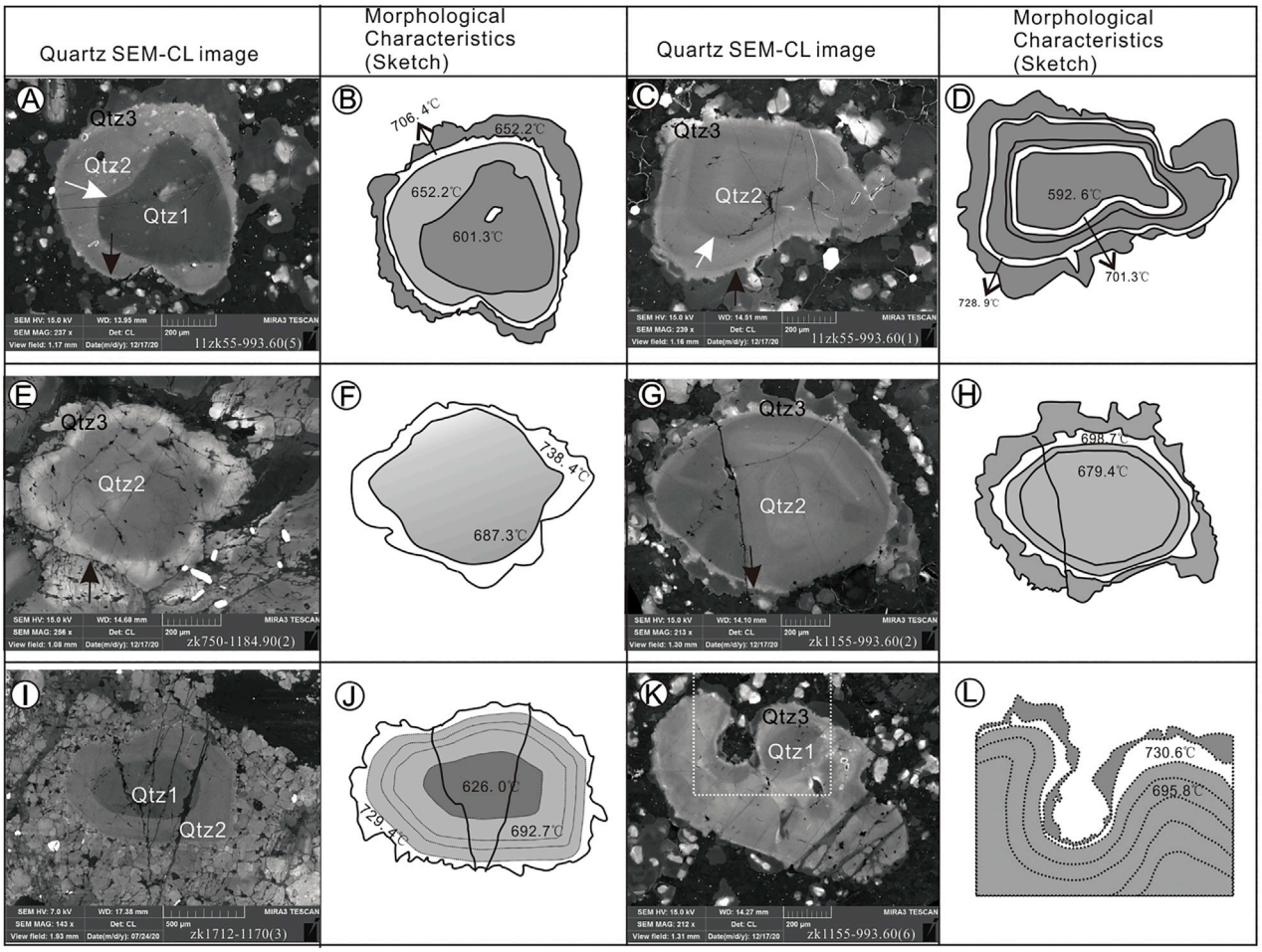

FIGURE 10 | Structure sketch and the temperature changes before and after resorption of quartz phenocrysts from the Hongniu–Hongshan deposit.

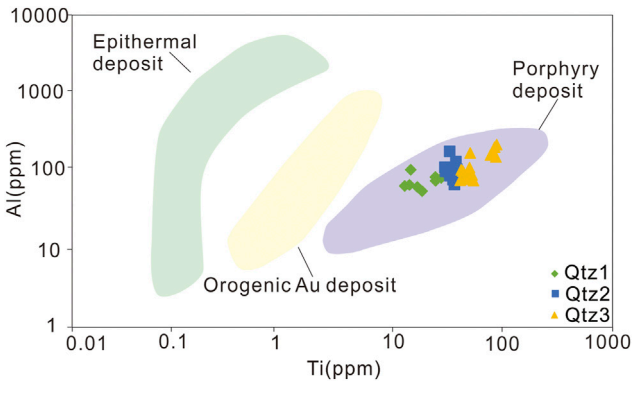

FIGURE 11 | Diagram of Ti vs Al contents of quartz in the Hongniu-Hongshan deposit compared with data from Rusk (2012) including porphyry-type deposits, orogenic Au deposits, and epithermal deposits.

pH, which may precipitate metal sulfides in hydrothermal deposits (Rusk et al., 2008). The Al content of quartz in porphyry deposits commonly ranges between 50 and 500 ppm, which is lower than that of orogenic gold deposits that assay 100–1,000 ppm Al. This may be due to the relatively Al-rich hydrothermal environment (Rusk, 2012). Hydrothermal quartz is mainly formed at high temperatures (500°–700°C) in porphyry deposits, and may be associated with K-alteration rather than Al-alteration (Rusk et al., 2008). Among the different types of deposits, the Al content of the low-temperature hydrothermal deposits is significantly variable. Some growth zones contain <50 ppm Al, while others contain >2000 ppm, with generally negligible amounts of Ti, Ge, and Mg (Francois and Larsen, 2009; Chen et al., 2011). Contrastingly, quartz always has a moderate concentration of Al in high-temperature hydrothermal deposits, which commonly assay several hundred ppm (**Supplementary Table S3**, **Supplementary Table S4**; **Figure 12**).

Although the Al and Ti assays of different types of deposits vary, it is difficult to distinguish magmatic quartz from hydrothermal quartz due to their overlap on the Al vs. Ti diagram in (**Figure 13A**, **Supplementary Table S5**). Previous studies show that the Li:Al atomic ratio of both magmatic and hydrothermal quartz does not exceed 1 (**Figure 13B**; Breiter and Mu¨ller, 2009; Jourdan et al., 2009; Breiter and Mu¨ller,

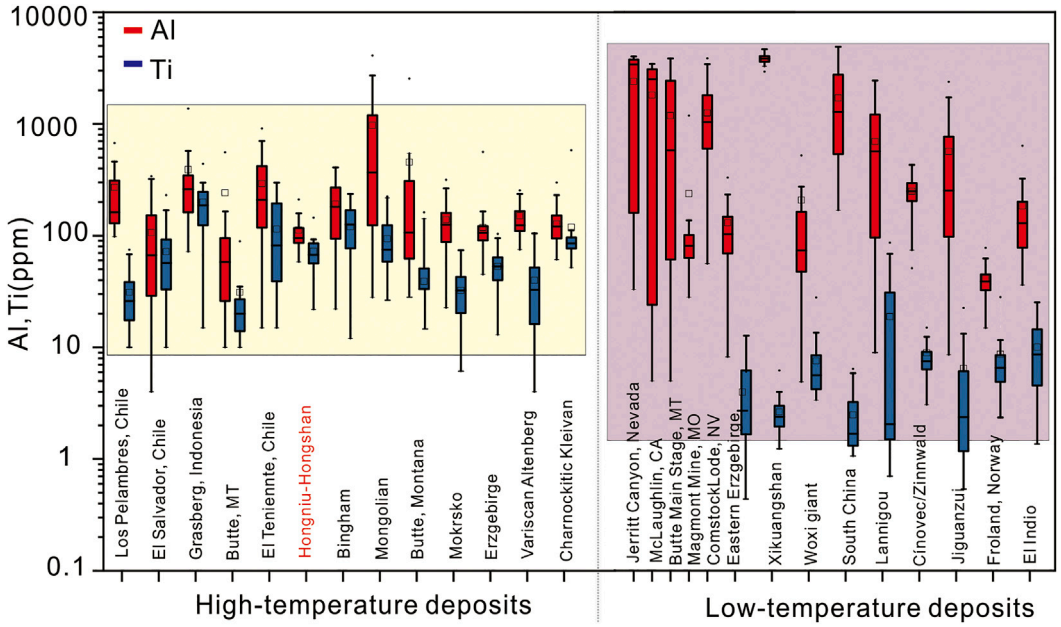

FIGURE 12 | Box diagram of Al and Ti concentrations of quartz from 20 hydrothermal deposits (A = after Rusk et al., 2008; Mariane and Thoms 2005; Rusk et al., 2008; Jacamon and Larsen, 2009; Müller et al., 2010; Peng et al., 2010a; Müller et al., 2018; Zhang et al., 2019; Fu and Yan 2020).

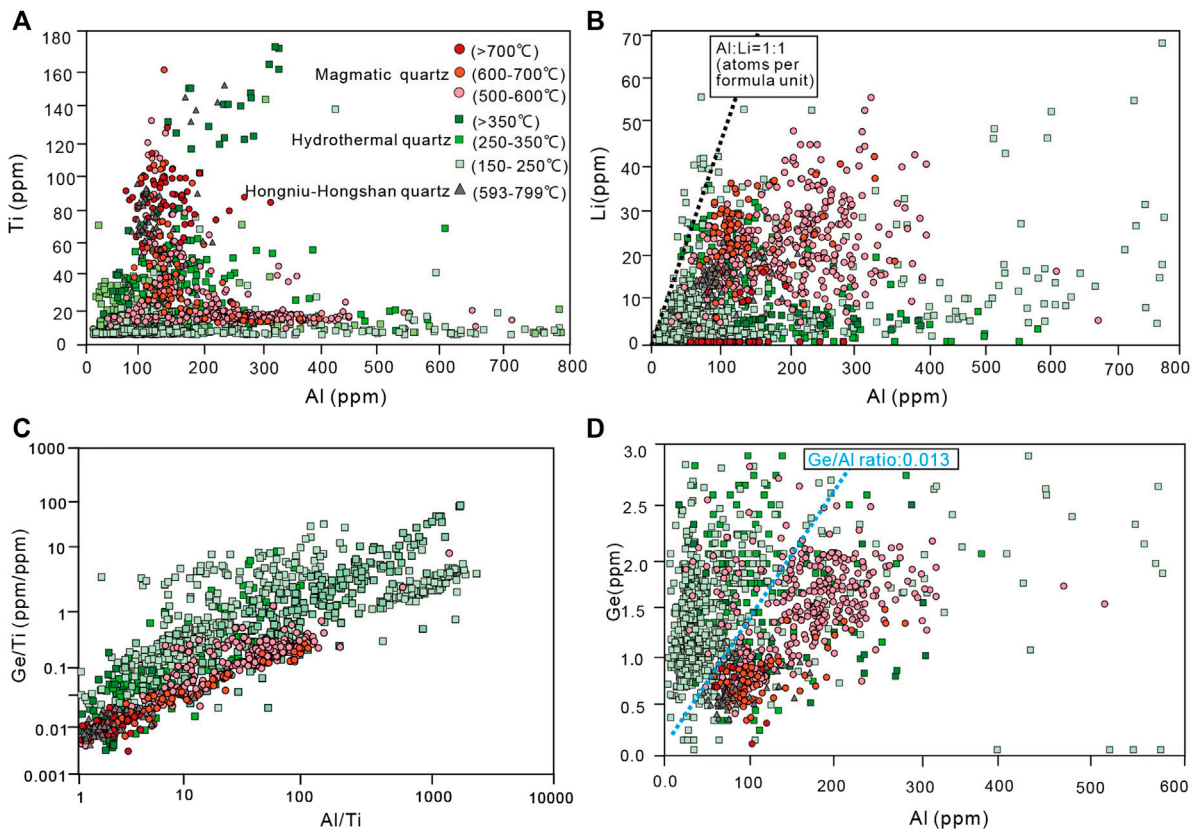

FIGURE 13 | Variability of trace element concentrations in magmatic and hydrothermal quartz from 14 deposits (data from Götze et al., 2004; Mariane and Thoms, 2005; Rusk et al., 2008; Jacamon and Larsen, 2009; Müller et al., 2008, 2010; Peng et al., 2010a; Breiter et al., 2012, 2017a; Wertich et al., 2018; Müller et al., 2018; Zhang et al., 2019; Fu and Yan, 2020). A.Al versus Ti plot. B. Al versus Li plot. C. Al/Ti versus Ge/Ti plot. D. Al versus Ge plot.

2009; Beurlen et al., 2011; Garate-Olave et al., 2017; Mu¨ller et al., 2018). This indicates that the Li uptake by quartz is limited by the amount of Al^{3+} substituting for Si^{4+}.

The positive correlation between Al and Ge in **Figure 13C** shows that progression between magmatic and hydrothermal quartz increases in the quartz's Ge content and decreases in the Al content. Thus, the magmatic quartz can be distinguished from hydrothermal quartz by its increased Ge content. The Ge/Al ratio in the two types of quartz increased systematically from high to low temperatures of quartz crystallization. Similar observations were made by Müller et al. (2018)who proposes magmatic and hydrothermal quartz populations can be distinguished by their Ge/Al weight ratio based on the study of the Late Palaeozoic Zinnwald/Cínovec Sn-W-Li greisen-type deposit: magmatic quartz has a Ge/Al ratio of < 0.008 whereas hydrothermal quartz a ratio of >0.008. The Ge assay varies from 0.35 to 1.17 ppm in the Hongniu-Hongshan deposit (**Supplementary Table S1**) and the average Ge/Al ratio is 0.006, which corresponds to the range reported from other magma-related deposits. On the basis of quartz composition collected for this study from 14 different deposits and our new dataset, we propose that magmatic quartz has a Ge/Al ratio of <0.013, and the hydrothermal quartz has a ratio of >0.013 (**Figure 13D**). The decreasing average Ge content of the hydrothermal quartz is consistent with the finding of Pokrovskii and Schott (1998), who attributed it to the decreasing solubility of Ge in the hydrothermal fluid with decreasing temperature. In the other words, Ge is preferentially incorporated in quartz compared with Al under hydrothermal conditions.

6. CONCLUSION

The quartz phenocrysts in the Hongniu–Hongshan porphyritic granite have Ti^{4+}–Al^{3+}–Li^{+}(–Na^{+}–K^{+}–H^{+}) substituting for Si4+ in the quartz lattice, where Ge2+ acts as a charge compensator for the substitution of Si^{4+} by Al^{3+}.

From the CL textures and trace element concentrations, three quartz generations and two mixing episodes involving a later hotter magma were identified in the porphyritic granite at the deposit. Before the first resorption, the average concentration of Ti in the quartz phenocryst core was 24 ppm, and that in the bright band halo at the rim of core was 56 ppm. This was at a temperature of 109°C higher than that at the pre-resorption stage. Furthermore, the Ti assay of the edge of the quartz phenocryst was 75 ppm before resorption. At the post-resorption stage, the average Ti content increased to 81 ppm at a temperature of 54°C higher than that at the pre-resorption stage.

Based on the quartz composition data collected from 14 different deposits, the magmatic quartz can be distinguished from the hydrothermal quartz using the Ge/Al ratio. The magmatic quartz has a Ge/Al ratio of <0.013, and the hydrothermal quartz has a Ge/Al ratio >0.013.

DATA AVAILABILITY STATEMENT

The original contributions presented in the study are included in the article/**Supplementary Material**, further inquiries can be directed to the corresponding author.

AUTHOR CONTRIBUTIONS

S-lW completed the original draft (first draft). H-jP completed the writing—review and editing. T-rW assisted in the pretreatment of samples and participated in the discussion. HZ made unique suggestions for the article. QZ finished sorting out the reference articles. D-jY completed the collection of partial data and the production of maps. SC assisted in the conception of the previous article and the analysis of samples. XT assisted in data analysis and made maps.

FUNDING

This study was supported by the National Natural Science Foundation of China (41972077 and 41502074).

ACKNOWLEDGMENTS

We thank the editors for their constructive recommendations that have improved this manuscript. We also thank general manager Yuan Qiuyun, of the Nanjing Hongchuang Geological Exploration Technology Service Company Limited, for assistance with the CL analysis, and Han Junjie, of the Institute of Geochemistry, Chinese Academy of Sciences for his help during LA-ICP-MS analyses.

SUPPLEMENTARY MATERIAL

The Supplementary Material for this article can be found online at: https://www.frontiersin.org/articles/10.3389/feart.2022.864118/full#supplementary-material

Supplementary Table S1 | Average trace element concentrations of quartz from the Hongniu–Hongshan deposit.

Supplementary Table S2 | Increase of the Ti contents and quartz crystallization temperatures before and after major resorption episodes documented by the chemical zoning of quartz phenocrysts.

Supplementary Table S3 | Corresponding relationship between formation temperature and Al/Ti content of 20 hydrothermal deposits.

Supplementary Table S4 | Date from Al and Ti concentrations of quartz from 20 hydrothermal deposits.

Supplementary Table S5 | Date from the quartz composition collected from 14 different deposits and our new dataset.

REFERENCES

Agangi, A., McPhie, J., and Kamenetsky, V. S. (2011). Magma Chamber Dynamics in a Silicic LIP Revealed by Quartz: the Mesoproterozoic Gawler Range Volcanics. *Lithos* 126, 68–83. doi:10.1016/j.lithos.2011.06.005

Andersson, U. B., and Eklund, O. (1994). Cellular Plagioclase Intergrowths as a Result of crystal-magma Mixing in the Proterozoic Land Rapakivi Batholith, SW Finland. *Contr. Mineral. Petrol.* 117, 124–136. doi:10.1007/bf00286837

Beurlen, H., Müller, A., Silva, D., and Da Silva, M. R. R. (2011). Petrogenetic Significance of LA-ICP-MS Trace-Element Data on Quartz from the Borborema Pegmatite Province, Northeast Brazil. *Mineral. Mag.* 75, 2703–2719. doi:10.1180/minmag.2011.075.5.2703

Blake, P., and Pincus, J. (1996). 'Neurology and Murderers': Reply. *Neurology* 47, 1611–1612.

Breiter, K., Durisova, J., Hrstka, T., Korbelova, Z., Vankova, M H., Galiovaa, M V., et al. (2017a). Assessment of Magmatic vs. Metasomatic Processes in Rare-Metal Granites: A Case Study of the Cinovec/Zinnwald Sn-W-Li Deposit, Central Europe. *Lithos* 292, 198–217.

Breiter, K., Korbelova, Z., Chladek, S., Uher, P., Knesl, I., Rambousek, P., et al. (2017b). Diversity of Ti-Sn-W-Nb-Ta Oxide Minerals in the Classic Granite-Related Magmatic-Hydrothermal Cinovec/Zinnwald Sn-W-Li Deposit (Czech Republic). *Europ. J. Mineral.* 29, 727–738.

Breiter, K. M., and Müller, A. (2009). Evolution of Rare-Metal Granitic Magmas Documented by Quartz Chemistry. *ejm* 21, 335–346. doi:10.1127/0935-1221/2009/0021-1907

Breiter, K., Svojtka, M., Ackerman, L., and Švecová, K. (2012). Trace Element Composition of Quartz from the Variscan Altenberg-Teplice Caldera (Krušné hory/Erzgebirge Mts, Czech Republic/Germany): Insights into the Volcano-Plutonic Complex Evolution. *Chem. Geology.* 326-327, 36–50. doi:10.1016/j.chemgeo.2012.07.028

Chen, J. F., and Zhang, H. (2011). Trace Elements in Quartz Lattice and Their Implications for Petrogenesis and Mineralization. *Gaoxiao Dizhi Xuebao* 17, 125–135. (in Chinese with English abstract).

Chen, X. D., Chen, Z. Y., Cheng, Y. B., and Ye, H. S. (2011). Characteristics and Applications of Trace Elements in Hydrothermal Quartz: Recognition and Progress. *Geol. Rev.* 5, 707–717. (in Chinese with English abstract).

Ciobanu, C. L., Cook, N. J., Kelson, C. R., Guerin, R., Kalleske, N., and Danyushevsky, L. (2013). Trace Element Heterogeneity in Molybdenite Fingerprints Stages of Mineralization. *Chem. Geology.* 347, 175–189. doi:10.1016/j.chemgeo.2013.03.011

Coulson, I. M., Edwards, P. R., and Lee, M. R. (2007). Preface: Recent Developments in Microbeam Cathodoluminescence with Applications to Mineralogy. *Am. Mineral.* 92, 233–234. doi:10.2138/am.2007.476

Flem, B., Larsen, R. B., Grimstvedt, A., and Mansfeld, J. (2002). *In Situ* analysis of Trace Elements in Quartz by Using Laser Ablation Inductively Coupled Plasma Mass Spectrometry. *Chem. Geology.* 182, 237–247. doi:10.1016/s0009-2541(01)00292-3

Francois, J., and Larsen, R. B. (2009). Trace Element Evolution of Quartz in the Charnockitic Kleivan Granite, SW-Norway: The Ge/Ti Ratio of Quartz as an index of Igneous Differentiation. *Lithos* 107, 28–291.

Fu, S. L., and Yan, J. (2020). Trace Element Chemistry of Hydrothermal Quartz and its Genetic Significance: A Case Study from the Xikuangshan and Woxi Giant Sb Deposits in Southern China. *Ore Geology. Rev.* 126, 103–112. doi:10.1016/j.oregeorev.2020.103732

Garate-Olave, I., Müller, A., Roda-Robles, E., Gil-Crespo, P. P., and Pesquera, A. (2017). Extreme Fractionation in a Granite-Pegmatite System Documented by Quartz Chemistry: The Case Study of Tres Arroyos (Central Iberian Zone, Spain). *Lithos* 286-287, 162–174. doi:10.1016/j.lithos.2017.06.009

Genna, D., and Gaboury, D. (2015). Deciphering the Hydrothermal Evolution of a VMS System by LA-ICP-MS Using Trace Elements in Pyrite: an Example from the Bracemac-McLeod Deposits, Abitibi, Canada, and Implications for Exploration. *Econ. Geology.* 110, 2087–2108. doi:10.2113/econgeo.110.8.2087

Götte(2016). Trace Element Composition of Authigenic Quartz in Sandstones and its Correlation With Fluid-Rock Interaction During Diagenesis (Book Chapter). *Geol. Soc. Spec. Publ.* 435, 373–387.

Götte, T., Pettke, T., Ramseyer, K., Koch-Muller, M., and Mullis, J. (2011). Cathodoluminescence Properties and Trace Element Signature of Hydrothermal Quartz: a Fingerprint of Growth Dynamics. *Am. Mineral.* 96, 802–813. doi:10.2138/am.2011.3639

Götte, T., and Ramseyer, K. (2012). Trace Element Characteristics, Luminescence Properties and Real Structure of Quartz. *Springer Geology.* 2197, 265–285. doi:10.1007/978-3-642-22161-3_12

Götze, J. (2009). Chemistry, Textures and Physical Properties of Quartz - Geological Interpretation and Technical Application. *Mineral. Mag.* 73, 645–671. doi:10.1180/minmag.2009.073.4.645

Götze, J., Plötze, M., Graupner, T., Hallbauer, D. K., and Bray, C. J. (2004). Trace Element Incorporation into Quartz: a Combined Study by ICP-MS, Electron Spin Resonance, Cathodoluminescence, Capillary Ion Analysis, and Gas Chromatography. *Geochimica et Cosmochimica Acta* 68, 3741–3759. doi:10.1016/j.gca.2004.01.003

Götze, J., Plötze, M., and Habermann, D. (2001). Origin, Spectral Characteristics and Practical Applications of the Cathodoluminescence (CL) of Quartz - a Review. *Mineralogy Pet.* 71, 225–250. doi:10.1007/s007100170040

Götze, J., Plötze, M., and Trautmann, T. (2005). Structure and Luminescence Characteristics of Quartz from Pegmatites. *Am. Mineral.* 90, 13–21. doi:10.2138/am.2005.1582

Gurbanov, A, Koschug, D, Williams, I, and Braun, J. (1999). A New Method for the Estimation of Cooling and Denudation Rates Using Paramagnetic Centers in Quartz: A Case Study on the Eldzhurtinskiy Granite, Caucasus. *J. Geophys. Res. Solid Earth* 104 (B8), 17531–17549.

Hayden, B., and Mathewes, R. (2005). The Rise and Fall of Complex Large Villages on the British Columbian Plateau: A Geoarchaeological Controversy. *Canad. J. Archaeol.* 33, 281–296.

Heinrich, C. A., Moritz, R., and Peytcheva, I. (2005). Geochronology and Geodynamics of Late Cretaceous Magmatism and Cu-Au Mineralization in the Panagyurishte Region of the Apuseni-Banat-Timok-Srednogorie Belt, Bulgaria. *Ore Geol. Rev.* 27, 95–126.

Hou, Z. Q., Gao, Y. F., and Meng, X. J. (2004). Genesis of Adakitic Porphyry and Tectonic Controls on the Gangdese Miocene Porphyry Copper belt in the Tibet an Orogen. *Acta Petrologica Sinica* 20, 239–248. (in Chinese with English abstract).

Hou, Z. Q. (2010). Metallogensis of Continent Al Collision. *Acta Geologica Sinica-English Edition* 84, 30–58. (in Chinese with English abstract).

Hou, Z., Zaw, K., Pan, G., Mo, X., Xu, Q., Hu, Y., et al. (2007). Sanjiang Tethyan Metallogenesis in S.W. China: Tectonic Setting, Metallogenic Epochs and deposit Types. *Ore Geology. Rev.* 31, 48–87. doi:10.1016/j.oregeorev.2004.12.007

Huang, R., and Audétat, A. (2012). The Titanium-In-Quartz (TitaniQ) Thermobarometer: A Critical Examination and Re-calibration. *Geochimica et Cosmochimica Acta* 84, 75–89. doi:10.1016/j.gca.2012.01.009

Huang, X., Xu, J., Chen, J., and Ren, J. (2012). Geochronology, Geochemistry and Petrogenesis of Two Periods of Intermediate-Acid Intrusive Rocks from Hongshan Area in Zhongdian Arc. *Acta Petrologica Sinica* 28, 1493–1506.

Jacamon, F., and Larsen, R. B. (2009). Trace Element Evolution of Quartz in the Charnockitic Kleivan Granite, SW-Norway: the Ge/Ti Ratio of Quartz as an index of Igneous Differentiation. *Lithos* 107, 281–291. doi:10.1016/j.lithos.2008.10.016

Jourdan, A.-L. V., Mullis, J., Ramseyer, K., Spiers, C. J., and Spiers, C. J. (2009). Evidence of Growth and Sector Zoning in Hydrothermal Quartz from Alpine Veins. *ejm* 21, 219–231. doi:10.1127/0935-1221/2009/0021-1881

Kretz, R. (1983). Symbols for Rock-Forming Minerals. *Am. Mineral.* 68, 277–279.

Lan, T. G., Hu, R. Z., Fan, H. R., Bi, X. W., Tang, Y. W., Zhou, L., et al. (2017). In-situ Analysis of Major and Trace Elements in Fluid Inclusion and Quartz: LA-ICP-MS Method and Applications to Ore Deposits. *Acta Petrologica Sinica* 33, 3239–3262. (in Chinese with English abstract).

Landtwing, M. R., and Pettke, T. (2005). Relationships between SEM-Cathodoluminescence Response and Trace-Element Composition of Hydrothermal Vein Quartz. *Am. Mineral.* 90, 122–131. doi:10.2138/am.2005.1548

Larsen, R. B., Henderson, I., Ihlen, P. M., and Jacamon, F. (2004). Distribution and Petrogenetic Behaviour of Trace Elements in Granitic Pegmatite Quartz from South Norway. *Contrib. Mineral. Petrol.* 147, 615–628. doi:10.1007/s00410-004-0580-4

Larsen, R. B., Polve, M., and Juve, G. (2000). Granite Pegmatite Quartz from Evje-Iveland: Trace Element Chemistry and Implications for the Formation of High-Purity Quartz. *Norges Geologiske Undersokelse* 436, 57–66.

Lehmann, K., Berger, A., Götte, T., Ramseyer, K., and Wiedenbeck, M. (2009). Growth Related Zonations in Authigenic and Hydrothermal Quartz Characterized by SIMS-, EPMA-, SEM-CL- and SEM-CC-Imaging. *Mineral. Mag.* 73, 633–643. doi:10.1180/minmag.2009.073.4.633

Lehmann, K., Pettke, T., and Ramseyer, K. (2011). Significance of Trace Elements in Syntaxial Quartz Cement, Haushi Group Sandstones, Sultanate of Oman. *Chem. Geology.* 280, 47–57. doi:10.1016/j.chemgeo.2010.10.013

Leng, C. B., Zhang, X. C., and Wang, S. X. (2008). Geochemical Characteristics of Porphyry Copper Deposits in the Zhongdian Area, Yunnan as Exemplified by the Xuejiping and Pulang Porphyry Copper Deposits. *Acta Mineralogica Sinica* 27, 415–442. (in Chinese with English abstract).

Li, W. C., Li, H. J., Yu, G. H., and Yin, G. H. (2013). Porphyry Metallogenic System of Geza Arc in the Sanjiang Region, Southwestern China. *Acta Petrologica Sinica* 29, 1129–1144. (in Chinese with English abstract).

Li, W. C., Yu, H. J., and Yin, G. H. (2012). Re-Os Dating of Molybdenite from Tongchanggou Mopolymetallic deposit in Northwest Yunnan and its Metallogenic Environment. *Mineral. Deposits* 31, 282–292. (in Chinese with English abstract).

Li, W. C., Zeng, P. S., Hou, Z. Q., and White, E. C. (2011). The Pulang Porphyry Copper deposit and Associated Felsic Intrusions in Yunnan Province, Southwest China. *Econ. Geology.* 106, 79–92.

Liang, Y., Wang, G., Liu, S., Sun, Y., Huang, Y., and Hoshino, K. (2014). A Study on the Mineralization of the Woxi Au-Sb-W Deposit, Western Hunan, China. *Resource Geology.* 65, 27–38. doi:10.1111/rge.12053

Liu, X. C., Xiong, X. L., Audetat, A., Li, Y., Song, M. S., Li, L., et al. (2008). Partitioning of Copper Between Olivine, Orthopyroxene, Clinopyroxene, Spinel, Garnet and Silicate Melts at Upper Mantle Conditions. *Geochim. Et Cosmochim. Acta.* 125, 1–22.

Mao, J., Pirajno, F., Lehmann, B., Luo, M., and Berzina, A. (2014). Distribution of Porphyry Deposits in the Eurasian Continent and Their Corresponding Tectonic Settings. *J. Asian Earth Sci.* 79, 576–584. doi:10.1016/j.jseaes.2013.09.002

Mariane, R. L., and Thoms, P. (2005). Relationships between SEM-Cathodoluminescence Response and Trace-Element Composition of Hydrothermal Vein Quartz. *Am. Mineral.* 90, 122–131. doi:10.2138/am.2005.1548

Marshall, D. J. (1988). Cathodoluminescence of Geological Materials. *Unwin Hyman. Geol. J.* 26, 351.

Meng, J. Y., Yang, L. Q., and Liu, L. (2013). Re-Os Dating of Molybdenite from the Hongshan Cu-Mo deposit in Northwest Yunnan and its Implications for Mineralization. *Acta Petrologica Sinica* 29, 1214–1222. (in Chinese with English abstract).

Monecke, T., Kempe, U., and Götze, J. (2002). Genetic Significance of the Trace Element Content in Metamorphic and Hydrothermal Quartz: a Reconnaissance Study. *Earth Planet. Sci. Lett.* 202, 709–724. doi:10.1016/s0012-821x(02)00795-1

Mü ller, A., Wiedenbeck, M., Van Den Kerkhof, A. M., Kronz, A., and Simon, K. (2003). Trace Elements in Quartz - a Combined Electron Microprobe, Secondary Ion Mass Spectrometry, Laser-Ablation ICP-MS, and Cathodoluminescence Study. *ejm* 15, 747–763. doi:10.1127/0935-1221/2003/0015-0747

Müller, A., Behr, H. J., and Kerkhof, A. M. (2009). The Evolution of Late Hercynian Granites and Royalties Documented by Quartz: A Review. *Earth Environ. Sci. Trans. R. Soc. Edinb.* 100, 3549. doi:10.1017/s1755691009016144

Müller, A., Breiter, K., Seltmann, R., and Pécskay, Z. (2005). Quartz and Feldspar Zoning in the Eastern Erzgebirge Volcano-Plutonic Complex (Germany, Czech Republic): Evidence of Multiple Magma Mixing. *Lithos* 80 (1), 201–227. doi:10.1016/j.lithos.2004.05.011

Müller, A., Herklotz, G., and Giegling, H. (2018). Chemistry of Quartz Related to the Zinnwald/Cínovec Sn-W-Li Greisen-type deposit, Eastern Erzgebirge, Germany. *J. Geochemical Exploration* 190, 357–373. doi:10.1016/j.gexplo.2018.04.009

Müller, A., Herrington, R., Armstrong, R., Seltmann, R., Kirwin, D. J., Stenina, N. G., et al. (2010). Trace Elements and Cathodoluminescence of Quartz in Stockwork Veins of Mongolian Porphyry-Style Deposits. *Miner Deposita* 45, 707–727. doi:10.1007/s00126-010-0302-y

Müller, A., and Koch-Müller, M. (2009). Hydrogen Speciation and Trace Element Contents of Igneous, Hydrothermal and Metamorphic Quartz from Norway. *Mineral. Mag.* 73, 569–583. doi:10.1180/minmag.2009.073.4.569

Müller, A., Seltmann, R., and Behr, H.-J. (2000). Application of Cathodoluminescence to Magmatic Quartz in a Tin Granite - Case Study from the Schellerhau Granite Complex, Eastern Erzgebirge, Germany. *Mineralium Deposita* 35, 169–189. doi:10.1007/s001260050014

Müller, A., Thomas, R., Wiedenbeck, M., Seltmann, R., and Breiter, K. (2006). Water Content of Granitic Melts from Cornwall and Erzgebirge: A Raman Spectroscopy Study of Melt Inclusions. *ejm* 18, 429–440. doi:10.1127/0935-1221/2006/0018-0429

Müller, A., Wiedenbeck, M., Flem, B., and Schiellerup, H. (2008). Refinement of Phosphorus Determination in Quartz by LA-ICP-MS through Defining New Reference Material Values. *Geostandards Geoanalytical Res.* 32, 361–376. doi:10.1111/j.1751-908x.2008.00901.x

Pagel, M., and Orberger, B. (2000). Diagenetic Evolution of Cretaceous Siltstones From Drill Core MAR 501 (South-Eastern France). *J. Geochem. Explor.* 69, 115–118.

Peng, H.-j., Mao, J.-w., Hou, L., Shu, Q.-h., Zhang, C.-q., Liu, H., et al. (2016). Stable Isotope and Fluid Inclusion Constraints on the Source and Evolution of Ore Fluids in the Hongniu-Hongshan Cu Skarn Deposit, Yunnan Province, China. *Econ. Geology.* 111, 1369–1396. doi:10.2113/econgeo.111.6.1369

Peng, H.-j., Mao, J.-w., Pei, R.-f., Zhang, C.-q., Tian, G., Zhou, Y., et al. (2014). Geochronology of the Hongniu-Hongshan Porphyry and Skarn Cu deposit, Northwestern Yunnan Province, China: Implications for Mineralization of the Zhongdian Arc. *J. Asian Earth Sci.* 79, 682–695. doi:10.1016/j.jseaes.2013.07.008

Peng, H.-j., Zhang, C.-q., Mao, J.-w., Santosh, M., Zhou, Y.-m., and Hou, L. (2015). Garnets in Porphyry-Skarn Systems: A LA-ICP-MS, Fluid Inclusion, and Stable Isotope Study of Garnets from the Hongniu-Hongshan Copper deposit, Zhongdian Area, NW Yunnan Province, China. *J. Asian Earth Sci.* 103, 229–251. doi:10.1016/j.jseaes.2014.10.020

Peng, H. J., Lin, H., Sun, C., Zou, H., Wang, T. R., and Ma, Z. Z. (2021). Geochemistry of Magnetite from the Hongniu-Hongshan Cu Skarn deposit in Yunnan Province, SW China. *Ore Geology. Rev.* 136 (2021), 104–237. doi:10.1016/j.oregeorev.2021.104237

Peng, H. J., Wang, X. W., Qin, Z. P., Hou, L., and Zhou, Y. (2010b). The Characteristics of Cathodoluminescence Visualized Microstructure in Quartz: A Case Study from the Jiama Igneous Rock in Tibet. *Bull. Mineralogy, Pet. Geochem.* 29 (3), 45–52. (in Chinese).

Peng, H. J., Wang, X. W., Qin, Z. P., Hou, L., and Zhou, Y. (2010c). *The Magmatic Hydrothermal Transition Evidence from Mineralogy of the Jiama Copper Polymetallic deposit in Tibet*. Unpublished: Journal of Chengdu University of Technology Science. (in Chinese with English abstract).

Peng, H. J., Wang, X. W., Tang, J. X., Qin, Z. P., Zhou, Y., and Hou, L. (2010a). The Application of Quartz Cathodoluminescence in Study of Igneous Rock. *Rock Mineral. Anal.* 29 (2), 65–73. (in Chinese with English abstract).

Penniston-Dorland, S. C. (2001). Illumination of Vein Quartz Textures in a Porphyry Copper Ore deposit Using Scanned Cathodoluminescence: Grasberg Igneous Complex, Irian Jaya, Indonesia. *Am. Mineral.* 86, 652–666. doi:10.2138/am-2001-5-606

Peppard, B. T., Steele, I. M., Davis, A. M., Wallace, P. J., and Anderson, A. T. (2001). Zoned Quartz Phenocrysts from the Rhyolitic Bishop Tuff. *Am. Mineral.* 86, 1034–1052. doi:10.2138/am-2001-8-910

Perny, B., Eberhardt, P., Ramseyer, K., Mullis, J., and Pankrath, R. (1992). Microdistribution of Al, Li, and Na in Alpha Quartz: Possible Causes and Correlation with Short-Lived Cathodoluminescence. *Am. Mineral.* 77, 534–544.

Pokrovski, G. S., and Schott, J. (1998). Thermodynamic Properties of Aqueous Ge(IV) Hydroxide Complexes from 25 to 350°C: Implications for the Behavior of Germanium and the Ge/Si Ratio in Hydrothermal Fluids. *Geochimica et Cosmochimica Acta* 62, 1631–1642. doi:10.1016/s0016-7037(98)00081-7

Qu, X. M., Jiang, J. H., Xin, H. B., and Chen, H. (2010). A Study of Two Groups of Adakite Almost Simulteneously Formed in Gangdese Collisional Orogen, Tibet: Why Does One Group Contain Copper Mineralization and the Other Not. *Mineral. Deposits* 29 (3), 382–390. (in Chinese with English abstract).

Ramseyer, K., and Müllis, J. (1990). Factors Influencing Short-Lived Blue Cathodoluminescence of Alpha-Quartz. *Am. Mineral.* 75, 791–800.

Remond, G., Cesbron, F., and Chapoulie, R. (1992). Cathodoluminescence Applied to the Micro Characterization of mineral Materials: A Present Status in Experimentation and Interpretation. *Scanning Microsc.* 6 (1), 23–68.

Rusk, B. (2012). Cathodoluminescent Textures and Trace Elements in Hydrothermal Quartz. *Springer Geology*. 2197-9545, 307–329. doi:10.1007/978-3-642-22161-3_14

Rusk, B. G., Lowers, H. A., and Reed, M. H. (2008). Trace Elements in Hydrothermal Quartz: Relationships to Cathodoluminescent Textures and Insights into Vein Formation. *Geol* 36, 547–550. doi:10.1130/g24580a.1

Rusk, B. G., Reed, A. H., Dilles, J. H., and Kent, A. J. R. (2006). Intensity of Quartz Cathodoluminescence and Trace-Element Content in Quartz from the Porphyry Copper deposit at Butte, Montana. *Am. Mineral.* 91, 1300–1312. doi:10.2138/am.2006.1984

Rusk, B., Koenig, A., and Lowers, H. (2011). Visualizing Trace Element Distribution in Quartz Using Cathodoluminescence, Electron Microprobe, and Laser Ablation-Inductively Coupled Plasma-Mass Spectrometry. *Am. Mineral.* 96, 703–708. doi:10.2138/am.2011.3701

Rusk, B., and Reed, M. (2002). Scanning Electron Microscope-Cathodoluminescence Analysis of Quartz Reveals Complex Growth Histories in Veins from the Butte Porphyry Copper deposit, Montana. *Geol* 30, 727–730. doi:10.1130/0091-7613(2002)030<0727:semcao>2.0.co;2

Sengör, A. M. C., and Natal, B. A. (1996). Paleotectonics of Asia: Fragments of a Synthesis. *World Reg. Geology*. 8, 486–640.

Smith, J. V., and Stenstrom, R. C. (1965). Electron-Excited Luminescence as a Petrologic Tool. *J. Geology*. 73, 627–635. doi:10.1086/627098

Smith, V. C., Shane, P., and Nairn, I. A. (2004). Reactivation of a Rhyolitic Magma Body by New Rhyolitic Intrusion before the 15.8 Ka Rotorua Eruptive Episode: Implications for Magma Storage in the Okataina Volcanic Centre, New Zealand. *J. Geol. Soc.* 161, 757–772. doi:10.1144/0016-764903-092

Soltani Dehnavi, A., McFarlane, C. R. M., Lentz, D. R., and Walker, J. A. (2018). Assessment of Pyrite Composition by LA-ICP-MS Techniques from Massive Sulfide Deposits of the Bathurst Mining Camp, Canada: from Textural and Chemical Evolution to its Application as a Vectoring Tool for the Exploration of VMS Deposits. *Ore Geology. Rev.* 92, 656–671. doi:10.1016/j.oregeorev.2017.10.010

Song, B., Cai, X., and Xu, X. (2006). Cenozoic Hot-spring Exhalative Mineralization Hongshan Copper-Polymetallic deposit in Zhongdian, NW Yunnan. *Chin. J. Geology*. 41, 700–710. (in Chinese with English abstract).

Takahashi, M., Mizuta, T., Ishiyama, D., Kimura, J., and Takada, J. (2002). Characteristics of Trace Elements in Quartz by LA-ICP-MS and the Origin of Ore Fluid Responsible for Gold Mineralization at the Hishikari Epithermal Gold deposit, Japan. *Resource Geology*. 52, 51–67. (in Japanese).

Thomas, J. B., Bruce Watson, E., Spear, F. S., Shemella, P. T., Nayak, S. K., and Lanzirotti, A. (2010). TitaniQ under Pressure: the Effect of Pressure and Temperature on the Solubility of Ti in Quartz. *Contrib. Mineral. Petrol.* 160, 743–759. doi:10.1007/s00410-010-0505-3

Tian, Z. D., Leng, C. B., Zhang, X. C., Zafar, T., and Lai, C. K. (2019). Chemical Composition, Genesis and Exploration Implication of Garnet from the Hongshan Cu-Mo Skarn deposit, SW China. *Ore Geology. Rev.* 112, 103–106. doi:10.1016/j.oregeorev.2019.103016

Ting, G. L., Rui, Z. H., and Xian, W. (2018). Metasomatized Asthenospheric Mantle Contributing to the Generation of Cu-Mo Deposits within an Intracontinental Setting: a Case Study of the ~128 Ma Wangjiazhuang Cu-Mo deposit, Eastern North China Craton. *J. Asian Earth Sci.* 160, 460–489.

Wang, P., Dong, G., Santosh, M., Liu, K., and Li, X. (2016). Copper Isotopes Trace the Evolution of Skarn Ores: a Case Study from the Hongshan-Hongniu Cu deposit, Southwest china. *Ore Geology. Rev.* 88, 822–831.

Wang, S. X., Bi, X. W., and Leng, C. B. (2011). LA-ICP-MS Zircon U-Pb Dating of Granite Porphyry in the Hongshan Cu-Polymetallic deposit, Zhongdian, Northwest Yunnan, China and its Geological Implication. *Acta Mineralogica Sinica* 31, 315–321. (in Chinese with English abstract).

Wang, S. X., Zhang, X. C., and Leng, C. B. (2008). Stable Isotopic Compositions of the Hongshan Skarn Copper deposit in the Zhongdian Area and its Implication for the Copper Mineralization Process. *Acta Petrologica Sinica* 24, 480–488. (in Chinese with English abstract).

Wark, D. A., Hildreth, W., Spear, F. S., Cherniak, D. J., and Watson, E. B. (2007). Pre-eruption Recharge of the Bishop Magma System. *Geology* 35, 235–238. doi:10.1130/g23316a.1

Wark, D. A., and Watson, E. B. (2006). TitaniQ: a Titanium-In-Quartz Geothermometer. *Contrib. Mineral. Petrol.* 152, 743–754. doi:10.1007/s00410-006-0132-1

Wertich, V., Leichmann, J., Dosbaba, M., and Götze, J. (2018). Multi-Stage Evolution of Gold-Bearing Hydrothermal Quartz Veins at the Mokrsko Gold Deposit (Czech Republic) Based on Cathodoluminescence, Spectroscopic, and Trace Elements Analyses. *Minerals* 8, 335. doi:10.3390/min8080335

Xiong, F. H., Ma, C. Q., Jiang, H. A., Liu, B., and Huang, J. (2014). Geochronology and Geochemistry of Middle Devonian Mafic Dykes in the East Kunlun Orogenic Belt, Northern Tibet Plateau: Implications for the Transition from Prototethys to Paleotethys Orogeny. *Chemie Der Erae-Geochem.* 74 (2), 225–235.

Xu, J., Xie, G. D., and Xiao, Y. (2018). Dynamic Analysis of Ecological Environment Quality Combined with Water Conservation Changes in National Key Ecological Function Areas in China. *Sustainability* 3987, 2071–2105.

Xu, Z. Q., Yang, J. S., and Li, H. Q. (2012). Indosinian Collision-Orogenic System of Chinese Continent and its Orogenic Mechanism. *Acta Petrologica Sinica* 28, 1697–1709. (in Chinese with English abstract).

Yang, Z. M., Hou, Z. Q., Li, Z. Q., Song, Y. C., and Xie, Y. L. (2008). Direct Record of Primary Fluid Exsolved from Magma: Evidence from Unidirectional Solidification Texture (UST) in Quartz Found in Qulong Porphyry Copper deposit, Tibet. *Mineral. Deposits* 27, 188–199. (in Chinese with English abstract).

Zhang, Y., Cheng, J., Tian, J., Pan, J., Sun, S., Zhang, L., et al. (2019). Texture and Trace Element Geochemistry of Quartz in Skarn System: Perspective from Jiguanzui Cu-Au Skarn deposit, Eastern China. *Ore Geology. Rev.* 109, 535–544. doi:10.1016/j.oregeorev.2019.05.007

Conflict of Interest: Author SC is currently employed by SW Resources and Hydropower Survey, Design and Research Institute Co. Ltd., China, but he was not employed here at the time of research.

The remaining authors declare that the research was conducted in the absence of any commercial or financial relationships that could be construed as a potential conflict of interest.

Publisher's Note: All claims expressed in this article are solely those of the authors and do not necessarily represent those of their affiliated organizations, or those of the publisher, the editors, and the reviewers. Any product that may be evaluated in this article, or claim that may be made by its manufacturer, is not guaranteed or endorsed by the publisher.

frontiers | Frontiers in Earth Science

ORIGINAL RESEARCH
published: 12 July 2022
doi: 10.3389/feart.2022.949660

Predicting Granitic Buried-Hill Reservoirs Using Seismic Reflection data—A Case Study From the Bongor Basin, Southwestern Chad

Yajie Wang[1,2,3]*, *Guosheng Xu*[1,2]*, *Wei Zhou*[1,2], *Jiaju Liang*[1,2], *Fanghao Xu*[1,2] and *Sai He*[1,2]

[1]College of Energy, Chengdu University of Technology, Chengdu, China, [2]State Key Laboratory of Oil and Gas Reservoir Geology and Exploitation, Chengdu University of Technology, Chengdu, China, [3]Overseas Business Department, Geophysical Research Institute, Bureau of Geophysical Prospecting, CNPC, Zhuozhou, China

Predicting the distribution of fractured and dissolved reservoirs in granitic buried hills is a prerequisite for finding high-quality hydrocarbon reservoirs and improving the success rate of exploration activities. Granitic buried-hill reservoirs in the Bongor Basin are characterized by strong heterogeneity and poor lateral continuity. Through the analysis of seismic, core, logging and dynamic production data, this study predicts the distribution of fractured reservoirs and fractured-cave reservoirs in the granitic buried hills in the BC Block of the Bongor Basin. In this study, we predict fractured reservoirs using coherence cubes and linearly enhanced attributes and identify fractured-cave reservoirs with single-frequency attribute bodies. Integrated predictions of fractured reservoirs and fractured-cave reservoirs are conducted using attribute fusion techniques. With these methods, good results have been achieved in reservoir prediction in BC buried hills. Furthermore, this study summarizes a set of granitic buried-hill reservoir prediction techniques for densely inverted rift basins in the Central African Rift System.

Keywords: granitic buried-hills, fractured reservoir prediction, fracture-cavity reservoir prediction, attribute fusion, inverted rift basin, Bongor Basin

OPEN ACCESS

Edited by:
Dongming Zhi,
Turpan-Hami oil company, PetroChina, China

Reviewed by:
Qi Li,
China University of Geosciences, China
Nan Jia,
Liaoning Technical University, China

***Correspondence:**
Yajie Wang
wangyajie01@cnpc.com.cn
Guosheng Xu
xgs@cdut.edu.cn

Specialty section:
This article was submitted to Economic Geology, a section of the journal Frontiers in Earth Science

Received: *21 May 2022*
Accepted: *21 June 2022*
Published: *12 July 2022*

Citation:
Wang Y, Xu G, Zhou W, Liang J, Xu F and He S (2022) Predicting Granitic Buried-Hill Reservoirs Using Seismic Reflection data—A Case Study From the Bongor Basin, Southwestern Chad. Front. Earth Sci. 10:949660. doi: 10.3389/feart.2022.949660

1 INTRODUCTION

Granite, as a dense rock formed by magma crystallization, has no primary pores. In addition, granite is hard to detect when buried thousands of metres underground, resulting in little attention to be paid during hydrocarbon exploration (Ye et al., 2020; Yi et al., 2021). However, with the development of global oil and gas exploration, breakthroughs have been made in granitic buried hills worldwide, and a few medium- to large-sized oil and gas fields have been discovered, such as the BachHo field in Vietnam, the Dongping gas field in China, the Penglai oil field in China, and the BC oilfield discovered in the Bongor Basin in Chad (Cuong and Warren, 2009; Dou et al., 2015; Chen et al., 2018; Guo et al., 2019; Li et al., 2021a; Dai et al., 2021). The exploration of buried-hill reservoirs in the basement has gradually become a new exploration field (Cuong and Warren, 2009; Dou et al., 2020; Ye et al., 2020).

In 2013, the success of hydrocarbon drilling in the northern slope of the basin by the China National Petroleum Corporation (CNPC) targeting Precambrian granitic reservoirs expanded the boundary of petroleum exploration in the Bongor Basin, and industrial amounts of oil and gas were obtained from the granitic reservoirs of five buried hills (Dou et al., 2015; Chen et al., 2018). This

reveals the huge exploration potential of the bedrock buried-hill reservoir in the Bongor Basin. Therefore, the Precambrian basement is a good reservoir for hydrocarbon accumulation (Li et al., 2017; Dou et al., 2018).

The Bongor Basin is an important hydrocarbon-rich basin in southwestern Chad. Preliminary exploration results reveal the huge exploration potential of bedrock buried-hill reservoirs in this area (Dou et al., 2015; Li et al., 2017; Chen et al., 2018; Dou et al., 2018). Scholars have reached an agreement that granitic reservoirs are mainly composed of secondary reservoir spaces, including structural fractures, weathering fractures, dissolved fractures and dissolved pores, and the physical properties change tremendously spatially, showing strong heterogeneity (Salah and Alsharhan, 1998; Cuong and Warren, 2009; Wang et al., 2018). Longitudinally, there is a certain zonality, but it is not obvious. Maerten and Panza proposed that the basement buried-hill reservoir consists mainly of structural fractures and caves formed by later modification. With the increase in depth below the buried hill surface, the type of basement buried-hill reservoir gradually transitions from a fractured-cave reservoir to a fractured reservoir. Through the calibration of the core and well seismic data, the oil-producing section of the well is mainly concentrated in the upper part of the buried hill (Wang et al., 2018; Dou et al., 2020). Therefore, the predictions of buried-hill reservoirs in the BC block are mainly fractured and fractured-cave reservoirs.

Fractures play a key role in basement buried-hill reservoirs and are important reservoirs and channels that communicate with reservoir space (Maerten et al., 2018; Panza et al., 2018; Shang et al., 2021). Therefore, the prediction of fractures is a key and difficult aspect of exploration and exploitation in basement buried-hill reservoirs (Salah and Alsharhan, 1998; Yan et al., 2019).

For the study of fractured reservoirs in the subsurface, outcrops and core observations were initially used, but they have the disadvantage of being less accurate and limited to areas with drilled wells. Logging evaluation is also an effective method for identifying and evaluating fractures. In recent years, emphasis has been placed on the combined application of multiple logging profiles to identify and evaluate fractured reservoirs (Li et al., 2021b). The combined application of multiple logs has improved the accuracy and precision compared to direct observation methods, but for areas with limited wells, only mathematical algorithms can be used to interpolate and predict the planimetric distribution of basement buried-hill reservoirs (Ye, 2019). The use of seismic detection technology for fracture prediction began later; however, because seismic data cover a much wider space than drilling data, have a greater range of applications and are more practical, they are more generally used (Gong et al., 2013; Zhang et al., 2022). At present, the main techniques for the fracture prediction of reservoirs using seismic data are shear wave exploration, multiwave and multicomponent detection, and three-dimensional p-wave fracture detection (Pu and Qing, 2008). The reservoir prediction in basement buried hills is limited by the heterogeneity of the reservoir and the quality of the seismic data, and the use of single-attribute prediction techniques will increase the multisolution nature of the reservoir prediction. Therefore, in this paper, multiple geophysical methods are first used to predict the spatial distribution of fractured and fractured-cave reservoirs in basement buried hills, and then they are combined to evaluate the granitic buried-hill reservoirs. This method achieves good results in predicting the granitic buried-hill reservoirs in the BC block of the Bongor Basin in southwestern Chad.

2 GEOLOGICAL SETTING

The Bongor Basin in southwestern Chad is an important hydrocarbon-bearing basin (**Figure 1A**). Tectonically, it is in the northern part of the middle Central African shear zone and is a Mesozoic-Cenozoic intracontinental rift basin developed under the influence of the Central African shear zone (Genik, 1992; Li et al., 2017; Chen et al., 2018; Dou et al., 2018).

The BC block is in the northeastern part of the Northern Slope belt of the Bongor Basin (Salah and Alsharhan, 1998) (**Figure 1B**). It developed at the bottom of the basin during the Precambrian period and shows the present structural-depositional morphology after long-term weathering denudation, subsidence, and sedimentary filling. Precambrian basement rock, Lower Cretaceous (P, M, K, R, and B formations) and Cenozoic strata are developed sequentially from bottom to top in the basin, while the Upper Cretaceous strata are absent after denudation (Chen et al., 2018) (**Figure 2**). According to the hydrocarbon exploration and investigation, three hydrocarbon plays are considered to have developed in the Bongor Basin, namely, the upper (R-K), lower (M-P) and basement rock plays (**Figure 2**). The target of this study is the basement rock play (Genik, 1992; Dou et al., 2014; Dou et al., 2018).

According to core observations, the lithology of the basement rock is mainly granite or mixed granite, and this rock features a brittle texture and is prone to develop structural fractures, joint fractures, and dissolution pores along these fractures. The crystalline basement of the Bongor Basin is mainly composed of metamorphic rocks with a high degree of metamorphism and magmatic rocks formed by remelting. Intercrystalline pores are difficult to retain, and the size of intercrystalline pores is small. In addition, due to the extent of drilling and coring, only a small amount of reservoir space of physical origin can be found in the cores of weathering crusts (Chen et al., 2018; Wang et al., 2018).

The FMI data show extensive development of horizontal to low-angle fractures in the basement rock (**Figures 3A,B**). The larger the fracture angle is, the more intense the dissolution is (Wang et al., 2018). The rocks at the intersection of faults are heavily fractured and easily form collapse caves (Dou et al., 2014; Dou et al., 2015; Li et al., 2017; Dou et al., 2020). Multistage and multiangle fractures and dissolution are superimposed on each other to form buried-hill fractured and fractured-cave reservoirs, which are often characterized by strong heterogeneity and limited distribution (Chen et al., 2018).

The most developed reservoir spaces in the basement rock are mainly structural fractures, intergranular pores and dissolution

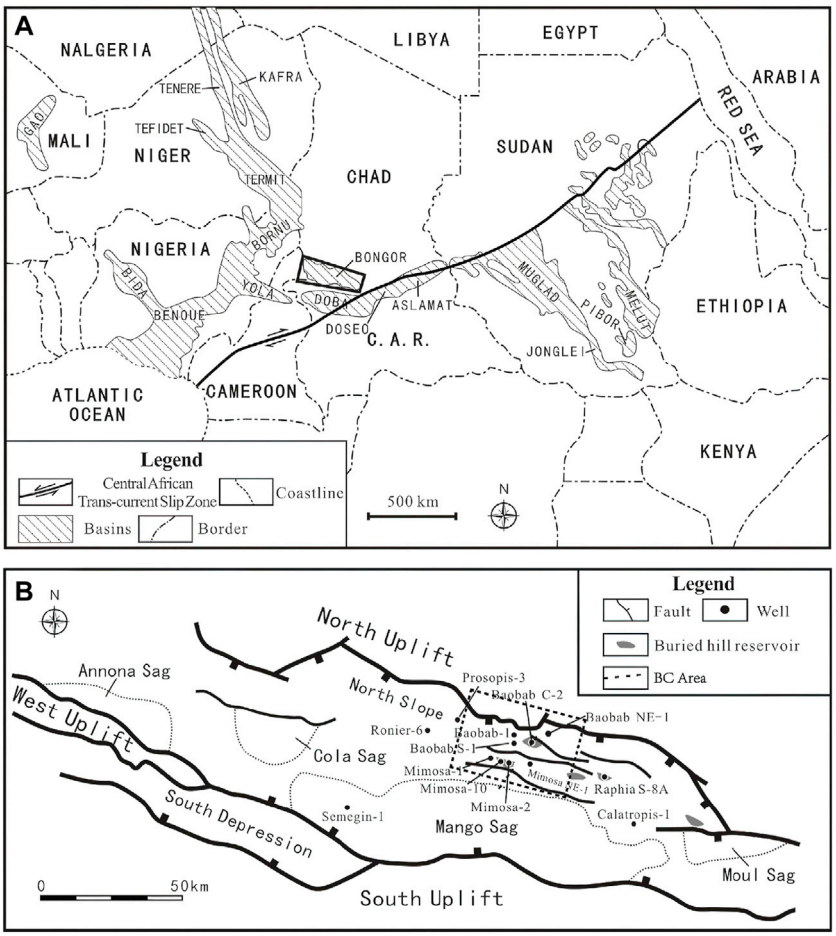

FIGURE 1 | Location map of the study area and study area with main faults. **(A)** Location of the Bongor Basin and Central African Trans-Current Slip zone and adjacent basins, such as the Termit, Muglad, and Melut basins. **(B)** The main faults, tectonic division, and location of the BC block in the Bongor Basin and the discovered buried-hill hydrocarbon reservoirs with wells (Modified from Chen et al., 2018).

pores formed by chemical dissolution (Dou et al., 2014). With the increase in depth below the buried hill surface, the type of basement buried-hill reservoir gradually transitions from a fractured-cave reservoir to a fractured reservoir. Through the calibration of the core and well seismic data, the oil-producing section of the well is mainly concentrated in the upper part of the buried hills (Wang et al., 2018; Dou et al., 2020). Therefore, the predicted types of pore space in the buried-hill reservoirs in the BC block are mainly fractures and dissolution pores.

At present, more than 30 wells exploring the basement rock of the BC block have obtained good oil and gas shows. Through years of research and drilling, it has been verified that basement buried-hill reservoirs in the BC block are typical fractured reservoirs with strong heterogeneity, large differences in oil-bearing layer thickness, and complex gas–water distributions (Chen et al., 2018). The accumulation degree of oil and gas is mainly controlled by the spatial distribution of reservoirs such as fractures and cavities. Therefore, the accurate prediction of the distributions of fractures and caves is key to the prediction of buried-hill reservoirs.

3 MATERIALS AND METHODS

3.1 Structure-Oriented Filtering Technology

A structure-oriented filter is a diffusion filtering process for seismic data anisotropy under the control of dip and azimuth bodies. The seismic data after structure-oriented filtering have the functions of directivity and edge detection directivity. It smooths the information parallel to the seismic in-phase axis and does not deal with the seismic information perpendicular to the fault or the main tectonic direction. This technology was first applied in the field of image processing and analysis (Höcker and Fehmers, 2002; Saleh et al., 2002; Fehmers and Höcker, 2003; Wang et al., 2021; Luo et al., 2022). During the early stage, linear operators were used to filter noisy images. However, although this method was good at reducing noise, edge information of images would be damaged. Later, a nonlinear operator defined by a nonlinear partial differential equation was developed to convolve the original image with a series of Gaussian kernel functions with different noise scales to obtain smooth images of the original

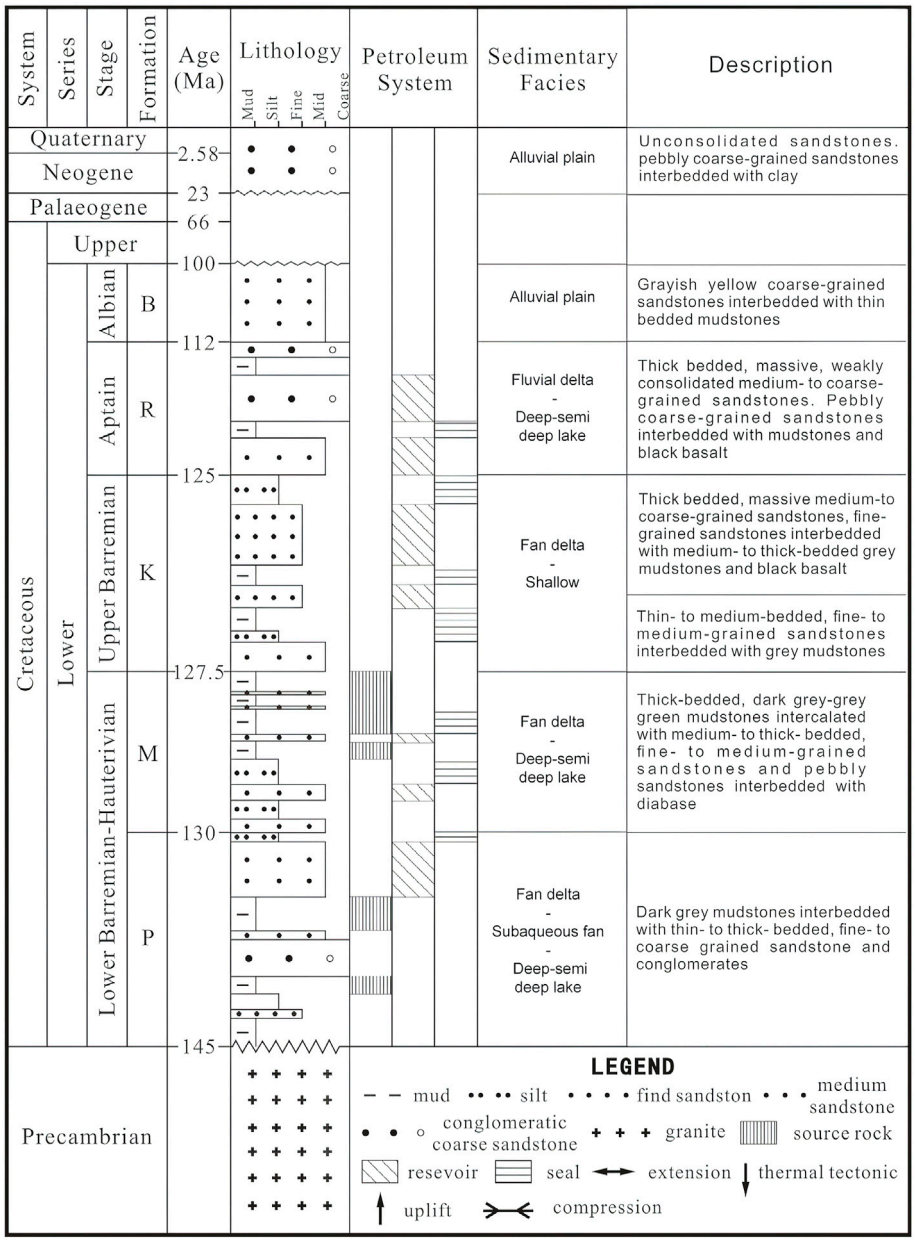

FIGURE 2 | Comprehensive stratigraphic histogram of the Bongor Basin (Modified from Chen et al., 2018).

image at different scales, which can effectively protect the structural information of the image (Höcker and Fehmers, 2002; Fehmers and Höcker, 2003; Zhou and Li, 2018; Luo et al., 2022). Structure-oriented filters have the advantages of reducing invalid signals, increasing effective signals, and highlighting small and microscale faults, which can effectively reduce the noise of seismic profiles, improve the quality of seismic data, improve the signal-to-noise ratio, improve the accuracy of small and microscale fault identification, and guide oil and gas exploration (Höcker and Fehmers, 2002; Chen, 2015; Zhou and Li, 2018; Luo et al., 2022).

3.2 Fractured Reservoir Prediction Technology

The BC buried-hill fractured reservoir prediction technique is based on poststack migration seismic data. First, spectrum analysis is used to determine the reasonable calculation parameters to fabricate coherence. Then, linear enhancement of the AFE module in Paradigm software is used to enhance the resolution of microfault recognition by coherence. Finally, the coherent slices of a certain time window are extracted from the linear enhanced coherence to predict fractured reservoirs based on seismic geometry attributes.

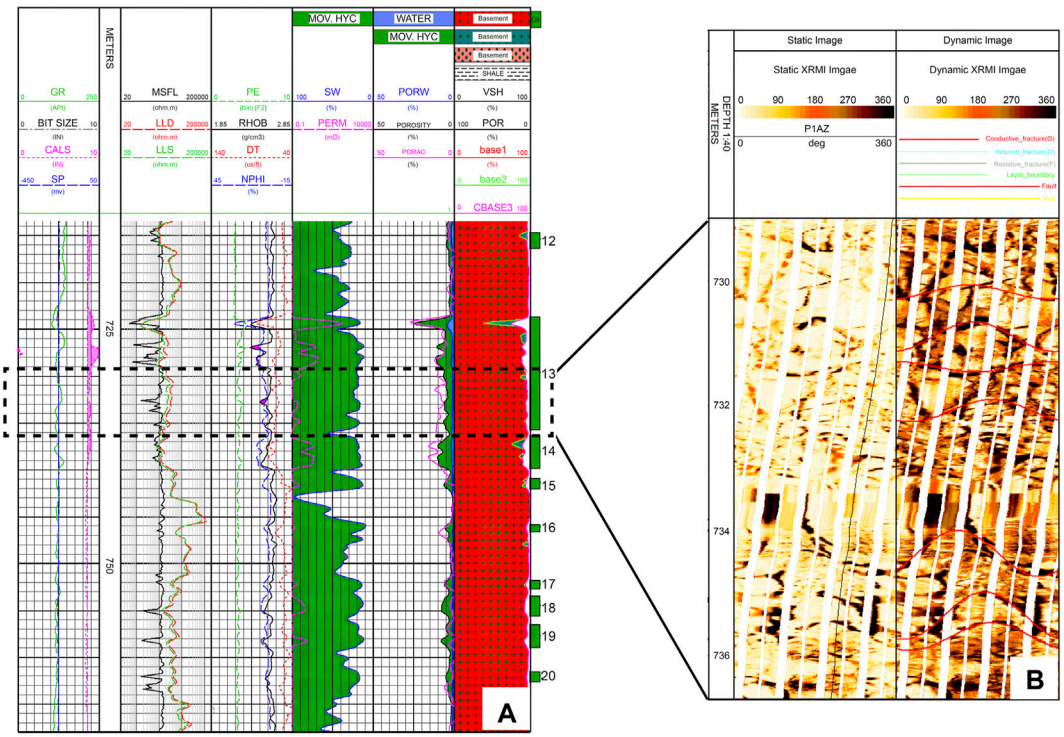

FIGURE 3 | (A) Well log interpretation of well Baobab C-2. **(B)** Image log of well Babab C-2 (729–737 m).

3.2.1 Coherence Attributes Technique

Coherence attributes reflect the similarity of adjacent seismic trace waveforms in the time window centered on the target point and can be used to obtain the discontinuous variation characteristics of the stratum through the similarity between waveforms (Bahorich and Farmer, 1995; Marfurt et al., 1999; Wang et al., 2016; Gao et al., 2018). The coherence data reflect the difference between adjacent seismic tracks. Mathematically, the difference value is mainly expressed by variance. The worse the continuity of the strata is, the greater the variance value. Coherence highlights discontinuities by emphasizing unrelated anomalies (Zhang et al., 2002; Wang et al., 2012; Gong et al., 2013; Wang et al., 2015). When the continuity of a stratum is broken, such as by a fault, pinching, intrusion, deformation, etc. causing seismic waves to change, sudden changes are evident at the edges.

The data used are the coherence attributes extracted from the resulting data after structure-oriented filtering using the eigenvalue algorithm of coherence attribute technology of GeoEast software. The number of coherence channels is 5 × 5, and the coherent time window is selected as 25 ms after the test (approximately 2/3 wavelength, the main frequency of the data is approximately 30 Hz).

3.2.2 Coherent Linear Enhancement Technique

The main function of the AFE module in Paradigm software is automatic fault extraction. The intermediate part of this module, linear reinforcement processing, supports the search for microcracks and can help predict the planar distribution of cracks. The discontinuity of seismic reflection events mainly contains two kinds of information: noise irrelevant to geological factors and fractures and faults. The main effect of linear reinforcement in the AFE module is to suppress noise and enhance and amplify the desired geological information. First, linear filtering is carried out; that is, according to the actual geological conditions, the noise distribution is correctly understood, and INLINE, XLINE, and BOTH are flexibly used in three ways to remove noise, save related geological information as much as possible, and improve the quality of the data. Then, through the line detection method and reasonable selection of the detection line length, linear strengthening is conducted to highlight the fracture information and solve the actual geological problems (Zhang et al., 2013; Shang et al., 2021).

The fabrication of coherence is the basis of the linear strengthening technique for crack detection. To obtain a higher-quality data volume sensitive to fractures, the coherence data volume should be further linearly enhanced. In the process of linear strengthening, noise suppression is mainly carried out along the direction of noise in the plane, and the direction perpendicular to the main measuring line is usually considered the main direction of noise. Its purpose is mainly to filter the noise that can be seen in the coherence data. The effect of noise filtering can be achieved by selecting the length of the noise filtering factor. In the

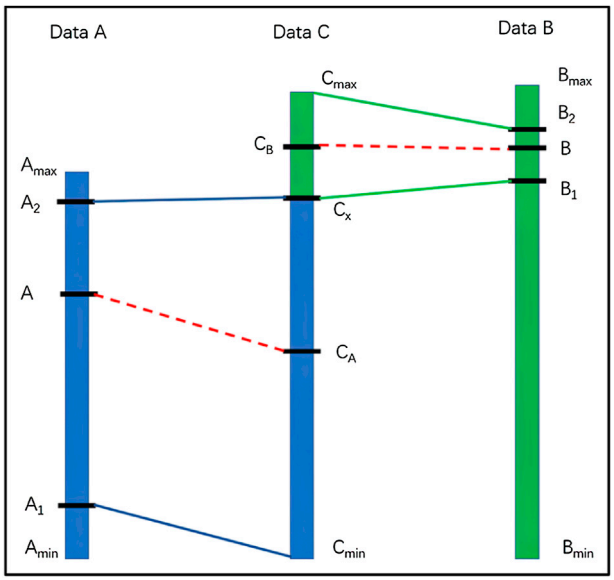

FIGURE 4 | Schematic diagram of attribute proportion fusion calculation.

process of linear strengthening, fracture seismic reflection in the direction of the main survey line is retained, and the noise information of fractures in other directions is suppressed to enhance the fracture information in the study area.

3.3 Spectral Decomposition

Fractures inside a buried hill are the main cause for the formation of a cavity, and the response characteristics of seismic data with different acquisition directions vary. The collection direction vertical to the cavity is most sensitive to the response characteristics of the cavity (Lu et al., 2007; Liu and Ning, 2009; Su et al., 2020). The technique of spectral decomposition transforms the seismic signal from the time domain to the frequency domain by mathematical transformation. The reservoir is characterized in the frequency domain to avoid the mutual interference of different frequencies in the time domain (Sinha et al., 2005; Zhang et al., 2017; Li et al., 2019; Wu et al., 2020). Therefore, the seismic response characteristics of the same cavity to seismic waves with different frequencies are also different. The low-frequency amplitude energy of the reservoir increases when oil and gas are present (Li et al., 2019; Luo et al., 2020). In other words, the energy of the low-frequency component of seismic waves passing through oil–gas reservoirs is stronger than that of seismic waves passing through nonreservoirs (Liu, 2013; Tian et al., 2016; Zheng et al., 2019). It is possible to predict the distribution of fractured-cave reservoirs by using weak seismic spectral variation (Wang et al., 2004; Liu, 2013). Based on the above understanding, it can be considered that seismic waves in the low-frequency segment have a clearer representation of fractures and caves. To clarify the distribution rules of buried hill cavities, the following research ideas are designed: the short-time Fourier transform (STFT) is applied to seismic data to obtain a single frequency attribute body of multiple frequencies, combined with along-layer slicing technology, to identify the cavity plane distribution of various time windows (theoretically, the frequency division information can reflect the aperture of the 1/4 wavelength specification) (Raeesi et al., 2012; Tian et al., 2016; Li et al., 2019; Yang et al., 2021).

3.4 Attribute Fusion Technology

The extraction of seismic attributes is mainly based on mathematical transformation, and the geological significance of a single attribute may be relatively fuzzy, which requires geological researchers to determine the attributes comprehensively according to experience and various data (Zhou et al., 2021). However, the mixed attribute generated after seismic attribute fusion has no specific geological meaning. The purpose is to enable different attributes to be displayed simultaneously in the same palette mode, which is convenient for researchers to conduct comprehensive analysis and consideration of multiple attributes.

The GeoEast system attribute fusion technology is, according to a certain proportion relationship, to fuse attribute A and attribute B to generate a new attribute C. An appropriate dividing line is selected within the value range of attribute C, and the value range to be displayed by data A and that by data B are placed on either side of the boundary point of data C (Meng et al., 2018) (**Figure 4**).

Amax, Amin: the maximum and minimum values of seismic attribute data A; Data between (A1, A2) in data A are selected for fusion; Amin ≤ A1 ≤ A2 ≤ Amax.

Bmax, Bmin: the maximum and minimum values of seismic attribute data B; Data between (B1, B2) in data B are selected for fusion; Bmin ≤ B1 ≤ B2 ≤ Bmax.

The maximum and minimum of data C after fusion are Cmax and Cmin.

In the program, the maximum and minimum of data C are designed to be equal to the maximum and minimum of attribute data A, that is, Cmax = Amax, Cmin = Amin.

Amax and Amin: maximum and minimum values of seismic attribute data A, respectively. Data between (A1, A2) in data A are selected for fusion, and Amin ≤ A1 ≤ A2 ≤ Amax.

Bmax and Bmin: the maximum and minimum values of seismic attribute data B; data between (B1, B2) in data B are selected for fusion, and Bmin ≤ B1 ≤ B2 ≤ Bmax.

The maximum and minimum of data C after fusion are Cmax and Cmin. In the program, the maximum and minimum of data C are designed to be equal to the maximum and minimum of attribute data A; that is, Cmax = Amax, Cmin = Amin.

To scale the attribute data A and B into data C, an appropriate value between the maximum and minimum of data C is selected as the cut-off point Cx, and Cmin < Cx < Cmax (or Amin < Cx < Amax). Then, the selected part of data A (A1, A2) is fused into the (Cmin, Cx) segment of data C, and the selected part of data B (B1, B2) is fused into the (Cx, Cmax) segment of data C. The specific calculation formula is as follows (Zhang et al., 2015; Meng et al., 2018) (**Formulas 1**, **2**):

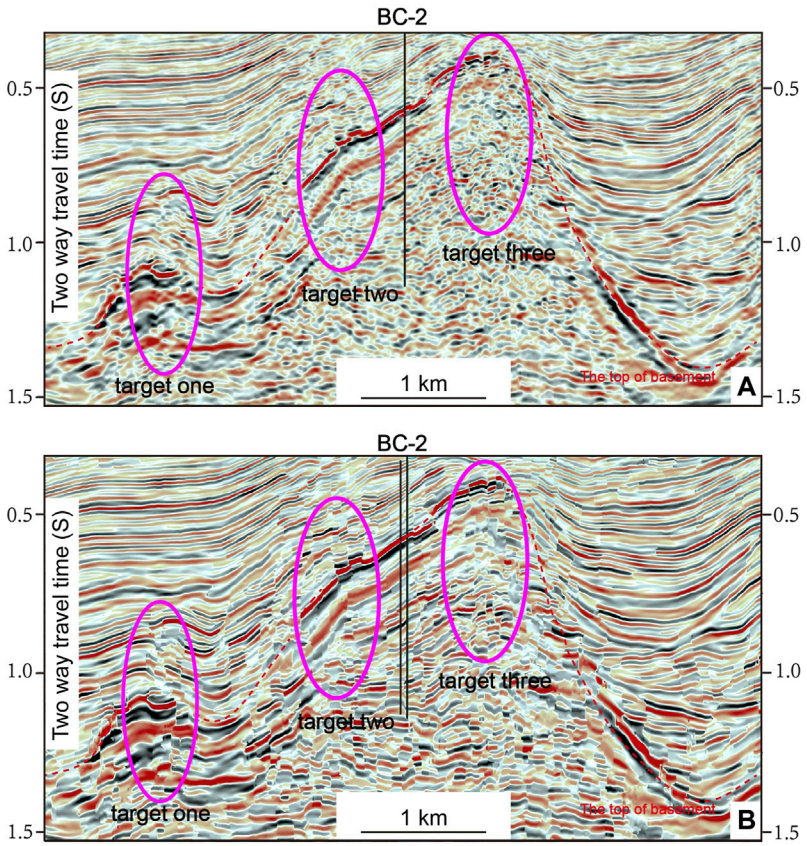

FIGURE 5 | Seismic profile before and after structure-oriented filtering. **(A)** Original seismic profile; **(B)** Seismic profile after structure-oriented filtering.

$$C_A = C_{min} + \frac{(\mathrm{A} - A_1)}{(A_2 - A_1)}(C_x - C_{min}) \quad (1)$$

$$C_B = C_x + \frac{(\mathrm{B} - B_1)}{(B_2 - B_1)}(C_{max} - C_x) \quad (2)$$

Cmin < Cx < Cmax, Amin ≤ A1 ≤ A2 ≤ Amax, Bmin ≤ B1 ≤ B2 ≤ Bmax.

4 RESULTS AND DISCUSSION

4.1 Seismic Data Preprocessing

In the BC block, there is a large difference in wave impedance between the granitic buried hill and the overlying clastic rocks in the P formation, which has a certain shielding effect on the seismic reflection characteristics of the underlying basement rock. As a result, the reflection signal is lost, and the resolution gradually decreases as the depth inside the buried hill increases. Seismic interpretation requires enhancement of the seismic reflections within the buried hill to maximize the accuracy of fracture prediction. Currently, the structure-oriented filtering technique is widely used for the preprocessing of seismic data because of its simplicity and effectiveness.

The signal-to-noise ratio of seismic data can be improved by structure-oriented filtering, thus improving the quality of the seismic data. Although the raw seismic data can reflect fault and fracture information to some extent, the resolution of the breakpoints is low (**Figure 5A**). Parameters suitable for the area were selected for structure-oriented filtering (**Figure 5B**). After filtering, the seismic profiles and breakpoints are clear. In addition, the continuity of seismic reflection events was improved, which provides a basis for subsequent prediction studies of buried-hill reservoirs.

4.2 Coherent Linear Enhancement

Figure 6A is the coherence attribute map along the top of the buried hill in the test area of the BC block, in which dark shadows represent low coherence, and bright areas represent high coherence. Because of the poor continuity of the reflected wave at the fault, it shows dark lines or curved features. Superposed with the fault system, the faults in the buried hill are found to have strikes of NW–SE and nearly E–W. This attribute is good for identifying large fractures but has a weak sensitivity response to fractures. Therefore, further linear strengthening technology is needed to improve the prediction accuracy of fractures.

Figure 6B shows the prediction plan of fracture development after coherent linear enhancement within 100 m below the upper surface of the buried hill in the test area of the BC block. In the figure, black areas represent areas with well-developed fractures,

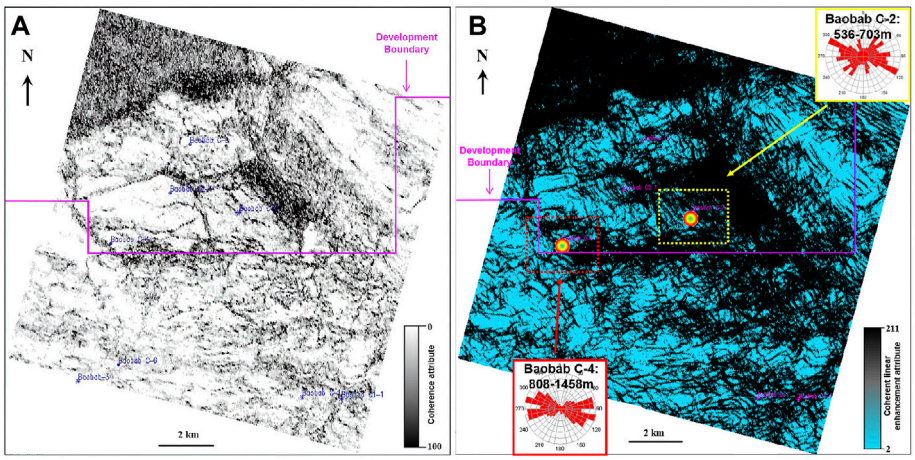

FIGURE 6 | Coherence attribute properties and coherent linear enhancement properties. **(A)** Coherence attribute properties on the top of the granitic buried hill in the BC2 well area. **(B)** Coherent linear enhancement properties of cracks on the top of granitic buried hill in the BC2 well area.

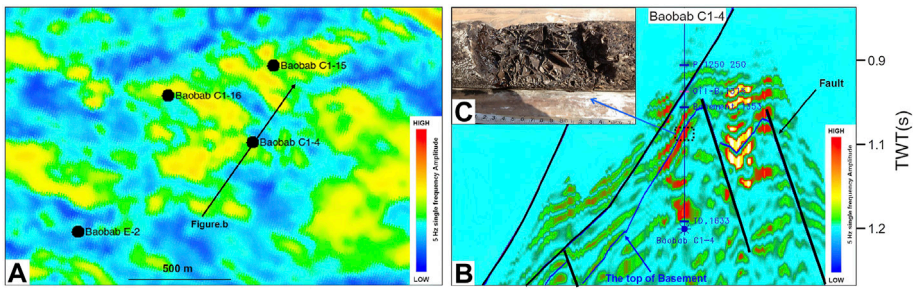

FIGURE 7 | (A) Plan view of the single-frequency volume in the area of well Baobab C1-4 (5 Hz). **(B)** Single-frequency profile of well Baobab C1-4. **(C)** Image of the core of well Baobab C1-4 (1,419.72 m–1420 m).

and blue areas represent areas with poorly developed fractures. The results of fracture prediction are verified by the high oil and gas production of well BC-4 and well BC-2 in the buried hill section. The results show that the degree of coincidence is high, which suggests the feasibility of this fracture prediction method, which can effectively predict the planar distribution of fractured reservoirs.

4.3 Fractured-Cave Reservoir Prediction

Combined with accurate reservoir calibration, the development location and seismic reflection characteristics of the cavity were determined. The GeoEast time-frequency analysis module was used to obtain the highest coincidence between the 5 Hz single frequency attribute body and the actual drilling core calibration, which can accurately reflect the plane distribution of the fractured-cave reservoir in the buried hill (**Figures 7A–C**).

Figure 7B shows the core photos of Well Baobab C1-4 and the 5 Hz frequency volume profile of well Baobab C1-4. Red and yellow represent abnormal bodies such as cavities, and green represents conventional strata. In the drilling of Well Baobab C1-4, multistage caving and mud leakage occurred, and holes were found in the drilling core at 1,419.72 m, which was consistent with the characteristics of the frequency attribute body at the corresponding position, indicating the sensitivity of low-frequency hole detection. Therefore, 5 Hz single-frequency attribute body data can be used to predict the distribution of fractures or cavities.

4.4 Comprehensive Prediction of Buried-Hill Reservoirs

The planar prediction results (as shown in **Figures 8A,B**) of the buried hill fractures and fractured caves in the BC block described above are used for attribute fusion. **Figure 9A** is a comprehensive evaluation diagram of buried-hill reservoirs in the BC block after splicing and fusion of the two types of reservoirs at depths of 0–100 m below the buried hill surface. The blue values indicate the development area of fractured reservoirs, which are mainly concentrated in the higher area in the northeast. The distribution characteristics are influenced by the NW–SE strike. Because the northeastern part of the section is strongly affected by tectonic stress, the buried hill is steep and narrow, and a series of large

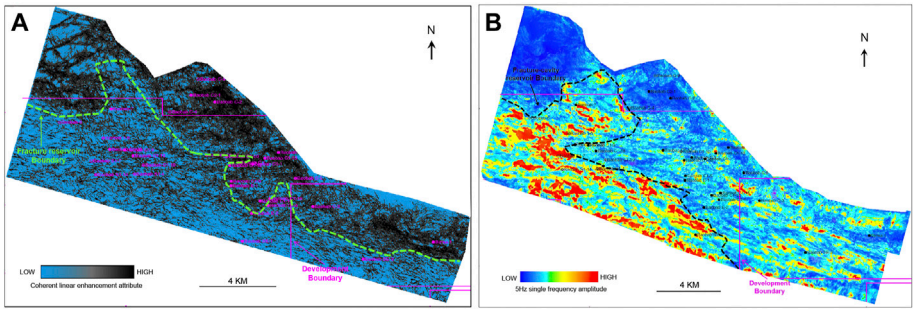

FIGURE 8 | (A) Prediction map of the fractured granitic buried-hill reservoirs in the BC block (100 m below buried-hill surface). **(B)** Prediction map of the fractured-cave granitic buried-hill reservoirs in the BC block (0–100 m below the buried-hill surface).

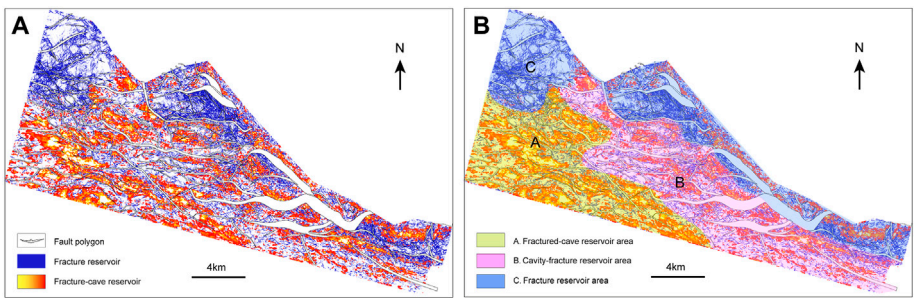

FIGURE 9 | (A) Overlap map of the buried-hill reservoirs in the BC block (0–100 m below the buried hill surface). **(B)** Planar distribution of the three types of buried-hill reservoirs in the BC block (0–100 m below the buried hill surface).

first-order faults are developed in the NW–SE direction. The strata adjacent to the large faults are seriously broken, and a fracture zone is developed. The buried hill landform in the southwestern section is relatively broad and has been weakly affected by tectonic stress. It is located at the tail end of the large fault, the strata are relatively intact, and the fracture development intensity is relatively weak. The fracture system around the long-term active fault associated with multistage tectonic movement is dense and complex and represents the final result of the crossing and superposition of multistage fractures (Sun et al., 2013). The red and yellow values indicate the development zones of fractured-cave reservoirs. **Figure 8B** shows that the basement rock pores in this area are mainly developed in the southwest of the section (West of the black dotted line in **Figure 8B**), are weakly developed in the East and are least developed in the North. The development degree of basement rock pores weakens from SW to NE.

Comprehensive analysis shows that the granitic rocks mainly host fractured reservoirs with little difference in development intensity. During the formation of the central African shear zone, the uplift height in the northeast of the section was greater than that in the southwest due to tectonic stress (Cuong and Warren, 2009). As the large fault developed, the formation fragmentation was more severe in the northeast than in the southwest. In the southwestern part of the section, the stress intensity has remained low, and the strata are relatively intact. Later developed faults or fractures intersect with early fractures, which is conducive to local formation dissolution and fractured-cave formation. The reservoir connectivity of the whole area gradually increases from southwest to northeast.

According to the above observations, the types of buried-hill reservoirs in the BC block are divided according to the relative development degree of fractures and caves. From southwest to northeast, the reservoirs gradually transition from the fractured-cave type to the fracture type. With gradually decreasing porosity, reservoirs are divided as follows: A) fractured-cave reservoir, B) cavity-fracture reservoir, and C) fracture reservoir. Finally, based on the comprehensive consideration of porosity and connectivity, it is considered that the B type (cavity-fracture reservoir) is the preferred high-quality reservoir (**Figure 9B**).

4.5 Application Effect Evaluation

Reservoir production dynamic data can effectively reflect the production characteristics of a large section of the play zone, which can further verify the reservoir prediction results (Guo et al., 2019). Wells BC1-10 and BC1-13 are located in the high part of the buried hill, and the fracture and frequency data are displayed in the fusion profile and on the horizontal plane (**Figures 10A,B**). Black represents the fractured reservoir response, and yellow–green represents the fractured-cave reservoir response. Fractures are well developed in both wells. However, the amplitude energy of the 5 Hz single-frequency

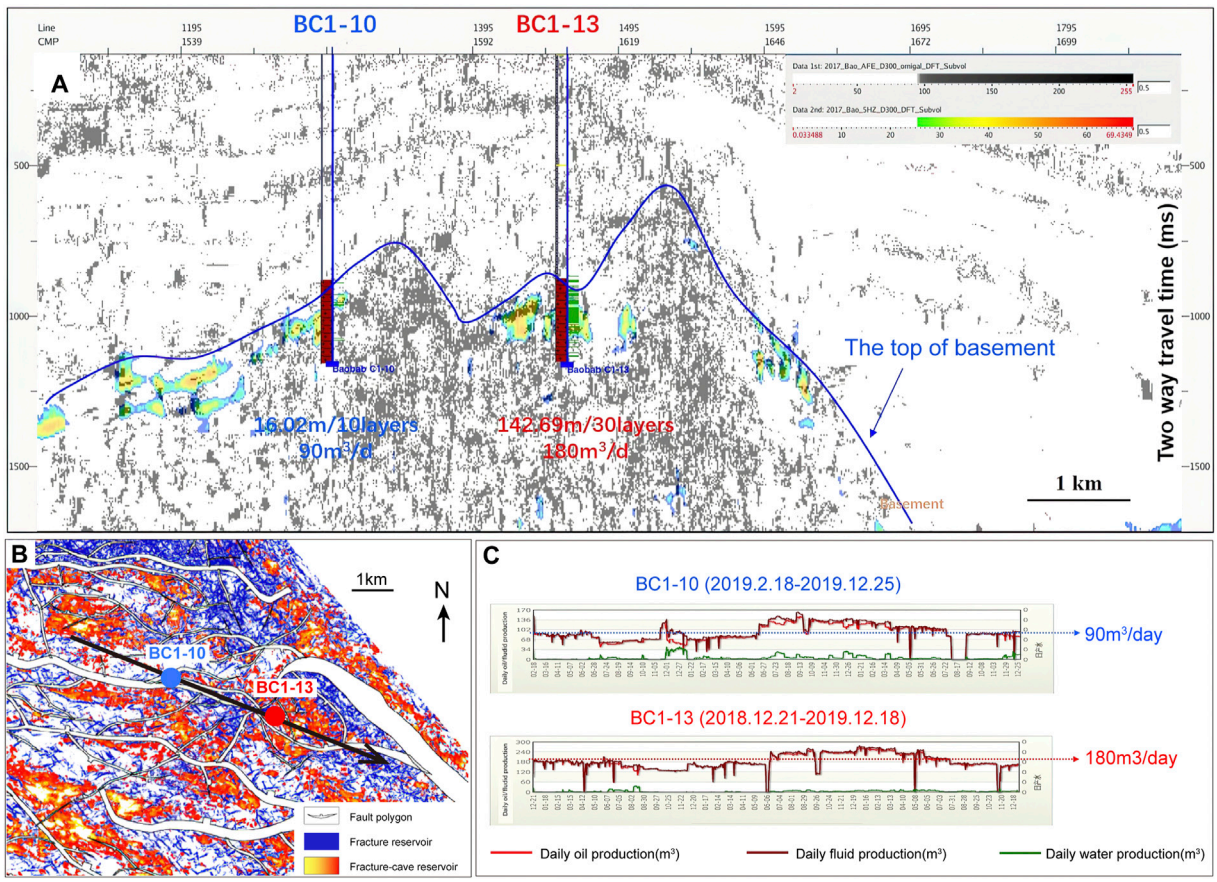

FIGURE 10 | (A) Fusion profile of fracture data and fractured-cave data through wells BC1-10 and BC1-13 (coherent linear enhancement attribute and 5 Hz frequency volume). **(B)** Reservoir overlap diagram of buried hills in the BC block. **(C)** Dynamic production curves of wells BC1-10 and BC1-13.

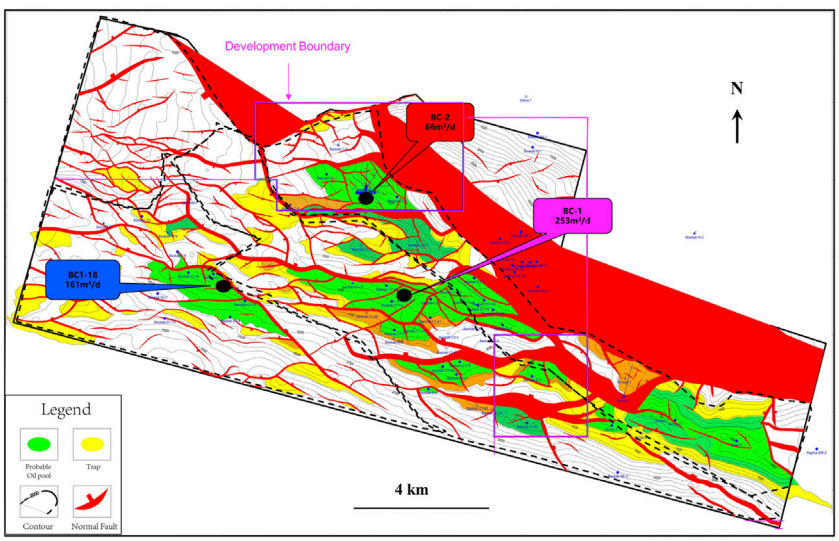

FIGURE 11 | Structural diagram of the top of the buried hill in the BC block (green indicates oil-bearing areas and yellow indicates traps).

attribute body in BC1-13 is stronger, suggesting that the fractured-cave reservoir is more developed, with better reservoir connectivity and better reservoir evaluation. The logging interpretation of the BC1-13 well buried-hill oil layer is 142.69 m, and that of the BC1-10 well buried-hill oil layer is 16 m. Based on the dynamic production curve statistics of the past year (**Figure 10C**), well BC1-10 averaged 90 m^3 of oil per day, while well BC1-13, which was predicted to have a more developed buried-hill formation, averaged 180 m^3/day, in line with the predrilling forecast.

The three types of reservoir areas are compared with the previous prediction results (**Figure 11**), combined with dynamic data from all producing wells in the field. The average daily oil production per well in the buried-hill type B reservoir is 253 m^3/day; the average daily oil production per well in the buried-hill type C reservoir area is 161 m^3/day; the average daily oil production per well in the buried-hill type A reservoir area is 66 m^3/day; and the average daily production of oil and gas per well decreases successively. This is consistent with the comprehensive prediction results of basement buried-hill reservoirs in the BC block area, which confirms the effectiveness of this method. Buried-hill oil and gas accumulations are controlled by structural location and reservoir type. In a buried-hill fault block with a high structure, the type of buried-hill reservoir is the main controlling factor affecting productivity change. The cavity-fracture reservoirs are characterized by the highest oil production.

5 CONCLUSION

(1) A set of reservoir prediction methods suitable for granitic buried-hill reservoirs is summarized. These methods have been successfully applied to predict the most favourable development zones in the BC block. According to the different types of basement buried-hill reservoirs, different methods can be used to predict the spatial distribution of fracture reservoirs and fractured-cave reservoirs in complicated and heterogeneous basement buried-hill reservoirs.

(2) The basement buried-hill reservoirs in the BC block are dominated by fractured reservoirs, with locally developed fractured-cave reservoirs. The fractured-cave reservoirs formed from fractured reservoirs and are mainly associated with tectonic faults in the southwestern part. The tectonic faults in the northeastern part are close to the tectonic stress release zone. The formation is heavily fractured. The reservoirs are mainly fractured. The overall connectivity is better in the northeast than in the southwest.

(3) A comprehensive study shows that the basement buried-hill reservoirs in the BC block can be divided into three types: A) fractured-cave reservoirs; B) cavity-fracture reservoirs; and C) fracture-type reservoirs. From the southwest to the northeast, the reservoirs gradually transition from the fractured-cave type to the fracture type, with a gradual decrease in porosity and a gradual increase in connectivity. Based on the comprehensive evaluation of porosity and connectivity, it is concluded that the B-type cavity-fracture reservoir is the best reservoir type. Actual drilling data are consistent with the predictions.

(4) The comprehensive reservoir prediction results show that the method proposed in this study can effectively predict the reservoir distribution in the depth range of 0–100 m from the top of the buried hill but still has some limitations (e.g., it cannot distinguish effective fractures from ineffective fractures).

(5) The reservoir potential of the Precambrian basement has been greatly underestimated. This favourable finding has potential implications for exploration in the future. The oil discovery in the fractured buried hills in the Precambrian basement of the Bongor Basin will aid the hydrocarbon exploration of new plays in the central African rift system. It is also a milestone in the onshore exploration of the central African rift system.

DATA AVAILABILITY STATEMENT

The datasets presented in this article are not readily available because 1. The original data involves trade secrets and shall not be disclosed without authorization. 2. The original data sets take up too much disk space to be easily transferred over the Internet. Requests to access the datasets should be directed to wangyajie01@cnpc.com.cn.

AUTHOR CONTRIBUTIONS

YW: Writing Original Draft, Formal analysis; Methodology, GX: Conceptualization; Reviewing and Editing. WZ: Verified the analytical methods. JL, FX, and SH: Technology support: provided critical feedback.

ACKNOWLEDGMENTS

We thank the editors for their constructive recommendations that have improved this manuscript. We also thank the CNPCIC for providing the data and allowing the publication of this article. Zhao Lin-Hai of the College of Energy, Chengdu University of Technology and senior engineer Hou Yun-Peng of the Geophysical Research Institute, Bureau of Geophysical Prospecting of Petro China have been of great assistance during the data analysis.

REFERENCES

Bahorich, M., and Farmer, S. (1995). 3-D Seismic Discontinuity for Faults and Stratigraphic Features: The Coherence Cube. *Lead. edge* 14, 1053–1058. doi:10.1190/1.1437077

Chen, C. (2015). Key Technique and Application of Structure Oriented Filter for Seismic Wave Field. Doctor's thesis. Changchun (China): Jilin University.

Chen, L., Ji, H., Dou, L., Du, Y., Xu, Z., Zhang, L., et al. (2018). The Characteristics of Source Rock and Hydrocarbon Charging Time of Precambrian Granite Reservoirs in the Bongor Basin, Chad. *Mar. Petroleum Geol.* 97, 323–338. doi:10.1016/j.marpetgeo.2018.06.003

Cuong, T. X., and Warren, J. K. (2009). BACH HOFIELD, A FRACTURED GRANITIC BASEMENT RESERVOIR, CUU LONG BASIN, OFFSHORE SE VIETNAM: A "BURIED-HILL" PLAY. *J. Petroleum Geol.* 32, 129–156. doi:10.1111/j.1747-5457.2009.00440.x

Dai, J., Ni, Y., Dong, D., Qin, S., Zhu, G., Huang, S., et al. (2021). 2021-2025 Is a Period of Great Development of China's Natural Gas Industry: Suggestions on the Exploration and Development of Natural Gas during the 14th Five-Year Plan in China. *J. Nat. Gas Geoscience* 6, 183–197. doi:10.1016/j.jnggs.2021.08.001

Dou, L., Li, W., and Cheng, D. (2020). Hydrocarbon Accumulation Period and Process in Baobab Area of Bongor Basin. *J. Afr. Earth Sci.* 161, 103673. doi:10.1016/j.jafrearsci.2019.103673

Dou, L., Shrivastava, C., Dai, C. S., Wang, J., Hammond, N., Anoliefo, C., et al. (2014). "Better Exploitation of Granitic Reservoirs: Understanding the Role of Stress Regime and Fractures," in Unconventional Resources Technology Conference, Denver, CO. doi:10.1306/02061817090

Dou, L., Wang, J., Wang, R., Wei, X., and Shrivastava, C. (2018). Precambrian Basement Reservoirs: Case Study from the Northern Bongor Basin, the Republic of Chad. *Bulletin* 102, 1803–1824. doi:10.1306/02061817090

Dou, L., Wei, X., Wang, J., Li, J., Wang, R., and Zhang, S. (2015). Characteristics of Granitic Basement Rock Buried-Hill Reservoir in Bongor Basin, Chad. *Acta Pet. Sin.* 36, 897–904+925.

Fehmers, G. C., and Höcker, C. F. W. (2003). Fast Structural Interpretation with Structure-oriented Filtering. *Geophysics* 68, 1286–1293. doi:10.1190/1.1598121

Gao, M., Cui, G., Liu, B., Han, J., Tian, Y., and Xu, L. (2018). Fault Block Trap Evaluation in Maozhou Oilfield. *Oil Geophys. Prospect.* 53, 170–178+113114. doi:10.13810/j.cnki.issn.1000-7210.2018.S1.028

Genik, G. J. (1992). Regional Framework, Structural and Petroleum Aspects of Rift Basins in Niger, Chad and the Central African Republic (C.A.R.). *Tectonophysics* 213, 169–185. doi:10.1016/0040-1951(92)90257-7

Gong, D., Xu, G., Xu, S., Wang, X., Zheng, L., Fu, H., et al. (2013). Seismic Geomorphology Analysis and its Application in Llanos Basin, Columbia. *Prog. Geophys.* 28, 2569–2578.

Guo, K., Fan, L., Li, Y., Zhang, M., Zhang, C., and Li, L. (2019). Comprehensive Prediction of Fracture of Tight Carbonate Reservoir in the H Block of Amu Darya Right Bank. *Geophys. Prospect. Petroleum* 58, 112–122+138.

Höcker, C., and Fehmers, G. (2002). Fast Structural Interpretation with Structure-Oriented Filtering. *Lead. edge* 21, 238–243. doi:10.1190/1.1463775

Li, H., Lin, C., Ren, L., Zhang, G., Chang, L., and Dong, C. (2021a). Quantitative Prediction of Multi-Period Tectonic Fractures Based on Integrated Geological-Geophysical and Geomechanics Data in Deep Carbonate Reservoirs of Halahatang Oilfield in Northern Tarim Basin. *Mar. Petroleum Geol.* 134, 105377. doi:10.1016/j.marpetgeo.2021.105377

Li, H., Niu, C., Xu, P., Liu, Q., Zhang, X., and Cui, H. (2021b). Discovery of Bozhong 13-2 Archean Large Monoblock Volatile Buried Hill Oilfield and its Oil and Gas Exploration Significance. *Nat. Gas. Ind. B* 8, 376–383. doi:10.1016/j.ngib.2021.07.008

Li, W., Dou, L., Wen, Z., Zhang, G., and Cheng, D. (2017). Use of a Geochemical Method to Analyze the Hydrocarbon Accumulation Process in the Bongor Basin, Chad. *Petroleum Sci. Technol.* 35, 2133–2138. doi:10.1080/10916466.2017.1386678

Li, W., Yue, D., Wang, W., Wang, W., Wu, S., Li, J., et al. (2019). Fusing Multiple Frequency-Decomposed Seismic Attributes with Machine Learning for Thickness Prediction and Sedimentary Facies Interpretation in Fluvial Reservoirs. *J. Petroleum Sci. Eng.* 177, 1087–1102. doi:10.1016/j.petrol.2019.03.017

Liu, A. (2013). Comprehensive Evaluation and Fluid Identification of Fracture-Cavity Carbonate Reservoir. Doctor's thesis. Chengdu (China): Chengdu University of Technology.

Liu, X., and Ning, J. (2009). A Review of Time Frequency Attributes and Their Applications in Seismic Data Interpretation for Oil & Gas Geology. *Prog. Explor. Geophys.* 32 (1), 18–22+83. (in Chinese with English abstract).

Lu, P., Yang, C., and Guo, A. (2007). The Present Research on Frequency-Spectrum Imaging Technique. *Prog. Geophys.* 22 (5), 1517–1521. (in Chinese with English abstract).

Luo, J., Wu, F., Zhang, D., Xu, M., Chen, H., Fan, J., et al. (2020). A Frequency-Divided Gas Prediction Technology Based on Resistivity Constraint. *Nat. Gas. Ind. B* 7, 127–132. doi:10.1016/j.ngib.2019.09.003

Luo, X., Chen, X., Zhang, J., Li, K., Lv, B., and Wen, H. (2022). A Target-Oriented Integrated Workflow for Seismic Delineation of Thin Tight Reservoirs in the Eastern Sichuan Basin, China. *J. Petroleum Sci. Eng.* 208, 109246. doi:10.1016/j.petrol.2021.109246

Maerten, L., Maerten, F., and Lejri, M. (2018). Along Fault Friction and Fluid Pressure Effects on the Spatial Distribution of Fault-Related Fractures. *J. Struct. Geol.* 108, 198–212. doi:10.1016/j.jsg.2017.10.008

Marfurt, K. J., Sudhaker, V., Gersztenkorn, A., Crawford, K. D., and Nissen, S. E. (1999). Coherency Calculations in the Presence of Structural Dip. *Geophysics* 64, 104–111. doi:10.1190/1.1444508

Meng, Y., Xu, Y., Li, J., Xu, T., Wang, H., and Wang, X. (2018). Fault Identification with OVT-Domain Seismic Attribute Analysis. *Oil Geophys. Prospect.* 53, 289–294+219. doi:10.13810/j.cnki.issn.1000-7210.2018.S2.045

Panza, E., Sessa, E., Agosta, F., and Giorgioni, M. (2018). Discrete Fracture Network Modelling of a Hydrocarbon-Bearing, Oblique-Slip Fault Zone: Inferences on Fault-Controlled Fluid Storage and Migration Properties of Carbonate Fault Damage Zones. *Mar. Petroleum Geol.* 89, 263–279. doi:10.1016/j.marpetgeo.2017.09.009

Pu, J., and Qing, Q. (2008). An Overview of Fracture Prediction Methods for Oil and Gas Reservoirs. *Special Oil Gas Reservoirs* 15 (3), 9–13+106. (in Chinese with English abstract).

Raeesi, M., Moradzadeh, A., Doulati Ardejani, F., and Rahimi, M. (2012). Classification and Identification of Hydrocarbon Reservoir Lithofacies and Their Heterogeneity Using Seismic Attributes, Logs Data and Artificial Neural Networks. *J. Petroleum Sci. Eng.* 82-83, 151–165. doi:10.1016/j.petrol.2012.01.012

Salah, M. G., and Alsharhan, A. S. (1998). The Precambrian Basement: A Major Reservoir in the Rifted Basin, Gulf of Suez. *J. Petroleum Sci. Eng.* 19, 201–222. doi:10.1016/S0920-4105(97)00024-7

Saleh, A. D., Kurt, J. M., and Luo, Y. (2002). 3-D Edge Preserving Smoothing for Seismic Edge Detection. *Seg. Tech. Program Expand. Abstr.*, 524–527. doi:10.1190/1.1817300

Shang, X., Long, S., and Duan, T. (2021). Fracture System in Shale Gas Reservoir: Prospect of Characterization and Modeling Techniques. *J. Nat. Gas Geoscience* 6, 157–172. doi:10.1016/j.jnggs.2021.06.001

Sinha, S., Routh, P. S., Anno, P. D., and Castagna, J. P. (2005). Spectral Decomposition of Seismic Data with Continuous-Wavelet Transform. *GEOPHYSICS* 70, P19–P25. doi:10.1190/1.2127113

Su, Z., Liu, Y., Han, J., Luo, H., Yang, F., Cui, Y., et al. (2020). Application of Ultra-deep Sandstone Reservoirs Prediction Technology under Controlled Seismic Facies in Yudong Block of Tabei Uplift, Tarim Basin, China. *J. Nat. Gas Geoscience* 5, 157–167. doi:10.1016/j.jnggs.2020.05.001

Sun, W., Li, Y., He, W., Hei, J., and Kong, K. (2013). Using P-Wave Azimuthal Anisotropy to Predict Fractures in Carbonate Reservoirs of the ZY Block. *Geophys. Prospect. Petroleum* 34 (1), 137–144. (in Chinese with English abstract).

Tian, F., Jin, Q., Lu, X., Lei, Y., Zhang, L., Zheng, S., et al. (2016). Multi-layered Ordovician Paleokarst Reservoir Detection and Spatial Delineation: A Case Study in the Tahe Oilfield, Tarim Basin, Western China. *Mar. Petroleum Geol.* 69, 53–73. doi:10.1016/j.marpetgeo.2015.10.015

Wang, J., Dou, L., Xu, J., Wei, X., Wang, Z., and Chen, H. (2018). Granitic Buried-Hill Reservoir Characterization Based on Broadband, Wide-Azimuth and High-Density Seismic Data:A Case Study of Bongor Basin in Chad. *Oil Geophys. Prospect.* 53, 320–329+222. doi:10.13810/j.cnki.issn.1000-7210.2018.02.013

Wang, S., Guan, L., and Zhu, H. (2004). Prediction of Fracture-Cavity System in Carbonate Reservoir: A Case Study in the Tahe Oilfield. *Appl. Geophys.* 1, 56–62. doi:10.1007/s11770-004-0032-y

Wang, S., Yuan, S., Yan, B., He, Y., and Sun, W. (2016). Directional Complex-Valued Coherence Attributes for Discontinuous Edge Detection. *J. Appl. Geophys.* 129, 1–7. doi:10.1016/j.jappgeo.2016.03.016

Wang, X., Gao, J., Chen, W., and Song, Y. (2012). An Efficient Implementation of Eigenstructure-Based Coherence Algorithm Using Recursion Strategies and the Power Method. *J. Appl. Geophys.* 82, 11–18. doi:10.1016/j.jappgeo.2012.03.009

Wang, X., Zhang, X., Zhao, X., Hu, F., Ren, C., Wang, G., et al. (2021). Key Technologies for Complex Surface Seismic Acquisition in the Sichuan Basin and Their Application Effect. *Nat. Gas. Ind. B* 8, 552–561. doi:10.1016/j.ngib.2021.11.003

Wang, Y., Lu, W., and Zhang, P. (2015). An Improved Coherence Algorithm with Robust Local Slope Estimation. *J. Appl. Geophys.* 114, 146–157. doi:10.1016/j.jappgeo.2015.01.015

Wu, D., Wu, Z., and Wu, Y. (2020). A New Method for High Resolution Well-Control Processing of Post-stack Seismic Data. *Nat. Gas. Ind. B* 7, 215–223. doi:10.1016/j.ngib.2019.11.003

Yan, L., Chang, Y., Tian, Z., Li, X., and Jin, J. (2019). Characteristics of Reservoir Spaces and Influencing Factors for Basement Rock of Bongor Basin in Chad. *J. Northeast Petroleum Univ.* 43 (2), 59–67+5859. doi:10.19509/j.cnki.dzkq.2019.0608

Yang, Y., Xie, J., Zhao, L., Huang, P., Zhang, X., Chen, C., et al. (2021). Breakthrough of Natural Gas Exploration in the Beach Facies Porous Dolomite Reservoir of Middle Permian Maokou Formation in the Sichuan Basin and its Implications: A Case Study of the Tridimensional Exploration of Well JT1 in the Central-Northern Sichuan Basin. *Nat. Gas. Ind. B* 8, 393–401. doi:10.1016/j.ngib.2021.07.010

Ye, T., Niu, C., and Wei, A. (2020). Characteristics and Genetic Mechanism of Large Granitic Buried-Hill Reservoir, a Case Study from PengLai Oil Field of Bohai Bay Basin, North China. *J. Petroleum Sci. Eng.* 189, 106988. doi:10.1016/j.petrol.2020.106988

Ye, Y. (2019). Comprehensive Prediction of Precise Reservoir Fracture and the Application Stduy on the Gas-Bearing Detection. Doctor's thesis. Chengdu (China): Chengdu University of Technology.

Yi, S., Li, M., Xu, S., Guo, X., Cui, B., Meng, Q. A., et al. (2021). Accumulation Condition and Model of Buried Hill in the Central Uplift, Songliao Basin, China. *J. Nat. Gas Geoscience* 6, 121–135. doi:10.1016/j.jnggs.2021.06.002

Zhang, H., Ma, J., Jiang, Z., Wang, T., Zhao, Z., and Li, B. (2017). Application of Spectral Decomposition Technique in Reservoir Characterization and Fluid Identification. *Complex Hydrocarb. reserv.* 10, 31–33. doi:10.16181/j.cnki.fzyqc.2017.01.006

Zhang, J., Liu, Y., Luo, X., Zhao, L., Li, S., and Yin, N. (2015). Application of Complex Fracture Characterization Technique provided by GeoEast in Dawan Oil-Field. *Petroleum Geol. Englineering* 29 (5), 31–32+37. (in Chinese).

Zhang, J., Tian, S., Zheng, D., and Qu, X. (2013). Seismic Attribute Predication Method for Fractured Reservoirs. *Journal Oil Gas Technol.* 35 (3), 79–84+166. (in Chinese with English abstract).

Zhang, K., Lin, N., Tian, G., Yang, J., Wang, D., and Jin, Z. (2022). Unsupervised-learning Based Self-Organizing Neural Network Using Multi-Component Seismic Data: Application to Xujiahe Tight-Sand Gas Reservoir in China. *J. Petroleum Sci. Eng.* 209, 109964. doi:10.1016/j.petrol.2021.109964

Zhang, Y., Li, S., Huang, G., Zhang, F., and Chi, Y. (2002). The Classification and Application Value of Seismic Slice. *Petroleum Geology and Recovery Efficiency* 9 (3), 67–69+61. (in Chinese with English abstract).

Zheng, S., Yang, M., Kang, Z., Liu, Z., Long, X., Liu, K., et al. (2019). Controlling Factors of Remaining Oil Distribution after Water Flooding and Enhanced Oil Recovery Methods for Fracture-Cavity Carbonate Reservoirs in Tahe Oilfield. *Petroleum Explor. Dev.* 46, 786–795. doi:10.1016/s1876-3804(19)60236-3

Zhou, L., Qian, Y., Zhang, L., Lan, X., Wu, Y., Wang, Q., et al. (2021). Seismic Prediction of Oolitic Beach Thin-Bed Reservoir Based on Favorable Facies Belt Constraints: Taking the Second Member of Feixianguan Formation in Jiulongshan Area, Northwest Sichuan, China. *J. Nat. Gas Geoscience* 6, 329–344. doi:10.1016/j.jnggs.2021.12.002

Zhou, Y., and Li, S. (2018). Simultaneous Deblending and Interpolation Using Structure-Oriented Filters. *J. Appl. Geophys.* 150, 230–243. doi:10.1016/j.jappgeo.2018.01.015

Conflict of Interest: The authors declare that the research was conducted in the absence of any commercial or financial relationships that could be construed as a potential conflict of interest.

frontiers | Frontiers in Earth Science

ORIGINAL RESEARCH
published: 08 August 2022
doi: 10.3389/feart.2022.945563

Stratigraphic Characteristics and Sediment-Filling Process of the Early Permian Fengcheng Formation in the Northwestern Margin of the Junggar Basin, Northwest China

Dongming Zhi[1,2], Mingxin Liu[3], Xinwei Chen[3], Nuru Said[4,5], Wenbin Tang[3], Chenhui Hu[3], Zhijun Qin[1], Hao Zou[3] and Deyu Gong[6]**

[1]Xinjiang Oilfield Company, PetroChina, Karamay, China, [2]Turpan-Hami Oilfield Company, PetroChina, Hami, China, [3]State Key Laboratory of Oil and Gas Reservoir Geology and Exploitation, Chengdu University of Technology, Chengdu, China, [4]Department of Mineral and Rocks, King Abdul-Aziz University, Jeddah, SaudiArabia, [5]Centre of Exploration Targeting, The University of Western Australia, Crawley, WA, Australia, [6]Research Institute of Petroleum Exploration and Development, PetroChina, Beijing, China

OPEN ACCESS

Edited by:
Shang Xu,
China University of Petroleum, China

Reviewed by:
Zeyang Liu,
Guangzhou Institute of Geochemistry (CAS), China
Kuanhong Yu,
China University of Petroleum, China

***Correspondence:**
Hao Zou
zouhao@cdut.edu.cn
Deyu Gong
deyugong@126.com

Specialty section:
This article was submitted to Economic Geology, a section of the journal Frontiers in Earth Science

Received: 16 May 2022
Accepted: 14 June 2022
Published: 08 August 2022

Citation:
Zhi D, Liu M, Chen X, Said N, Tang W, Hu C, Qin Z, Zou H and Gong D (2022) Stratigraphic Characteristics and Sediment-Filling Process of the Early Permian Fengcheng Formation in the Northwestern Margin of the Junggar Basin, Northwest China. Front. Earth Sci. 10:945563. doi: 10.3389/feart.2022.945563

The Permian Fengcheng Formation in the Mahu sag of the Junggar Basin is a crude oil reservoir and source rock. However, its stratigraphic characteristics, the boundary marks of the three members (lower, middle, and upper), and the sediment-filling processes are unclear. This study presents the sedimentary systems and sediment-filling processes in an intracontinental rift basin of this area using sedimentary-faces analysis, sequence stratigraphy, well logs, and two-dimensional seismic interpretations. The results show that the Fengcheng Formation consists of three third-order sequence stratigraphy (SQf1, SQf2, and SQf3). The lowest member of the Fengcheng Formation is composed of gray to dark gray thin middle layers of tuff, lacustrine dolomitic mudstone, and argillaceous dolomite near the depocenter. Tuff, siltstone, a small amount of fan–delta glutenite, volcanic breccia, and basalt are present near the fault zone. The logging curve is characterized by a high gamma-ray (GR) value, high amplitude, wavelength growth, and medium frequency. Near the depocenter, the middle member of the Fengcheng Formation comprises gray and gray–black thin layers of lacustrine muddy dolomite and dolomitic mudstone and thin sandstone and mudstone interbedded between tuff and gravel near the orogenic belt. The logging curve displays high-to-low GR values, high amplitude, short wavelength, and high frequency. The upper member of the Fengcheng Formation is not characterized by lesser tuffaceous and dolomitic components but by an increased fan–delta sandy content. Next, the bottom of the upper member is composed of lacustrine mudstone and siltstone interbedded between dolomitic mudstones; whereas, the top of the upper member is dominated by fan–delta coarse sandstone and sandy conglomerate. The logging curve shows low GR values, small amplitude, and continuous stability. The sediment-filling process of the Fengcheng Formation is controlled by fault activity. Overall, the lower and middle members of the Fengcheng Formation expand during the sediment-filling process of the lake basin of the Mahu sag; whereas, the upper member contracts. The strong uplift of the Horst near the Baiquan and Mahu orogenic

belts led to an increase in provenance supply, resulting in a contraction of the southwestern margin of the lake basin during the sedimentation period from lower member to upper member of Fengcheng Formation.

Keywords: stratigraphic characteristics, sediment-filling process, Mahu sag, early Permian Fengcheng Formation, Junggar Basin

1 INTRODUCTION

Junggar Basin is a large petroliferous superimposed basin in northwest China (Cao et al., 2006; Jia et al., 2010; Zhang et al., 2010; Zhang et al., 2015; Li, 2022). The Permian delta sandstone, shore–shallow lacustrine, and semideep lacustrine mudstone developed in the Junggar Basin are the most critical reservoirs and source rocks, respectively (Gong et al., 2018; Gong et al., 2020). The volume of Permian oil and gas resources ranks first among all strata in the Junggar Basin. The Mahu sag, in the northwestern margin of the Junggar Basin, is a hydrocarbon-rich sag with the highest organic-matter content (Lei et al., 2014; Fang et al., 2019). The alkaline lacustrine sediments of the early Permian Fengcheng Formation in the Mahu sag are important source rocks for forming Karamay–Wuerhe and Mahu oil fields at the northwestern margin of the basin (Lei et al., 2005; Kuang and Qi, 2006; Zhang, 2013; Ouyang et al., 2018; Li et al., 2020; Tang et al., 2020). A detailed study of oil and gas exploration indicates that the Fengcheng Formation is a high-quality source rock and reservoir, forming conventional structural lithologic and unconventional tight/shale oil reservoirs (Wei et al., 2018; Zhi et al., 2019). Zhi et al. (2021) presented the orderly coexistence and accumulation models for conventional and unconventional hydrocarbons in the Lower Permian Fengcheng Formation. The Fengcheng Formation is divided into three members based on different lithologic assemblages (Cao et al., 2015), the characteristics of the sedimentary environment, and the development of the reservoir, tectonics, volcanism, and genesis of the rock, which are well documented (Xian, 1985; Niu et al., 2009; Liu et al., 2013; Gong et al., 2014). Chen et al. (2010) attempted to establish the sequence-division scheme of the Permian in the Wuxia area, in the northwest margin of the Junggar Basin, using a comprehensive analysis of well-seismic and -framework sequence. However, stratigraphic sequences and sediment-filling processes of the Fengcheng Formation are poorly understood.

The division of these three members is important for accurate stratigraphic correlation and refined exploration. This study presents a detailed stratigraphic framework for the Fengcheng Formation based on core observation, logging curve, and seismic data. The objective of this study is to determine the stratigraphic characteristics and sedimentary-filling process of the early Permian Fengcheng Formation.

2 GEOLOGICAL SETTING

The Junggar Basin, located in northern Xinjiang, China (**Figure 1A**) (He et al., 2004a), is an important part of the Central Asian Orogenic Belt (Shi et al., 2017; Pei et al., 2018; Zhang et al., 2020). It is located at the junction of Kazakhstan, Siberian, and Tarim Blocks (**Figure 1B**) (He et al., 2018). The basin is a late Paleozoic, Mesozoic, and Cenozoic superimposed basin (Cao et al., 2006; Zhang et al., 2010; Jin., 2011; Lu et al., 2019). The triangular Junggar Basin demonstrates an east–west extension, a width, and an area of ca. 700, 370, and 1.3×10^5 km^2, respectively. It is surrounded by the Zaire and Hala'alate mountains to the northwest; the Altai, Qingggelidi, and Kelamaili mountains to the northeast; and the Yilin Block, Biergen, and Bogda mountains to the south (**Figure 1C**). The Mahu sag is a second-order structural unit in the Junggar Basin, located at the northwest margin of the Junggar Basin (**Figure 1C**). The Mahu sag is a gentle-slope structure with monocline tilting to the southeast. Kebai (Karamay–Baikouquan) and Wuxia (Wuerhe–Xiazijie) fault zones are the main factors controlling the distribution and variation of the Permian–Triassic stratigraphic units (He et al., 2004b; Yu et al., 2016; Liang et al., 2020). The southeast slope belt of the sag is adjacent to the Shiyingtan uplift, Yingxi sag, Sanquan uplift, Xiayan uplift, and Dabasong uplift, from north to south (Gong et al., 2019) (**Figure 1D**).

Since the late Carboniferous, after the southwestern part of the Central Asian orogenic belt was amalgamated, the Junggar Basin experienced multistage intraplate tectonic deformation (Hendrix et al., 1992; Carroll et al., 1995; Han et al., 2010; Wang et al., 2018). Thus, the Mahu sag has changed from an early Permian syn-rift basin to a middle Permian postrift basin, and the sedimentary range has expanded, ending with the tectonic inversion, from the late Permian to early Triassic (Tang et al., 2020, 2021a, b, c). The basement of the Mahu sag is a late Carboniferous arc-basin system (Li et al., 2016; Tang et al., 2020). The Carboniferous strata are sequentially overlain by the Permian Jiamuhe (P_1j), Fengcheng (P_1f), Xiazijie (P_2x), lower Wuerhe (P_2w), upper Wuerhe (P_3w), Triassic Baikouquan (T_1b), Karamay (T_2k), and Baijiantan (T_3b) Formations (**Figure 2**). The maximum thickness of the sedimentary center of the Mahu sag is more than 6,000 m. The Lower Permian Fengcheng Formation is the sedimentary response to the syn-rift II stage (Tang et al., 2021a). From the bottom to the top, the Fengcheng Formation of the Lower Permian can be divided into three members: the lower (P_1f^1), middle (P_1f^2), and upper members (P_1f^3). The P_1f^2 is dominated by mafic-intermediate volcanic rocks, coarse clastic rocks, organic-rich mudstones interbedded with dolomitic mudstones, tuffs, ignimbritic flows, and uniform organic-rich mudstone interval with interbedded tuff (He et al., 2018). The P_1f^2 is characterized by organic-rich mudstones and dolomitic mudstones with turbidite sandstones (Zhang et al., 2018). Next, the P_1f^3 contains mudstones with interbedded dolomitic mudstones in the lower part and terrigenous clastic rocks in the upper part (Cao et al., 2015).

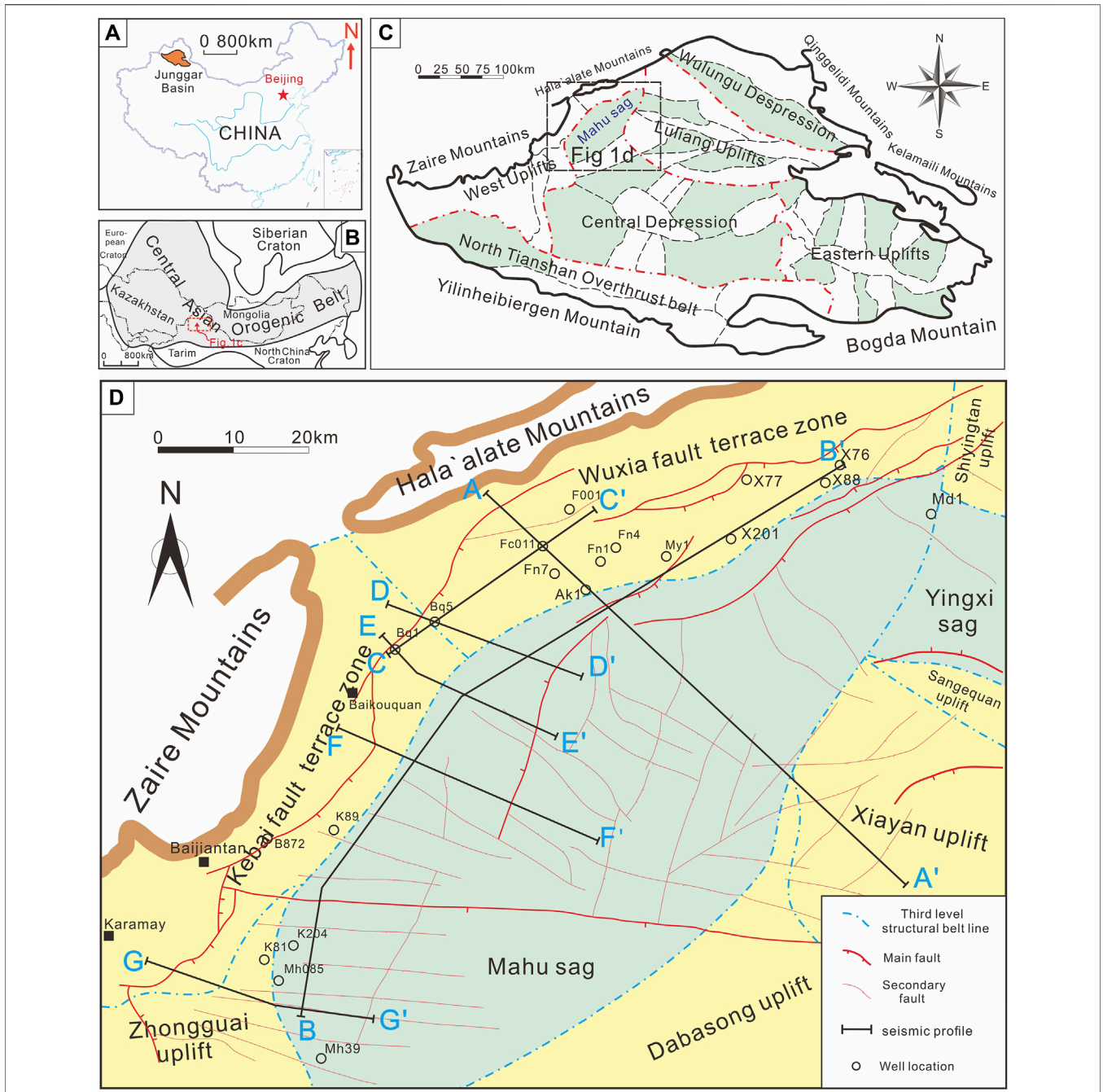

FIGURE 1 | Geological background of the study area. **(A)** the location of the Junggar Basin in China. **(B)** the location of the study area in the Central Asian orogenic belt. **(C)** the tectonic unit of Junggar Basin and the location of Mahu sag. **(D)** Geological background and distribution of drilling and seismic profiles in Mahu sag (modified from Feng et al., 2019; Liang et al., 2020; Tang et al., 2020, Tang et al., 2021a).

3 MATERIALS AND METHODS

Investigation of the sedimentary characteristics, sequence stratigraphy, and filling process of the Fengcheng Formation is based on the analysis of two-dimensional (2D) seismic data, well logging, and core descriptions obtained from the Xinjiang Oil Company, PetroChina (**Figure 1D** for the location). Moreover, the seismic lines that were studied covered most of the western margin of the Mahu sag. The 2D seismic profiles (SE-trending 110 km and NE-trending 290 km) demonstrated a record length of 7,500-m two–way travel. Therefore, penetration and resolution in all profiles are sufficient to image the Fengcheng Formation, representing our target. In addition, in this study, data from ten boreholes were combined and applied.

Sequence-boundary identification is the first step in the study of sequence stratigraphy (Vail, 1988). The base level is an

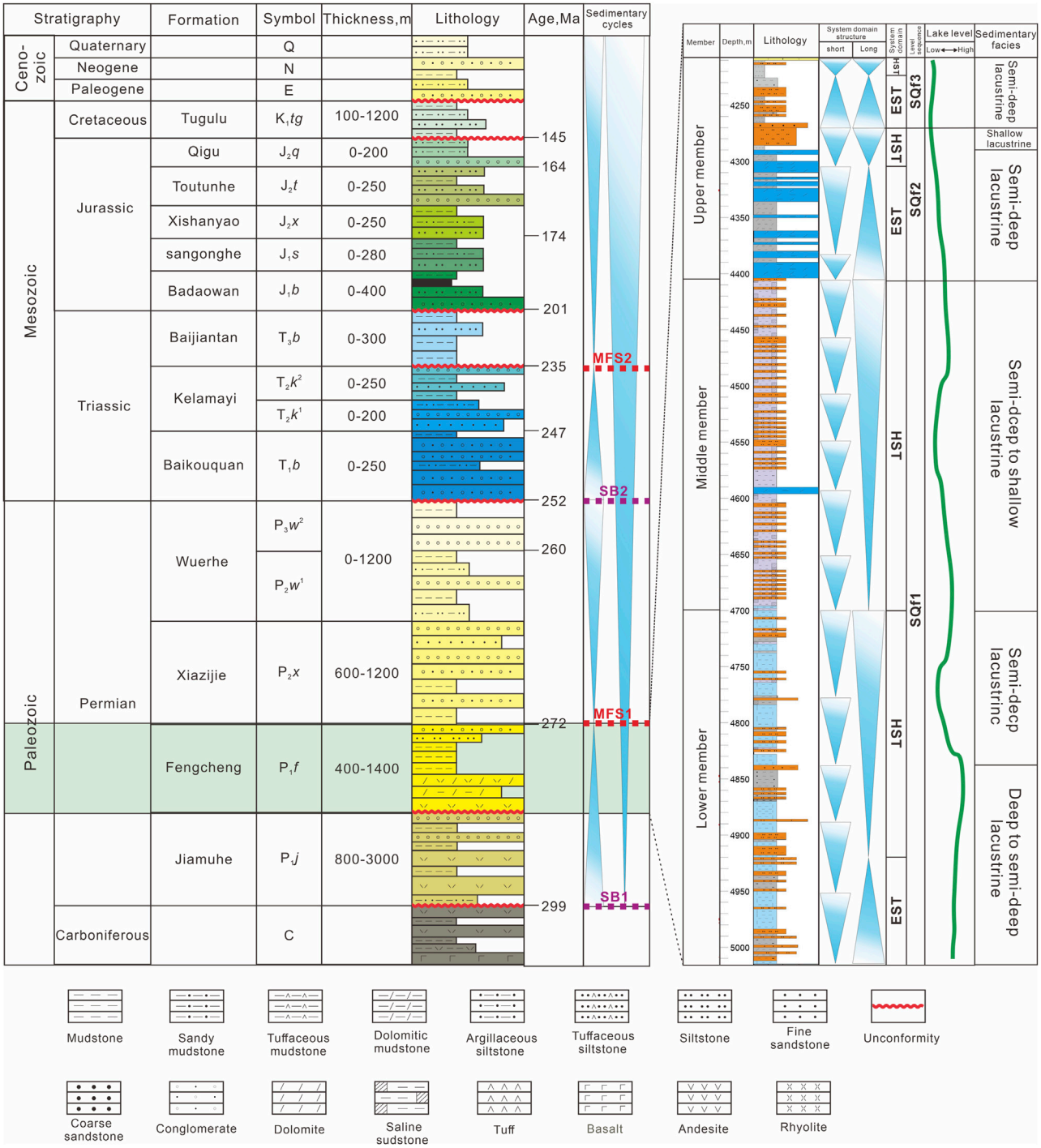

FIGURE 2 | Stratigraphic framework of the Paleozoic to Cenozoic in the Mahu sag (right) and lithologic column, sequence, and sedimentary facies of Fengcheng Formation in Fn7 well (left); SB, sequence boundary; MFS, maximum flooding surface (modified from Cao et al., 2015; Liang et al., 2020; Huang et al., 2021).

important basis for forming depositional sequences, and a stratigraphic sequence corresponds to a cycle of change in stacking patterns, recorded as variation in lithological characteristics and logging curves (Catuneanu et al., 2009). In most cases, a single study of the sequence is insufficient for determining the sequence interface. Therefore, critically integrating data from various sources is necessary (Zheng et al., 2000; Zheng et al., 2001). Moreover, unlike subaerial basins, no outcrops are found in the Mahu sag, and the sequence stratigraphic surfaces, such as weathering crusts,

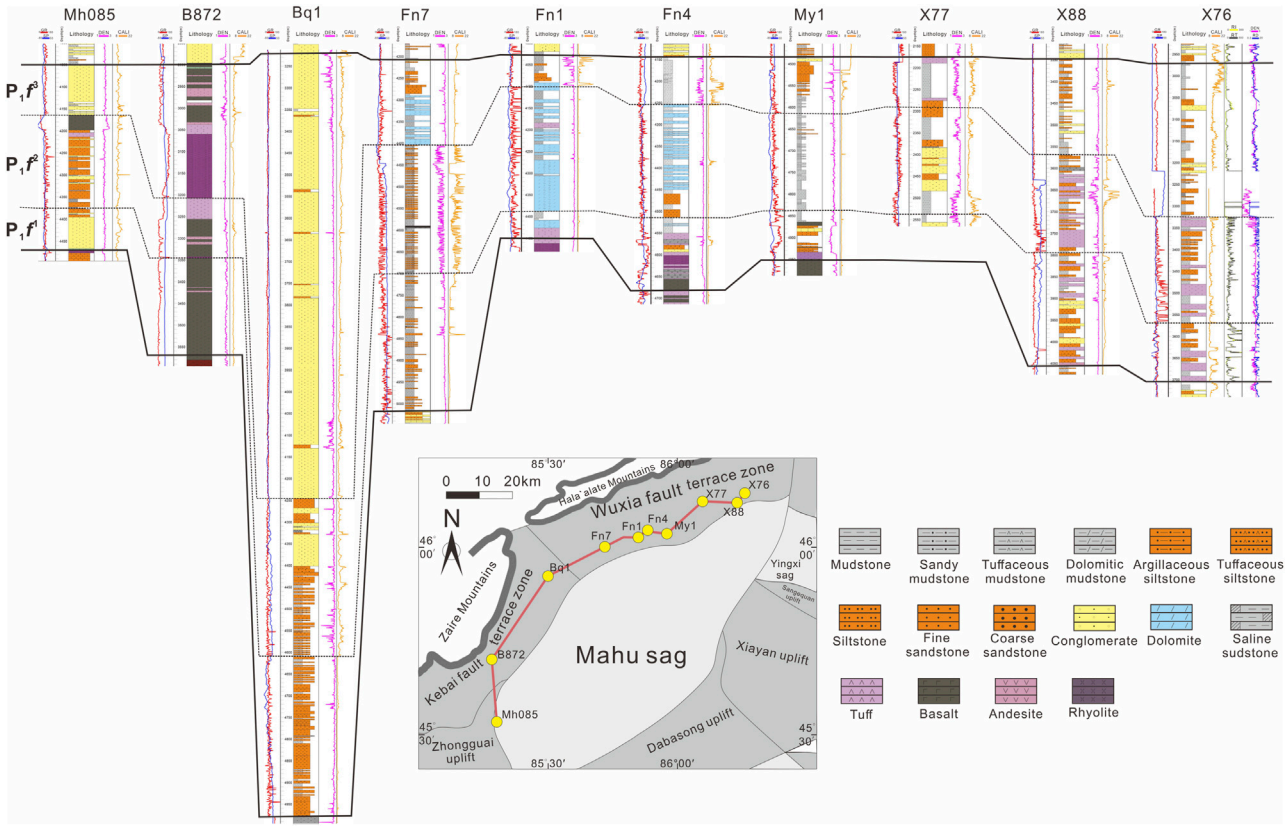

FIGURE 3 | Stratigraphic correlation of Lower Permian Fengcheng Formation in the western margin of Mahu sag. Wells X77, x88, and x76 are located in the Xiazijie area; wells My1, Fn4, Fn1, and Fn7 are located in the Fengcheng area; well Bq1 is located in the Baiquan area; wells B872 andMh085 are located in the Mahu area; GR, natural gamma-ray; SP, spontaneous potential; DEN, density; CALI, borehole diameter; RT, true formation resistivity.

cannot be easily observed. Therefore, the stratigraphic sequence framework was determined by tracing and comparing the sequence boundaries based on the variations of logging curves (Van Wagoner et al., 1990; Miller et al., 2013; Zhu et al., 2017; Zou et al., 2020; Zou et al., 2021) and the contact relationships from cuttings and seismic data interpretation. Moreover, sedimentary facies are inferred from the observation of the drill cuttings and interpretation of the logging curves.

4 RESULTS

4.1 Stratigraphic Correlation

The Fengcheng Formation demonstrates an unconformable contact with the P_1j. The P_1j is composed of pyroclastic rock, andesite, and sandstone at the bottom and sandstone at the top, respectively (**Figure 2**). The overlying strata of P_1f is the P_2x. P_1f exhibits an unconformable contact with P_2x. Next, the P_2x is a set of gray–brown and brown–gray glutenite with a small amount of gray, brown–gray mudstone and sandstone.

The drilling of the Fengcheng Formation is distributed in the western margin of the Mahu sag, including the Xiazijie (wells X76, X88, X77, and X201), Fengcheng (wells Fn7, Fn4, Fn1, and Fn7), Baiquan (Bq1), and Mahu areas (wells B872 and Mh085) (**Figure 1D**).

The P_1f^1 is composed of a gray, dark gray thin layer of tuff, dolomitic mudstone, and argillaceous dolomite near the sedimentary center; whereas, near the orogenic belt, tuff and siltstone are interbedded between thin layers glutenite, volcanic breccia, and basalt. Moreover, their logging curve shows high natural gamma ray (GR) and amplitude values, wave growth, and medium frequency (**Figure 3**).

The P_1f^2 is composed of deep gray and gray–black thin layers of muddy dolomite and dolomitic mudstone near the sedimentary center. Near the orogenic belt, it contains thin sandstone and mudstone interbedded between tuff and gravel. The logging curve of these rocks displays the following features: high-to-low GR values, high amplitude, short wavelength, and high frequency (**Figure 3**).

Next, the tuffaceous and dolomitic components of the P_1f^3 decrease; whereas, the sandy content increases. The bottom of the P_1f^3 is composed of mudstone and siltstone interbedded between dolomitic mudstone, whereas, its top is coarse sandstone and sandy conglomerate. The logging curve shows a low GR value, small amplitude, and continuous stability (**Figure 3**).

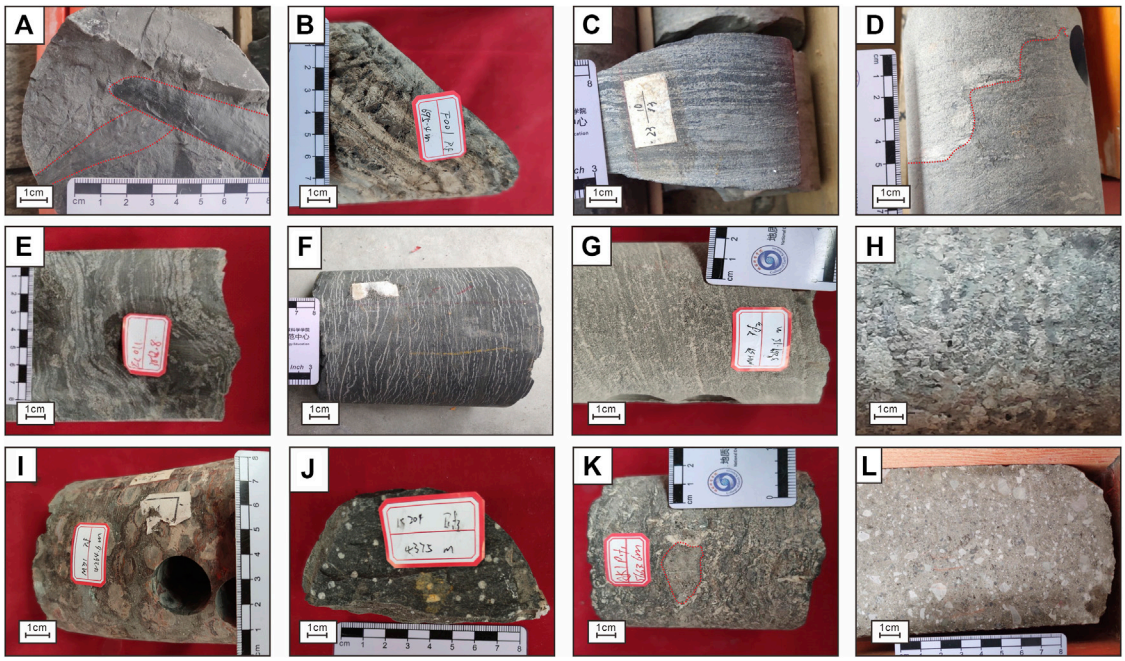

FIGURE 4 | Core photos of different lithology of Fengcheng Formation. **(A)** mudstone, plant leaf fossils can be seen on the cross section, well Mh39 at 5,269.68 m. **(B)** bituminous dolomitic mudstone with developed fractures and invaded by high concentration heavy oil, well F001 at 696.65 m. **(C)** fine sandy migmatite with a slightly thicker grain size and thin calcareous layer, well Fn1 at 4,421.85 m. **(D)** dolomitic siltstone, dolomitic strip filling can be seen on the boundary, local light under-invasion surface denudation dark top, dark part contains more dolomitic lenses, well Fn1 at 4,327 m. **(E)** dolomitic mudstone, see the crumpled structure. The dolomite is clumpy and irregularly laminated, well Fn011 at 3,862.8 m. **(F)** Fine sandy migmatite, well Fc011 well at 3,862.8 m. **(G)** tuffaceous gravel sandstone, well Fc011 well at 3,862.8 m. **(H)** breccia, well Bq5 at 3,575.4 m. **(I)** dark gray lava with accretionary volcanic gravel average particle size 1 cm, maximum particle size 2 cm, undeveloped stomata, well Md1 at 4,269 m. **(J)** basalt, undeveloped pores, and cryptocrystalline structure, well K204 at 4,375.0 m. **(K)** dolomitic gravel sandstone, coring depth, see the crumpled structure, well Ak1 at 5,666.8 m. **(L)** tuffaceous volcanic breccia, containing a large number of angular light-colored volcanic debris, well B872 at 3,250 m.

4.2 Sedimentary-Facies Analysis

During the sedimentation period of the Fengcheng Formation, the Mahu sag experienced complex tectonic activity, strong volcanic activity, and consequently formed various lithofacies. According to petrological characteristics and sedimentary structure, the sedimentary facies of the Fengcheng Formation are divided into two: lacustrine and fan–continental delta facies. Next, the lacustrine facies can be divided into semideep lake to deep lake and shore–shallow lake subfacies. The fan delta can be divided into fan–delta front subfacies and fan–delta plain subfacies.

4.2.1 Semideep Lake–Deep Lake Subfacies

The main lithofacies of semideep lake–deep lake subfacies are dark gray mudstone, gray–black mudstone, and gray–white dolomitic siltstone (**Figures 4A–C**). Semideep lake–deep lake subfacies are distributed in the Fengcheng area. Next, fossilized plant leaves can be seen in the dark gray mudstone (**Figure 4A**). In the F001 well, fissures in dolomitic mudstone are developed, and most of them are invaded by a high concentration of heavy oil (**Figure 4B**). In Fn1, light and dark dolomitic siltstone and dolomitic strip filling can be seen on the boundary. Moreover, the local light part under the invasion surface denudates the dark part, and the dark part contains more dolomitic lenses (**Figure 4D**).

4.2.2 Shore–Shallow Lake Subfacies

The shore–shallow lacustrine subfacies are distributed in most Mahu sag areas. The lithology is gray–white dolomitic mudstone, light gray–green fine sandy mixed rock, and gray–green mudstone. Next, soft-sedimentary deformation and folded structures are found in dolomitic mudstone (**Figure 4E**). Thin calcareous layers are present in gray–green fine sandy migmatite (**Figure 4C**). The gray–green mudstone contains several calcareous horizontal layers (**Figure 4F**). Wave sand ripple bedding, slump deformation structure, and antigrain sequence cycles are common in sand bodies.

4.2.3 Fan–Delta Facies

The fan delta refers to the fan body advancing from the adjacent mountain area to the stable water body, developed near the synsedimentary fault in the margin of the depression. The fan–delta front facies are composed of sandy conglomerate and dolomitic sandstone. The dolomitic sandstone exhibits a crumpled structure. Next, dolomite is clumpy and irregularly laminated. The grinding cycle of gravel is insufficient, and the gravel sorting is medium (**Figure 4K**). The subfacies rock types of fan–delta plain include fine, massive, and tuffaceous sand conglomerates (**Figure 4H**).

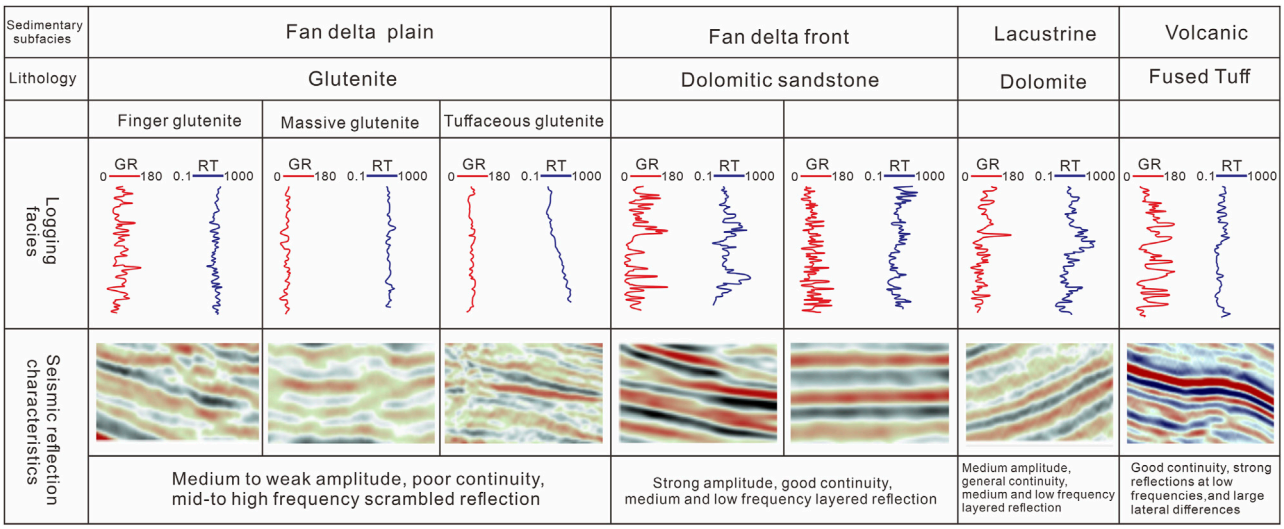

FIGURE 5 | Characteristics of lithofacies seismic reflection and logging curve of Fengcheng Formation; GR, natural gamma curve; RT, true formation resistivity.

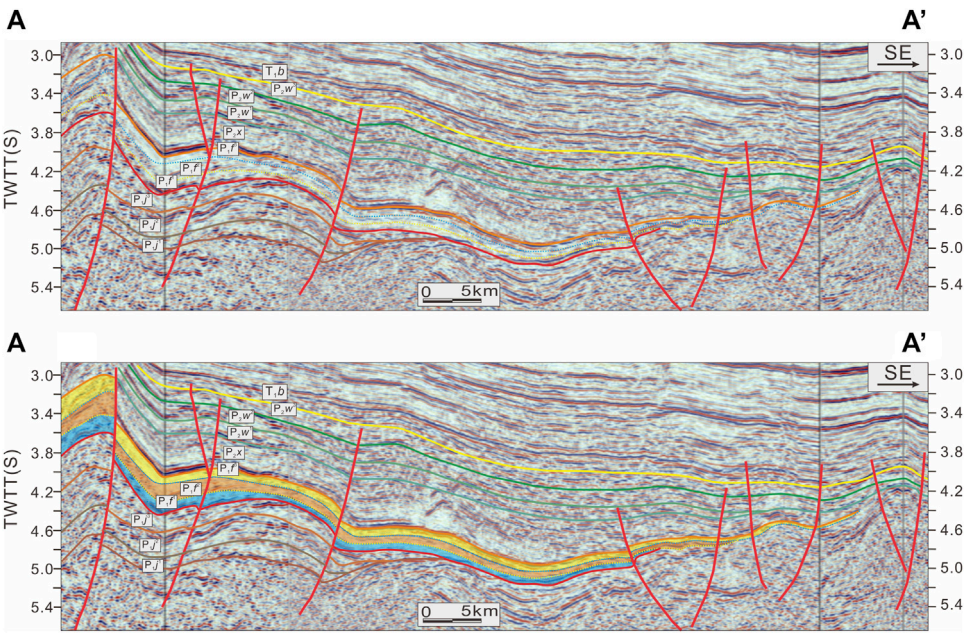

FIGURE 6 | Stratigraphic and structural interpretation of the seismic reflection section **(A)**. See **Figure 1D** for the location.

4.2.4 Volcanic Facies

The volcanic rocks of P_1f^1 and P_1f^2 members are developed in the Mahu sag, containing massive molten gray breccia tuff, basalt, and volcanic breccia. The dark gray lava contains proliferated volcanic gravel, with an average particle size of 1 cm and a maximum particle size of 2 cm, with undeveloped pores (**Figure 4I**). The basalt demonstrated undeveloped stomata and a cryptocrystalline structure (**Figure 4J**). The surface section of the core was half-filled with white calcite. Light gray tuffaceous volcanic breccia contains several angular light volcanic debris, demonstrating a matrix-support characteristic (Figure 4L).

4.3 Seismic Interpretation

Sections A and D–G are distributed from northwest to southeast, perpendicular to the extensional direction of the Mahu sag and the strike of the Kebai Fault (**Figure 1D**). Sections B and C are distributed in the northeast direction (**Figure 1D**).

The physical characteristics of sandy conglomerate, dolomitic sandstone, dolomitic mudstone, and volcanic

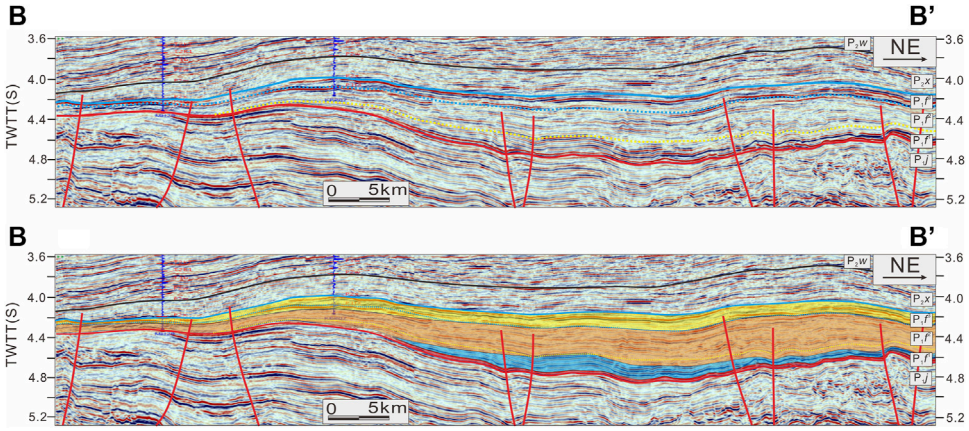

FIGURE 7 | Stratigraphic and structural interpretation of the seismic reflection section **(B)**. See **Figure 1D** for the location.

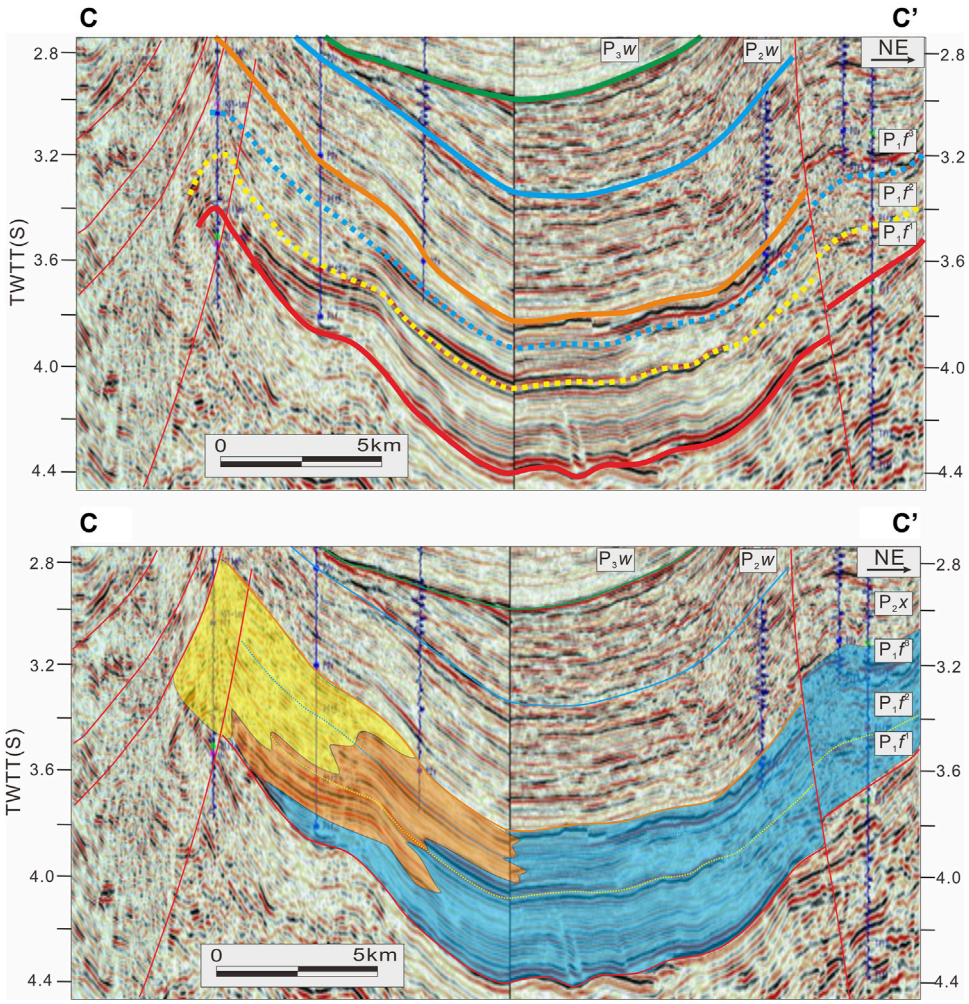

FIGURE 8 | Stratigraphic and structural interpretation of the seismic reflection section **(C)**. See **Figure 1D** for the location. The legend is the same as **Figure 9**.

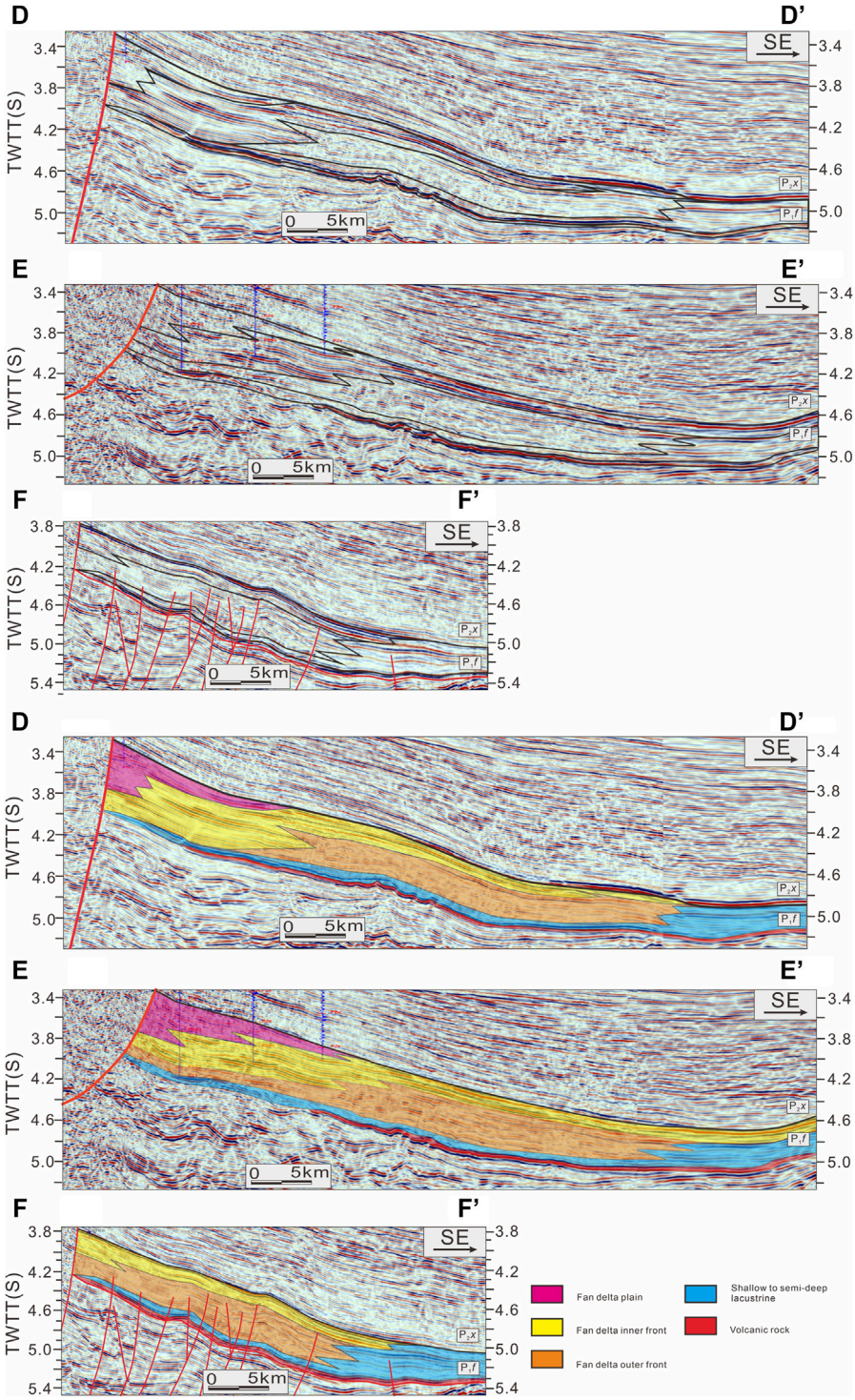

FIGURE 9 | Stratigraphic and structural interpretation of the seismic reflection section **(D–F)**. See **Figure 1D** for the location.

rocks in the Fengcheng Formation are different, and they demonstrate apparent reflection characteristics in the seismic profiles (**Figure 5**). Different sedimentary facies correspond to different lithologic assemblages. Therefore, combined with the logging curve, we identify four kinds of sedimentary facies on the seismic profile (**Figure 5**). The reflection characteristics of subfacies' seismic profiles in fan–delta plain are medium and weak amplitude, poor

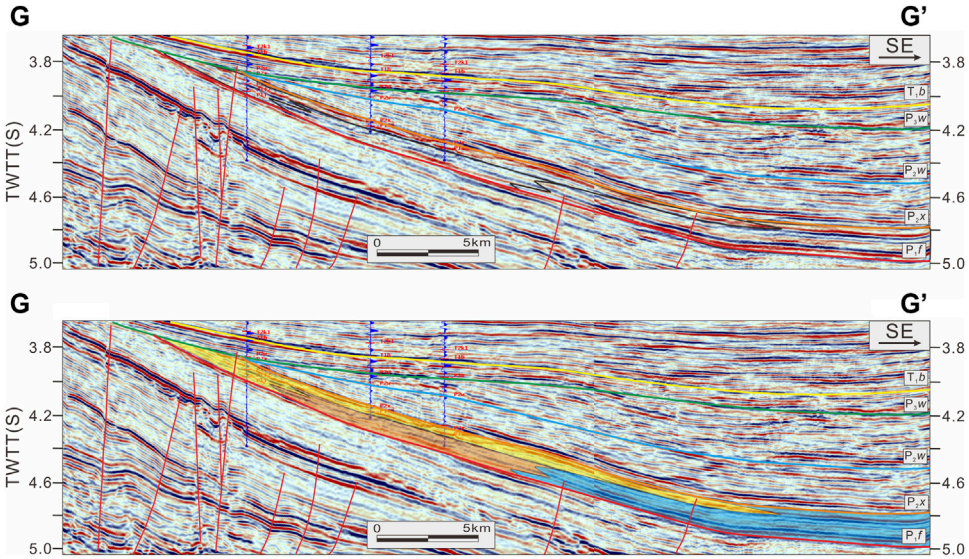

FIGURE 10 | Stratigraphic and structural interpretation of the seismic reflection section **(G)**. See **Figure 1D** for the location. The legend is the same as **Figure 9**.

continuity, and disorderly reflection of medium and high frequencies (**Figure 5**). Next, the fan–delta front facies show low GR value, low true formation resistivity (RT) value, and straight curve in the logging facies. The seismic reflection of fan–delta front facies exhibits strong amplitude, good continuity, and medium- and low-frequency layered reflection (**Figure 5**). Volcanic rocks show good continuity, strong low-frequency reflection, and significant lateral differences in seismic profile (**Figure 5**).

Next, Section A is located north of the sag, extending from the Wuxia Fault to the entire Mahu sag up to the Xiayan uplift and extending 60 km. This section can identify the Permian strata in the study area and every member of the Fengcheng Formation. **Figure 6** shows the whole profile shape of the Fengcheng Formation, which deepens from the orogenic belt to the depression. Moreover, currently, the strata of the Fengcheng Formation are deformed by faults. The three members of the Fengcheng Formation overlap and pinch out layer by layer to the west edge of the lake basin, from top to bottom. The distribution of $P_1 f^3$ is the most extensive, followed by $P_1 f^2$ and $P_1 f^1$, respectively.

Section B (**Figure 7**) extends south to north along the sag's western margin and extends 80 km. This shows that the Fengcheng Formation in the north of the sag is thicker than that in the south. In addition, it also shows that the thickness of $P_1 f^2$ is more significant than those of $P_1 f^1$ and $P_1 f^3$.

Next, Section C is located in the Fengcheng area of the sag. Glutenite accumulates near the fault zone, and the range of lacustrine facies decreases from the $P_1 f^1$ to $P_1 f^3$ (**Figure 8**), showing the process of lake regression.

Then, Sections D, E, and F are located in the Huangyangquan fan in the central Mahu sag (**Figure 1D**) and identify the Fengcheng Formation fan–delta inner–front sand conglomerate, fan–delta outer–front sand gravel, and shallow lake–semideep lacustrine dolomitic shale (**Figure 9**). Section G is located in the south of the sag, which can identify the glutenite in the inner front of the fan delta, glutenite in the outer front of the fan delta, and dolomitic mudstone of the shore–shallow lake (**Figure 10**). The sedimentary thickness of the south of the sag is thinner than that of the north, and the sand–conglomerate range of the inner front of the fan delta in the $P_1 f^3$ expands in the later stage. In addition, it shows that the outer-front dolomitic sandstone is covered with lacustrine mudstone (**Figure 10**).

4.4 Sequence Stratigraphy

4.4.1 Sequence Boundaries

The sequence boundary is defined by the contact relationship, which is revealed by the core, logging curve, and seismic profiles (**Figure 11**). Sequence boundary 1 (SB1) is the regional conformity between the $P_1 f^2$ and $P_1 f^3$ members of the Fengcheng Formation (**Figure 11**). SB1 appears at the bottom of the $P_1 f^3$, where large-scale alkaline evaporates and fan deltas are developed. The overall shape of the basal unconformity SB1 in the seismic profiles indicates a half-graben structure with NE–SW trending master faults (**Figure 6**). Sequence boundary 2 (SB2) is in the $P_1 f^3$.

The maximum flooding surfaces divide a backstepping retrogradational sequence pattern at the base from a progradational sequence pattern at the top (Catuneanu et al., 2009). Three maximum flooding surfaces (MFS) can be traced throughout the area, and they form the upper boundary for the transgressive system tracts (**Figures 11–13**). MFS is placed at the maximum GR response.

4.4.2 Sequence Stratigraphy Framework

The SQf1 is further divided into one expansion system tract (EST1) and two high-stand system tracts (HST1). The SQf2 and

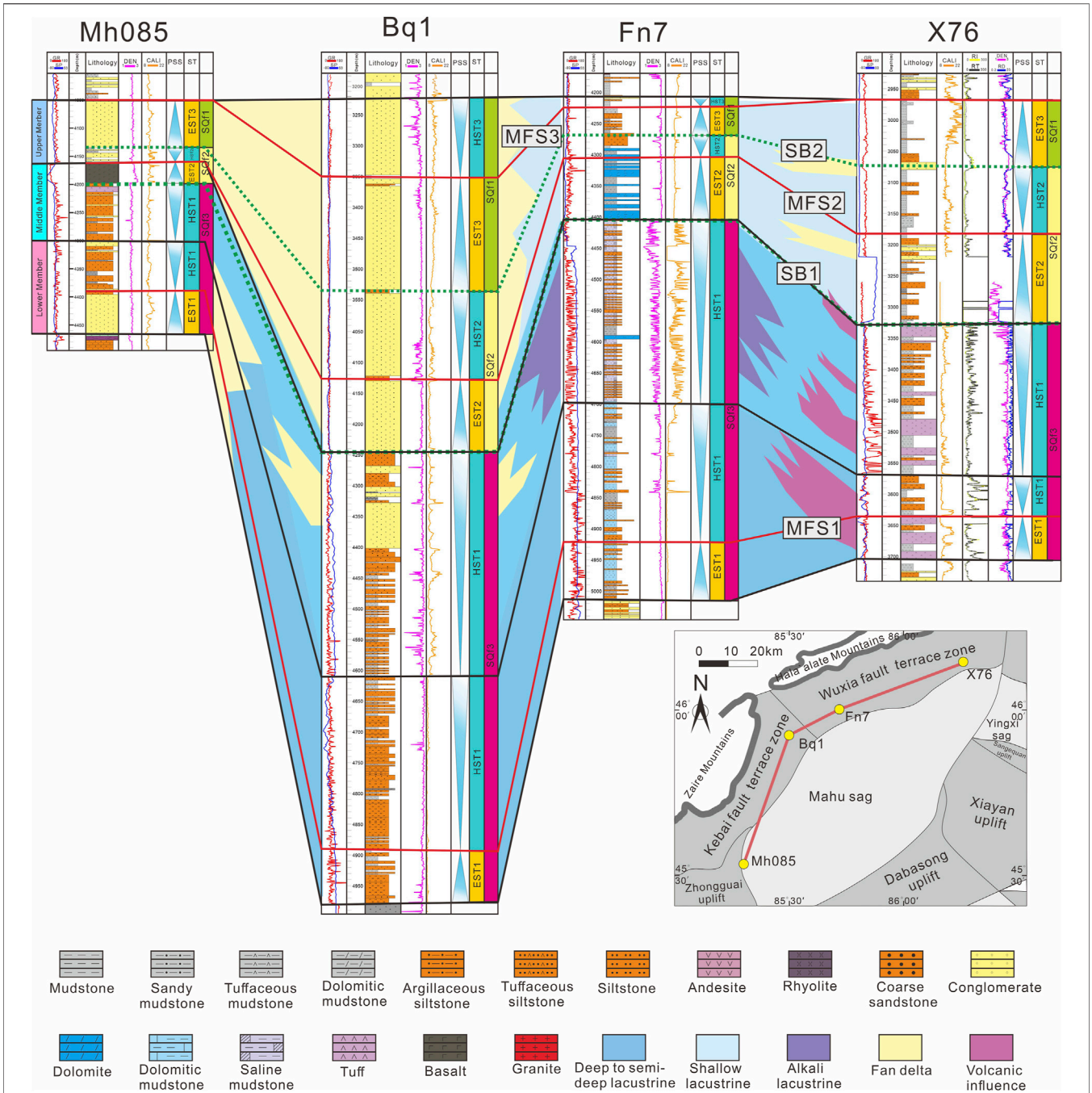

FIGURE 11 | The sequence stratigraphic connecting sections of wells X76, Fn7, Bq1, and Mh085 and the location of the well is shown in **Figure 1D**; PSS, parasequence set; ST, systems tract; EST, expansion system tract; HST, high-stand system tracts.

SQf3 are further divided into an expansion system tract (EST2 and EST3) and a high-stand system tract (HST2 and HST3).

EST1 is bounded above by MFS1. EST2 is bounded above and below by MFS2 and SB1, respectively. EST3 is bounded above and below by MFS3 and SB2, respectively (**Figures 11–13**). This unit comprises a retrogradational and fining-upward succession. In SQf1, EST1 is deposited in semideep lacustrine facies in the Xiazijie, Fengcheng, and Baiquan areas; whereas, fan–delta front facies are in the Mahu area. Then, SQf2, SQf3, EST2, and EST3 are deposited as shallow lacustrine facies in Xiazijie, Fengcheng and the fan–delta facies in the Mahu and Baiquan areas. The units show lateral thickness variation, with the most significant thickness on the slope of the Fengcheng area.

HST1 is bounded below by MFS1 and above by SB1. HST2 is bounded below by MFS2 and above by SB2.

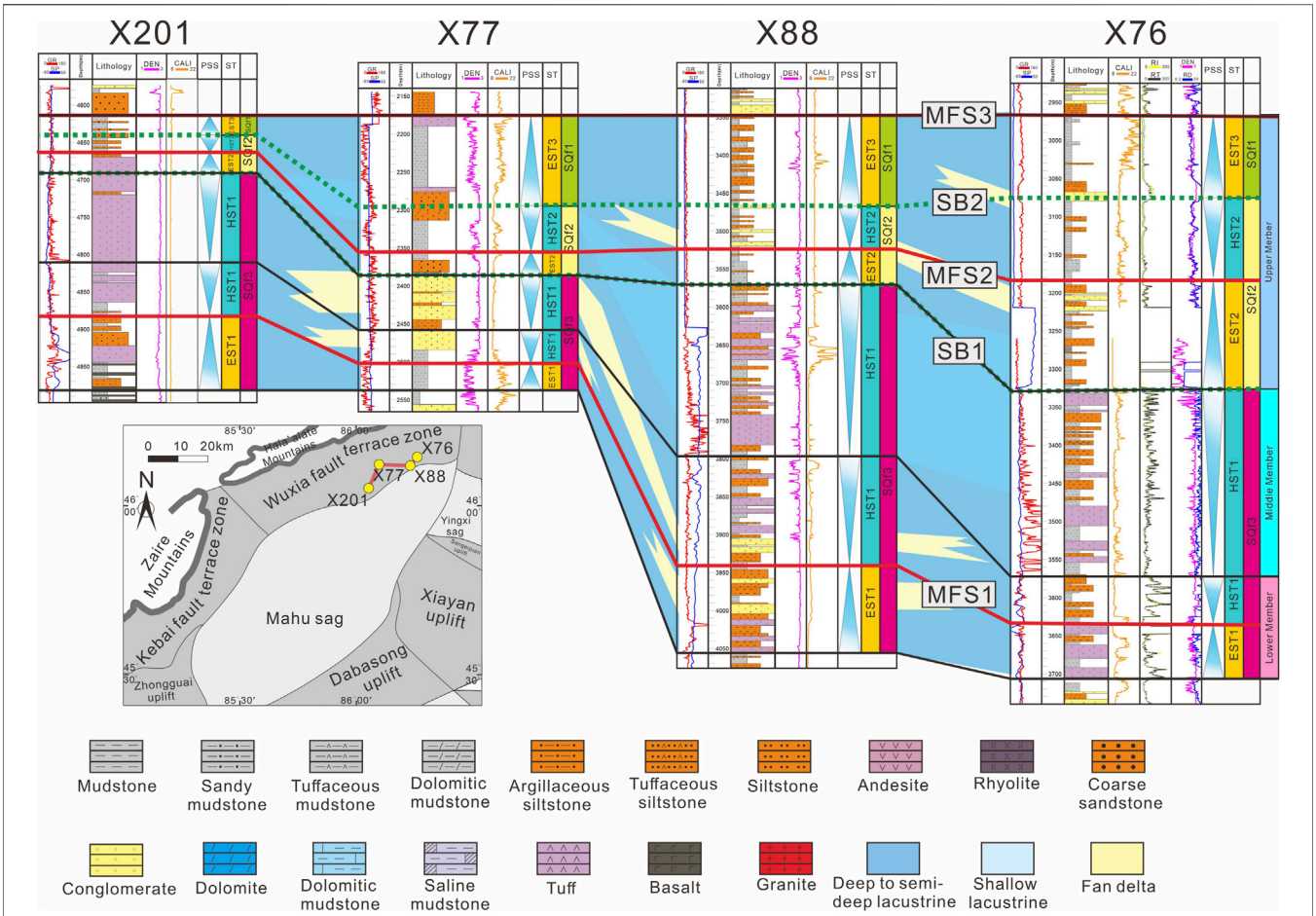

FIGURE 12 | The sequence stratigraphic connecting sections of wells X201, X77, X88, and X76 and the location of the wells is shown in **Figure 1D**.

HST3 is bounded below by MFS3 (**Figures 11–13**). HST1 is progradational, with a coarsening upward trend. In SQf1, HST1 is deposited near the alkaline lake, and more alkaline evaporite is distributed in the Fengcheng and Baiquan areas. The Xiazijie and Mahu areas are dominated by fan–delta front facies deposits. In SQf2 and SQf3, HST2 and HST3 are typical lacustrine deposits in the Fengnan and Xiazijie areas and thick fan–delta plain–facies deposits in the Baiquan and Mahu areas.

5 DISCUSSION

5.1 Sedimentary Evolution and Paleogeography

Through complete lithofacies' description and interpretation, stratigraphic sequence framework, and 2D seismic–reflection profile identification, we draw new lateral and vertical sedimentary-facies evolution maps of $P_1 f^1$, $P_1 f^2$, and $P_1 f^3$ in the Mahu sag (**Figure 14**). In addition, the potential provenances and transport routes of the Mahu sag were traced through previous provenance studies (Tang et al., 2020). These provide necessary sedimentary face variations for the sedimentary-filling process described in this study.

During the sedimentary period of $P_1 f$ in the Xiazijie area, the lithology into pyroclastic deposits. $P_1 f^1$ is composed of tuff, followed by tuffaceous mudstone and siltstone. These sedimentary characteristics indicate that the Xiazijie area was in an evaporated shore–shallow lacustrine environment during the $P_1 f^1$. Next, volcanic activity was reduced as reflected in the decreased amount of tuff. At the beginning of $P_1 f^2$, the sedimentary grain size was reduced, and the content of tuffaceous rocks increased, indicating that the lake level rose, and volcanic activity increased. In $P_1 f^3$, little tuff and more sandy conglomerate is found, indicating that volcanic activity almost stopped, and the fan delta expanded. In the Xiazijie area, the provenance appears to be the Hala'alate mountains and volcanic materials in the Luliang uplift (Lu, 2018).

In the Fengcheng area, the bottom of $P_1 f^1$ contains limestone, mudstone, and sandstone, and the top of $P_1 f^1$ contains interbedded dolomitic mudstone and sandstone. This reflects that the $P_1 f^1$ is a semideep lake–deep lake environment with weak hydrodynamics and weak volcanic activity. In $P_1 f^2$, alkaline lacustrine deposits and salt-bearing mudstones reflect

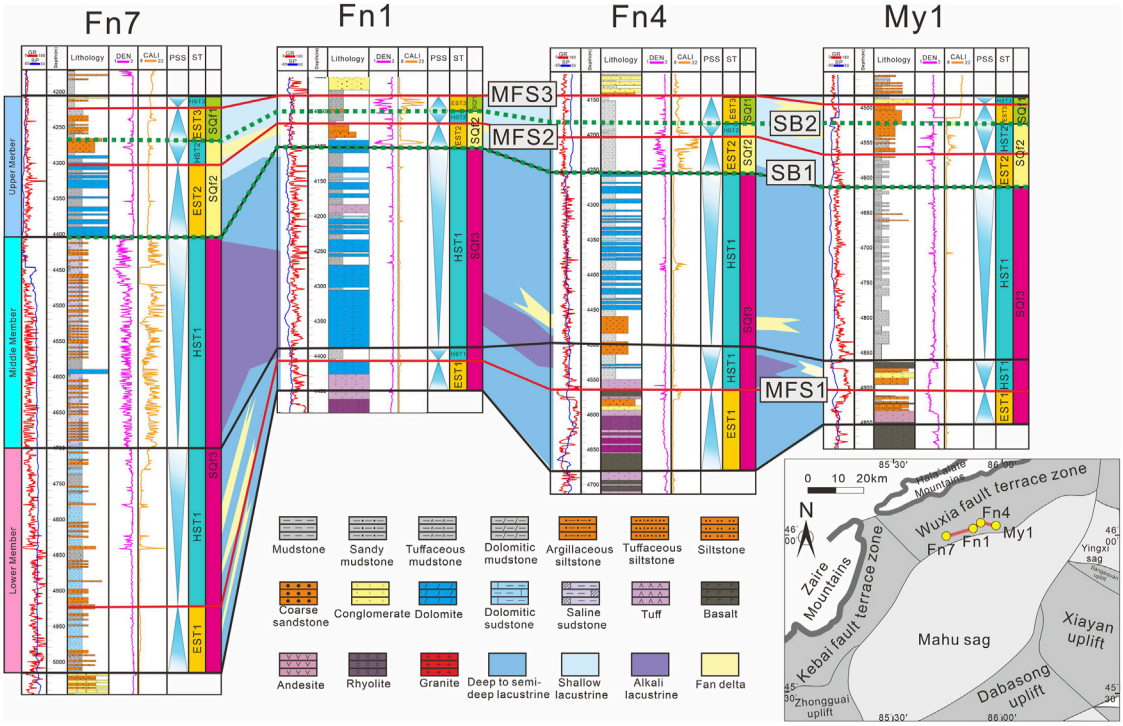

FIGURE 13 | The sequence stratigraphic connecting sections of wells Fn7, Fn1, Fn4, and My1 and the location of the wells is shown in **Figure 1D**.

a dry climate, with low-lake levels and high salinity that encouraged the formation of unique alkaline minerals. These alkaline minerals may be affected by deep hydrothermal fluids (Chang et al., 2016; Zhang et al., 2018; Tang et al., 2020). P_1f^3 consists of lacustrine dolomite in the early stage and terrigenous clastic rock in the late stage, reflecting the decrease of lacustrine facies and the development of fan delta. It can be seen from Sections B (**Figure 7**) and C (**Figure 8**) that the Fengcheng area is the sedimentation center.

The Baiquan area is close to the Kebai fault zone and is located at the edge of the sedimentary lacustrine basin. P_1f^1 is composed of dolomitic sandstone and a small amount of dolomitic mudstone. At the bottom of P_1f^2, interbeds of cloud sand and mudstone are found, and the top is tuffaceous coarse sandstone. P_1f^3 is a thick sandy conglomerate. Therefore, in P_1f^1, the Baikouquan area is shore–shallow lacustrine facies. P_1f^2 volcanic activity developed, and fan deltas began to develop. P_1f^3 fan delta developed further. This is consistent with the change in sedimentary facies interpreted using the seismic profile. In Sections C–G (**Figures 8–10**), lacustrine deposits are deposited at the bottom of P_1f^1, and a large area of lacustrine facies is transformed into fan–delta front facies within a short time. From P_1f^2 to P_1f^3, the fan–delta outer-front developed into the fan–delta inner front. In P_1f^3, Sections D and E (**Figure 9**) develop fan–delta plain facies near the fault zone. Moreover, the provenance of the Baiquan area likely originated from the West Junggar block and Zaire mountains.

In the Mahu area, P_1f^1 is deposited in shallow lacustrine facies. The tuffaceous sandy conglomerate is developed during the early stage, and tuffaceous mudstone is developed in a low-energy environment. During the P_1f^2 period, volcanic activity was frequent, and pyroclastic rocks were abundant. Volcanic rocks were developed at the top of P_1f^2 in wells Mh085 (**Figure 3**). Therefore, the volcanic activity was intense during the deposition of upper P_1f^2. During the deposition of P_1f^3, the volcanic activity ceased, and the lake level dropped. The deposition is characterized by the fan–delta facies. Section G (**Figure 10**) shows that the sedimentary process of the Mahu area is similar to that of the Baiquan area. Thus, the fan delta was developed in the southern sag during the deposition of P_1f^2 and P_1f^3.

In summary, the P_1f^1 deposition center was between the Baiquan and Fengcheng areas, and the lake reached its maximum depth. During this period, volcanic activity was frequent, and volcanic material provided part of the source. The fluvial delta deposits on the eastern slope originated from the Luliang uplift and flew through the river toward the center of the Mahu sag (Tang et al., 2021a). Next, during the deposition of P_1f^2 and P_1f^3, provenance increased in the southern Mahu and Baiquan areas, and fan deltas with a considerable thickness were developed (**Figure 11**). This provenance may come from the Zaire mountains.

5.2 Sediment-Filling Process and Sedimentary Model

Sections A and B (**Figures 6** and **7**) reflect the architecture of the Fengcheng Formation in the Mahu sag, which is deposited from the West Junggar terrane to the lake (**Figure 1D**). The distribution of the

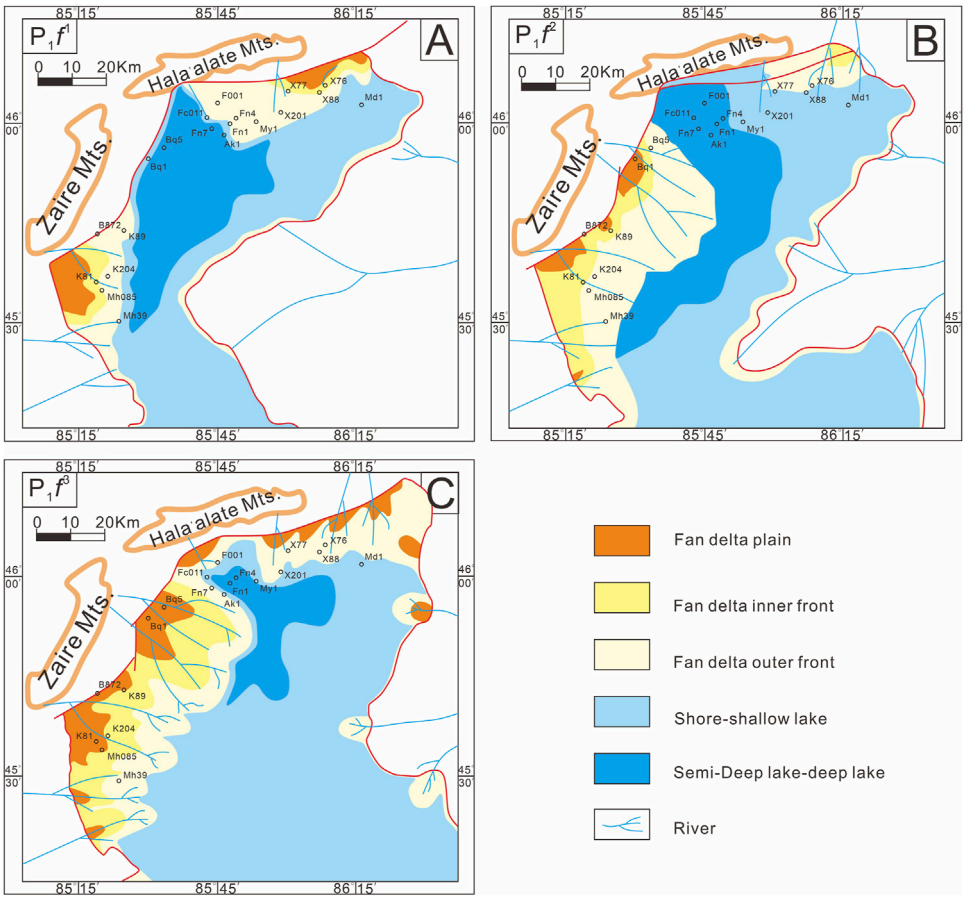

FIGURE 14 | Palaeogeographic evolution of the Fengcheng Formation (modified from Tang et al., 2020). **(A)** Palaeogeographic evolution of the Lower Member of Fengcheng Formation. **(B)** Palaeogeographic evolution of the Middle Member of Fengcheng Formation. **(C)** Palaeogeographic evolution of the Upper Member of Fengcheng Formation.

Fengcheng Formation in the north is controlled by paleogeomorphology and faults, and the depocenter is in the Fengcheng area of the Mahu sag. Moreover, the east–west seismic profile reveals that the characteristics of multiple half-graben structures in the lower Permian strata are pronounced (**Figure 6**). Unidirectional and single boundary faults control these structures. Next, the activity of the northwest-trending marginal–fault system in the late Permian led to the tectonic inversion of rift-related depressions in the early Permian (Liang et al., 2020). The half-graben structure and faulting style revealed by the seismic profiles (**Figure 6**), the paleogeographic reconstruction in the stratigraphic sequence framework (**Figure 11**), and the identification of soft-sediment deformation structures indicate that the early Permian Mahu sag was a rift basin (Yu et al., 2016; Liang et al., 2020; Tang et al., 2020, Tang et al., 2021a).

Figure 11 shows that P_1f^1 is a set of lacustrine deposits with its depocenter in the Fengcheng area, and only a small part of P_1f^1 was deposited in a fan–delta environment in the southern Mahu sag (**Figure 15A**). In P_1f^2, the range of the lacustrine facies continues to expand (**Figure 15B**), and the area of the lake basin reaches the maximum (**Figure 11**). Tang et al. (2020) proposed that most of the soft-sediment deformation structures in P_1f^2 are caused by frequent earthquakes, indicating basin-bounding normal fault activities in the depocenter, creating maximal accommodation. Next, geochemical data and alkaline minerals show that the P_1f^2 member of the Mahu sag is an alkaline lake basin with high salinity (Gong et al., 2014; Cao et al., 2015; Zhang et al., 2018). At the beginning of the deposition of P_1f^3, the range of lacustrine facies shrinks, and the Xiazijie and Fengcheng areas are shore–shallow lacustrine deposits. The Baiquan and Mahu areas were the fan–delta facies' deposits, and the lake basin began to shrink (**Figure 15C**).

During the syn-rift stage of a rift basin, due to gravity isostasy, the continuous subsidence of the half-graben will lead to the uplift of the horst, increasing the sedimentary supply from the proximal horst sources (Chao et al., 2021). Based on the detrital zircon U–Pb chronology of the Fengcheng Formation, Tang et al. (2021c) demonstrated a transition from distant axial provenance areas to proximal lateral horsts in West Junggar during the syn-rifting processes in the Mahu sag. Next, Sections C–F (**Figures 8** and **9**) in the Baikouquan area and Section G (**Figure 10**) in the Mahu area show different filling processes in the margin of the basin. In the Baiquan area, fan–delta sequences accumulate toward the depocenter in the Mahu sag (**Figures 8** and **9**). The rock grain size became coarser and evolved from lacustrine facies to fan–delta

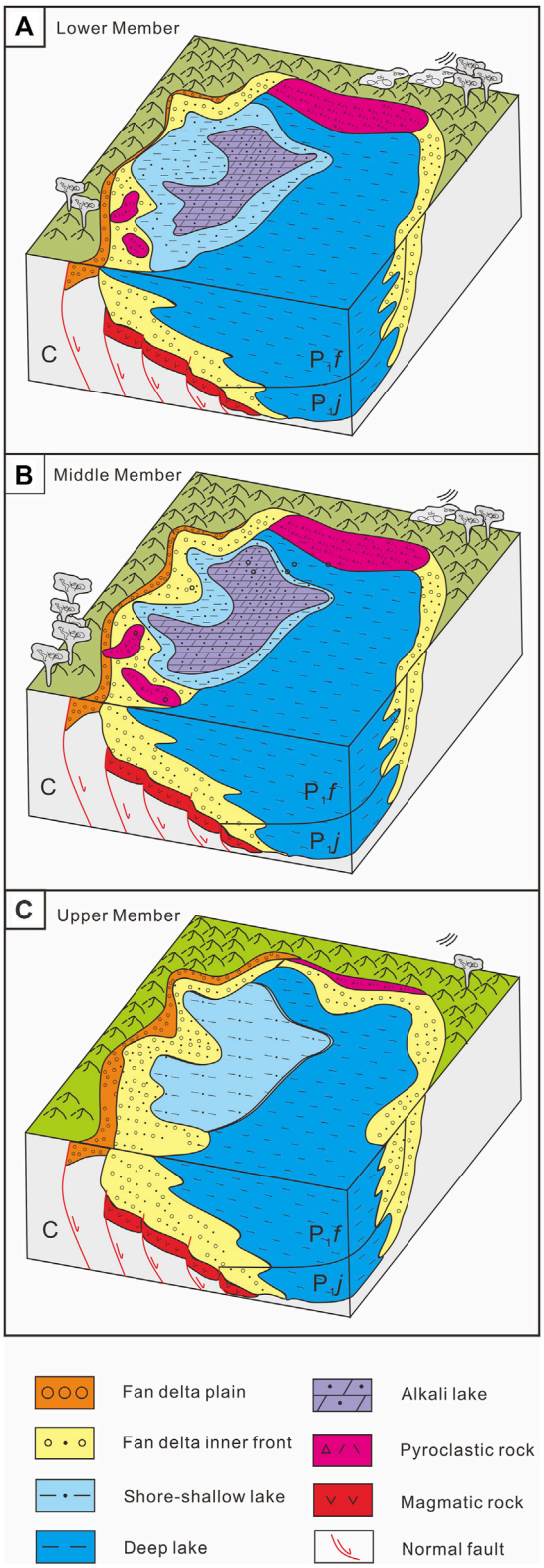

FIGURE 15 | (A) Sedimentary-filling model map of the Lower Member of Fengcheng Formation. **(B)** sedimentary-filling model map of the Middle Member of Fengcheng Formation. **(C)** sedimentary-filling model map of the Upper Member of Fengcheng Formation.

front facies in P_1f^1 and P_1f^2 and finally to fan–delta plain facies in P_1f^3, suggesting that the rate of sedimentary supply is higher than subsidence, which is consistent with the filling processes in the margin of a rift basin.

Therefore, the sediment-filling process of the Fengcheng Formation is controlled by fault activity. The Fengcheng Formation experienced a lake-basin expansion during the deposition of P_1f^1 and P_1f^2 and a shrinkage stage during the deposition of P_1f^3 (**Figure 15**).

6 CONCLUSION

The Fengcheng Formation consists of three third-order sequence stratigraphy (SQf1, SQf2, and SQf3). The SQf1 is divided into one expansion system tract (EST1) and two high-stand system tracts (HST1). The SQf2 consists of EST2 and HST2. The SQf3 consists of EST3 and HST3. In SQf1, EST1 was deposited in semideep lacustrine facies in the Xiazijie, Fengcheng, and Baiquan areas. Fan–delta front facies are in the Mahu area, HST1 is deposited near the alkaline lake, and more alkaline evaporite is distributed in the Fengcheng and Baiquan areas. The Xiazijie and Mahu areas are dominated by fan–delta front facies deposits. In SQf2 and SQf3, EST2 and EST3 were deposited as shallow lacustrine facies in Xiazijie and Fengcheng and fan–delta facies in the Mahu and Baiquan areas; HST2 and HST3 are typical lacustrine deposits in the Fengcheng and Xiazijie areas and thick fan–delta plain–facies deposits in the Baiquan and Mahu areas.

The deposition center was between the Baiquan and Fengcheng areas. During the sedimentary period of P_1f^1 and P_1f^2, volcanic activity was frequent, and volcanic material provided part of the source. During the deposition of P_1f^2 and P_1f^3, provenance increased in the southern Mahu and Baiquan areas and developed fan delta.

The sedimentary-filling model of the Fengcheng Formation in Mahu sag is controlled by the fault. Next, the lake basin of the Mahu sag experienced a sedimentary-filling process from the expansion of P_1f^1 and P_1f^2 to the contraction of P_1f^3. Sedimentary supply rate at the margin of Mahu sag is higher than subsidence, which is consistent with the filling processes at the margin of a rift basin.

DATA AVAILABILITY STATEMENT

The original contributions presented in the study are included in the article/supplementary material; further inquiries can be directed to the corresponding authors.

AUTHOR CONTRIBUTIONS

WT and ML are responsible for writing and drawing, while XC, CH, NS, WT, and ZQ are responsible for content revision and sample collection. DZ and DG are responsible for the review of the content of the article.

FUNDING

This research is supported by the Chinese National Natural Science Foundation (No. 41802177), the Prospective and Fundamental Project of PetroChina (2021DJ0206), and the Fund for Basic Science Research of PetroChina (2020D-5008-04).

ACKNOWLEDGMENTS

We thank the editor-in-chief and the two reviewers for their constructive comments and careful corrections that led to significant improvement of the manuscript. We thank Xinjiang Oilfield, China National Petroleum Corporation for providing drill cores, wireline logs and seismic profiles.

REFERENCES

Cao, J., Hu, W. X., Yao, S. P., Zhang, Y. J., Wang, X. L., Zhang, Y. Q., et al. (2006). Evolution of Petroleum Migration and Accumulation in the Northwestern Margin of the Junggar Basin Fluid Inclusion Geochemistry. *Geol. Rev.* 2006 (05), 700–707. doi:10.16509/j.georeview.2006.05.023

Cao, J., Lei, D. W., Li, Y. W., Tang, Y., Wang, T, Chang, Q. S., et al. (2015). Ancient High-Quality Alkaline Lacustrine Source Rocks Discovered in the Lower Permian Fengcheng Formation, Junggar Basin. *Acta Pet. Sin.* 36 (07), 781–790. doi:10.7623/syxb201507002

Carroll, A. R., Graham, S. A., Hendrix, M. S., Ying, D., and Zhou, D. (1995). Late Paleozoic Tectonic Amalgamation of Northwestern China: Sedimentary Record of the Northern Tarim, Northwestern Turpan, and Southern Junggar Basins. *Geol. Soc. Am. Bull.* 107, 571–594. doi:10.1130/0016-7606(1995)107<0571:lptaon>2.3.co;2

Catuneanu, O., Abreu, V., Bhattacharya, J. P., Blum, M. D., Dalrymple, R. W., Eriksson, P. G., et al. (2009). Towards the Standardization of Sequence Stratigraphy. *Earth-Sci Rev.* 92 (1), 1–33. doi:10.1016/j.earscirev.2008.10.003

Chang, H. L., Zheng, R. C., Guo, C. L., and Wen, H. G. (2016). Characteristics of Rare Earth Elements of Exhalative Rock in Fengcheng Formation, Northwestern Margin of Jungger Basin. *Geol. Rev.* 62 (03), 550

Chao, D., Zhu, R. X., Han, J. H., Shu, Y., Wu, Y. X., Hou, K. F., et al. (2021). Impact of Basement Thrust Faults on Low-Angle Normal Faults and Rift Basin Evolution: a Case Study in the Enping Sag, Pearl River Basin. *Solid earth.* 12, 2327–2350. doi:10.5194/se-12-2327-2021

Chen, J. F., Han, B. F., Ji, J. Q., Zhang, L., Xu, Z., He, G. Q., et al. (2010). Zircon U–Pb Ages and Tectonic Implications of Paleozoic Plutons in Northern West Junggar, North Xinjiang, China. *Lithos* 115 (1-4), 137–152. doi:10.1016/j.lithos.2009.11.014

Fang, X., Yang, Z., Yan, W., Guo, X., Wu, Y., and Liu, J. (2019). Classification Evaluation Criteria and Exploration Potential of Tight Oil Resources in Key Basins of China. *J. Nat. Gas Geoscience* 4 (6), 309–319. doi:10.1016/j.jnggs.2019.11.002

Feng, C., Lei, D., Qu, J., and Huo, J. (2019). Controls of Paleo-Overpressure, Faults and Sedimentary Facies on the Distribution of the High Pressure and High Production Oil Pools in the Lower Triassic Baikouquan Formation of the Mahu Sag, Junggar Basin, China. *J. Petroleum Sci. Eng.* 176, 232–248. doi:10.1016/j.petrol.2019.01.012

Gong, B. S., Wen, H. G., Li, C. L., Wang, L., Zheng, R. C., and Qi, L. Q. (2014). Sedimentary Environment of Fengcheng Formation in Urho Area, Junggar Basin. *Lithol. Reserv.* 26 (02), 59

Gong, D., Li, J., Ablimit, I., He, W., Lu, S., Liu, D., et al. (2018). Geochemical Characteristics of Natural Gases Related to Late Paleozoic Coal Measures in China. *Mar. Petroleum Geol.* 96, 474–500. doi:10.1016/j.marpetgeo.2018.06.017

Gong, D. Y., Wang, X. L., Zhou, C. M., Chen, G., Wu, W. A., and Liu, Y. H. (2020). Hydrocarbon Generation Potential of Middle Triassic Karamay Formation in the Northwestern Junggar Basin. *J. China U Min. Techno* 49 (2), 328

Gong, D. Y., Zhang, Y. Q., Guo, W. J., Song, Z. H., Lu, S., and Wu, W. S. (2019). The Identification of Secondary Microbial Methane and biodegradation:Case Study of Luliang Oil and Gas Field, Junggar Basin. *Nat. Gas. Geosci.* 30 (7), 1006

Han, B.-F., Guo, Z.-J., Zhang, Z.-C., Zhang, L., Chen, J.-F., and Song, B. (2010). Age, Geochemistry, and Tectonic Implications of a Late Paleozoic Stitching Pluton in the North Tian Shan Suture Zone, Western China. *Geol. Soc. Am. Bull.* 122, 627–640. doi:10.1130/b26491.1

He, D. F., Yin, C., Du, S. K., Shi, X., and Ma, H. S. (2004b). Characteristics of Structural Segmentation of Foreland Thrust Belts-A Case Study of the Fault Belts in the Northwestern Margin of Junggar Basin. *Earth Sci.Front.* (03), 91

He, D. F., Zhang, L., Wu, S. T., Li, D., and Zhen, Y. (2018). Tectonic Evolution Stages and Features of the Junggar Basin. *Oil Gas. Geol.* 39 (5), 845–861. doi:10.11743/ogg20180501

He, G. Q., Chen, S. D., Xu, X., Li, J. Y., and Hao, J. (2004a). *An Introduction to Tectonic Map of Xinjiang and its Neighboring Area (1: 250 000)*. Beijing: Geological Publishing House, 65.

Hendrix, M. S., Graham, S. A., Carroll, A. R., Sobel, E. R., McKnight, C. L., Schulein, B. J., et al. (1992). Sedimentary Record and Climatic Implications of Recurrent Deformation in the Tian Shan: Evidence from Mesozoic Strata of the North Tarim, South Junggar, and Turpan Basins, Northwest China. *Geol. Soc. Am. Bull.* 104, 53–79. doi:10.1130/0016-7606(1992)104<0053:sracio>2.3.co;2

Huang, H., Gao, Y., Ma, C., Niu, L., Dong, T., Tian, X., et al. (2021). Astronomical Constraints on the Development of Alkaline Lake during the Carboniferous-Permian Period in North Pangea. *Glob. Planet. Change* 207, 103681. doi:10.1016/j.gloplacha.2021.103681

Jia, F. j., Yao, W. j., Liang, Z. L., Zhang, S. C., Fang, L. H., and Shi, J. A. (2010). Diagenic Feature and Evolution of Reservoir Pore of Permian Reservoir under the Kebai Fault in the Northwestern Margin Junggar Basin. *Nat. Gas. Geosci.* 21 (03), 458–463. doi:10.1016/j.petrol.2020.107599

Kuang, J., and Qi, X. F. (2006). The Structural Characteristics and Oil-Gas Explorative Direction in Junggar Foreland Basin. *Xinjiang Pet. Geol.* 2006 (01), 5

Lei, D. W., Abulimiti, B, Tang, Y., Chen, J., and Cao, J. (2014). Controlling Factors and Occurrence Prediction of High Oil-Gas Production Zones in Lower Triassic Baikouquan Formation of Mahu Sag in Junggar Basin. *Xinjiang Pet. Geol.* 35 (05), 495

Lei, Z. Y., Lu, B., Wei, Y. J., Zhang, L. P., and Shi, X. (2005). Tectonic Evolution and Development and Distribution of Fans on Northwestern Edge of Junggar Basin. *Oil Gas. Geol.* (01), 86. doi:10.3969/j.issn.1001-3873.2006.01.002

Li, L. (2022). Development of Natural Gas Industry in China: Review and Prospect. *Nat. Gas. Ind. B* 9 (2), 187–196. doi:10.1016/j.ngib.2022.03.001

Li, W., Yu, Z., Wang, X., Yu, Z., Lu, X., and Feng, Q. (2020). Formation Mechanisms of Deep and Ultra-deep over Pressure Caprocks and Their Relationships with Super-large Gas Fields in the Petroliferous Basins of China. *Nat. Gas. Ind. B* 7 (5), 443–452. doi:10.1016/j.ngib.2020.09.002

Li, Y., Xu, Q., Liu, J., Wang, R., and Xiang, K. (2016). Redefinition and Geological Significance of Jiamuhe Formation in Hala'alate Mountain of West Junggar, Xinjiang. *Earth Sci.* 41 (09), 147–1488. doi:10.3799/dqkx.2016.516

Liang, Y., Zhang, Y., Chen, S., Guo, Z., and Tang, W. (2020). Controls of a Strike-Slip Fault System on the Tectonic Inversion of the Mahu Depression at the Northwestern Margin of the Junggar Basin, NW China. *J. Asian Earth Sci.* 198, 104229. doi:10.1016/j.jseaes.2020.104229

Liu, M., Zhang, S. C., Kong, Y. H., and Shi, J. A. (2013). The Sedimentary Faceis Research of Fengcheng Formation of Permian in Fengcheng Area, the Northwestern Margin of Junggar Basin. *Xingjiang Geol.* 31 (03), 236

Lu, X., Sun, D., Xie, X., Chen, X., Zhang, S., Zhang, S., et al. (2019). Microfacies Characteristics and Reservoir Potential of Triassic Baikouquan Formation, Northern Mahu Sag, Junggar Basin, NW China. *J. Nat. Gas Geoscience* 4 (1), 47–62. doi:10.1016/j.jnggs.2019.03.001

Lu, Y. (2018). *Permian Chronostratigraphic Framework and Sedimentary Filling Evolution in Mahu-Shawan and Adjacent Area, Junggar Basin [MasterThesis]*. Beijing: China University of Geosciences Beijing, 132.

Miller, K. G., Browning, J. V., Mountain, S. G., Bassetti, M. A., Monteverde, D., Katz, M. E., et al. (2013). Sequence Boundaries Are Impedance Contrasts: Core-Seismic-Log Integration of Oligocene-Miocene Sequences, New Jersey Shallow Shelf. *Geosphere* 9 (5), 1257–1285. doi:10.1130/GES00858.1

Niu, H. Q., Chen, S. Y., Zhang, P., and Yan, J. H. (2009). Analysis of the Pemian Reservoir Characteristics and Controlling Factors in Wuxia Area, Junggar Basin. *J. Palaegeogr.* 1 (4), 425–434. doi:10.7605/gdlxb.2009.04.007

Ouyang, Y., Tian, W., Sun, B., Wang, B., Qi, L., Sun, Q., et al. (2018). Accumulation Characteristics and Exploration Strategies of Coal Measure Gas in China. *Nat. Gas. Ind. B* 5 (5), 444–451. doi:10.1016/j.ngib.2018.03.003

Pei, L., Gang, W., Zhu, C., Liu, Y., He, W., Dong, Y., et al. (2018). Carbon Isotope and Origin of the Hydrocarbon Gases in the Junggar Basin, China. *J. Nat. Gas Geoscience* 3 (5), 253–261. doi:10.1016/j.jnggs.2018.11.002

Shi, J. a., Sun, G., Zhang, S., Guo, H., Zhang, S., and Du, S. (2017). Reservoir Characteristics and Control Factors of Carboniferous Volcanic Gas Reservoirs in the Dixi Area of Junggar Basin, China. *J. Nat. Gas Geoscience* 2 (1), 43–55. doi:10.1016/j.jnggs.2017.03.001

Tang, W. B., Song, Y., He, W. J., Tang, Y., Guo, X. G., Pe-Piper, G., et al. (2021a). Source-to-sink Evolution of Syn-Rift Alkaline Lake Sediments in the Lower Permian Fengcheng Formation, Junggar Basin, NW China: Evidence from Petrology, Detrital Zircon Geochronology and Geochemistry. *J. Asian Earth Sci.* 232, 105049. doi:10.1016/j.jseaes.2021.105049

Tang, W., Zhang, Y., Pe-Piper, G., Piper, D. J. W., Guo, Z., and Li, W. (2021c). Permian Rifting Processes in the NW Junggar Basin, China: Implications for the Post-accretionary Successor Basins. *Gondwana Res.* 98, 107–124. doi:10.1016/j.gr.2021.06.005

Tang, W., Zhang, Y., Pe-Piper, G., Piper, D. J. W., Guo, Z., and Li, W. (2021b). Permian to Early Triassic Tectono-Sedimentary Evolution of the Mahu Sag, Junggar Basin, Western China: Sedimentological Implications of the Transition from Rifting to Tectonic Inversion. *Mar. Petroleum Geol.* 123, 104730. doi:10.1016/j.marpetgeo.2020.104730

Tang, W., Zhang, Y., Pe-Piper, G., Piper, D. J. W., Guo, Z., and Li, W. (2020). Soft-sediment Deformation Structures in Alkaline Lake Deposits of Lower Permian Fengcheng Formation, Junggar Basin, NW China: Implications for Syn-Sedimentary Tectonic Activity. *Sediment. Geol.* 406, 105719. doi:10.1016/j.sedgeo.2020.105719

Vail, P. R. (1988). *AAPG Annual Convention Short Course: Sequence Stratigraphy Interpretation of Seismic Stratigraphy Interpretation Procedure*. Houston, TX: AAPG Bull.-Am. Assoc. Petr.

Van Wagoner, J. C., Mitchum, R. M., and Campion, K. M. (1990). "Siliciclastic Sequence Stratigraphy in Well Logs, Cores and Outcrops," in *American Association of Petroleum Geologists Methods in Exploration Series*. Editors J. Helwig and G. D. Howell (Oklahoma, OK: AAPG Bull.-Am. Assoc. Petr. Geol), 7, 2–8. doi:10.1306/mth7510

Wang, Y., Jia, D., Pan, J., Wei, D., Tang, Y., Wang, G., et al. (2018). Multiple-phase Tectonic Superposition and Reworking in the Junggar Basin of Northwestern China-Implications for Deep-Seated Petroleum Exploration. *Bulletin* 102, 1489–1521. doi:10.1306/10181716518

Wei, G., Li, J., She, Y., Zhang, G., Shao, L., Yang, G., et al. (2018). Distribution Laws of Large Gas Fields and Further Exploration Orientation and Targets in China. *Nat. Gas. Ind. B* 5 (5), 485–498. doi:10.1016/j.ngib.2018.04.014

Xian, J. Y. (1985). Discussion on Rock Ore and Reservoir Characteristics of Fengcheng Formation in Fengcheng Area. *Xinjiang Pet.Geol.* (03), 28

Yu, Y., Wang, X., Rao, G., and Wang, R. (2016). Mesozoic Reactivated Transpressional Structures and Multi-Stage Tectonic Deformation along the Hong-Che Fault Zone in the Northwestern Junggar Basin, NW China. *Tectonophysics* 679, 156–168. doi:10.1016/j.tecto.2016.04.039

Zhang, G., Jin, L., Lan, L., and Zhao, Z. (2015). Analysis of the Orderly Distribution of Oil and Gas Fields in China Based on the Theory of Co-control of Source and Heat. *Nat. Gas. Ind. B* 2 (1), 49–76. doi:10.1016/j.ngib.2015.02.005

Zhang, S. W. (2013). Identification and its Petroleum Geologic Significance of the Fengcheng Formation Source Rocks in Hala' Alt Area, the Northern Margin of Junggar Basin. *Oil Gas. Geol.* 34 (02), 145. doi:10.11743/ogg20130201

Zhang, S., Zhang, S., Fang, L., Lu, X., Guo, H., and Shi, J. a. (2020). Petrological and Geochemical Constraints on Tectonic Settings of the Late Carboniferous-Early Permian, Central Junggar, China. *J. Nat. Gas Geoscience* 5 (1), 1–10. doi:10.1016/j.jnggs.2019.12.002

Zhang, Y. J., Cao, J., and Hu, W. X. (2010). Timing of Petroleum Accumulation and the Division of Reservoir-Forming Assemblages, Junggar Basin, NW China. *Pet. Explor. Dev.* 37 (03), 257–262. doi:10.1016/S1876-3804(10)60031-6

Zhang, Z. J., Yuan, X. J., Wang, M. S., Zhou, C. M., Tang, Y., Chen, X. Y., et al. (2018). Alkaline-lacustrine Deposition and Paleoenvironmental Evolution in Permian Fengcheng Formation at the Mahu Sag, Junggar Basin, NW China. *Pet. Explor. Dev.* 45 (06), 972–984. doi:10.1016/s1876-3804(18)30107-1

Zheng, R. C., Peng, J., and Wu, C. R. (2001). Grade Divisions of Base-Level Cycle of Terrigenous Basin and its Implications. *Acta Sedimentol. Sin.* 2, 249

Zheng, R. C., Wu, C. R., and Ye, M. C. (2000). Research Think of Highresolition Sequence Stratigraphy about a Sterrigenous Basin. *J. Chengdu Univ. Technol. Sci. Ed.* 3, 241

Zhi, D. M., Song, Y., He, W. J., Jia, X. Y., Zou, Y., and Huang, L. L. (2019). Geological Characteristics, Resource Potential and Exploration Direction of Shale Oil in Middle-Lower Permian, Junggar Basin. *Xinjiang Pet. Geol.* 40 (04), 389–401. doi:10.7657/XJPG20190402

Zhi, D. M., Tang, Y., He, W. J., Guo, X. G., Zheng, M. L., and Huang, L. L. (2021). Orderly Coexistence and Accumulation Models of Conventional and Unconventional Hydrocarbons in Lower Permian Fengcheng Formation, Mahu Sag, Junggar Basin. *Pet. Explor. Dev.* 48 (01), 38–51. doi:10.1016/s1876-3804(21)60004-6

Zhu, X., Zeng, H., Li, S., Dong, Y., Zhu, S., Zhao, D., et al. (2017). Sedimentary Characteristics and Seismic Geomorphologic Responses of a Shallow-Water Delta in the Qingshankou Formation from the Songliao Basin, China. *Mar. Petroleum Geol.* 79, 131–148. doi:10.1016/j.marpetgeo.2016.09.018

Zou, H., Li, Q.-L., Bagas, L., Wang, X.-C., Chen, A.-Q., and Li, X.-H. (2021). A Neoproterozoic Low-δ18O Magmatic Ring Around South China: Implications for Configuration and Breakup of Rodinia Supercontinent. *Earth Planet. Sci. Lett.* 575, 117196. doi:10.1016/j.epsl.2021.117196

Zou, H., Wang, J., Chen, A., Zhong, Y., Chen, H., Liu, S., et al. (2020). Sedimentology of the Deltaic Paleogene Shahejie Formation in the D-1 Area of Liaodong Bay, East China. *Geol. J.* 55 (12), 7738–7759. doi:10.1002/gj.3901

Conflict of Interest: DZ was employed by Xinjiang Oilfield Company.

DZ was employed by Turpan-Hami Oilfield Company.

The remaining authors declare that the research was conducted in the absence of any commercial or financial relationships that could be construed as a potential conflict of interest.

frontiers | Frontiers in Earth Science

ORIGINAL RESEARCH
published: 08 August 2022
doi: 10.3389/feart.2022.950305

Effect of Volcanic Activity on Hydrocarbon-Forming Organisms in Organic-Rich Shale: A Case Study of Dalong Formation in Northwestern Sichuan Basin, China

Chuanwen Zhang[1,2,3], Qingqiang Meng[2], Xuan Tang[3]*, Zuoyu Sun[4], Qian Pang[5], Dawei Lyu[6], Dongya Zhu[2], Jiayi Liu[2], Jiachun Li[4] and Bin Jiang[1]*

[1]State Key Laboratory of Organic Geochemistry, Guangzhou Institute of Geochemistry, Chinese Academy of Sciences, Guangzhou, China, [2]Sinopec Petroleum Exploration and Development Research Institute, Beijing, China, [3]School of Energy and Resources, China University of Geosciences, Beijing, China, [4]School of Earth Science and Spatial Information, Peking University, Beijing, China, [5]School of Earth Science and Technology, Southwest Petroleum University, Chengdu, China, [6]School of Earth Science and Engineering, Shandong University of Science and Technology, Qingdao, China

OPEN ACCESS

Edited by:
Dongming Zhi,
PetroChina, China

Reviewed by:
Yingkun Fu,
University of Alberta, Canada
Qi Fu,
University of Houston, United States

***Correspondence:**
Qingqiang Meng
mengqq2004@163.com
Xuan Tang
tangxuan@cugb.edu.cn

Specialty section:
This article was submitted to Economic Geology, a section of the journal Frontiers in Earth Science

Received: *22 May 2022*
Accepted: *13 June 2022*
Published: *08 August 2022*

Citation:
Zhang C, Meng Q, Tang X, Sun Z, Pang Q, Lyu D, Zhu D, Liu J, Li J and Jiang B (2022) Effect of Volcanic Activity on Hydrocarbon-Forming Organisms in Organic-Rich Shale: A Case Study of Dalong Formation in Northwestern Sichuan Basin, China. Front. Earth Sci. 10:950305. doi: 10.3389/feart.2022.950305

Hydrocarbon-generating material determines the elemental composition and hydrocarbon-generating potential of kerogens in a source rock, and it is the key material basis to control the hydrocarbon-generating capacity of the source rock. Previous studies have shown that many intervals of high-quality source rocks generally contain a varying number of volcanic ash layers. The impact of these volcanic ash layers on the development of high-quality source rocks has attracted extensive attention. However, these studies mainly focused on the development of hydrocarbon-forming organisms and the preservation of organic matters but rarely dealt with the differential development of hydrocarbon-forming organisms between multiple volcanic ash layers. The Permian Dalong Formation in the northwestern Sichuan Basin, China, is a set of high-quality source rocks with multiple volcanic sedimentary layers. To understand the differential development of hydrocarbon-forming organisms between volcanic ash layers, with the Dalong Formation in the Longfeng quarry section, Guangyuan, the Sichuan Basin as an example, this study analyzes the types of hydrocarbon-generating materials of high-quality source rocks of the Dalong Formation and the reasons why volcanic activities affected the growth of hydrocarbon-forming organisms and explores the impact of volcanic activities on the development of different types of hydrocarbon-forming organisms. The results show that the TOC of the Longfeng quarry section is 0.05%–15.46%, with an average of 4.76%, and the average TOC of the Dalong Formation is as high as 5.16%, which belongs to high-quality source rocks. The hydrocarbon-forming organism association in the Dalong Formation source rocks is mainly composed of floating algae and benthic algae and vertically divided into three parts: a few radiolarians and trace fossils occasionally in the lower part; a large number of radiolarians, calcium spheres, and algal debris in the middle part; and mainly foraminifera and gastropods in the upper part. There are 36 volcanic ash layers in the Dalong Formation of the study area. In the process of volcanic activity, the “fertilization” effect of volcanic ash made the nutrient elements in the volcanic ash enter

water, increasing the number of hydrocarbon-forming organisms, causing the differential development of various hydrocarbon-forming organisms, and promoting the formation of reducing water to support the preservation of organic matters. The development of hydrocarbon-forming organisms is controlled by the changes of element types and abundances caused by magmatic properties. The time interval of volcanic activities also has an important impact on the development of hydrocarbon-forming organisms.

Keywords: volcanic activity, hydrocarbon-forming organism, differential development, Dalong Formation, Guangyuan, Sichuan Basin

1 INTRODUCTION

The generation and evolution of source rocks experience a long and complex process under the control of many factors. Previous studies have shown that high-quality source rocks contain multiple volcanic ash layers, such as the Eagle Ford Formation in the Gulf Coast Basin, U.S. (Dawson et al., 2000; Duggen et al., 2007; Lee et al., 2018), the Qingshankou Formation (Gao et al., 2009) and Yingcheng Formation (Shan et al., 2014) in the Songliao Basin, the Shahejie Formation in the Bohai Bay Basin (Du et al., 2014), the Yanchang Formation in the Ordos Basin (Zhang et al., 2009; Qiu et al., 2010; Liu et al., 2013; Xue et al., 2020), the Wufeng–Longmaxi Formations (Lyu et al., 2020; Qiu et al., 2020) and Dalong Formation in the Sichuan Basin (Pang, 2019), and the Haerjiawu Formation (Li, 2010) and Lucaogou Formation (Wu et al., 2012) in the Santanghu Basin, China. This indicates that the formation of organic-rich source rocks might be strongly affected by volcanic activity.

The Sichuan Basin is an important conventional and unconventional oil and gas province in China (Hu et al, 2021b; Xie et al., 2021). The high-quality source rocks of the Dalong Formation in northwestern Sichuan Basin have a good potential for shale oil and gas exploration and development (Fu et al., 2010). Previous studies and stratigraphic sections revealed the presence of multiple volcanic ash interlayers in the Dalong Formation. Deep fluid activities such as volcanic activity can significantly promote the formation of organic-rich shale and the proliferation of hydrocarbon-forming organisms (Liu et al., 2019a; Liu et al., 2019b; Liu et al., 2022). However, for the Dalong Formation high-quality source rocks, further efforts are needed to clarify the relationship between types of hydrocarbon-generating materials and volcanic ash interlayers. The Dalong Formation was deposited successively the overlying Triassic Feixianguan Formation, and it is also the boundary between Permian and Triassic (Li et al., 2020; Zhou et al., 2021). The study on the relationship between types of

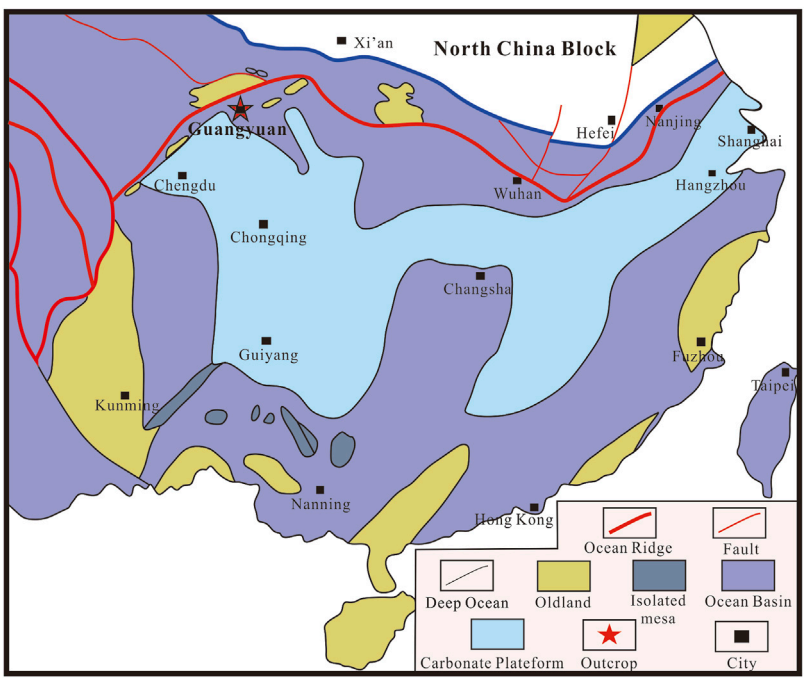

FIGURE 1 | Outcrop location (modified after Meng et al., 2022).

TABLE 1 | Inorganic elements of Dalong Formation in Longfeng quarry section.

Sample no.	Na_2O	MgO	Al_2O_3	SiO_2	K_2O	CaO	TiO_2	Fe_2O_3	MoEF	UEF	VEF
TY-091	0.58	10.10	7.08	25.55	1.54	20.86	0.39	4.15	0.63	1.10	0.44
TY-090	0.62	1.72	21.84	54.00	4.17	2.78	0.53	2.31	0.31	1.05	0.38
TY-089	0.64	1.07	12.79	67.05	2.79	3.86a	0.36	2.99	1.53	0.74	0.28
TY-088	0.28	2.27	24.61	49.16	4.48	2.45	0.61	2.38	1.76	1.50	0.13
TY-087	0.35	0.81	4.58	81.24	0.99	4.70	0.17	1.15	11.88	0.98	0.53
TY-086	0.19	0.30	2.41	68.26	0.49	14.88	0.08	0.72	12.64	3.59	0.61
TY-085	0.17	0.64	1.94	18.32	0.40	43.08	0.06	0.79	3.95	4.23	0.50
TY-084	0.28	0.59	7.33	72.28	1.69	7.01	0.25	1.73	3.00	1.48	0.43
TY-083	0.31	2.22	2.90	35.11	0.62	30.70	0.10	1.36	3.84	5.34	0.53
TY-082	0.29	0.79	1.58	16.27	0.26	44.41	0.03	0.60	9.93	42.95	1.01
TY-081	0.36	1.27	2.16	12.56	0.40	45.51	0.08	0.87	12.67	8.81	0.59
TY-080	0.38	0.67	2.10	10.37	0.34	47.57	0.06	1.02	8.25	13.77	0.95
TY-079	0.85	0.69	7.16	36.51	1.43	26.85	0.22	2.05	11.76	15.73	1.60
TY-078A	0.26	8.02	2.81	11.85	0.61	37.02	0.10	1.68	17.60	4.96	0.63
TY-078	0.21	1.11	0.43	1.54	0.04	53.70	0.01	0.88	35.88	36.62	0.86
TY-077	0.58	0.99	6.19	57.99	1.18	14.68	0.24	2.33	25.20	3.65	2.70
TY-076	0.75	0.62	10.18	59.78	1.86	2.98	0.32	4.43	96.64	7.41	6.90
TY-075	0.40	2.16	3.81	57.31	0.67	16.81	0.12	1.30	37.60	4.49	1.85
TY-074	0.38	0.51	7.72	75.85	1.60	1.40	0.25	1.77	15.87	1.26	2.03
TY-073	0.26	0.84	2.86	59.29	0.54	18.73	0.08	0.65	17.31	5.00	1.23
TY-072	0.36	0.28	2.06	69.16	0.30	14.60	0.06	0.68	25.94	18.21	1.96
TY-071	0.27	0.31	1.49	68.13	0.22	15.93	0.05	0.57	64.69	9.94	1.67
TY-070	0.40	1.31	2.33	57.06	0.32	19.31	0.06	0.64	23.69	26.33	121.52
TY-069	0.59	0.59	3.83	71.34	0.63	10.99	0.09	0.87	41.17	3.97	51.58
TY-068	0.34	0.56	2.99	63.98	0.74	15.76	0.10	0.92	46.22	15.10	166.58
TY-067	0.33	0.55	2.14	76.61	0.32	5.55	0.08	2.43	789.72	23.47	1,015.59
TY-066	0.47	0.41	7.52	71.12	1.20	1.19	0.23	2.07	136.37	6.01	668.71
TY-065	0.22	0.21	1.29	90.89	0.22	2.18	0.04	0.92	293.10	7.14	156.94
TY-064	0.22	0.27	3.41	82.03	0.74	2.46	0.12	1.62	331.41	5.97	584.46
TY-063	0.54	0.49	8.70	70.38	1.45	0.29	0.27	1.44	123.86	5.00	814.47
TY-062	0.32	0.45	2.74	75.62	0.55	7.53	0.10	2.66	265.27	12.83	502.25
TY-061	0.18	0.17	1.21	83.77	0.20	4.84	0.04	1.15	709.96	67.26	461.51
TY-060–1	0.27	8.69	2.86	37.71	0.73	19.41	0.12	2.22	370.31	17.75	848.90
TY-060	0.18	0.18	1.85	80.27	0.42	3.32	0.08	1.66	895.79	18.39	633.86
TY-059	0.18	0.19	2.79	80.20	0.79	0.74	0.13	2.87	947.15	16.22	660.90
TY-058	0.45	0.19	4.38	80.58	0.92	3.82	0.15	1.31	61.47	4.25	377.26
TY-057–1	0.50	0.27	5.80	79.42	1.20	1.78	0.19	1.79	48.22	16.52	593.92
TY-057	0.58	0.46	7.97	67.01	1.62	0.22	0.29	2.95	176.94	9.62	1,695.21
TY-056	0.23	0.22	1.87	81.67	0.37	6.13	0.07	1.19	431.52	12.49	261.13
TY-055	0.20	0.88	2.59	78.22	0.55	4.45	0.10	2.41	263.88	14.29	670.35
TY-054	0.33	0.74	3.87	72.92	0.84	3.90	0.14	2.90	387.15	11.92	967.56
TY-053	0.37	0.37	2.34	51.72	0.36	22.57	0.08	1.24	204.45	57.28	307.97
TY-052	0.63	0.68	9.88	57.45	1.92	0.10	0.42	3.01	333.74	5.30	1,397.78
TY-051	0.20	0.21	1.25	74.87	0.21	11.00	0.04	0.79	155.85	47.82	183.72
TY-050	0.13	7.92	0.50	7.19	0.07	42.62	0.02	0.29	483.96	34.53	128.27
TY-049	0.20	1.27	2.38	79.41	0.53	3.05	0.11	1.92	393.36	10.35	713.42
TY-048	0.27	1.41	2.99	63.68	0.57	13.05	0.10	1.53	273.99	10.54	653.77
TY-047	0.14	0.24	1.77	75.40	0.33	8.66	0.06	1.51	229.17	15.49	27.86
TY-046	0.30	0.28	3.32	71.81	0.68	6.32	0.14	2.97	313.80	12.42	15.20
TY-045	0.45	0.87	6.67	60.33	1.22	5.30	0.22	3.58	233.02	7.18	15.66
TY-044	0.49	0.87	6.10	64.18	1.16	4.38	0.22	4.65	195.53	4.38	9.75
TY-043–1	0.31	1.39	3.83	64.68	0.76	9.24	0.15	3.10	184.66	8.27	23.92
TY-043	0.20	1.25	2.10	81.18	0.41	3.78	0.09	1.43	233.58	9.08	20.61
TY-042	0.19	9.97	2.20	36.33	0.55	20.01	0.07	1.25	273.72	12.64	17.33
TY-041A	0.14	0.35	1.67	75.90	0.36	8.45	0.06	1.94	441.55	22.47	26.19
TY-041	0.45	0.61	6.50	66.63	1.25	5.01	0.21	2.35	52.17	6.47	7.19
TY-040A	0.22	0.22	1.65	84.58	0.32	3.67	0.07	0.89	113.68	14.23	13.38
TY-040	0.38	0.50	7.09	70.04	1.36	1.43	0.23	2.27	39.11	4.44	7.49
TY-039	0.23	0.86	3.52	80.92	0.85	1.70	0.14	1.26	43.24	4.17	7.39
TY-038	0.45	0.31	5.94	63.70	1.49	0.49	0.24	6.06	309.28	6.60	24.98
TY-037	0.46	0.48	4.91	43.82	1.25	18.41	0.21	3.62	181.30	10.74	17.26
TY-036	0.43	0.57	5.60	43.80	1.54	15.34	0.23	5.02	234.97	8.56	22.73
TY-035	0.73	9.77	5.89	15.40	0.87	29.52	0.11	1.26	12.60	5.78	3.17

(Continued on following page)

TABLE 1 | (*Continued*) Inorganic elements of Dalong Formation in Longfeng quarry section.

Sample no.	Na_2O	MgO	Al_2O_3	SiO_2	K_2O	CaO	TiO_2	Fe_2O_3	MoEF	UEF	VEF
TY-034	0.67	0.82	8.76	50.09	2.11	7.41	0.38	6.89	103.28	4.81	12.53
TY-033	0.58	3.52	6.25	47.40	1.53	15.05	0.24	2.93	53.65	42.92	9.58
TY-032	0.32	0.85	1.35	14.12	0.31	45.84	0.06	1.15	289.98	36.42	12.41
TY-031	0.37	1.57	6.16	49.19	1.49	12.34	0.38	6.07	191.60	11.37	14.33
TY-030	0.39	1.21	7.50	50.81	1.79	13.96	0.60	5.20	73.02	10.97	8.61
TY-029	0.49	0.83	9.70	46.99	2.27	7.73	0.83	8.71	84.89	7.26	10.87
TY-028	0.19	0.57	1.67	76.01	0.34	9.56	0.07	1.50	163.39	7.91	19.87
TY-027	0.32	0.59	8.35	65.43	2.05	0.22	0.37	3.14	67.35	3.70	10.44
TY-026	0.24	0.44	1.37	48.90	0.34	26.40	0.06	0.58	159.19	29.17	10.10
TY-025	0.06	0.46	0.04	1.06	0.02	56.18	0.00	0.06	122.43	324.60	27.10
TY-024	0.21	0.39	5.23	74.81	1.69	0.13	0.25	1.94	41.71	4.02	11.01
TY-023	0.22	0.81	3.98	75.72	1.08	3.87	0.20	1.49	48.51	3.38	9.71
TY-022	0.24	0.54	5.69	65.13	2.41	8.87	0.19	1.55	33.11	3.93	449.93
TY-021	0.23	0.52	4.06	51.61	1.30	16.47	0.19	2.25	145.47	9.35	1,173.62
TY-020	0.25	0.58	5.12	45.73	1.58	6.96	0.23	3.06	169.93	8.24	1,526.37
TY-019	0.14	0.87	0.48	4.74	0.12	52.49	0.02	0.50	357.41	60.93	192.19
TY-018	0.27	0.49	4.56	55.73	1.35	14.98	0.21	2.00	68.09	12.70	639.38
TY-017	0.29	0.65	6.64	63.65	2.04	2.72	0.32	2.60	30.55	8.08	585.37
TY-016	0.24	0.65	4.40	58.46	1.43	15.43	0.19	1.65	40.02	4.60	331.14
TY-015	0.25	0.46	5.86	39.33	2.36	18.79	0.28	3.23	106.42	23.06	691.16
TY-014	0.31	1.49	6.38	61.68	2.05	10.92	0.27	2.23	45.12	4.78	369.44
TY-013–1	0.20	0.69	1.85	10.20	0.51	47.60	0.07	0.63	38.76	14.81	124.38
TY-013	0.38	0.66	5.86	33.55	2.05	26.36	0.24	2.40	31.34	20.30	296.65
TY-012	0.18	0.74	0.84	6.58	0.23	49.41	0.04	0.57	121.18	77.07	114.52
TY-011	0.23	0.78	2.63	22.74	0.96	37.99	0.12	2.30	216.22	25.33	262.24
TY-010	0.28	0.67	6.26	41.81	2.10	23.21	0.24	2.01	12.22	3.51	170.12
TY-009	0.22	0.96	6.97	27.85	1.82	32.40	0.18	2.72	7.68	7.62	46.80
TY-008	0.13	14.79	1.35	4.29	0.32	34.93	0.05	0.92	4.05	6.19	13.90
TY-007	0.16	3.05	2.79	29.91	0.82	32.80	0.10	1.47	4.18	3.49	19.16
TY-006	0.23	0.65	5.03	67.15	1.24	12.31	0.21	1.65	7.47	3.01	43.36
TY-005	0.10	0.80	0.49	1.62	0.12	53.86	0.02	0.40	15.55	22.43	4.44
TY-004	0.17	0.51	2.74	37.22	0.87	32.00	0.12	0.97	3.46	7.19	38.76
TY-003	0.18	0.78	0.75	3.56	0.16	52.18	0.03	0.66	3.88	6.29	7.73
TY-002	0.09	0.55	1.48	16.24	0.47	44.97	0.07	0.63	11.78	6.21	28.43
TY-001	0.14	0.78	0.82	6.09	0.26	51.00	0.04	0.51	2.74	6.26	10.03

hydrocarbon-forming organisms and volcanic activity in the Dalong Formation will enrich the efforts in biological extinction and recovery in the Permian–Triassic boundary (PTB) and then help to strengthen the understanding of the Earth's ecological environment in this major transition of geological history.

2 GEOLOGICAL SETTING

In the Upper Permian, the Sichuan Basin was a marine craton basin (Li et al., 2015), with mainly carbonate rocks deposited. According to the fossil community and habitat types in Shangsi, Guangyuan, classified by Yan et al. (2008), and the habitat type classification of Yin and Tong (1995), the Dalong Formation indicates lower shallow sedimentary environment in the lower and upper parts and intra-platform basin sedimentary environment in the middle part.

This thesis takes the Shangsi Dalong Formation in Guangyuan, Sichuan Province, as the research object (**Figure 1**). Dalong Formation is mainly distributed as two strips in northwestern and northern Sichuan Basin. The study area is located in the Kuangshanliang-Liangping area, Guangyuan, in a narrow coverage striking NW-SE, where the strata are about 10–40 m thick and gradually thin to the southwest and northeast (Fu et al., 2010) (**Table 1**).

Except for the Dalong Formation, the Xuanwei Formation is mainly developed in the Upper Permian in the Emei-Junlian area, western Sichuan Basin, and it is composed of argillaceous sandstone and shale, as well as coal seams, with rich Gigantopterisian flora (Yang, 2016). The bottom of the Xuanwei Formation is tuff or conglomerate, which is in disconformable contact with the Emeishan basalt. Approaching the top, the coal seam gradually disappears until the overlying Kayitou Formation and Dongchuan Formation. In central Sichuan Basin, the Upper Permian strata are Longtan Formation and Changxing Formation from the bottom to the top. The Longtan Formation is believed to be transitional sedimentary facies, mainly depositing black silty mud shale, with a few limestone and occasionally intercalated with coal streaks, and it is in parallel unconformable contact with the underlying Maokou Formation (Yang et al., 2021). The Changxing Formation is of marine platform sedimentary facies, represented by marl and sandy mudstone, and it has

rich biological fossils, including foraminifera, brachiopods, and bivalves (Zhang and Zhang, 1992; Ma et al., 2006; Ran et al., 2021). The Changxing Formation and the overlying Feixianguan Formation are bounded by thin mudstone and marl (**Figure 2**).

3 SAMPLES AND METHOD

The outcrop section in Xibei Township of Guangyuan includes the Permian and Triassic strata. The top of Permian Changxing Formation, the whole Dalong Formation, and the bottom of Triassic Feixianguan Formation were measured, with the thickness of 30.80 m. The Permian Changxing Formation at the bottom of the section is about 2.50 m thick and contains mainly gray limestone with chert strip (**Figure 3A**). Upward, the Dalong Formation appears, with a total thickness of about 27.80 m, and mainly contains black mudstone and shale, with a high silicon content. There is an argillaceous limestone section of about 1.00 m at the bottom of the Dalong Formation (**Figure 3B**). Silicon content increases toward the middle of the Dalong Formation. There are massive black shale and black siliceous mud shale with limestone lens in the middle (**Figure 3C**), and two thin layers of limestone are found. The top of the Dalong Formation is gray limestone of about 4.00 m. Triassic stratum is deposited at the top of the section, with a thickness of about 0.50 m, and containing mainly gray marl. **Figure 3D** shows a part of volcanic ash samples collected.

A total of 113 samples were acquired from the field outcrop, including 98 shale samples and 15 volcanic ash (tuff) samples. The shale samples were numbered as TY-001 to TY-091 in a descending order of age (**Figure 4**), the thickness of volcanic ash layer is between 1 and 5 cm, and it is concentrated in 1–3 cm. They were analyzed for TOC and XRF measurement, kerogen pyrolysis, rock slice, and maceral observation. The pyrolysis test was conducted in China University of Petroleum (Beijing), and the XRF and ICP-MS tests were conducted in China University of Geosciences (Wuhan). Specifically, the XRF test was completed using PANalytical Zetium and the Super Q 6 analysis software, with the sample preparation steps as follows: 1) pre-oxidation and melting; and 2) determination of loss on ignition. The ICP-MS and pyrolysis tests were completed according to the procedures described by Govindaraju (1994) and Song et al. (2012).

4 RESULTS

4.1 Organic Matter Content, Total Sulfur, and Rock Pyrolysis

The Longfeng quarry section is found with obvious cyclicity of lithology, roughly as a succession (from the bottom to the top) of limestone–mud shale–limestone–mud shale–mud shale interbedded with limestone lens–limestone (**Figure 4**). The silicon content is generally high. TOC varies obviously with lithology, and exhibits relatively higher value in black shale.

The analysis results show that the TOC value is universally high in the section, ranging from 0.1% to 15.5%, with an average of 4.8% (5.2% in the Dalong Formation). The highest TOC value (15.5%) is demonstrated in the middle part of the Dalong Formation. The total sulfur content (TS) is 1.2% on average, but it changes greatly in the vertical direction. In other words, the appearance of volcanic ash layer rapidly increases the TS. The minimum and maximum of TS in the Dalong Formation are 0.1% and 4.7%, respectively, and reveal the largest difference of 3.6% between two neighbor samples, typically near the N11 volcanic ash layer.

The results of rock pyrolysis show that the hydrocarbon-generating potential (S1 + S2) of the Dalong Formation is 0.04–19.76 mg/g, with an average of 5.78 mg/g, the peak temperature (Tmax) of thermolysis changes little in the Dalong Formation, with an average of about 446°C, and S1/(S1 + S2) ranges between 0.1 and 0.2, indicating that the Dalong Formation stays at the peak or late stage of hydrocarbon generation, with a high maturity of organic matters. The HI value ranges from 33.86 to 1,139.47, primarily in 80–120, with an average of 108.13, and it increases obviously in the rocks below to above the volcanic ash layers—even from 44.04 to 587.83, especially near the N20 volcanic ash layer (**Figure 5**).

4.2 Inorganic Elements

For major elements, SiO_2, Al_2O_3, and Fe_2O_3 account for relatively high proportions, being about 55.13%, 4.47%, and 2.10%, respectively; the proportions of K_2O, MgO, Na_2O, and TiO_2 are relatively low, accounting for 1.02%, 1.21%, 0.33%, and 0.17%, respectively. Moreover, the CaO content is high, with an average of about 15.43%, and it is higher in the upper and lower parts than in the middle part of the Dalong Formation. For trace elements, MOEF, UEF, and VEF are 148.72, 16.71, and 226.75 on average, respectively, with higher enrichment coefficient, and all values are higher in the layers above the volcanic ash layer than those beneath the volcanic ash layer.

5 DISCUSSION

5.1 Geochemical Characteristics of Source Rocks in Dalong Formation

Under normal thermal evolution conditions, the abundance of organic matter in rock is directly proportional to the hydrocarbon-generating capacity (Mukhopadhyay et al., 1985), and the conventional indicators for evaluating the abundance of organic matter include TOC, chloroform asphalt "A," hydrocarbon-generating potential (S1 + S2), and total hydrocarbon (Liu et al., 2008; Liu et al., 2016). However, in the case of high-evolution degree, TOC becomes the main indicator to evaluate the hydrocarbon-generating potential of source rocks (Fu et al., 2010).

In this thesis, TOC was mainly used to evaluate the hydrocarbon-generating potential of the Dalong Formation, which has a high thermal evolution degree (Fu et al., 2010). As shown in **Figures 4** and **5**, the appearance of volcanic ash layer affects TOC, TS, pyrolytic hydrocarbon (S2), and HI of the Dalong Formation. For samples from the strata above the volcanic ash layer, both TOC and TS increase to a certain extent. For samples adjacent to volcanic ash above the

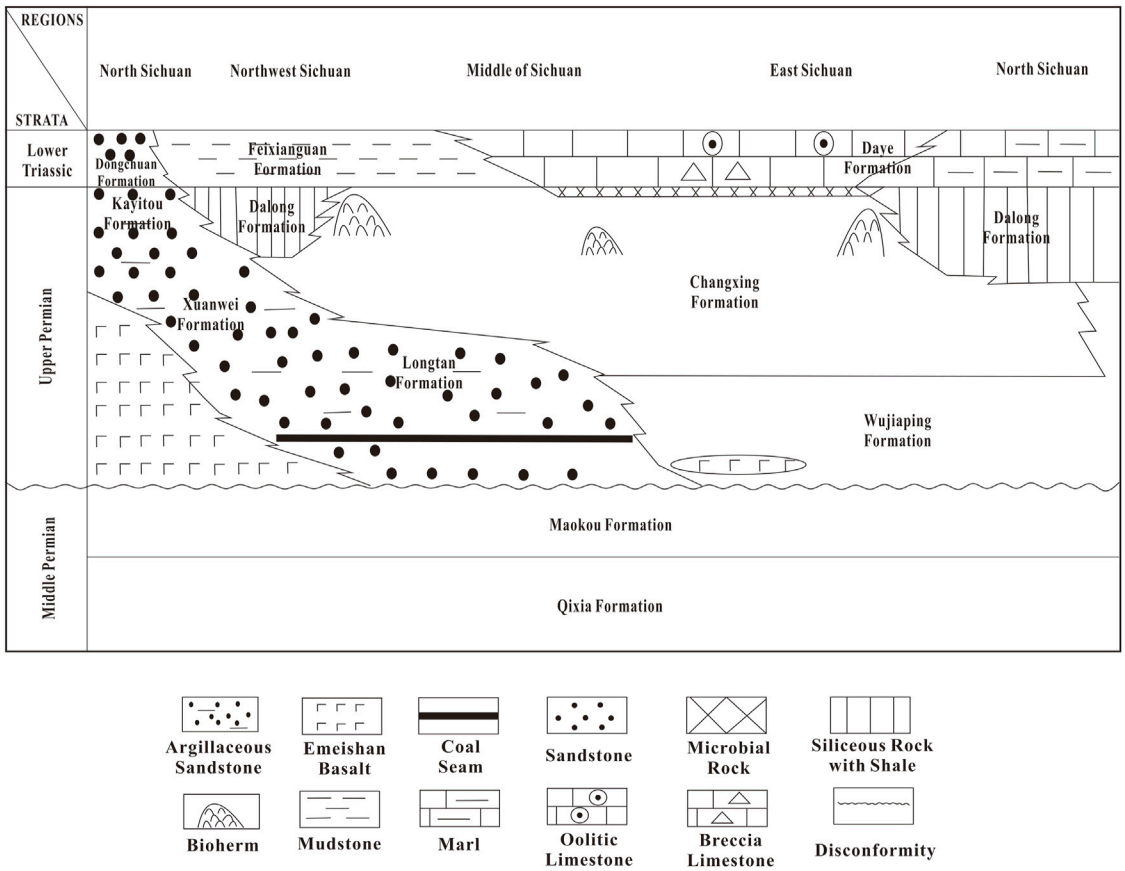

FIGURE 2 | Stratigraphic division of Sichuan Basin (modified after Yang, 2016).

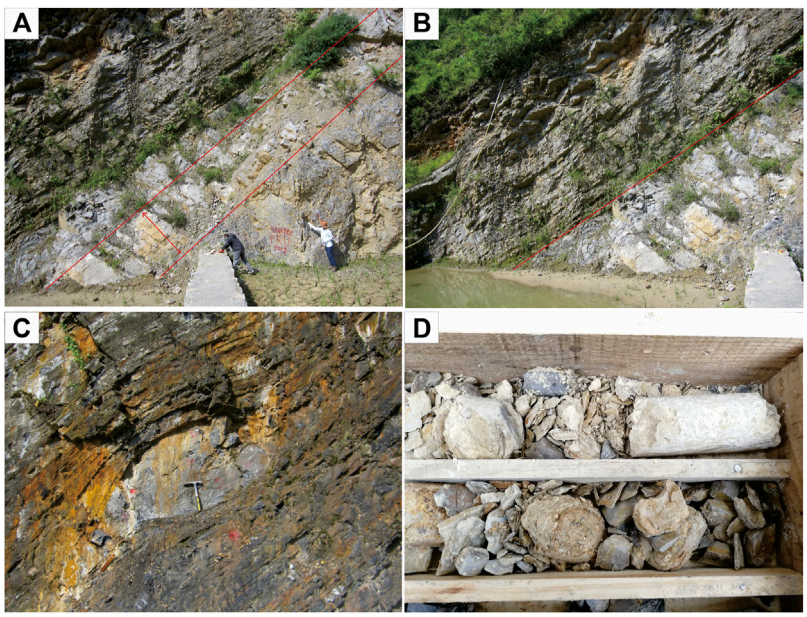

FIGURE 3 | Longfeng quarry section near Shangsi, Guangyuan.

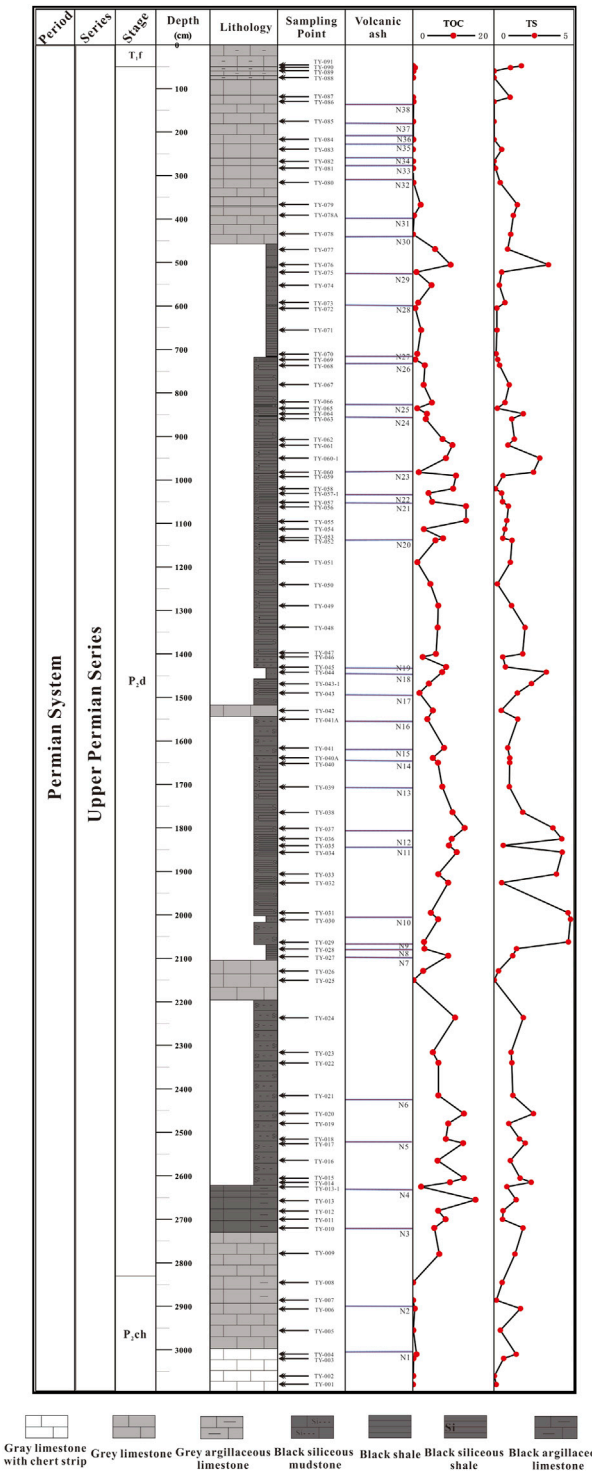

FIGURE 4 | Longfeng quarry profile sampling location and sample TOC and TS data.

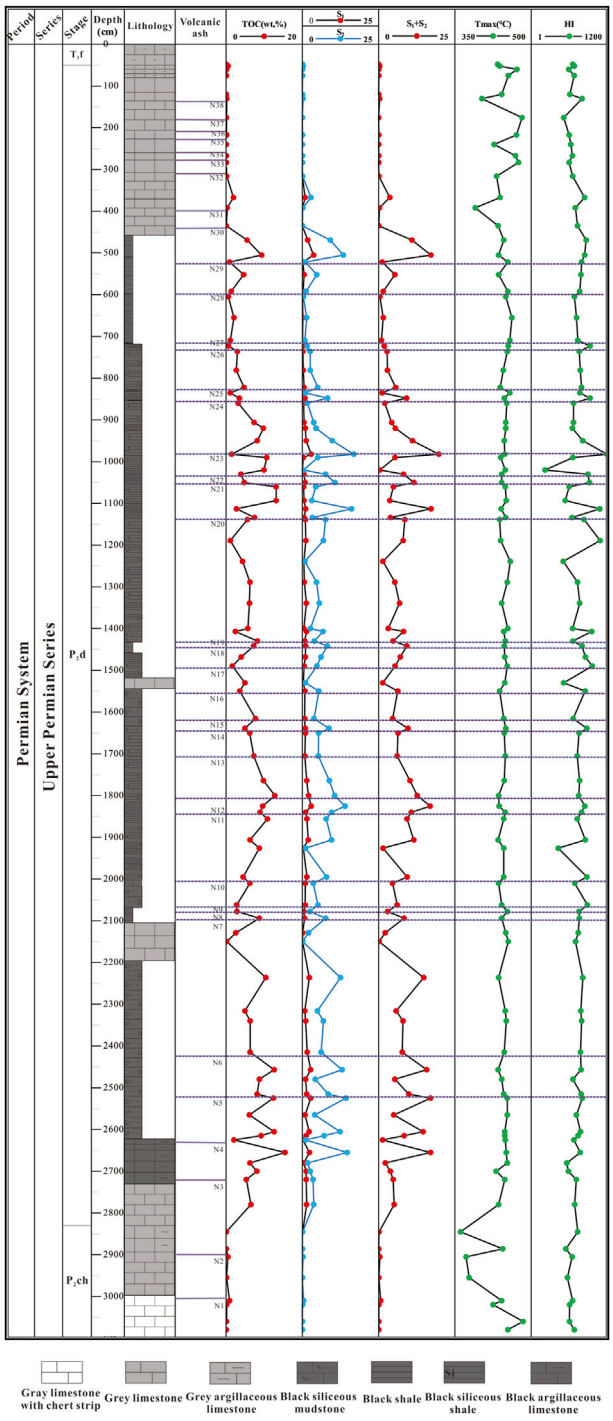

FIGURE 5 | Rock pyrolysis data of Longfeng quarry profile samples.

volcanic ash layer, TOC increases slightly, but S2 and HI increase rapidly. This phenomenon, different from the common viewpoint that TOC should change in the same trend as S2, may be attributed to the fact that the huge input of insoluble substances by volcanic eruption into water greatly diluted TOC, while the facilitation of volcanic ash to the growth of hydrocarbon-forming organisms (at this time, the hydrocarbon-generating potential was increasing) resulted in the increase of S2. Moreover, a higher HI represents a higher

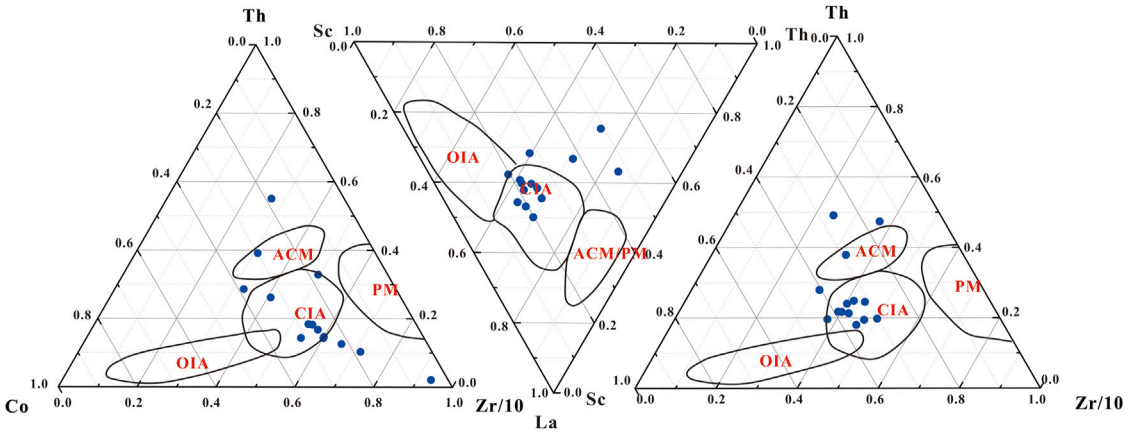

FIGURE 6 | Tectonic setting of Permian Dalong Formation in Longfeng quarry section. (Bhatia, 1984; Roser and Korsch, 1988). OIA, ocean island arc; CIA, continental island arc; ACM, active continental margin; PM, passive margin.

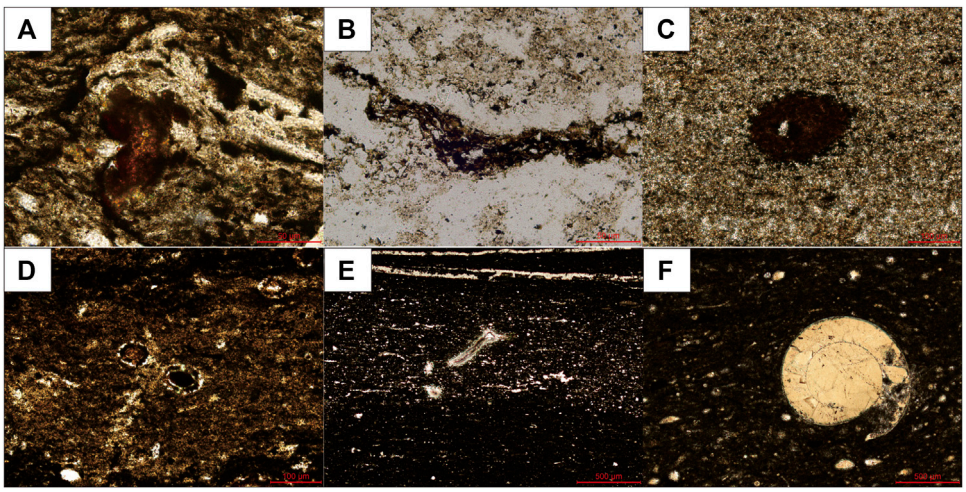

FIGURE 7 | Biological fossils of Dalong Formation in Longfeng quarry section. **(A)** Planktonic algae; **(B)** benthic algae; **(C)** acritarchs; **(D)** radiolaria; **(E)** sponge spicule; and **(F)** foraminifera.

hydrocarbon-generating capacity. For example, bacteria and algae show high HI value due to their high lipid contents, and the change in types of hydrocarbon-forming organisms/organic matters can be expressed by HI (Peters et al., 2005). The samples above the volcanic ash layer reflect apparently increasing HI, indicating that the association of hydrocarbon-forming organisms and the proportions of organisms changed, with planktonic algae taking a higher share in hydrocarbon-forming organisms (Meng et al., 2022).

5.2 Tectonic Setting of Source Rocks in Dalong Formation

Previous studies have shown that some trace elements (e.g., Th, V, Co., and Zr) have stable properties and are not easy to migrate. The triangular diagrams of Th–Co–Zr/10, La–Th–Sc, and Th–Sc–Zr/10 can be used to distinguish the tectonic setting of the provenance (Ross and Bustin, 2009).

It can be seen from **Figure 6** that the samples of the Dalong Formation are mainly distributed in ACM and CIA. The data processing results correspond to the frequent plate activity during the deposition of the Late Permian Dalong Formation in the Sichuan Basin, and they are consistent with the characteristics of frequent volcanic activity and multi-stage distribution of volcanic ash in the study area. Comprehensive analysis indicates that the element mass fraction of the Dalong Formation is closer to the characteristic values of ACM and CIA. It is thus determined that the Dalong Formation was deposited under a tectonic setting of ACM and CIA. This conclusion is consistent with the research results of Liu et al. (2019) on the Dalong Formation in western Hubei Province, which is covered in the same tectonic range as Shangsi of Guangyuan, both in the central-north of the Yangtze plate.

5.3 Regular Vertical Distribution of Hydrocarbon-Forming Organisms in Dalong Formation

Abundant fossils of biota (including plankton and benthos) and other organisms (including sponge spicule, ammonite, and brachiopod) are identified in the Dalong Formation of the Longfeng quarry section.

Combined with previous studies and the thin section identification of organic petrology in this study, it is found that the hydrocarbon-forming organisms of the Dalong Formation are mainly planktonic and benthic. The thin sections reveal the thalluses of planktonic algae (**Figure 7A**) and benthic algae (**Figure 7B**), as well as biological fossils, such as acritarchs that are suspected to be derived from planktonic algae (**Figure 7C**), radiolarians (**Figure 7D**), sponge spicules (**Figure 7E**), and planktonic foraminifera (**Figure 7F**).

The Dalong Formation in Shangsi, as a whole, was deposited in shallow sea and shelf facies sedimentary environment (Hu G. et al, 2021). Most of the fauna lived in the lower part of shallow sea, and the association and distribution of organisms show that the Dalong Formation was always in a reducing and low-energy environment during its deposition.

The hydrocarbon-forming organisms in Dalong Formation vary obviously in vertical direction. In the lower part near the Changxing Formation, there are few volcanic ash layers, which acted at large time intervals, giving rise to organisms with low content and single types (dominantly minor radiolarians and some algal fragments). In the middle part, due to frequent volcanic activity, multiple volcanic ash layers with smaller spacing appeared, and the organism association is dominated by radiolarians, calcium spheres, and algal debris, of which radiolarians take a very high proportion in the biological community because siliceous organisms could grow without competitors, especially in the water area with sufficient clay supply (Cai et al., 2011). In the upper part, there are also numerous volcanic ash layers, and organisms are abundant in quantity and species, which are mainly foraminifera, gastropods, conodonts, calcium spheres, and radiolarians, as well as association of other biological fossils; the proportion of radiolarians is high, but far less than that in the middle part (**Figure 8**).

5.4 Volcanic Activity-Related Development of Hydrocarbon-Forming Organisms in Dalong Formation

A total of 98 shale samples were taken from 30.80 m thick strata in the Longfeng quarry section, and revealed 38 layers of volcanic ash and tuff, including 36 layers in the Dalong Formation. Considering the higher accuracy of sampling than thin section observation, typical samples above and below the representative N17–N19 and N22 volcanic ash (tuff) layers were selected for depiction. These layers were chosen because of the following reasons: 1) TOC and TS increase significantly after the deposition of these layers; 2) TOC and TS increase step-like continuously due to the N17–N19 volcanic ash layers which are adjacent with each other and thus can be analyzed to verify whether the influence of volcanic ash layers can be stacked; and 3) TOC curve shows a trend of sharp increase–slow increase–sharp

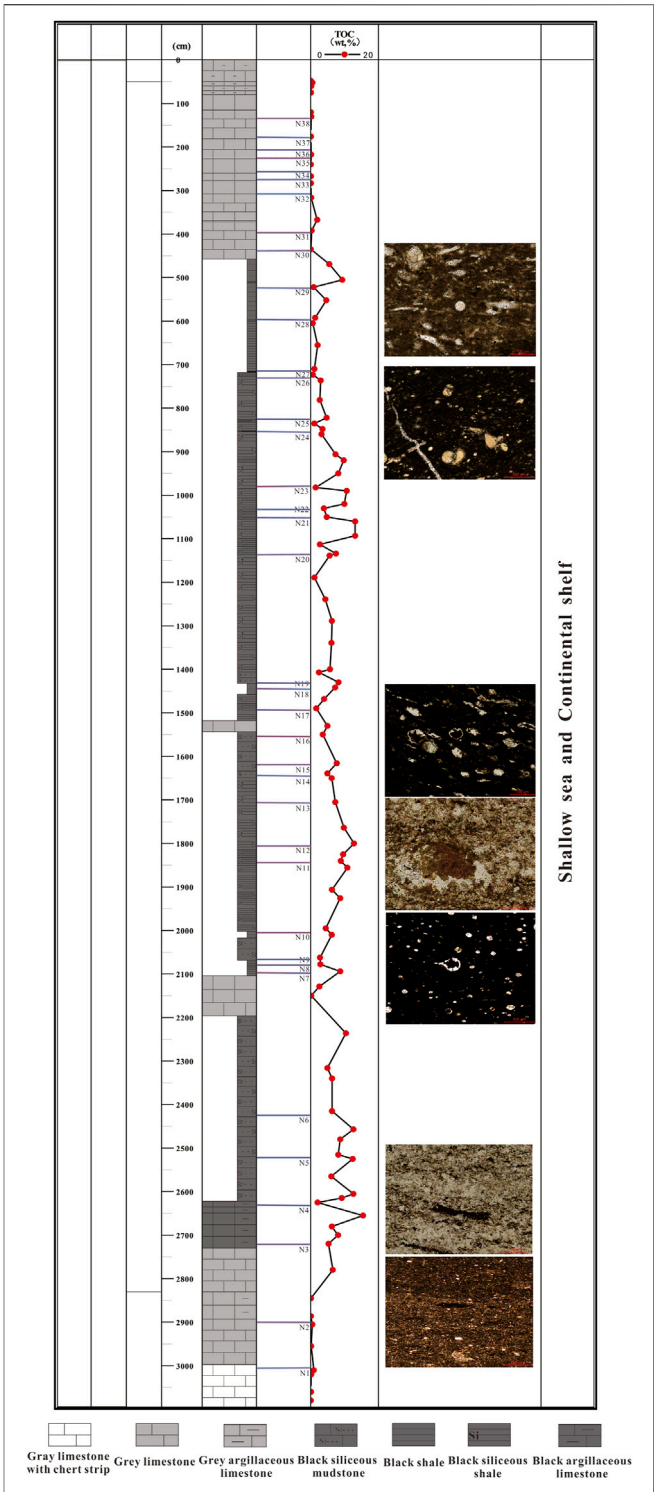

FIGURE 8 | Vertical variation of organism types in Dalong Formation in Longfeng quarry section.

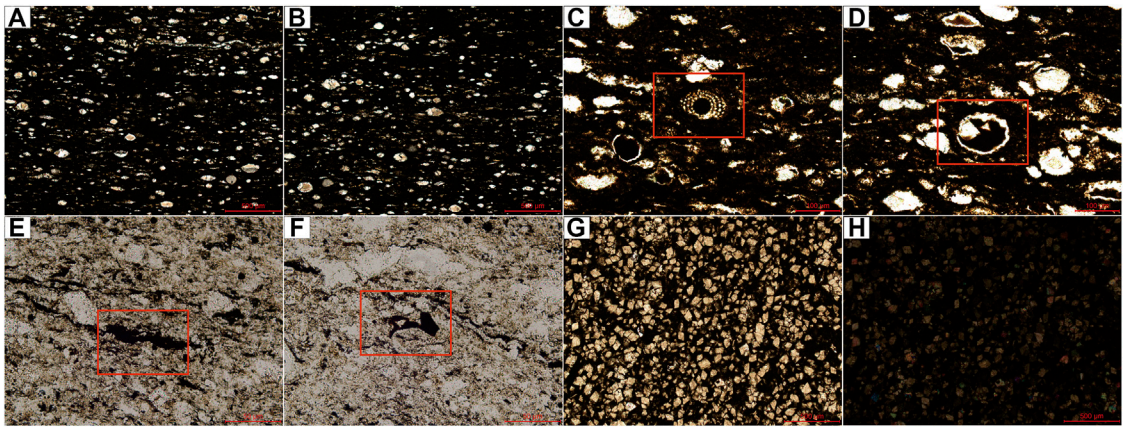

FIGURE 9 | Hydrocarbon-forming organisms above and below N17–N19 volcanic ash layers. **(A,B)** Radiolaria, above N19; **(C)** foraminifera, above N18; **(D)** radiolaria, above N18; **(E)** algal debris, above N17; **(F)** biological nail plate, above N17; **(G,H)** stellate organic matter, below N17.

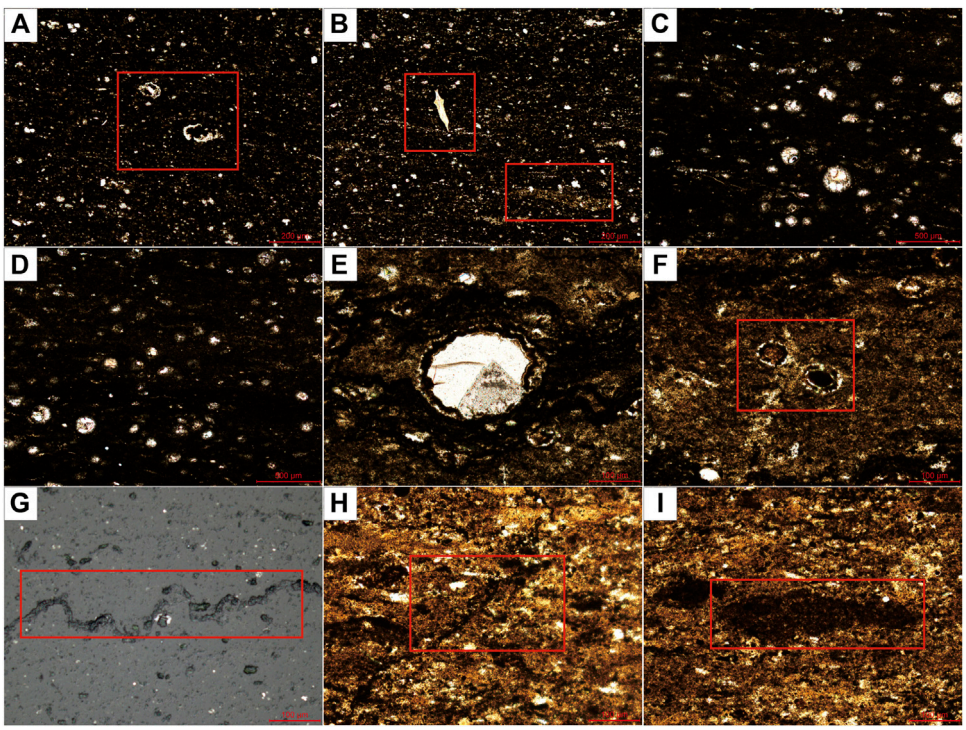

FIGURE 10 | Hydrocarbon-forming organisms above and below N22 volcanic ash layer. **(A,B)** Biological nail plate and algal debris, above N22 and close to N23; **(C–F)**: radiolaria, above N22; **(G)** worm trail, below N22; **(H,I)** benthic algal thallus, below N22.

decrease, under the control of the N22 volcanic ash layer, which can be analyzed to find out the reason why this TOC trend occurs.

5.4.1 Different Hydrocarbon-Forming Organisms Below and Above Volcanic Ash Layers

The N17, N18, and N19 volcanic ash (tuff) layers are densely distributed, with TOC increasing in a step-like manner, which may be due to the stacked effect of volcanic ash. Below N17, TOC is 1.65%; above N17, TOC increases to 3.96%, nearly doubled. After N18, TOC increases again to 7.25%. After N19, TOC increases slightly again, from 7.25% to 8.22%. Below and above N17 and N18, there are obvious changes in the number and type of hydrocarbon-forming organisms. Below N17, TOC is low, thin sections are rarely observed with traces of biological fossils and biological activities, and organic matters are dispersed and stellate embedded in the mineral matrix (**Figures 9A,B**).

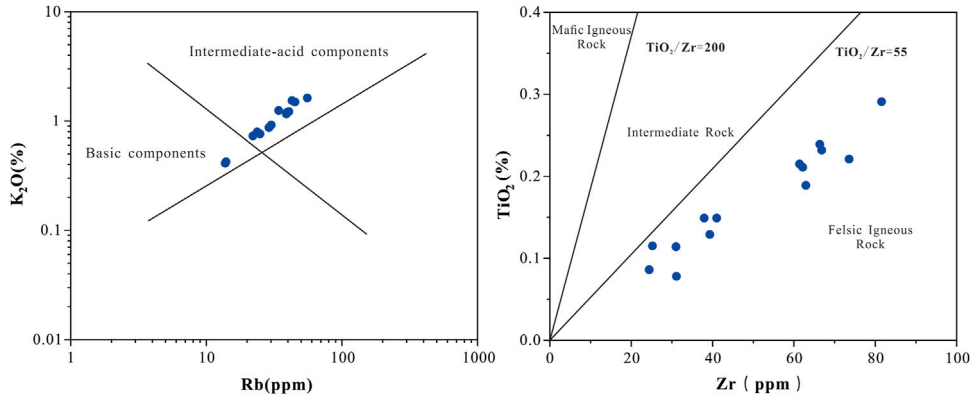

FIGURE 11 | K_2O–Rb and TiO_2–Zr diagram of Longfeng quarry section.

TABLE 2 | Components of magma by types.

Magma type	SiO_2 content	Features of other components
Ultrabasic magma	<45%	Rich Fe and Mg, low Ca, and poor K and Na
Basic magma	45%–53%	High Fe, Mg, and Ca and low K and Na
Intermediate magma	53%–66%	Moderate Fe, Mg, Ca, Na, and K
Acidic magma	>66%	Low Fe, Mg, and Ca and high K and Na

Above N17, obvious biological fossils are observed, mainly broken biological nail plates of suspected benthic organisms (**Figure 9C**) and fragments of benthic algae and thallus (**Figure 9D**). Near the top of the Dalong Formation, the major observed organisms are foraminifera and radiolarians (**Figures 9E,F**). After N18, the concentration of nutrient elements further increases and the number of hydrocarbon-forming organisms increases sharply; thin sections show a large number of radiolarians with great density and many biological trace fossils such as calcium spheres and algal debris (**Figures 9G,H**).

After N22, TOC also changes significantly—from 3.90% to 9.95%, nearly tripled. It is noteworthy that such sharp increase of TOC lasted only for a short period, followed by a slow increase to 10.65% and finally a sharp decrease to 1.48%. With the thin section observation, this TOC variation is speculated to occur in the process as follows: the content of nutrient elements in water surged in a short time after the partial dissolution of volcanic ash, which brought quickly a large number of nutrient elements to planktons and benthos, making them grow rapidly in quantity; when the biological density approached the level the water could bear, the growth of these hydrocarbon-forming organisms slowed down apparently; after the biological density reached the extreme level the environment could carry, the organisms no longer increased, and massive organisms died as a result of huge oxygen consumption in biological respiration.

The aforementioned speculation was verified by thin section observations of samples from rocks above and below N22. A small quantity of scattered fragments of planktonic algae, foraminifera, radiolarians, and traces of biological activities were observed in the stratum below N22 (**Figures 10A–C**). In the stratum above N22, there are much more hydrocarbon-forming organisms, which are mainly radiolarians, and also abundant siliceous radiolarian shells (**Figures 10D,G**), which is also one of the reasons for the extremely developed siliceous rocks in the Dalong Formation of Longfeng quarry section. After a period since the deposition of N22, TOC decreased rapidly, and only sporadic biological nail plates and traces of algae (e.g., algal debris and leaf residues) were developed (**Figures 10H,I**), as evidenced by the corresponding thin sections.

5.4.2 Factors Affecting the Development of Hydrocarbon-Forming Organisms

There is sufficient evidence to justify the positive impact of volcanic ash on the development of hydrocarbon-forming organisms. For example, the eruption of Kasatochi volcano in 2008 prompted the algae bloom in an area of (1.5–2.0) × 106 km^2 in northeastern Pacific Ocean (Langmann, 2013). However, it is still not clear why and how the hydrocarbon-forming organisms were affected by volcanic ash. Here, the possible factors are preliminarily discussed from the perspective of element geochemistry.

5.4.2.1 Magmatic Properties

Generally, the Emeishan large igneous province is mainly composed of subalkaline and meta-alkaline basic volcanic lavas and pyroclastic rocks (Mei, 1973; Meng et al., 2018). However, acidic volcanic rocks were also exposed in the late stage of

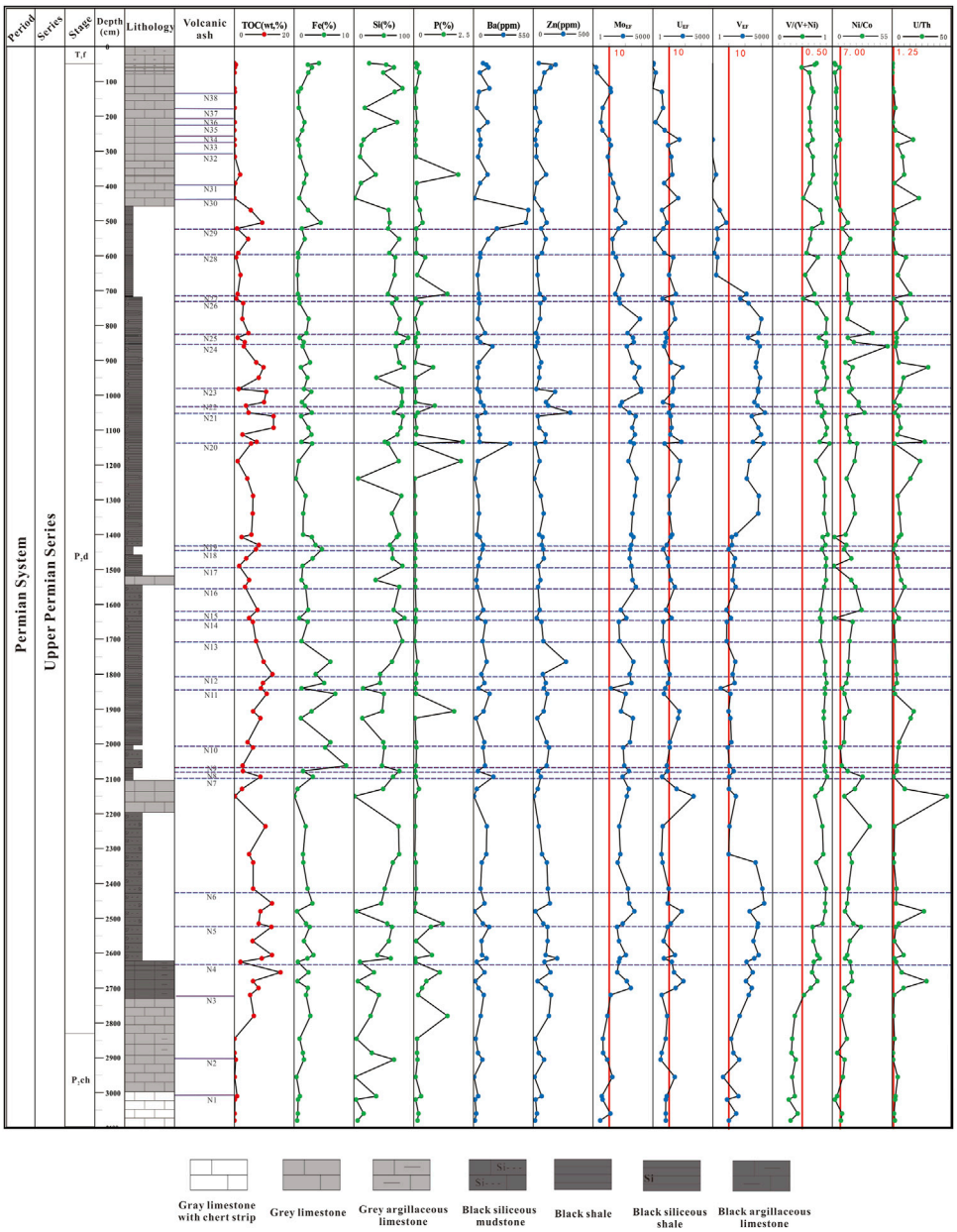

FIGURE 12 | Geochemical element indexes of Longfeng quarry profile.

magmatism. They coexist with basic volcanic rocks and show the bimodal features (Xu et al., 2010).

Acidic volcanic rocks are mainly trachyte and rhyolite. They are somewhat different from basic basalt in composition. Trachyte contains significantly less MgO, Fe2O3, P2O5, TiO2, and CaO and reflects obvious Eu negative anomaly and strong loss of Sr, Ti, and other elements (Xu et al., 2013). Different types of magma are distinct in components (Hu et al., 2019).

Based on the chart of Taylor et al. (1985), the K_2O–Rb and $Zr–TiO_2$ diagrams were obtained from the data of Longfeng quarry section (**Figure 11**). It can be seen that K_2O accounts for 0.1%–8.0%, and Rb is concentrated at 10–100 ppm, it shows that the three symbolic volcanic ash layers mentioned above are intermediate-acid components. According to the $Zr–TiO_2$ diagram, the three marked volcanic ash layer combinations of Dalong formation are dominated by felsic igneous rocks, which also indicate acidic magma. Combined with the compound composition of the Dalong Formation and the components of magma in **Table 2**, it can be basically determined that the volcanic ash affecting the development of hydrocarbon-forming organisms in the Longfeng quarry section is mainly acidic magma.

It is found that the magma of N17–N19 and N22 all fall in the region of intermediate-acid components. The intermediate-acid

magma can play a better role in promoting the development of hydrocarbon-forming organisms, possibly because they could provide sufficient and comprehensive nutritional elements, including Si, Fe, Mg, Ca, Na, and K, of which Fe is decisive for biological growth.

5.4.2.2 Different Element Inputs

The deposition of N22, TOC, Si, Zn, and Mo increased (**Figure 12**), which proves that volcanic ash can indeed cause the increase of element concentration in a certain period and promote the growth of hydrocarbon-forming organisms. However, Fe and P decreased to some extent, which is not attributable to the probability that the volcanic ash did not carry these elements, but more likely that these elements were consumed faster than that before volcanic ash deposition. Particularly, the decrease of P lasted for a long time, while the decrease of Fe only lasted for a short time, possibly because Fe was not the controlling element at this time, but the large input of Zn promoted the utilization of phosphate by algae, resulting in the reduction of P. Referring to **Figure 10**, after the deposition of N22, more traces of benthic algae, planktonic algae, and radiolarian were found in the stratum. After the deposition of N17, TOC, Fe, Cu, Zn, and Mo all increased greatly, P was always at a low level, and Si decreased significantly, indicating that P was the most likely element restricting the growth of organisms at this time, and the input of Si enriched the nutrients for hydrocarbon-forming organisms (Meng et al., 2009). Referring to **Figure 8**, after volcanic ash deposition, the number of radiolarians and foraminifera of benthic and planktonic species increased owing to the input of Si, Mo, Fe, and other elements.

5.4.2.3 Time Interval of Volcanic Activities

Observation of spacing between volcanic ash layers indicates that during the deposition of N30–N38 volcanic ash layers, the curves of TOC and elements show minor variation. However, this phenomenon rarely occurs in other layers, and it is presumably caused by the too short time interval of volcanic activities. On the one hand, the deposition of multiple volcanic ash layers in a short time would cause the incomplete release of nutrients, and exert an inconspicuous effect in promoting the growth of hydrocarbon-forming organisms. On the other hand, multiple volcanic activities in a short time might induce a higher concentration of toxic substances inhibiting the growth of hydrocarbon-forming organisms in water. The microscopic identification results of hydrocarbon-forming organisms shown in **Figure 10** also suggest that algae is very rare in the thin-section view of samples from above N22 with frequent volcanic activities (**Figures 10A–H**), while algae can be seen in samples from below N22 (**Figures 10G–I**). Nonetheless, further efforts are needed to determine which action ultimately led to the TOC reduction in layers with dense volcanic ash.

6 CONCLUSION

(1) The samples of the Dalong Formation taken from the Longfeng quarry section in Shangsi of Guangyuan, Sichuan Basin, were analyzed in light of major trace elements, the enrichment coefficients of paleo-productivity indicator elements (N, P, and Fe etc.) and redox indicator elements (Mo, U, and V), and V/(V + Ni), Ni/Co, and U/Th. It is found that volcanic activity contributed to the increase of TOC and made the sedimentary environment highly reducing.

(2) The hydrocarbon-generating materials of the Dalong Formation include benthic algae, planktonic algae, acritarchs, radiolarians, and foraminifera, of which radiolarians take a high proportion. Vertically, at the bottom of the Dalong Formation, hydrocarbon-forming organisms are small in quantity and single in types; in the middle part, hydrocarbon-forming organisms are dominated by plankton and benthos, with radiolarians as the biological fossil with the largest proportion; in the middle–upper part, hydrocarbon-forming organisms are mainly plankton and acritarchs, with abundant foraminifera and broken nail plates of various organisms.

(3) According to the analysis of the components of magma formed by volcanic eruptions in different periods during the deposition of the Dalong Formation, the magma type has an impact on the development of hydrocarbon-forming organisms. It is preliminarily determined that the intermediate (intermediate-acid) magma has a better effect on promoting the development of hydrocarbon-forming organisms. In addition to magmatic properties, different element inputs and time intervals of volcanic activities may have significant impact on the number and types of hydrocarbon-forming organisms. Specifically, different element inputs would induce the development of different aquatic plankton and benthos. Too small time interval of volcanic activities might make the nutrient elements of volcanic ash fail to release completely, or the accumulation of elements inhibiting the development of hydrocarbon-forming organisms brought by volcanic ash might result in the worse growth of hydrocarbon-forming organisms.

DATA AVAILABILITY STATEMENT

The original contributions presented in the study are included in the article/supplementary material; further inquiries can be directed to the corresponding authors.

AUTHOR CONTRIBUTIONS

CZ carried out the experiment and wrote the manuscript. QM designed the whole research, set up the tech geological model, and modified the manuscript. ZS analyzed other paleontology other than algae, such as foraminifera. XT analyzed the source rock type and the favorable factors for organic matter enrichment. QP analyzed the characteristics of algae. DL analyzed the sedimentary environment, and DZ and JYL jointly processed the primary color characteristics of the rock. JCL collected samples and performed pretreatment. BJ systematically processed the elemental analysis data.

FUNDING

This work is jointly funded by the National Key R&D Program (2019YFA0708504), the National Natural Science Foundation Project (41872164), and the Open Fund of the State Key Laboratory of Organic Geochemistry (SKLOG202125).

ACKNOWLEDGMENTS

This work was completed with the help of Professor Hu Guang of Southwest Petroleum University in treatment and identification of hydrocarbon-forming organisms and the assistance of Yu Xin of Peking University in field outcrop measurement.

REFERENCES

Bhatia, M. R. (1984). Composition and Classification of Paleozoic Flysch Mudrocks of Eastern Australia: Implications in Provenance and Tectonic Setting Interpretation. *Sediment. Geol.* 41, 249–268. doi:10.1016/0037-0738(84)90065-4

Cai, X. F., Feng, Q. L., Gu, S. Z., and Luo, Z. J. (2011). Regressive Shelf Facies: an Important Part of the Formation of Source Rocks—Taking the Dalong Formation of the Upper Permian on the Northern Margin of the Middle and Upper Yangtze Region as an Example. *Oil gas Geol.* 32, 29–37.

Du, J. X., Shi, W. W., Zhou, H., Wang, Q. L., Xia, Q. J., et al. (2014). Zircon Chronology and Formation Model of Volcanic Rocks in Nanpu Sag, Bohai Bay Basin. *Oil Gas Geol.* 35, 742–748.

Duggen, S., Croot, P., Schacht, U., Hoffmann, L., and Hoffmann, L. (2000). Subduction Zone Volcanic Ash Can Fertilize the Surface Ocean and Stimulate Phytoplankton Growth: Evidence from Biogeochemical Experiments and Satellite Data. *Geophys. Res. Lett.* 34, 1–5. doi:10.1029/2006GL027522

Duggen, S., Croot, P., Schacht, U., and Hoffmann, L. (2007). Subduction Zone Volcanic Ash Can Fertilize the Surface Ocean and Stimulate Phytoplankton Growth: Evidence from Biogeochemical Experiments and Satellite Data. *Geophys. Res. Lett.* 34, 5–1612. doi:10.1029/2006GL027522

Fu, X. D., Qin, J. Z., Teng, G. E., and Wang, X. F. (2010). Evaluation of Source Rocks of Dalong Formation of Upper Permian in the Northern Margin of Sichuan Basin. *Pet. Exp. Geol.* 32, 566–571.

Gao, Y., Wang, P., Cheng, R., Wang, G., Wan, X., Wu, H., et al. (2009). Description of Cretaceous Sedimentary Sequence of the First Member of the Qingshankou Formation Recovered by CCSD-SK-Is Borehole in Songliao Basin: Lithostratigraphy, Sedimentary Facies, and Cyclic Stratigraphy. *Earth Sci. Front.* 16, 314–323. doi:10.1016/s1872-5791(08)60081-0

Govindaraju, K. (1994). 1994 Compilation of Working Values and Sample Description for 383 Geostandards. *Geostand. Newslett* 18, 1–158. doi:10.1046/j.1365-2494.1998.53202081.x-i1

Hu, D., Wang, L., Zhang, H., Duan, J., Xia, W., Liu, Z., et al. (2021a). Discovery of Carbonate Source Rock Gas Reservoir and its Petroleum Geological Implications: A Case Study of the Gas Reservoir in the First Member of Middle Permian Maokou Formation in the Fuling Area, Sichuan Basin. *Nat. Gas. Ind. B* 8 (1), 13–23. doi:10.1016/j.ngib.2020.07.001

Hu, G., He, F., Mi, J., Yuan, Y., and Guo, J. (2021b). The Geochemical Characteristics, Distribution of Marine Source Rocks and Gas Exploration Potential in the Northwestern Sichuan Basin, China. *J. Nat. Gas Geoscience* 6 (4), 199–213. doi:10.1016/j.jnggs.2021.07.004

Hu, Z. Y., Fu, W., Luo, P., Cai, Q., and Feng, M. (2019). Symbiotic Enrichment Characteristics and Genesis of Ilmenite and Rare Earth in Igneous Weathering Crust in Southeast Guangxi. *Rare earth* 40, 16–27.

Langmann, B. (2013). Volcanic Ash Versus Mineral Dust: Atmospheric Processing and Environmental and Climate Impacts. *Isrn Atmos. Sci.* 2013, 1–17. doi:10.1155/2013/245076

Lee, C.-T. A., Jiang, H., Ronay, E., Minisini, D., Stiles, J., and Neal, M. (2018). Volcanic Ash as a Driver of Enhanced Organic Carbon Burial in the Cretaceous. *Sci. Rep.* 8. doi:10.1038/s41598-018-22576-3

Li, G. Y. (2010). *Formation Conditions and Main Controlling Factors of Upper Carboniferous Volcanic Rock Reservoir in Malang Sag*. Santanghu Basin. Beijing: China University of Geosciences (Beijing) Press.

Li, J., Yang, S., Qi, Z., Zhao, G., Yin, B., and Mo, F. (2020). A Calculation Model for Water Breakthrough Time of Gas Wells in Gas Reservoirs with Edge Water Considering Interlayer Heterogeneity: A Case Study of the Lower Triassic Feixianguan Gas Reservoirs in the Puguang Gas Field. *Nat. Gas. Ind. B* 7 (6), 631–638. doi:10.1016/j.ngib.2020.04.005

Li, W., Liu, J. J., Deng, S. H., Zhang, B. M., and Zhou, H. (2015). Nature and Function of Tectonic Movement in Sichuan Basin and its Adjacent Areas from Late Sinian to Early Cambrian. *J. petroleum* 36, 546–556.

Liu, Q., Jin, Z., Liu, W., Lu, L., Meng, Q., Tao, Y., et al. (2013). Presence of Carboxylate Salts in Marine Carbonate Strata of the Ordos Basin and Their Impact on Hydrocarbon Generation Evaluation of Low TOC, High Maturity Source Rocks. *Sci. China Earth Sci.* 56, 2141–2149. doi:10.1007/s11430-013-4713-3

Liu, Q., Li, P., Jin, Z., Sun, Y., Hu, G., Zhu, D., et al. (2022). Organic-rich Formation and Hydrocarbon Enrichment of Lacustrine Shale Strata: A Case Study of Chang 7 Member. *Sci. China Earth Sci.* 65, 118–138. doi:10.1007/s11430-021-9819-y

Liu, Q., Qin, S., Li, J., Liu, W., Zhang, D., Zhou, Q., et al. (2008). Natural Gas Geochemistry and its Origins in Kuqa Depression. *Sci. China Ser. D-Earth Sci.* 51, 174–182. doi:10.1007/s11430-008-5003-3

Liu, Q., Zhu, D., Jin, Z., Liu, C., Zhang, D., and He, Z. (2016). Coupled Alteration of Hydrothermal Fluids and Thermal Sulfate Reduction (TSR) in Ancient Dolomite Reservoirs - an Example from Sinian Dengying Formation in Sichuan Basin, Southern China. *Precambrian Res.* 285, 39–57. doi:10.1016/j.precamres.2016.09.006

Liu, Q., Zhu, D., Jin, Z., Meng, Q., and Li, S. (2019b). Influence of Volcanic Activities on Redox Chemistry Changes Linked to the Enhancement of the Ancient Sinian Source Rocks in the Yangtze Craton. *Precambrian Res.* 327, 1–13. doi:10.1016/j.precamres.2019.02.017

Liu, Q., Zhu, D., Meng, Q., Liu, J., Wu, X., Zhou, B., et al. (2019a). The Scientific Connotation of Oil and Gas Formations under Deep Fluids and Organic-Inorganic Interaction. *Sci. China Earth Sci.* 62, 507–528. doi:10.1007/s11430-018-9281-2

Liu, W. Q., Qiao, Y., Bo, J. F., Mu, C. L., Tong, J. N., et al. (2019). Geochemical Characteristics of Argillaceous Rocks of Dalong Formation of Upper Permian in Enshi Area, Western Hubei and its Indication to Weathering, Provenance and Tectonic Setting. *J. Lanzhou Univ. Nat. Sci. Ed.* 55, 158–167.

Lyu, C., Zhang, Y., Li, C., Chen, G., Zhou, Q., Ma, M., et al. (2020). Pore Characterization of Upper Ordovician Wufeng Formation and Lower Silurian Longmaxi Formation Shale Gas Reservoirs, Sichuan Basin, China. *J. Nat. Gas Geoscience* 5 (6), 327–340. doi:10.1016/j.jnggs.2020.11.002

Ma, Y. S., Mou, C. L., Guo, X. S., Tan, Q. Y., and Yu, Q. (2006). Sedimentary Characteristics and Sedimentary Pattern of Changxing Period in Northeast Sichuan Basin. *Geol. Rev.*, 1, 25–29.

Mei, H. J. (1973). Relationship between Petrochemical Characteristics of Two Series of Dark Rock Abyss Differentiation in Southwest China and Iron Nickel Mineralization. *J. Geochem.*, 4, 219–253.

Meng, Q., Jing, J., Li, J., Zhu, D., Zou, A., Zheng, L., et al. (2018). New Exploration Strategy in Igneous Petroliferous Basins - Enlightenment from Simulation Experiments. *Energy Explor. Exploitation* 36, 971–985. doi:10.1177/0144598718758338

Meng, Q., Pang, Q., Hu, G., Jin, Z., Zhu, D., Liu, J., et al. (2022). Rhyolitic Ash Promoting Organic Matter Enrichment in a Shallow Carbonate Platform: A Case Study of the Maokou Formation in Eastern Sichuan Basin. *Front. Earth Sci.* 10. doi:10.3389/feart.2022.879654

Meng, Q. Q., Ma, B. L., Zou, A. D., and Li, Z. F. (2009). Comparison of Characteristics of Hydrocarbon Generation for Different Alga. *Petroleum Geol. Exp.* 30, 291.

Mukhopadhyay, P., Hagemann, H., and Jr, G. (1985). Characterization of Kerogens as Seen Under the Aspect of Maturation and Hydrocarbon Generation. *Erdol Kohle Erdgas Petrochem.* 38, 7–18.

Pang, Q. (2019). *Characteristics of Hydrocarbon-Generating Materials of Wufeng Formation and Longmaxi Formation in Changning Area and Their Influence on Organic Matter Pores*. Chengdu: Southwest Petroleum University Press.

Peters, K. E., Peters, K. E., Walters, C. C., and Moldowan, J. (2005). *The Biomarker Guide*. Cambridge, United Kingdom: Cambridge University Press.

Qiu, X. W., Liu, C. Y., Mao, G. Z., Deng, Y., and Wang, F. F. (2010). Enrichment Characteristics of Th Element in Tuff Interlayer of Yanchang Formation of Upper Triassic in Ordos Basin. *Geol. Bull.* 29, 1185–1191.

Qiu, Z., Zou, C., Wang, H., Dong, D., Lu, B., ChenLiu, Z. D. X., et al. (2020). Discussion on the Characteristics and Controlling Factors of Differential Enrichment of Shale Gas in the Wufeng-Longmaxi Formations in South China. *J. Nat. Gas Geoscience* 5 (3), 117–128. doi:10.1016/j.jnggs.2020.05.004

Ran, Q., Tao, X., Xu, C., Zhang, L., Huang, T., Liu, S., et al. (2021). Fine Description of Ramp-type Small Bioherms and Breakthrough of "two Bioherms in One Well" in High-Yield Gas Wells: A Case Study of the Changxing Formation Small Bioherm Group in the Eastern Sichuan Basin. *Nat. Gas. Ind. B* 8 (4), 384–392. doi:10.1016/j.ngib.2021.07.009

Roser, B. P., and Korsch, R. J. (1988). Provenance Signatures of Sandstone-mudstone Suites Determined Using Discriminant Function Analysis of Major-Element Data. *Chem. Geol.* 67, 119–139. doi:10.1016/0009-2541(88)90010-1

Ross, D. J. K., and Bustin, R. M. (2009). Investigating the Use of Sedimentary Geochemical Proxies for Paleoenvironment Interpretation of Thermally Mature Organic-Rich Strata: Examples from the Devonian-Mississippian Shales, Western Canadian Sedimentary Basin. *Chem. Geol.* 260, 1–19. doi:10.1016/j.chemgeo.2008.10.027

Shan, X. L., Li, J. Y., Chen, S. M., Ran, Q. C., Chen, G. B., et al. (2014). Continental Underwater Volcanic Eruption and Influence on the Formation of High-Quality Source Rocks: a Case Study of Yingcheng Formation in Xujiaweizi Fault Depression, Songliao Basin. *Sci. China Earth Sci.* 44, 2637–2644.

Song, D. F., He, D. F., Wang, S. R., Li, D., Wang, Z. Y., et al. (2012). Evaluation of Carboniferous Source Rocks in Santanghu Basin. *Xinjiang Pet. Geol.* 3, 305–309.

Taylor, S., McLennan, S. M., Mclennan, J. R., and Hatch, J. S. (1985). The Continental Crust: Its Composition and Evolution Relationship between Inferred Redox Potential of the Depositional Environment and Geochemistry of the Upper Pennsylvanian (Missourian) Stark Shale Member of the Dennis Limestone, Wabaunsee County, Kansas. *U.S.A. Chem. Geol.* 99, 65–82.

Wu, L. G., Li, X. S., Guo, X. B., Luo, Q. S., Liu, X. J., et al. (2012). Diagenetic Evolution and Dissolution Pore Formation Mechanism of Shale Oil Reservoir of Lucaogou Formation in Malang Sag. *J. China Univ. Petroleum* 36, 38–43.

Xie, Z., Yang, C., Li, J., Zhang, L., Guo, J., Jin, H., et al. (2021). Accumulation Characteristics and Large-Medium Gas Reservoir-Forming Mechanism of Tight Sandstone Gas Reservoir in Sichuan Basin, China: Case Study of the Upper Triassic Xujiahe Formation Gas Reservoir. *J. Nat. Gas Geoscience* 6 (5), 269–278. doi:10.1016/j.jnggs.2021.10.001

Xu, Y.-G., Chung, S.-L., Shao, H., and He, B. (2010). Silicic Magmas from the Emeishan Large Igneous Province, Southwest China: Petrogenesis and Their Link with the End-Guadalupian Biological Crisis. *Lithos* 119, 47–60. doi:10.1016/j.lithos.2010.04.013

Xu, Y. G., He, B., Luo, Z. Y., and Liu, H. Q. (2013). Research Progress and Prospect of Igneous Provinces and Mantle Plumes in China. *Bull. mineral rock Geochem.* 32, 25–39.

Xue, P., Zhang, L., Liang, Q., Sun, X., Zhao, Q., and Qi, P. (2020). Thermodynamic Characteristics of CH4 Adsorption by Continental Shale: A Case Study of the Upper Triassic Yanchang Shale in the Yanchang Gasfield, Ordos Basin. *Nat. Gas. Ind. B* 7 (3), 269–277. doi:10.1016/j.ngib.2019.10.009

Yan, J. X., Ma, Z. X., Xie, X. N., Xue, W. Q., Li, B., et al. (2008). Subdivision of Permian Fossil Communities and Habitat Types in Northeast Sichuan, South China. *J. China Univ. Geosciences Engl. Ed.* 19, 441–450. doi:10.1016/S1002-0705(08)60049-7

Yang, W. (2016). *Study on the Evolution and Dynamic Mechanism of Marine Benthic Fauna in the Eastern Sichuan Basin in the Late Permian*. Chengdu: Southwest Petroleum University Press.

Yang, Y., Xie, J., Zhao, L., Huang, P., Zhang, X., Chen, C., et al. (2021). Breakthrough of Natural Gas Exploration in the Beach Facies Porous Dolomite Reservoir of Middle Permian Maokou Formation in the Sichuan Basin and its Implications: A Case Study of the Tridimensional Exploration of Well JT1 in the Central-Northern Sichuan Basin. *Nat. Gas. Ind. B* 8 (4), 393–401. doi:10.1016/j.ngib.2021.07.010

Yin, H. F., and Tong, J. N. (1995). Relationship between Sequence Stratigraphic Boundary and Chronostratigraphic Boundary. *Sci. Bull.* 40, 539–541.

Zhang, W., and Zhang, X. L. (1992). *Permian Reefs and Paleoecology in Southern China*, BeiJing: BeiJing Publishing House, 7, 157.

Zhang, W. Z., Yang, H., Peng, P. A., Yang, Y. H., Zhang, H., et al. (2009). Influence of Late Triassic Volcanic Activity on the Development of Chang 7 High-Quality Source Rocks in Ordos Basin. *J. Geochem.* 38, 573.

Zhou, L., Qian, Y., Zhang, L., Lan, X., Wu, Y., Wang, Q., et al. (2021). Seismic Prediction of Oolitic Beach Thin-Bed Reservoir Based on Favorable Facies Belt Constraints: Taking the Second Member of Feixianguan Formation in Jiulongshan Area, Northwest Sichuan, China. *J. Nat. Gas Geoscience* 6 (6), 329–344. doi:10.1016/j.jnggs.2021.12.002

Conflict of Interest: The authors declare that the research was conducted in the absence of any commercial or financial relationships that could be construed as a potential conflict of interest.

Publisher's Note: All claims expressed in this article are solely those of the authors and do not necessarily represent those of their affiliated organizations, or those of the publisher, the editors, and the reviewers. Any product that may be evaluated in this article, or claim that may be made by its manufacturer, is not guaranteed or endorsed by the publisher.

frontiers | Frontiers in Earth Science

TYPE Original Research
PUBLISHED 25 August 2022
DOI 10.3389/feart.2022.944701

OPEN ACCESS

EDITED BY
Dongming Zhi,
PetroChina, China

REVIEWED BY
Zhanfeng Qiao,
PetroChina Hangzhou Research Institute of Geology, China
Xiucheng Tan,
Southwest Petroleum University, China
Yuefeng Shen,
Hefei University of Technology, China

*CORRESPONDENCE
Youli Wan,
wanyouli@cdut.edu.cn
Jiashan Lin,
sumlin_2021@163.com

SPECIALTY SECTION
This article was submitted to Economic Geology, a section of the journal Frontiers in Earth Science

RECEIVED 15 May 2022
ACCEPTED 11 July 2022
PUBLISHED 25 August 2022

CITATION
Wan Y, Lin J, Zhao Z and Wang Z (2022), Origin of the dolomite in the Buqu Formation (Mid-Jurassic) in the south depression of the Qiangtang Basin, Tibet: Evidence from petrographic and geochemical constraints.
Front. Earth Sci. 10:944701.
doi: 10.3389/feart.2022.944701

Origin of the dolomite in the Buqu Formation (Mid-Jurassic) in the south depression of the Qiangtang Basin, Tibet: Evidence from petrographic and geochemical constraints

Youli Wan[1,2]*, Jiashan Lin[1,2]*, Zhan Zhao[1,2] and Zhonglin Wang[1,3]

[1]Key Laboratory of Sedimentary Basin and Oil and Gas Resources, Ministry of Natural and Resources, Chengdu, China, [2]Chengdu Center, China Geological Survey, Chengdu, China, [3]College of Earth Sciences, Chengdu University of Technology, Chengdu, China

The Qiangtang Mesozoic sedimentary basin is a new field of hydrocarbon exploration, in which the Buqu Formation dolostone reservoirs have attracted increasing attention in recent years. To determine the origin of these reservoirs, petrographic study, fluid inclusion thermometry dating, and C-O and Sr isotopic dating were performed. The results revealed the genesis and evolution of different types of dolomite matrix and cement, as follows: 1) The dolomite texture in the study area is closely related to its formation environment and process and can be categorized as primary fabric well-preserved dolomite (Rd1), primary fabric poorly-preserved dolomite, and dolomite filling. The primary fabric-poorly-preserved dolomite includes fine-grained euhedral dolomite (Rd2), fine-grained planar subhedral dolomite (Rd3), and medium-to coarse-grained anhedral dolomite (Rd4). The dolomite filling includes fine-grained planar subhedral cave-filling dolomite (Cd1) and medium-to coarse-grained anhedral, saddle dolomite (Cd2). 2) Rd1 has $\delta^{13}C$ ‰$_{PDB}$ of 3.42‰–4.23‰, $\delta^{18}O$‰$_{PDB}$ from −4.22‰ to −3.37‰, and $^{87}Sr/^{86}Sr$ of 0.707654–0.708176 and was formed in the contemporaneous or penecontemporaneous stage at low temperatures by mimic replacement related to seawater evaporation. Abundant supersaturated dolomitization fluids favored the preservation of its primary dolomite texture. 3) Rd2 has $\delta^{13}C$‰$_{PDB}$ of 3.18‰–4.11‰, $\delta^{18}O$‰$_{PDB}$ from −4.56‰ to −4.23‰, and $^{87}Sr/^{86}Sr$ (0.707525–0.708037), while Rd3 has $\delta^{13}C$‰$_{PDB}$ of 2.72‰–4.42‰, $\delta^{18}O$ ‰$_{PDB}$ from −6.57‰ to −5.56‰, and $^{87}Sr/^{86}Sr$ of 0.707432–0.707990. Both were formed at low temperatures in the shallow-burial stage, when the dolomitization fluid was mainly derived from seawater. Excessive dolomitization during the late shallow-burial stage caused the destruction of the dolomite crystals from euhedral to subhedral. 4) Rd4 has $\delta^{13}C$‰$_{PDB}$ of 3.24‰–4.14‰, $\delta^{18}O$‰$_{PDB}$ from −8.22‰ to −6.37‰, and $^{87}Sr/^{86}Sr$ of 0.707234–0.707884 and resulted from dolomitization or recrystallization at high temperatures in the medium-to deep-burial stage. The crystal curvature

was caused by high environmental temperatures. 5) Cd1 has $\delta^{13}C‰_{PDB}$ of 3.02‰, $\delta^{18}O‰_{PDB}$ of −5.13‰, and $^{87}Sr/^{86}Sr$ of 0.708147 and was formed during cavern filling before the shallow-burial stage. Cd2 has $\delta^{13}C‰_{PDB}$ of −0.09‰–3.38‰, $\delta^{18}O‰_{PDB}$ from −10.41‰ to −8.56‰, and $^{87}Sr/^{86}Sr$ of 0.708180–0.708876 and was related to the collisional orogeny between the Lhasa termite and the Qiangtang Basin in the late Early Cretaceous. Fluids in the overlying and underlying clastic strata of the Buqu Formation were driven by the thermal hot spot during compressional tectonic setting. These fluids caused negative shifts in the oxygen isotope compositions of the earlier dolomite.

KEYWORDS

dolomitization, dolomite texture, geochemistry, Buqu Formation, Qiangtang basin

1 Introduction

Dolostone reservoirs are an important target for carbonate oil and gas exploration (Dai et al., 2020; Fu et al., 2021; Liu et al., 2021; Yang et al., 2021; Yue et al., 2021). In 1791, French geologist Déodat de Dolomieu discovered and named the dolomite mineral in the Dolomieu mountain in Italy. For more than two centuries, the "dolomite problem" has challenged geologists and oil explorers. The complexity of dolomite has made it difficult to determine its origin, which has become a core topic of debate (Huang et al., 2021). Hence, based on petrographic and geochemical data, researchers worldwide have reported on the driving mechanisms of dolomitization fluid, favorable dolomitization environments, and corresponding macro-level dolomitization models, including the sabkha (McKenzie et al., 1980; Patterson and Kinsman, 1982; Mutti and Simo, 1994), mixed water (Hanshaw et al., 1971; Badiozamani, 1973; Choquette and Steinen, 1980), microbial (organic) (Vasconcelos and McKenzie, 1997), reflux (Adams and Rhodes, 1960; Jones et al., 2003), seawater dolomitization (Purser et al., 1994; Gregg et al., 2001), burial dolomitization (Land, 1985; Morrow, 1998; Mountjoy et al., 1999), and tectonic hydrothermal dolomitization (Qing and Mountjoy, 1994; Lonnee and Machel, 2004; L´opez-Horgue et al., 2010) models, among others. These findings have improved our understanding of dolomite origin and the mechanisms by which dolostone reservoirs are formed. Compared to these macro-scale aspects, little consideration has been given to the genetic implication of dolomite textures, which may be attributed to inadequate textural descriptions (Huang et al., 2011). However, dolomite textures may preserve unique information on the environment, crystallization, crystal growth, and fluid during the formation process, which can be used to study the formation environments and mechanisms (Friedman, 1965; Gregg and Sibley, 1984; Sibley and Gregg, 1987; Huang Q Y. et al., 2014; Lu et al., 2020; Huang et al., 2020; Qiao et al., 2021b; Xiong et al., 2021).

Friedman (1965) was the first to describe the significance of dolomite crystal textures. Using the classification terminology for migmatite and metamorphic rocks, he divided dolomites into three basic textures: euhedral, subhedral, and anhedral. Based on dolomite synthetic experiments, Gregg and Sibley (1984) and Sibley and Gregg (1987) combined the kinetic theory of crystal growth to propose a more detailed classification scheme based on the crystal size distributions, shapes, and boundary features. First, dolomites were divided into unimodal and multimodal types based on the size distributions of their crystals. They were then divided into planar euhedral (planar-e), planar subhedral (planar-s), and nonplanar anhedral (nonplanar-a) based on their boundary shapes and crystal features. The planar type refers to a straight crystal boundary, whereas the nonplanar/curved type refers to the bent, terraced, or other irregular crystal boundaries. Planar and nonplanar dolomites can exist in the form of cement. This classification scheme defines the critical temperature for crystal transformation from planar type to nonplanar type; namely, the critical temperature of anhedral crystal growth (around 50–60°C). Planar-e or planar-s dolomite is formed below this critical temperature, whereas nonplanar-a dolomite is formed above this critical temperature. Huang S. et al. (2014) assumed a maximum critical temperature of 73°C. Wright (2001) also defined a transition type from planar-s to nonplanar-a, which was supplementary to the scheme proposed by Gregg and Sibley. This classification scheme is highly valued for its easy use and description with certain significance regarding its origin (Amthor and Friedman, 1991; Warren, 2000; Machel, 2004; Huang Q. Y. et al., 2014). Recently, several scholars have studied the relationship between dolomite texture and origin in China. Based on the morphological characteristics of a single dolomite crystal, Wang et al. (2010) developed a structural-genetic classification for dolomites in the burial stages and investigated the relationship between dolomite shapes and the forming environment. Huang et al. (2011) studied the Permian–Triassic dolostones in the Sichuan Basin and analyzed the differences between different dolomites and their relationship in the dolomitization process. However, these studies lacked corresponding geochemical data. The structural-genetic concept was not thoroughly introduced until Huang S. et al. (2014) described a structural classification based

on the Cambrian–Ordovician dolostones in the central uplift region of the Tarim Basin combined with C-O-Sr isotope data to investigate the origin of different types of dolomites (Yu et al., 2020).

The Qiangtang Mesozoic Marine sedimentary basin is the least explored oil-bearing basin in China. In recent years, dolostone paleo-reservoirs were discovered in the middle Jurassic Buqu Formation in the southern Qiangtang depression, providing a new direction for oil and gas exploration in the basin (Chen et al., 2018; Wang and Fu, 2018; Sun et al., 2020; Wang et al., 2020; Yi and Xia, 2022). The dolostone reservoir in the Buqu Formation has attracted attention as a high-quality reservoir under the overall dense background of oil and gas reservoirs in the Qiangtang Basin (Tan et al., 2004; Sun et al., 2020; Yi and Xia, 2022). Many researchers have conducted fruitful studies on this reservoir regarding the sedimentary environment, dolomite genesis, reservoir characteristics, etc. However, controversy remains about the dolomite genesis, including the mixed water model (Yi et al., 2004; Zhang et al., 2005; Chen et al., 2006; Liu et al., 2008a, b, c, 2010; Peng et al., 2008), high-temperature formation water (Yi et al., 2014; Li et al., 2018), tectonic hydrothermal fluids (Tian et al., 2019; Ji et al., 2020), burial dolomitization (Sun et al., 2020), and multi-stage dolomitization superimposes (Wan et al., 2017a, b, 2018a, b, 2020, 2021), all of which have restricted the discovery of oil and gas. The core dispute centers on the source and formation environment of dolomitization fluid; namely, whether it is seawater, concentrated brine trapped by strata, or meteoric water. Moreover, questions remain regarding whether the dolomite formed in a shallow-burial low-temperature environment or deep-burial high-temperature environments and if dolomitization occurred under a normal geothermal gradient or abnormal high-temperature hydrothermal condition.

This study investigated the petrography, geochemistry, and origin of various types of dolomites collected from the QZ11, QZ12, and QK-1 wells using various methods, including core description; petrographic observation; cathodoluminescence imaging; and carbon (C), oxygen (O), and strontium (Sr) isotope analyses. Combined with fluid inclusion measurement and salinity analysis, this study aimed to reveal the genetic mechanism of the dolostone in the Buqu Formation and provide a geological basis for the evaluation of the dolostone reservoir.

2 Geological setting

The Qiangtang Basin, located in the hinterland of the Qinghai-Tibet Plateau, is a marine sedimentary basin formed in the Mesozoic Era on the pre-Ordovician crystalline basement (Tan et al., 2016). The Qiangtang Basin is bounded by the Kekexili–Jinsha River suture zone (KJS) in the north and the Bangong Lake–Nujiang suture zone (BNS) in the south (Yang et al., 2000). Its structural framework can be divided into four first-order tectonic units: the northern fold and thrust belt, the northern depression belt, the central uplift belt, and the southern depression belt (Wang, et al., 2007; Wan et al., 2021). Overall, the basin presents a tectonic pattern of "two depressions interlocked with one uplift". The study area was located in the southern depression belt (Figure 1A).

In the early Norian Age of the late Triassic Period, the Qiangtang Basin was under tension due to the opening of the Bangong Lake-Nujiang Oceanic Basin in the south. The Southern Qiangtang Depression entered the rift valley stage. Until the late Norian Age–the early Rhaetian Age, the Northern Qiangtang Rift Basin developed, and both the Northern and Southern Qiang Basins simultaneously sank and became sedimentary depressions to form the structural framework in the Qiangtang Basin (Wang et al., 2007). From the early Jurassic Period to the Kimmeridgian Age of the late Jurassic Period, the entire Qiangtang Basin was in a stable uniform environment (Wang et al., 2020). In the Bathonian age of the middle Jurassic Period and the Oxfordian Age–the Kimmeridgian Age of the late Jurassic Period, two large-scale marine transgressions occurred. Seawater submerged the Central Uplift, forming the sedimentary sequence of clastic rocks - carbonate rocks - clastic rocks - carbonate rocks (Table 1).

In the Bathonian Age of the middle Jurassic Period, the first and largest marine transgression occurred in the Qiangtang Basin, which was nearly submerged by seawater. With the reduction in the terrigenous detritus supply, a stable carbonate platform deposition developed in the basin under a hot and arid-semiarid paleoclimate (Pan et al., 2015). Carbonate deposition with a restricted water body developed near the boundary of the open platform in the study area (Chen et al., 2020), which was controlled by the high-frequency relative sea-level change. The underwater plateau in the platform developed into intra-platform beaches and the water body in the intra-beach depression was under salinization in the late high stand systems tract. Due to deposition, the Buqu Formation was impacted by multiple diagenetic fluid media and tectonic movements in the burial-uplift process, forming high-quality reservoirs in the overall tight background of Mesozoic oil and gas reservoirs in the Qiangtang Basin (Wan et al., 2017; Wang et al., 2020). The second stage of the Yanshan Movement and the third stage of the Himalayan Movement had the most significant impacts (Wu et al., 2014, 2016; Ji et al., 2019; Zhao W. Z. et al., 2020).

3 Materials and methods

The dolomite samples used in this study were collected from wells QZ11, QZ12, and QK-1 and sections SNP (Figure 1A) and BGP (Figure 1B). We examined 284 thin sections and classified

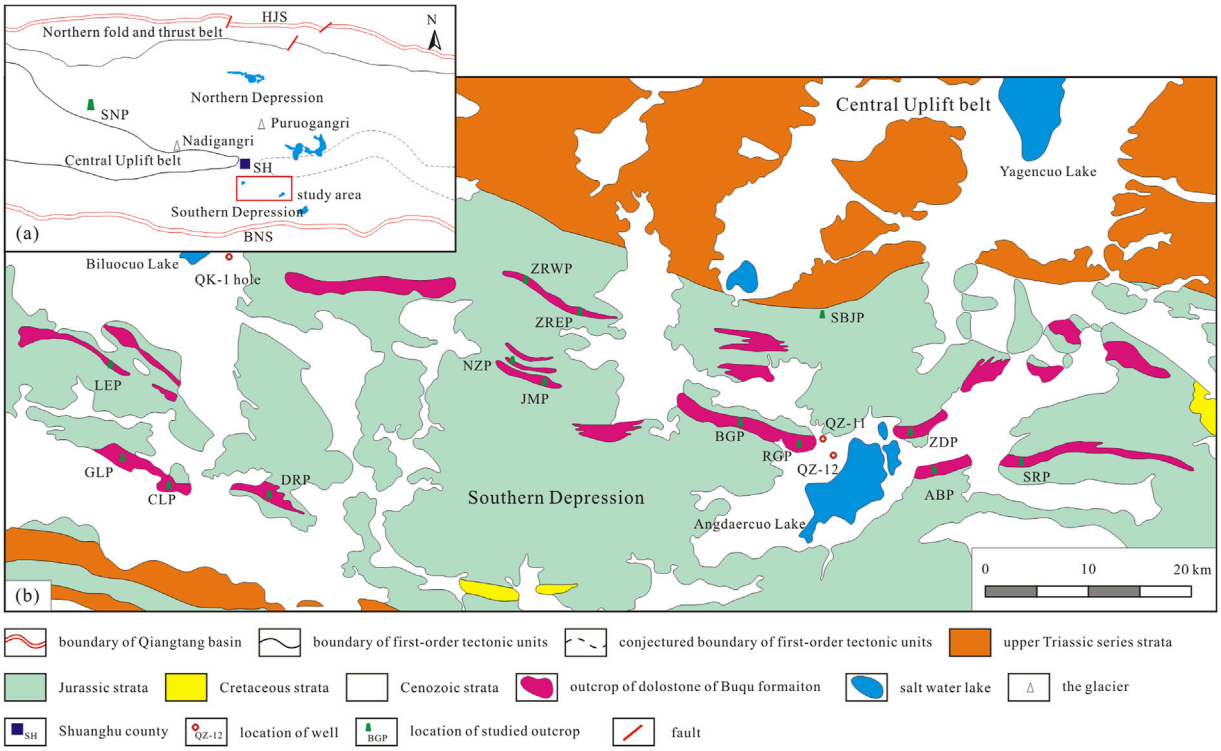

FIGURE 1
Tectonic location of the Qiangtang Basin **(A)**, and distribution and well location of the Buqu Formation dolostone section assessed in the study area **(B)** (**(A)** modified from Wan et al., 2018a **(B)** modified from Ji et al., 2020). Buqu Formation dolostone section: SNP, Suonahu lake section; SBJP, Saibangji section; LEP, Long'eni section; GLP, Geluguanna section; CLP, Chalai section; NZP, Nianzha section; JMP, Jiamu'erqie section; ZRWP, Zharen west section; ZREP, Zharen east section; BGP, Bagedijiari section; RGP, Riga'erbao section; ZDP, Zhadonglaima section; ABP, Angbacundong section; SRP, Sairen section.

the textural types of well-preserved fabric, poorly preserved fabric, and texture-destroyed fabric according to classification system proposed by Gregg and Sibley (1984) and Sibley and Gregg (1987), as well as the replacive dolomite and void-filling dolomite cement classification. Fluid inclusion thin sections (33 pieces) of different dolomite texture types were also selected for temperature measurement of the fluid inclusions. Dolomite samples with cavities and fractures filled with high purity and little influence by diagenetic epigenesis (without "misty center and clear rim") were selected. Micro-sampling was performed with a dental drill (0.05–0.1 mm) to eliminate the influence of filling or transformation by other minerals after dolomitization. A total of three limestone samples and 19 matrix dolomite samples were obtained. Five dolomite filling (cement) and five sparry calcite veins filled with fractures and cavities were used for C-O and Sr isotope analyses. Carbon and oxygen isotope analyses were performed on five granular dolomite samples collected from the SNP sections.

The petrographic and fluid inclusion thin sections were prepared in the State Key Laboratory of Oil and Gas Reservoir Geology and Exploitation of the Chengdu University of Technology. Thin section identification, cathodoluminescence analysis, scanning electron microscope observation, and fluid inclusion temperature measurement were completed at the Southwest Mineral Resources Supervision and Testing Center, Ministry of Natural Resources. The temperature measurements (homogenization temperature and ice-final melting temperature) of the dolomite fluid inclusions were conducted by LINKAM THMS600 Hot & Cold Stage to measure the misty center and clear rim of the dolomite, respectively.

Carbon and oxygen isotope analyses of 27 samples, including limestone, matrix dolomite, and dolomite filling (cement), and Sr isotope analyses of 32 samples were performed at the State Key Laboratory of Oil and Gas Reservoir Geology and Exploitation at the Chengdu University of Technology. The carbon and oxygen isotope analyses were performed on a MAT253, which performed the Sr isotope analyses by thermoelectric ionization solid isotope mass spectrometry (TIMS). Carbon and oxygen isotope analyses of five granular dolomite samples and five sparry calcite veins filled samples were completed by MAT252 isotope mass spectrometry analyzer in the Experimental Testing Center, School of Earth Science and Technology, Southwest Petroleum University. For C-O isotope analyses, pure phosphoric acid was

TABLE 1 Generalized stratigraphic column of the Qiangtang Basin.

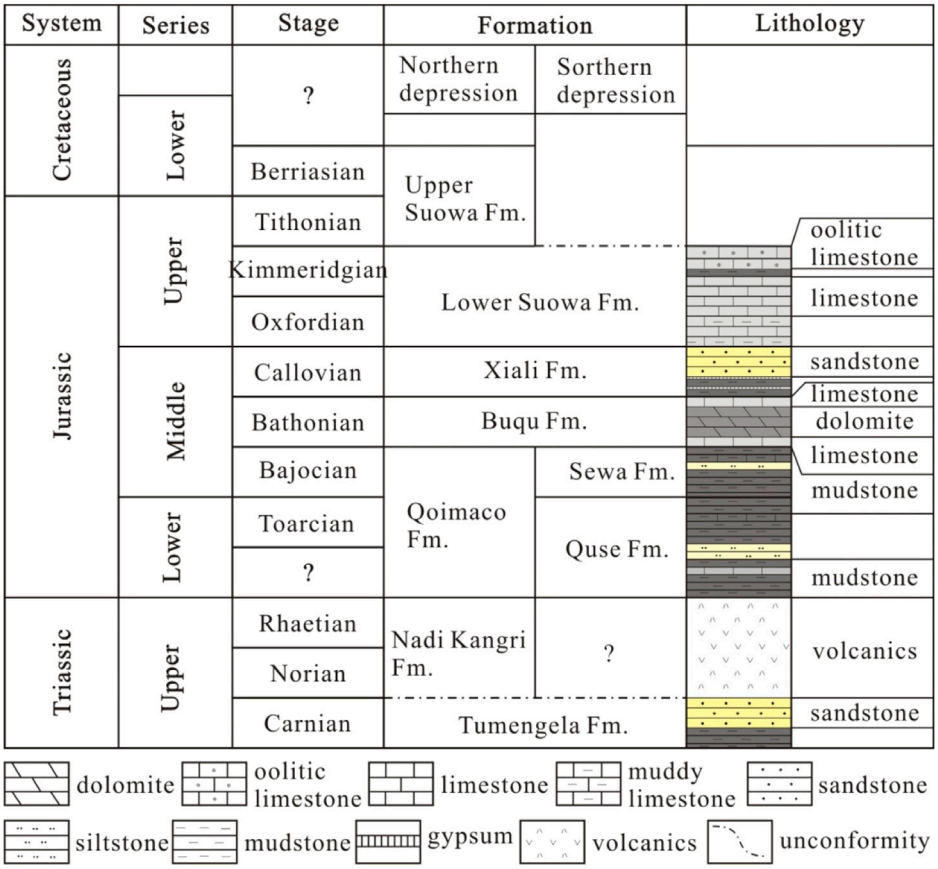

used to generate CO_2. The results were presented in δ‰ values as per PDB standards. The test was taken as per DZ/T0184.17–1997, with an analytical error of ±0.0005%. Sr isotope analyses were performed as per the standard Sample NBS987 of the US National Bureau of Standards, with an analytical error of the specific value of $^{87}Sr/^{86}Sr$ of ±0.002%.

4 Petrographic study

According to the profile geological survey data (BGP section) (Figure 1), the dolostone of the Buqu Formation in this study area was mainly fine crystal dolomite (Wan et al., 2017a). Core observation showed that the formation dip angle of the Buqu Formation encountered in well QZ12 was >50°, with enlarged thickness of severely weathered strata. The profile of a single well showed that the dolomite of the Buqu Formation developed at well depths of 213.56–4.25 m, with 81 "limestone-dolomite" meter-level lithologic cycles. In each cycle, thin-bedded "micritic limestone to micritic arenaceous limestone to sparry arenaceous limestone to calcareous dolomite to dolomite (fine-grained dolomite or medium-coarse grained dolomite)" developed from the bottom to the top, with the thicknesses of each lithologic segment ranging from 40 to 80 cm (Wan et al., 2017a; Wan et al., 2018a; Wan et al., 2020). Under the microscope, the samples from well QZ12 were mainly composed of fine-grained euhedral dolomite and fine-grained subhedral dolomite, followed by medium-coarse-grained dolomite and a small amount of microcrystalline dolomite. Only six of the 154 samples were saddle dolomite. The 600.00–575.00 m section of well QZ11 was pinhole dolomite, with saddle dolomite filling commonly observed. Saddle dolomite was found in half of the 64 samples in the core of the QK-1 hole, with equal fine-grained and medium-coarse-grained dolomite.

Two different varieties of dolomite were identified according to the primary fabric preservation (Huang Q. Y. et al., 2014): fabric-well-preserved dolomite (Rd1) and fabric-poorly preserved or fabric-destructive dolomite. Three different varieties of five different types of dolomite and fabrics were identified according to the crystal size distribution (unimodal or polymodal) and crystal boundary shape (planar or nonplanar) (Sibley and Gregg, 1987).

According to the preservation of the primary fabric, the dolomite was divided into Rd1 and poorly preserved fabric or

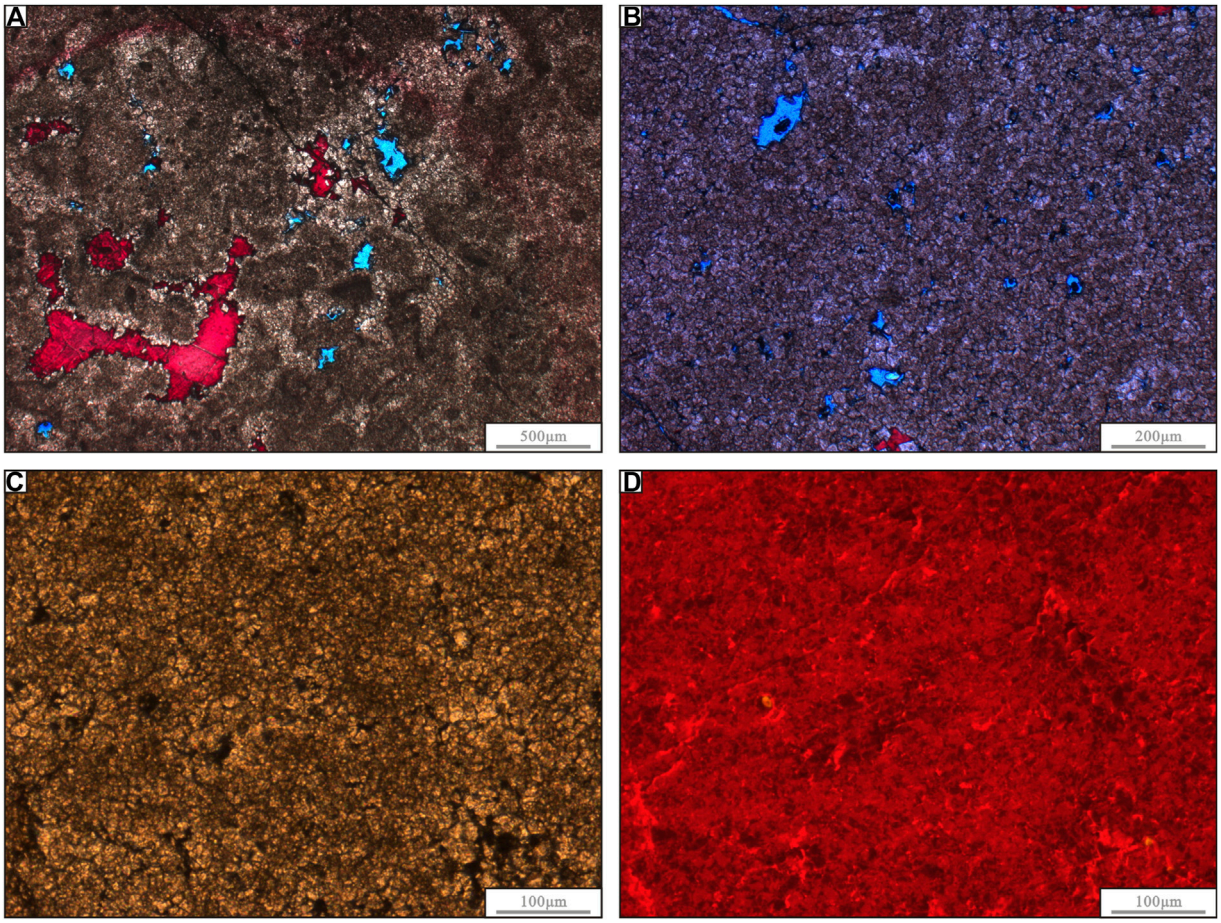

FIGURE 2
Petrological characteristics of Rd1. **(A)**. Plane-polarized-light image of an Rd1 sample showing nonplanar-a textures in small areas, with some calcite-filled pores. The sample was obtained from well QZ12 in the Buqu Formation at a depth of 140.86 m. **(B)**. Plane-polarized-light image of an Rd1 sample showing nonplanar-a textures in most areas and an algal stromatolitic texture in some areas, with a few calcite-filled pores. The sample was obtained from well QZ12 in the Buqu Formation at a depth of 65.00 m. **(C)**. Plane-polarized-light image of an Rd1 sample containing relatively dense peloids replaced by nonplanar-a dolomite to varying degrees, as well as scattered asphaltenes. The sample was obtained from well QZ12 in the Buqu Formation at a depth of 134.58 m **(D)**. Cathodoluminescence image of the Rd1 sample in **(C)**. These crystals show a dull-dull orange light, which is brighter along the grain edge. In contrast, the asphaltene shows no luminescence.

fabric-destructive dolomite (Huang S. et al., 2014). Rd1 preserves primary fabrics well, while poorly preserved fabric or fabric-destructive dolomite is subdivided based on the crystal size and structural features of the dolomite. The crystal textures were classified as proposed by Sibley and Gregg (1987) and adjusted and simplified based on the actual situations in the research area. The crystal textures included euhedral (planar-e crystal), subhedral (mainly planar-s crystal, with some nonplanar-a crystal), and anhedral (nonplanar-a crystal) types. In addition, dolomite can also appear as filling of holes and cracks, which is significant in the analysis of dolomite origin. For instance, saddle-shaped dolomite is often thought to be linked to hydrothermal transformation (Davies and Smith, 2006). Thus, based on dolomite filling (cement), the dolomite of the Buqu Formation in the study area was categorized as Rd1, fine-grained euhedral crystalline dolomite (Rd2), fine-grained subhedral dolomite (Rd3), medium-to coarse-grained anhedral dolomite (Rd4), and dolomite fillings. The dolomite fillings included fine-grained euhedral-subhedral dolomite (Cd1) and medium-coarse grained saddle-shaped dolomite (Cd2) filling. The preliminary study for this work included an analysis of the trace elements and rare Earth elements for different types of dolomite, which can be mutually verified with this study (Wan et al., 2017b; 2018b).

4.1 Fabric well-preserved dolomite (Rd1)

The fabric-well-preserved dolomite inherits and/or retains the structural characteristics of the precursor limestone, which helps to reconstruct its sedimentary environment.

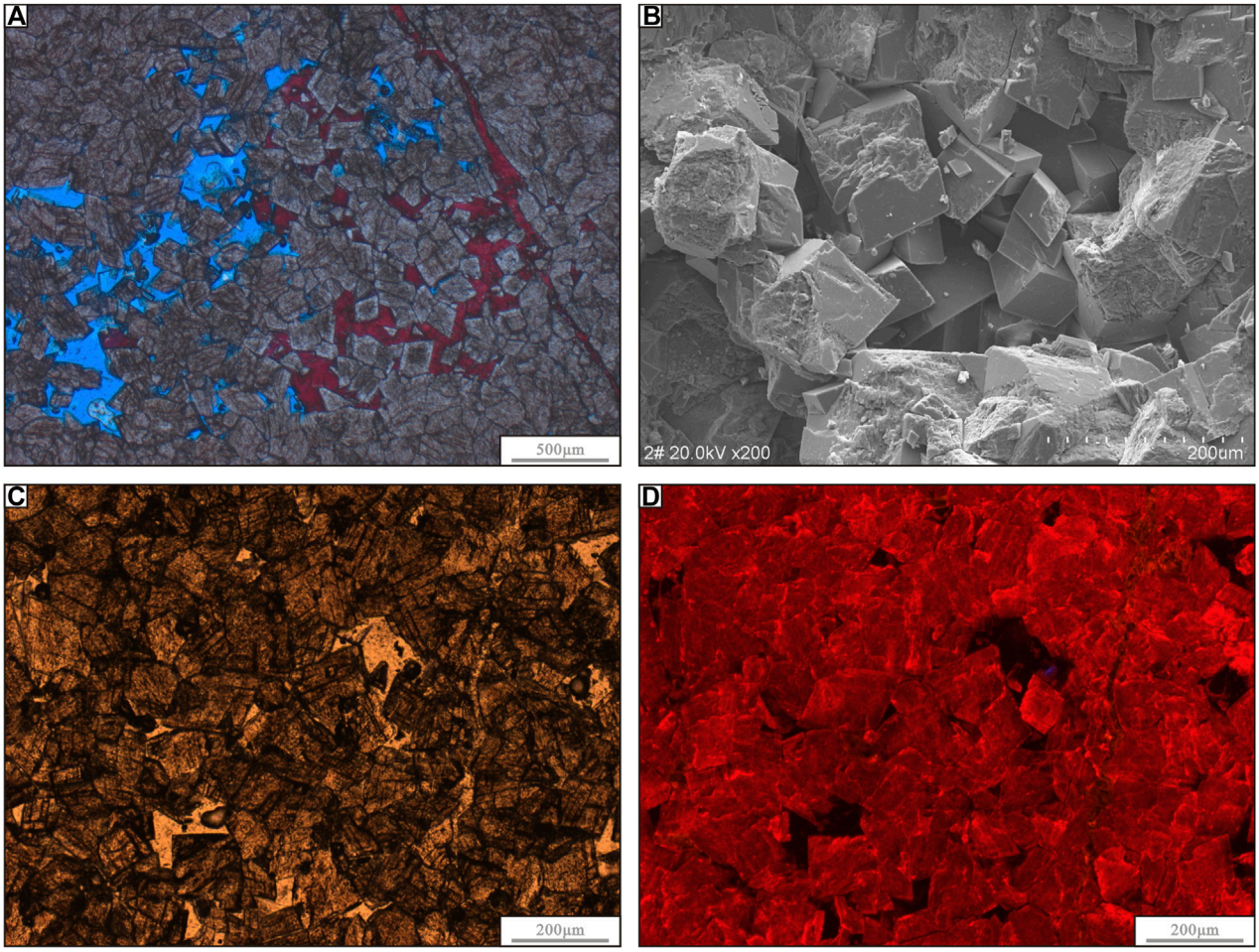

FIGURE 3
Petrological characteristics of Rd2. **(A)**. Plane-polarized-light image of an Rd2 sample with fine crystalline size and showing planar euhedral textures, some dolomites with misty center and clear rim, and some calcite-filled pores. The sample was obtained from well QK-1 in the Buqu Formation at a depth of 352.74 m. **(B)**. Scanning electron microscope image of an Rd2 sample showing planar euhedral textures, some mostly rhombohedral dolomite, and partially dissolved dolomite. The sample was obtained from well QZ11 in the Buqu Formation at a depth of 597.34 m. **(C)**. Plane-polarized-light image of an Rd2 sample with fine crystalline size showing planar euhedral textures, a few dolomite areas with misty center and clear rim, and unfilled pores. The sample was obtained from well QZ11 in the Buqu Formation at a depth of 581.69 m. **(D)**. Cathodoluminescence image of the Rd2 sample in **(C)**. These crystals show a very dull-dull orange light that is brighter along the crystalline edge. In contrast, the pore shows no luminescence.

Different intensities of metasomatism of the residual structures in the study area lead to different degrees of recognition of precursor limestone particles or plaster (Bi et al., 2001; Yang et al., 2021). The results of the petrographic examination showed fabric-well-preserved dolomite in the study area in the Buqu Formation, which was further divided into two subtypes.

The first subtype of dolomite (Rd1) has intact grain or a stucco outline; some scholars have termed the internal structure "mimic/mimetic replacement" (Kaldi and Gidman, 1982; Sibley, 1991). Combined with the inferred primordia fabric of the precursor limestone, this subtype contains granular (Figure 2A) and mud-silty (Figures 2B,C) dolomites. The muddy-silty dolomite in the Buqu Formation in the study area mostly retained the primary fabric of the residual precursor limestone, and single muddy-silty dolomite was rarely observed. This type of dolomite mainly consists of muddy-silty dolomite (0.001–0.05 mm) with tiny, mostly subhedral-anhedral, crystals. The other subtype, residual grain dolomite, only retains the shape or outline of the original particles with unrecognizable internal structures. It is rarely observed in the Buqu Formation. Primary Rd1 in this study refers to the mimetic crystal metasomatic dolomite.

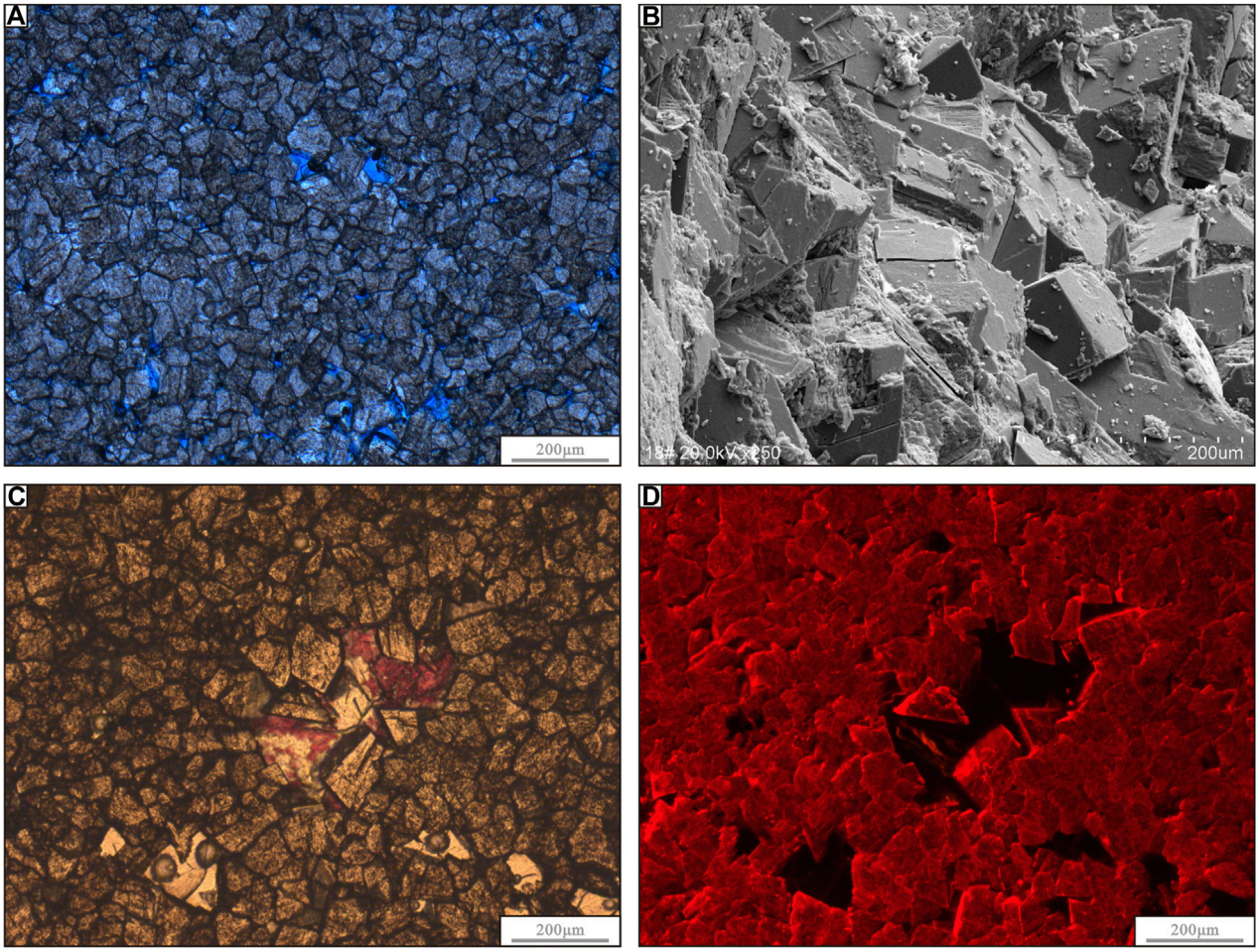

FIGURE 4
Petrological characteristics of Rd3. **(A)**. Plane-polarized-light image of an Rd3 sample with fine crystalline size showing planar subhedral textures, several dolomite areas with misty centers and clear rims, as well as unfilled pores. The sample was obtained from well QK-1 in the Buqu Formation at a depth of 351.94 m. **(B)**. Scanning electron microscope image of an Rd3 sample showing planar subhedral textures due to dense dolomite overgrowth. The sample was obtained from well QZ12 in the Buqu Formation at a depth of 105.02 m. **(C)**. Plane-polarized-light image of an Rd3 sample with fine crystalline size showing planar subhedral textures, several areas of dolomite with misty centers and clear rims, and some calcite-filled pores. The sample was obtained from well QZ12 in the Buqu Formation at a depth of 54.86 m. **(D)**. Cathodoluminescence image of the Rd2 sample in **(C)**. These crystals show a very dull-dull orange, which is brighter in a few dolomite areas along the crystalline edge. The pores and calcite cement show no luminescence.

4.2 Fabric poorly preserved or fabric-destructive dolomite

4.2.1 Euhedral planar crystalline dolomite (Rd2)

This type of dolomite (Rd2) is also referred to as "sugar" dolostone (Ji et al., 2020). The core sample and field profiles showed light-dark gray, medium to thick layers or lumpy occurrence, with locally visible traces of biodisturbance or fossil fragments of shell organisms. Rd2 contained mostly fine grains (0.05–0.25 mm) and a small number of powdered crystals, with a high degree of self-morphism and sugar-like characteristics under a microscope. The crystals were highly euhedral and saccharoidal. Bright fine rings or "misty center and clear rim" structures were observed at the edge of some crystals (Figure 3A), with intercrystalline point/line contacts and pores. Under scanning electron microscopy, Rd2 was mostly composed of rhombohedral dolomite with flat crystal boundaries (Figure 3B). Cathodoluminescence showed uniform medium brightness and orange to dark red color (Figures 3C,D).

4.2.2 Fine-grained subhedral planar crystalline dolomite (Rd3)

In the core sample and the field cross-section, dolomite (Rd3) was mainly dark gray to gray in color and is slightly deeper than or interbedded with the fine crystal and euhedral dolomites. The crystals were mainly fine (0.05–0.25 mm), with minor medium

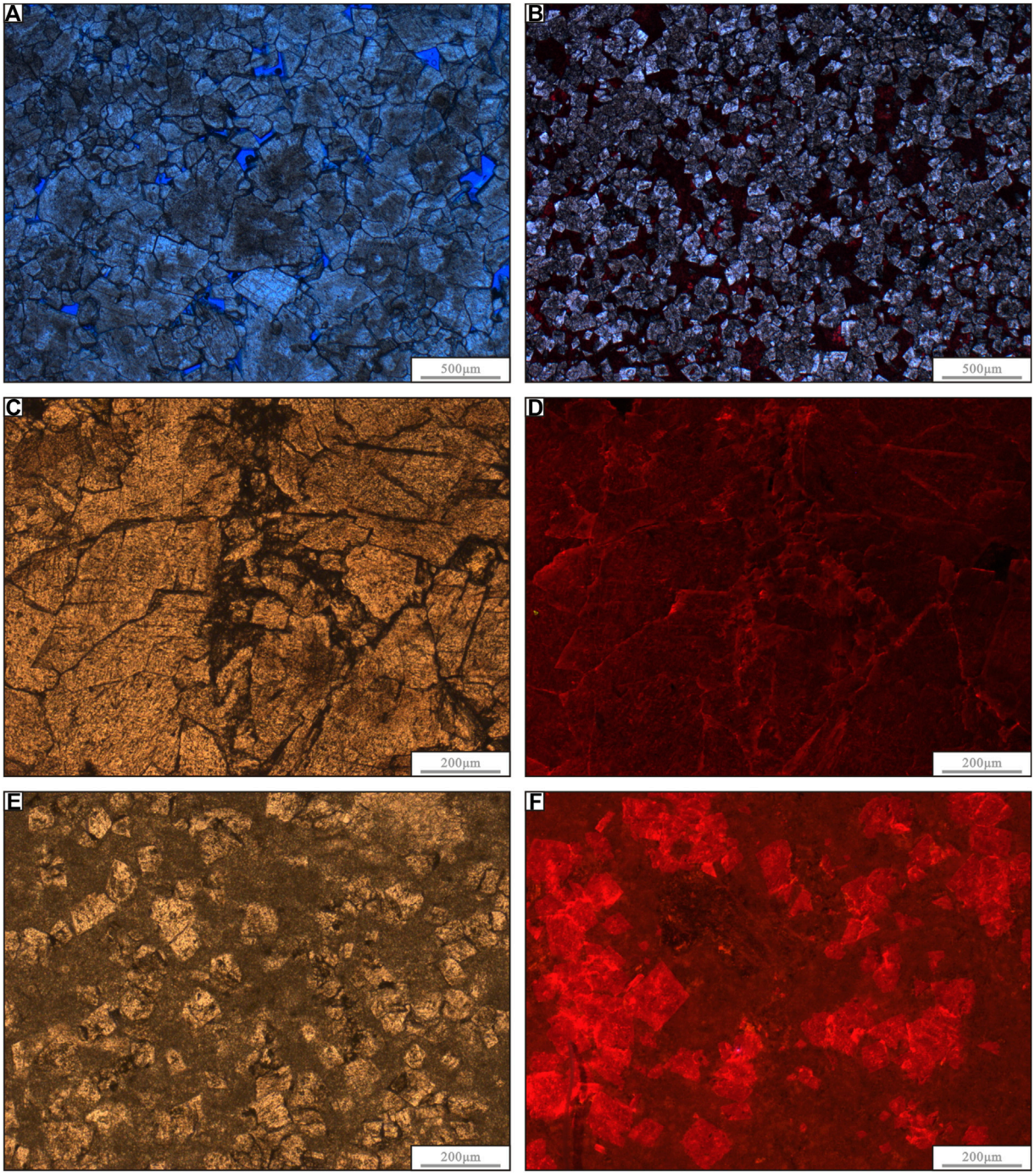

FIGURE 5
Petrological characteristics of Rd4. **(A)**. Plane-polarized-light image of an Rd4 sample with medium-coarse crystalline size showing anhedral texture, some dolomite with misty centers and clear rims, and unfilled pores. The sample was obtained from well QK-1 in the Buqu Formation at a depth of 308.97 m. **(B)**. Plane-polarized-light image of an Rd4 sample showing incomplete dolomitization, and the accumulation of a fine dolomite crystal mosaic. The sample was obtained from well QZ12 in the Buqu Formation at a depth of 105.02 m. **(C)**. Plane-polarized-light image of an Rd4 sample with coarse crystalline size showing planar subhedral textures and asphalt-filled microcracks. The sample was obtained from well QZ12 in the Buqu Formation at a depth of 54.86 m. **(D)**. Cathodoluminescence image of the Rd4 sample in **(C)**. These crystals show a very dull red, which is brighter in a few dolomite areas along the crystalline edge. **(E)**. Plane-polarized-light image of an Rd4 sample showing fine crystal dolomite with incomplete dolomitization. The sample was obtained from well QZ12 in the Buqu Formation at a depth of 66.26 m. **(F)**. Cathodoluminescence image of the Rd4 sample in **(E)**. These crystals show a dull red, while the calcite does not emit light.

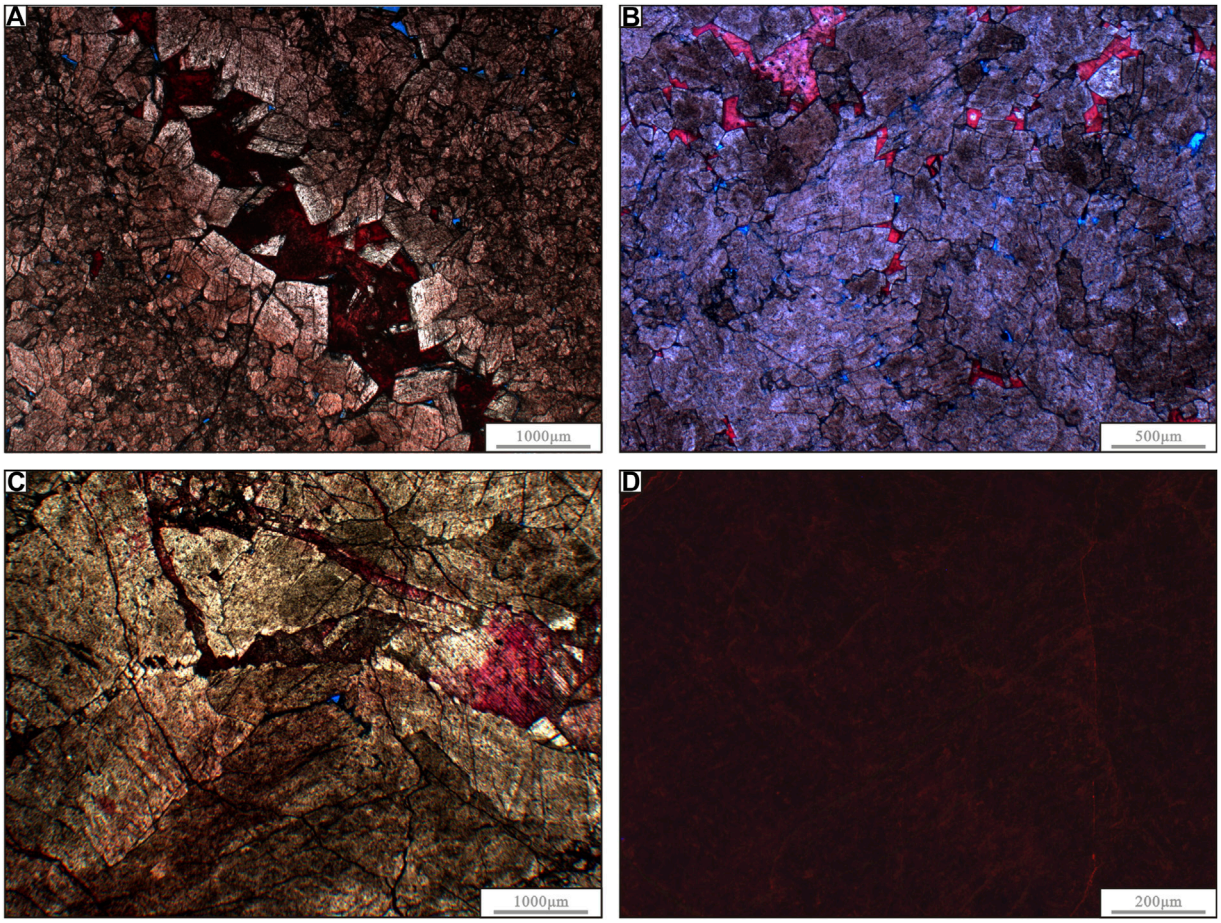

FIGURE 6
Petrological characteristics of void-filling dolomite/dolomite cement. **(A)**. Plane-polarized-light image of a Cd1 sample with fine-medium crystalline size showing dolomite cement filling along the inner wall of the calcite-filled fracture. The sample was obtained from well QZ12 in the Buqu Formation at a depth of 62.75 m. **(B)**. Plane-polarized-light image of a Cd2 sample showing filled saddle dolomite in Rd3, The fractures are well developed and filled with calcite. The sample was obtained from well QZ12 in the Buqu Formation at a depth of 73.38 m. **(C)**. Plane-polarized-light image of a Cd2 sample showing saddle dolomite with calcite-filled fractures. The sample was obtained from well QZ11 in the Buqu Formation at a depth of 580.90 m. **(D)**. Cathodoluminescence image of the Cd2 sample in **(C)**. These crystals show no visible cathodoluminescence.

grains (0.25–0.5 mm) and powder (0.006–0.05 mm). The crystals were mainly subhedral and anhedral and mainly in point or line contact, with some parts in embedded contact. The intercrystalline pores were drastically reduced compared to those in Rd2 (Figure 4A). The dolomite was tightly accumulated in scanning electron microscope examination. Although some crystals showed straight grain boundaries, they were restricted by their growing space. The crystal morphology was incomplete, or they were embedded in neighboring crystals and occupied the original interstitial space. Perfect rhombohedral crystals were observed in the direction toward the intercrystalline pores. (Figure 4B). The cathodoluminescence of such dolomite was predominately dark red in color, similar to or weaker than that of Rd2 (Figures 4C,D).

4.2.3 Medium-to coarse-grained anhedral crystalline dolomite (Rd4)

Rd4 was mainly composed of allomorphic dolomite with a poor degree of crystallography. Medium-/coarse-grained dolomite (0.25–2 mm) was dominant, followed by fine dolomite (0.05–0.25 mm). Rd4 showed two occurrences. One was a transitional type between limestone and dolostone due to incomplete or selective dolomitization. The mottled rock generally developed in the core of well QZ12 (Figures 5B–E), which presented as two-tone punctate, plaque, or ribbon. Microscopic observation showed that the dolomite grain was relatively thin, with mostly fine-medium grains, poor crystal automorphism, and well-developed intergranular pores (Figure 5B). The cathodoluminescence of Rd4 was mainly dark red in color or speckled, with bright orange bands or

TABLE 2 Homogenization and ice-final melting temperatures of fluid inclusions in different dolomites.

Dolomite texture	Occurrence	Homogenization, ˚C			Ice-final melting temperatures, ˚C			Salinity,%	Features of fluid inclusions	
		Mean	Maximum	Minimum	Mean	Maximum	Minimum		Number	Degree of development
RD1	Replacive									Very low
RD2-misty left	Replacive	73.24	83	65.5	−17.6	−16.2	−20.1	20.64	5	Low
RD2-clear rim	Recrystal	122.25	123.4	121.1	−20.15	−20	−20.3	22.48	2	Very High
RD3-misty left	Replacive	90.18	98	82.9	−17.05	−13	−19.7	20.21	19	Low
RD3-clear rim	Recrystal	126.75	157	102.8	−17.8	−12.8	−21.1	20.75	22	Very High
RD4-misty left	Replacive	102.67	117	84	−18.15	−13.6	−21.3	21.03	52	High
RD4-clear rim	Recrystal	130.15	145	118	−18.69	−10	−21.5	21.37	37	Very High
CD1	Cements	113.5	116.7	110.2	−20	−19.9	−20.1	22.38	3	High
CD2-misty left	Cements	140.43	165	121	−18.58	−13.3	−20.9	21.34	26	Very High
CD2-clear rim	Recrystal	105.15	119.4	89	−18.19	−14.8	−20.4	21.06	26	High

spots visible at the crystal edges or contacts. The overall cathodoluminescent intensity was slightly higher than that of the non-metasomatized limestone (Figure 5F).

The other occurrence of Rd4 was in gray or dark gray massive medium to thick beds. The fractures and dissolution pores in the upper layers of the core were highly developed, accompanied by saddle dolomite filling. Under the microscope, Rd4 showed fine crystals, with medium, and predominantly coarse grains (Figures 5A–C). Some parts of the samples showed double number distributions, with coarse grains surrounding fine grains, namely between coarse grain dolomite packages or around the fine dolomite crystals, with some individuals differing under the coarse grain dolomite in the orthogonal polarization extinction phenomenon. This indicated the influence of recrystallization. This kind of dolomite crystal is dominated by curved plane boundaries. Rd4 showed entirely dark cathodoluminescence, with local dark red patches (Figure 5D).

4.3 Void-filling dolomite/dolomite cement

For the dolostone of the Buqu Formation in the study area, it was difficult to determine whether the dolomite growing around the inwall of a cavern or a crack was generated by cementation or metasomatism. Hence, it was described as “filling” rather than “cement” (Wan et al., 2018a). Although only a small amount of dolomite was present in the dolostone, it played a significant role in determining the property of the diagenetic fluid and identifying the evolutionary process of the formation and cavern filling. This study revealed two types of dolomite fillings in the dolostone of the Buqu Formation.

Fine planar subhedral crystalline cavern-filling dolomite generally acted as the cavern or crack filling by growing on its in-wall (Cd1). These mostly contained fine grains with little silty grains or medium grains and high euhedral degree (straight boundary) in the direction of the holes (Figure 6A). All crystals were clean with fewer impurities and predominant dark red cathodoluminescence with local glowing rings, similar to those observed Rd3.

In the core, the medium-coarse anhedral saddle dolomite filling (Cd2) was mostly light gray and mainly grew along the inner wall of the fracture or dissolution cavity, forming a shell around or filling the cavity. However, the crystal surface was dirty under plane-polarized light, wherein massive solid or liquid inclusions were seen. Microcracks and cleavages had developed inside the crystals. The grain boundary was bending in a sickle shape. Wavy extinction was obvious under cross-polarized light. The dark red ray was predominant in cathodoluminescence, with no light locally (Figure 6D). The saddle dolomite in the Buqu Formation in the study area was in abrupt contact with the surrounding rock, with matrix dolomite filling material (Figure 6B), indicating that the saddle dolomite was formed after matrix dolomite due to late reconstruction.

TABLE.3 C- O and Sr isotope data for the different carbonate rocks in the Buqu Formation.

Sample ID	Sample position	Rock type	$\delta^{13}C‰_{PDB}$	$\delta^{18}O‰_{PDB}$	$^{87}Sr/^{86}Sr$	Remarks
YP-33	Yanshiping area	micrite limestone	2.10	−7.40		Tan et al. (2004)
YP-34	Yanshiping area	micrite limestone	2.60	−6.40		Tan et al. (2004)
YP-37-1	Yanshiping area	micrite limestone	2.30	−6.30		Tan et al. (2004)
YP-37-2	Yanshiping area	shell limestone	0.90	−10.20		Tan et al. (2004)
3	Yichangma area	bioclast-bearing	0.86	−12.05		Zhang et al. (2006)
4	Yichangma area	micrite limestone	1.24	−9.70		Zhang et al. (2006)
9	Yichangma area		2.52	−4.02		Zhang et al. (2006)
5	Yichangma area	micrite limestone	1.16	−10.28		Zhang et al. (2006)
6	Yichangma area	micrite limestone	1.79	−7.06		Zhang et al. (2006)
7	Yichangma area	micrite limestone	1.33	−6.24		Zhang et al. (2006)
8	Yichangma area	micrite limestone	2.49	−3.79		Zhang et al. (2006)
22	Yichangma area	micrite limestone	1.41	−10.24		Zhang et al. (2006)
GP32-B1	this study area	bioclast limestone	1.84	−9.04		Ji et al. (2020)
5	this study area	micrite limestone	2.30	−10.30		Ji et al. (2020)
16	this study area	micrite limestone	1.80	−10.90		Ji et al. (2020)
26	this study area	micrite limestone	2.70	−9.90		Ji et al. (2020)
34	this study area	micrite limestone	3.00	−10.50		Ji et al. (2020)
54	this study area	micrite limestone	2.50	−11.90		Ji et al. (2020)
55	this study area	micrite limestone	2.50	−10.50		Ji et al. (2020)
57	this study area	micrite limestone	2.00	−9.10		Ji et al. (2020)
59	this study area	micrite limestone	2.30	−10.20		Ji et al. (2020)
BD30-2	this study area	micrite limestone	0.89	−13.02		Ji et al. (2020)
P9-B1	this study area	micrite limestone	0.46	−11.86		Ji et al. (2020)
P6-B1	this study area	sparry arenaceous limestone	2.06	−11.99		Ji et al. (2020)
P15-B2	this study area	sparry arenaceous limestone	1.71	−9.68		Ji et al. (2020)
BD16-B4	this study area	sparry arenaceous limestone	2.27	−10.71		Ji et al. (2020)
BP-4	this study area	Straticulate doloston	3.75	−9.07		Ji et al. (2020)
AD03-B	this study area	crystal powder dolomite	4.06	−8.51		Ji et al. (2020)
AD03-D	this study area	crystal powder dolomite	4.23	−7.90		Ji et al. (2020)
LP3-B1	this study area	fine-crystalline dolomite	3.21	−8.69		Ji et al. (2020)
LP5-B	this study area	fine-crystalline dolomite	3.02	−8.51		Ji et al. (2020)
LP8-B1	this study area	fine-crystalline dolomite	3.02	−8.94		Ji et al. (2020)
P13-B	this study area	fine-crystalline dolomite	3.46	−9.79		Ji et al. (2020)
GP18-Bb	this study area	fine-crystalline dolomite	4.26	−9.56		Ji et al. (2020)
BD16-B3	this study area	fine-crystalline dolomite	3.28	−9.13		Ji et al. (2020)
DT-257	this study area	fine-crystalline dolomite	2.30	−9.50		Ji et al. (2020)
DT-282	this study area	fine-crystalline dolomite	3.20	−8.90		Ji et al. (2020)
LE-2	this study area	meso-crystalline dolomite	2.40	−10.6		Ji et al. (2020)
AD03-B3	this study area	coarse-grained dolomite	3.30	−7.96		Ji et al. (2020)
BD30-1	this study area	coarse-grained dolomite	2.84	−10.12		Ji et al. (2020)
BD30-4	this study area	coarse-grained dolomite	3.38	−10.28		Ji et al. (2020)
BD30-5	this study area	coarse-grained dolomite	3.21	−9.80		Ji et al. (2020)
P11-B4	this study area	coarse-grained dolomite	3.86	−9.96		Ji et al. (2020)
GP20-B	this study area	coarse-grained dolomite	4.41	−8.84		Ji et al. (2020)
DT-224	this study area	coarse-grained dolomite	3.60	−7.90		Ji et al. (2020)
LE-1	this study area	coarse-grained dolomite	2.50	−8.7		Ji et al. (2020)
BG-10	this study area	coarse-grained dolomite	3.30	−8.10		Ji et al. (2020)
GL01-27	this study area	coarse-grained dolomite	3.10	−10.00		Ji et al. (2020)

(Continued on following page)

TABLE.3 (*Continued*) C- O and Sr isotope data for the different carbonate rocks in the Buqu Formation.

Sample ID	Sample position	Rock type	$\delta^{13}C‰_{PDB}$	$\delta^{18}O‰_{PDB}$	$^{87}Sr/^{86}Sr$	Remarks
GL01-33	this study area	coarse-grained dolomite	3.10	−10.40		Ji et al. (2020)
GL01-21	this study area	coarse-grained dolomite	3.10	−10.10		Ji et al. (2020)
Geluguanna	GLP section	saddle dolomite	4.29	−10.02		Ji et al. (2020)
Geluguanna	GLP section	saddle dolomite	3.36	−10.65		Ji et al. (2020)
Geluguanna	GLP section	saddle dolomite	3.49	−10.31		Ji et al. (2020)
Deruri	DRP section	saddle dolomite	3.22	−7.51		Ji et al. (2020)
	QZ12-232.16 m	sparry calcite veins	−1.15	−13.04		wan et al. (2020)
	QZ12-075.32 m	filled fractures	−1.18	−9.42		wan et al. (2020)
	QZ12-070.96 m		1.64	−10.75		wan et al. (2020)
16D-13	QZ12-075.22 m	micrite limestone	1.19	−8.25	0.707765	this study
16D-20	QZ12-130.83 m	micrite limestone	1.96	−8.62	0.707763	this study
16D-21	QZ12-131.46 m	sparry arenaceous limestone	2.57	−7.47	0.707850	this study
15S-2	SNP section	granular dolomite	3.75	−0.24		this study
15S-3	SNP section	granular dolomite	3.71	0.36		this study
15S-4	SNP section	granular dolomite	4.02	0.01		this study
15S-6	SNP section	granular dolomite	3.69	0.12		this study
15S-7	SNP section	granular dolomite	3.52	−0.47		this study
16D-14	QZ12-096.21 m	Rd1	3.42	−3.84	0.708176	this study
16D-07	QZ12-058.24 m	Rd1	3.74	−4.22	0.707747	this study
16D-25	QZ12-198.13 m	Rd1	4.23	−3.37	0.707654	this study
16D-06	QZ12-057.31 m	Rd2	4.11	−4.56	0.707525	this study
16D-15	QZ12-100.63 m	Rd2	3.64	−4.33	0.707667	this study
16D-17	QZ12-102.02 m	Rd2	3.18	−4.23	0.707572	this study
16D-22	QZ12-143.12 m	Rd2	3.33	−4.25	0.708037	this study
16D-23	QZ12-151.71 m	Rd2	3.83	−4.31	0.707686	this study
16D-02	QZ12-026.57 m	Rd3	4.42	−5.87	0.707432	this study
16D-03	QZ12-030.24 m	Rd3	4.18	−6.26	0.707609	this study
16D-05	QZ12-043.43 m	Rd3	3.95	−6.23	0.707990	this study
16D-16	QZ12-101.12 m	Rd3	3.28	−5.56	0.707780	this study
16D-24	QZ12-190.37 m	Rd3	2.72	−6.57	0.707593	this study
16D-01	QZ12-024.29 m	Rd4	3.24	−7.22	0.707303	this study
16D-04	QZ12-043.43 m	Rd4	4.05	−7.65	0.707884	this study
16D-10	QZ12–067.73 m	Rd4	3.92	−8.22	0.707752	this study
16D-12	QZ12-072.73 m	Rd4	3.85	−6.56	0.707234	this study
16D-18	QZ12-107.14 m	Rd4	4.14	−8.16	0.707593	this study
16D-27	QZ11-581.62 m	Rd4	3.68	−6.37	0.707865	this study
16D-19	QZ12-122.84 m	Cd1	3.02	−5.31	0.708147	this study
16D-08	QZ12-060.65 m	Cd2	-0.09	−10.41	0.708518	this study
16D-09	QZ12-060.64 m	Cd2	3.38	−9.58	0.708876	this study
16D-11	QZ12-069.33 m	Cd2	1.27	−9.25	0.708562	this study
16D-26	QZ11-580.95 m	Cd2	1.86	−8.56	0.708180	this study
QZ12-026	QZ12-105.02 m	Calcite cement filled dolomite intercrystalline pores	3.73	−5.38	0.707574	this study
QZ12-001-2	QZ12-232.16 m	Sparry calcite veins filled in fractures	−0.85	−11.97	0.708912	this study
QZ12-005	QZ12-219.76 m		−1.35	−11.33	0.709233	this study
QZ12-007	QZ12-219.81 m		0.57	−10.62	0.708128	this study
QZ12-013	QZ12-195.75 m		1.89	−10.45	0.708041	this study

5 Dolomite geochemistry

5.1 Fluid inclusion characteristics

Fluid inclusions are poorly developed in the dolomite of the Buqu Formation in the Qiangtang Basin (Table 2). Among the 33 thin sections of different dolomite samples, only 17 samples contain fluid inclusions. Fluid inclusions were identified in replaced dolomite and dolomite cement, including Rd2, Rd3, Rd4, Cd1, and Cd2, but not in Rd1. As described previously, misty centers and clear rims were observed in Rd2, Rd3, Rd4, and Cd2. The fluid inclusions in the healed trails in these dolomites were carefully avoided. The fluid inclusions that were isolated and in clusters in the misty center were interpreted to be of primary origin. In the clear rim, inclusions occurring along the boundary between the misty center and clear rim, as well as those in clusters, were interpreted to be of primary origin. These fluid inclusions in the misty center and clear rim were liquid-vapor inclusions with gas-liquid ratios of <10% and were chosen for further microthermometric analysis to reflect the diagenetic temperature and fluid salinity when they were captured (Liu, 1995; Braithwaite and Rizzi, 1997; Goldstein, 2001).

Among crystalline dolomites, the homogenization temperature of Rd2 types was low (lowest value 65.5°C), which is also the lowest homogenization temperature among the fluid inclusions observed in this study. Meanwhile, its ice-final melting temperature (−16.2°C) was also low. The highest homogenization temperature was 83°C, the average homogenization temperature was 73.24°C, and the lowest ice-final melting temperature was −20.1°C. The average corresponding salinity was 20.64%. The homogenization temperatures of the clear rim part of Rd2 dolomite ranged between 121.1 and 123.4°C (average 122.25°C), The ice-final melting temperatures were between −20.3°C and −20°C (average −20.15°C), with a corresponding salinity of 22.48%. While this study obtained only three fluid inclusion temperature measurements for the clear rim part of dolomite, which may not be statistically significant, these data indicated a higher formation temperature of the clear rim part of the dolomite compared to that of the misty center part.

The homogenization temperatures of fluid inclusions in Rd3 dolomite ranged from 82.9 to 98°C (average 90.18°C), slightly higher than those in Rd2 dolomite. Meanwhile, the ice-final melting temperatures, ranging from −19.7°C to −13°C (average −17.05°C), were also slightly higher than those in Rd2. The corresponding average salinity was 20.21%, slightly lower than that in Rd2. The homogenization temperatures of the clear rim part of Rd3 dolomite with "misty center and clear rim" were 102.8–157°C (average 126.75°C). The ice-final melting temperatures were between −21.1°C and −12.8°C (average of −17.8°C), with a corresponding salinity of 20.75%. These data indicated that the formation temperature of the clear rim part of Rd3 was higher than that of Rd3.

The homogenization temperatures of Rd4 dolomite inclusions were higher than those of Rd2 and Rd3, ranging from 84 to 117°C (average 102.67°C.) The salinity ranged from −13.6 to −21.3°C (average −18.15°C), corresponding to an average salinity of 21.03%. The homogenization temperatures of the clear rim part of Rd4 dolomite with a "misty center and clear rim" were 118–145°C (average 130.15°C). The ice-final melting temperatures were between −21.5°C and −10°C (average −18.69°C), with a corresponding salinity of 21.37%. These indicated that the formation temperatures of the clear rim of Rd4 were higher than those of Rd4 and similar to those of Rd3 dolomite. The homogenization temperatures of the clear rim part of the Rd4 dolomite with a "misty center and clear rim" were generally higher than the maximum formation temperatures of granular dolomite, indicating that the formation environment of the clear rim might have been altered by a high-temperature environment during burial.

For dolomite fillings/cements, the homogenization temperatures of Cd1 partially coincided with those of Rd4, ranging from 110.2 to 116.7°C (average 113.5°C). The ice-final melting temperatures ranged from −20.1 to −19.9°C (average −20°C), corresponding to an average salinity of 22.38%. The homogenization temperatures of Cd2 differed significantly from those of crystalline dolomite and Cd1 filling, ranging from 121 to 165°C (average 140.43°C). Comparatively, the corresponding ice-final melting temperatures ranging from −20.9°C to −13.3°C did not differ significantly, indicating that the fluid properties of Cd2 were not significantly different from those of crystalline dolomite and Cd1. This may be related to the warming of tectonic thermal events under the background of tectonic compression. Under the microscope, part of Cd2 was broken into coarse near-regular rhomboid dolomite crystals with a "misty center and clear rim" structure. The homogenization temperatures of the fluid inclusions at the clear rim (between 89 and 119.4°C) were much lower than those of Cd2 but similar to those of Rd3. The ice-final melting temperature was similar to that of Cd2, with an average corresponding salinity of 21.06%. These also indicated that the genetic fluids in the clear rim of Cd2 did not involve meteoric water.

5.2 Isotope geochemical characteristics

5.2.1 Oxygen and carbon isotope

Table.3 shows the carbon, oxygen, and strontium isotope data obtained in this study and the carbon and oxygen isotope data collected from published literature. The δ^{13}C‰PDB of micritic limestone in the Buqu Formation of Qiangtang Basin ranged from 1.16‰ to 3‰ (average 2.08‰) and the δ^{18}O‰PDB ranged from −11.9‰ to −3.79‰ (average −8.77‰). The carbon isotope δ^{13}C‰PDB of SNP grain dolomite (Figure 1A) was

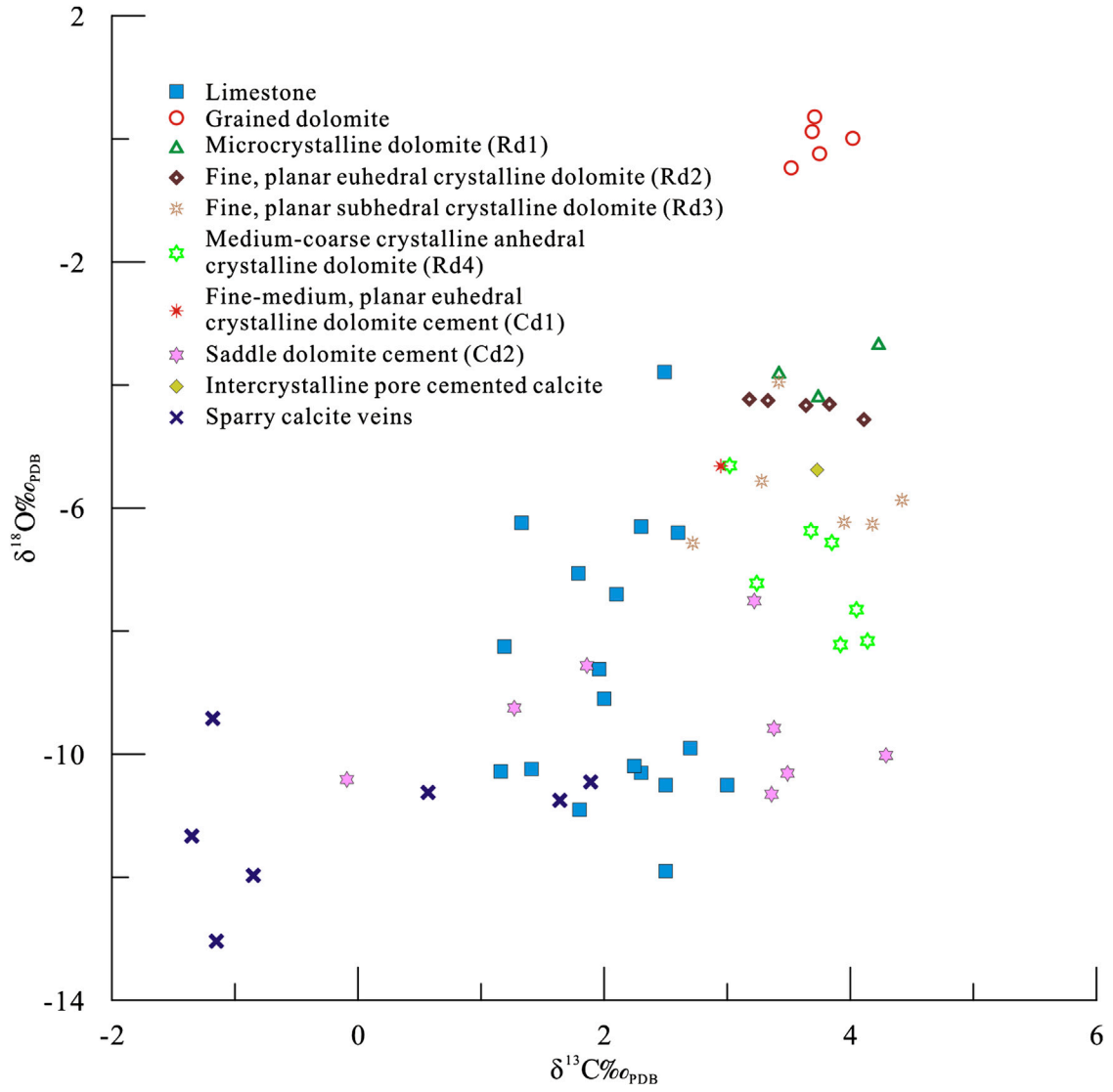

FIGURE 7
Cross-plot showing $^{87}Sr/^{86}Sr$ vs. $\delta^{18}O$ for different carbonate rocks in the study area.

3.52‰–4.02‰ (average 3.74‰). The oxygen isotope $\delta^{18}O‰$ PDB was −0.47‰– 0.36‰ (average −0.04‰). The carbon isotope $\delta^{13}C‰PDB$ of Rd1 ranged from 3.42 to 4.23‰ (average 3.8‰). The oxygen isotope $\delta^{18}O‰PDB$ of Rd1 ranged from −4.22‰ to −3.37‰ (average −3.81‰). The $\delta^{13}C‰PDB$ ranged from 3.18 to 4.11‰ (average of 3.62‰) in Rd2 and varied from 2.72 to 4.42‰ (average 3.71‰). The oxygen isotope $\delta^{18}O‰PDB$ of Rd3 ranged from −6.57‰ to −5.56‰ (average -6.10‰). The $\delta^{13}C‰PDB$ of medium-coarse anhedral dolomite (Rd4) ranged from 3.24 to 4.14‰ (average 3.81‰). The $\delta^{18}O‰PDB$ ranged from -8.22‰ to -6.37‰ (average −7.36‰).

The $\delta^{13}C‰PDB$ and $\delta^{18}O‰PDB$ of Cd1 were 3.02‰ and −5.13‰, respectively. The $\delta^{13}C‰PDB$ of Cd2 ranged from −0.09 to 3.38‰ (average 1.61‰), while the $\delta^{18}O‰PDB$ ranged from −10.41‰ to −8.56‰ (average −9.45‰). The calcite cement filling in the dolomite intercrystalline pores had a $\delta^{13}C‰$ PDB of 3.73‰ and an $\delta^{18}O‰PDB$ of −5.38‰. The sparry calcite veins filling the core fractures of well QZ12 had an $\delta^{13}C‰PDB$ of between -1.35‰ and −1.89‰ (average −0.06‰) and an $\delta^{18}O‰$ PDB between −13.04‰ and −9.42‰ (average −11.08‰).

5.2.2 Strontium isotope

Unlike C and O isotopes, Sr isotopes are not prone to fractionation or isotope exchange due to changes in biology, salinity, temperature, and pressure in geological history; thus, they are an effective tracer of carbonate diagenetic fluid (Huang

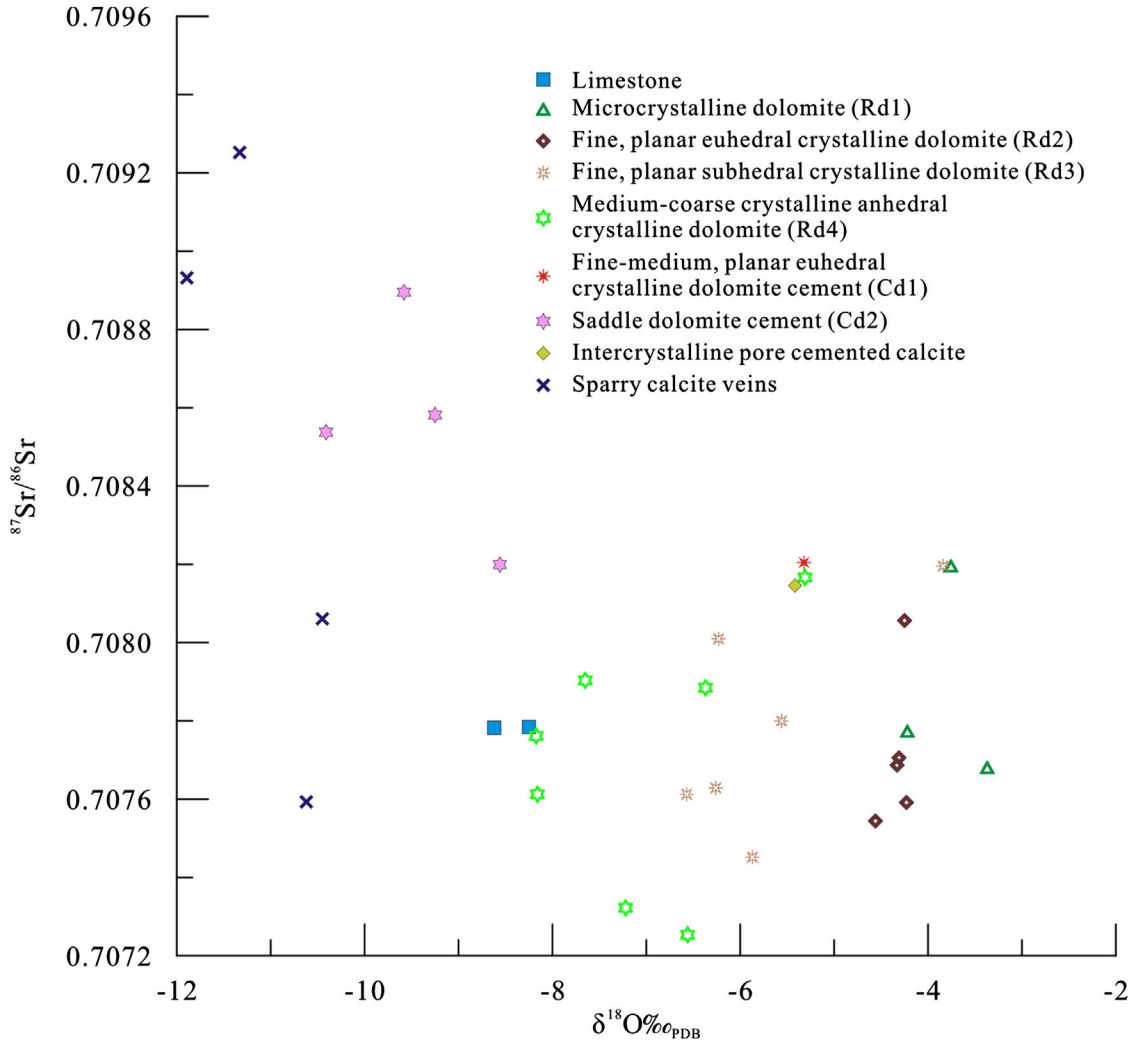

FIGURE 8
Cross-plot showing $\delta^{18}O$ vs. $\delta^{13}C$ for different carbonate rocks in the study area.

S. et al., 2014). During the deposition of the Buqu Formation in the middle Jurassic, due to the further expansion of the Bangonghu-Nujiang ocean basin in the south of the Qiangtang Basin, large-scale transgression in the basin resulted in a large, flooded area and weakened weathering. This led to a decreased proportion of Sr supplied by aluminum-siliceous rocks in the continental crust, which has high $^{87}Sr/^{86}Sr$ ratios. The Sr isotopic composition of carbonate rocks deposited in this period was controlled by mantle-derived materials with a low $^{87}Sr/^{86}Sr$ ratio in the Bangonghu-Nujiang ocean basin, resulting in a reduced $^{87}Sr/^{86}Sr$ ratio, comparable to that reported worldwide (Wan et al., 2018a).

The $^{87}Sr/^{86}Sr$ ratios of micritic limestone in the Buqu Formation in the study area ranged from 0.707763 to 0.707850 (average 0.707793). Rd1 dolomite with original fabric preserved showed $^{87}Sr/^{86}Sr$ ratios of 0.707654–0.708176 (average 0.707859). The ranges of $^{87}Sr/^{86}Sr$ ratios in Rd2, Rd3, and Rd4 were 0.707525–0.708037, 0.707432–0.707990, and 0.707234–0.707884, respectively. The average $^{87}Sr/^{86}Sr$ ratios were 0.707697 (Rd2), 0.707681 (Rd3), and 0.707605 (Rd4). The $^{87}Sr/^{86}Sr$ ratio of Cd1 was 0.708147, while the ratios of Cd2 ranged from 0.70818 to 0.708876 (average 0.708534). The $^{87}Sr/^{86}Sr$ ratio of the calcite cement filling the dolomite intergranular pores was 0.707574. The $^{87}Sr/^{86}Sr$ ratios of sparry calcite veins filling the fractures were 0.708041–0.709233 (average 0.708579). Except for samples 16D-14 (Rd1), 16D-22 (Rd2), dolomite fillings, and fissure fillings of sparry calcite veins, all other samples showed $^{87}Sr/^{86}Sr$ ratios within the range of seawater (0.707–0.708) (Veizer et al., 1999).

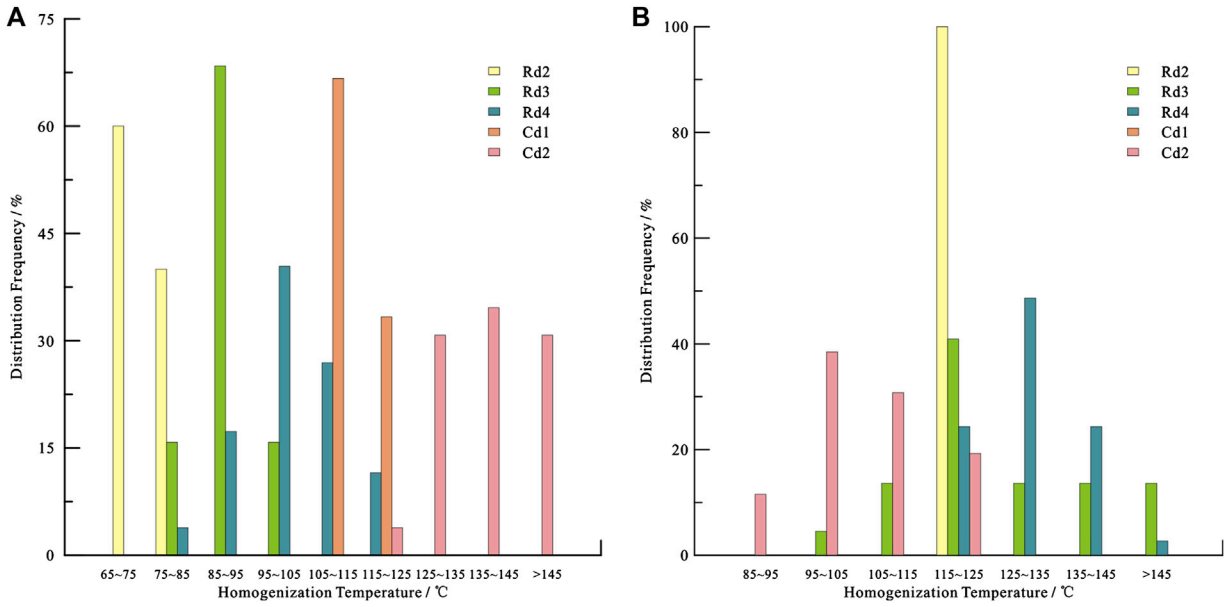

FIGURE 9
Histogram of the homogenization temperatures for fluid inclusions in different dolomite phases. **(A)** Various dolomites without misty centers and clear rims. **(B)** Clear rim parts of dolomite samples with misty centers and clear rim structures.

6 Discussion

6.1 Genesis of fabric well-preserved dolomite

Rd1 comprises fine dolomite that preserves the primary fabric of the precursor limestone. A fine dolomite grain can be interpreted as the result of dolomitization under near-surface, low temperature, and high salinity conditions (Gregg and Shelton, 1990). Moreover, fine-grained dolomite might be formed by consolidated or half-consolidated marls in metasomatism. Sibley et al. (1987) and Amthor and Friedman (1991) reported that the tiny grains had a larger surface area, which was favorable for rapid dolomite nucleation. Furthermore, a non-luminance or uniform dark red ray under cathodoluminescence also reflected a marine diagenetic environment with very low manganese content (Huang et al., 2008), indicating the early formation of this type of dolomite. The well-preserved fabric of the precursor limestone might be related to mimetic metasomatism (Sibley, 1991) and lower diagenetic temperature (Machel, 2004). Metasomatism generally requires a high-density dolomite nucleus to ensure the preservation of the complex inner texture of calcium carbonate grains and cement (Sibley, 1991). The high-density nucleation was related to the highly soluble reactive and supersaturated dolomitization fluid. For instance, the bioclastic grain comprising high magnesium calcite was often first replaced by dolomite with a well-preserved primary fabric (Tucker and Wright, 1990).

Only a few fabric-well-preserved dolomites had developed and no associated evaporated salt was observed in the study area. However, the granular dolomite was associated with evaporite in the Suonahu section. The freezing temperatures of fluid inclusions in the granular dolomites suggested a higher diagenetic fluid salinity, indicating high seawater salinity and large Mg^{2+}/Ca^{2+} ratios in the study area. These conditions are required for the formation of a highly saturated dolomitization fluid. The isotope geochemical data also supported this hypothesis. The $^{87}Sr/^{86}Sr$ ratios of 0.707763–0.707850 were close to the contemporaneous seawater ratios (0.707–0.708) (Veizer et al., 1999) (Figure 7), whereas the C-O isotope values were significantly biased/shifted (Figure 8). The positive excursion of the C isotope values might be related to an evaporative environment as in such restricted and oxygen-deficient conditions, the degradation of isotopically light carbon from organic matter in the water would have been significantly inhibited (Mckenzie, 1981; Warren, 2000; Xiong et al., 2021, 2022). Rd1 is a mimetic replacement dolomite related to evaporated seawater in the contemporaneous or penecontemporaneous stage and resulted from high salinity seawater metasomatism formed by the strong evaporation of restricted water bodies in carbonate platforms under hot and arid-semiarid conditions (Pan et al., 2015).

6.2 Genesis of fabric poorly preserved or fabric-destructive dolomites

The straight crystal boundaries, loosely stacked saccharoidal crystals, uniform red-dark red cathodoluminescence, and deficient

stylolite of Rd2 indicated its formation before strong compaction and pressure solution. The homogenization temperatures of the fluid inclusions were low (65.5°C) and the freezing temperature indicated a salinity of 19.6% (Table.2; Figure 9A), suggesting that Rd2 was formed as a result of dolomitization at low temperature in the early diagenetic stage. The texture was similar to that of the typical dolomite formed by the backflow of high salinity evaporated seawater (Adams and Rhodes, 1960). Although associated evaporated salts did not develop in the dolostone of the Buqu Formation in the study area, the salinity of the fluid inclusions was 3–7 times higher than that of normal seawater (Table 2), indicating that seawater salinity might not reach the degree of large precipitation of evaporite when the dolomitization fluid was brackish water or mildly evaporated seawater. Therefore, it is difficult to explain the origin of such dolomite using the traditional hypersaline water backflow model. However, an increasing number of studies have shown the potential for dolomitization in medium salinity or mildly evaporated seawater (Whitaker and Smart, 1990; Qing et al., 2001). Similarly, in terms of isotopes, Rd2 showed slightly heavier oxygen isotope compositions than that of the contemporaneous marine calcite but similar strontium isotopes as that of contemporaneous seawater (Figure 7, Figure 8), indicating a correlation between its origin and slightly evaporated seawater. Medium salinity dolomitization fluid could also prevent excessive dolomitization favorable for the preservation of massive intercrystalline pores and the formation of loosely stacked saccharoidal crystals. Consequently, Rd2 was formed in a low-temperature environment in the early diagenetic stage. The backflow or infiltration diffusion of slightly evaporated seawater in the shallow burial stage might be the major mode of dolomitization, in which "appropriate" dolomitization was favorable for the development and preservation of the intercrystalline pores.

Rd3 has similar cathodoluminescence and O-Sr isotope compositions as those of Rd2, suggesting a similarity in their diagenetic environment and dolomitization fluid properties with predominant marine fluid in the shallow burial stage. Compared to Rd2, Rd3 had lighter O isotope compositions, related to the increased burial depth and temperature during its formation (Table.2; Figure 8, Figure 9A). With the increased burial depth, the continuous supply of dolomitization fluid and the increasing diagenetic temperature enabled dolomite to proceed to cementation accretion after it replaced calcite, resulting in excessive dolomitization. This excessive dolomitization led to the growth of new dolomite around the initially formed dolomite and the formation of enlarged rims or crustose zones, causing dolomite to transform from euhedral to subhedral crystal and intercrystalline pores to continuously decrease. However, Rd3 developed relatively straight crystal boundaries, indicating that the formation temperature did not reach the critical temperature for crystal curvature. Therefore, such dolomite was likely formed in the late shallow burial stage. The origins of Rd3 and Rd2 were similar and successive. In the burial process, excessive dolomitization was the major reason for the less-euhedral crystals.

Rd4 mainly comprised nonplanar-curved anhedral dolomite, significantly different from the abovementioned dolomite in texture. Previous studies reported high formation temperature (Gregg and Sibley, 1984; Sibley and Gregg, 1987), highly saturated dolomitization fluid (Shukla, 1986), and competitive growth of crystals for growing space as factors leading to crystal curvature (Jones, 2005). The coarse grains, wavy extinction, and associated pressure solution stylolite indicated that Rd4 dolomite in the Buqu Formation in the Qiangtang Basin was formed with increasing temperature in the medium-deep burial stage (Fairchild, 1980; Qing and Mountjoy, 1989). The oxygen isotope of Rd4 was significantly negatively biased, and reduced by 2‰ compared to that of fine dolomite. The carbon isotope of Rd4 does not differ significantly compared to the abovementioned dolomite, which also indicated the correlation between its origin and high temperature (Figure 8, Figure 9). In particular, the $^{87}Sr/^{86}Sr$ ratio was close to or slightly higher than that of contemporaneous seawater (Figure 7), indicating that no deep mantle source fluid or atmospheric freshwater participated in the formation of such dolomite. The slightly increasing Sr isotope ratios might be related to diagenetic alteration in the burial process (Qing et al., 1998) or the participation of a neutron-rich radioactive ^{87}Sr fluid in the overlying or underlying clastic strata (Davies and Smith, 2006). Many high-temperature fluids participated in the formation of Rd4, as reflected by the homogenization temperatures of the fluid inclusions (average 102.67°C) and salinity of 21.03% (Table 2). In addition to the direct replacement of the precursor limestone, Rd4 might also be the result of recrystallization of the fine-grained dolomite formed at an early stage (Mazzullo, 1992; Hartig et al., 2011). Therefore, Rd4 was characterized by a bimodal granularity distribution. Moreover, the oxygen and strontium isotopes of some dolomite overlapped to different degrees, which might result from recrystallization due to the late dolomitization fluids alternating the early formed dolomite.

6.3 Genesis of dolomite filling

Cd1 often grew along the inwall of caverns and cracks as the first filling of caverns. Its crystal texture and cathodoluminescence were like those of fine-grained euhedral or subhedral dolomite. The freezing temperature and carbon and strontium isotopes of the fluid inclusions were also similar to those of thlarities, suggesting that Cd1 and fine-grained dolomite probably have a similar origin as that of fine-grained dolomite. These were similar to those of dolomitization fluid. However, the homogenization temperature of Cd1 was higher than that of fine-grained euhedral or subhedral dolomites and the oxygen isotope was negatively skewed compared to that of fine-grained or medium-to coarse-grained dolomites (Table 2; Figure 8,

	Matrix dolomite				Void-filling Dolomite/Dolomite Cement	
Dolomite type	Rd1	Rd2	Rd3	Rd4	Cd1	Cd2
Crystal size	micrite/ microcrystal	fine grain/ fine crystlline	fine grain/ fine crystlline	medium to coarse grained	fine grain/ fine crystlline	medium to coarse grained
Crystal type		euhedral	subhedral	anhedral	euhedral	anhedral saddle
Crystal surface morphology	planar	planar	planar	planar-curved	planar	curved
Contact relationship between crystals		point	point-line	concavo-convex	point-line	concavo-convex
Pore abundance	very poor	well	well to medium	medium to poor	poor	poor
Genetic mechanism	metasomatic genesis	metasomatic genesis	metasomatic genesis	metasomatic genesis / recrystallization	recrystallization	hydrothermal origin
Developmental stage	penecontemporaneous	shallow buried	late shallow burial	middle to deep burial	late shallow burial	tetonic thermal event (79.03Ma B. P.)
Schematic diagram of crystal texture	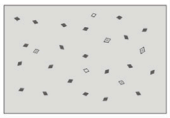	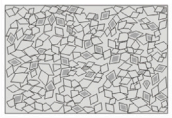		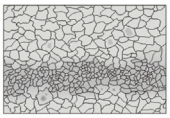		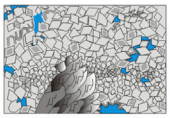

FIGURE 10
Model showing the evolution of diagenetic fabrics among representative dolomites from the study area.

Figure 9), indicating that Cd1 experienced diagenetic transformations such as recrystallization in the deep burial stage, where the higher formation temperature resulted in the fractionation of heavy oxygen isotopes.

The unique crystal texture of Cd2 indicated a unique growing environment. The crystallographic and geochemical features illustrated that such a crystal was rapidly formed in a highly supersaturated solution (Searl, 1989), but a small quantity of Cd2 might be related to the self-regulation effect of the host dolomite (Qing and Chen, 2010) and thermochemical sulfate reduction in the burial and compaction process (Machel, 1987; Machel and Lonnee, 2002). The dolomite in the Qiangtang Basin has higher homogenization temperatures compared to the saddle-shaped dolomite with limestone as the host mineral in North America and salinity of nearly 7 times higher than the contemporaneous seawater, indicating the formation was related to thermal fluids (Wang et al., 2010). However, dolomite in the Qiangtang basin, in general, might be formed by the recrystallization of previous matrix dolomite or directly in a thermal fluid rather than by replacing limestone. The Cd2 in the Tarim Basin formed during the Cambrian–Ordovician periods has similar oxygen and strontium isotopes as Rd4, and the saddle-shaped dolomite of the Buqu Formation in the Qiangtang Basin has similar carbon isotopes as grained dolomite. However, Cd2 has higher strontium isotopes but significantly lower (2‰) oxygen isotope than that of medium-coarse-grained dolomite (Figures 7, 8). These results further indicate that the saddle-shaped dolomite fillings (Cd2) in the Buqu Formation dolomite in the Qiangtang Basin were formed with the participation of external thermal fluids.

If the foreign fluid was from the deep mantle-derived fluids, the saddle-shaped dolomite formed should be characterized by a low $^{87}Sr/^{86}Sr$ ratio. If the saddle dolomite flowed through the ^{87}Sr-rich clastic rocks of the Lower Fuqu and Sewa formations, it would have absorbed a large amount of ^{87}Sr and showed an increased $^{87}Sr/^{86}Sr$ ratio in the foreign fluid. However, this is inconsistent with our findings of lower $^{87}Sr/^{86}Sr$ ratios but a wider range in the saddle dolomite compared to those of the matrix dolomite (Table 3; Figure 7). In addition, the distribution range and average ice-final melting temperature of saddle-shaped dolomite were similar to those of Rd3 and Rd4, indicating the saddle-shaped dolomite fluid was a contemporaneous marine fluid trapped in the Buqu Formation without the involvement of atmospheric water. The Yanshan and Himalayan tectonic movements occurred after the Jurassic deposition in the Qiangtang Basin. The Yanshan Movement formed the intrusive rocks (Andesite?-porphyrite) in the Buqu Formation of the SBJP section, which may have provided a heat source for saddle dolomite genetic fluid. The tectonic compression then drove the movement of marine fluid trapped in the Buqu Formation. During this migration, the marine fluid passed through the ^{87}Sr-enriched clastic strata of the overlying Xiali Formation, the underlying the Quse Formation, and the Sewa Formation. A schematic diagram of the evolution of dolomite texture in the study area of the Qiangtang basin is shown in Figure 10.

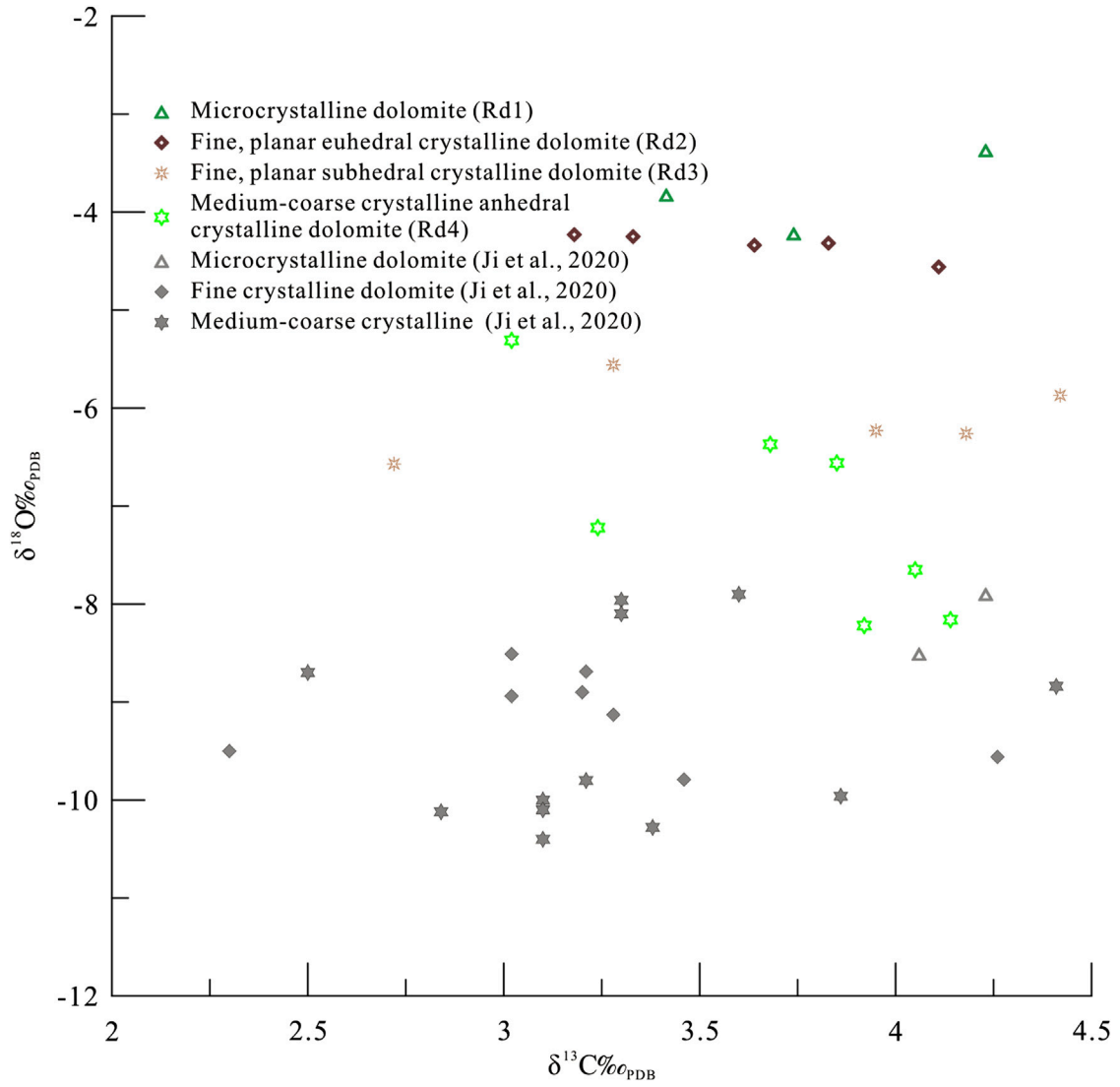

FIGURE 11
Comparisons of cross-plots showing $\delta^{18}O$ vs. $\delta^{13}C$ for different types of dolomite without misty centers and clear rims with previous research results.

6.4 Revelation of the misty center and clear rim

The granular dolomite and broken saddle dolomite in the study area in the Buqu Formation area tended to show a misty center and clear rim structure (Figure 2A). Dolomite crystals with clear rims have higher fluid formation temperatures compared to dolomite without the misty center and clear rim structure (Table.2; Figure 9B), or even higher than Rd4 and Cd2. Thus, the clear rim formation of the granular dolomite of the Buqu Formation was related to tectonic thermal events. The ice-final melting temperatures and corresponding salinity of the fluids forming the clear rim of the grain dolomite barely varied, indicating that these fluids were tectonic thermal fluids. The formation time was consistent with that of Cd2, indicating that tectonothermal events related to Cd2 significantly impacted the early dolomites, especially oxygen isotopic composition (Figure 11). The tectonothermal events may have caused high-temperature heat transfer fluid in the early dolomite oxygen isotope fractionation. The clear rim of dolomite formed in the high-temperature thermal fluid flow showed lower oxygen isotopic values, resulting in the lower oxygen isotope values of the dolomite with clear rim structures compared to those of the dolomite without misty center clear rim structures.

Two tectonic activities in the Yanshan and Himalayan periods occurred after the deposition of Jurassic strata in the Qiangtang Basin (Fang et al., 2002), especially the late Cretaceous Yanshan

Movement (Act II) that produced many thrust nappe structures (Wu et al., 2014, 2016; Ji et al., 2019; Zhao Z. et al., 2020; Wan et al., 2021). Broken after a nearly perfect diamond saddle dolomite, the clear rim portion of the fluid inclusions has a homogenization temperature far below the formation temperature of the saddle dolomite (Table 2; Figure 9). The clear rim of the saddle dolomite formed later than the saddle dolomite, and the corresponding freezing temperature and salinity suggest that the saddle dolomite was broken. During this period, the fault lines that connect atmospheric water were not formed and atmospheric freshwater did not infiltrate the Buqu Formation, suggesting that the ancient oil reservoir was not destroyed at this time. Zircon U-Pb dating of andesitic porphyrite in the SBJP section of the Buqu Formation in the northern part of the study area (Figure 1B) determined the ages for the first time at 78–64 Ma B. P. (Wan et al., 2018a; Wan et al., 2020; Wan et al., 2021). Our latest research determined the intrusive age of andesitic porphyrites in this section of 79.03 Ma (this will be described separately in other articles), indicating that the saddle-shaped dolomite was formed at about 79.03 Ma and was possibly related to the intraplate-collision orogeny between the Lhasa and Qiangtang terranes. Moreover, U-Pb isotope (LA-ICP-MS) dating of saddle-shaped dolomite showed (Qiao et al., 2020; Qiao et al., 2021a) that the saddle-shaped dolomite was formed at about 80 Ma B. P (This will be described separately in other articles), further confirming that the saddle-shaped dolomite was formed during the late stage of early the Cretaceous. All these data support that the formation of the paleo-reservoirs of oil in the southern Qiangtang Depression was related to the collision between the Indian subcontinent and the Eurasian plate and the uplift of the Qinghai-Tibet Plateau in the Cenozoic.

7 Conclusion

1) According to the primary fabric of the precursor limestone, the dolostone of the Buqu Formation in the Qiangtang Basin is divided into fabric-well-preserved (residual) and fabric-poorly preserved or fabric-destructive dolomite. The fabric-well-preserved dolomite is mainly residual dolomite (Rd1) consisting of muddy–silty crystals. The other dolomites include fine-grained euhedral dolomite (Rd2), fine-grained subhedral dolomite (Rd3), and medium-to coarse-grained anhedral dolomite (Rd4). In addition, two types of dolomite fillings developed in the study area: fine-grained euhedral-subhedral dolomite filling (Cd1) and medium-to coarse-grained saddle-shaped dolomite filling (Cd2).
2) Rd1 was formed in the penecontemporaneous stage as a result of mimetic metasomatism related to seawater evaporation. The flow of massive highly saturated dolomitization fluids was favorable for the preservation of the primary fabric. Among the fabric-poorly preserved or fabric-destructive dolomite, Rd2 and Rd3 were formed in a low-temperature environment at the shallow burial stage. The backflow or infiltration diffusion might be the major driving mechanism of dolomitization fluids. Moderate dolomitization was favorable for the formation and preservation of holes, whereas excessive dolomitization resulted in the transformation from euhedral to subhedral crystals and gradually blocked holes. Medium-coarse-grained anhedral dolomite was mostly related to high temperature and recrystallization in the medium-deep burial stage and the higher formation temperature of curved crystals.
3) Cd1 was formed in the shallow burial stage. Cd2 was related to the collisional orogeny between the Lhasa and Qiangtang terranes in the late Early Cretaceous (79.03 Ma). The thermal fluid was the marine fluid trapped in the overlying and underlying clastic rocks driven by the tectonothermal event during this period. Cd2 was mainly formed by recrystallization or direct precipitation from thermal fluids.
4) The tectonothermal events of the late Early Cretaceous greatly influenced the dolomites formed in the early stage, leading to the development of the clear rim with a misty center. The geochemical characteristics of the clear rim structure that formed after the fracture of saddle-shaped dolomites indicate that the formation of the southern Qiangtang oil paleo-reservoir belt was related to the Himalayan movement.

Data availability statement

The raw data supporting the conclusions of this article will be made available by the authors, without undue reservation.

Author contributions

All authors listed have made a substantial, direct, and intellectual contribution to the work and approved it for publication.

Funding

This article was funded by the National Natural Science Foundation of China (“The mechanism of pores formation and preservation during dolomitization: a case study from Buqu formation dolomite reservoirs, Southern Qiangtang depression”, No. 41902138).

Conflict of interest

The authors declare that the research was conducted in the absence of any commercial or financial relationships that could be construed as a potential conflict of interest.

Reviewer XT declared a shared affiliation with author JW to the handling editor at the time of review

Publisher's note

References

Adams, J. E., and Rhodes, M. L. (1960). Dolomitization by seepage refluxion. *AAPG Bull.* 44 (12), 1912–1920. doi:10.1306/0bda6263-16bd-11d7-8645000102c1865d

Amthor, J. E., and Friedman, G. M. (1991). Dolomite-rock textures and secondary porosity development in Ellenburger Group carbonates (Lower Ordovician), west Texas and southeastern New Mexico. *Sedimentology* 38 (2), 343–362. doi:10.1111/j.1365-3091.1991.tb01264.x

Badiozamani, K. (1973). The dorag dolomitization model, application to the middle Ordovician of Wisconsin. *J. Sediment. Res.* 43 (4), 965–984. doi:10.1306/74d728c9-2b21-11d7-8648000102c1865d

Bi, Y. Q., Tian, H. Q., Zhao, Y. S., Ma, Y. X., Yu, W. Q., and Hu, S. Y. (2001). On the micrite envelope to restoration of primary texture character of secondary dolomites and its significance. *Acta Petrol. Sin.* 17 (3), 491–496.

Braithwaite, C. J. R., and Rizzi, G. (1997). The geometry and petrogenesis of hydrothermal dolomites at Navan, Ireland. *Sedimentology* 44 (3), 421–440. doi:10.1046/j.1365-3091.1997.d01-30.x

Chen, H., Chen, M., Sun, W., and Wang, Y. K. (2018). Sedimentary facies and palaeogeography of the middle jurassic Buqu formation in the longeni - esima ancient oil reservoirs zone, Qiangtang basin, northern xizang. *Geol. Tethyan Geol.* 38 (2), 74–81. (in Chinese with English abstract).

Chen, M., Sun, W., Chen, H., and Song, C. Y. (2020). Sedimentary characteristics and oil-gas geological significance of the middle jurassic Buqu formation in the ersma area, southern Qiangtang basin, tibet. *Geol. Tethyan Geol.* 40 (3), 96–101. (in Chinese with English abstract).

Chen, W. B., Yang, P., Zhang, Y. J., and Peng, Z. M. (2006). Dolostone reservoirs and their Genesis in the Zaring oil pool in southern Qiangtang Basin. *Sediment. Geol. Tethyan Geol.* 26 (2), 43–46. (in Chinese with English abstract).

Choquette, P. W., and Steinen, R. P., 1980. Mississippian non-supratidal dolomite, ste. Genevieve limestone, Illinois basin: Evidence for mixed-water dolomitization. doi:10.2110/pec.80.28.0163

Dai, J. X., Ni, Y. Y., Dong, D. Z., Qin, S. F., Zhu, G. Y., Huang, S. P., et al. (2021). 2021-2025 is a period of great development of China's natural gas industry: Suggestions on the exploration and development of natural gas during the 14th five-year plan in China. *J. Nat. Gas Geoscience* 6 (4), 183–197. doi:10.1016/j.jnggs.2021.08.001

Dai, X. F., Du, B. Q., Zhang, M., Li, J., Tang, T. K., Xu, Y. P., et al. (2020). Reunderstanding and significance of high-quality reservoirs of the inner dengying Formation in the anyue gas field. *Nat. Gas. Ind. B* 7 (2), 109–119. doi:10.1016/j.ngib.2020.03.001

Davies, G. R., and Smith, L. B., Jr (2006). Structurally controlled hydrothermal dolomite reservoir facies: An overview. *Am. Assoc. Pet. Geol. Bull.* 90 (11), 1641–1690. doi:10.1306/05220605164

Dolomieu, D. D. (1981). Sur un genre de Pierres calcaires tres-peu effervescentes avec les Acides, & phosphorescentes par la collision. *J. Phys.* 29 (1), 4–10. 3–10. Translation of Dolomieu's paper with notes reporting his discovery of dolomite by Carozzi, A.V. & Zenger, D.H. 1981. Journal of Geological Education. 29. doi:10.5408/0022-1368-29.1.4

Fairchild, I. J. (1980). Stages in a precambrian dolomitization, scotland: Cementing versus replacement textures. *Sedimentology* 27 (6), 631–650. doi:10.1111/j.1365-3091.1980.tb01652.x

Fang, X. M., Lu, B., Liu, C. Y., and Liu, Z. (2002). Evolution of the central dome in the Qiangtang basin and its importance in oil-gas exploration. *Geol. Rev.* 48 (3), 279–283. (in Chinese with English abstract). doi:10.16509/j.georeview.2002.03.010

Friedman, G. M. (1965). Terminology of crystallization textures and fabrics in sedimentary rocks. *J. Sediment. Res.* 35 (3), 643–655. doi:10.1306/74d7131b-2b21-11d7-8648000102c1865d

Fu, L., Li, J. Z., Xu, W. L., Guo, W., Li, N. X., Zhang, Y. Q., et al. (2021). Characteristics and main controlling factors of Ordovician deep subsalt reservoir in central and eastern Ordos Basin, China. *J. Nat. Gas Geoscience* 6 (1), 13–25. doi:10.1016/j.jnggs.2021.03.001

Goldstein, R. H. (2001). Fluid inclusions in sedimentary and diagenetic systems. *Lithos* 55 (1-4), 159–193. doi:10.1016/s0024-4937(00)00044-x

Gregg, J. M., and Shelton, K. L. (1990). Dolomitization and dolomite neomorphism in the back reef facies of the Bonneterre and Davis formations (Cambrian), southeastern Missouri. *J. Sediment. Res.* 60 (4), 549–562. doi:10.1306/212f91e2-2b24-11d7-8648000102c1865d

Gregg, J. M., Shelton, K. L., Johnson, A. W., Somerville, I. D., and Wright, W. R. (2001). Dolomitization of the waulsortian limestone (lower carboniferous) in the Irish midlands. *Sedimentology* 48 (4), 745–766. doi:10.1046/j.1365-3091.2001.00397.x

Gregg, J. M., and Sibley, D. F. (1984). Epigenetic dolomitization and the origin of xenotopic dolomite texture. *J. Sediment. Res.* 54 (3), 908–931. doi:10.1306/212f8535-2b24-11d7-8648000102c1865d

Guo, X. S., Hu, D. F., Huang, R. C., Wei, Z. L., Duan, J. H., Wei, X. F., et al. (2020). Deep and ultra-deep natural gas exploration in the Sichuan Basin: Progress and prospect. *Nat. Gas. Ind. B* 7 (2), 419–432. doi:10.1016/j.ngib.2020.05.001

Hanshaw, B. B., Back, W., and Deike, R. G. (1971). A geochemical hypothesis for dolomitization by ground water. *Econ. Geol.* 66 (5), 710–724. doi:10.2113/gsecongeo.66.5.710

Hartig, K. A., Soreghan, G. S., Goldstein, R. H., and Engel, M. H. (2011). Dolomite in Permian paleosols of the Bravo Dome CO2 Field, USA: Permian reflux followed by late recrystallization at elevated temperature. *J. Sediment. Res.* 81 (4), 248–265. doi:10.2110/jsr.2011.24

Huang, B., Zhang, S., Lu, Z., Ye, N., Zhu, B., Ding, X., et al. (2021). Origin of dolomites in lower-middle ordovician carbonate rocks in the yingshan formation, gucheng area, Tarim Basin: Evidence from petrography and geochemical data. *Mar. Petroleum Geol.* 134, 105322. doi:10.1016/j.marpetgeo.2021.105322

Huang Q Y.Zhang, S. N., Zhang, S. Y., Liu, D., and Ye, N. (2014). Textural control on the development of dolomite reservoir: A study from the cambrian-ordovician dolomite, central Tarim Basin, NW China. *Nat. Gas. Geosci.* 25 (3), 341–350. (in Chinese with English abstract).

Huang, S. J., Lü, J., and Lan, Y. F. (2011). The main texture of dolomite of middle permian, Western Sichuan Basin: Concurrently on the differences with upper permian-triassic, northeast Sichuan Basin. *Acta Petrol. Sin.* 27 (8), 2253–2262.

Huang, S., Huang, K., Lü, J., and Lan, Y. (2014). The relationship between dolomite textures and their formation temperature: A case study from the permian-triassic of the Sichuan Basin and the lower paleozoic of the Tarim Basin. *Pet. Sci.* 11 (1), 39–51. doi:10.1007/s12182-014-0316-7

Huang, S. J., Qing, H. R., Hu, Z. W., Pei, C. R., Wang, Q. D., Wang, C. M., et al. (2008). Cathodoluminescence and diagenesis of the carbonate rocks in feixianguan formation of triassic, eastern Sichuan Basin of China. *Earth Science—Journal China Univ. Geosciences* 33 (1), 26–34.

Ji, C. J., Chen, C., Wu, Z. H., Yi, H. S., Xia, G. Q., and Zhao, Z. (2020). Carbon and oxygen isotopes analysis of the fluid inclusions in Middle Jurassic saccharoidal dolostone of Qiangtang Basin and discussion on the Genesis of dolostone. *Geol. Rev.* 66 (5), 1186–1198. (in Chinese with English abstract).

Ji, C. J., Wu, Z. H., Liu, Z. W., and Zhao, Z. (2019). Structural features of thrust nappes in the Qiangtang basin and hydrocarbon resources effect. *J. Geomechanics* 25 (S1), 66–71. (in Chinese with English abstract).

Jones, B. (2005). Dolomite crystal architecture: Genetic implications for the origin of the tertiary dolostones of the Cayman Islands. *J. Sediment. Res.* 75 (2), 177–189. doi:10.2110/jsr.2005.014

Jones, G. D., Smart, P. L., Whitaker, F. F., Rostron, B. J., and Machel, H. G. (2003). Numerical modeling of reflux dolomitization in the Grosmont platform complex (Upper Devonian), Western Canada sedimentary basin. *Am. Assoc. Pet. Geol. Bull.* 87 (8), 1273–1298. doi:10.1306/03260302007

Kaldi, J., and Gidman, J. (1982). Early diagenetic dolomite cements; examples from the permian lower magnesian limestone of england and the pleistocene carbonates of the Bahamas. *J. Sediment. Res.* 52 (4), 1073–1085. doi:10.1306/212f80da-2b24-11d7-8648000102c1865d

Land, L. S. (1985). The origin of massive dolomite. *J. Geol. Educ.* 33 (2), 112–125. doi:10.5408/0022-1368-33.2.112

Li, X., Yi, H. S., Jin, F., Ji, C. J., and Li, K. Y. (2018). Diagenetic characteristics of dolomite in the Long'eni-Angdar Co ancient reservoir, Qiangtang Basin, China. *J. Chengdu Univ. Technol. Sci. Technol. Ed.* 45 (2), 142–153. (in Chinese with English abstract).

Liu, D. H. (1995). Fluid inclusion studies: An effective means for basin fluid investigation. *Earth Sci. Front.* 2 (4), 149–154. (in Chinese with English abstract).

Liu, J. Q., Chen, W. B., Yang, P., Chen, W. X., and Fu, X. G. (2008a). The dolomite fabric characteristics and lead isotope significance of the ancient oil accumulation in Long'eni- angdar lake Qiangtang basin. *Acta Geosci. Sin.* 29 (1), 72–80. (in Chinese with English abstract).

Liu, J. Q., Chen, W. B., Yang, P., Chen, W. X., and Fu, X. G. (2008b). The Longeni-Aangdaerco paelo-oil dolomite geochemical characteristcs in southern part of the center uplift zone of Qiangtang basin and it's significance. *Acta Petrol. Sin.* 24 (06), 1379–1389. (in Chinese with English abstract).

Liu, J. Q., Jia, B. J., Yang, P., Chen, W. B., Chen, W. X., and Fu, X. G. (2008c). Characteristics of the paleo-oil dolomite REE geochemistry of Buqu formaiton in southern part of the central uplift zone of Qiangtang basin and it's sigificance. *Acta Sedimentol. Sin.* 26 (1), 28–38. (in Chinese with English abstract).

Liu, J. Q., Yang, P., Chen, W. B., Chen, W. X., and Fu, X. G. (2010). The characteristics of Longen-i Angdaercuo paleo-oil dolomite in southern part of the central uplift zone of Qiangtang Basin and its forming mechanism, China University of Geosciences (Beijing):Peking University. *Earth Sci. Front.* 17 (1), 311–321. (in Chinese with English abstract).

Liu, X. Y., Wei, L. B., Liu, B. X., Zhang, L., Guo, W., Zhang, J. W., et al. (2021). Characteristics of natural gas accumulation in the Cambrian weathered crust in southwestern Ordos Basin. *Nat. Gas. Ind. B* 8 (5), 421–430. doi:10.1016/j.ngib.2021.08.001

Long, S. X., Cheng, Z., Xu, H. M., and Chen, Q. (2020). Exploration domains and technological breakthrough directions of natural gas in SINOPEC exploratory areas, Sichuan Basin, China. *J. Nat. Gas Geoscience* 5 (6), 307–316. doi:10.1016/j.jnggs.2020.10.002

Lonnee, J., and Machel, H. G., 2004. Dolomitization by halite-saturated brine and subsequent hydrothermal alteration in the devonian slave point formation, clark lake gas field, British columbia. In CSPG-CHOA-CWLS Joint Conference Abstracts (Vol. 13).

Lu, F. F., Tan, X. C., Zhong, Y., Luo, B., Zhang, B. J., Zhang, Y., et al. (2020). Origin of the penecontemporaneous sucrosic dolomite in the Permian Qixia formation, northwestern Sichuan Basin, SW China. *Petroleum Explor. Dev.* 47 (6), 1218–1234. doi:10.1016/s1876-3804(20)60131-3

L´opez-Horgue, M. A., Iriarte, E., Schr¨oder, S., Fern´andez-Mendiola, P. A., Caline, B., Corneyllie, H., et al. (2010). Structurally controlled hydrothermal dolomites in Albian carbonates of the Asón valley, Basque Cantabrian Basin, Northern Spain. *Mar. Petroleum Geol.* 27 (5), 1069–1092. doi:10.1016/j.marpetgeo.2009.10.015

Machel, H. G. (2004). Concepts and models of dolomitization: A critical reappraisal. *Geol. Soc. Lond. Spec. Publ.* 235 (1), 7–63. doi:10.1144/gsl.sp.2004.235.01.02

Machel, H. G., and Lonnee, J. (2002). Hydrothermal dolomite a product of poor definition and imagination. *Sediment. Geol.* 152 (3-4), 163–171. doi:10.1016/s0037-0738(02)00259-2

Machel, H. G. (1987). Saddle dolomite as a by-product of chemical compaction and thermochemical sulfate reduction. *Geol.* 15 (10), 936. doi:10.1130/0091-7613(1987)15<936:sdaabo>2.0.co;2

Mazzullo, S. J. (1992). Geochemical and neomorphic alteration of dolomite: A review. *Carbonates Evaporites* 7 (1), 21–37. doi:10.1007/bf03175390

Mckenzie, J. A. (1981). Holocene dolomitization of calcium carbonate sediments from the coastal sabkhas of abu dhabi, UAE: A stable isotope study. *J. Geol.* 89, 185–198. doi:10.1086/628579

McKenzie, J. A., Hsü, K. J., and Schneider, J. F. (1980). Movement of subsurface waters under the sabkha Abu Dhabi, UAE, and its relation to evaporative dolomite Genesis. *Concepts Models Dolomitization*, 11–30. doi:10.2110/pec.80.28.0011

Morrow, D. (1998). Regional subsurface dolomitization: Models and constraints. *Geosci. Can.*

Mountjoy, E. W., Machel, H. G., Green, D., Duggan, J., and Williams-Jones, A. E. (1999). Devonian matrix dolomites and deep burial carbonate cements: A comparison between the rimbey-meadowbrook reef trend and the deep basin of west-central alberta. *Bull. Can. Petroleum Geol.* 47 (4), 487–509.

Mutti, M., and Simo, J. A. (1994). Distribution, petrography and geochemistry of early dolomite in cyclic shelf facies, Yates Formation (Guadalupian), Capitan Reef Complex, USA. Dolomites. *A Volume Honour Dolomieu*, 91–107. doi:10.1002/9781444304077.ch7

Pan, J. Q., Song, C. H., Bao, J., Ma, L. F., Yan, M. D., Fang, X. M., et al. (2015). Geochemical characteristics and salt- forming analysis of jurassic strata in Qiangtang basin. *Acta Geol. Sin.* 89 (11), 2152–2160. (in Chinese with English abstract).

Patterson, R. J., and Kinsman, D. J. J. (1982). Formation of diagenetic dolomite in coastal sabkha along Arabian (Persian) Gulf. *AAPG Bull.* 66 (1), 28–43.

Peng, Z. M., Liao, Z. L., Chen, M., Liu, J. Q., Zhang, Y. J., Chen, W. B., et al. (2008). Origin of the jurassic dolostone reservoirs in the Qiangtang basin on the qinghai-xizang plateau. *Geol. Tethyan Geol.* 28 (4), 1–6. (in Chinese with English abstract).

Purser, B., Tucker, M., and Zenger, D. (1994). Dolomites. International association of sedimentologists. Oxford: Blackwell Scientific Publications, 451.

Qiao, Z. F., Shao, G. M., Luo, X. Y., Cao, P., Sun, X. W., and Shen, A. J. (2021a). Genetic classification and large-scale reservoir development law of burial dolomite: Cognition based on LA-ICP-MS trace elemental mapping and U-Pb dating. *Nat. Gas. Ind.* 41 (9), 46–56. (in Chinese with English abstract).

Qiao, Z. F., Zhang, S. N., Shen, A. J., Hu, A. P., Liang, F., Luo, X. Y., et al. (2020). Laser ablate U-Pb dating-based determination of burial dolomitization process: A case study of lower ordovician penglaiba formation of yonganba outcrop in Tarim Basin. *Acta petrol. Sinia* 36 (11), 3493–3509. (in Chinese with English abstract).

Qiao, Z. F., Zhang, S. N., Shen, A. J., Shao, G. M., She, M., Cao, P., et al. (2021b). Features and origins of massive dolomite of lower ordovician penglaiba Formation in the northwest Tarim Basin: Evidence from petrography and geochemistry. *Petroleum Sci.* 18, 1323–1341. doi:10.1016/j.petsci.2021.03.001

Qing, H. R., and Chen, D. Z. (2010). Non- hydrothermal saddle dolomite: Petrological and geochemical evidence from the ordovician yeoman formation, southeastern saskatchewan, canda. *Acta Sedimentol. Sin.* 28 (5), 980–986.

Qing, H. R., Barnes, C. R., Buhl, D., and Veizer, J. (1998). The strontium isotopic composition of ordovician and silurian brachiopods and conodonts: Relationships to geological events and implications for coeval seawater. *Geochimica cosmochimica acta* 62 (10), 1721–1733. doi:10.1016/s0016-7037(98)00104-5

Qing, H. R., Bosence, D. W. J., and Rose, E. P. F. (2001). Dolomitization by penesaline sea water in Early Jurassic peritidal platform carbonates, Gibraltar, Western Mediterranean. *Sedimentology* 48 (1), 153–163. doi:10.1046/j.1365-3091.2001.00361.x

Qing, H. R., and Mountjoy, E. W. (1989). Multistage dolomitization in rainbow buildups, middle devonian keg river formation, alberta, Canada. *J. Sediment. Res.* 59 (1), 114. doi:10.1306/212f8f30-2b24-11d7-8648000102c1865d

Qing, H. R., and Mountjoy, E. W. (1994). Rare Earth element geochemistry of dolomites in the middle devonian presqu'ile barrier, western Canada sedimentary basin: Implications for fluid-rock ratios during dolomitization. *Sedimentology* 41 (4), 787–804. doi:10.1111/j.1365-3091.1994.tb01424.x

Searl, A. (1989). Saddle dolomite: A new view of its nature and origin. *Mineral. Mag.* 53 (5), 547–555. doi:10.1180/minmag.1989.053.373.05

Shukla, V., Gregg, J. M., and Sibley, D. F. (1986). Epigenetic dolomitization and the origin of xenotopic dolomite texture; discussion and reply. *J. Sediment. Res.* 56, 733–736. doi:10.1306/212f8a30-2b24-11d7-8648000102c1865d

Sibley, D. F., Dedoes, R. E., and Bartlett, T. R. (1987). Kinetics of dolomitization. *Geol.* 15 (12), 1112. doi:10.1130/0091-7613(1987)15<1112:kod>2.0.co;2

Sibley, D. F., and Gregg, J. M. (1987). Classification of dolomite rock textures. *J. Sediment. Res.* 57 (6), 967–975.

Sibley, D. F. (1991). Secular changes in the amount and texture of dolomite. *Geol.* 19 (2), 151. doi:10.1130/0091-7613(1991)019<0151:scitaa>2.3.co;2

Sun, W., Chen, M., Wan, Y. L., He, J. L., Lan, Y. F., Wei, H. W., et al. (2020). Closed-system dolomitization process and the significance for petroleum geology, an example from dolostone in the Middle Jurassic Buqu Formation in southern Qiangtang Depression. *Geol. Rev.* 66 (5), 1218–1230. (in Chinese with English abstract).

Tan, F. W., Wang, J., Wang, X. L., and Du, B. W. (2004). Analysis of carbon and oxygen isotope composition and sedimentary environment of the Yanshiping area of the Qiangtang basin in Middle-Late Jurassic. *Acta Geosci. Sin.* 25 (2), 119–126. (in Chinese with English abstract).

Tan, F. W., Zhang, R. H., Wang, J., Si, C. S., and Ma, L. Q. (2016). Discussion on basement structures of the late Triasic- early Cretaceous Qiangtang rift basin in Tibet, China. *J. Chengdu Univ. Technol. Sci. Technol. Ed.* 43 (5), 513–521. (in Chinese with English abstract).

Tian, K. Z., Ji, C. J., Yi, H. S., Tan, M., Jin, F., and Fan, L. S. (2019). Origin of grained dolomite from the Buqu Formation of Zaring area in southern Qiangtang depression. *Geol. China* 46 (2), 398–406. (in Chinese with English abstract).

Tucker, M. E., and Wright, V. P. (1990). *Carbonate sedimentology*. Oxford: Wiley-Blackwell.

Vasconcelos, C., and McKenzie, J. A. (1997). Microbial mediation of modern dolomite precipitation and diagenesis under anoxic conditions (Lagoa Vermelha, Rio de Janeiro, Brazil). *J. Sediment. Res.* 67 (3), 378–390.

Veizer, J., Ala, D., Azmy, K., Bruckschen, P., Buhl, D., Bruhn, F., et al. (1999). $^{87}Sr/^{86}Sr$, $\delta^{13}C$ and $\delta^{18}O$ evolution of Phanerozoic seawater. *Chem. Geol.* 161 (1-3), 59–88. doi:10.1016/s0009-2541(99)00081-9

Wan, Y. L., Wang, J., Fu, X. G., Tan, F. W., and Wang, Z. W. (2018a). *J. Chengdu Univ. Technol. Sci. Technol. Ed.* 45 (2), 129–141. (in Chinese with English abstract).

Wan, Y. L., Wang, J., Fu, X. G., and Wang, D. (2020). Geochemical tracing of isotopic fluid of dolomite reservoir in the Middle Jurassic Buqu Formation in southern depression of Qiangtang Basin. *Oil Gas Geol.* 41 (1), 189–200. (in Chinese with English abstract).

Wan, Y. L., Wang, J., Fu, X. G., and Wang, D. (2018b). Trace element geochemical signatures and significance of the Buqu Formation dolostones in southern Qiangtang depression. *Sediment. Geol. Tethyan Geol.* 38 (2), 23–35. (in Chinese with English abstract).

Wan, Y. L., Wang, J., Tan, F. W., Fu, X. G., and Wang, Z. W. (2017a). Dolomite reservoir formation mechanism and pore evolution feature of Buqu formation in the Long'eni- Angdaerco area, Qiangtang basin. *J. Northeast Petroleum Univ.* 41 (3), 21–33. (in Chinese with English abstract).

Wan, Y. L., Wang, J., Wan, F., Fu, X. G., Wang, Z. W., and Shen, L. J. (2017b). Characteristics and indications of rare Earth elements in carbonates in the Buqu Formation, southern Qiangtang Basin. *Petroleum Geol. Exp.* 39 (5), 655–665. (in Chinese with English abstract).

Wan, Y. L., Zhao, Z., Hu, Z. Z., and Li, X. R. (2021). Controlling factors and their geological significances of order degrees and unit-cell parameters of dolomites in the Middle Jurassic Buqu Formation in Qiangtang Basin. *Sediment. Geol. Tethyan Geol.* 41 (4), 512–523. (in Chinese with English abstract).

Wang, D., Wang, X., and Chen, D. Z. (2010). Characteristics of saddle dolomite cements in the Cambrian ordovician carbonates in tabei and tazhong area of Tarim Basin. *Chin. J. Geol.* 45 (02), 580–594. (in Chinese with English abstract).

Wang, J., and Fu, X. G. (2018). Sedimentary evolution of the Qiangtang basin. *Geol. China* 45 (2), 237–259. (in Chinese with English abstract).

Wang, J., Fu, X. G., Shen, L. J., Tan, F. W., Song, C. Y., and Chen, W. B. (2020). Prospect of the potential of oil and gas resources in Qiangtang basin, xizang(tibet). *Geol. Rev.* 66 (5), 1091–1113. (in Chinese with English abstract).

Wang, J., Wang, Z. J., Chen, W. X., Fu, X. G., and Chen, M. (2007). New evidences for the age assignment of the NadiKangri Formation in the north Qiangtang Basin, northern tibet, China. *Geol. Bull. China* 26 (4), 404–409

Wang, X. T., Zhang, Q. S., Zhang, J., Zhou, S. X., and Li, J. W. (2000). Character study and analysis of dolomite of mesozoic in qingzang plateau. *Acta Sedimentol. Sin.* 18 (4), 555–559. (in Chinese with English abstract).

Warren, J. (2000). Dolomite: Occurrence, evolution and economically important associations. *Earth-Science Rev.* 52 (1-3), 1–81. doi:10.1016/s0012-8252(00)00022-2

Whitaker, F. F., and Smart, P. L. (1990). Active circulation of saline ground waters in carbonate platforms: Evidence from the Great Bahama Bank. *Geol.* 18 (3), 200. doi:10.1130/0091-7613(1990)018<0200:acosgw>2.3.co;2

Wright, W. R. (2001). *Dolomitization, fluid-flow and mineralization of the lower carboniferous rocks of the Irish midlands and dublin basin regions*. Doctoral dissertation, University College Dublin.

Wu, Z. H., Gao, R., Lu, Z. W., Ye, P. S., Lu, L., and Yin, C. Y. (2014). Structures of the Qiangtang basin and its significance to oil- gas exploration. *Acta Geol. Sin.* 88 (6), 1130–1144. (in Chinese with English abstract).

Wu, Z. H., Liu, Z. W., Zhao, Z., Ji, C. J., and Ye, P. S. (2016). Thrust and uplift of the lung'eni-angdarco paleo-oil reservoirs in the Qiangtang basin. *Acta Geol. Sin.* 90 (4), 615–627. (in Chinese with English abstract).

Xiong, Y., Tan, X. C., Zhong, S. K., Xiao, D., Wang, B. B., Yang, M. Y., et al. (2022). Dynamic paleokarst geochemistry within 130 Myr in the middle ordovician shanganning carbonate platform, north China. *Palaeogeogr. Palaeoclimatol. Palaeoecol.* 591, 110879. doi:10.1016/j.palaeo.2022.110879

Xiong, Y., Wang, L. C., Tan, X. C., Liu, Y., Liu, M. J., Qiao, Z. F., et al. (2021). Dolomitization of the ordovician subsalt majiagou Formation in the central ordos basin, China: Fluid origins and dolomites evolution. *Pet. Sci.* 18 (2), 362–379. doi:10.1007/s12182-020-00522-1

Yang, R. H., Li, C., Yang, D. M., He, Z. H., Ren, Y. S., and Liu, J. (2000). Mesozoic tectonic-petrographic evolution and oil- gas perspective in Qiangtang basin, tibet. *J. Changchun Univ. Sci. Technol.* 30 (3), 237–242. (in Chinese with English abstract).

Yang, W., Liu, M. C., Wei, G. Q., Jin, H., Xie, W. R., Wu, S. J., et al. (2021). Lithofacies paleogeography and characteristics of large-scale reservoirs of the middle triassic leikoupo Formation in Sichuan Basin, China. *J. Nat. Gas Geoscience* 6 (5), 255–268. doi:10.1016/j.jnggs.2021.09.002

Yang, Y., Xie, J. R., Zhao, L. Z., Huang, P. H., Zhang, X. H., Chen, C., et al. (2021). Breakthrough of natural gas exploration in the beach facies porous dolomite reservoir of middle permian maokou Formation in the Sichuan Basin and its implications: A case study of the tridimensional exploration of well JT1 in the central-northern Sichuan Basin. *Nat. Gas. Ind. B* 8 (4), 393–401. doi:10.1016/j.ngib.2021.07.010

Yi, H. S., Chen, Z. Y., Ji, C. J., Yang, X. P., Xiong, G. Q., and Wu, C. H. (2014). New evidence for deep burial origin of sucrosic dolomites from Middle Jurrasic Buqu Formation in southern Qiangtang basin. *Acta Petrol. Sin.* 30 (3), 737–746. (in Chinese with English abstract).

Yi, H. S., Gao, C. W., Zhang, X. Q., and Li, J. H. (2004). Microscopic diagenetic fabrics of dolomite reservoir from Shuanghu paleo-oil pool of Qiangtang basin and its petroleum exploration implications. *J. Chengdu Univ. Technol. Sci. Technol. Ed.* 31 (6), 611–615. (in Chinese with English abstract).

Yi, H. S., and Xia, G. Q. (2022). Stratigraphic position of higher quality source rocks and and distribution of oil-bearing dolomites in the Qiangtang Basin. *Sediment. Geol. Tethyan Geol.* (in Chinese with English abstract). doi:10.19826/j.cnki.1009-3850.2022.04005

Yu, Z., Zhou, J. G., Ding, Z. C., Wei, L. B., Wei, Y., Wu, X. N., et al. (2020). Reservoir characteristics and Genesis of the Ordovician M_5^{4-1a} in the central and eastern parts of the Ordos Basin, China. *J. Nat. Gas Geoscience* 5 (5), 285–297. doi:10.1016/j.jnggs.2020.09.001

Yue, H., Liu, F., Zhang, H. L., Zhou, C. L., Chen, W. H., Xiao, Z. H., et al. (2021). Specified staged acid fracturing of horizontal well for strong-heterogeneity carbonate gas reservoirs: A case study on the gas reservoir of the fourth member of upper sinian dengying Formation in gaoshiti-moxi area of the central Sichuan Basin. *Nat. Gas. Ind. B* 8 (5), 484–493. doi:10.1016/j.ngib.2021.08.010

Zhang, L. Q., Ji, Y. L., and Li, Y. T. (2001). Reservoir characteristics of the jurassic dolomite in the Qiangtang basin. *Petroleum Geol. Exp.* 23 (4), 384–389. (in Chinese with English abstract).

Zhang, X. Q., Yi, H. S., and Zhu, Y. T. (2005). Study on reservoir characterritics of the dolomite in the Shuanghu area, Qiangtang basin. *J. Southwest Petroleum Univ. Sci. Technol. Ed.* 27 (5), 10–13. (in Chinese with English abstract).

Zhang, Y. X., Li, Y., Zhang, K. J., and Li, Y. L. (2006). Characteristics of mid-upper jurassic carbonate rocks in the yichangma area, Qiangtang basin, tibet: Implications for the sedimentary environment. *Geol. China* 33 (2), 393–400. (in Chinese with English abstract).

Zhao, W. Z., Wang, Z. C., Jiang, H., Fu, X. D., Xie, W. R., Xu, A. N., et al. (2020). Exploration status of the deep Sinian strata in the Sichuan Basin: Formation conditions of old giant carbonate oil/gas fields. *Nat. Gas. Ind. B* 7 (5), 462–472. doi:10.1016/j.ngib.2020.09.004

Zhao, Z., Wu, Z. H., Yang, Z. Y., and Ji, C. J. (2020). Establishing the chronostratigraphic framework of the continental red beds in Central Qiangtang Basin: Constrained by zircon U-Pb ages. *Geol. Rev.* 66 (5), 1155–1171. (in Chinese with English abstract).

Zhu, J. Q., and Li, Y. T. (2000). Types, origin and reservoir characteristics of the jurassic dolostones in the Qiangtang basin, north tibet. *J. Palaeogeogr.* 2 (4), 30–42. (in Chinese with English abstract).

frontiers | Frontiers in Earth Science

TYPE Original Research
PUBLISHED 06 September 2022
DOI 10.3389/feart.2022.987020

OPEN ACCESS

EDITED BY
Deyu Gong,
Research Institute of Petroleum Exploration and Development (RIPED), China

REVIEWED BY
Xiaoqun Yang,
Institute of Geology and Geophysics (CAS), China
M. A. Baojun,
Hebei GEO University, China

*CORRESPONDENCE
Fei Ning,
ningfei037@aliyun.com

SPECIALTY SECTION
This article was submitted to Economic Geology,
a section of the journal
Frontiers in Earth Science

RECEIVED 05 July 2022
ACCEPTED 04 August 2022
PUBLISHED 06 September 2022

CITATION
Ning F, Lin H, Zhou C, Yun J, Li P and Song H (2022), Characteristics of strike-slip fault-related reservoirs and the significance for hydrocarbon accumulation in the central Tarim Basin: Insights from the modern karst model. *Front. Earth Sci.* 10:987020. doi: 10.3389/feart.2022.987020

Characteristics of strike-slip fault-related reservoirs and the significance for hydrocarbon accumulation in the central Tarim Basin: Insights from the modern karst model

Fei Ning[1,2]*, Huixi Lin[1], Cunjian Zhou[3], Jinbiao Yun[1], Peng Li[4] and Haiming Song[1]

[1]Exploration and Production Research Institute, SINOPEC, Beijing, China, [2]Laboratory of Structural and Sedimentological Reservoir Geology, Exploration and Production Research Institute, SINOPEC, Beijing, China, [3]State Key Laboratory of Oil and Gas Reservoir Geology and Exploitation, Chengdu University of Technology, Chengdu, China, [4]Geology and Geophysics Department, University of Wyoming, Laramie, WY, United States

Proven to be closely linked to hydrocarbon accumulation, strike-slip faults are important hydrocarbon accumulation zones. In order to clarify the controlling effects of strike-slip faults on reservoirs, characteristics of two types of reservoirs, including strike-slip fault-controlled fracture caverns and strike-slip fault-dissolved fracture caverns in the central Tarim Basin, are delineated through detailed analyses of seismic data, tectonic evolution, and observations of the core and thin sections. High-density electrical logging was utilized for the modern karst area of South China to identify the development characteristics of the fractured-cavernous carbonate reservoirs. The development model of modern karst reservoirs was applied in the study of the Ordovician carbonate paleokarst in Tarim Basin to build the karst reservoir development model related to strike-slip faults. Modern karst investigation confirmed that the network of fracture systems formed by strike-slip faults was conducive to developing karst pores, while the tectonic slope provided hydrodynamic conditions for karstification. The karst fracture formed along the dissolved fractures at the top of the cave is not easily filled with debris, making it an important reservoir space outside the large karst caves. The Ordovician epikarst fracture-cavernous system is an important reservoir in the area from Shuntuoguole slope in the north of Tazhong uplift to the Tabei Uplift of the Tarim Basin. The reservoir, strike-slip faults, and unconformities together constitute a three-dimensional hydrocarbon accumulation system, which facilitates the migration and accumulation of oil and gas from deep source rocks to Ordovician karst fracture caverns and plays a significant role in hydrocarbon migration and accumulation.

KEYWORDS

strike-slip (fault), characteristics of reservoirs, modern karst environment, development model, carbonate layer, Tarim Basin

Introduction

Whether formed by tension torsion or compression torsion, strike-slip faults always damaged the surrounding rocks on both sides of fault planes during formation so as to induce the development of fractures and caverns (Peacock, 1991). Fractures and caverns not only provide major migration pathways and reservoirs for petroleum and natural gas but also are the main controlling factor for fluid seepage. The degree of development, distribution patterns, and connectivity of fractures and caverns control the migration and accumulation of oil and gas and affect the distribution of oil and gas reservoirs. In recent years, several wells of thousand-ton oil/gas production have been found in the strike-slip fault area in Tarim Basin, providing abundant evidence that the oil and gas reservoirs controlled by strike-slip faults, as a new type of reservoirs, have great exploration potential. These reservoirs controlled by strike-slip faults have long been an area where exploration and development of ultra-deep carbonate rocks in Tarim Basin are directed toward (Qi, 2020; Yang et al., 2020). Moreover, the exploration practices in reservoirs controlled by strike-slip faults in the Tarim Basin have also inspired the study of similar reservoirs in the Sichuan Basin and the Ordos Basin (Ma et al., 2018; He et al., 2021). In recent years, the generation and evolution of strike-slip faults inside basins and the mechanism for hydrocarbon accumulation have gradually become a focus point in structural geology and petroleum geology (Zhu et al., 2011; Ma D. et al., 2019; Han et al., 2019; He et al., 2019; Gu et al., 2020; Ma et al., 2020; Wu et al., 2020; Zhu et al., 2020). Controlled by the activities of strike-slip faults of multi-stages and fluid reformation, large-scale reservoirs were formed in the Ordovician carbonate rocks in Tazhong, Shuntuoguole, and Tabei uplifts of the Tarim Basin (Lu et al., 2017; Ding et al., 2020; Qi, 2020). The strike-slip fault system not only connects vertically with the source rock in the deep part but also has controlling effects on the migration and accumulation of oil and gas (Deng et al., 2018; Ma Y. et al., 2019; Han et al., 2019; Deng et al., 2021a). Although the discovered ultra-deep fault-controlled carbonate reservoir has reached 1 billion tons (Qi, 2020; Yang et al., 2020), the understanding of the control mechanism of strike-slip faults on fracture-cavernous reservoirs still lags behind exploration practice. Different from the conventional fault-related traps, the core issue for hydrocarbon enrichment in the strike-slip fault zone is the carbonate fracture-cavernous reservoir formed by the strike-slip faults, where the primary surrounding rock is the seal. It is of great guiding significance to establish the geological model for the distribution, spatial range, and morphology of fracture-cavernous reservoirs related to strike-slip faults in accordance of geological principles as it clarifies the enrichment patterns of strike-slip fault-controlled reservoirs and drives effective exploration and development.

Guizhou is located in the center of the southwest region of China's bare karst area, where carbonate rocks are well developed. Through the study of karst development characteristics, main controlling factors, and models around strike-slip faults in the modern low-uplift areas of southern Guizhou, China, the development model for karst fracture caverns controlled by strike-slip faults is built, from which references can be drawn for the exploration and development of marine paleo-karst reservoirs in the deep strata of Tarim Basin.

Geological background

The Tarim basin is a large-scale superimposed basin evolved with the Tarim craton. In episode I of the middle Caledonian, the West Kunlun of the southwestern margin combined with the Tarim craton (Sobel and Arnaud, 1999; Mattern and Schneider, 2000; Li et al., 2018; Qiu et al., 2019), forming multiple paleo-uplifts in the Tarim Basin. The NE-trending regional compression principal stress laid the foundation for the development of strike-slip faults in the Tarim Basin (Figure 1B). Later, the Tarim Basin was reconstructed by the superposition of multi-stage collision orogenic events (Gehrels et al., 2003; Yin et al., 2007; Wu et al., 2016), such as the combination of the Altun (in the southeastern margin) and the Tarim in episode III of the middle Caledonian, and the closure of the scissor-like difference of the southern Tianshan Ocean (in the northern margin) from east to west during the Hercynian. In the Indosinian-Himalayan period, Tarim Basin was mainly affected by the remote effect of the closure of the Paleo-Tethys Ocean and the Neo-Tethys Ocean (Mattauer et al., 1985; Hacker et al., 2000; Ratschbacher et al., 2003; Xiao et al., 2003, 2015; Zhu et al., 2021). The superimposed reformation of multi-stages in the Tarim Basin from Caledonian provides the dynamic source for the evolution of strike-slip faults inside the craton.

Under this background, strike-slip faults are widely developed inside the Tarim craton, which in the eastern part are primarily in the Tazhong Uplift and its north, the Shuntuoguole Uplift, and the Tabei Uplift (Figure 1C). Primarily in the NNE-trending near-parallel faults in the Tazhong Uplift and its northern slope and the NNE-NNW trending X-shaped faults in Tuoputai-Halahatang area of the Tabei Uplift, the strike-slip fault system is mainly developed in the middle and lower Ordovician carbonate rocks formed by the tectonic movement in the middle Caledonian (He et al., 2006; Jia et al., 2007) and experienced multiple activities in the later period (Deng, et al., 2021b; Wu, et al., 2021). Superimposed by multi-stages of fluid reformation, large-scale reservoirs were formed in the Ordovician carbonate rocks in the northern slope of the Tazhong Uplift, the Shuntuoguole Low Uplift, and the Tabei Uplift of the Tarim Basin (Lu et al., 2017; Ding, et al., 2020; Qi,

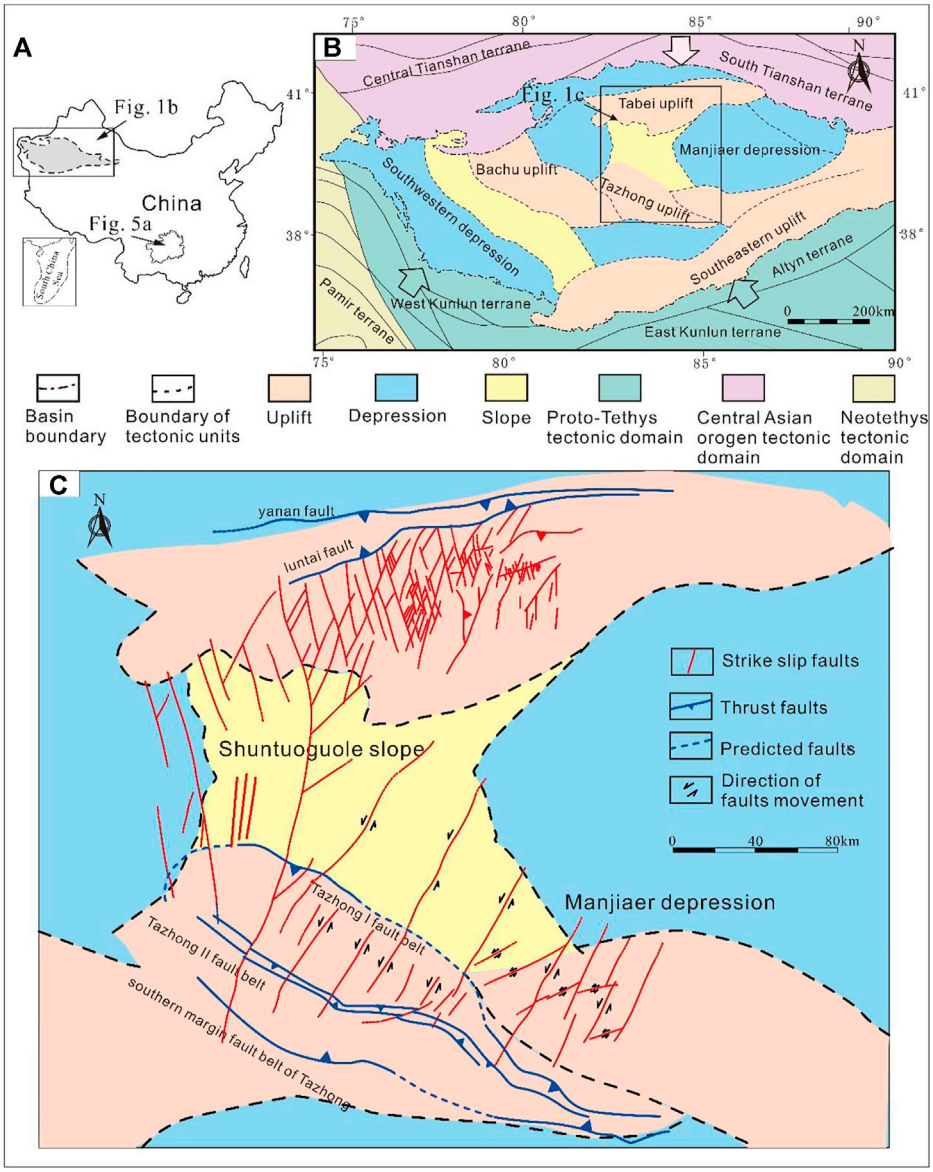

FIGURE 1
Distribution of strike-slip faults in Tarim Basin; **(A)** location of the Tarim Basin and Guizhou Province; **(B)** map showing the distribution and structural background of the Tarim Basin; **(C)** detailed map of distribution of the strike-slip fault belts in the eastern part of the Tarim Basin based on the interpretation of seismic data.

2020), which played an important role in hydrocarbon accumulation.

The Ordovician strata in the Tarim Basin are well-developed, with a few distinctive classifications of Ordovician lithostratigraphic units in Tazhong and Tabei areas representative of different paleogeographic environments and sedimentary types. The Ordovician in the Tazhong area is entirely comparable to that in the Tabei area, and both can be divided into three series and six formations (Table 1): The Lower Ordovician Penglaiba Formation, the Lower-Middle Ordovician Yingshan Formation, the Middle Ordovician Yijianfang Formation, the Upper Ordovician Sangtamu Formation, the Qiaerbake Formation, and the Lianglitage Formation. The Upper Yingshan-Qiaerbake Formation is absent in Tazhong area as it is only developed in the Shuntuoguole Low Uplift. The Lianglitage Formation in the Tazhong area has a great thickness and can be divided into three sections, namely, the argillaceous-banded limestone section, the granular limestone section, and the argillaceous limestone section. The Lianglitage Formation in the northern Tarim Basin is thin, only equivalent to

TABLE 1 Ordovician stratigraphic column of the study area.

System	Series	Formation	Symbol	Age (Ma)	Lithology	Tectonic movement
Ordovician	Upper	Sangtamu	O_3s	443.8		Middle Caledonian (II phase)
		Lianglitage	O_3l			
		Qiaerbake	O_3q	460.9		Middle Caledonian (I phase)
	Middle	Yijianfang	O_2yj			
		Yingshan	O_2ys	471.8		
	Lower	Penglaiba	O_1p	488.3		Early Caledonian
Cambrian	Upper	Qiulitage		501		
	Middle	Awatage	$\in_2a$			
		Shayilike	$\in_2s$	513		
	Lower	Wusonggeer	$\in_1w$			
		Xiaoerbulake	$\in_1x$			Kuluketage movement
		Yuertusi	$\in_1y$	542		

mudstone sand stone limestone dolomite gypsum gypsum-bearing salt

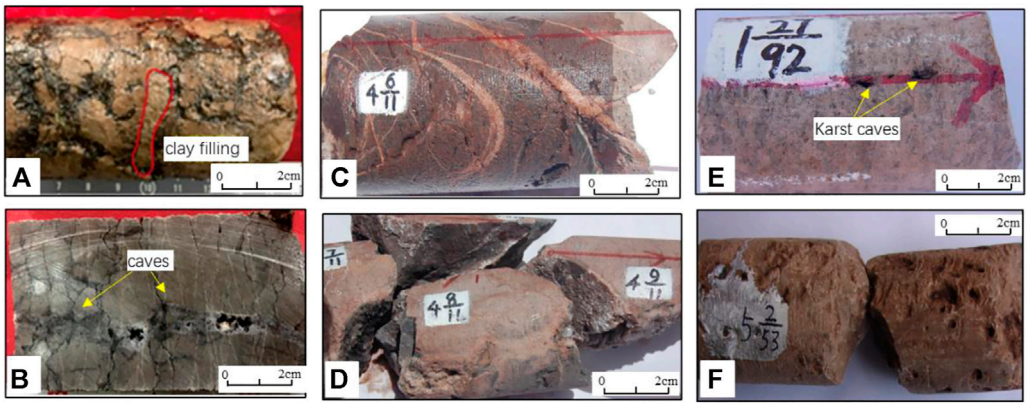

FIGURE 2
Core pictures show the characteristics of different types of reservoirs in Tarim Basin; **(A,B)** fractures and caves controlled by the strike-slip faults; clay filling can be seen in **(A)**. Hydrothermal dissolved and modified reservoir controlled by the strike-slip faults can be seen in core pictures **(C,D)**; **(E,F)** karst reservoir controlled by the strike-slip faults; karst caves can be seen in the core picture **(E)**.

the argillaceous-banded limestone with in the Tazhong area. In Shuntuoguole area, the Upper Ordovician can be divided into upper and lower sections with the exception of the Middle and Lower Ordovician, equivalent to the Santamu Formation and the Lianglitage Formation, respectively.

The periods of reservoir formation are coinciding with the tectonic movement periods experienced by the basin, and the hydrocarbon distribution is closely related to fault activities. As one of the important fault types inside the craton basin, the strike-slip faults affect the reformation of carbonate rocks that

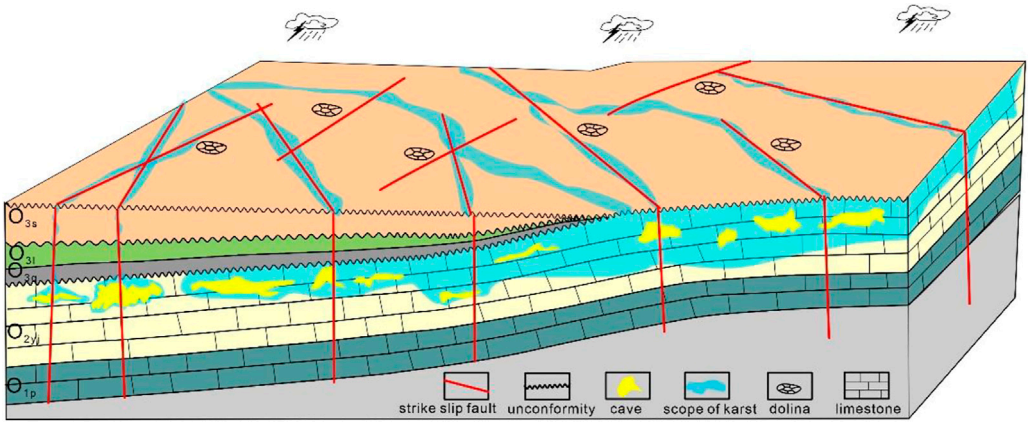

FIGURE 3
Model of reservoir reformation by the downstream fluid.

leads to the development of a broken breccia zone and an induced fracture zone and the formation of aggregated fractures, cavities, and caves distributed along the fault plane. More importantly, it provides longitudinal pathways for upward and downward fluids and forms high-quality reservoir space for the dissolution and reformation of the carbonate rock.

Characteristics of reservoirs

The strike-slip faults are mostly developed in the carbonate strata of the Tarim Basin. Due to the different properties of the diagenetic fluid inside the fault zone, two types of reservoirs were developed in the Ordovician carbonate rock in the deep horizon, namely, the fault-controlled fracture caverns (Figures 2A,B) and the fault-dissolved fracture caverns (Figures 2C–F). Among them, the reservoir space types of carbonate reservoirs from the Tabei uplift to the southern Tahe area and Shuntuoguole area are dominated by large caves along the fault plane of major faults in the deep horizons, which are typical reservoirs of the fault-controlled fracture caverns (Deng, et al., 2018; Qi, 2020). In the core samples containing hydrothermal minerals such as the giant-crystal calcite and the authigenic quartz from multiple wells along the strike-slip fault zone in the northern slope of the Tazhong Uplift, there is dissolution along the fractures, and hydrothermal mineral filling or metasomatic bedrock can be observed (Figures 2C,D). This indicates an upward hydrothermal dissolution and reformation along the strike-slip faults. The reservoirs with well-developed dissolution pores and fractures in the lower part are classified as fault-dissolved fracture caverns (Li, et al., 2015). The characteristic of the fault-controlled fracture caverns is that the extensional breccia can be seen on the core picture (Figure 2A); meanwhile, intergranular fractures/pores and high-angle structural fractures are developed with a weak dissolution phenomenon on the core picture. The fault-dissolved fracture caverns, however, are developed by dissolution caused by meteoric freshwater or deep hydrothermal fluids. In addition, the net-shape strike-slip fault system is developed in the Tabei area of the Tarim Basin. Affected by the fault activities, the karstification of the Ordovician weathering crust is strong, with an increasing dissolution depth, forming a “lamination-like” distribution in the reservoir. The reservoir property is better along the faults, which embodies the control of the downward fluid by the strike-slip faults. The reservoir is dissolved by atmospheric freshwater, where the major reservoir spaces are dissolution pores, caves, and fractures (Figures 2E,F).

Three stages of karstification have been developed in the Tabei uplift (He, et al., 2019), the middle Caledonian, the early Hercynian, and the late Hercynian. During episode I of karstification in the middle Caledonian, the Middle-Lower Ordovician was exposed, where dissolved pores filled with grayish green argillaceous were developed in the top of the Yijiangfang Formation and large-scale caves along the faults, evidently controlled by the faults. In episode II of middle Caledonian, the uplifting of tectonic activity was more robust, leading to a greater difference in topographic elevation and better hydrodynamic conditions. However, surface water could only dissolve the early karst fracture caverns through faults and fractures because Middle-Lower Ordovician in most areas of the southern part in the Tabei uplift was covered by the formation with good water insulation. In the structural highs, the Lianglitage Formation and the Qiaerbake Formation of Upper Ordovician may have been completely eroded, which allowed the atmospheric fresh water to directly enter the Middle-Lower Ordovician for dissolution and reformation, where the karstification was strong. Due to the global ice age of the Late Ordovician-Early Silurian, the hydrodynamic and paleoclimate conditions were not favorable for karstification. In

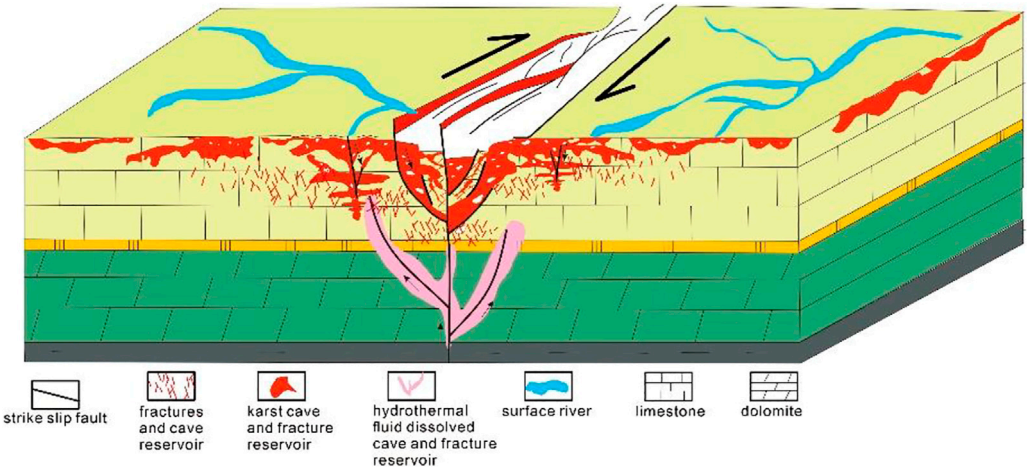

FIGURE 4
Reservoir model of different types controlled by strike-slip faults in the Tarim Basin.

these areas covered by the Upper Ordovician, atmospheric fresh water primarily entered the Middle-Lower Ordovician along the fault. In the exposed area in the northern part, atmospheric fresh water directly dissolved and reformed the Middle-Lower Ordovician. The karstification of this stage is weak, while the faulting is strong (Figure 3).

The early Hercynian tectonic activities have the characteristic of uplifting by stages, which enables the development of multiple karst systems. The karstification is constrained by the upper Ordovician mudstone and marlite aquifuge. The lithology of the upper Ordovician is complex. With thick mudstone existing in the Sangtamu Formation and the carbonate rocks in the Lianglitage Formation and the Qiaerbake Formation not being pure due to argillaceous, the development and extension length of fractures are limited. The fluid pathways can be easily filled by argillaceous, limiting the flow and dissolution along fractures. The fluid mainly dissolved and reformed the Middle-Lower Ordovician along the faults. The Middle-Lower Ordovician is a set of pure and tight carbonate rock, which is conducive for the development and extension of fractures and karstification.

There are also upstream fluid reformed reservoirs. The eruption of large-scale basalts in the Tarim Basin took place around 290–288 Ma (Yang, et al., 2007; Li, et al., 2008), mainly distributed in the western part of Tabei, Tazhong, and western regions of the basin. Several NE and NE strike-slip faults were developed in Shuntuoguole area, with high and steep occurrences. Places near the strike-slip fault were favorable for fracture development and deep fluid migration. At the end of the Late Ordovician, the underlying silicon-rich hydrothermal fluid of Cambrian rose along these NE strike-slip faults, and the fluid expanded and dissolved along the fractures. The reformation effect of the silicon-rich hydrothermal fluid on carbonate rocks was dissolution–metasomatism–cementation by acidic components on limestone, forming a porous silicified reservoir with diverse reservoir spaces (Figure 4).

Modern karst model construction

Methodology

In order to investigate the development characteristics of fault-controlled karst fracture caverns in carbonate reservoirs, underground high-density electrical logging was conducted in the karst of Neibanzhai Village, Maolan Nature Reserve, Libo County, Guizhou Province, China (Figure 5). Guizhou province, located in the southeast margin of the Yangtze Plate, is the most developed exposed karst area in China. There are three large NE-trending transpressional faults across the study area (Figure 5C), which belong to the Neocathaysian structure in terms of the structural system. Influenced by Yanshan movement and Indosinian movement, the main structures in the study area occurred, developed, and formed during this period (Liu, et al., 2010). The landform of this area is characterized by peak cluster depression (Figure 5B) mainly composed of Carboniferous carbonate rocks. The NE-trending Banzhai compression-torsion faults are developed in this area, where the main fault strike is about 35°, the dip ranges from 110° to 140°, the dip angle is larger than 60°, the length is more than 10 km, and the width of the fracture zone is between 10 and 40 m. The fault is filled with mylonite and breccia, with calcite vein and argillaceous filled in some parts. The breccia, composed of dolomitic limestone, varies in width. Affected by the Banzhai compression-torsion fault, fractures are relatively developed in the bedrock. There is karst development in the fracture zone, and micro-geomorphologies such as water-falling caves and karst caves are frequently observed in depressions.

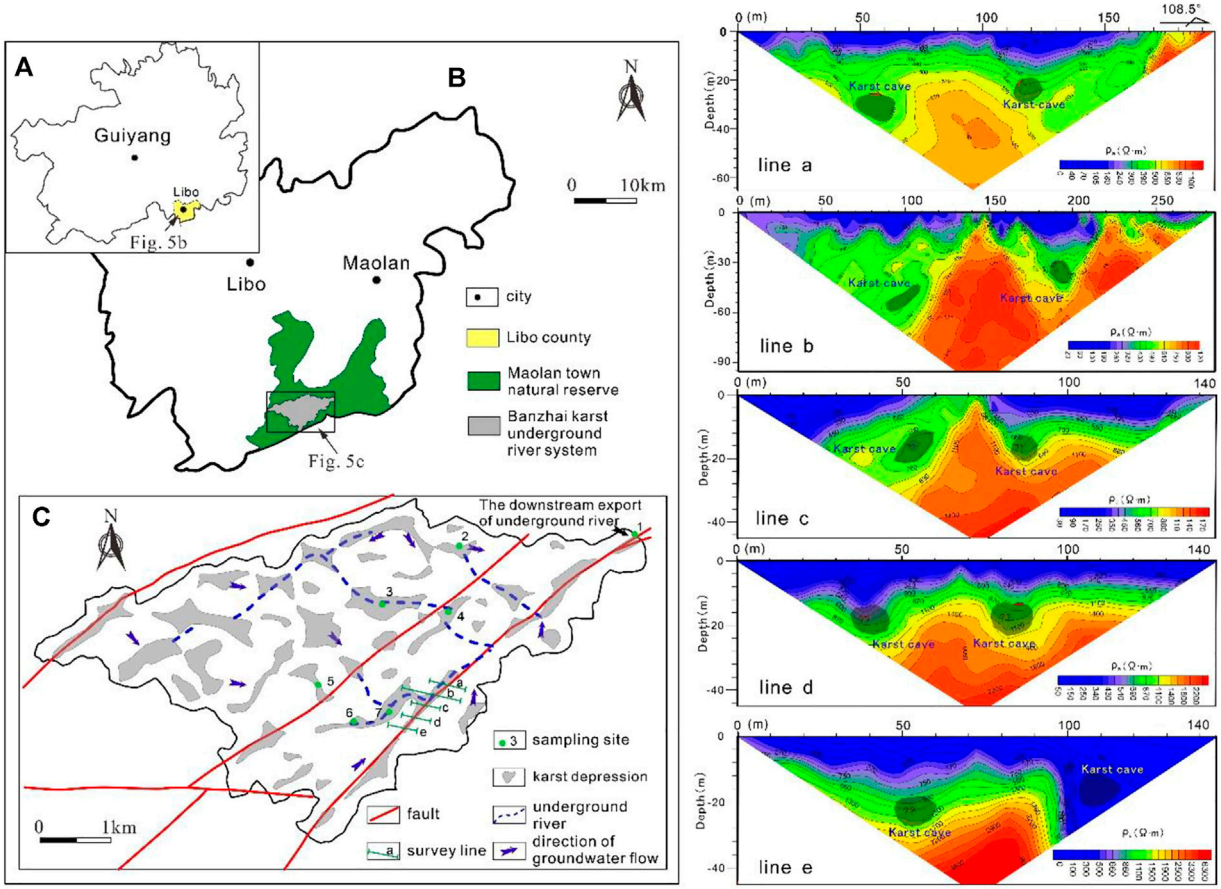

FIGURE 5
Location of the karst-developed areas in Banzhai village and the apparent resistivity quasi-section intersected by the Banzhai fault; the geographical location of Figure 5A is shown in Figure 1A; **(A)** geographic outline of Guiyang Province; **(B)** location and geographic outline of Libo county and Maolan natural reserve; **(C)** hydrogeological sketch map of the Banzhai underground River system, where there is the target area.

TABLE 2 Hydrochemical Parameters of Important Water Points of the Underground River Basin in Banzhai (The sampling positions are shown in Figure 5C).

No.	Type	Water temperature (°C)	pH	Electric conductivity (μS/cm)	Ca^{2+} (mg/L)	HCO_3^- (mg/L)	SIc	Pco_2 (Pa)
1	Karst spring on the surface	17.4	7.18	508	68	384	0.007	2197.9
2	Outlet of ground water	19.4	7.40	394	78	232	0.117	826.0
3	Sinkhole of underground river	19.6	7.57	374	60	226	0.171	545.8
4	Pond	20.5	7.33	400	68	244	0.028	1,037.5
5	Karst spring	18.5	7.38	430	60	250	0.010	926.8
6	Karst spring	18.2	7.57	403	60	268	0.217	635.3
7	Karst spring	18.8	7.23	478	70	323	0.023	1,686.6

Five profile lines perpendicular to the Banzhai fault were surveyed using high-density resistivity logging, all of which were located in the flat valley of the fault zone, crossing the valley in the NW-SE direction (Figure 5C). The length of profile a is 200 m, that of profile b is 300 m, and those of profiles c and d are 150 m. The topography in the valley has little fluctuation. As shown in

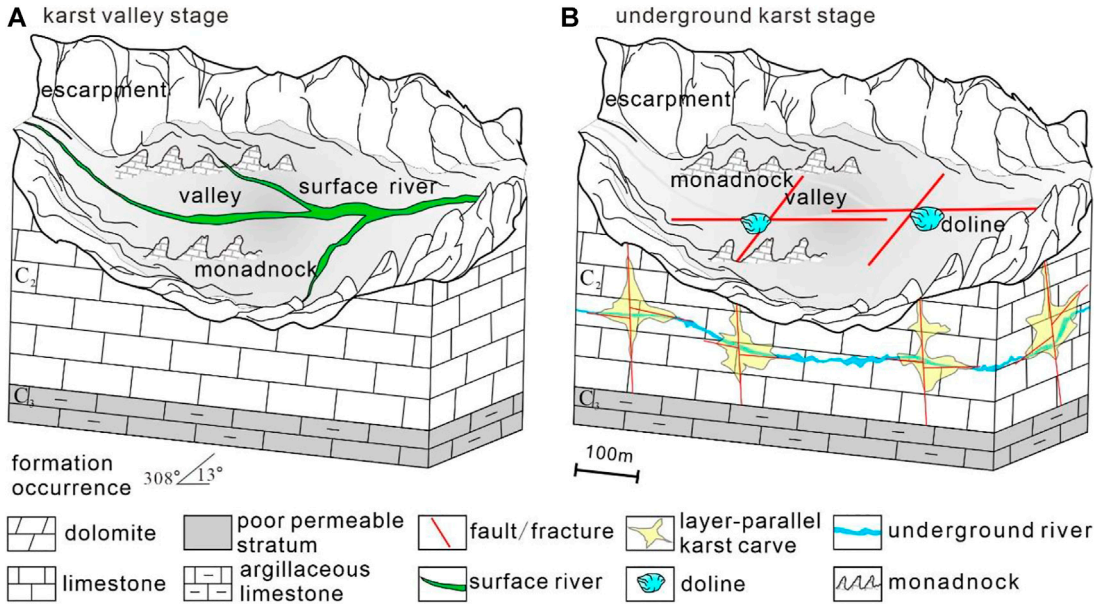

FIGURE 6
Development model of modern karst controlled by strike-slip faults; **(A)** karst valley stage, an extensional depression is developed at the junction of the two faults, and the river dissolves along the fracture; **(B)** underground karst stage, underground river is dissolved along the fault and karst depression is developed, typical geological phenomena such as monadnocks and dolines developed in karst depression.

Figure 5, horizons in each profile are clear. The thickness of the overburden strata is between 0 and 8 m, showing low resistivity, where the apparent resistivity is mostly below 200 Ω m. The apparent resistivity of deep bedrock is high, mostly above 500 Ω m. The relatively low resistivity in the deep high resistivity can be inferred as karst anomaly caused by low-resistivity fillers such as water or muddy and sandy sediments in the karst. Based on the comprehensive analysis of the apparent resistivity quasi-section of each profile, combined with characterization of physical properties of rocks and previous learnings of this area, it is concluded that two sets of karst caves (karst conduits) were developed in the valley, located on both sides of the core of the fault zone. These two sets of karst caves are expected to be interconnected, constituting the underground river system of Banzhai.

Karst geochemical analysis

Because water capable of erosion is one of enabling conditions for karst development, the evaluation of water erosivity is an important foundational work in karst research. The driving force of karstification is provided by the karst dynamic system consisting of three phases: the solid phase, the liquid phase, and the gas phase. When the CO_2 gas phase in the system reaches chemical equilibrium with liquid and solid phases, nine kinds of ions or molecules would be found in liquid-phase water, and the chemical equilibrium involves three phases and nine equilibrium constants. Calcite saturation index *SIc* and partial pressure of carbon dioxide Pco_2 are two important indicators in karst hydrology and geochemistry.

In this study, seven outcrop samples of groundwater were collected from the karst underground river basin area near the Banzhai fault in Libo County, Qiannan Prefecture, Guizhou Province, and the geological, structural, and hydrogeological characteristics of the underground river system were systematically analyzed.

The karst groundwater system in the karst underground river basin near the Banzhai fault is an epikarst system chemically driven by CO_2. The major fault system has a significant controlling effect on karstification, which is demonstrated in the controlling effect the large compressional torsional faults and joint systems have on the distribution of depressions and major runoff channels. Hydrogeochemical characteristics are representative of this macro-control effect to a certain extent. The calcite saturation index of the main water points in the study area is between 0.007 and 0.217 (Table 2), less than 0.8, which has not met the favorable conditions for large-scale deposition of calcium carbonate, indicating that the system is still under the process of dissolution and migration of carbonate rocks, and karst is still developing in progress.

The karst valley is controlled by the geochemical characteristics of surface water and the elevation differences in the landform during its development. In the upstream region of

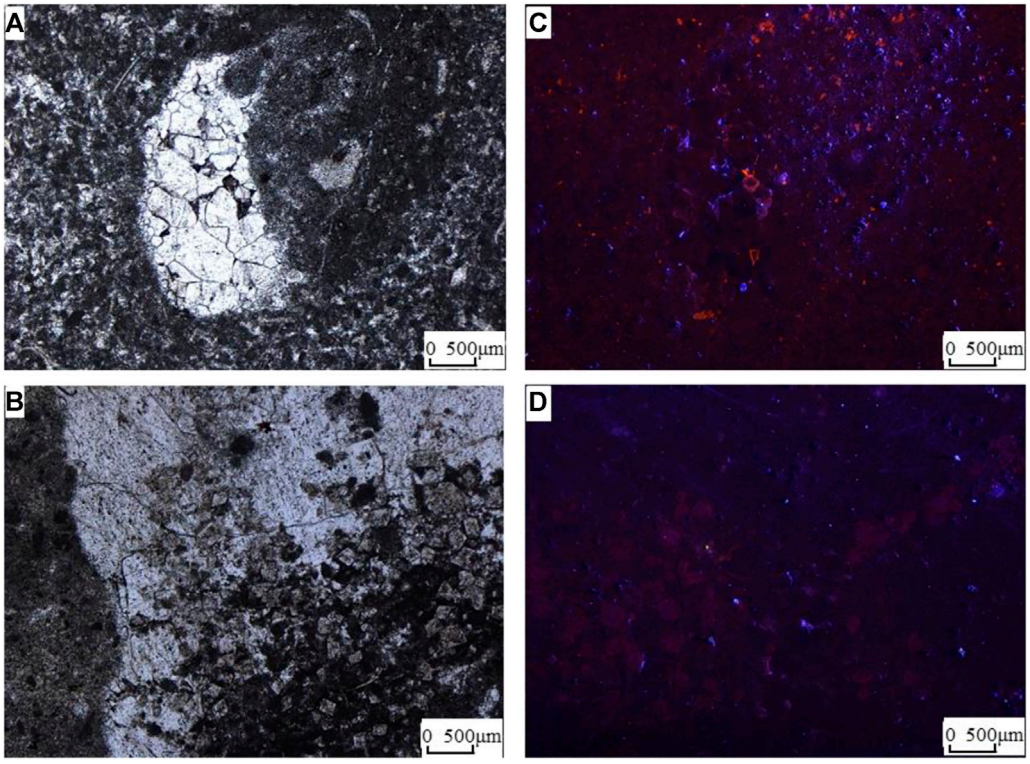

FIGURE 7
Fillings in Ordovician carbonate karst caves of Shuntuoguole area. **(A)** Bottom structure of atmospheric water karst; the bottom of the dissolved cave (upper corner on the right) is filled with dissolved residual, and the top of the dissolved pore (lower corner on the left of the pore) was filled by calcite, Shunbei area, O2yj. **(B)** Bottom structure for karst of atmospheric water; the dissolution residual is filled in dolomite particles at the bottom of dissolution pore (lower corner on the right), and calcite is filled at the top of the dissolution pore, Shunbei area, O1y. **(C)** Filled calcite at the top of the dissolved pore is not luminous, and the residue at the bottom is bright blue, as a clay debris residue, Shunbei area, O2yj. **(D)** Bottom structure for atmospheric karst; dissolved residuals are filled in dolomite particles at the bottom of dissolved pores (lower corner on the right) without luminosity, and calcite is filled in dissolved pores in at the top without luminosity, Shunbei area, O1y.

the Banzhai underground river basin, there is less surface water runoff, a low partial pressure of CO_2, a high $CaCO_3$ saturation index, and relatively slow karst development rates. In contrast, in the downstream flooded dam and the outlet of the underground river, there is more surface water runoff corresponding with a high partial pressure of CO_2 and a low $CaCO_3$ saturation index, resulting in a strong dissolution ability.

Modern karst model

Faulting is foundational to modern karst development. Affected by regional stress, strike-slip faulting results in the development of a series of rhombus-shaped pull-apart regions around the fault zone. Under the atmospheric precipitation and karst reformation in the later stage, these pull-apart regions were further developed into rhombus-shaped karst valleys. The Genggan valley in Banzhai, Libo, Guizhou, is the most representative of this phenomenon. The lengths and widths of the karst valleys developed in the pull-apart areas generally range from hundreds of meters to 2–3 km. While the karst valley formed in the pull-apart area, the surrounding remains turned into mountains that are hundreds to thousands of meters high. In the karst valley formed under the regional major faults, the karst further expands along the fractures or jointed karst pore fissures, forming abundant karst pores, while karst caves of underground streams can be developed from multiple secondary faulting (Figure 6).

Similar geological conditions for karst development can be found in the north slope of Tazhong toward Tabei area of the Tarim Basin. The NNE near-parallel fault system in the Tazhong Uplift and its northern slope and the NNE-NNW trending X-shaped faults in Tuoputai-Halahatang area of the Tabei Uplift provide the foundation for karstification. Multiple strike-slip faults were interconnected. From the Taibei Uplift to Shuntuoguole area, the Ordovician carbonate strata gradually transitioned from uplifted to buried. The development of the tectonic slope in Ordovician carbonate provided hydrodynamic

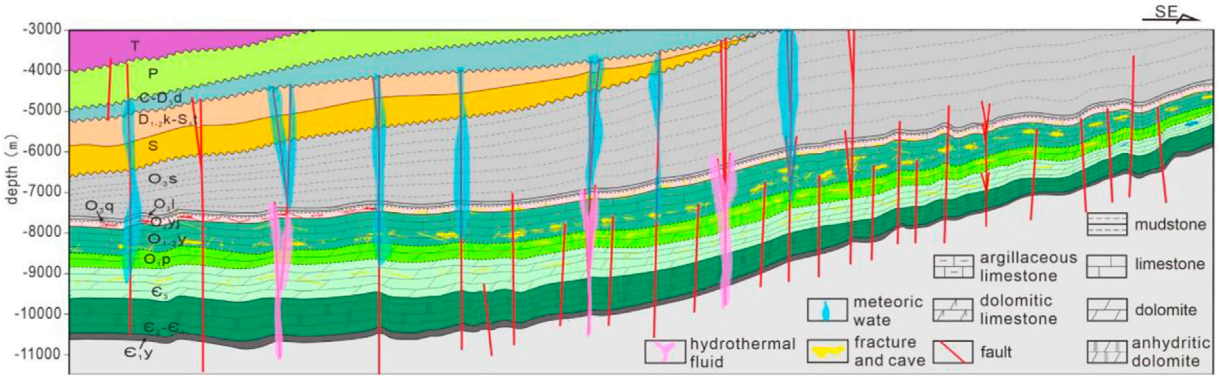

FIGURE 8
Patterns of hydrocarbon accumulation related to strike-slip faults in Tarim Basin.

conditions for karstification, which is consistent with the modern karst model. Controlled by fault connection and the tectonic slope in carbonate rock, atmospheric precipitation continues to percolate from the exposure area in the uplift of Tabei into the buried area of Shuntuoguole area in the south, forming a certain degree of karstification in Ordovician carbonate rocks in Shuntuoguole area, improving the reservoir.

In fact, many drilling data from the Tabei uplift to Shuntuoguole have confirmed the presence of kartisfication in Ordovician carbonate rocks. The middle-lower part of the Yijianfang Formation and the top of Yingshan Formation is dominated by intra-platform shoal by drilling data on the Shuntuoguole, where the lithology is mainly bright crystal algal limestone, with an average porosity of 3.4% and a permeability of 3.64×10^{-3} μm^2. Thin core sections of the calcite showed no luminosity during cathodoluminescence experiments, and the main reservoir space is intragranular micro-pores of algal debris. It may be related to the quasi-syngenetic exposure and dissolution. The dissolution of atmospheric precipitation karst can be seen in all the carbonate rocks from multiple wells in the Yijianfang Formation and the Yingshan Formation (Figure 7). The bottom of the dissolved pores is karst residual material, and the top is filled with calcite. No luminosity can be obtained in cathodoluminescence experiments, indicating a result of the dissolution and reformation from atmospheric precipitation.

In addition, according to the modern karst model, nearly vertical karst fractures with meters wide can be developed via dissolution at the top of large karst fracture caves, where it is less likely be filled by debris. These vertical fractures can be well sustained, making it a great reservoir space outside the large karst caves. With the strike slip fault activities in Shuntuogol area of Tarim Basin, a large number of nearly vertical fracture systems can be developed in the Shuntuoguole area of the Tarim Basin following strike-slip faulting, producing abundant karst fractures along these fracture systems which are excellent reservoirs with significant opportunities for oil and gas accumulation.

Significance for hydrocarbon accumulation

The core issue for oil and gas enrichment in the fault zone of Shuntuoguole of the Tarim Basin is high-quality carbonate fracture caverns formed by strike-slip faults. The superposition of three stages of tectonic movements and the paleokarst in the middle Caledonian resulted in a large number of dissolved pores, large caves, and dissolved fractures in the middle-lower Ordovician strata, forming large-scale karst fracture-cavernous reservoirs that provide the basis for oil and gas accumulation. Large faults and regional unconformities provide advantageous migration pathways favorable for hydrocarbon accumulation (Figure 8). Inside the large strike-slip faults or at the intersections of conjugate faults where karst fracture-cavernous reservoirs are developed, oil and gas production is higher than that of nearby wells, indicating that these deep and large faults are the main pathways for upward migration of oil and gas. Three regional unconformities developed in the middle Caledonian, together with deep and large strike-slip faults and the Ordovician karst fracture-cavern system, constitute a three-dimensional oil and gas conduction system enabling oil and gas to migrate from deep source rocks to Ordovician karst fracture-cavernous reservoirs.

Reservoir quality

The dissolution caused by the downstream fluid or karstification induced by the upstream fluid is common in Ordovician carbonate rocks in the strike-slip faults area of the

Tarim Basin. It is also the most essential reservoir-forming mechanism, primarily developed in Tabei of the Tarim Basin with the characteristic of developing in multiple stages that can be roughly categorized into four. The first stage is the dissolution of atmospheric water or atmospheric water–seawater mix controlled by parasequences resulting from sea level changes, which is marked by intergranular dissolved pores and dissolved pores in dolomite of the Penglaiba Formation and dissolved pores in granular limestone of the Yijianfang Formation, the Lianglitage Formation, and the Sangtamu Formation. The second stage is the dissolution of atmospheric water controlled by the unconformities in the middle Caledonian, marked by the dissolved pores or dissolved fracture caverns in the upper part of the Yijianfang Formation and the upper part of the Lianglitage Formation. The third stage is the dissolution of atmospheric water controlled by the angle unconformity of the early Hercynian. However, this stage of karst in southern Tahe is not the leading effect like the main area because Shuntuoguole area had been located below the phreatic surface. It plays a secondary role and is characterized by fracture-controlled karst locally. The fourth stage is the hydrothermal karstification related to hydrothermal activities after the Hercynian. Most strike-slip faults in Shuntuoguole area were faulted through the bedrock, providing a pathway for upward hydrothermal fluids. However, their contribution to the reservoir is limited due to the fact that the dissolution of hydrothermal fluids is always accompanied by metasomatism and cementation. Among these four stages, the first two, especially the second stage of middle Caledonian, have the greatest effects on the development of the Ordovician carbonate reservoir in the southern Tahe area.

Migration condition

The strike-slip faults in the study area are well developed, where the fault network is composed of small dissolved collapse faults and major faults. The major faults can be faulted downward through Cambrian or deeper and upward to Carboniferous, which very well connects the Cambrian-Ordovician source rocks and the Ordovician reservoir vertically. The analysis of fault activities reveals that these faults can be active for multi-stages, from the early Hercynian to the period after the end of Hercynian. They are compatible with a large amount of multi-stage oil and gas generation by forming an effective vertical migration system. The development of vertical structural fractures in multi-stages and high-angle oblique horizons improves the condition of the vertical migration system. Based on the core observations, it can be revealed that the tectonic fractures in the Ordovician carbonate profile in the area are characterized by vertical and high-angle oblique planes, regardless of whether calcite is fully filled or partially filled in the structural fractures. The comprehensive study of the petrological relationship and geochemical characteristics show that these are the result of tectonic stress after stages of the Caledonian, the early Hercynian, the Indosinian-Yanshanian, and the Himalayan. These fractured calcites are rich in hydrocarbon inclusions or have hydrocarbons of several stages preserved in effective fractures, which validates the important role these fractures play in the hydrocarbon migration in practice via improving the conditions to complement the faults in constituting a complete vertical conduction system.

Second, the development of multi-stages of unconformities makes a superior lateral conduction condition. The top of the Yijianfang Formation is a parallel unconformity formed in stage I of the Middle Ordovician, and the top of the Lianglitage Formation is a parallel unconformity formed in stage II of the Middle Ordovician, both of which play an important role not only in the formation of the Ordovician reservoir but also in the entrapment, migration, and accumulation of oil and gas in the Ordovician enabling the oil and gas lateral conduction system to be effectively developed. Carbonate rocks nearby the underneath of the unconformity become good reservoirs after leaching and corrosion by atmospheric water, forming the lateral conduction system for oil and gas. Karstification and reformation from atmospheric water in the Hercynian was robust, characterized by the development of large cave systems horizontally or nearly horizontally. On one hand, they created excellent reservoir conditions; on the other hand, they also formed a good lateral conduction system.

Conclusion

(1) Under the combined action from strike-slip faulting and the underground fluid, the strike-slip faults not only affect the upstream hydrothermal dissolution and reformation but also conduct the dissolution of the downstream fluid by atmospheric freshwater, resulting in the development of fault-controlled fractured-cavernous reservoirs, fault-dissolved fracture-cavernous reservoirs, or fault-controlled fracture-porous reservoirs in dense carbonate rocks and the development of dissolved pores, caves, and fractures.

(2) According to the modern karst model, the network fault system formed by strike-slip faults is conducive to the development of karst pores, while the tectonic slope provides hydrodynamic conditions for karstification. Karst fractures developed by dissolution along fractures can be formed in the top of the caves, which are less likely to be filled by debris, making it an important reservoir space outside the large karst caves.

(3) The quality of reservoirs formed by the downstream fluid in carbonate rocks is better than that of the upstream hydrothermal fluid, which has a relatively positive impact on hydrocarbon accumulation. The Ordovician karst fracture-cavernous system, unconformities, and strike-slip faults together constitute a three-dimensional oil and gas conduction system that provides conditions for oil and gas migration and accumulation from the deep source rock to the Ordovician karst reservoir.

Data availability statement

The original contributions presented in the study are included in the article/supplementary material; further inquiries can be directed to the corresponding author.

Author contributions

FN: conceptualization, methodology, investigation, writing—Original Draft. HL: supervision; CZ: formal analysis; JY: investigation; PL: geophysical research, HS: investigation, data curation.

Funding

This research was funded by the National Natural Science Foundation of China (Nos. 41972128, 41872161), with additional support from the Strategic Priority Research Program of the Chinese Academy of Sciences (Grant No. XDA14010402).

Conflict of interest

The authors declare that the research was conducted in the absence of any commercial or financial relationships that could be construed as a potential conflict of interest.

Publisher's note

All claims expressed in this article are solely those of the authors and do not necessarily represent those of their affiliated organizations or those of the publisher, the editors, and the reviewers. Any product that may be evaluated in this article or claim that may be made by its manufacturer is not guaranteed or endorsed by the publisher.

References

Deng, S., Li, H., Zhang, Z., Wu, X., and Zhang, J. (2018). Characteristics of differential activities in major strike-slip fault zones and their control on hydrocarbon enrichment in Shunbei area and its surroundings, Tarim Basin. *Oil Gas. Geol.* 39 (5), 38–48. (in Chinese with English abstract). doi:10.11743/ogg20180503

Deng, S., Liu, Y., Liu, J., Han, J., Wang, B., and Zhao, R. (2021a). Structural styles and evolution models of intracratonic strike-slip faults and the implications for reservoir exploration and appraisal: A case study of the Shunbei area, Tarim basin. *Geotect. Metallogenia* 45 (6), 1111–1126. doi:10.16539/j.ddgzyckx.2020.05.015 (in Chinese with English abstract)

Deng, S., Zhao, R., Kong, Q., Li, Y., and Li, B. (2021b). Two distinct strike-slip fault networks in the Shunbei area and its surroundings, Tarim Basin: Hydrocarbon accumulation, distribution and controlling factors. *Am. Assoc. Pet. Geol. Bull.* 106 (1), 77–102. doi:10.1306/07202119113

Ding, Z., Wang, R., Chen, F., Yang, J., Zhu, Z., Yang, Z., et al. (2020). Origin, hydrocarbon accumulation and oil-gas enrichment of fault-karst carbonate reservoirs: A case study of ordovician carbonate reservoirs in south Tahe area of halahatang oilfield. *Tarim Basin. Pet. Explor. Dev.* 47 (2), 78–88. doi:10.11698/PED.2020.02.07 (in Chinese with English abstract)

Gehrels, G. E., Yin, A., and Wang, X. (2003). Magmatic history of the northeastern Tibetan Plateau. *J. Geophys. Res.* 108 (B9), 2423. doi:10.1029/2002jb001876

Gu, Y., Huang, J., Jia, C., Shao, Z., Sun, Y., and Lu, Q. (2020). Research progress on marine oil and gas accumulation in Tarim Basin. *Pet. Geol. Experi.* 42 (1), 1–12. doi:10.11781/sysydz202001001 (in Chinese with English abstract)

Hacker, B. R., Ratschbacher, L., Webb, L., McWilliams, M. O., Ireland, T., Calvert, A., et al. (2000). Exhumation of ultrahigh-pressure continental crust in east central China: Late Triassic-Early Jurassic tectonic unroofing. *J. Geophys. Res.* 105 (B6), 13339–13364. doi:10.1029/2000jb900039

Han, J., Su, Z., Chen, L., Guo, D., Zhang, Y., Ji, Y., et al. (2019). Reservoir-controlling and accumulation-controlling of strike-slip faults and exploration potential in the platform of Tarim Basin. *Acta Pet. Sin.* 40 (11), 1296–1310. doi:10.1016/j.marpetgeo.2017.08.033 (in Chinese with English abstract)

He, D., Zhou, X., Zhang, C., Yang, W., and Shi, X. (2006). Characteristics of geologic framework of multicycle superimposed basin in Tarim basin. *China Pet. Explor.* 11 (1), 316–417. (in Chinese with English abstract).

He, F., Qi, R., Wang, F., Deng, J., Cheng, L., and Hu, T. (2021). Tectonic genesis of triassic yanchang formation valley systems, southern Ordos Basin. *Oil Gas. Geol.* 42 (05), 1056–1062. doi:10.11743/ogg20210504 (in Chinese with English abstract)

He, Z., Yun, L., You, D., Peng, S., Zhang, H., Wang, K., et al. (2019). Genesis and distribution prediction of the ultra-deep carbonate reservoirs in the transitional zone between the Awati and Manjiaer depressions, Tarim Basin. *Earth Sci. Front.* 26 (1), 13–21. doi:10.13745/j.esf.sf.2018.12.20 (in Chinese with English abstract)

Jia, C., Li, B., Zhang, X., and Li, C. (2007). Formation and evolution of the Chinese marine basins. *Chin. Sci. Bull.* 52 (S1), 1–11. (in Chinese). doi:10.1007/s11434-007-6012-x

Li, S., Zhao, S., Liu, X., Cao, H., Yu, S., Li, X., et al. (2018). Closure of the proto-Tethys Ocean and early paleozoic amalgamation of microcontinental blocks in east asia. *Earth. Sci. Rev.* 186, 37–75. doi:10.1016/j.earscirev.2017.01.011

Li, Y., Ye, N., Yuan, X., Huang, Q., Su, B., and Zhou, R. (2015). Geological and geochemical characteristics of silicified hydrothermal fluids in Well Shunnan 4, Tarim Basin. *Oil Gas. Geol.* 36 (06), 934–944. doi:10.11743/ogg20150608 (in Chinese with English abstract)

Li, Z., Yang, S., Chen, H., Yu, X., and Langmuir, C. H. (2008). Chronology and geochemistry of taxdnan basalts from the Tarim Basin: Evidence for permian plume magmatism. *Acta Petrol. Sin.* 24 (5), 959–970. (in Chinese with English abstract).

Liu, L. P., Li, S. Z., Dai, L. M., Wang, Y., J., Liu, B., Jin, C., et al. (2010). Structural characteristics and evolution in Guizhou province, west of xuefeng mountain. *Chin. J. Geol.* 45 (1), 228–242. (in Chinese with English abstract).

Lu, X., Wang, Y., Tian, F., Li, X., Yang, D., Li, T., et al. (2017). New insights into the carbonate karstic fault system and reservoir formation in the Southern Tahe area of the Tarim Basin. *Mar. Pet. Geol.* 86, 587–605. doi:10.1016/j.marpetgeo.2017.06.023

Ma, D., Wang, Z., Duan, S., Gao, J., Jiang, Q., Jiang, H., et al. (2018). Strike-slip faults and their significance for hydrocarbon accumulation in Gaoshiti-Moxi area, Sichuan Basin, SW China. *Petroleum Explor. Dev.* 45 (5), 851–861. (in Chinese with English abstract). doi:10.1016/s1876-3804(18)30088-0

Ma, D., Wu, G., Zhu, Y., Tao, X., Chen, L., Li, P., et al. (2019). Segmentation characteristics of deep strike slip faults in the Tarim basin and its control on hydrocarbon enrichment: Taking the ordovician strike slip fault in the halahatang oilfield in the Tabei area as an example. *Earth Sci. Front.* 26 (1), 225–237. doi:10.13745/j.esf.sf.2019.1.10 (in Chinese with English abstract)

Ma, Y., He, Z., Zhao, P., Zhu, H., Han, J., You, D., et al. (2019). A new progress in formation mechanism of deep and ultra-deep carbonate reservoir. *Acta Pet. Sin.* 40 (12), 1415–1425. doi:10.7623/syxb201912001 (in Chinese with English abstract)

Ma, Y., Li, M., Cai, X., Xu, X., Hu, D., Qu, S., et al. (2020). Mechanisms and exploitation of deep marine petroleum accumulations in China: Advances, technological bottlenecks and basic scientific problems. *Oil Gas. Geol.* 41 (04), 655683–656672. doi:10.11743/ogg20200401 (in Chinese with English abstract)

Mattauer, M., Matte, P., Malavieille, J., Tapponnier, P., Maluski, H., Qin, X. Z., et al. (1985). Tectonics of the qinling belt: Build-up and evolution of eastern asia. *Nature* 317 (6037), 496–500. doi:10.1038/317496a0

Mattern, F., and Schneider, W. (2000). Suturing of the proto- and paleo-tethys oceans in the western Kunlun (xinjiang, China). *J. Asian Earth Sci.* 18 (6), 637–650. doi:10.1016/s1367-9120(00)00011-0

Peacock, D. C. P. (1991). Displacements and segment linkage in strike-slip fault zones. *J. Struct. Geol.* 13 (9), 1025–1035. doi:10.1016/0191-8141(91)90054-m

Qi, L. (2020). Characteristics and inspiration of ultra-deep fault-karst reservoir in the Shunbei area of the Tarim Basin. *China Pet. Explor.* 25 (1), 102–111. (in Chinese with English abstract).

Qiu, H., Deng, S., Cao, Z., Yin, T., and Zhang, Z. (2019). The evolution of the complex anticlinal belt with crosscutting strike-slip faults in the central Tarim Basin, NW China. *Tectonics* 38, 2087–2113. doi:10.1029/2018tc005229

Ratschbacher, L., Hacker, B. R., Calvert, A., Webb, L. E., and Hu, J. (2003). Tectonics of the qinling (Central China): Tectonostratigraphy, geochronology, and deformation history. *Tectonophysics* 366 (1–2), 1–53. doi:10.1016/S0040-1951(03)00053-2

Sobel, E. R., and Arnaud, N. (1999). A possible middle Paleozoic suture in the Altyn Tagh, NW China. *Tectonics* 18 (1), 64–74. doi:10.1029/1998tc900023

Wu, C., Yin, A., Zuza, A. V., Zhang, J., Liu, W., and Ding, L. (2016). Pre-Cenozoic geologic history of the central and northern Tibetan Plateau and the role of Wilson cycles in constructing the Tethyan orogenic system. *Lithosphere* 8 (3), 254–292. doi:10.1130/l494.1

Wu, G., Ma, B., Han, J., Guan, B., Chen, X., Yang, P., et al. (2021). Origin and growth mechanisms of strike-slip faults in the central Tarim cratonic basin, NW China. *Petroleum Explor. Dev.* 48 (3), 595–607. (in Chinese with English abstract). doi:10.1016/s1876-3804(21)60048-4

Wu, G., Zhang, T., Zhu, Y., Wan, X., and Xiong, C. (2020). The architecture, distribution and growth of carbonate fault damage zone. *Chin. J. Geol.* 55 (1), 68–80. (in Chinese with English abstract).

Xiao, W. J., Windley, B., Hao, J., and Zhai, M. G. (2003). Accretion leading to collision and the permian solonker suture, inner Mongolia, China: Termination of the central asian orogenic belt. *Tectonics* 22, 1069–1089. doi:10.1029/2002tc001484

Xiao, W., Windley, B. F., Sun, S., Li, J., Huang, B., Han, C., et al. (2015). A tale of amalgamation of three permo-triassic collage systems in central asia: Oroclines, sutures, and terminal accretion. *Annu. Rev. Earth Planet. Sci.* 43 (1), 477–507. doi:10.1146/annurev-earth-060614-105254

Yang, H., Deng, X., Zhang, Y., Xie, Z., Li, Y., Li, S., et al. (2020). Great discovery and its significance of exploration for Ordovician ultra-deep fault-controlled carbonate reservoirs of Well Manshen 1 in Tarim Basin. *China Pet. Explor.* 25 (3), 17–27. (in Chinese with English abstract).

Yang, S., Li, Z., Chen, H., Santosh, M., and Yu, X. (2007). Permian bimodal dyke of Tarim Basin, NW China: Geochemical characteristics and tectonic implications. *Gondwana Res.* 12 (1), 113–120. doi:10.1016/j.gr.2006.10.018

Yin, A., Manning, C. E., Lovera, O., Menold, C. A., Chen, X. H., and Gehrels, G. E. (2007). Early Paleozoic tectonic and thermomechanical evolution of ultrahigh-pressure (UHP) metamorphic rocks in the northern Tibetan Plateau, Northwest China. *Int. Geol. Rev.* 49 (8), 681–716. doi:10.2747/0020-6814.49.8.681

Zhu, G., Sun, C., Zhao, B., Li, T., Chen, Z., Yang, H., et al. (2020). Formation, evaluation technology and preservation lower limit of ultra-deep ancient fracture-cavity carbonate reservoirs below 7000 m. *Nat. Gas. Geosci.* 31 (5), 5–19. doi:10.11764/j.issn.1672-1926.2020.04.013 (in Chinese with English abstract)

Zhu, G., Yang, H., Zhu, Y., Gu, L., Lu, Yu., Su, J., et al. (2011). Study on petroleum geological characteristics and accumulation of carbonate reservoirs in Hanilcatam area, Tarim basin. *Acta petro. Sin.* 27 (03), 827–844. (in Chinese with English abstract).

Zhu, R., Zhao, P., and Zhao, L. (2021). Tectonic evolution and geodynamics of the Neo-Tethys Ocean. *Sci. China Earth Sci.* 52 (1), 1–24. (in Chinese with English abstract). doi:10.1007/s11430-021-9845-7

frontiers | Frontiers in Earth Science

TYPE Original Research
PUBLISHED 12 September 2022
DOI 10.3389/feart.2022.959602

OPEN ACCESS

EDITED BY
Dongming Zhi,
PetroChina, China

REVIEWED BY
Xiaoqi Wu,
SINOPEC Petroleum Exploration and Production Research Institute, China
Pingping Li,
China University of Petroleum, China

*CORRESPONDENCE
Fanghao Xu,
13618043318@163.com

SPECIALTY SECTION
This article was submitted to Economic Geology,
a section of the journal
Frontiers in Earth Science

RECEIVED 01 June 2022
ACCEPTED 20 July 2022
PUBLISHED 12 September 2022

CITATION
Xiao H, Xu F, Fu X, Li W, Chen C, Zhang J, Wang Y and Zhou K (2022), Main factors controlling hydrocarbon accumulation in the Northwestern Sichuan Basin. *Front. Earth Sci.* 10:959602. doi: 10.3389/feart.2022.959602

Main factors controlling hydrocarbon accumulation in the Northwestern Sichuan Basin

Hang Xiao[1], Fanghao Xu[1]*, Xiaodong Fu[2], Wenzheng Li[2], Cong Chen[3], Jianyong Zhang[2], Yajie Wang[1,4] and Kuan Zhou[1]

[1]State Key Laboratory of Oil and Gas Reservoir Geology and Exploitation, Chengdu University of Technology, Chengdu, China, [2]Hangzhou Institute of Geology, PetroChina, Hangzhou, China, [3]PetroChina Southwest Oil and Gas Field Company, Chengdu, China, [4]Overseas Business Department, Geophysical Research Institute, Bureau of Geophysical Prospecting, CNPC, Zhuozhou, China

The basin-mountain transition regions of foreland basins are hot spots for hydrocarbon exploration worldwide, while the complex geological features and hydrocarbon accumulation rules make hydrocarbon exploration very difficult. The Northwestern Sichuan Basin is a typical case where the unclear distribution rules restrict the further exploration of natural gas. In this study, geochemistry and seismic profile data were comprehensively used to reveal the main factors controlling hydrocarbon accumulation in the Northwestern Sichuan Basin. The Lower Cambrian and the Upper- Middle Permian source rocks have different carbon isotope compositions, indicating that they have different kerogen types, sapropelic kerogen for the Lower Cambrian source rocks, mixed kerogen for the Middle Permian source rocks and humic kerogen for the Upper Permian source rocks. The Northwestern Sichuan Basin can be divided into the unfaulted belt, the thrust front belt and the thrust nappe belt. The thrust nappe belt develops many large thrust faults, and the natural gas there mainly originates from the Lower Cambrian source rocks. However, due to different denudation of regional caprocks, hydrocarbons in the area adjacent to the Longmen Mountain fold-and-thrust system were destroyed, while in the area adjacent to the thrust front belt, they had good preservation conditions. The thrust front belt and the unfaulted belt develop a few or few thrust faults, and the natural gas there mainly originates from the Upper-Middle Permian source rocks and has good preservation conditions due to no denudation of regional caprocks. The distribution of thrust faults controls the natural gas origins in different areas, and the preservation conditions determine whether the gas reservoirs can survive to the present. These conclusions can provide guidance for natural gas exploration in the Northwestern Sichuan Basin and other basin-mountain transition regions in foreland basins worldwide.

KEYWORDS

foreland basin, basin-mountain transition regions, gas source correlation, hydrocarbon accumulation process, carbon isotope

1 Introduction

The basin-mountain transition regions of the foreland basins have favorable hydrocarbon accumulation conditions and are regarded as hot spots for hydrocarbon exploration worldwide (Wei et al., 2019; Wei et al., 2020). Many large oil or gas fields have been discovered there, such as the Pineview oil field in the western Green River Basin of the United States (Deming and Chapman, 1988), the Chemchemal gas field in the Zagross Fold Belt of North Iraq (Al-ameri and Zumberge, 2012) and the Alade oilfield in the Northwestern Junggar Basin of China (Guo et al., 2021). However, these regions are characterized by intense tectonic movement, complex geological evolution and intricate hydrocarbon accumulation processes, which make hydrocarbon exploration very difficult (Decelles and Gilest, 1996; Macclay, 2004; He and Jia, 2005; Picha, 2011; Guo et al., 2020).

The Sichuan Basin is a large superimposed basin with abundant hydrocarbon resources, and its Northwestern region (the Northwestern Sichuan Basin) is a typical basin-mountain transition region between the Longmen Mountain and the eastern foreland basin. The Northwestern Sichuan Basin has a long history of natural gas exploration dating back to the 1970s. At that time, under the guidance of the traditional exploration idea that hydrocarbon exploration should be at the structural high point, some exploration wells were drilled in the hanging wall of the thrust nappe belt, such as the Kuangshanliang area, but there were no major exploration breakthroughs except for very few wells with high production of natural gas. However, exploration wells drilled in the Shuangyushi area of the thrust front belt have achieved major success, indicating huge natural gas exploration prospects in the thrust front belt. This suggests that complex and various hydrocarbon accumulation rules exist in different regions of the Northwestern Sichuan Basin, which restricts the further exploration of natural gas. Determining the major factors controlling natural gas accumulation is the key to subsequent natural gas exploration in the Northwestern Sichuan Basin.

On the basis of research on the chemical composition of natural gas, carbon isotope features of source rocks and natural gas, and geological feature differences between different regions in the Northwestern Sichuan Basin, this paper attempts to 1) determine the genesis and origins of natural gas in different regions; 2) clarify the hydrocarbon accumulation process in the Northwestern Sichuan Basin; and 3) explore the main factors controlling natural gas accumulation in the Northwestern Sichuan Basin.

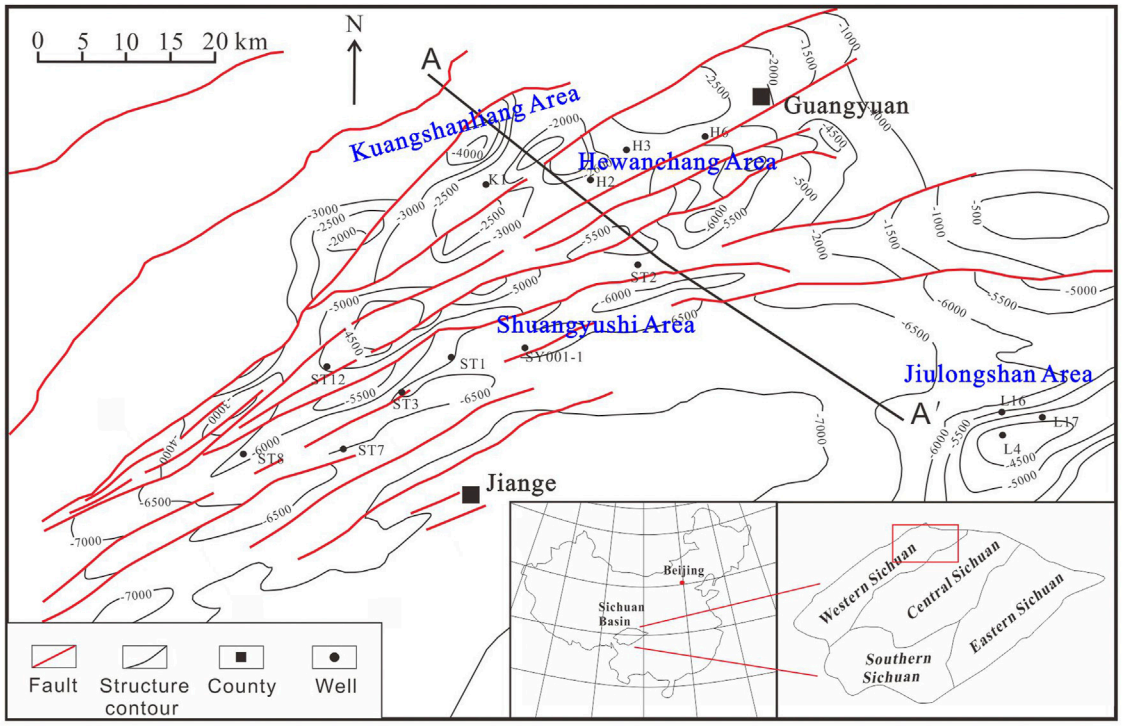

FIGURE 1
Regional position of the Northwestern Sichuan Basin. Note the top structure contours of the Qixia Formation.

2 Geological setting

The Sichuan Basin, located in southwestern China (Figure 1), is a large and petroliferous basin, with total natural gas reserves of approximately 53477.4 × 10^8 m^3 (Li B. et al., 2020). It has proven reserves of 16497.52 × 10^8 m^3 and has tremendous potential for natural gas exploration (Li B. et al., 2020). The Sichuan Basin is bounded by the Longmen Mountain orogenic belt to the northwest, the Micanshan uplift and Daba Mountain thrust belt to the northeast, and the Hunan-Guizhou-Hubei fold belt to the southeast (Wu et al., 2021). The Northwestern Sichuan Basin is located at the intersection of the Micangshan uplift belt and the Longmen Mountain fault-fold belt and consists of Wangcang, Jiange, Guanyuan and Cangxi counties.

The Northwestern Sichuan Basin experienced two tectonic stages: the craton basin stage (Neoproterozoic to early Mesozoic) and the foreland basin stage (middle Mesozoic to the present) (Chen X. Z. et al., 2019). The superimposed stratigraphic sequences were developed in the Northwestern Sichuan Basin and mainly consist of marine deposits from the Sinian to the Middle Triassic and continental deposits from the Upper Triassic to the present (Figure 2) (Li et al., 2022; Miao et al., 2022). The Lower Cambrian shales, the Upper-Middle Permian coal measures and marlstones, and the Upper Triassic shales are the main source rocks, while the Sinian and Paleozoic carbonate rocks and the Devonian and Mesozoic sandstones are good reservoirs for hydrocarbons (Figure 2) (Chen X. Z. et al., 2019; Li W. et al., 2020; Deng et al., 2022; Miao et al., 2022).

The Northwestern Sichuan Basin has experienced multiple tectonic events, such as the Emei Taphrogeny, Indo–Yanshanian orogeny and Himalayan orogeny (Wang et al., 2018; Xiao et al., 2021). During the Indo–Yanshanian orogeny, the Northwestern Sichuan Basin became a foredeep basin, and during the Himalayan orogeny, affected by the Longmen Mountain fold-and-thrust system, the Northwestern Sichuan Basin can be divided into three structural belts: the unfaulted belt, the thrust front belt and the thrust nappe belt (Figure 3) (Xiao et al., 2021; Li et al., 2022). The Hewanchang, Shuangyushi, Jiulongshan and Kuangshanliang areas are important gas-bearing structures in the Northwestern Sichuan Basin. The Kuangshanliang and Hewanchang areas are located in the thrust nappe belt, the Shuangyushi area is located in the thrust front belt, and the Jiulongshan area is located in the unfaulted belt (Figure 1).

The Qiongzhusi Formation ($\in_1$q) in the Lower Cambrian, the Qixia (P_2q) and Maokou (P_2m) formations in the Middle Permian and the Longtan Fomation (P_3l) in the Upper Permian develop the major source rocks for the Palaeozoic reservoirs in the Northwestern Sichuan Basin (Figure 2) (Hu et al., 2021; Xiao et al., 2021). The$\in_1$q source rocks are black, dark gray marine shale, and the P_2q and P_2m source rocks are gray black marine marlstones. The P_3l source rocks are black coal measures. The P_2q and P_2m also develop the most important reservoirs for natural gas in the Northwestern Sichuan Basin (Figure 2). P_2q is mainly composed of platform margin beach deposits, with the main lithology of brown–gray, light gray fine/mesocrystalline dolomite and medium/coarse-crystalline dolomite. The porosity and permeability of the P_2q reservoirs range from 0.42 to 16.51% (avg. 3.58%) and from 1.51 mD to 784 mD (avg. 10.9 mD), respectively (Chen C. et al., 2019). P_2m mainly consists of the deposits of platform margin beach and gentle slope. The natural gas reservoirs in P_2m can be divided into two kinds: limestone fracture-type reservoirs deposited in gentle slope facies and dolomite pore-type reservoirs deposited in platform margin beach facies (Huo et al., 2018). The former mainly belong to reservoirs with ultralow porosity and low permeability, while the latter mainly belong to reservoirs with medium porosity and medium permeability (Huo et al., 2018).

3 Samples and analytical methods

Twenty-one source rock samples from the Lower Cambrian and the Upper-Middle Permian of the Northwestern Sichuan Basin were selected for the carbon isotopic test. Seven natural gas samples from the Qixia Formation in the Shuangyushi area were selected for analyzing the chemical compositions. Six natural gas samples from the Hewanchang area and fifteen natural gas samples from the Shuangyushi area were also collected for the carbon isotopic test.

The carbon isotopic composition of the source rock samples was determined on a Finnigan Delta Plus mass spectrometer. The source rock samples were combusted at 1000°C to generate carbon dioxide after decalcification, which was used to determine the carbon isotopic composition of organic matter. The carbon isotopic compositions were reported in the δ notation in per mil (‰) relative to the VPDB standard, and the accuracy for the measurement was ±0.1‰.

The Chemical composition of the natural gas samples was analyzed by a Hewlett Packard 6890 II gas chromatograph equipped with a flame ionization detector and a thermal conductivity detector. The gaseous alkanes were separated by using a capillary column (PLOT Al_2O_3 50 m × 0.53 mm). The GC oven temperature was initially set to 30°C for 5 min, then programmed to increase to 180°C at 10°C/min, and finally kept at 180°C for 10 min.

The carbon isotopic composition of gaseous alkanes was determined on a Finnigan MAT-253 mass spectrometer. The gaseous alkanes were separated through a fused silica capillary column (PLOT Q 30 m × 0.32 mm). Helium was used as the carrier gas. The GC oven temperature was programmed to 160°C increasing from 40°C at 10°C/min and finally kept at 160°C for 10 min. The natural gas samples were measured in triplicate, and the carbon isotopic compositions were reported in the δ notation in per mil (‰) relative to the VPDB standard. The accuracy for the measurement was ±0.5‰.

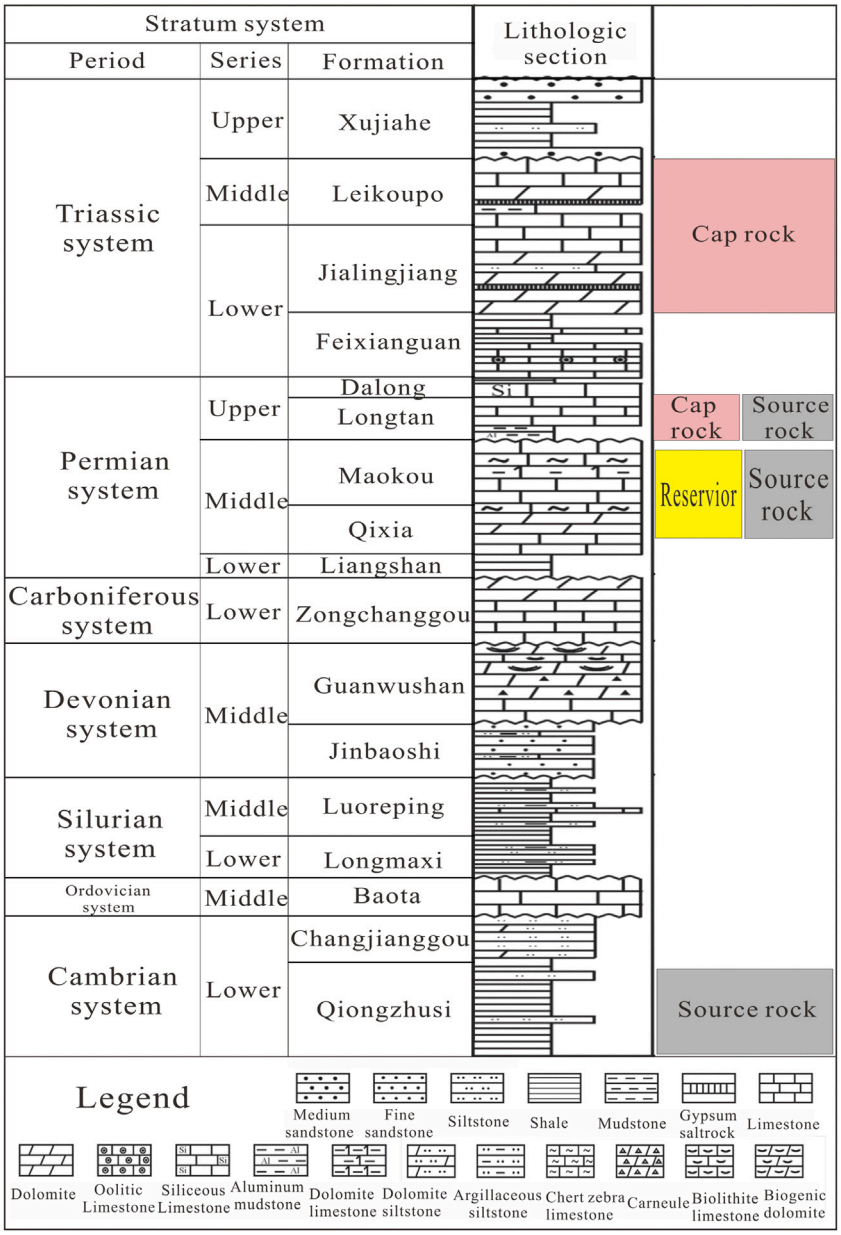

FIGURE 2
A generalized stratigraphic column of the Northwestern Sichuan Basin.

4 Results

4.1 Differences in geological features between different regions

Due to the distance from the Longmen Mountain fold-and-thrust system increasing from the thrust nappe belt to the thrust front belt and the unfaulted belt, the tectonic stress gradually decreases in the same order. Various tectonic stresses cause the above three regions to have different geological features, mainly in the distribution of thrust faults and the uplift of formations (Figure 3).

The thrust nappe belt is closest to the Longmen Mountain fold-and-thrust system and experiences the most intense tectonic stress. Therefore, under the influence of such intense tectonic stress, the strata uplifted violently, and many large thrust faults developed in the thrust nappe belt (Figure 3). Note that the denudation of strata varied in different areas, and the closer to the

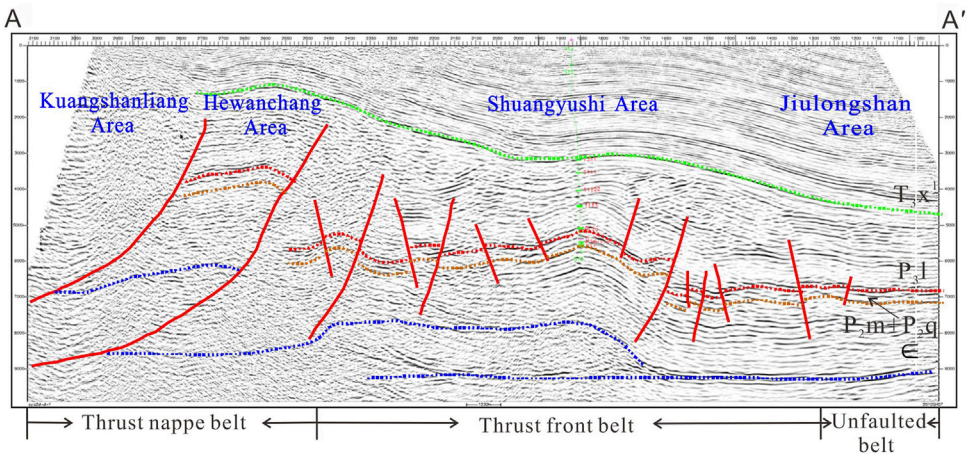

FIGURE 3
A seismic profile in the NW direction of the Northwestern Sichuan Basin to show the distribution of thrust faults and the uplift of formations in different areas Figure 1 for profile location.

Longmen Mountain fold-and-thrust system, the more serious denudation the strata suffered. The thrust front belt is farther from the orogenic belt than the thrust nappe belt, so tectonic stress there turned relatively weak. Therefore, the stratum experienced little or no uplift and denudation, and only a few thrust faults developed in the thrust front belt (Figure 3). The unfaulted belt is furthest from the orogenic belt and suffered the weakest tectonic stress, under the influence of which the unfaulted belt became a low hump and few thrust faults developed there (Figure 3).

4.2 Chemical composition of natural gas

The Chemical composition of natural gas from different regions in the Northwestern Sichuan Basin is shown in Table 1. The natural gas in the P_2q Formation of the Shuangyushi area are typical dry gas with gas dryness [$C_1/\Sigma(C_1–C_5)$] greater than 0.95%. The ethane content ranges from 0.10 to 0.11%, with an average of 0.11%. CO_2 is the most abundant nonhydrocarbon gas, with the average content of 1.24%. The content of H_2S is very low, with the gas souring index [GSI = 100 × $H_2S/(H_2S + CH_4 + C_2H_6 + C_3H_8)$] (Worden et al., 1995) values ranging from 0 to 0.008.

The natural gas in the P_2m Formation of the Hewanchang area are also typical dry gas. The ethane content is relatively high, ranging from 0.19 to 1.32%, with an average of 0.73%. N_2 is the most abundant nonhydrocarbon gas, with an average content of 1.16%. The content of H_2S is also very low, with GSI values ranging from 0 to 0.003.

The natural gas in the P_2m and P_2q Formations of the Jiulongshan area are typical dry gas as well, with ethane contents ranging from 0.1 to 0.94% (avg. 0.25%). N_2 is also the most abundant nonhydrocarbon, avg. 0.98%. H_2S has low content, with GSI values ranging from 0 to 0.009.

4.3 Carbon isotopic composition of source rocks and natural gas

The carbon isotopic compositions of source rocks from different stratigraphic intervals are shown in Table 2. The $\delta^{13}C$ values of the Lower Cambrian source rocks range from −38.8‰ to −34.9‰, avg. −36.5‰. The $\delta^{13}C$ values of the Middle Permian source rocks are larger than those of the Cambrian source rocks, ranging from −29.2‰ to −24.2‰, with an average of −26.9‰. The $\delta^{13}C$ values of the Upper Permian source rocks have the largest $\delta^{13}C$ values, ranging from −26.1‰ to −24.8‰, with an average of −25.4‰.

The carbon isotopic composition of natural gas from different areas is shown in Table 1. The $\delta^{13}C_1$ and $\delta^{13}C_2$ values of the natural gas samples from the Hewanchang area range from −36.7‰ to −32.9‰ (avg. −35.1‰) and from −36.7‰ to −32.5‰ (avg. −34.3‰), respectively. The natural gas samples from the Shuangyushi area have larger $\delta^{13}C_1$ and $\delta^{13}C_2$ values, ranging from −32.5‰ to −29.7‰ (avg. −30.5‰) and from −28.6‰ to −25.9‰ (avg. −27.3‰), respectively. The natural gas samples from the Jiulongshan area have $\delta^{13}C_1$ and $\delta^{13}C_2$ values ranging from −28.8‰ to −27.3‰ (avg. −28.2‰) and from −29.3‰ to −25.2‰ (avg. −27.3‰), respectively.

TABLE 1 Compositions and carbon isotopes of natural gas samples from different areas.

Area	Wactell	Strata	Hydrocarbon gases/%		Non-hydrocarbon gases/%					GSI	$\delta^{13}C_1$/‰	$\delta^{13}C_2$/‰	Data source
			CH_4	C_2H_6	N_2	CO_2	He	H_2	H_2S				
Shuangyushi	ST12	P_2q	96.56	0.11	0.85	1.71	0.03	0	0.74	0.008	−29.7	−26.8	This study
	SY132	P_2q	96.72	0.11	1.09	1.68	0.02	0	0.37	0.004	−30.4	−27.2	
	ST1	P_2q	96.65	0.1	0.87	2	0.03	0	0.34	0.004	−30.1	−28.2	
	ST3	P_2q	96.81	0.1	0.8	1.87	0.02	0.01	0.39	0.004	−30.5	−28.5	
	SY001-1	P_2q	97.14	0.11	0.95	1.4	0.02	0	0.38	0.004	−29.8	−28	
	ST7	P_2q	97.53	0.11	0	0	0.47	1.45	0.02	0.0002	−30.0	−27.1	
	ST8	P_2q	97.18	0.1	0	0	0.52	1.77	0.02	0.0002	−29.9	−26.7	
	ST1	P_2m	-	-	-	-	-	-	-	-	−32.5	−26.2	
	ST1	P_2m	-	-	-	-	-	-	-	-	−30.3	−26.3	
	ST1	P_2m	-	-	-	-	-	-	-	-	−30.2	−26.1	
	ST3	D_2g	-	-	-	-	-	-	-	-	−32.3	−28.6	
	ST3	D_2g	-	-	-	-	-	-	-	-	−31.1	−27.9	
	ST12	P_2q	-	-	-	-	-	-	-	-	−31.0	−25.9	
	ST12	P_2q	-	-	-	-	-	-	-	-	−30	−28.4	
	ST12	P_2q	-	-	-	-	-	-	-	-	−29.9	−28.2	
Hewanchang	H2	P_2m	-	-	-	-	-	-	-	-	−36.7	−32.8	
	H2	P_2m	-	-	-	-	-	-	-	-	−35.5	−33.4	
	H2	P_2m	-	-	-	-	-	-	-	-	−-32.9	−32.5	
	H3	O	-	-	-	-	-	-	-	-	−35.6	−36.7	
	H3	P_2ch	-	-	-	-	-	-	-	-	−35.3	−35.2	
	H3	O	-	-	-	-	-	-	-	-	−35.7	−36.4	
	H2	P_2m	97.08	0.65	1.7	0.36	0.04	0.01	0.05	0.001	−35.7	−33.4	Xiao et al. (2021)
	H2	P_2m	97.21	0	1.27	0.06	0.03	0.14	0	0	−33.7	-	
	H2	P_2m	96.01	1.32	1.43	0.21	0.05	0.13	0	0	−34.5	−34.7	
	H2	P_2m	97.67	0.69	1.38	0.06	0	0.16	0.05	0.001	−35.5	−33.6	
	H3	P_2m	97.82	0.56	1.18	0.33	1.18	0	0.05	0.001	−35.5	-	
	H6	P_2m	98.28	0.97	0.37	0.07	0.37	0.23	0	0	-	-	
	K1	P_2m	95.22	0.19	0.48	3.79	0.48	0	0.3	0.003	-	-	
Jiulongshan	LT1	P_2q	96.22	0.15	1.02	1.69	0.02	0.01	0.88	0.009	−28.8	−27.3	
	L004-X1	P_2m	98.1	0.14	0.72	0.48	0.02	0.01	0.54	0.005	27.3	−28.2	
	L004-X1	P_2m	96.94	0.14	1.34	0.04	0.04	0	0.74	0.008	–	-	
	L004-X1	-	-	-	-	-	-	-	-	-	−27.8	−27.7	
	L004-X1	-	-	-	-	-	-	-	-	-	−28.2	−29.3	
	L004-X1	-	-	-	-	-	-	-	-	-	−28.4	−28.5	
	L4	P_2m	97.5	0.15	1.01	0.02	0.03	0	0.72	0.007	-	-	
	L4	P_2m	98.45	0.94	0.44	0.02	0	0	0.01	0.0001	-	-	
	L4	-	-	-	-	-	-	-	-	-	−27.7	−26.3	
	L4	-	-	-	-	-	-	-	-	-	−28.8	−28.4	
	L4	-	-	-	-	-	-	-	-	-	−28.8	−25.2	
	L16	P_2m	97.42	0.14	0.92	0.68	0.02	0.01	0.82	0.008	−28.8	−28.4	
	L16	-	-	-	-	-	-	-	-	-	−27.7	−26.3	
	L17	P_2q	97.16	0.1	1.38	0.96	0.04	0.01	0.37	0.004	−28.3	−25.2	

Note: GSI = 100 × $H_2S/(H_2S + CH_4 + C_2H_6 + C_3H_8)$.

5 Discussion

5.1 Origins of natural gas

5.1.1 Crude oil cracking gas or kerogen cracking gas

Oil-type gas can be derived from oil cracking or kerogen cracking, whereas the coal-type gas is mainly derived from the kerogen cracking. Therefore, it is necessary to judge the organic matter type of its source rocks before judging the genetic mechanism of natural gas. The crossplot of $\delta^{13}C_1$ versus $\delta^{13}C_2$ shows that the natural gas from the Hewangchang Area is oil-type gas and the natural gas from the Shuangyushi and Jiulongshan areas is the mixture of oil-type gas and coal-type gas (Figure 4). The crossplots of ln (C_1/C_2) versus $\delta^{13}C_1$ and ln (C_1/C_2) versus $\delta^{13}C_2$ can be used to distinguish the oil cracking gas and kerogen cracking gas (Liu et al., 2018). According to the crossplots, the natural gas from the Hewangchang Area is oil cracking gas, and the natural gas from the Shuangyushi and Jiulongshan areas is not typical oil cracking gas (Figure 5), which may be influenced by mixture with natural gas generated by humic kerogen cracking.

Some nonhydrocarbon gas can also indicate the origin of natural gas (Wang et al., 2018; Xiao et al., 2021). For example, natural gas generated by kerogen cracking is usually characterized by higher N_2 content than those generated by crude oil cracking. Kerogen in argillaceous rocks contains more nitrogen compounds than the crude oil, so under pyrolysis reactions, the denitrification of the kerogen can result in high N_2 contents in the kerogen cracking gas (Chen et al., 2000; Wang et al., 2018). The Devonian natural gas in the Northwestern Sichuan Basin is the typical crude oil cracking gas, whose N_2 and CO_2 contents are very low, less than 2.4% (Li et al., 2019). However, the Sinian natural gas in the southwestern Sichuan Basin is the typical kerogen cracking gas, which has high N_2 and CO_2 contents of more than 4% (Yin et al., 2001). The natural gas from the Shuangyushi, Hewanchang and Jiulongshan areas are all characterized by low N_2 and CO_2 contents, ranging from 0 to 1.43% and from 0 to 3.79%, respectively (Figure 6), which indicates that the natural gas from the above three areas were generated by crude oil cracking.

According to the above discussion, we suggest that the natural gas from the Hewanchang area is oil cracking gas, while the natural gas from the Shuangyushi and Jiulongshan areas is a mixture of oil cracking gas and humic kerogen cracking gas.

5.1.2 Originating from the lower cambrian source rocks or the upper-middle permian source rocks

There exist multiple sets of source rocks in the Sichuan Basin (Wei et al., 2018; Xu et al., 2018; Zheng et al., 2019), but considering the distribution and organic matter abundance, the Lower Cambrian and Upper-Middle Permian source rocks are the major source rocks for the natural gases in the Northwestern Sichuan Basin (Hu et al., 2021). Carbon isotopic composition of kerogen can indicate the type of organic matter (Kotarba and Clayton, 2003; Misz-Kennan and Fabianska, 2011). In general, the sapropelic kerogen has $\delta^{13}C_{kerogen}$ values less than −28‰, the mixed kerogen has $\delta^{13}C_{kerogen}$ values between −28‰ and −26‰, while the humic kerogen has $\delta^{13}C_{kerogen}$ values greater than −26‰ (Borjigen et al., 2014; Li et al., 2015a). The $\delta^{13}C_{kerogen}$ values of the ϵ_1q source rocks range from −38.7‰ to −34.9‰ (avg. −36.5‰), implying the sapropelic kerogen type (Table 2; Figure 7). The $\delta^{13}C_{kerogen}$ values of the P_2q and P_2m source rocks range from −29.2‰ to −24.2‰ (avg. −26.5‰), implying that they mainly contain the mixed kerogen (Table 2; Figure 7). However, the $\delta^{13}C_{kerogen}$ values of the P_3l source rocks range from −26.1‰ to −24.8‰ (avg. −26.9‰), implying humic kerogen type, which is consistent with the lithology of coal measure (Table 2; Figure 7). The methane $\delta^{13}C$ value of natural gas is affected by maturity, while the ethane carbon isotopes have a relatively strong inheritance from parent material type (Stahl, 1977; Li et al., 2019). Therefore, ethane carbon isotopes of natural gas are usually used to indicate the origin of natural gas. Ethane carbon isotopes can be affected by thermochemical sulphate reduction of sulphate minerals by hydrocarbons at elevated temperatures (Liu et al., 2014; Li et al., 2015b; Gong et al., 2018; Wu et al., 2019). The GSI value of 0.01 was proposed as the threshold of TSR (Liu et al., 2013, 2019) and the GSI values of natural gas in the Permian reservoirs of the Northwestern Sichuan Basin is less than 0.01 (Table 1), so the natural gas has not undergone TSR, which cannot affect the ethane carbon isotopes.

The $\delta^{13}C_2$ values of natural gas samples in the Hewanchang area range from −36.7‰ to −31.5‰, similar to the $\delta^{13}C_{kerogen}$ values of the ϵ_1q source rocks (Figures 4, 7), implying the natural gases mainly originate from the ϵ_1q source rocks. The $\delta^{13}C_2$ values of natural gas samples in the Shuangyushi area range from −28.6‰ to −25.9‰, similar to the $\delta^{13}C_{kerogen}$ values of the P_2q and P_2m source rocks (Figures 4, 7), implying the natural gases mainly originate from the Upper Permian source rocks, but the contribution from P_3l source rocks cannot be excluded only by carbon isotope data. The $\delta^{13}C_2$ values of natural gas samples in the Jiulongshan area have a relatively wide range compared to those in the Shuangyushi area, from −29.3‰ to −25.2‰, which is similar to the $\delta^{13}C_{kerogen}$ values of the P_2q, P_2m and P_3l source rocks (Figures 4, 7), indicating that the natural gases mainly originate from the above three sets of source rocks.

Biomarker analysis is an effective method for determining the origin of hydrocarbon (Chen et al., 2018; Adriana et al., 2020; Schwangler et al., 2020). The relative content of steranes can indicate the origins of organic matter (Li et al., 2022). The C_{27} sterane are mainly originated from lower aquatic organisms and algal organic matter, the C_{28} sterane are mainly related to specific

TABLE 2 Carbon isotopes of source rock samples from different tratigraphic intervals.

Series	Formation	Lithology	$\delta^{13}C$/‰
Lower Cambrian	Qiongzhusi	shale	−36.3
Lower Cambrian	Qiongzhusi	shale	−37.6
Lower Cambrian	Qiongzhusi	shale	−38.7
Lower Cambrian	Qiongzhusi	shale	−37.2
Lower Cambrian	Qiongzhusi	shale	−36.7
Lower Cambrian	Qiongzhusi	shale	−36.9
Lower Cambrian	Qiongzhusi	shale	−35.1
Lower Cambrian	Qiongzhusi	shale	−36.7
Lower Cambrian	Qiongzhusi	shale	−35.6
Lower Cambrian	Qiongzhusi	shale	−35.8
Lower Cambrian	Qiongzhusi	shale	−34.9
Middle Permian	Qixia	marlstones	−24.2
Middle Permian	Qixia	marlstones	−25.2
Middle Permian	Qixia	marlstones	−27.4
Middle Permian	Maokou	marlstones	−27.2
Middle Permian	Maokou	marlstones	−28.3
Middle Permian	Maokou	marlstones	−29.2
Upper Permian	Longtan	coal	−25.2
Upper Permian	Longtan	coal	−25.6
Upper Permian	Longtan	coal	−26.1
Upper Permian	Longtan	coal	−24.8

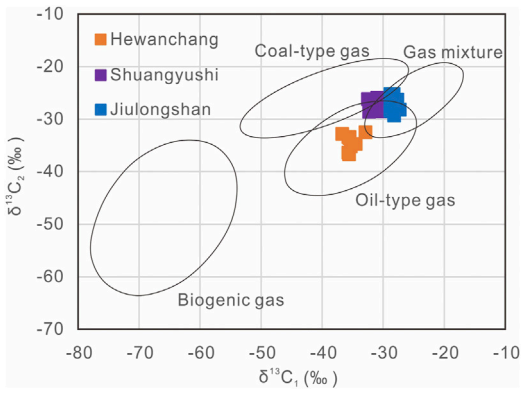

FIGURE 4
Cross-plot of $\delta^{13}C_1$ vs. $\delta^{13}C_2$ for natural gas samples from different areas to indicate the genetic types and origins of natural gas. The genetic types of natural gas are described in Liu et al., 2019.

phytoplankton such as diatoms, while the C_{29} sterane are mainly associated with higher plants as well as microalgae and blue-green algae (Huang and Meinschein, 1979; Grantham and Wakefield, 1988; Li et al., 2022). The Gam/C_{31}H and Ts/Tm ratios are the common biomarker parameters for oil-source correlation, which can indicate the salinity of water body and lithology respectively (Peters, et al., 2005). Li et al. (2022) analyzed the origins of Permian natural gas in different belts of the Northwest Sichuan Basin by the above biomarker characteristics of source rocks and Permian solid bitumen. The solid bitumen in the thrust nappe belt has abundant C_{29} steranes and large Gam/C_{31}H and Ts/Tm values, which resembles to those of theϵ_1q source rocks (Figures 8A,B), indicating that the natural gas in the thrust nappe belt is originated from theϵ_1q source rocks. The solid bitumen in the thrust front belt and unfaulted belt has both abundant C_{27} and C_{29} steranes and small Gam/C_{31}H and Ts/Tm ratios (Figures 8A,B), which resembles to those of the P_2q and P_2m source rocks, indicating that the natural gas in the thrust front belt and unfaulted belt is originated from the P_2q and P_2m source rocks. These results are basically consistent with those obtained by carbon isotope correlation.

5.2 Hydrocarbon accumulation process

Accurate determination of hydrocarbon charging time is the key to study hydrocarbon generation history and accumulation process. Fluid inclusion is one of the most common and effective methods to determine hydrocarbon charging period and time (Ni et al., 2016; Li et al., 2021; Pang et al., 2021). Chen et al. (2019b) found that the homogenization temperatures of brine inclusions associated with hydrocarbon inclusions in the reservoirs of the Shuangyushi Area are mainly distributed at 140–150°C and 160–170°C (Figure 9), indicating two stages of hydrocarbon charging. The GOI value in the first stage is larger than that in the second stage, indicating more hydrocarbons charged in the first stage. Combined with the burial and thermal history, it can be seen that the first hydrocarbon charging event occurred at late Triassic, while the second hydrocarbon charging event occurred at Early-Middle Jurassic (Figure 10).

The tectonic evolution of the Northwestern Sichuan Basin controlled the whole process of hydrocarbon accumulation, and combined the tectonic evolution history, the hydrocarbon accumulation process in the Northwestern Sichuan Basin can be divided into the following three stages (Figure 11).

5.2.1 Crude oil charging stage

In the late indosinian period, the slip nappe structure in the Northwestern Sichuan Basin was deformed, and a large-scale (large fault block) thrust nappe structure was formed under the control of the slip layer. At this time, the Lower Cambrian and the Upper-Middle Permian source rocks had entered the mature stage and the ϵ_1q, P_2q and P_2m source rocks generated large amounts of oils, while the P_3l source rocks of coal measures can only generate a certain amount of natural gas. Due to the existence of large thrust faults in the thrust nappe belt, the oil generated from the ϵ_1q source rocks can migrated along the thrust faults to the overlying reservoirs. However, there is few faults in the thrust front belt and unfaulted belt, so the Permian

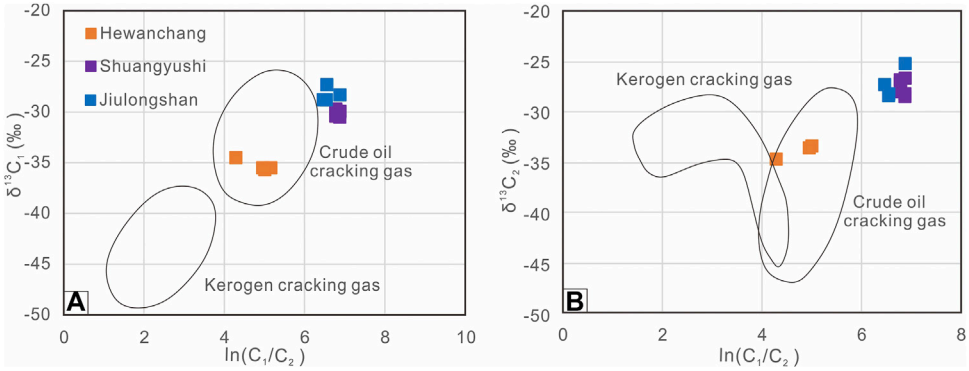

FIGURE 5
Cross-plots of ln (C_1/C_2) vs. $\delta^{13}C_1$ **(A)** and ln (C_1/C_2) vs. $\delta^{13}C_2$ **(B)** for natural gas samples from different areas to indicate the genetic types of natural gas. The distribution ranges of different genetic types of natural gas are referred to Liu et al. (2018).

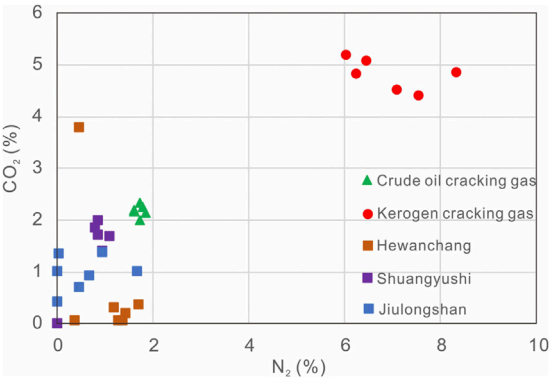

FIGURE 6
Cross-plot of N_2 vs. CO_2 for natural gas samples from different areas, showing the genetic types of natural gas. Samples of crude oil cracking gas and kerogen cracking gas are according to Li et al. (2019) and Yin et al. (2001), respectively.

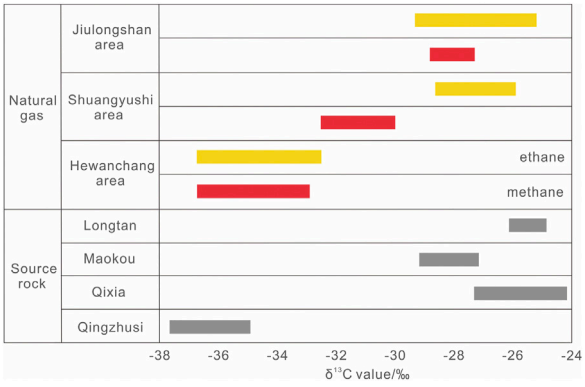

FIGURE 7
Carbon isotopes of source rock samples from different stratigraphic intervals and natural gas samples from different areas to indicate the origins of natural gas.

reservoirs there can only receive the oils and gas generated from the Upper-Middle Permian source rocks.

5.2.2 Oil cracking stage

In the Yanshanian period, the nappe further extends southeast. With the increase of the buried depth, the formation temperature increases continuously, resulting to the crude oil cracking to generate natural gas. The newly generated natural gas migrated a short distance to accumulate in the appropriate traps.

5.2.3 Gas reservoir adjustment stage

During the Himalayan period, with the continuous advance of the Longmen Mountain fold belt toward the passive margin, the strata in the Northwestern Sichuan Basin suffered severe deformation, resulting to the adjustment and destruction of large amounts of traps. The gas reservoirs were destroyed in the Kuangshanliang Area and went through large-scale adjustment in the other areas.

5.3 Main factors controlling the natural gas accumulation

5.3.1 Distribution of thrust faults

Faults can transport the hydrocarbons generated by the source rocks in deep layers to the reservoirs in shallow layers, and are the most important vertical migration pathways for hydrocarbons (Li et al., 2021). The faults and the associated fractures control the migration and subsurface location of hydrocarbon in carbonate and evaporate lithologies (Ameen, 2003; Lunn et al., 2008; Zhang et al., 2022). During the

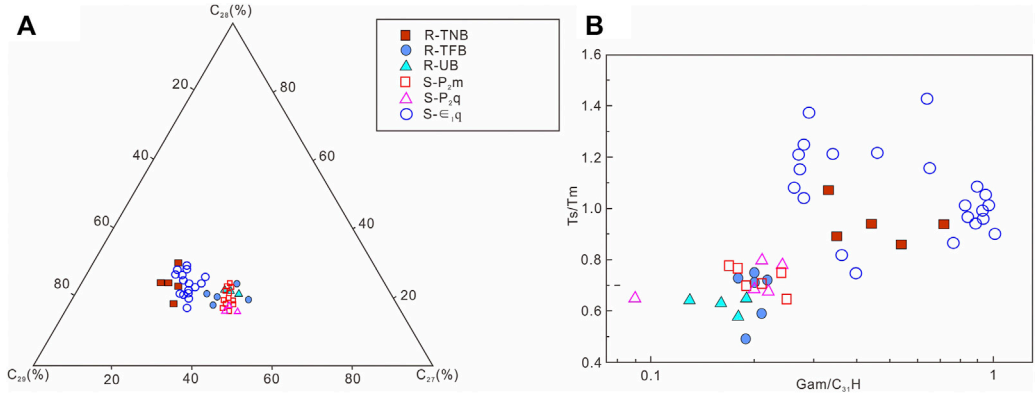

FIGURE 8
Biomarker characteristics for source rocks in different stratigraphic intervals and reservoir solid bitumen in different structural belts for determining the origins of natural gas (modified by Li et al., 2022). **(A)** Ternary plot of C_{27}–C_{28}–C_{29} steranes. **(B)** Cross plot of Gam/C_{31}H vs. Ts/Tm.

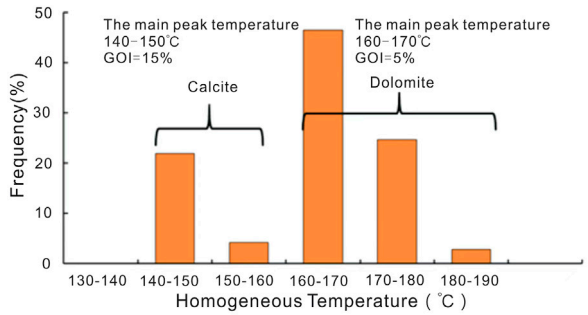

FIGURE 9
Homogenization temperature distribution of brine inclusions associated with hydrocarbon inclusions in the gas reservoirs of the Shuangyushi area (According to Chen et al., 2019b).

Indo–Yanshanian orogeny, under the influence of the large-scale subduction of the adjacent orogenic belt into the basin, a huge horizontal compressive stress field formed in the Northwestern Sichuan Basin (Gu et al., 2016; Li B. et al., 2020), creating large amounts of thrust faults. With the decreasing of the compressional stress from the thrust nappe belt to the thrust front belt and the unfaulted belt, the number and size of thrust faults decrease in the same order (Figures 3, 11).

The Hewanchang area is located in the thrust front belt, and develops many large thrust faults which extend down through the Cambrian strata and up to the Triassic and overlying strata. These thrust faults are favorable vertical migration paths for hydrocarbons generated by the ϵ_1q source rocks to enter the Permian reservoirs (Figure 11). Therefore, the natural gases in the Hewanchang area originate from the ϵ_1q source rocks. The Shuangyushi area is located in the thrust front belt. Although some thrust faults develop there, few of them extend down to the Cambrian strata. Therefore, hydrocarbons generated by theϵ_1q source rocks cannot migrate upward to the Permian reservoirs, which result to the fact that the natural gases in the Shuangyushi area mainly originate from the P_2q, P_2m and P_3l source rocks (Figure 11). However, the Jiulongshan area is located in the unfaulted belt and few thrust faults develop there. Therefore, the Permian reservoirs in the Jiulongshan area can only receive the hydrocarbons generated by the P_2q, P_2m and P_3l source rocks (Figure 11). According to the above discuss, it is the distribution of thrust faults that controls the hydrocarbon origins in different areas.

5.3.2 Preservation condition

The marine basins of China are usually located in the plates with small scale. Affected by multi-stage and multi-direction compressional tectonic movement such as the paleo-Asian ocean tectonic domain, western Pacific tectonic domain and Tethys tectonic domain, these basins are characterized by old age, multi-cycle evolution, complex basin-mountain structure, multi-period activity and poor stability, which makes the preservation condition an indispensable key factor for the large accumulation of hydrocarbons in the marine basins of China (Jia et al., 2006; Liu et al., 2011; Zhao et al., 2015). The Sichuan Basin is a typical marine basin during the Sinian to the Middle Triassic in China and the Northwestern Sichuan Basin is located in the transition region between the basin and mountain, so intense tectonic movement during the Himalayan orogeny caused the stratum deformation, fragmentation and denudation, which make a challenge for hydrocarbon preservation (Luo et al., 2020).

The Hewanchang area is in the thrust nappe belt adjacent to the thrust front belt. Although the stratum there were lifted up during the Himalayan orogeny, the regional caprocks of the thick shale in the Longtan Formation of the Upper Permian and the gypsum rocks in the Lower-Middle Triassic suffered little or no denudation and still owned strong sealing ability (Figure 11) (Luo

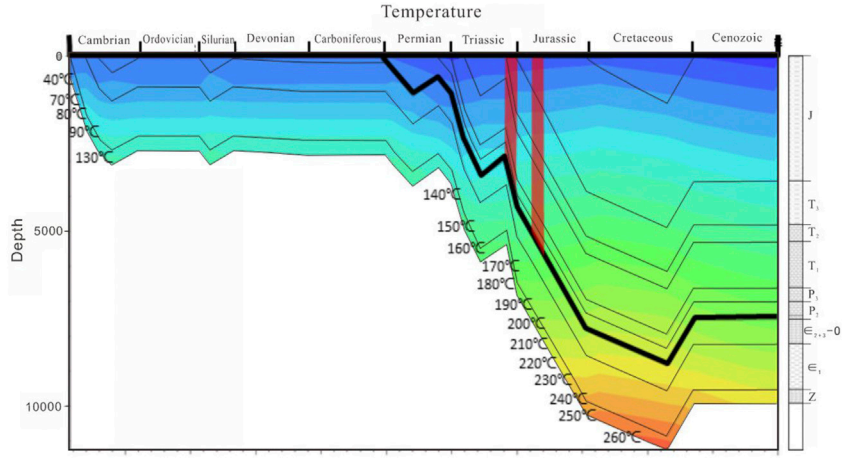

FIGURE 10
Burial and thermal history of the Northwestern Sichuan Basin to show the hydrocarbon charging stage and time.

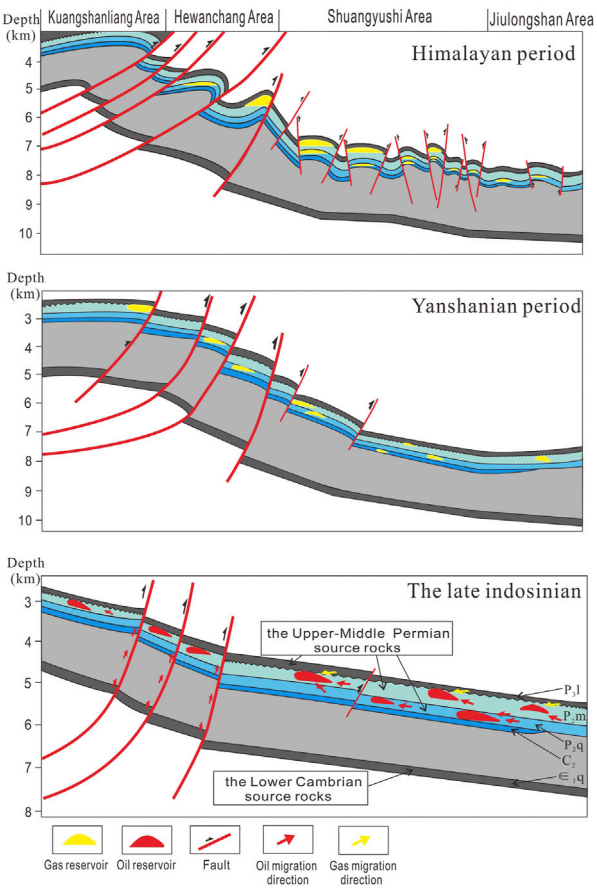

FIGURE 11
Hydrocarbon accumulation process in different periods and in different areas of the Northwestern Sichuan Basin.

et al., 2020). Therefore, natural gases can be preserved well after accumulation in the Hewanchang area. However, in the Kuanshanliang area, which is in the thrust nappe belt adjacent to the Longmen Mountain fold-and-thrust system, intense tectonic movement caused the opening of large deep thrust faults and the serious denudation of the regional caprocks due to violent stratum uplift (Figure 11) (Chen X. Z. et al., 2019). These caused the destruction of trap integrity, and then resulted to the oxidation and degradation of hydrocarbons to form exposed oil sands, oil seedlings and bitumen (Li et al., 2020a, b). In addition, due to weak compressional stress during the Himalayan orogeny, the stratum in the Shuangyushi area of the thrust front belt and the Jiulongshan area in the unfaulted belt suffered little or no uplift (Figure 11), so the regional caprocks of the Upper Permian and the Lower-Middle Triassic had a strong sealing ability and the natural gases in the Permian reservoirs owned a good preservation condition. This can be verified by the fact that the pressure coefficients of the gas reservoirs in the Shuangyushi area range from 1.4 to 1.8 and those in the Jiulongshan area range from 1.8 to 2.0 (Chen X. Z. et al., 2019).

5.4 Implications for natural gas exploration

Foreland basins are very important petroliferous basins over the world and the basin-mountain transition regions are key areas for hydrocarbon exploration in the foreland basins. The above discuss clearly reveals that the distribution of thrust faults and the preservation condition are the main factors controlling the natural gas accumulation in the Northwestern Sichuan Basin, a typical basin-mountain transition region. The distribution of

thrust faults controls the natural gas origins in different areas and the preservation condition determines whether the gas reservoirs can survive to the present or not. Under the influence of the large-scale subduction of the adjacent orogenic belt into the basin, the Northwestern Sichuan Basin can be divided into three regions, and different regions own unique geological features and gas accumulate rules.

The thrust nappe belt develops many large thrust faults extending down through the Low Cambrian source rocks, so the natural gases mainly originate from the Lower Cambrian source rocks. The area adjacent to the Longmen Mountain fold-and-thrust system suffered the most intense compressional stress and the regional caprocks suffered the serious uplift and denudation. Therefore, the natural gases cannot be preserved well and this area is not worth exploring the natural gas. However, the regional caprocks in the area adjacent to the thrust front belt suffered little or no denudation, so the natural gases in this area can be preserved well and are worth being explored.

The thrust front belt and the unfaulted belt only develops a few or few thrust faults, which cannot transport enough gases generated by the Low Cambrian source rocks to the overlying reservoirs. Therefore, the natural gases in the above two regions mainly originate from the Upper-Middle Permian source rocks. The regional caprocks there suffered little or no uplift and denudation, so the natural gases in the above two regions can be preserved well and are worth being explored.

6 Conclusion

The Northwestern Sichuan Basin is a typical basin-mountain transition region, with complex hydrocarbon accumulation rules. Under the influence of the large-scale subduction of the adjacent orogenic belt into the basin, the Northwestern Sichuan Basin can be divided into three structural belts: the unfaulted belt, the thrust front belt and the thrust nappe belt. Multiple sets of source rocks exist: Lower Cambrian source rocks containing sapropelic kerogen, Middle Permian source rocks containing mixed kerogen, and Upper Permian source rocks containing humic kerogen. The natural gas in the thrust nappe belt were mainly crude oil cracking gas, while the natural gas in the thrust front belt and the unfaulted belt were a mixture of crude oil cracking gas and humic kerogen cracking gas. The distribution of thrust faults controls the natural gas origins in different regions. The natural gas in the thrust nappe belt developing many large thrust faults mainly originates from the Lower Cambrian source rocks, while the natural gas in the thrust front belt and the unfaulted belt only developing a few or few thrust faults mainly originates from the Upper-Middle Permian source rocks. The preservation condition determines whether the gas reservoirs can survive to the present. The natural gas has poor preservation conditions in the thrust nappe belt adjacent to the Longmen Mountain fold-and-thrust system, where the regional caprocks suffered serious denudation, so this area is not worth exploring for natural gas. However, the natural gas can be preserved well in the thrust nappe belt adjacent to the thrust front belt, the thrust front belt and the unfaulted belt, where the regional caprocks suffered little or no denudation, so these areas have good prospects for natural gas exploration.

Data availability statement

The original contributions presented in the study are included in the article/supplementary material, further inquiries can be directed to the corresponding author.

Author contributions

HX is the first author of this article, responsible for the preparation of the full text. FX directed the research work of this paper and served as the corresponding author. XF, JZ, WL, and CC provide data support for this study. YW and KZ were responsible for the data collation of the study.

Funding

This study was funded by the PetroChina Project. The authors sincerely thank the collaboration and enthusiastic support from staff in the Hangzhou Institute of Geology and Southwest Oil and Gas Field Company of PetroChina. The funder had the following involvement in the study: financial support, study design and collecting project data. The funder was not involved in data analysis and interpretation, the writing of this article or the decision to submit it for publication.

Conflict of interest

XF, JZ, and WL were employed by the company PetroChina. CC was employed by the company PetroChina Southwest Oil and Gas Field Company. YW was employed by the company CNPC.

The remaining authors declare that the research was conducted in the absence of any commercial or financial relationships that could be construed as a potential conflict of interest.

Publisher's note

References

Adriana, M., Santos, M., Caroline, A., Eliane, S., Martins, L. L., and Rene, R. (2020). Degradation-resistant biomarkers in the Pirambóia Formation tar sands (Triassic) and their correlation with organic facies of the Irati Formation source rocks (Permian), Paraná. Brazil. *J. S. Am. Earth Sci.* 104, 102873. doi:10.1016/j.jsames.2020.102873

Al-ameri, T. K., and Zumberge, J. (2012). Middle and upper jurassic hydrocarbon potential of the Zagross Fold belt, North Iraq. *Mar. Petroleum Geol.* 36 (1), 13–34. doi:10.1016/j.marpetgeo.2012.04.004

Ameen, M. (2003). Fracture and *in-situ* stress characterization of hydrocarbon reservoirs: Definitions and introduction. *Geol. Soc. Lond. Spec. Publ.* 209, 1–6. doi:10.1144/gsl.sp.2003.209.01.01

Borjigen, T., Qin, J., Fu, X., Yang, Y., and Lu, L. (2014). Marine hydrocarbon source rocks of the Upper Permian Longtan Formation and their contribution to gas accumulation in the northeastern Sichuan Basin, southwest China. *Mar. Petroleum Geol.* 57, 160–172. doi:10.1016/j.marpetgeo.2014.05.005

Chen, C., Zhang, J., and Luo, B. (2019). Middle triassic-paleozoic pressure chamber and hydrocarbon accumulation in northwestern Sichuan Basin. *Nat. Gas. Ind.* 39 (04), 37–47. doi:10.3787/j.issn.1000-0976.2019.04.005

Chen, S. J., Fu, X. W., and Shen, Z. G. (2000). Molecular nitrogen Genesis in natural gas and relationship with gas accumulation history in Tarim Basin. *Acta Sedimentol. Sin.* 18, 615–618. (in Chinese with English abstract). doi:10.14027/j.cnki.cjxb.2000.04.024

Chen, X., Hao, F., Guo, L., Wang, D., Yin, J., Yang, F., et al. (2018). Origin of petroleum accumulation in the chaheji-gaojiapu structural belt of the baxian sag, bohai bay basin, China: Insights from biomarker and geological analyses. *Mar. Pet. Geol.* 93, 1–13. doi:10.1016/j.marpetgeo.2018.02.010

Chen, X. Z., Li, W., Wang, L. N., Lei, Y., Yang, G., Zhang, B., et al. (2019). Structural geology and favorable exploration prospect belts in Northwestern Sichuan Basin, SW China. *Petroleum Explor. Dev.* 46 (2), 413–425. doi:10.1016/s1876-3804(19)60022-4

Decelles, P. G., and Gilest, K. A. (1996). Foreland basin systems. *Basin Res.* 8, 105–123. doi:10.1046/j.1365-2117.1996.01491.x

Deming, D., and Chapman, D. S. (1988). Inversion of bottom-hole temperature data; the Pineview Field, Utah-Wyoming thrust belt. *Geophysics* 53 (5), 707–720. doi:10.1190/1.1442504

Deng, J., Liu, M., Ji, Y., Tang, D., Zeng, Q., Song, L., et al. (2022). Controlling factors of tight sandstone gas accumulation and enrichment in the slope zone of foreland basins: The Upper Triassic Xujiahe Formation in Western Sichuan Foreland Basin, China. *J. Petroleum Sci. Eng.* 214, 110474. doi:10.1016/j.petrol.2022.110474

Gong, D., Li, J., Ablimit, I., He, W., Lu, S., Liu, D., et al. (2018). Geochemical characteristics of natural gases related to Late Paleozoic coal measures in China. *Mar. Petroleum Geol.* 96, 474–500. doi:10.1016/j.marpetgeo.2018.06.017

Grantham, P. J., and Wakefield, L. L. (1988). Variations in the sterane carbon number distributions of marine source rock derived crude oils through geological time. *Org. Geochem.* 12 (1), 61–73. doi:10.1016/0146-6380(88)90115-5

Gu, Z., Yin, J., Jiang, H., Zhang, B., Li, Q., Yuan, M., et al. (2016). Tectonic evolution from late sinian to early paleozoic and natural gas exploration in northwestern Sichuan Basin, SW China. *Petroleum Explor. Dev.* 43 (1), 1–12. doi:10.1016/s1876-3804(16)30001-5

Guo, R., Wang, Q., and Wang, J. (2021). Oil-source correlation and stages of reservoir formation of the Alade oilfield in the Northwestern Junggar Basin of China. *J. Northeast Petroleum Univ.* 45 (3), 54–61. doi:10.3969/j.issn.2095-4107.2021.03.006

Guo, X., Hu, D., Huang, R., Wei, Z., Duan, J., Wei, X., et al. (2020). Deep and ultradeep natural gas exploration in the Sichuan Basin: Progress and prospect. *Nat. Gas. Ind. B* 7 (5), 419–432. doi:10.1016/j.ngib.2020.05.001

He, D., and Jia, C. (2005). Thrust tectonics and hydrocarbon accumulation. *Petroleum Explor. Dev.* 32 (2), 55–62. doi:10.3321/j.issn:1000-0747.2005.02.013

Hu, G., He, F., Mi, J., Yuan, Y., and Guo, J. (2021). The geochemical characteristics, distribution of marine source rocks and gas exploration potential in the Northwestern Sichuan Basin, China. *J. Nat. Gas Geoscience* 6 (4), 199–213. doi:10.1016/j.jnggs.2021.07.004

Huang, W., and Meinschein, W. (1979). Sterols as ecological indicators. *Geochimica Cosmochimica Acta* 43 (5), 739–745. doi:10.1016/0016-7037(79)90257-6

Huo, F., Yang, X., and Wang, C. (2018). Characteristics and main controlling factors of the middle permian Maokou formation reservoir in northwestern Sichuan Basin, China. *J. Chengdu Univ. Technol. Sci. Technol. Ed.* 45 (1), 45–52. (in Chinese with English abstract). doi:10.3969/j.issn.1671-9727.2018.01.04

Jia, C. Z., He, D. F., Shi, X., Yang, G., and Zhang, C. (2006). Characteristics of China's oil and gas pool formation in latest geological history. *Sci. China (Series D)* 49 (9), 947–959. doi:10.1007/s11430-006-0947-7

Kotarba, M. J., and Clayton, J. L. (2003). A stable carbon isotope and biological marker study of Polish bituminous coals and carbonaceous shales. *Int. J. Coal Geol.* 55, 73–94. doi:10.1016/s0166-5162(03)00082-x

Li, B., Mei, W., and Li, Q. (2020a). Influence of tectonic evolution of foreland basin in Northwestern Sichuan Basin on Paleozoic marine hydrocarbon accumulation. *Nat. Gas. Geosci.* 31 (7), 993–1003. doi:10.11764/j.issn.1672-1926.2020.02.008

Li, C. Z., Xu, G. S., Xu, F. H., Yu, Q., and Liang, H. (2021). A model for faults to link the Neogene reservoirs to the Paleogene organic-rich sediments in low-relief regions of the south Bohai Sea, China. *J. Petroleum Sci. Eng.* 200, 108360. doi:10.1016/j.petrol.2021.108360

Li, P., Hao, F., Guo, X., Zou, H., Yu, X., and Wang, G. (2015b). Processes involved in the origin and accumulation of hydrocarbon gases in the Yuanba gas field, Sichuan Basin, southwest China. *Mar. Petroleum Geol.* 59, 150–165. doi:10.1016/j.marpetgeo.2014.08.003

Li, P., Hao, F., Zhang, B., Zou, H., Yu, X., and Wang, G. (2015a). Heterogeneous distribution of pyrobitumen attributable to oil cracking and its effect on carbonate reservoirs: Feixianguan Formation in the Jiannan gas field, China. *Am. Assoc. Pet. Geol. Bull.* 99, 763–789. doi:10.1306/11051414018

Li, Q., Li, B., Mei, W., and Liu, Y. (2022). Genesis and sources of natural gas in fold-and-thrust belt: The Middle Permian in the NW Sichuan Basin. *Mar. Petroleum Geol.* 140, 105638. doi:10.1016/j.marpetgeo.2022.105638

Li, W., Yu, Z., Wang, X., Lu, X., and Feng, Q. (2020c). Formation mechanisms of deep and ultradeep over pressure caprocks and their relationships with superlarge gas fields in the petroliferous basins of China. *Nat. Gas. Ind. B* 7 (5), 443–452. doi:10.1016/j.ngib.2020.09.002

Li, Y., Chen, S., Wang, Y., Qiu, W., Su, K., He, Q., et al. (2019). The origin and source of the Devonian natural gas in the Northwestern Sichuan Basin, SW China. *J. Petroleum Sci. Eng.* 181, 106259. doi:10.1016/j.petrol.2019.106259

Li, Y., Chen, S., Wang, Y., Su, K., He, Q., Qiu, W., et al. (2020b). Relationships between hydrocarbon evolution and the geochemistry of solid bitumen in the Guanwushan Formation, NW Sichuan Basin. *Mar. Petroleum Geol.* 111, 116–134. doi:10.1016/j.marpetgeo.2019.08.018

Liu, Q., Jin, Z., Wang, X., Yi, J., Meng, Q., Wu, X., et al. (2018). Distinguishing kerogen and oil cracked shale gas using H, C-isotopic fractionation of alkane gases. *Mar. Petroleum Geol.* 91, 350–362. doi:10.1016/j.marpetgeo.2018.01.006

Liu, Q., Wu, X., Wang, X., Jin, Z., Zhu, D., Meng, Q., et al. (2019). Carbon and hydrogen isotopes of methane, ethane, and propane: A review of genetic identification of natural gas. *Earth-Science Rev.* 190, 247–272. doi:10.1016/j.earscirev.2018.11.017

Liu, Q. Y., Worden, R. H., Jin, Z. J., Liu, W., Li, J., Gao, B., et al. (2014). Thermochemical sulphate reduction (TSR) versus maturation and their effects on hydrogen stable isotopes of very dry alkane gases. *Geochimica Cosmochimica Acta* 137, 208–220. doi:10.1016/j.gca.2014.03.013

Liu, Q. Y., Worden, R. H., Jin, Z. J., Liu, W., Li, J., Gao, B., et al. (2013). TSR versus non-TSR processes and their impact on gas geochemistry and carbon stable isotopes in Carboniferous, Permian and Lower Triassic marine carbonate gas reservoirs in the Eastern Sichuan Basin, China. *Geochimica Cosmochimica Acta* 100, 96–115. doi:10.1016/j.gca.2012.09.039

Liu, S., Deng, B., and Li, Z. (2011). The texture of sedimentary basin-orogenic belt system and its influence on oil/gas distribution: A case study from Sichuan basin. *Acta Petrol. Sin.* 27 (3), 621–635.

Lunn, R. J., Willson, J. P., Shipton, Z. K., and Moir, H. (2008). Simulating brittle fault growth from linkage of preexisting structures. *J. Geophys. Res.* 113 (B7), B07403. doi:10.1029/2007jb005388

Luo, B., Wen, L., and Zhang, Y. (2020). Differential gas accumulation process of the middle permian Qixia Formation, northwestern Sichuan Basin. *Oil gas Geol.* 41 (2), 393–406. doi:10.11743/ogg20200215

Macclay, K. R. (2004). Thrust tectonics and hydrocarbon systems. *AAPG Mem.* 82. doi:10.1306/M82813

Miao, Z., Pei, Y., Su, N., Sheng, S., Feng, B., Jiang, H., et al. (2022). Spatial and temporal evolution of the Sinian and its implications on petroleum exploration in the Sichuan Basin, China. *J. Petroleum Sci. Eng.* 210, 110036. doi:10.1016/j.petrol.2021.110036

Misz-Kennan, M., and Fabianska, M. J. (2011). Application of organic petrology and geochemistry to coal waste studies. *Int. J. Coal Geol.* 88, 1–23. doi:10.1016/j.coal.2011.07.001

Ni, Z. H., Wang, T. G., Li, M. J., Fang, R. H., Li, Q. M., Tao, X. W., et al. (2016). An examination of the fluid inclusions of the well RP3-1 at the Halahatang Sag in Tarim Basin, northwest China: Implications for hydrocarbon charging time and fluid evolution. *J. Petroleum Sci. Eng.* 146, 326–339. doi:10.1016/j.petrol.2016.04.038

Pang, Y., Shi, B., Guo, X., Zhang, X., Han, Z., Cai, L., et al. (2021). Source–reservoir relationships and hydrocarbon charging history in the central uplift of the south Yellow Sea basin (East Asia): Constrained by machine learning procedure and basin modeling. *Mar. Petroleum Geol.* 123, 104731. doi:10.1016/j.marpetgeo.2020.104731

Peters, K. E., Walters, C. C., and Moldowan, J. M. (2005). *The biomarker guide, biomarkers and isotopes in Petroleum exploration and Earth history*. Cambridge: Cambridge University Press.

Picha, F. J. (2011). Late orogenic faulting of the foreland plate: An important component of petroleum systems in orogenic belts and their forelands. *Am. Assoc. Pet. Geol. Bull.* 95 (6), 957–981. doi:10.1306/11191010006

Schwangler, M., Harris, N. B., and Waldron, J. W. F. (2020). Source rock characterization and oil-to-source rock correlation of a Cambrian -Ordovician fold-and-thrust belt petroleum system, Western Newfoundland. *Mar. Pet. Geol.* 115, 104283. doi:10.1016/j.marpetgeo.2020.104283

Stahl, W. J. (1977). Carbon and nitrogen isotopes in hydrocarbon research and exploration. *Chem. Geol.* 20, 121–149. doi:10.1016/0009-2541(77)90041-9

Wang, Q., Zhang, D. Y., and Wang, J. (2018). Hydrocarbon and nonhydrocarbon characteristics for comprehensive identification about kerogen pyrolysis gas and oil cracked gas. *Nat. Gas. Geosci.* 29, 1231–1239. (in Chinese with English abstract). doi:10.11764/j.issn.1672-1926.2018.07.003

Wei, G., Wang, Z., Li, J., Yang, W., and Xie, Z. (2018). Characteristics of source rocks, resource potential and exploration direction of Sinian-Cambrian in Sichuan Basin, China. *J. Nat. Gas Geoscience* 2 (5-6), 289–302. doi:10.1016/j.jnggs.2018.02.002

Wei, G., Yang, W., Liu, M., Xie, W., Jin, H., Wu, S., et al. (2020). Distribution rules, main controlling factors and exploration directions of giant gas fields in the Sichuan Basin. *Nat. Gas. Ind. B* 7 (1), 1–12. doi:10.1016/j.ngib.2020.01.001

Wei, Y., Yang, T., and Guo, S. (2019). Oil and gas resource potentials, exploration fields and favorable zones in foreland thrust belts. *China Pet. Explor.* 24 (1), 46–59.

Worden, R. H., Smalley, P. C., and Oxtoby, N. H. (1995). Gas souring by thermochemical sulfate reduction at 140°C. *AAPG Bull.* 79, 854–863. doi:10.1306/8D2B1BCE-171E-11D7-8645000102C1865D

Wu, A., Cao, J., and Zhang, J. (2021). Bedding-parallel calcite veins indicate hydrocarbon–water–rock interactions in the overmature Longmaxi shales, Sichuan Basin. *Mar. Petroleum Geol.* 133, 105303. doi:10.1016/j.marpetgeo.2021.105303

Wu, X., Liu, Q., Liu, G., and Ni, C. (2019). Genetic types of natural gas and gas-source correlation in different strata of the Yuanba gas field, Sichuan Basin, SW China. *J. Asian Earth Sci.* 181, 103906. doi:10.1016/j.jseaes.2019.103906

Xiao, D., Wen, L., Zhang, Y., Xie, C., Tan, X., and Cao, J. (2021). Natural gas accumulation in the basin–mountain transition zone, Northwestern Sichuan Basin, China. *Mar. Petroleum Geol.* 133, 105305. doi:10.1016/j.marpetgeo.2021.105305

Xu, Q., Qiu, N., Liu, W., Shen, A., and Wang, X. (2018). Thermal evolution and maturation of sinian and cambrian source rocks in the central Sichuan Basin, southwest China. *J. Asian Earth Sci.* 164, 143–158. doi:10.1016/j.jseaes.2018.06.015

Yin, C. H., Wang, T. D., Wang, S. Y., and Lin, F. (2001). Differences between Kerogen and oil cracked gases in Sinian reservoirs of Weiyuan and Ziyang area. *Acta Sedimentol. Sin.* 19 (1), 156–160. (in Chinese with English abstract). doi:10.14027/j.cnki.cjxb.2001.01.028

Zhang, L., Liao, Z., Long, K., Carpenter, B. M., Zou, H., and Hao, F. (2022). Fundamental constraints of lithologically controlled fault networks on gas migration and accumulation for fractured carbonates in the Western Sichuan Basin, China. *J. Petroleum Sci. Eng.* 208, 109502. doi:10.1016/j.petrol.2021.109502

Zhao, W. Z., Hu, S. Y., Liu, W., Wang, T., and Jiang, H. (2015). The multistaged "golden zones" of hydrocarbon exploration in superimposed petroliferous basins of onshore China and its significance. *Petroleum Explor. Dev.* 42 (1), 1–13. doi:10.1016/s1876-3804(15)60001-5

Zheng, T., Ma, X., Pang, X., Wang, W., Zheng, D., Huang, Y., et al. (2019). Journal of petroleum science and engineering organic geochemistry of the upper triassic T_3x^5 source rocks and the hydrocarbon generation and expulsion characteristics in Sichuan Basin, central China. *J. Petroleum Sci. Eng.* 173, 1340–1354. doi:10.1016/j.petrol.2018.10.070

frontiers | Frontiers in Earth Science

TYPE Original Research
PUBLISHED 21 September 2022
DOI 10.3389/feart.2022.987822

OPEN ACCESS

EDITED BY
Hao Zou,
Chengdu University of Technology, China

REVIEWED BY
Xiaoqi Wu,
SINOPEC Petroleum Exploration and Production Research Institute, China
Piotr Krzywiec,
Institute of Geological Sciences (PAN), Poland

*CORRESPONDENCE
Jian Cao,
jcao@nju.edu.cn
Yiming Ablimiti,
ablmt@petrochina.com.cn

SPECIALTY SECTION
This article was submitted to Economic Geology, a section of the journal Frontiers in Earth Science

RECEIVED 06 July 2022
ACCEPTED 30 August 2022
PUBLISHED 21 September 2022

CITATION
Ablimiti Y, He W, Li N, Ma D, Liu H, Bian B, Ding X, Jiang M, Wang J and Cao J (2022), Mechanisms of deep oil–gas accumulation: New insights from the Carboniferous Central Depression, Junggar Basin, China.
Front. Earth Sci. 10:987822.
doi: 10.3389/feart.2022.987822

Mechanisms of deep oil–gas accumulation: New insights from the Carboniferous Central Depression, Junggar Basin, China

Yiming Ablimiti[1]*, Wenjun He[1], Na Li[1], Delong Ma[2], Hailei Liu[1], Baoli Bian[1], Xiujian Ding[3], Mengya Jiang[1], Jiangtao Wang[1] and Jian Cao[4]*

[1]Research Institute of Exploration and Development, PetroChina Xinjiang Oilfield Company, Karamay, China, [2]PetroChina Research Institute of Petroleum Exploration and Development—Northwest, Lanzhou, China, [3]Key Laboratory of Deep Oil and Gas, School of Geosciences, China University of Petroleum, Qingdao, China, [4]State Key Laboratory for Mineral Deposits Research, School of Earth Sciences and Engineering, Nanjing University, Nanjing, China

To investigate the mechanisms of deep oil–gas accumulation in superimposed basins in western China, and identify deep oil–gas reserves in the Junggar Basin, this study examined Carboniferous reservoirs in the Central Depression of the basin. We determined the hydrocarbon physical properties and geochemical characteristics, and controlling factors on hydrocarbon accumulation in the deep part of the Central Depression. We present a geological model of oil–gas accumulation based on analog modeling of reservoir formation. The deep hydrocarbons in the study area are mainly light–medium oil and wet natural gas, which were mainly derived from Permian and Carboniferous source rocks. The hydrocarbon source rocks and their thermal evolution led to hydrocarbon accumulation in the study area. Adjacent source–reservoir rocks on both sides of faults were key to vertical hydrocarbon migration and multi-stage charging. Suitable reservoir–cap rock assemblages were also important for reservoir preservation. The hydrocarbon accumulation model involves a source–reservoir link along faults, late charging, and paleo-uplifts. The reservoir types include those linked to source rocks by large-scale faults and those in paleo-uplifts surrounded by oil-generating depressions, which both have good exploration prospects. This accumulation model may be applicable to deep parts of other superimposed basins.

KEYWORDS

hydrocarbon accumulation mechanism, deep strata, analog modeling, fault, Carboniferous, Junggar Basin

1 Introduction

Deep oil–gas accumulation usually means the hydrocarbon resources buried below 4,500 m in sedimentary basins (Jia and Pang, 2015; Pang et al., 2015). Recent years, the deep parts of sedimentary basins are increasingly important sites for global oil–gas exploration, and attract much attention (Ma et al., 2018; Zheng et al., 2018; Zhu et al., 2021). However, many questions still in confusion, such as the formation and evolution of deep-buried traps, the efficiency of large-scale reservoirs, the types of migration pathways and hydrocarbon accumulation processes. In China, superimposed petroliferous basins have experienced multiple stages of tectonism and sedimentation, which have led to the development of multiple sets of source and reservoir rocks. These complex geological conditions make the hydrocarbon accumulation mechanism in the deep buried strata still unclear. Lateral hydrocarbon migration and accumulation have been affected by faulting and, as such, the hydrocarbon migration and accumulation processes are complex (Zhang et al., 2021).

The Junggar Basin is a typical superimposed petroliferous basin in western China and an important area for onshore oil–gas exploration. Deep strata exploration began in the 1990s, when the first ultra-deep well (6,010 m; the Lu 3 well) was drilled in the basin, specifically in the Luliang Uplift of the Central Depression where deep Carboniferous strata were targeted. Based on this well, the Carboniferous reservoirs in the Shixi area were discovered and developed. However, subsequent deep oil–gas exploration has been limited by technological and economic constraints. In 2005, the deepest onshore exploration well in China at that time (i.e., the Moshen1 well) was drilled in the Carboniferous anticline of the Mosuowan Uplift in the Central Depression to a depth of 7,500 m, which yielded a good oil–gas show. Although there was no oil flow, it was confirmed that effective source rocks and reservoirs occur in (ultra)-deep parts of the Central Depression of the basin. Since 2005, the PetroChina Xinjiang Oilfield Company has increased exploration in many areas of the deep basin, which has led to the establishment of many producing oil–gas wells. In particular, in the past 2 years, discoveries have been made in the Chetan 1, Shatan 1, Kangtan 1, Gaotan 1, and Hutan 1 wells in Carboniferous–Triassic strata around the Shawan and Fukang sags, and in Jurassic–Cretaceous strata in the southern thrust belt (Du et al., 2019a; Du et al., 2019b; Zhi et al., 2019; Hu et al., 2020; He et al., 2021; Zhi et al., 2021). This highlights the considerable exploration potential of the deep basin strata, and necessitates further improvements in our geological understanding of the deep structures, source and reservoir rocks, and hydrocarbon accumulation in such settings. Although previous exploration and studies have indicated the deep Carboniferous strata in the Central Depression are a potential exploration area, key factors such as the state of the oil–gas phases and hydrocarbon accumulation processes remain unclear and hinder hydrocarbon exploration. This is a common problem for (ultra)-deep oil–gas exploration worldwide.

As such, this study investigated deep Carboniferous reservoirs in the Central Depression of the Junggar Basin, China, in what is the first study of the hydrocarbon accumulation mechanisms in this region. To guide deep oil–gas exploration, analog modeling of reservoir formation was undertaken to constrain the processes of oil–gas accumulation and enrichment.

2 Geological setting

The Junggar Basin is part of the Central Asia Orogenic Belts (CAOB) and located in northwestern China, and has an area of 13.6×10^4 km^2. The basin has experienced numerous tectonic events from the Carboniferous to Quaternary, and has evolved from a transitional marine–continental facies basin to an intracontinental depression basin with multiple depocenters, a large depression basin that underwent multiple cycles of subsidence, and finally a foreland basin (Chen et al., 2002; Chen et al., 2005; He et al., 2018; Wang et al., 2018). The strata in the Central Depression are Carboniferous to Quaternary in age, and the oldest strata intersected by drilling are early Carboniferous. The Carboniferous rocks consist mainly of andesite, basalt, tuff, and occasional clastic sedimentary rocks. In the early Carboniferous, the Junggar Basin was in a marine environment, in which marine clastic and carbonate rocks were deposited, and volcanic rocks were erupted. In the late Carboniferous, the ocean basin closed and a foreland basin formed (Li et al., 2012; Li et al., 2015a; Li et al., 2015b). At the end of the Carboniferous, the basin was strongly deformed and erosion was widespread (He et al., 2010a; Lu et al., 2013). During the early–middle Permian, the Junggar Basin had multiple depositional and subsidence centers in the Mahu, Shawan, Penyijingxi, Fukang, Jimusar, and Zhangbei–Shishugou regions, in which the best source rocks in the basin were deposited (Wang et al., 2012; Xia et al., 2020a; Xia et al., 2020b; Cao et al., 2020; Tang et al., 2021; Xia et al., 2022). In the Mesozoic, the Junggar Basin were developed as an intracontinental depression due to the compression from northwest and northeast (Allen and Vincent, 1997; Liu et al., 2017). The strata were mainly composed of conglomerate, sandstone, mudstone and so on. From Late Jurassic to Early Neogene, the compression stress became gradually weak and changed to slightly extension, developing NS- and EW-trending normal faults (Liu et al., 2017). The strata also were mainly composed of conglomerate, sandstone and mudstone, with coal beds developed in the Jurassic. From Neogene to Quaternary, the Junggar Basin changed into a rejuvenated foreland basin (Wu et al., 2005).

Based on the extent of exploration and data availability, this study focused on Carboniferous reservoirs in the Penyijingxi Sag and surrounding areas. The Penyijingxi Sag is one of units in the

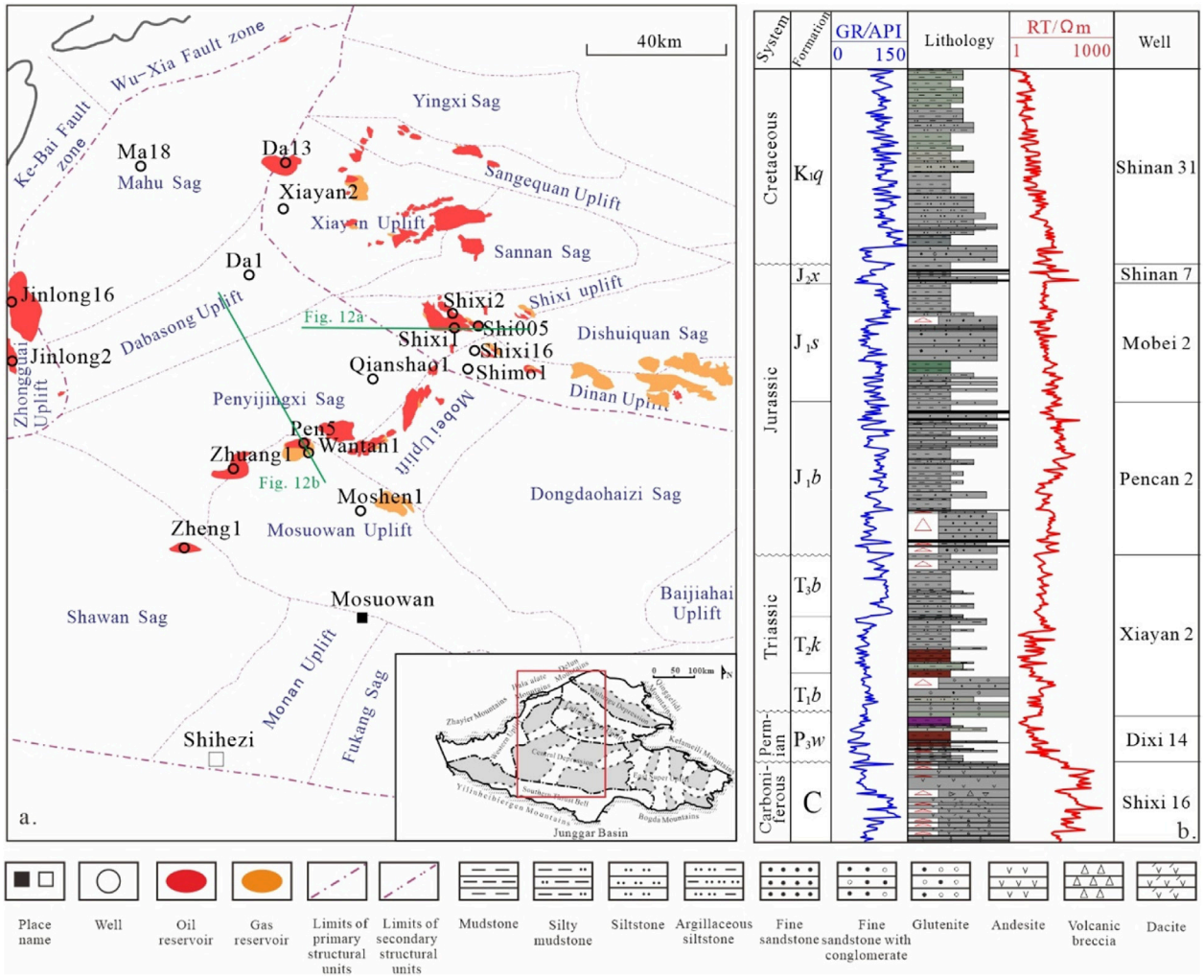

FIGURE 1
(A) Location and **(B)** stratigraphy of the study area.

Central Depression, and is surrounded by the Mosuowan, Mobei, Shixi, Dabasong, and Xiayan uplifts. Several large-scale and high-output oil–gas fields, such as the Pen 5 gas field and Shixi oilfield, have been discovered in the uplift belt around the Penyijingxi Sag (Figure 1). The oil and gas are distributed in several Carboniferous–Jurassic reservoirs.

3 Geochemistry and origin of the oil–gas

3.1 Geochemistry and origins of the crude oils

Typical crude oils in Carboniferous reservoirs in the Penyijingxi Sag occur in the Zhongguai, Shixi, and Mosuowan uplifts. The crude oils have a low densityand a medium wax content (Figure 2). The physical properties of the crude oil vary laterally, and the crude oil density decreases with depth (Figure 2). The crude oil at < 3,100 m depth is medium oil, at 3,100–3,900 m is light oil, and below 4,400 m is mainly condensate. Therefore, it can be inferred that condensate and natural gas reservoirs with poorer physical properties exist at greater depth (Figure 2).

The crude oil from the Zhongguai Uplift was derived from a mixture of Carboniferous and the lower Permian Fengcheng Formation (P_1f) source rocks, and those from the Shixi and Mosuowan uplifts were derived from a mixture of Permian and Carboniferous source rocks. In general, the oils from the Zhongguai Uplift have pristane (Pr) with $<nC_{17}$, phytane (Ph) with $<nC_{18}$, high Ts/Tm ratios, and moderate β-carotene contents. The Pr and Ph contents are low, with $Pr/nC_{17} < 1$ (0.4–1.2), $Ph/nC_{18} < 1$ (0.2–1.0),

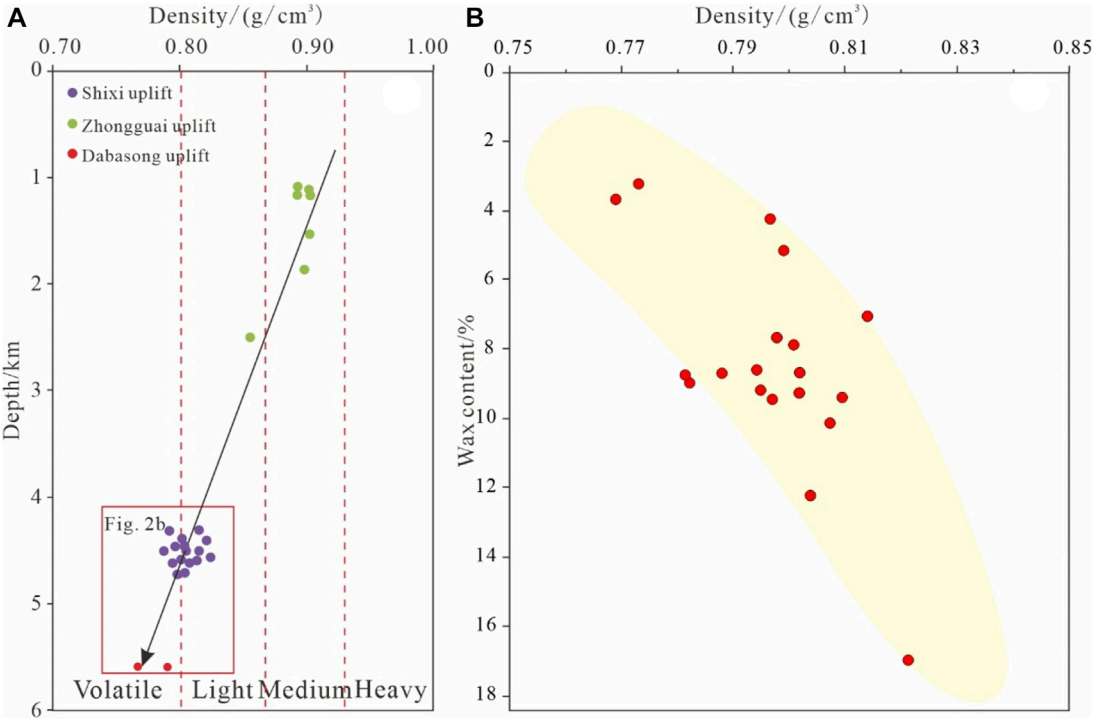

FIGURE 2
Oil density versus **(A)** depth and **(B)** wax content for Carboniferous crude oils in the Penyijingxi Sag.

pristane/phytane (Pr/Ph) = 0.8–1.2, and gammacerane index (gammacerane/C_{30} hopane) values of 0.2–0.6. Crude oils from the Shixi and Mosuowan uplifts have low Pr/Ph ratios, high Ts/Tm ratios, and low gammacerane and β-carotene contents. These crude oils have Pr/Ph < 1, gammacerane index values of < 0.2, and Ts/Tm = 0.4–1.2. Most of the samples do not contain β- or γ-carotene.

In addition, the crude oils contain a wide range of *n*-alkanes that are normally distributed, with light/heavy *n*-alkane ratios of >1.5. The *n*-alkanes exhibit no obvious odd–even predominance and the carbon preference index (CPI) is 1.0–1.2, which is indicative of mature oil. Pr/Ph values of 1.0–2.0 indicate that the source rocks formed in a reducing, lacustrine sedimentary environment. There are no clear differences in Pr/Ph values between the oil fields, although the deep oil in the northern part of the sag has slightly lower Pr/Ph values, Pr/Ph values in the Shixi oilfield are <1.2, and Pr/Ph values of oils from the other areas are 1.2–2.0. The crude oil biomarkers have similar characteristics in all three uplifts. C_{19} tricyclic terpene contents are lower than C_{20} and C_{21} tricyclic terpene contents, with a peak at C_{20}, C_{21}, and C_{23} tricyclic terpenes. The abundance of C_{24} tetracyclic terpenes is low and the abundance of the 25-norhopane series is high. The crude oils containing 25-norhopane have higher contents of tricyclic terpenes, Ts, and gammacerane, whereas those not containing 25-norhopane have lower contents of these biomarkers. C_{29} is the carbon number of the most abundant regular sterane, and the abundance of C_{28} sterane is slightly lower than that of C_{29}. C_{27} sterane is low in abundance and diasteranes are almost absent. These biomarker characteristics are typical of Permian crude oil. The carbon isotopic ($\delta^{13}C$) compositions of the crude oils are light, with $\delta^{13}C$ values of most crude oils varying from −30‰ to −29‰, but some condensates and light oils have values heavier than −29‰. The biomarker characteristics of the Carboniferous crude oils in this area are different from those in other areas of the Junggar Basin. For example, the crude oil from the northern slope of the Zhongguai Uplift in the western Penyijingxi Sag has high Pr and Ph contents with Pr/Ph ≤ 1, and low Ts and high β-carotene and gammacerane contents (e.g., the Jin 102 well). The crude oil from the southern Zhongguai Uplift has low Pr and Ph, high Ts, low β-carotene, and moderate gammacerane contents (e.g., the Jinlong 103 well). The crude oil in the northern Zhongguai Uplift typically has high β-carotene, low Pr and Ph, low Ts, and high gammacerane contents (e.g., the Jinlong 16 well) (Figure 3).

3.2 Geochemistry and origins of the natural gas

Methane is the most abundant component in the natural gas in the study area, with contents of 60%–95%. The methane content decreases with increasing depth, and

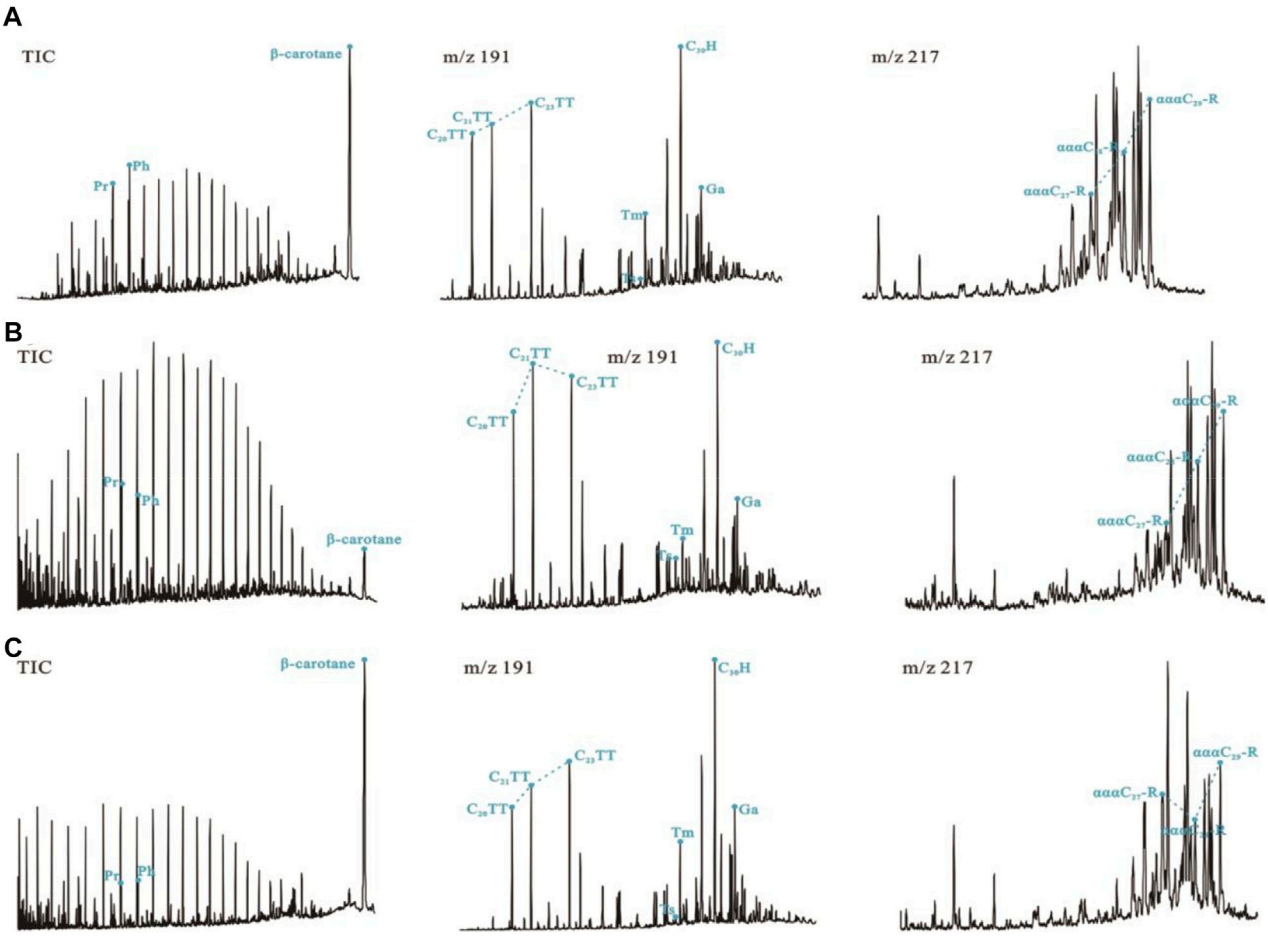

FIGURE 3
Biomarker chromatograms for Carboniferous crude oils in the Penyijingxi Sag. **(A)** Well Jin102, 1,470–1,510 m, Carboniferous, oil; **(B)** Well Jinlong103, 3,118–3,130 m, Carboniferous, oil; **(C)** Well Jinlong16, 2548–2556 m, Carboniferous, oil. Pr is pristane; Ph is phytane; C_{20}TT is C_{20} tricyclic terpane; C_{21}TT is C_{21} tricyclic terpane; C_{23}TT is C_{23} tricyclic terpane; Ts is 18α(H)-22,29,30-trinorneohopane; Tm is 17α(H)-22,29,30-trinorhopane; C_{30}H is C_{30} hopance; Ga is gammacerane; C_{27}-R is C_{27} steranes; C_{28}-R is C_{28} steranes; C_{29}-R is C_{29} steranes.

below 4,500 m is <80%. The ethane content of the natural gas is <10% and gradually increases with increasing depth. The propane content is <10%, and mostly <5%. The propane content increases gradually with burial depth. The dryness coefficient is a commonly used parameter to characterize the relative methane contents in natural gas. The dryness coefficient of natural gas in the study area is 0.7–1.0, and decreases gradually with increasing depth. However, the natural gas is generally wet (Figure 4).

In general, natural gas can be divided into oil-type, coal-type, and mixed gas, based on the hydrocarbon source materials (Dai, 1993). In the Shixi and Mobei oil fields, and Mosuowan gas field (Figure 5) the carbon isotopic compositions of the natural gas are variable. The carbon isotopic compositions of methane ($\delta^{13}C_1$) vary from –42‰ to –33‰, and for ethane ($\delta^{13}C_2$) from –27.5‰ to –25.0‰, indicating that the natural gas is generally mature.

The source of the natural gas is relatively complex. Based on the light hydrocarbons associated with natural gas in the Mobei and Mosuowan uplifts, it can be inferred the hydrocarbons were mainly derived from a mixture of lacustrine lower organisms and terrestrial higher organisms. The crude oils associated with gas in the Mosuowan Uplift have low Pr and Ph contents, low Ts/Tm ratios, low gammacerane contents, and a V-shaped distribution of C_{27}–C_{28}–C_{29} cholestanes (Figure 6). The biomarker characteristics of the light hydrocarbons and crude oils associated with the natural gas suggest that the natural gas in the Penyijingxi Sag was mainly derived from the Fengcheng Formation and other Carboniferous source rocks.

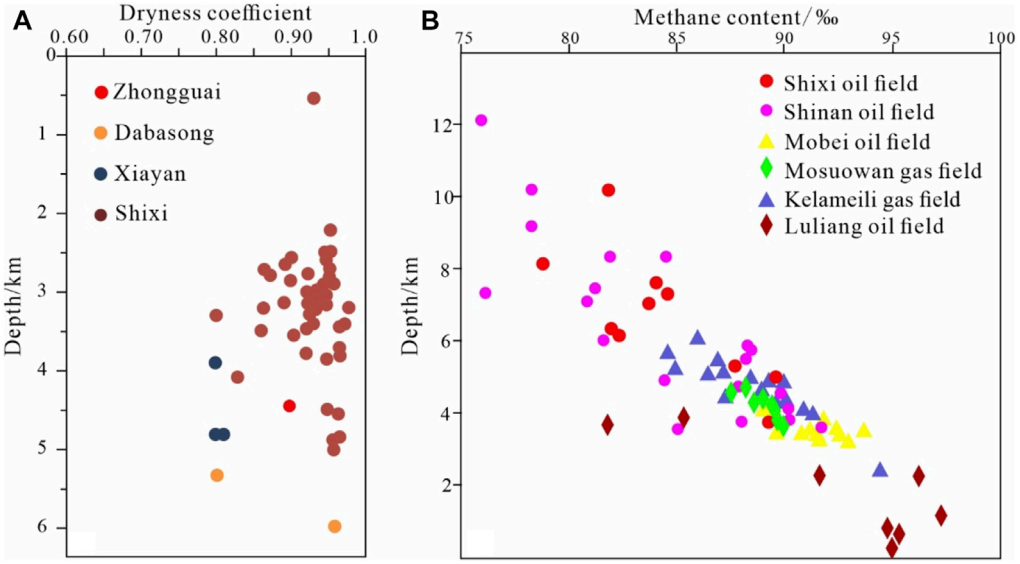

FIGURE 4
(A) Dryness coefficient and **(B)** methane content versus depth in the Penyijingxi Sag.

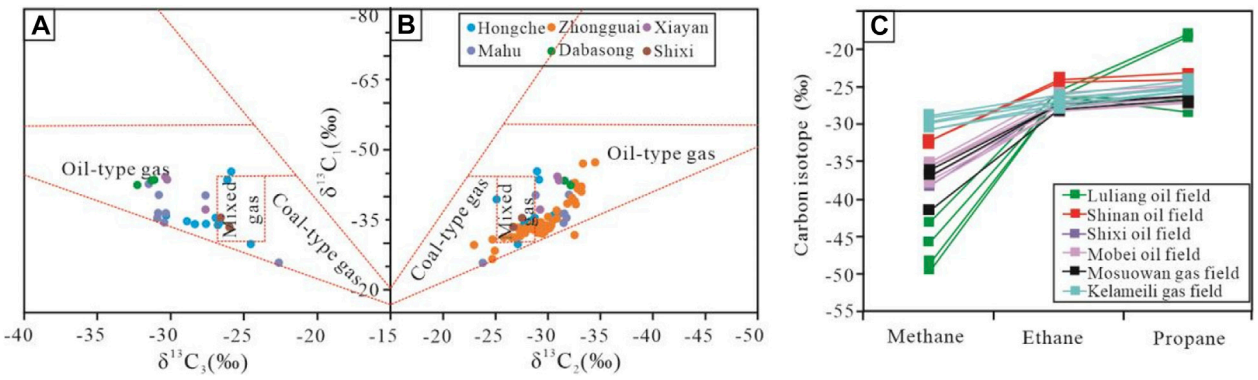

FIGURE 5
(A) Carbon isotopic compositions of propane ($\delta^{13}C_3$) and **(B)** carbon isotopic compositions of ethane ($\delta^{13}C_2$) versus carbon isotopic compositions of methane ($\delta^{13}C_1$) in Carboniferous and Permian reservoirs in the Penyijingxi Sag; **(C)** Carbon isotopic compositions of natural gas in Carboniferous and Permian reservoirs in the Penyijingxi Sag.

4 Factors controlling hydrocarbon accumulation

4.1 Hydrocarbon sources and degree of thermal evolution

Source rocks have a key role in hydrocarbon formation (Kuang et al., 2007; He et al., 2010a; He et al., 2010b; Wang et al., 2010; Zhao et al., 2011; Wang et al., 2012; Yang et al., 2014; Chen et al., 2016). The Penyijingxi Sag is surrounded by paleo-uplifts, which are close to the hydrocarbon generation sag. The oil–gas was derived from deep Carboniferous–Permian source rocks in the sag. In the early stages of exploration, shallow gas reservoirs (e.g., those in the Pen5 and Qianshao wells) were found in the Penyijingxi Sag. The gas was derived from a mixture of Permian and Carboniferous source rocks, and secondary gas reservoirs formed by the upward modification of deeper gas reservoirs (Cao et al., 2007; Ablimiti et al., 2019). More recent exploration of the central area of the sag has identified condensate reservoirs with high gas/oil ratios at depth. In particular, the Shixi 16 well at the eastern margin of the

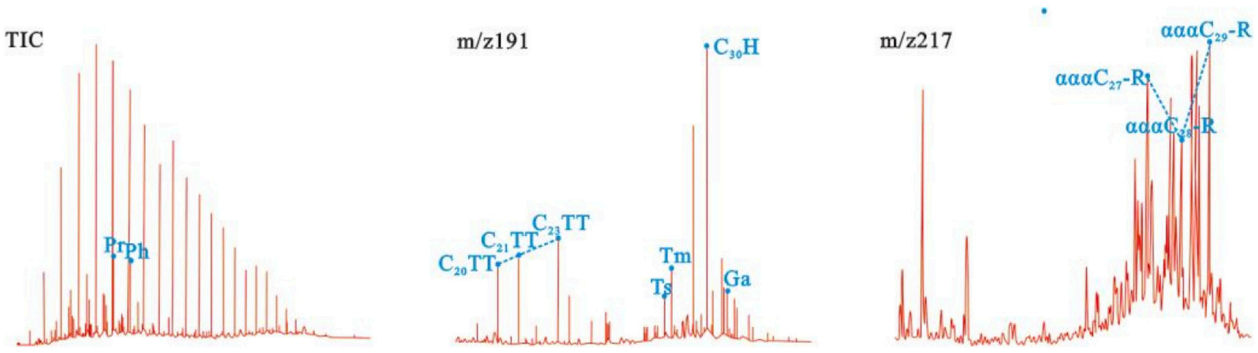

FIGURE 6
Biomarker spectra of natural gas and associated crude oils in the Mosuowan Uplift (Well Moshen1; 7209 m).

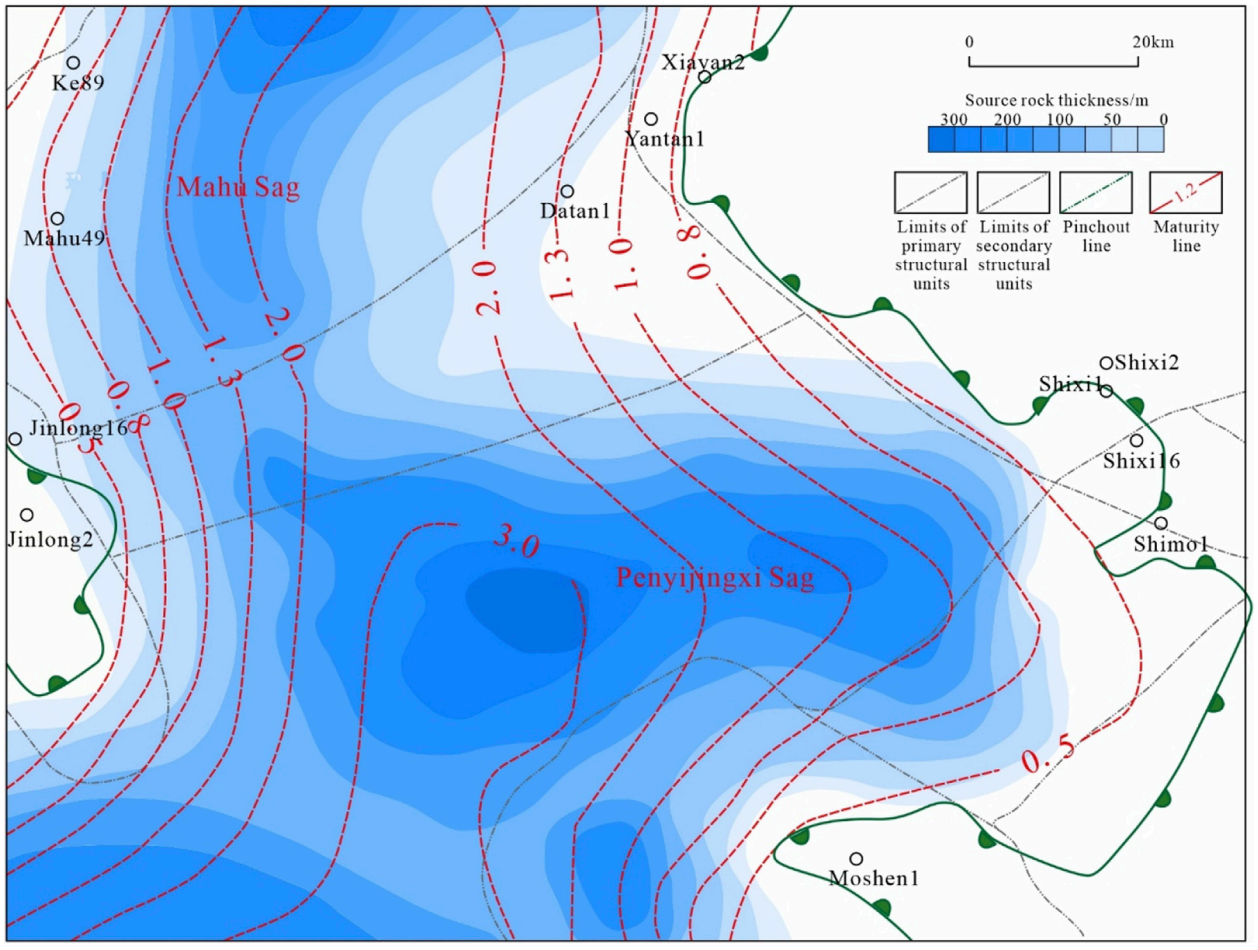

FIGURE 7
Map showing the source rock thickness and maturity in the Fengcheng Formation in the Penyijingxi Sag.

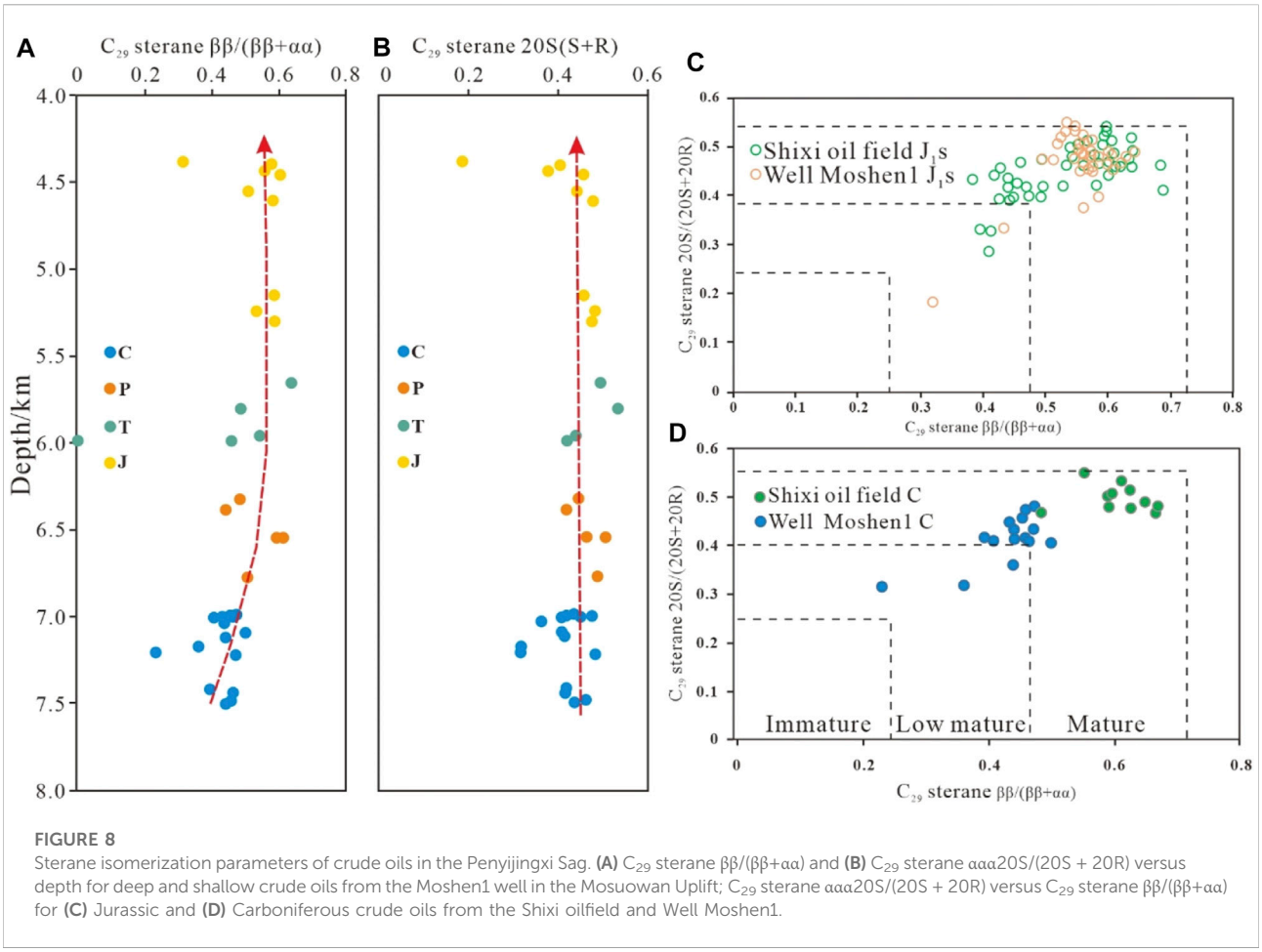

FIGURE 8
Sterane isomerization parameters of crude oils in the Penyijingxi Sag. **(A)** C_{29} sterane ββ/(ββ+αα) and **(B)** C_{29} sterane ααα20S/(20S + 20R) versus depth for deep and shallow crude oils from the Moshen1 well in the Mosuowan Uplift; C_{29} sterane ααα20S/(20S + 20R) versus C_{29} sterane ββ/(ββ+αα) for **(C)** Jurassic and **(D)** Carboniferous crude oils from the Shixi oilfield and Well Moshen1.

Penyijingxi Sag yielded high oil–gas flows from two Carboniferous intervals, which are large-scale condensate gas reservoirs. This indicates that from the margin to the center of the sag, the maturity of the crude oil increases gradually, the oil changes from light oil to condensate, and the proportion of natural gas increases. Therefore, condensate and gas reservoirs exist at depth. The density of crude oil in the Shixi 16 well is 0.80 g/cm^3 and the dryness coefficient is 0.88. The density of crude oil in the Qianshao 2 well in the sag is 0.77 g/cm^3 and the dryness coefficient is > 0.93. The gas/oil ratio increases gradually from the uplift area to the sag. As such, the oil–gas in the deep part of the paleo-uplift were affected by the distribution of source rocks and their maturity (Figure 7). In the central area, deep gas reservoirs are more likely to occur due to the high maturity of the source rocks.

4.2 Source–reservoir rocks linked by faults

A comparison of the C_{29} sterane isomerization parameters for deep and shallow crude oils from the Moshen 1 well in the Mosuowan Uplift (Figure 8) shows that the C_{29} sterane ααα20S/(20S + 20R) ratios of the deep and shallow crude oils are similar. However, the C_{29} sterane ββ/(ββ+αα) ratio decreases with increasing depth. The former parameter is mainly affected by the degree of thermal evolution, which increases with increasing thermal maturity. However, the latter is affected not only by the degree of thermal evolution but also hydrocarbon migration. During oil–gas migration, the C_{29} sterane ββ/(ββ+αα) ratio increases with migration distance. Therefore, the deep and shallow crude oils have a similar maturity and source. However, the C_{29} sterane ββ/(ββ+αα) ratio increases gradually from the deep to shallow crude oil as a result of oil migration, which was controlled by faults (Figure 9).

Based on the reservoir distribution and faults identified in previous studies, it is inferred that faults controlled the distribution of oil–gas reservoirs, leading to the formation of a belt of oil reservoirs in the northeastern Penyijingxi Sag (Figure 9A). Based on an analysis of the hydrocarbon accumulation factors in the deep reservoirs of the Shixi, Mobei, and Mosuowan oil–gas fields, the source–reservoir rocks are inferred to have been linked by faults. This linked

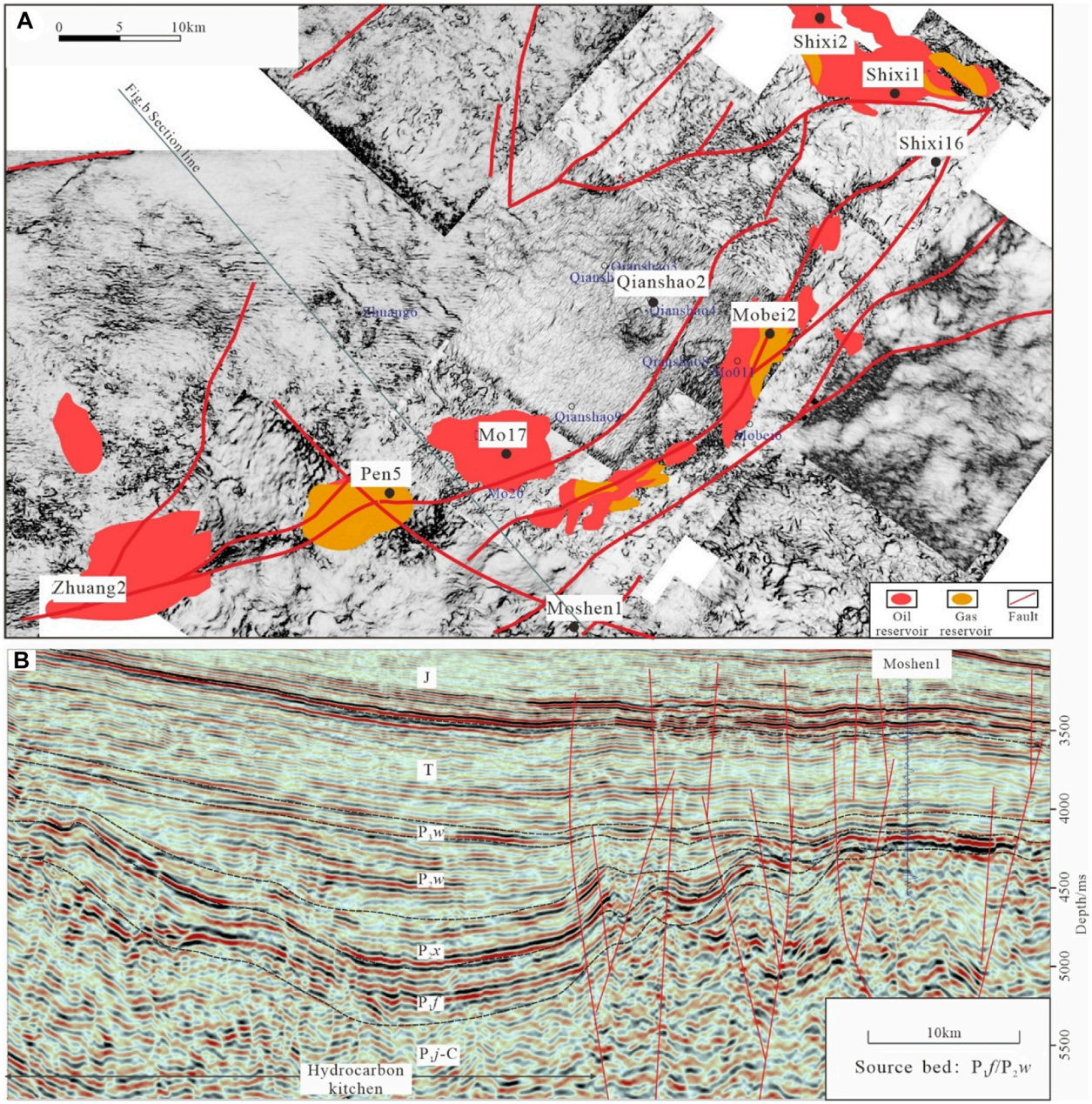

FIGURE 9
(A) Distribution of deep and large faults (basemap is the top of Carboniferous) and reservoir rocks, and an **(B)** interpreted seismic section of the source rock–fault relationships in the Penyijingxi Sag.

the source and reservoir rocks and allowed the hydrocarbons to migrate into the reservoirs. Therefore, the reservoirs formed near the source rocks. If no late oil–gas charging occurred along faults, then hydrocarbon accumulation would have been limited. Typical examples of this are the Moshen1 and Shixi 16 wells. The Moshen1 well is located 28 km from the main hydrocarbon source rocks (Figure 9B), and the grains containing oil inclusions (GOI) value of the Carboniferous reservoir in the Moshen1 well are as high as 20%. This indicates that large-scale oil–gas accumulation has occurred. During the Yanshanian orogeny, which occurred after reservoir formation, the oil–gas at depth migrated to shallower levels along faults. Oil–source rock correlations and the timing of hydrocarbon accumulation indicate the crude oil in the Moshen 1 well was derived from the overlying Fengcheng Formation source rocks. There was only one stage of oil–gas charging, and oil–gas at depth were later

modified (Wang et al., 2011). This might explain why the Moshen 1 well is not productive.

The Shixi Uplift underwent multiple stages of oil–gas charging from a variety of source rocks. The early oil–gas that accumulated in the Carboniferous reservoirs were also modified by the Yanshanian orogeny. High-mature oil–gas from the Lower Wuerhe Formation also charged and accumulated in the Carboniferous reservoirs. The maturity of the Carboniferous crude oil in the Shixi Uplift is much higher than that in the Mosuowan Uplift (i.e., the Moshen1 well). The residual Carboniferous oil–gas in the Moshen 1 well were low-mature in the early stages of charging and there was no later charging of high-mature oil–gas. Late-stage hydrocarbon accumulation involved near-source charging of mature and high-mature hydrocarbons.

4.3 Reservoir–cap rock relationships

The deep Carboniferous strata contain mainly volcanic rock reservoirs, which are less affected by compaction as compared with clastic and dolomitic reservoirs. The widely developed unconformity at the top of these strata, which formed by meteoric water leaching, improved the reservoir properties (Yao et al., 2011; Lei et al., 2013; He et al., 2017; Jin et al., 2018; Ablimiti et al., 2019). Porosity and permeability data show that the volcanic reservoirs at the top of the Carboniferous strata have the best physical properties, and the properties degrade strongly with increasing depth. The hydrocarbon reservoirs with porosity of >10% and permeability of >0.1 mD are located at a depth that is within 150 m of the unconformity at the top of the Carboniferous strata. The physical properties of the weathering crust on the volcanic rocks has affected the oil–gas distribution. A statistical analysis shows that oil production in different test intervals is positively correlated with the reservoir physical properties. For example, the daily oil production of the Shixi 2 and Shi00 5 wells is 19.49 and 31.89 t, respectively, whereas the daily oil production of the Xiayan 2 well is 11.36 t. The reservoir properties of the Shixi2 and Shi005 wells are much better than those of the Xiayan 2 well. In summary, reservoirs consisting of volcanic rocks with a weathering horizon were favorable for deep oil–gas enrichment in the Penyijingxi Sag of Central Depression, and good reservoir quality is essential for high production levels of oil–gas.

Most of the deep oil–gas reservoirs have experienced multi-stage tectonism, and contain light oil–gas. The cap rocks and extent of reservoir preservation controlled the deep oil–gas accumulation. A statistical analysis and comparison of the lithologies, physical properties, and thicknesses of the overlying cap rocks of discovered oil–gas reservoirs and unproductive wells in the western Central Depression shows that the overlying cap rocks of the high-yielding oil–gas reservoirs are thick mudstone. Most of the unproductive wells do not have mudstone cap rocks, and their reservoirs are directly overlain by sandstone, conglomerate, and volcanic rocks. These latter cap rocks have a poor sealing ability, and thus the oil–gas was not preserved in the reservoirs. For the Xiayan 2 well in the Xiayan Uplift, the two Carboniferous test intervals yielded 11.4 and 12.7 t/day of oil, and the Carboniferous reservoirs are directly overlain by 60 m of mudstone and marl of the Fengcheng Formation. The mudstone cap rocks of the Fengcheng Formation and Carboniferous volcanic reservoir rocks form a good reservoir–cap rock assemblage. The four Carboniferous test intervals in the Shixi 1 well yielded 82.9, 67.4, 41.5, and 16.8 t/day of oil. The cap rock of the volcanic reservoir in this well comprises 112 m of mudstone of the Karamay Formation.

In summary, deep reservoir formation and the reservoir types were controlled by the thermal evolution of the source rocks, which generated oil–gas. In addition, source–reservoir linkages and vertical hydrocarbon migration through faults were important for efficient hydrocarbon accumulation in the Carboniferous reservoirs. A comparison of the Shixi oilfield, Shixi 16 gas reservoir, Shimo1 gas field, Pan 5 gas field, and Moshen 1 well confirmed that the migration distance between the source rocks and hydrocarbon traps also affected the accumulation of high-mature oil–gas, due to differences in the accumulation process and multi-stage charging.

5 Hydrocarbon migration and accumulation patterns

5.1 Analog modeling of reservoir formation

Based on the above analysis of the factors controlling hydrocarbon accumulation and the example of the Shixi Uplift, analog modeling of deep oil–gas migration and accumulation were undertaken to investigate the formation of deep oil- and gas-bearing reservoirs. The experiments were conducted at the PetroChina Research Institute of Petroleum Exploration and Development—Northwest Branches. These experiments are the basis for the establishment of a deep hydrocarbon accumulation model.

Using the Penyijingxi Sag and northeastern Shixi and Mobei uplifts as examples, analog modeling of hydrocarbon injection and accumulation was designed at scale of 1:10000 based on the actual structural geology (Figures 10A,B). The oil–gas injection point corresponds to the Penyijingxi Sag; the F1 oil–gas migration pathway corresponds to the Shixi Fault; the F2 oil–gas migration pathway corresponds to the Mobei Fault; the No. 1 volcanic rock body represents the Shixi oil field; the No. 2 volcanic rock body represents the oil–gas reservoir in the Shixi 16 well; and the No. 3 volcanic rock body represents the uncharged trap in the Shimo1 well. In the sandbox model,

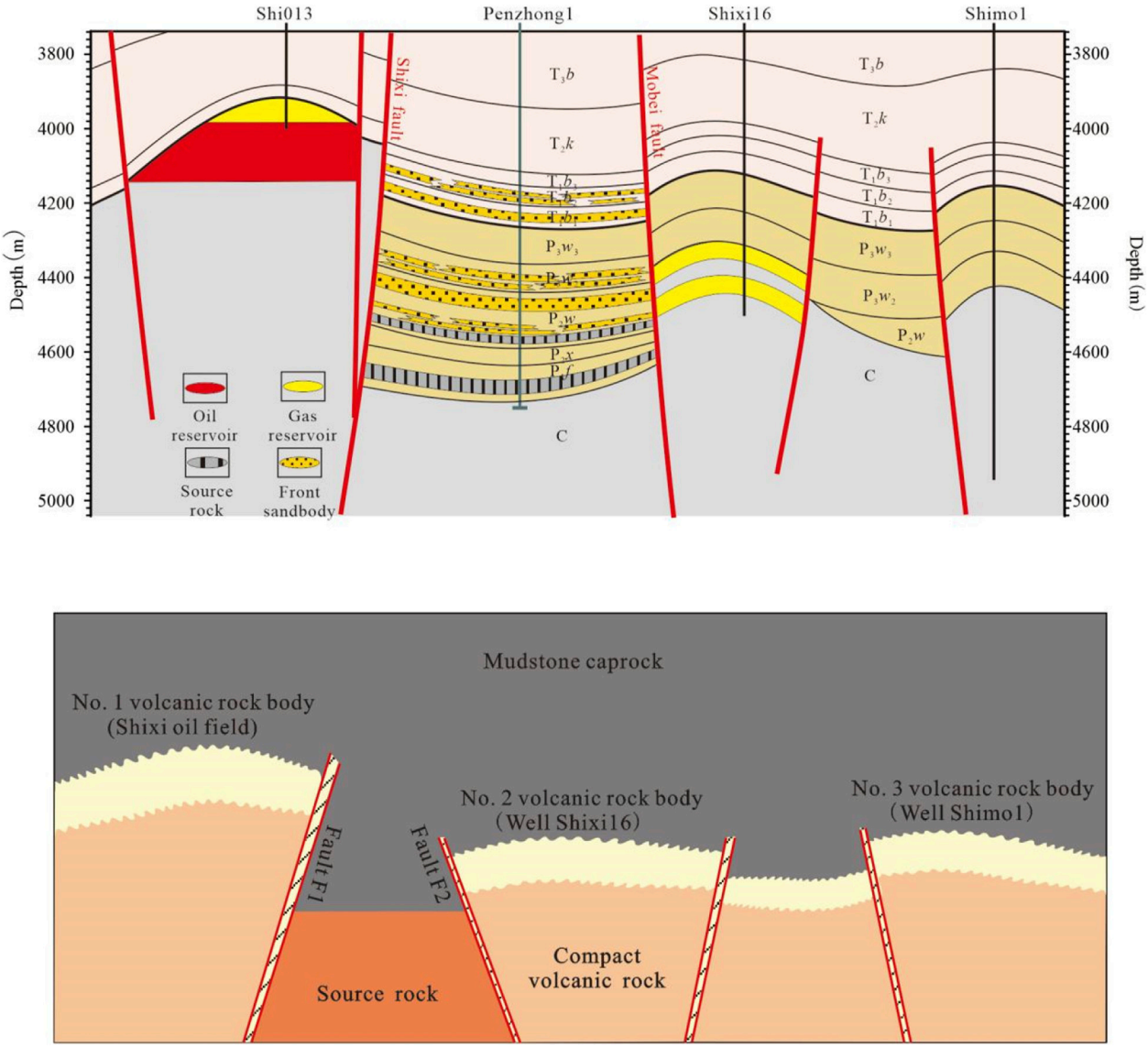

FIGURE 10
Geological model of oil–gas migration and accumulation.

400 mesh glass beads were used to represent the Carboniferous weathering crust reservoir and fault channels (particle size of 0.038 mm and 15% porosity); silica powder was used to represent the cap rocks; and brown corundum powder was used to represent the overlying strata. The initial experimental model was saturated with $CaCl_2$ with a salinity of 21,303.6 mg/L, similar to the formation waters in the Shixi 16 well. The sandbox model was left to settle for 12 h, and then oil injection was carried out. The white oil was stained with Sudan red. The oil density was 824 kg/cm^3, oil viscosity was 6.266 mPa s, oil surface tension was 27.8 mN/m, oil injection rate was 2.0 ml/min, and oil injection duration was 5 h. Subsequent gas injection (i.e., air) began after 5 h at a rate of 2.0 ml/min. The process of oil–gas migration and accumulation were recorded by taking photographic images during the experiment.

Oil and gas accumulation in the Shixi Uplift involved early oil charging and late high-mature natural gas charging. Therefore, the analog modeling of oil–gas migration and accumulation were conducted in two stages. At the beginning of the experiments, the sandbox reservoir was saturated with formation waters and the source channel was saturated with crude oil, which was charged at a constant rate of 2.0 ml/min. After 50 min, the oil migrated upwards along the F1 and F2 faults. After 100 min, the F1 and F2 faults were filled with oil, and crude oil began to accumulate in

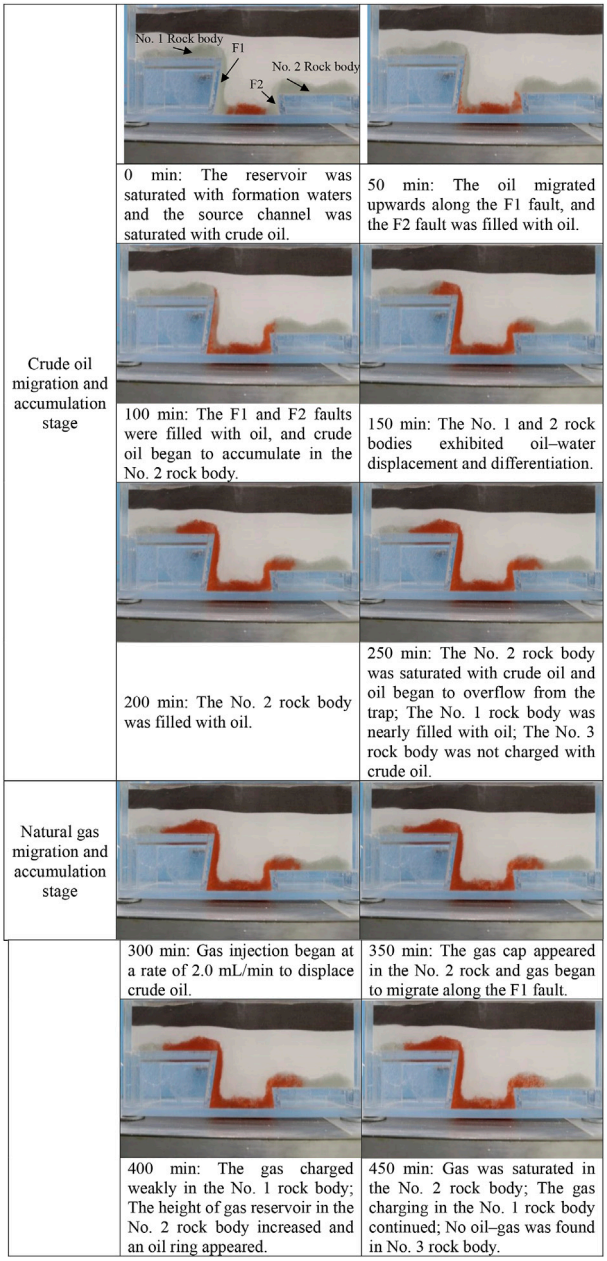

FIGURE 11
Analog modeling of deep petroleum migration and accumulation.

the No. 2 rock body. After 150 min, the F1 fault gradually became saturated with crude oil, and the No. 1 rock body began to charge. The No. 1 and 2 rock bodies exhibited oil–water displacement and differentiation, with crude oil preferentially migrating along the bottom of the trap. After 200 min, the No. 2 rock body was filled with oil. After 250 min, the No. 2 rock body was saturated with crude oil and oil began to overflow from the trap, and the No. 1 rock body was nearly filled with oil. The No. 3 rock body was not charged with crude oil during the entire process (Figure 11). The gas injection began at 300 min. The gas migration rate was much higher than that of the crude oil, and gas migrated rapidly along the top of the reservoir and hanging wall of the fault. After 350 min, the color of the upper part of the F1 fault and entire F2 fault became lighter due to gas filling. In addition, the color at the top of the No. 2 rock became lighter, but gas was not saturated in the rock body. After 400 min, the color of the No. 2 rock body became lighter, the degree of gas filling increased, the gas–oil interface migrated downward, the height of the gas column increased, and an oil ring formed. The color of the No. 1 rock body began to become lighter. After 450 min, the color of the No. 2 rock body stabilized and gas was saturated in the rock body. The gas charging in the No. 1 rock body continued, but the gas migration efficiency and saturation of the trap were low. With further gas filling, the model changed little and became stable, and the experiment was stopped.

The analog modeling of oil–gas migration and accumulation exhibited some similarities and differences with observations in the Shixi Uplift. Vertical migration of crude oil occurred along the faults in the model, but lateral migration was limited. The migration efficiency of the natural gas was high, and involved rapid and unidirectional diffusion. The migration of the deep oil and natural gas showed characteristics of near-source accumulation. After early oil has accumulated and formed charged reservoirs, late natural gas charging can drive oil migration if the cap rock is effective. This gradually transforms the oil reservoir into a gas reservoir. In general, deep oil–gas accumulation produced large-scale oil reservoirs in higher traps, which are underlain by oil–gas reservoirs. Large-scale gas reservoirs occur at depth, close to the source rocks.

5.2 Model of hydrocarbon accumulation and implications for exploration

Based on the factors that controlled hydrocarbon accumulation and the analog modeling of migration and accumulation, the paleo-uplifted regions around the Penyijingxi Sag are inferred to have been favorable sites for hydrocarbon accumulation. We propose a model of deep reservoir formation for the western Central Depression. Most of the deep oil–gas migrated laterally and converged in the paleo-uplifts, which may have moved upward due to tectonism. The preservation conditions of the early oil–gas reservoirs and whether there was large-scale, late oil–gas charging were key factors for the deep accumulation of oil–gas. Based on differences of source-reservoir relationship in the different structural belts, Carboniferous oil–gas accumulation in the Penyijingxi Sag and adjacent strata can be divided into two types.

The first type involves the source and reservoir rocks being connected over a long distance by faults, in which the source rocks have a large hydrocarbon window. Typical examples of this

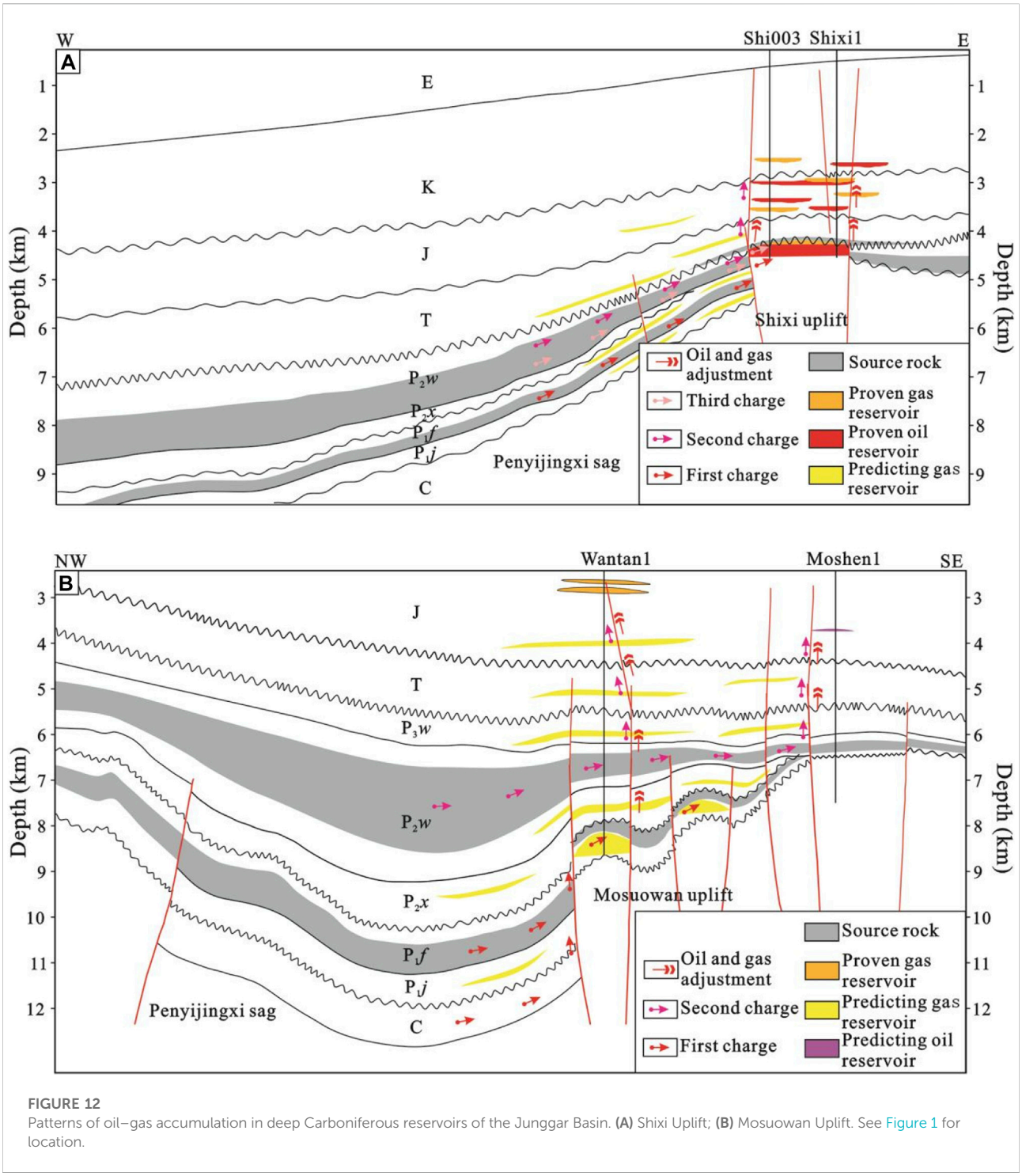

FIGURE 12
Patterns of oil–gas accumulation in deep Carboniferous reservoirs of the Junggar Basin. **(A)** Shixi Uplift; **(B)** Mosuowan Uplift. See Figure 1 for location.

are the Mosuowan, Mobei, and Shixi uplifts, which are connected to hydrocarbon generation sags by large faults. These faults directly link Carboniferous reservoir and Permian source rocks, which was favorable for hydrocarbon accumulation. The hydrocarbon window of the Carboniferous reservoir and Fengcheng Formation source rocks in the Shixi Uplift encompasses 700 m, and that of the lower Wuerhe Formation source rocks is 500 m. The oil–gas generated by these two sets of source rocks migrated and accumulated in Carboniferous volcanic reservoirs. The large hydrocarbon windows in the Mosuowan and western Mobei uplifts are also similar to this type (Figure 12A). For this type of accumulation, the

hydrocarbon window of the source rocks is large and the hydrocarbon charging is strong. After the early oil–gas was dispersed, later oil–gas charging occurred again. The Shixi oilfield reservoir in the Shixi Uplift is a typical example of a late-charging reservoir. The reservoir and source rocks on the western side of the Mosuowan Uplift show a much better lateral alignment than those in the Moshun 1 well.

The second type is where a paleo-uplift is bounded by hydrocarbon-generating sags. For example, the Dabasong Uplift is located between two hydrocarbon-rich sags (i.e., the Mahu and Penyijingxi sags; Figure 12B). Large faults that controlled the structural development occur on both sides of the uplift, and the reservoirs are laterally connected to the Carboniferous source rocks (i.e., the Jiamuhe, Fengcheng, and Lower Wuerhe formations). Large-scale oil–gas reservoirs formed due to the long-term presence and high abundance of oil–gas. In this type of accumulation, hydrocarbons are supplied to the paleo-uplift from two sides, and earlier charged hydrocarbons may have been displaced upwards and dissipated due to the effects of the Hercynian orogeny. Subsequently, hydrocarbon charging occurred again, cap rocks formed, and the oil–gas preservation conditions were good.

There are five paleo-uplifts developed around the Penyijingxi Sag, which are the Zhongguai, Mosuowan, Mobei, Shixi, and Dabasong uplifts. The Carboniferous source rocks in the nose-salient and depression area are connected over a wide area. The hydrocarbon source rocks in the depression areas generated oil–gas, and these areas were intersected by deep faults and surrounded by paleo-uplifts. This situation was favorable for lateral, near-source hydrocarbon accumulation. High-resolution seismic data indicate a favorable exploration area of nearly 700 km^2 over six anticlinal structures. At present, these targets have not all been explored, except for the Shixi uplift and Shixi 16 well. In addition to the advantage of near-source accumulation and direct linkage *via* deep and large faults, the Permian and Carboniferous source rocks in the Penyijingxi Sag have entered the large-scale gas generation stage. Based on the thermal and hydrocarbon generation history of source rocks in the Fengcheng Formation, the gas generation at depths of >6,500 m might be as high as 20×10^8 m^3/km^2. The source rocks in the Lower Wuerhe Formation are mainly a humic type, with a lower maturity than the Fengcheng Formation and a greater capacity for gas generation. The early low-mature to mature crude oil and middle–late high-maturity light oil–gas were continuously charged into the Carboniferous paleo-nose salient to form light condensate reservoirs. Due to rapid burial in the Jurassic, anomalously high pressure exists in pre-Jurassic strata in the Penyijingxi Sag, which makes the Carboniferous oil–gas reservoirs highly productive and facilitates effective development. In 2021, the Shixi 161H horizontal well was drilled around the Shixi 16 well. The horizontal section of the well runs along the reservoir at the top of the Carboniferous strata. The horizontal section is 500 m long and, after fracturing, the daily oil–gas production is 2000 t. This indicates that the Carboniferous structures are important exploration targets, despite their great burial depth.

6 Conclusion

The crude oil in the deep Carboniferous reservoirs of the Junggar Basin is mainly light–medium oil, and the natural gas is wet. The hydrocarbons were derived from Permian and Carboniferous source rocks. The source rocks and their thermal evolution controlled deep hydrocarbon accumulation, and source–reservoir rock linkages *via* faults allowed vertical hydrocarbon migration and multiple stages of hydrocarbon charging. Good reservoir-cap rock assemblages were important for the preservation of the deep oil–gas reservoirs. The deep Carboniferous paleo-uplifts in the Central Depression of the Junggar Basin were favorable sites for oil–gas accumulation.

The preservation conditions of the early oil–gas reservoirs and whether later, large-scale oil–gas charging occurred were key factors for the deep oil–gas accumulation. The Junggar Basin contains two types of deep reservoir: those linked to source rocks by large-scale faults and those in paleo-uplifts surrounded by oil-generating depressions. Potential exploration targets are the Mosuowan, Shixi, and Dabasong uplifts, although these are high risk.

Data availability statement

The original contributions presented in the study are included in the article/supplementary material, further inquiries can be directed to the corresponding author.

Author contributions

YA: Writing—original draft, Data curation, and Formal analysis. WH: Methodology, and Data curation. NL: Resources. DM: Methodology, and Resources. HL: Visualization, and Investigation. BB: Resources. XD: Methodology, and Data curation. MJ: Resources. JW: Resources. JC: Writing—review and; editing, Conceptualization, Data curation, Funding acquisition, and Supervision.

Acknowledgments

We thank editors and reviewers for insightful comments in improving the manuscript. This work was funded by PetroChina Science and Technology Major Project (Grant Nos. 2019E-2602 and 2021DJ0108).

Conflict of interest

YA, WH, NL, HL, BB, MJ, and JW was empolyed by PetroChina Xinjiang Oilfield Company.

The remaining authors declare that the research was conducted in the absence of any commercial or financial relationships that could be construed as a potential conflict of interest.

Publisher's note

All claims expressed in this article are solely those of the authors and do not necessarily represent those of their affiliated organizations, or those of the publisher, the editors and the reviewers. Any product that may be evaluated in this article, or claim that may be made by its manufacturer, is not guaranteed or endorsed by the publisher.

References

Ablimiti, Y. M., Zha, M., Yang, F., Yin, H., Ding, X. J., and Bian, B. L. (2019). Carboniferous igneous reservoir distribution and its controlling factors in Mahu-Dabasong Area, Junggar Basin. *Xinjiang Pet. Geol.* 40, 564–569. doi:10.7657/XJPG20190509

Allen, M. B., and Vincent, S. J. (1997). Fault reactivation in the junggar region, northwest China: The role of basement structures during mesozoic-cenozoic compression. *J. Geol. Soc. Lond.* 154, 151–155. doi:10.1144/gsjgs.154.1.0151

Cao, J., Hu, W. X., Yao, S. P., Zhang, Y. J., Wang, X. L., Zhang, Y. Q., et al. (2007). Carbon, oxygen and strontium isotope composition of calcite veins in the carboniferous to Permian source sequences of the Junggar Basin: Implications on petroleum fluid migration. *Acta Sedimentol. Sin.* 25, 722–729.

Cao, J., Xia, L., Wang, T., Zhi, D., Tang, Y., and Li, W. (2020). An alkaline lake in the late paleozoic ice age (lpia): A review and new insights into paleoenvironment and petroleum geology. *Earth-Science Rev.* 202, 103091. doi:10.1016/j.earscirev.2020.103091

Chen, F. J., Wang, X. W., and Wang, X. W. (2005). Prototype and tectonic evolution of the Junggar Basin, northwestern China. *Earth Sci. Front.* 12, 77–89. doi:10.3321/j.issn:1005-2321.2005.03.010

Chen, J. P., Wang, X. L., Deng, C. P., Liang, D. G., Zhang, Y. Q., Zhao, Z., et al. (2016). Geochemical features of source rocks and crude oil in the Junggar Basin, Northwest China. *Acta Geol. Sin.* 90, 37–67. doi:10.3969/j.issn.0001-5717.2016.01.003

Chen, X., Lu, H. F., Shu, L. S., Wang, H. M., and Zhang, G. Q. (2002). Study on tectonic evolution of Junggar basin. *Geol. J. China Univ.* 8, 257–267. doi:10.3969/j.issn.1006-7493.2002.03.003

Dai, J. X. (1993). Carbon and hydrogen isotope characteristics of natural gas and identification of different types of natural gas. *Nat. Gas. Geosci.* 4, 1–40.

Du, J. H., Zhi, D. M., Li, J. Z., Yang, D. S., Tang, Y., Qi, X. F., et al. (2019a). Major breakthrough of Well Gaotan 1 and exploration prospects of lower assemblage in southern margin of Junggar Basin, NW China. *Petroleum Explor. Dev.* 46, 216–227. doi:10.1016/s1876-3804(19)60003-0

Du, J. H., Zhi, D. M., Tang, Y., Jia, C. M., Xu, Y., and Ablimiti, Y. M. (2019b). Prospects in upper permian and strategic discovery in shawan sag, Junggar basin. *China Pet. Explor.* 24, 24–35. doi:10.3969/j.issn.1672-7703.2019.01.004

He, D. F., Chen, X. F., Kuang, J., Yuan, H., Fan, C., Tang, Y., et al. (2010b). Distribution of Carboniferous source rocks and petroleum systems in the Junggar Basin. *Petroleum Explor. Dev.* 37, 397–408. doi:10.1016/s1876-3804(10)60041-9

He, D. F., Chen, X. F., Kuang, J., Yuan, H., Wu, X. Z., Du, P., et al. (2010a). Characteristics and exploration potential of Carboniferous hydrocarbon plays in Junggar Basin. *Acta Pet. Sin.* 31, 1–11. doi:10.7623/syxb201001001

He, D. F., Zhang, L., Wu, S. T., Li, D., and Zhen, Y. (2018). Tectonic evolution stages and features of the Junggar Basin. *Oil Gas Geol.* 39, 845–861. doi:10.11743/ogg20180501

He, H. Q., Zhi, D. M., Tang, Y., Liu, C. W., Chen, H., Guo, X. G., et al. (2021). A great discovery of well kangtan 1 in Fukang sag in the Junggar basin and its significance. *China Pet. Explor.* 26, 1–11. doi:10.3969/j.issn.1672-7703.2021.02.001

He, X. Y., Liu, Y., Xu, X. L., Liu, B. X., and Zhang, S. C. (2017). Controlling factors of carboniferous volcanic reservoirs and favorable reservoir prediction in Xiquan area, Junggar Basin. *Lithol. Reserv.* 29, 42–51. doi:10.3969/j.issn.1673-8926.2017.03.006

Hu, S. Y., Wang, X. J., Cao, Z. L., Li, J. Z., Gong, D. Y., and Xu, Y. (2020). Formation conditions and exploration direction of large and medium gas reservoirs in the Junggar Basin, NW China. *Petroleum Explor. Dev.* 47, 266–279. doi:10.1016/s1876-3804(20)60045-3

Jia, C. Z., and Pang, X. Q. (2015). Research processes and main development directions of deep hydrocarbon geological theories. *Acta Pet. Sin.* 12, 1457–1469. doi:10.7623/syxb201512001

Jin, J., Wang, J., Yang, Z., Liu, J., Ji, H. C., Jia, H. B., et al. (2018). Well logging identification of Carboniferous volcanic inner buried-hill reservoirs in Ke-Bai fault zone in Junggar Basin. *Lithol. Reserv.* 30, 85–92. doi:10.12108/yxyqc.20180210

Kuang, L. C., Xue, X. K., Zou, C. N., and Hou, L. H. (2007). Oil accumulation and concentration regularity of volcanic lithostratigraphic oil reservoir: A case from upper-plate carboniferous of KA-Bai fracture zone, Junggar basin. *Petroleum Explor. Dev.* 34, 285. doi:10.3321/j.issn:1000-0747.2007.03.003

Lei, D. W., Yang, D. S., Chen, Z. H., Gu, X. P., Liu, W., and Luo, X. P. (2013). Reservoir space characteristics of carboniferous volcanic rocks in the central-east part of Junggar basin, NW China. *Xinjiang Geol.* 31, 231–235. doi:10.3969/j.issn.1000-8845.2013.03.017

Li, D., He, D. F., Santosh, M., Ma, D. L., and Tang, J. Y. (2015a). Tectonic framework of the northern Junggar basin part I: The eastern Luliang uplift and its link with the east junggar terrane. *Gondwana Res.* 27, 1089–1109. doi:10.1016/j.gr.2014.08.015

Li, D., He, D. F., Santosh, M., and Ma, D. L. (2015b). Tectonic framework of the northern Junggar Basin Part II: The island arc basin system of the Western Luliang Uplift and its link with the West Junggar terrane. *Gondwana Res.* 27, 1110–1130. doi:10.1016/j.gr.2014.08.019

Li, D., He, D. F., Tang, Y., Fan, C., and Kong, Y. H. (2012). Genesis of early carboniferous volcanic rocks of the di'nan uplift in Junggar basin: Constraints to the closure time of kalamaili ocean. *Acta Petrol. Sin.* 28, 2340–2354.

Liu, Y., Wu, K. Y., Wang, X., Liu, B., Guo, J. X., and Du, Y. N. (2017). Architecture of buried reverse fault zone in the sedimentary basin: A case study from the hong-che fault zone of the Junggar basin. *J. Struct. Geol.* 105, 1–17. doi:10.1016/j.jsg.2017.11.002

Lu, H. T., Xia, H. P., Chen, Z. H., Lai, S. X., Zhang, Y., and Mao, H. B. (2013). Stratigraphic division, correlation and distribution of the Carboniferous system in the Junggar Basin. *J. Stratigr.* 37, 353–360.

Ma, Y. S., Cai, X. Y., and Zhao, P. R. (2018). China's shale gas exploration and development: Understanding and practice. *Petroleum Explor. Dev.* 45, 589–603. doi:10.1016/s1876-3804(18)30065-x

Pang, X. Q., Jia, C. Z., and Wang, W. Y. (2015). Petroleum geology features and research developments of hydrocarbon accumulation in deep petroliferous basins. *Pet. Sci.* 12, 1–53. doi:10.1007/s12182-015-0014-0

Tang, Y., Cao, J., He, W. J., Guo, X. G., Zhao, K. B., and Li, W. W. (2021). Discovery of shale oil in alkaline lacustrine basins: The late paleozoic Fengcheng Formation, Mahu sag, Junggar basin, China. *Petroleum Sci.* 18, 1281–1293. doi:10.1016/j.petsci.2021.04.001

Wang, B., Wu, M., Wang, X. L., Zhang, Y. Q., and Cao, J. (2011). Source rock features and evaluation of Triassic strata in the central Junggar basin. *J. Southwest Petroleum Univ.* 33, 12–20. doi:10.3863/j.issn.1674-5086.2011.02.002

Wang, X. L., Zha, M., Xia, H. P., Chen, Z. H., Kong, Y. H., and Jiang, R. F. (2012). Forecast and assessment of oil and gas resources in Carboniferous, northern Xinjiang. *Adv. Earth Sci.* 27, 80–85.

Wang, X. L., Zhao, M. J., Xiang, B. L., Da, J., Jiang, Y. Q., and Liu, C. M. (2010). Carboniferous source rocks in the Ludong-Wucaiwan area, Junggar basin, NW China. *Petroleum Explor. Dev.* 37, 523–530. doi:10.1016/s1876-3804(10)60052-3

Wang, Y. J., Jia, D., Pan, J. G., Wei, D. T., Tang, Y., Wang, G. D., et al. (2018). Multiple-phase tectonic superposition and reworking in the Junggar Basin of northwestern China-Implications for deep-seated petroleum exploration. *Am. Assoc. Pet. Geol. Bull.* 102, 1489–1521. doi:10.1306/10181716518

Wu, K. Y., Zha, M., Wang, X. L., Qu, J. X., and Chen, X. (2005). Further researches on the tectonic evolution and dynamic setting of the Junggar basin. *Acta Geosci. Sin.* 26, 217–222. doi:10.3321/j.issn:1006-3021.2005.03.004

Xia, L., Cao, J., Bian, L., Hu, W., Wang, T., Zhi, D., et al. (2022). Co-evolution of paleo-environment and bio-precursors in a Permian alkaline lake, Mahu mega-oil

province, Junggar Basin: Implications for oil sources. *Sci. China Earth Sci.* 65, 462–476. doi:10.1007/s11430-021-9861-4

Xia, L., Cao, J., Lee, C., Stüeken, E. E., Zhi, D., and Love, G. D. (2020a). A new constraint on the antiquity of ancient haloalkaliphilic green algae that flourished in a ca. 300 Ma Paleozoic lake. *Geobiology* 19, 147–161. doi:10.1111/gbi.12423

Xia, L., Cao, J., Stüeken, E. E., Zhi, D., Wang, T., and Li, W. (2020b). Unsynchronized evolution of salinity and pH of a permian alkaline lake influenced by hydrothermal fluids : A multi-proxy geochemical study. *Chem. Geol.* 541, 119581. doi:10.1016/j.chemgeo.2020.119581

Yang, H. B., Xiang, B. L., Bao, H. J., and Pang, H. (2014). Hydrocarbon resources potential in carboniferous igneous inner reservoirs in Ludong Area of Junggar Basin. *Xinjiang Pet. Geol.* 35, 1–4.

Yao, W. J., Fan, C. H., Dang, Y. F., Qin, Q. R., and Zhao, L. (2011). Characteristics and main control factors of Carboniferous volcanic reservoirs of Zhongguai uplift in the northeastern margin of Junggar Basin. *J. Oil Gas Technol.* 33, 32–36. doi:10.3969/j.issn.1000-9752.2011.09.007

Zhang, D. D., Liu, W. H., Wang, X. F., Luo, H. Y., Wang, Q. T., Li, Y. N., et al. (2021). Genetic types and characteristics of deep oil and gas plays. *Oil Gas Geol.* 42, 1169–1180. doi:10.11743/ogg20210514

Zhao, M. J., Wang, X. L., Da, J., Xiang, B. L., Song, Y., and Qin, S. F. (2011). Genetic origin of natural gas and its filling history in Dinan Uplift-Wucaiwan of Junggar Basin. *Nat. Gas. Geosci.* 22, 595–601.

Zheng, M., Li, J. Z., Wu, X. Z., Wang, S. J., Guo, Q. L., Yu, J. D., et al. (2018). China's conventional and unconventional natural gas resources: Potential and exploration targets. *J. Nat. Gas Geoscience* 3, 295–309. doi:10.1016/j.jnggs.2018.11.007

Zhi, D. M., Song, Y., He, W. J., Jia, X. Y., Zou, Y., and Huang, L. L. (2019). Geological characteristics, resource potential and exploration direction of shale oil in middle-lower permian, Junggar basin. *Xinjiang Pet. Geol.* 40, 389–401. doi:10.7657/XJPG20190402

Zhi, D. M., Tang, Y., He, W. J., Guo, X. G., Zheng, M. L., and Huang, L. L. (2021). Orderly coexistence and accumulation models of conventional and unconventional hydrocarbons in lower permian Fengcheng Formation, Mahu sag, Junggar basin. *Petroleum Explor. Dev.* 48, 43–59. doi:10.1016/s1876-3804(21)60004-6

Zhu, G. Y., Li, J. F., and Zhang, Z. Y. (2021). Origin of deep oil and gas phase state diversity and evaluation of secondary geochemical intensity—A case study of marine oil and gas in tarim basin. *Earth Sci.* (In Press).

frontiers | Frontiers in Earth Science

TYPE Original Research
PUBLISHED 09 January 2023
DOI 10.3389/feart.2022.999135

OPEN ACCESS

EDITED BY
Hao Zou,
Chengdu University of Technology, China

REVIEWED BY
Ziliang Liu,
Chengdu University of Technology, China
Jian Cao,
Nanjing University, China
Youli Wan,
Key Laboratory of Sedimentary Basin and Oil and Gas Resources, China

*CORRESPONDENCE
Wenyuan He,
hewenyuan@petrochina.com.cn
Jianhua Zhong,
957576033@qq.com

SPECIALTY SECTION
This article was submitted to Economic Geology, a section of the journal Frontiers in Earth Science

RECEIVED 20 July 2022
ACCEPTED 28 September 2022
PUBLISHED 09 January 2023

CITATION
He W, Zhong J and Sun N (2023), Discovery and significance of tempestites and storm deposits in the Qingshankou Formation of the Gulong Sag, northeastern China.
Front. Earth Sci. 10:999135.
doi: 10.3389/feart.2022.999135

Discovery and significance of tempestites and storm deposits in the Qingshankou Formation of the Gulong Sag, northeastern China

Wenyuan He[1,2,3]*, Jianhua Zhong[4,5]* and Ningliang Sun[6]

[1]Daqing Oilfield Co., Ltd., PetroChina, Daqing, China, [2]Heilongjiang Provincial Key Laboratory of Shale Oil and Tight Oil Accumulation, Daqing, China, [3]China National Oil and Gas Exploration and Development Company Ltd., Beijing, China, [4]School of Geosciences, China University of Petroleum, Qingdao, Shandong, China, [5]School of Resources and Material, Northeastern University at Qinhuangdao, Qinghuangdao, Hebei, China, [6]Key Laboratory of Ministry of Education on Safe Mining of Deep Metal Mines, School of Resources and Civil Engineering, Northeastern University, Shenyang, Liaoning, China

The Qingshankou Formation in the Gulong Sag has attracted significant attention due to its rich shale oil reserves. However, several fundamental geological problems associated with shale from the Qingshankou Formation remain unresolved. The Qingshankou Formation in the Gulong Sag is a set of deep-lake and semi-deep-lake fine-grained deposits primarily composed of mudstone and shale. Recent studies have shown that tempestites and storm deposits commonly occur in the Qingshankou Formation. Fine liquefaction veins often occur at the bottom of the tempestite, indicating that storm-shaking liquefaction is expected in the swale structure. Meanwhile, the mudstone and shales primarily have a sand structure with fine grain size, indicating that the environment is exposed to an undercurrent activity, with a water flow velocity of 20–55 cm s^{-1}. Unlike previous studies, we posit that the ancient water depth was only 20–30 m or shallower. These phenomena have significance for understanding the formation environment and diagenetic process of shale in the first member of the Qingshankou Formation, which provides a reference for oil and gas exploration and development.

KEYWORDS

tempestite, storm deposit, shale oil, Qingshankou Formation, Gulong Sag

Introduction

Storm deposits and tempestites are not new concepts. Kelling and Mullin (1975) proposed the idea of storm (flow) deposits, and Aigner (1980) defined storm deposits as tempestites. Allen (1981), Dott and Bourgeois (1982), Aigner and Reineck (1982), and Aigner (1980), Aigner (1985a), Aigner (1985b) conducted systematic studies on the characteristics of tempestites, the genesis of hummocky stratification, and the vertical sequence of tempestites.

Based on a summary of the palaeogeographic distribution of storm deposition in the Paleozoic and Mesozoic, Klein and Marsaglia (1987) suggested that the hurricane zone was limited to a latitude range of 25°–45° in the western margin of the ocean. This region is characterized by the combined activities of hurricanes and winter storms. The Paleozoic storm sedimentation system shows that 70% occurred in the paleo-hurricane and winter storm belt. Next, tempestites and storm deposits were concentrated in carbonate environments. Only in the last 30 years have domestic scholars focused on tempestites and storm deposits, primarily concentrating on lacustrine tempestites (Zhang et al., 1988; Jiang et al., 1990; Chen et al., 2008; Yang et al., 2009; Zheng et al., 2010; Fang et al., 2011; Feng et al., 2011; Guo and Guo, 2011; Liu et al., 2012; Zhong et al., 2018, 2020a,b).

The presence of hummocky and swale cross-bedding is the most important marker for distinguishing tempestites from storm deposits. Hummocky cross-bedding is also known as "concave cross-bedding," a construction first discovered, described and explained by Gilbert (1899). In the 1970s, studies confirmed this phenomenon as a genesis perspective, which was thought to form *via* storm activity. Due to its shape, this is referred to as "hummocky cross-bedding." This bedding was previously called "crazy-bedding" or "truncated wave ripple lamination." Identifying knoll cross-bedding will be inaccessible if the knoll shape's presence is insufficient, at which time it must be combined with the internal structure. Various international studies have termed the weak hummocky shape, with a surface <1 cm in the very thin silt layer with a cm-scale thickness, as hummocky cross-bedding (Osamu and Takanobu, 2007). However, after observing many samples, various uncertainties have arisen in the term and concept of hummocky cross-bedding.

Tempestites and storm sediments have two types of hummocky bottoms. The first is constructive hummocky bottoms formed *via* storm sediments, characterized by hummocky bottoms and internal or hummocky cross-bedding. The second is a destructive storm eroded hummocky bottom shape, which has a domal bottom shape. However, the internal structure does not have typical bedding characteristics. This shape is unstable in the thin layer, yet shows a dome shape at the bottom and interior of the structure with the influence of a storm. This often occurs without any internal bedding structure. Hummocky bottoms formed *via* storm erosion are common in the tempestites and storm deposits from the Ordos Basin, Mentougou (Beijing), and the Qingsong Cement plant (east of Urumqi, Xinjiang) (Fang et al., 2011; Zhong et al., 2020a). Therefore, "hummocky structure" is typically preferred for describing storm-formed sedimentary structures developed *via* storm erosion without hummocky cross-bedding. The hummocks can form *via* storm deposition or storm erosion. There are also many cases in the Gulong Sag.

Storm deposits and tempestites were first discovered in marine facies. However, they have also been recently found in the lacustrine facies. Storm deposits and tempestites in lakes were first discovered in cores (Greenwood and Sherman, 1986), with several follow-up studies (Zhang et al., 1988; Jiang et al., 1990; Feng et al., 2011; Liu et al., 2012). Allen (1981) probably first discovered lake storm deposits but was unsure about them. Detecting HSC (hummocky cross-stratification) and SCS (swale cross-stratification) on a core of approximately 10 cm in diameter is difficult and requires careful observation. Greenwood and Sherman. (1986) performed observational experiments on storm deposition in the Canadian Great Lakes, characterizing the relationship between typical HCS and SCS layers and their combinations and storm flow parameters. There was also a significant storm in 2016 at Lake Erie. Every November, winds around the Great Lakes can reach 45–50 km h^{-1}, while the surface temperature remains approximately 11°C, and lake waves can reach a maximum of 25 m. However, the recent discovery of a storm on Lake Erie (passing storm) contradicts this theory. The development of storm sedimentary structures and bodies is objective, based on the characteristics of lake sediments; therefore, we confirm that the development of lake storm sediments and tempestites is indisputable.

Typical hummocky and swale structures are small in scale, ranging from tens of centimeters to 1–2 m (Allen, 1981; Dott and Bourgeois, 1982), and may be a remnant of a base eroded by a storm. Many tempestites and hummocky structures in storm deposits do not have hummocky cross-beddings. Additionally, there are two types of knoll cross-beddings: classic knoll cross-bedding with the interface of a fine layer and the knoll, and knoll cross-bedding for which the thin layer is parallel to the hillock interface. Swale cross-bedding is less developed in areas where tempestites or storm deposits are developed than hummocky cross-bedding. In theory, swale structure and hummocky cross-bedding should develop equally. However, this is not the case: hummocky cross-bedding tends to have a flat bottom between them, which differs from swale cross-bedding.

Storm deposits are helpful indicators for facies and palaeogeographic analysis (Aigner, 1980, 1985a, b; Myrow et al., 2008; Immenhauser, 2009). Additionally, tempestites are essential reservoirs for stratigraphic traps (Aigner, 1985a,b; Mohseni and Al-Aasm, 2004). Therefore, studies on tempestites and storm deposits are of great significance. Additionally, there are relatively few studies on storm deposits and tempestites at the core scale; therefore, performing research in this discipline is highly necessary and significant. This is especially the case for the cores in the study area, which can be used for three-dimensional (3-D) observations and descriptions. Therefore, based on core observations, this study discussed typical storm deposits and tempestites of the Qingshankou Formaiton in the Gulong Sag.

The Qingshankou Formation in the Songliao Basin is rich in shale oil with 15.3 billion tons reserves, a crucial replacement resource for the Daqing Oilfield. The K_2qn shale has >90% oil-

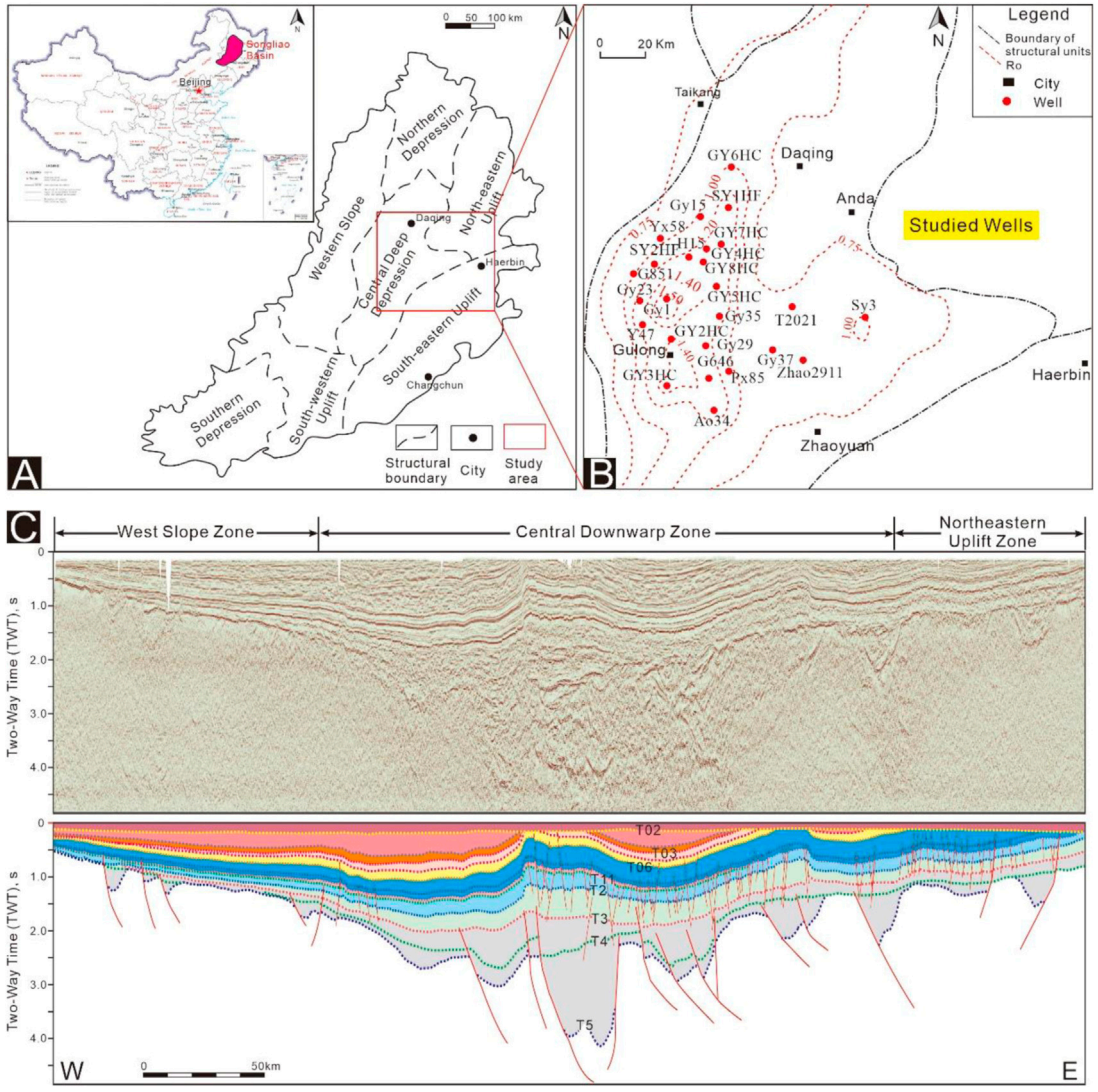

FIGURE 1
Geological background of the study area. **(A)** The structural units of the Songliao Basin. **(B)** The R_o (%) contour map of the Qingshankou Formation. **(C)** EW-trending seismic profile and its interpretation in the Songliao basin (T2–T11) are the Qingshankou Group.

source/reservoir ratio and <0.20 m single sand body thickness generally, which is a typical pure (type III) shale oil (Wang et al., 2020). Many vital advancements have been made while examining the formation, reservoirs, and shale oil in the Qingshankou Formation (Liu et al., 2012; Sun, 2020; Wang et al., 2020; He et al., 2021, 2022a,b; He, 2022). However, some basic geological problems remain unresolved, including the sedimentary environment. It is unclear whether a simple deep-lake, semi-deep-lake facies with quiet water sediments, or more complex environmental differentiation occurred, which is not similar to the other shale-oil-bearing basins in China (Xue et al., 2020; Cui et al., 2021; Liu et al., 2021, 2022; Nie et al., 2021; Tao et al., 2021; Zhi et al., 2021). This paper discusses an influential, unrecognized phenomenon known as storm deposition and tempestite. This phenomenon is significant for understanding the formation environment and diagenetic process of the K_2qn^1 shale, providing a reference for oil and gas exploration and development.

Geological setting

The discovery of mudstone oil in the Gulong Sag in the Daqing Oilfield occurred quite early. Gao (1984) first reported the fractured mudstone oil reservoir in the Gulong Sag, which was later examined by Chen et al.

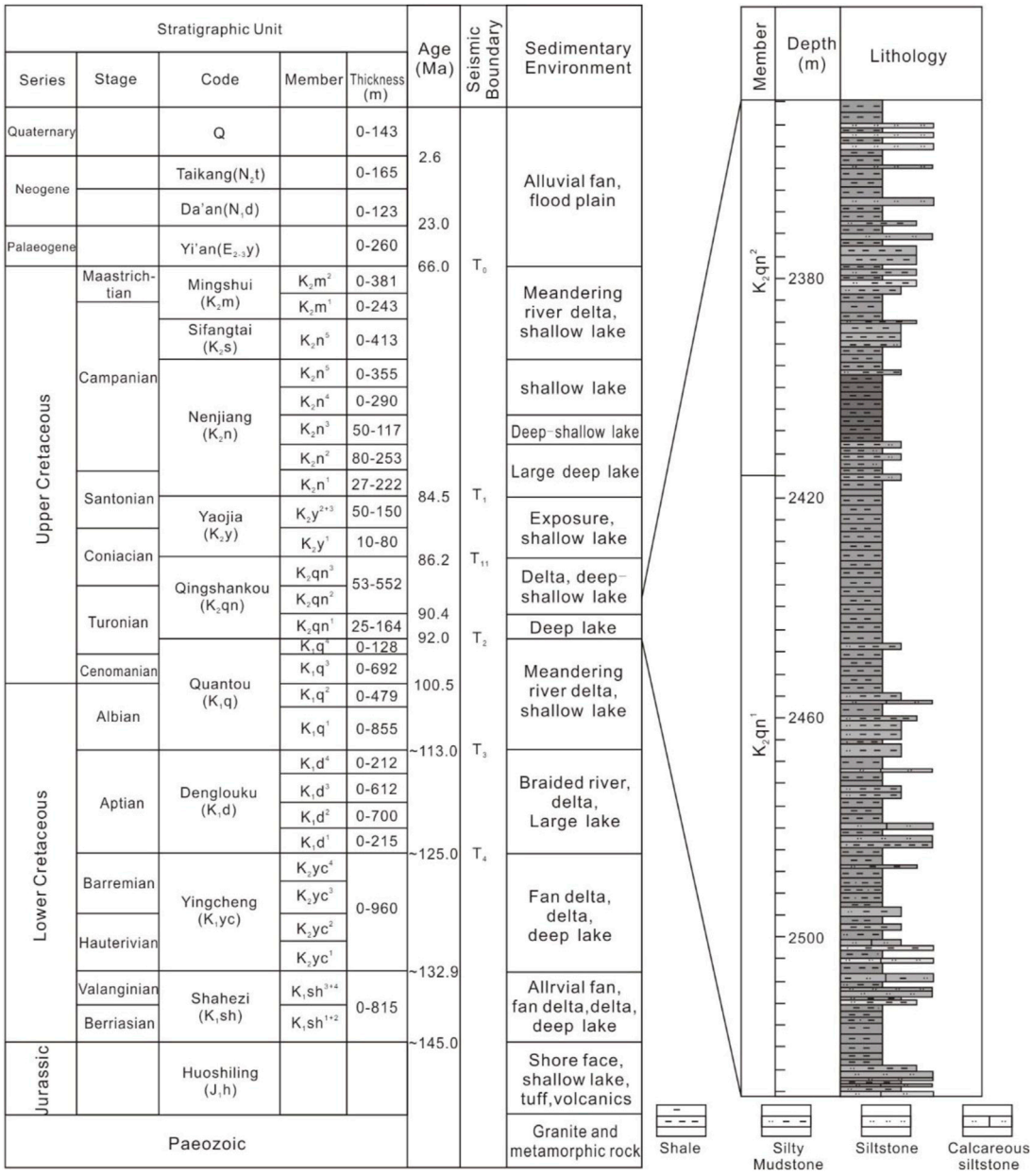

FIGURE 2
Generalized stratigraphic column of the Songliao Basin (modified from Zhao et al., 2020)

(1988), providing a prelude to the discovery, exploration, and development of shale oil in the Gulong Sag. The recently constructed Wells Songye Oil 1HF and Guye Youping one have led to breakthroughs in shale oil exploration, especially the Well Guye Youping, which has substantial strategic significance (Sun., 2020). The northern Songliao Basin, with an area of $11.95 \times 10^4\ km^2$, is a Meso–Cenozoic inland fault-swale structure superimposed basin that can be divided into five first-order tectonic units: the central swale structure, western slope, northern dip, northeast uplift, and southeast uplift areas (Figure 1).

The Songliao Basin is a Cenozoic development in the Paleozoic and a former Paleozoic metamorphic rock series with a base of large proliferous basins. Its development was a breakthrough, with a swale structure and inversion during three tectonic evolutionary stages, forming a series of stretching, squeezing, and inversion tectonics. The tectonic deformation of the geometry and kinematics characteristics substantially

influenced sedimentation. The tectonic inversion occurred at the end of the Nenjiang Formation. Consequently, the Songliao Basin changed from extensional subsidence to compressive uplift (Figure 1), resulting in the uplift and folding of the Sifangtai, Mingshui, Yi'an, Da'an, and Taikang Formations, as well as the development of four unconformities. Here the NWW–SEE compression caused the development of a series of NNE anticlines, as represented by the Changyuan and Aogula. The Qingshankou Formation (K_2qn) in the Gulong Sag, adjacent to the Aogula and Changyuan anticlines, suffered from a strong NWW–SEE lateral compression (Figure 1). A series of conjugate shear fractures and bedding slips formed by the NWW–SEE extrusion developed, yielding many bedding fractures, which significantly improved the reservoir capacity of the K_2qn shale.

We examine the influence of the tectonic movement on the deposition, diagenesis, and accumulation of the Qingshankou Formation, as well as its impact and control over the bedding shear fracture and lateral compression-conjugate fracture in the Qingshankou Formation based on previous studies. From the Quantou to the Nenjiang Formations, the Songliao Basin is dominated by swale structures; deep-water and semi-deep-water fine-grained sediments rich in organic matter, as represented in the Qingshankou and Nenjiang Formations, established a solid foundation for the formation of shale oil in the Songliao Basin.

Two significant lake transgressions occurred during the sedimentary period of the swale structure; a large area from the deep to the semi-deep lake was generated in the central area of the basin (Figure 2), forming two sets of large-scale lacustrine deposits in the Qingshankou and Nenjiang Formations. These were the basin's primary periods for source rock deposition and the primary shale oil development horizon. The Qingshankou Formation is the main shale oil development interval. Meanwhile, the first member of the Qingshankou Formation (K_2qn^1) is mainly composed of black-gray–black mud shale (Figure 2) with high organic matter content and three or four layers of shale at the bottom, representing the primary shale oil development interval.

3 Storm deposits

3.1 Characteristics of tempestites and storm deposits in the Qingshankou Formation

The primary basis for determining storm deposition is the cross-bedding on a hummocky or swale structure. However, such characteristics are absent in some storm deposits and tempestites (Zhong et al., 2018). Therefore, the identification and differentiation of storm deposits and tempestites cannot be solely based on the development of hummocky or swale cross-bedding.

Tempestites were discovered in the Songliao Basin (Liu et al., 2012) more than 1 decade ago. However, evidence regarding the cause of these deposits appears to be limited. Therefore, obtaining more reliable evidence is necessary, especially for the K_2qn black shale of the Gulong Sag with >100 m thickness. The development of the tempestite must provide sufficient evidence because the shale oil formation occurs under continuous sedimentary reduction. Storm characteristics can affect the growth or even terminate hydrocarbon source rocks. Therefore, the oil content of the K_2qn shale is negatively affected. Based on many core observations, we can conclude that the K_2qn deposits in the Gulong Sag have the following characteristics.

3.1.1 Hummocky or swale cross-bedding on the flank of a core

The cross-bedding on a hummocky or swale structure is an essential symbol for storm deposits and tempestites, often observed in the K_2qn^1, Gulong Sag (Figure 3). The fine layers in the hummocky and swale structures are thin and converge at the edge, revealing the attenuation of storm waves. The two hummocks of the cross-bedding in Figure 3 are thicker at the "ridge" and thinner at the edge, most noticeably at the region that converted to the sag cross-bedding, distinguishing them from ordinary sand wave-bedding and sand wave lenses. The hummocky structures are often easily eroded by the next storm due to the intense erosion effect of storm deposition; the top of the hummocky structures often erode, thin out, and lose their vital characteristics (Figures 3C,D). This phenomenon is even more pronounced during the storm deposition on Lingshan Island, Qingdao, Shandong Province (Zhong et al., 2020a,b).

Additionally, small core sizes can only be partially preserved, thus making it challenging to observe a perfect hummocky cross-bedding. Figure 3E shows that the entire bedding has a highly symmetrical lenticular shape, which is raised in the center and thinner and pinched on both sides while converging to a point. This reflects the inflection point from the storm's crest to the power's trough. Figure 3F shows a dome-like structure formed by storm compound flow. The lower portion is a one-way cross-bedding with a fore deposit, related to storm wave drift from right to left. The upper layer has hummocky bedding. In addition to the hummocky and depressed-shaped cross-bedding formed by storms, the fine layers are hummocky and convex on the top or depressed-shaped and concave on the bottom. The key is convergence and thinning on both sides, forming a point or line.

A hummocky or depression cross-bedding was observed in the storm deposits and rocks in the Qingshankou Formation of the Gulong Sag (Figure 4), with the following characteristics: 1) The hummocky shape is poor with an overall small size, and the height is approximately 1 cm, and width of several centimeters to >10 cm. Notably, some flat bedding strip silt layers may be

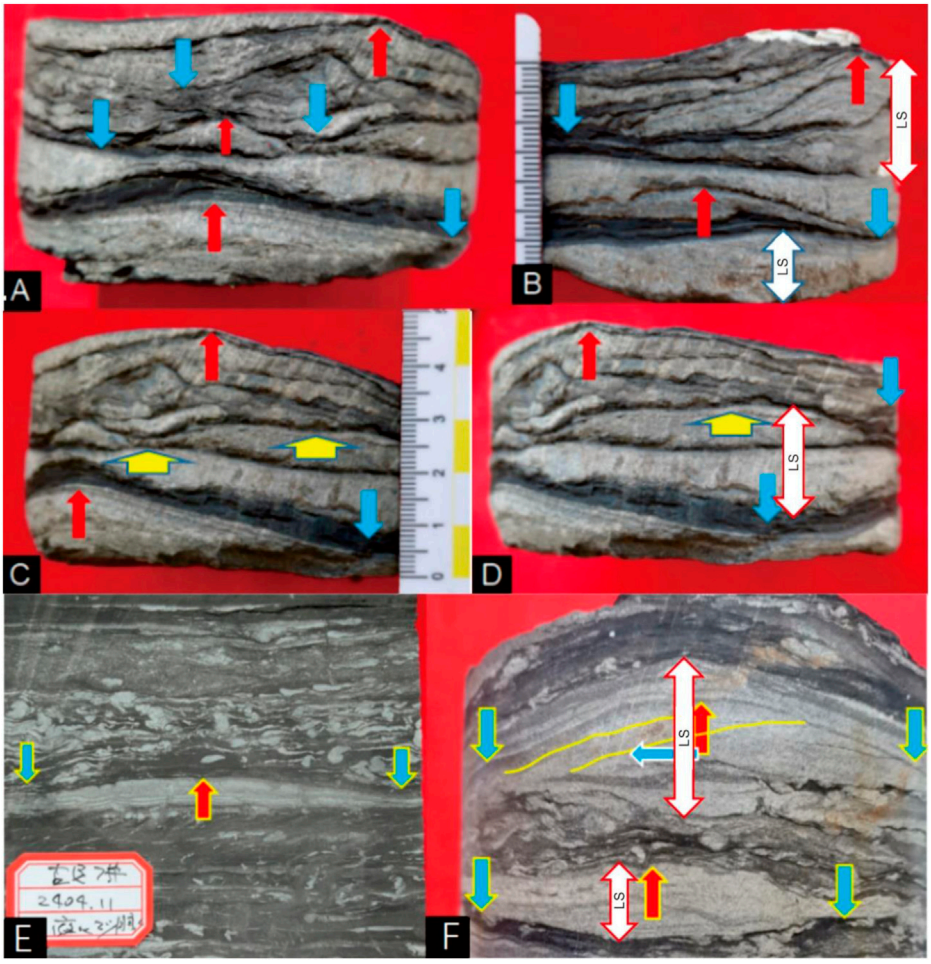

FIGURE 3
HSC and WSC structures of the K_2qn shale in the Gulong Sag (LS, lenticular structures). **(A)** Hummocky and swale structures; three hummocky structures (red arrows), with the largest and better-developed base, approximately 10 cm wide with a 2 cm high symmetry. The hummocky structure consists of gray calcareous silty sand in the lower region and black clay in the upper region. The bottom has an erosional wash surface. Hummocky cross-bedding is developed in the upper part of the thin gray siltstone layer. The swale structure (blue arrow) is slightly smaller in width at 6–7 cm and a height of 1–2 cm. **(B)** Back view of core in(A). The slope structure changes along the side, and an erosional scour surface develops. The lenticular bodies of the hummocks suddenly and thinly pinch out within a few centimeters, revealing that the hummocks are isolated lenticular structures formed over a black mud bottom. The lateral variation in the sand lenses in the swale structure is as sharp as that in the hummocky structure. A lenticular or ocular structure forms when a 180° phase difference is superimposed. **(C)** Left 45° rotation of (A) showing slight lateral changes in the hummocky and swale structures. **(D)** (A) rotated 90° to the left, showing continuous lateral changes in the hummocky and swale structures. The lower swale structures are well-formed; unlike the hummocks, they have reverse grain sequences, with black clay at the base and gray calcareous silty sand at the top. The concave base is convex, and the top is flat; the concave structure is convex and lenticular. Lenticular or ocular structures were formed when a 180° phase difference was superimposed. **(E)** Hummocky cross-bedding, highly slender, but well developed. Convergent merging on both sides, especially thinning on the right side where convergent merging is optimal. There are 56 vertical fine liquefied sand veins. **(F)** Hummocky cross-bedding. Under the influence of compound flow from right to left (solid yellow line), fore deposit cross-bedding developed. However, the symmetry of the dome was not destroyed; the dome cross-bedding enveloped the top.

larger hummocky structures, i.e., the core diameter is too small to show the overall structural characteristics. 2) Unlike hummocky or swale cross-bedding, the layers are thin and merge at the edges. Consequently, the thin layers are eroded and truncated at the top, even when pinched out (Figure 4B). 3) There is an erosional cross-section at the bottom, indicating that erosion may occur at the beginning of the storm. 4) Common hilly structures occur as inverted wide "U" and "buckled" shapes on the dark mudstone (Figures 4E,F), which do not converge to a single point but spread out and are distributed along a plane. This phenomenon is also common on Lingshan Island, Qingdao (Zhong et al., 2020a,b). In contrast, Zalmai and Schieber (2017) suggested that this structure forms *via* sliding shear. 5) Symmetrical flow forms wavy stratification without convergence (Figures 4G,H) or cross-stratification *via* unidirectional flow (Figure 4H). 6) Dark sand-grade mud is expected in the fine layers or lamina,

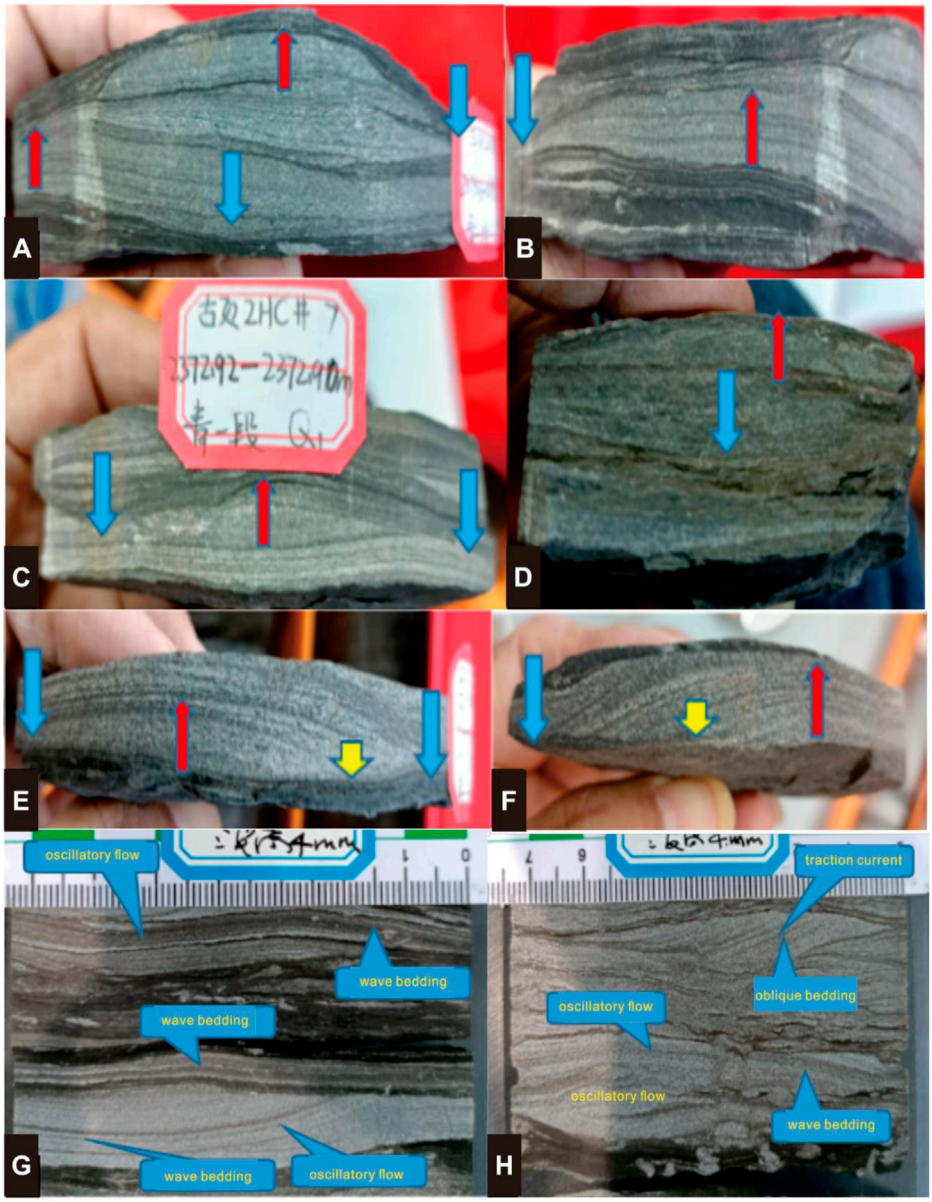

FIGURE 4
Hummocky structures and cross-bedding of the K_2qn^1 shale in the Gulong Sag. **(A)** Hummocky and swale cross-bedding. The three layers cut into each other and developed in the gray siltstone but contain half of the sand-grade mud particles, with fine storm erosion of the lake-bottom ooze. **(B)** Continuation behind the lower series in (A). Imperfect hummocky cross-bedding, which pinches out on the left, formed *via* the erosion of the upper hummocky structure. There are abundant sand-grade mud particles in the fine layer, which formed *via* erosion of the lake-bottom ooze from fine storm activity. **(C)** Hummocky and swale cross-bedding: there is abundant sand mud in the fine layer. Fine storm erosion formed the lake-bottom ooze. **(D)** The reverse side of (C). Three layers can be observed: the lower two are swale structure cross-beddings, and the upper is a hummocky cross-bedding. **(E)** Hummocky cross-bedding. The right and fine layers are suddenly in contact with the grayish-black mudstone system below (yellow arrows), formed *via* the oscillation of the storm crest over the mud deposits. The layers that are at 90° laterally in **(E)** and **(F)** show the fine layers and the abrupt contact of these layers with the lower gray mud-leaf layers (yellow arrows). There is a large amount of sand-grade mud clastic in the fine layer, i.e., >50%. **(G)** Wave-bedding and oscillating flow did not converge in the hummocky and swale cross-bedding. **(H)** Wave-bedding and oscillating flow did not converge with the hummocky and swale cross-bedding.

accounting for more than half of all particles, revealing the intense erosion, transport, and mixing of lake-bottom mud due to the storm's activity.

3.1.2 Hummocky structures at the core level

The hummocky structure and hummocky sag cross-bedding observed on the core facade cannot be easily distinguished from

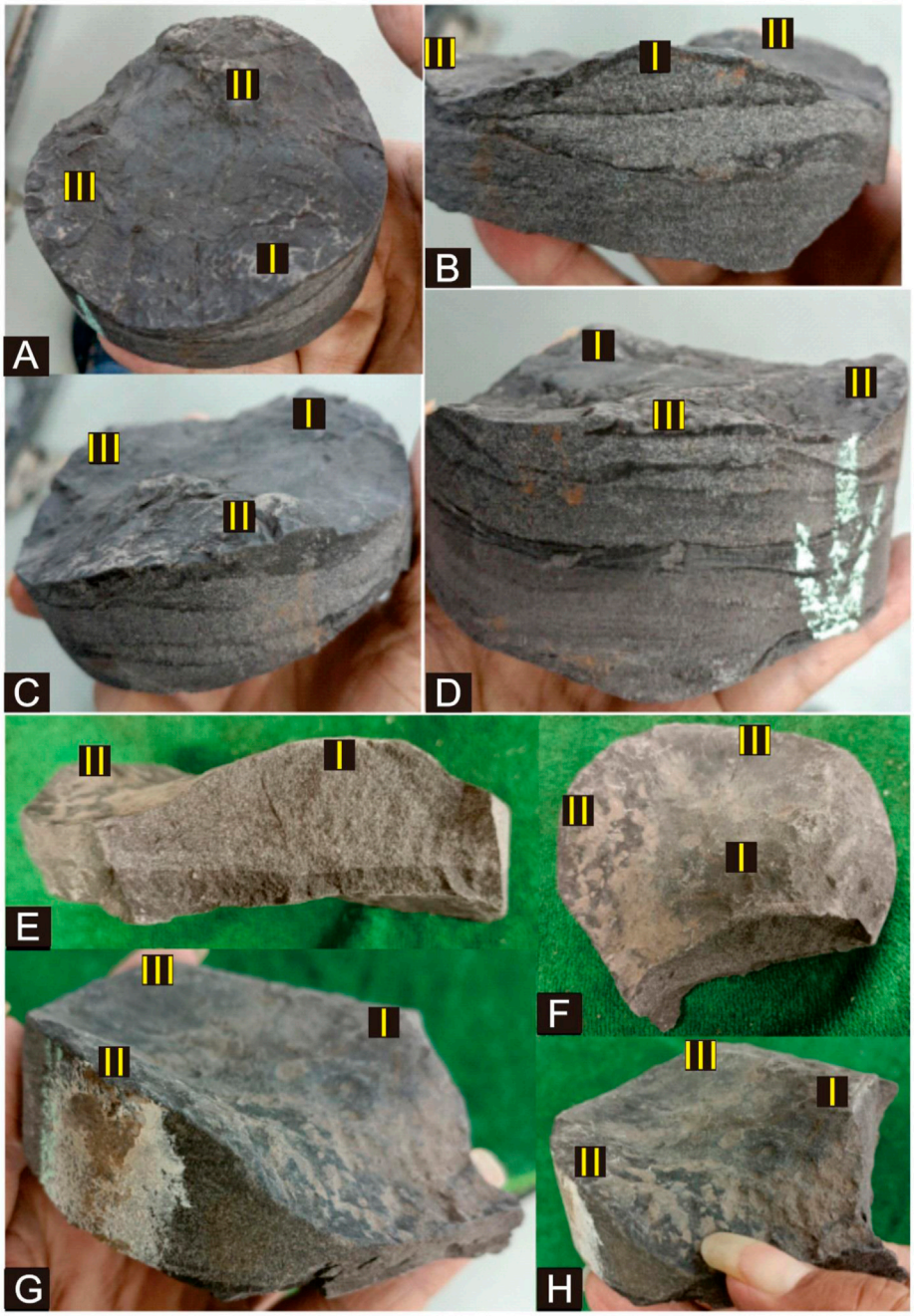

FIGURE 5
Three-dimensional hummocky structure and related structures formed *via* storm activity (LS: lenticular structures). **(A)** Three hummocky structures and their interlaying swale structures are 4–5 cm in diameter and 0.5 cm in height. **(B)** The hummocky type is notable on the side of the hummocky structure I in the *middle of* **(A)**. Sandwiched between the three hummocks is a distinct swale (blue arrow). **(C)** On the side and top of the hummocky structure II in the middle of **(A)**, the hummocky structure is notable, while the silty sand body has been pinched out and has disappeared. **(D)** On the side and top of the hummocky structure III in the middle of **(A)**, the hummocky type, which may have been eroded, is not evident and flat. **(E)** The hummocky structure is dense and massive without any cross-bedding, revealing that the silty sand at the bottom of the lake is sufficient. **(F)** The top surface of E shows a highly symmetrical small hummocky shape (~6–7 cm in diameter), not a sand wave bread shape. A distinct swale structure (blue arrow) is sandwiched between the three hummocks. **(G)** Three other hummocky structures are sandwiched by a swale structure (blue arrow). **(H)** A 90° view on the right side of **(G)** shows notable swale structures.

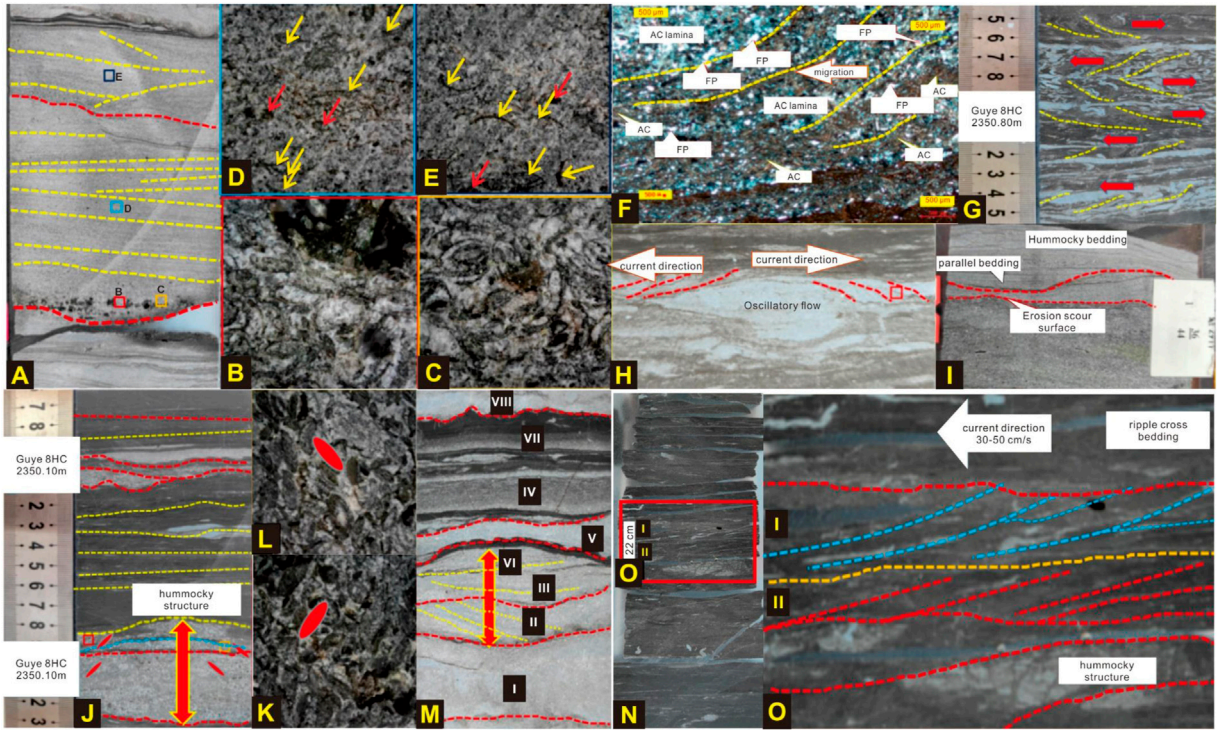

FIGURE 6
Beddings associated with a storm deposit in the K_2qn shale of Well Guye 8HC, Gulong Sag (AC: Algea-clastic; FP: Felsic particle). **(A)** Storm-calcareous siltstone, developed with an erosional surface, parallel-bedding, complex low-angle cross-bedding, fine gravel, and Ostracoda fossils. **(B,C)** Dense Ostracoda fossils in the red and yellow boxes in (A) are mostly intact. **(D)** Green box in (A) magnified ×30. Siltstones containing Ostracoda fragments (red arrows). A large amount of black silt-grade mud is also visible. **(E)** The basket in (A) magnified ×30. Siltstones containing Ostracoda fragments: some are complete (yellow arrows) and a few incomplete (red arrows). There is also a large amount of black silt-grade mud. **(F)** Bidirectional oblique bedding and oscillating flow. **(G)** Unidirectional oblique bedding, slightly increasing, reflecting rich sediments and a weak water flow capacity. **(H)** Bidirectional oblique bedding, showing the formation of inlet and backward flows. **(I)** Erosional scour surface, parallel-bedding, and hummocky bedding. **(J)** Parallel-bedding, erosion surfaces, and hummocky and swale structures formed via storm activity. Ostracods are arranged in a hedged imbricate shape on both sides of the hummocky structure. **(K,L)** The ostracods on both sides of (J) are arranged in a hedged imbricate structure with a steep dip angle between 45° and 50°, which is larger than the dip angle of the imbricate structures formed via traction flow (34°). **(M)** A complete storm sequence, decaying rapidly. The scour surface at the bottom is developed, the sequence thickness is large, and the grain size decreases sharply upward. Inclined and swale structure bedding, formed via traction flow, are developed in the middle part, reflecting the activities of compound flow. **(N)** Strom deposits **(O)** in background sediment of gray-black shale. **(O)** Strom deposits, showing hummocky cross-stratification grow upwards to uni-directional micro cross-stratification deposited by waning current flow.

the sand lens and sand wave-bedding. Therefore, the characteristics of the plane should be combined. Small hummocky and swale structures can also be observed in the plane. Unlike the sand-wave lens formed by lakeside waves, the sand-wave lens formed by storms has an equiaxed 3-D convex shape, a linear sand bar in three dimensions, and notably exhibits linear extending peaks and troughs. Only a few sand lenses occur on the core's facade, whereas three raised hummocky structures can be observed on the plane (Figure 5). Hence, these sand lenses are quasi-equiaxed hummocky structures in three dimensions, which further shows that the waves forming these dunes are equiaxed oscillatory flows formed by storms rather than ordinary linear waves. Each silty lens is separated by gray-black mudstone owing to intermittent "still water" deposits formed *via* small or stagnant waves between the storms.

An out-of-phase superposition creates complex sand formations that yield a pod-like storm sequence (Figures 4A–D). Lenticular or ocular structures can form when the difference is 180° (Figures 4B,D,F, 5B), i.e., the thickness will suddenly increase or decrease when the hummocky and swale structures of the two storm systems are superimposed. For example, between 2,408.00 and 2,408.10 m in the Well Gupage 7, the maximum thickness can reach 4.5 cm when the difference between the hummocky and swale structures is 180°, whereas the lateral thickness of 4 cm thins to 3 cm and the thickness decreases by 1.5 cm (Figure 5B). A further 90° lateral rotation shows that the thickness of the swale structure decreases sharply in the center and on both sides, from 1.5 to 4 cm laterally to 0.0 cm, while the thickness decreases by 1.5 cm (Figure 5B), yielding the pod-like swale structure. The superimposed

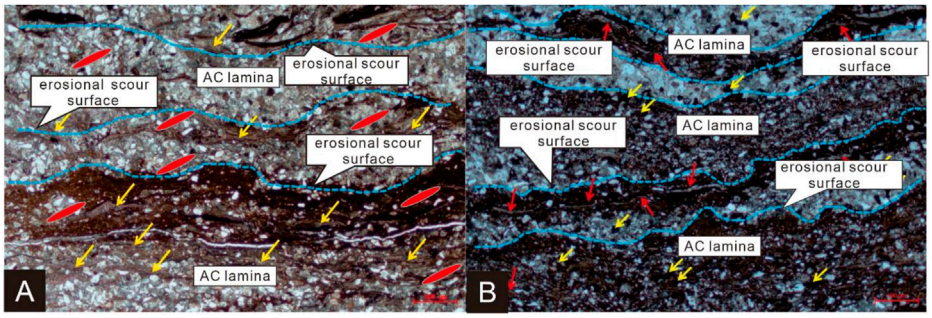

FIGURE 7
Erosional surface of an algal tempestite (dotted blue line).

relationship of the thin sand layer is highly complicated, and the thickness changes significantly since hummocky and swale structures are frequently superimposed in different phases. Moreover, the thickness, shape, and continuity of the single hummocky structure change considerably due to the storm activity's erosion and cutting. This is a piece of critical evidence that distinguishes the storm's activity from ordinary wave activity.

In addition to hummocky or swale cross-bedding, storm sediments have some associated and symbiotic bedding (Figure 6), such as parallel-bedding (Figures 4, 6A,D,J), cross-bedding with notable lateral deposition (Figure 6F), bidirectional bedding (Figures 6G,H), and sand wave bedding, among others, revealing and recording the changes in the storm flow. In summary, the stratification of storm deposits is complex, indicating complex changes in the flow direction and velocity. However, it is generally characterized by oscillating flow: fine layers dip bidirectionally in the vertical plane and multi-directionally in the 3-D plane. The storm-calcareous siltstones in Figure 6A develop erosional scour surfaces, parallel-bedding, and complex low-angle cross-bedding, revealing an intense storm wave activity, rapid underflow, and abundant silt. The erosion and scour surface has fine gravel development and contains many Ostracoda and its debris (Figures 6B,C).

3.1.3 Erosion and scouring surfaces

Erosion and scour surfaces are essential features of storm activity. These surfaces are developed in almost all areas characterized by storm activity (Zhong et al., 2020a,b). This phenomenon is expected in the Qingshankou Formation of the Gulong Sag, in which erosional and scour surfaces occur at the bottom of almost every swale structure (Figures 6A,I,J,M, 7). The interaction between the storm and wave is the base level, i.e., the original depth of more significant "standing water" fine particle deposition (clay and mud mass particles) erosion. This transports the original fine-grained sediment (Figure 7), as well as intraclasts and crumbs (including shallow algae crumbs and Ostracod debris), mixed deposits, thus forming a storm deposit at the bottom of the erosional scour surface (Figure 7). Sedimentation begins as the storm abates, forming hummocky structures and associated bedding. Erosional and scour surfaces develop at the bottom of each storm sequence and are often uneven (Figures 6A,I,J,M, 7), so the sediment size is coarser, and felsic and algal debris are more common (Figure 7). Silt is also the primary component.

3.4 AC represents Algea-clastic

3.1.4 Storm deposition sequence, grain sequence, and grain arrangement

Storm activity is a concept characterized by specific time and space constraints. Specifically, the storm activity in a lake has a process of occurrence and extinction. This process forms *via* a combination of several sub-storm deposits: each sub-storm deposit is a tiny stage of a significant storm deposit. High-energy erosion is dominated at the bottom, and storm deposits begin to form on the erosional and scouring surface. Coarser particles are deposited first due to the corresponding storm's high energy. Fine gravel with a diameter of 2–3 mm can sometimes be observed in the Gulong Sag (Figure 6A). Moreover, we can occasionally observe 1–2 cm diameter or large boulders ranging from 1 to >10 cm in diameter. The sediment size gradually becomes smaller as the storm weakens, transforming into black or gray-black fine grain deposits at the top (Figures 6M, 7, and 8). In the storm deposits of the Qingshankou Formation, each storm sequence is composed of multiple to several centimeter-level normal cycles (Figure 7). A complete storm deposit generally has 7–9 cycles. Each sequence is usually 1–2 cm thick, with the largest reaching 3–5 cm or >10 cm. Many storm-deposited calcareous silty layers are thin lamellar beds rather than lenticular (Figures 9E,F). Most liquefied sand veins are developed at the bottom, indicating that they are storm deposits resulting from wave oscillation (Figure 9F).

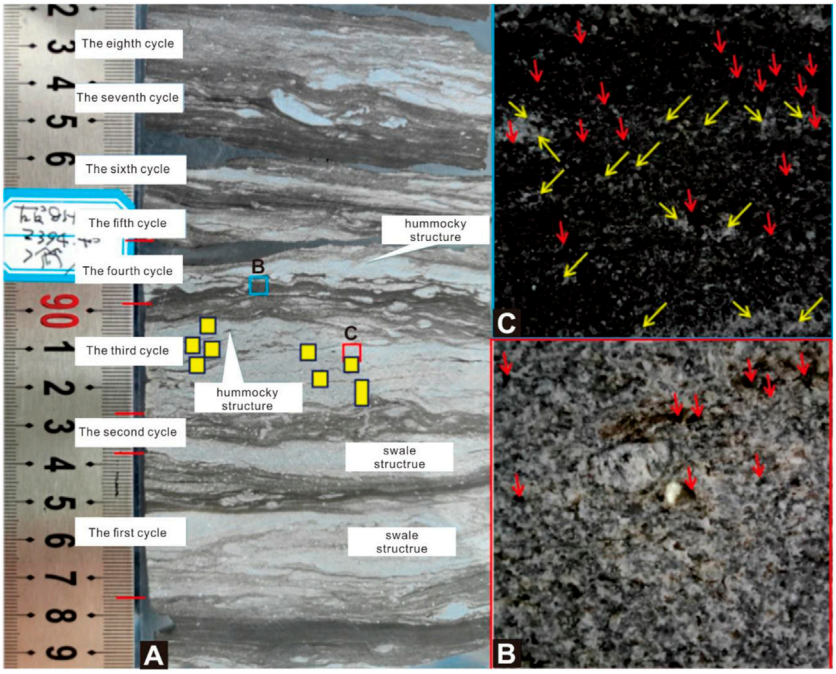

FIGURE 8
Cycle and structures of a storm deposition for the K_2qn shale in the Gulong Sag. **(A)** A storm's sedimentary sequence is composed of eight relatively complete cycles, among which the lower two are swale structures formed *via* the oscillating currents of storm troughs, whereas the upper two are hummocky structures formed *via* the oscillations of storm peaks. Each cycle is composed of two elements: the lower coarse-grained element and the upper fine-grained element, corresponding to the high and quiet periods of the storm, respectively. For example, the third cycle develops *via* the superposition of eight sub-cycles. **(B)** In the third sequence, the magnified photo of the red box at ×30 magnification shows two types of black and white particles, most ranging from 0.01 to 0.03 mm. The black particles are primarily clay (red arrows), and the white particles are calcite or dolomite and exist as cement. In terms of the area ratio, the content of black mud particles is ≥50%, and the content of the white calcite or dolomite particles is also approximately 50%. **(C)** Magnified view of the blue box in (A); the apparently uniform and dense mudstone is also composed of a series of silty clays (red arrows) often coated with calcite (yellow arrows).

Generally, the sequence at the bottom is thicker and coarser, with a normal grain sequence.

Typically, the storm sequence has a notable normal grain sequence. Above the erosional surface is gray calcareous siltstone, sometimes containing fine gravel, with gray-brown or gray-black mud shale above it. The grain size is smaller than the gray calcareous siltstone at the bottom, sometimes containing fine gravel (Figure 9A).

During the storm deposition, particles have certain arrangement rules; most have imbricated structures (Figures 9B–D), which reveals that, in most cases, storm waves are not simple oscillations of symmetry but have specific unidirectional and composite flow properties. However, sometimes visible ostracods are arranged in an "A" shape, and fossil ostracods hedge into a reverse imbricate structure on both sides of the dome structure, similar to an "A" shape (red ellipse in Figures 10A–C). This reveals the role of oscillation flow: high structure types occur in the cyclone storm flow on both sides of the high structure hedge. Fossil ostracods produced are in response to the oscillating flow against the imbricate structure.

3.1.5 Sand-scale mud clastic common in sandstones storm deposits

In the Qingshankou Formation, Gulong Sag, sand-grade mud clastic is generally developed in the storm deposits as gray-light gray siltstone formed *via* storm activity, sometimes reaching more than 50% content. The particle size of the sand-grade mud clastic mostly ranges from 0.01 to 0.03 m, within the range of the coarse silty sand. Therefore, a unique phenomenon occurs; the sandstone has some of the mineralogical and chemical composition of the clay while being classified structurally only as sandstone. This is a highly homogeneous mudstone at the macroscopic level but highly heterogeneous at the microscopic level. It can be divided into three distinct components: silty mud, argillaceous felsic silt, and a large amount of algal and Ostracoda debris. Sand and mud are reversed; mud has a silt size and silt has a mud size. Therefore, the siltstone formed *via* storms can intercalate with poorer physical properties than mudstone (Lu et al., 2020).

The diameter of most mud clastic is approximately 0.01–0.03 mm, which is between the coarse silt and is more significant than the felsic particles. The black and brown slivers

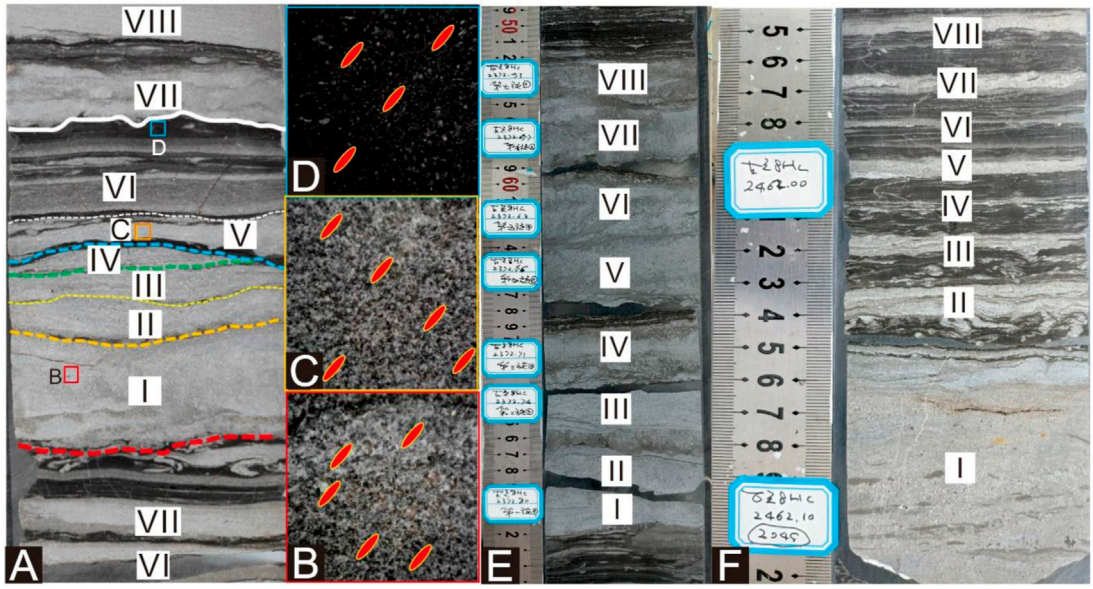

FIGURE 9
Complete storm sequence for the K_2qn shale in the Gulong Sag. **(A)** When the storm is at its most intense activity, the energy is at a maximum, wave oscillation yields liquefied sand, falling sand veins form at the bottom, and the liquefaction and drainage deformation form on the interior. There are approximately eight secondary sequences. **(B)** The red box in the first storm sequence in (A) magnified ×30, with abundant gray-black silty silt in the calcareous silt. The flake minerals have a notable left-leaning preponderance arrangement, revealing wave washing from left to right. **(C)** The orange box in the V storm sequence in (A) magnified ×30, which also has a left-leaning imbricated arrangement with a large amount of gray-black silt-grade mud. **(D)** The blue box at the top of the VI storm sequence magnified ×30, with substantial silty mud clastic and lamellar minerals, which have a weak left-imbricated structure. **(E)** The inner liquefaction of the silty sand is strong, and the bedding disappears. The bottom erosional surface is still well developed. **(F)** The first sequence at the bottom is the most developed, up to 7 cm thick, with discontinuous oblique bedding. A good liquefaction sand vein is developed at the bottom of the second sequence. There is also significant liquefaction at the bottom of sequences III and IV. Several of the upper sequences also have liquefied sand veins, indicating that these thin flat calcareous silts, without storm cross-bedding and dune structures, also formed during the storm.

on the sliders indicate that the two have different origins. The black sliders are derived from deep-water areas inside the swale structure, while the brown sliders originate from shallow water areas in the swale structure. Felsic and carbonate particles surround the mud clastic, forming a unique "Tangyuan structure (hard shell and soft core)," which requires further analysis concerning its influence on reservoirs and fracturing.

There is a large amount of silty mud in the mudstone, which can be divided into two types according to the color: organic-rich mud with black edges near the center of the swale structure and brown rounded silty mud, which originates in the organic-poor mud at the edge of the swale structure and is transported into the swale structure *via* turbidity currents (Figure 11).

3.1.6 General developments in gray-black mud shales

Except for the hummocky structure and cross-bedding developed at the bottom of the K_2qn in a set of sandstones, the hummocky structure and cross-bedding characteristics of the Qingshankou Formation are all developed as a set of dark gray or gray-black mud shale, indicating that the storm deposits formed *via* a reduction of clay in the lake deposits. Reducing clays are *in situ* deposits, whereas storm deposits are ectopic deposits. Due to abundant silty mud and calcareous cementation, the porosity and permeability of the storm sediments in the Gulong Sag are poorer than that of the shale, which forms special intercalation. In the K_2qn shale oil reservoir, the proportion of gray calcareous siltstone deposited by storms is only approximately 5%, primarily developed in the second and third members of the Qingshan Formation (K_2qn^2 and K_2qn^3), especially in the K_2qn^3; the proportion is relatively small in the K_2qn^1. Therefore, calcareous siltstones deposited by such storms have a negligible influence on hydrocarbon generation and storage.

3.1.7 Sand vein development at the base of storm systems

This phenomenon cannot be observed in ordinary storm deposits or tempestites but is expected in the Qingshankou Formation. Liquefaction sandstone veins often occur at the bottom of a storm's sedimentary system (Figure 12), characterized as follows: 1) Generally small in size; the diameter of sand veins in the core is 1–2 mm; the larger is 3–4 mm, and some are 7–8 mm or even >1 cm (Figures 12A,B) and >10 cm. 2) The vertical surface of the core is mostly

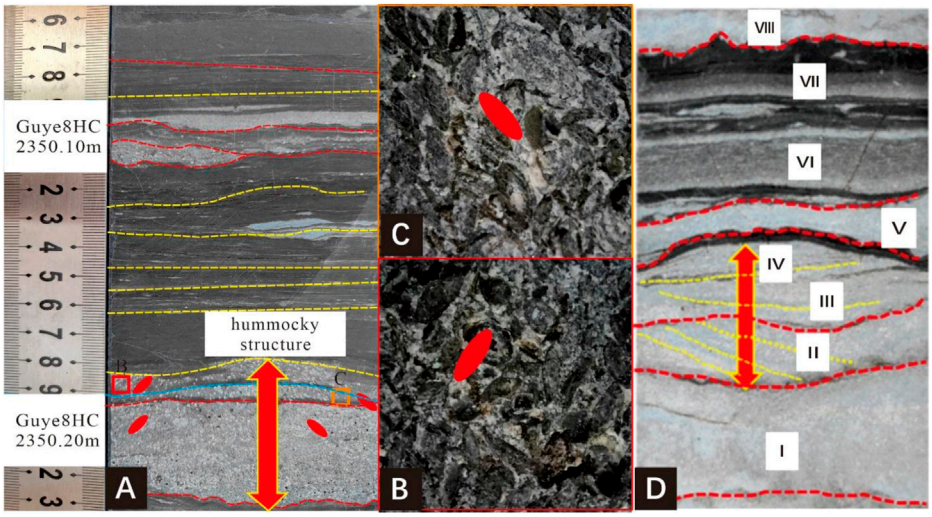

FIGURE 10
Hummocky structures with Ostracoda on either side arranged in reverse imbricated structures for the K_2qn shale in the Gulong Sag. **(A)** The storm formed an Ostracoda limestone hummock with a significant erosional surface and normal grain sequence. Ostracoda on both sides of the hummocky structure is inversely imbricated. **(B)** Magnified view of the red box in (A) showing that the Ostracoda fossils have a distinct left-imbricated structure. **(C)** Magnified view of the orange square in (A) showing the Ostracoda fossils with a right-leaning imbricate structure. **(D)** Storm deposits with distinct hummocky and swale structures. Sequences ii and iii have notable unidirectional oblique bedding formed *via* a composite flow.

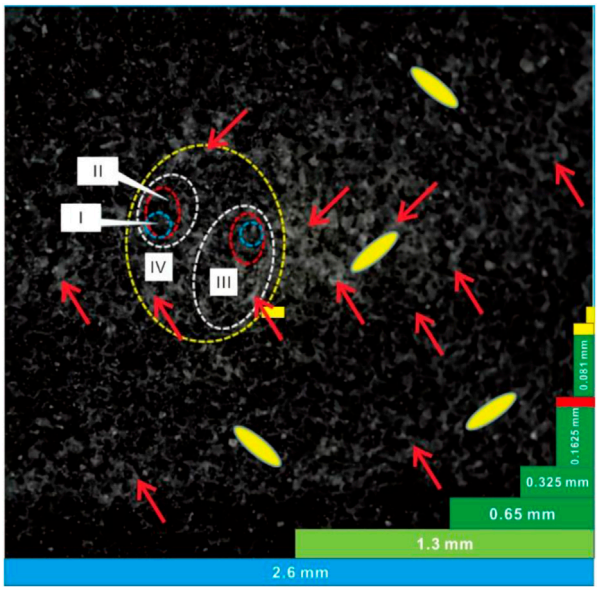

FIGURE 11
Silt-grade fragments and structure of sand-grade mud particles from I to IV.

intestinal, primarily due to compaction. This vein has a curved plate shape (Figure 12). 3) Contains a prolific gray-black mud shale, often from the bottom of the silt to the bottom of the fine dark mud shale, with several occurring in thin (cm-scale) sandstones (Figures 12C,D) and occasionally in dolomite nodules. 4) A gut shape is visible on the core facade, while a strip or wide worm-like shape is present on the core layer (Figures 12E,F). 5) Normally inclined characteristics, indicating that sand veins were subjected to bedding shear after their formation (He et al., 2021, 2022a,b,He, 2022). 6) Few gravity falling veins pass through two or three mud shale beds or even 3–4 silt beds. Additionally, due to prevalent liquefication wave oscillation or storm layer liquefaction, storm deposits often develop at the bottom of the silt layer with subsided liquefied sand veins (Figure 12) rather than from the bottom up as is common with general sand vein injections (Zhong et al., 2020a,b), referred to as "sand liquefaction gravity fall veins" or "vein of liquefied sand fall" (Figure 12).

Sand veins rarely developed at the bottom of storm siltstones in the Qingshankou Formation. This is an essential feature of the shale oil reservoir in the Gulong Sag. Various mechanisms exist for sand liquefaction (Zhong et al., 2020a, b). However, the small, liquefied sand veins at the bottom of the storm deposits in the Gulong Sag form *via* subsidence from top to bottom under gravity, which is opposite to that of high-pressure filling from the bottom to the top in most sand veins. Primarily, this vein of liquefied sand falls from the top down (Figure 12). The continuous activities of storm oscillation on the deposited fine silt allow it to liquefy and lose its internal viscosity, resulting in flow and liquefaction deformation. This can result in liquefaction flow

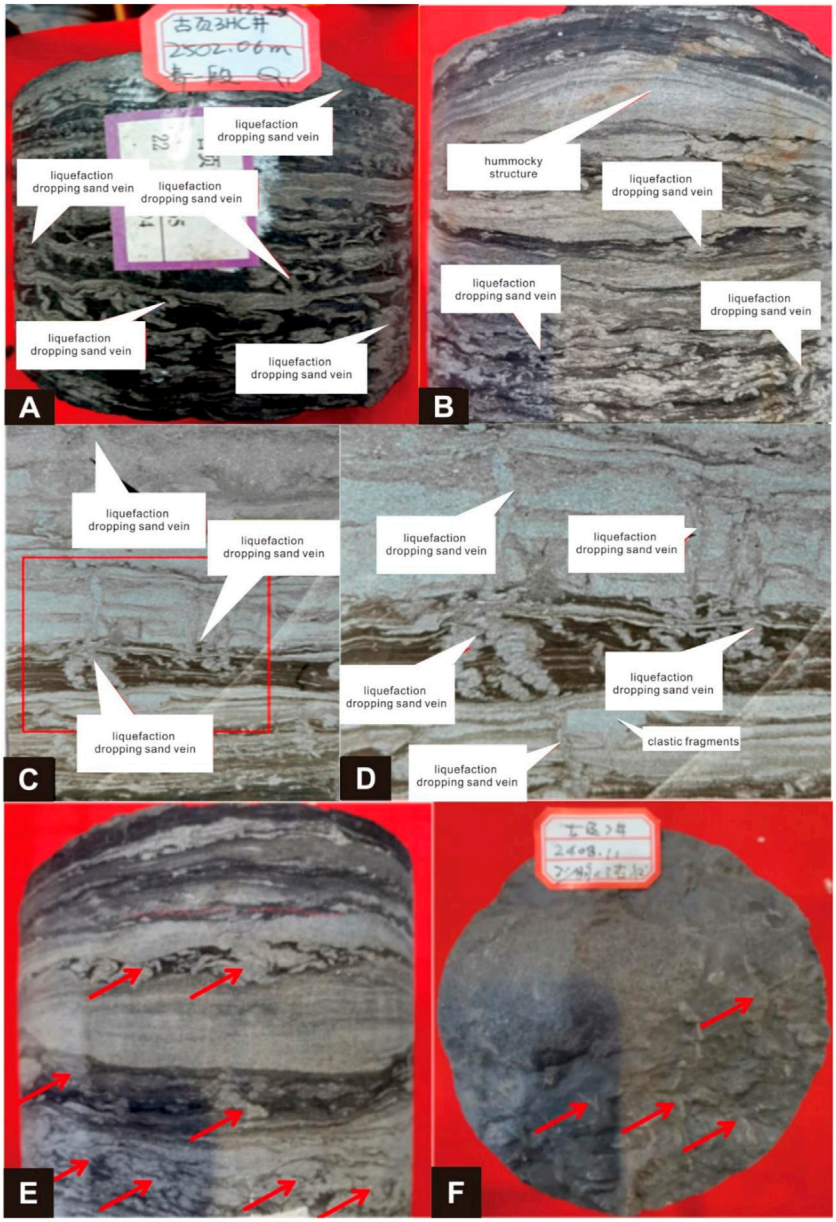

FIGURE 12
Veins of liquefied gravity falling sand formed *via* storm activity. **(A)** Hummocky and swale structures, but the hummocky and swale cross-bedding is not well developed. Liquefied sand veins at the bottom (red arrow) are well developed, indicating that the sediment at the bottom experienced oscillatory liquefaction of the storm and is soft; deposition during the low energy period between storms. **(B) (A)** rotated 90°: liquefied sand veins are at the bottom of each layer. Due to erosion at the storm's peak, the development of gray-black mud shale at the bottom is not good or the erosion is too strong and thin, which is ideal for developing liquefied sand veins. **(C)** Veins of liquefied sand, which pass through the silty sand, reveal that the silty sand was also liquefied simultaneously and into the gray-black shale. The vertical veins of sand are greatly shortened and overlapped to form chitterlings (red arrow) due to intense compaction. **(D)** A magnified view of the red box in **(C)** shows that the liquefied sand penetrates the thin layer of silty sand into the gray-black mud shale, forming intestinal veins. **(E)** Thin silty layer of liquefied sand veins curled and folded into chitterlings (red arrow) at the bottom, resulting from intense compaction. This also reveals that the grayish-brown mudstone with sand veins has a high compaction rate. **(F)** Sand veins at the base of the storm deposits (red arrows), projecting downward into a worm-like pattern, indicating denser subsidence.

in the sand layer and an upward flow of discharge water. Due to its increased density, it then falls into the lower mud or silt layer, forming liquefied sand veins (Figures 12C,D). Such liquefied sand veins are often mistaken for insect tracks. Additionally, there are negligible liquefied sand veins, often mistaken for seismites. This phenomenon is rare elsewhere.

Storm oscillation liquefaction occurs *via* wave fluctuation; small deformation bedding formed by wave oscillation is often observed in modern sediments of the Yellow River (Zhong et al., 2018). Macquaker et al. (2010) also observed that wave oscillation could enhance sediment gravity flow, which is partially related to oscillation liquefaction. Therefore, wave oscillation liquefaction is plausible.

4. Storm deposition dynamics

One of the most critical factors regarding storm deposition is its magnitude. Therefore, the K_2qn formation conditions are significant, i.e., the storm wave size (wave height and wave width) and water depth during the formation. Storm waves and their dynamic characteristics have been recovered by examining their hilly cross-bedding. Studies have shown that the orbital radius, D_0, at the bottom of the waves controls the wavelength, λ_0, of hummocky cross-bedding (or hummocky bodies); this relationship is represented by Eq. 1 (Dumas et al., 2005):

$$\lambda_0 = 0.52D_0 + 38.5\text{cm} \quad (1)$$

The simplest means of estimating the wavelength and wave height is to equate the hummocky structure's crest and trough to the bottom orbit of the wave.

We used the general width of the hummocky structure in the core of the Gulongqing section as a parameter for simple calculation. The typical width was 0.05 m (Figures 3–5). The core has 0.10 m maximum diameter (Figures 3–5), with a radius of ~0.05 cm. Substituting the latter value into Eq. 1 yielded a λ_0 ratio of 38.53 cm.

Therefore, a storm with a wave width of 0.10 m (Figures 3–5) would have a wavelength of ~0.39 m, i.e., approximately four times the width of the hummocks. The maximum orbital velocity (Komar, 1998) under shallow and moderate water depths can be represented as Eq. 2:

$$U_w = \pi d_0/T \quad (2)$$

where U_w denotes water velocity. Therefore, the wave period (T) must be calculated for the velocity. Immenhauser (2009) proposed a formula to calculate the storm wave period, i.e., $L_0 \approx 1.56\,T^2$, where L_0 is the wavelength and T is the storm wave cycle, yielding the following:

$$T = (L_0/1.56)^{1/2} \quad (3)$$

This formula calculates the period according to the wavelength of deep water, which is more consistent with the characteristics of the Gulong Sag. If we substitute a storm wavelength of 0.43 m, we obtain a wave period (T) of 0.50, which is reasonable. We substituted this value into Eq. 2 and obtained a U_w value of 0.55 m s^{-1}. This is the bottom flow velocity caused by storm waves that form small hummocky structures in the Qingshankou Formation.

According to the base-shape stability diagram proposed by Dumas et al. (2005), the wave velocity during the formation of the HCSs generally does not exceed 1 m s^{-1}. Therefore, U_w can be set as 1 m $s^{-1,}$ and d_0 = 0.43 m can be substituted into Eq. 2, yielding the following:

$$1 = \pi d_o/T \quad (4)$$

$$T = 0.43\pi/1 = 3.14 \times 0.43 = 1.35\text{s} \quad (5)$$

Using this value in Eq. 2, we obtained the following:

$$Uw = \pi d_0/T = 3.14 \times 0.10/1.35 = 0.25\text{ms}^{-1} \quad (6)$$

A value of 0.0139 m s^{-1} can also be obtained using the formula proposed by Allen (1981). We used the methods of Lowe (1975) and Allen (1981) to calculate the minimum fluidization velocity (V_{mf}) from silt to gravel with a diameter of 4 cm. Table 1 shows that the V_{mf} decreases from gravel to fine sand and silt by 5–6 orders of magnitude. It should be noted that V_{mf} values of silt and fine sand are almost zero and may represent a storm moving away from the source area (Shore lake) of the silt deposited near the storm wave base plane, forming the lower fine-grained hummocky cross-bedding (Figures 3–5). To determine the extent to which the bottom gravel layer forms under reflux with upward suspension, we obtained several empirical formulas based on our experiments, among which $D = 0.0954\,V^{1.7627}$ had the highest correlation of 0.9969. In this formula, D is the particle diameter (m), and V is the minimum upward movement velocity of the water flow ($m{\cdot}s^{-1}$). Therefore, from our experimental results (Table 1), we can see that V_{mf} increased by more than 40 times from silt to 4 mm diameter gravel, which is much smaller than the results of Allen (1981) and Lowe (1975).

To determine the horizontal component of the upward velocity of the wave or current, the velocity of water points can be obtained by calculating the ellipse of the water points:

$$X^2/a^2 + Y^2/b^2 = 1 \quad (7)$$

where X and Y represent the position of the water quality point in the horizontal and vertical directions, respectively. For example, to establish a model based on the parameters of the hummocky structure or cross-bedding in Figures 3–5, we substituted the values a = 0.05 m and b = 0.01 m into Eq. 7:

$$X^2/0.05^2 + Y^2/0.001^2 = 1 \quad (8)$$

To obtain the velocity of the mass point, the first derivative of time, T, was needed, thus yielding Eq. 9:

$$2X/0.0025dt + 2Y/0.001dt = 0 \quad (9)$$

Based on this, we obtained the following:

$$800Xdt = 2,000Ydt \quad (10)$$

TABLE 1 V_{mf} values of particles with different particle sizes.

Particle diameter (mm)	0.125	0.25	0.50	1	2	10	20	30	40
V_{mf} (Lowe, 1975)	0.185	0741	0.296	0.119	0.474	0.119	0.474	0.107	0.191
(m/s)	E-6	E-6	E-5	E-4	E-4	E-2	E-2	E-1	E-1
V_{mf} (Allen, 1985)	0.135	0.539	0.216	0.864	0.346	0.864	0.346	0.778	0.139
(m/s)	E-6	E-6	E-5	E-4	E-4	E-2	E-2	E-2	E-1
This paper (m/s)	**0.023**	0.045	0.063	**0.107**	0.143	0.443	0.557	0.835	1.013

The bold values represented the particle diameter (mm), for example, the diameter of siltstone particle is 0.125 mm.

Dividing both sides by dt, we obtained:

$$800X = 2,000Y \tag{11}$$

If we substitute Y = 0.023, as the negative sign only represents the direction, it has no practical significance. Therefore, we obtained the X and Y values as 0.0575 m s^{-1} and 0.023 m s^{-1}, respectively.

Therefore, the storm flow velocity is 0.0575 m s^{-1} and 0.023 m s^{-1} in the horizontal and vertical directions, respectively when forming silt-sand mini-hummocky structures at the bottom of the shale in the Gulong Sag. The velocity along the lake bottom is 0.0575 m s^{-1}, indicating that the horizontal motion is 2.5 times faster than vertical motion. In the K_2qn shale, clay particles with a diameter of 1 mm acting on medium sand particles are often observed. Therefore, based on Table 1, Y = 0.107 m/s and X = 0.107 × 0.0575/0.023 = 0.2675 (m·s^{-1}).

During the deposition of the Qingshankou Formation, the horizontal and vertical velocities of the bottom water in the ancient lake ranged from 0.0575 to 0.2675 m s^{-1}; the transport velocity of 1 mm particles was nearly consistent with the Jurstrom diagram, at approximately 0.18–55 m s^{-1}. It can be seen that the horizontal velocity of transporting 1 mm particles obtained through experiments and calculations is 0.2675 m s^{-1}, which is close to the lower velocity of 1 mm particles shown in the Jurstrom diagram. These velocities will significantly increase if we consider the clay particle's surface viscosity.

Based on the Jurstrom diagram, the transport velocities of the 0.0039 to 0.0001 mm mud particles ranged from 0.30 to 3.5 m/s, revealing that the particle size of clay is inversely proportional to the transport velocities due to the viscosity. Moreover, using the silt particles (0.005–0.05) in the K_2qn, the water flow velocity was 20–55 cm s^{-1} (Zalmai and Schieber, 2017). Therefore, the depositional velocity of the K_2qn^3 in the Gulong Sag was at least 20–55 cm s^{-1}.

Strong recombination flows are likely to form asymmetric HCSs (Arnott and Southard, 1990; Dumas and Arontt, 2006). Composite wave marks are distinguished from wave marks formed *via* oscillating flow by their circular ridges, convex hyperboloid, and strong local erosion (square box shape) on the inflow surface.

5 Formation depth of small hummocky structures

The water depth for the formation of hummocky cross-bedding has always been a topic of debate in storm sediment and tempestite studies (Bourgeois, 1980; Hunter and Clifton, 1981). Bourgeois (1980) suggested that the maximum water depth of ocean tempestite was 50 m, while others have proposed depths of >10 m. Hunter and Clifton. (1982) established a relationship diagram between the storm wave period, wave height, and water depth. For a particular wave height, a longer wave period corresponds to a larger water depth (Myrow et al., 2008), implying that the height of the hummocky structure is related to both the wave size and water depth. Long-period waves can form in deeper water, whereas short-period waves can form hummocky structures of the same height in shallower water. Therefore, water depth cannot be simply evaluated by the height of the hummocky structure. Additionally, from Eqs 1, 2, we can infer that under a specific wave height, the greater the wavelength, the greater the water depth. Therefore, the hummocky structure's height and width should be considered when examining water depth from a hummocky structure perspective.

Makoto et al. (2001) proposed that the wavelength of such bedding increases with an increase in the thickness of storm sediments. However, it decreases with an increase in the paleo-water depth. Its wavelength was considered a function of the bottom oscillating water flow track diameter caused by the storm surge. The effective storm wave base depth was one-third of the storm wavelength (Alberto and Fernando, 2012). However, this information does not allow us to infer the water depth of the Gulong Sag from a hummocky structure scale.

Greenwood and Sherman (1986) observed that typical hummocky cross-bedding with a wave height of several

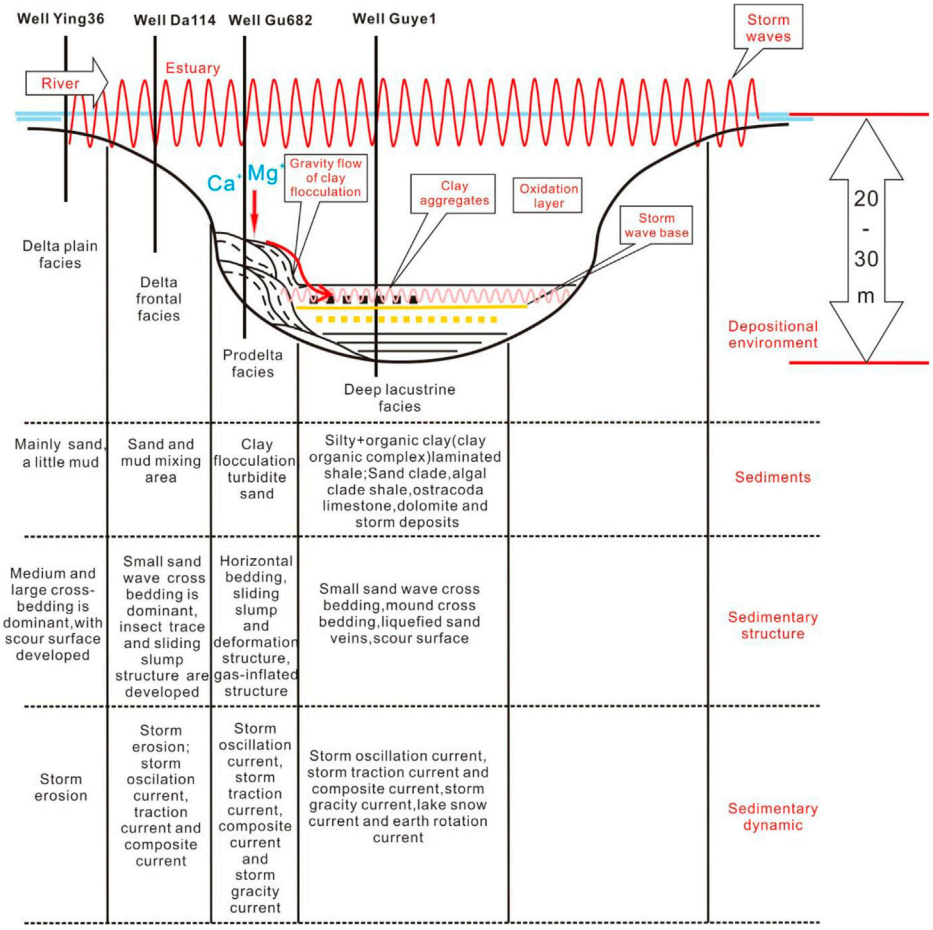

FIGURE 13
Model of salt lake storm deposition in the Qingshankou Formation, Gulong Sag.

centimeters and 0.3–0.6 m wavelength could form in a lake at a 2.0 m depth. The ripple index ranged from 8 to 10, and the ratio of the water depth to the HSC wave height was approximately 1/30 (calculated in this study). 1:100 was used for reliability; the water depth for hummocky cross-bedding at 0.02 m height should be approximately 2.00 m. Therefore, the water depth of the Gulong Sag during the K_2qn sedimental period should be approximately 2.00 m, which may not be consistent with the situation at that time. Nevertheless, this indirectly reveals that the depth of the Gulong Sag at that time was not great. Based on studies of wave activity in the modern Yellow River, the ratio of the sand wave height to the water depth is approximately 10–20. Therefore, this provides evidence that the depth of the K_2qn^1 is not overly large. Recently, five current closed lakes near Daqing were investigated; clay deposits at the bottom of the lakes were in a reductive phase when the water depth was shallow. When fresh, the clay deposits were black and smelled like hydrogen sulfide and ammonia. This information was insufficient to distinguish deep water based on the fine grain size and high matrix content of the sediments. Bourgeois (1980) indicated that the maximum depth of Gulong Lake does not exceed 50 m. Therefore, the ancient water depth of Gulong Lake during the Qingshankou stage should have been 2–50 m.

In conclusion, restoring the water depth through HSCs is significant for lake palaeography, paleodeposition, and the development of source rocks. Through this study, we propose a model diagram of storm deposition of the K_2qn shale oil reservoir in the Gulong Sag (Figure 13).

6 Conclusion

Many storm deposits are developed in the Qingshankou Formation, Gulong Sag, primarily composed of gray calcareous silt, silty mud, ostracods, and algal debris. Storms that affected the Qingshankou Formation formed many small hummocky structures and cross-beddings, with a width of several centimeters and height of <1 cm. The width of the largest

bedding was 10 cm, with a 2 cm height. There were also many relatively hummock/swale structures and hummocky/swale cross-bedding as flat thin siltstones. The storm sediments of the Qingshankou Formation have abundant silt-sized mud, which formed *via* the re-fragmentation of lake-bottom mud disturbed by the storm. Tiny veins of liquefied silt developed at the bottom of most storm-deposited silt layers. The silty veins formed *via* gravity deposition after the liquefaction of the silty storm layer, rather than classic liquefaction overpressure injection from the bottom to the top. Black and gray-black mud shale symbiosis with, or adjacent to, storm deposits also had a sand structure. The mud particles mostly ranged between 0.01 and 0.03 mm, unique internal debris formed by storm stirring and crushing. Storm activity and deposition significantly influenced the shale oil reservoir in the Gulong Sag. Even the grayish-brown, grayish-black, and black shales in the gray siltstone without storm deposition all had sand structures, indicating that storms and other bottom currents significantly influenced lakeside deposits. The sub-lacustrine flow velocity due to storm waves in the Qingshankou Formation was between 0.20 and 0.55 cm s^{-1}.

Data availability statement

The original contributions presented in the study are included in the article/supplementary material, further inquiries can be directed to the corresponding authors.

Author contributions

WH: Conceptualization, Resources, Project administration JZ: Writing Original Draft, Formal analysis NS: Investigation, Data Curation.

Funding

This work was supported by National Natural Science Foundation of China (Grant No.42072138; 41572088).

Acknowledgments

We gratefully acknowledge the Research Institute of Exploration and Development, Daqing Oilfield Company Limited for providing geological data and samples. Special thanks give also to the editor and reviewers for handing our manuscript and for the constructive comments.

Conflict of interest

Author WH was employed by Daqing Oilfield Co., Ltd., PetroChina and China National Oil and Gas Exploration and Development Company Ltd.

The remaining authors declare that the research was conducted in the absence of any commercial or financial relationships that could be construed as a potential conflict of interest.

Publisher's note

References

Aigner, T. A., and Reineck, H. E. (1982). Proximality trends in modern storm sands from the Helgoland Bight (North Sea) and their implications for basin analysis. *Senckenberg. Marítima* 14, 83

Aigner, T. A. (1985b). Storm depositional systems: Dynamic stratigraphy in modern and ancient shallow-marine sequences: Berlin. *Lect. Notes Earth Sci.* 3, 174.

Aigner, T. (1985a). *Storm depositional systems*. Berlin: Springer-Verlag, 119.

Aigner, T. (1980). *Storm deposits as a tool in facies analysis*. Abstracts: International Association of Sedimentologists 1st European Meeting, 44

Alberto, P., and Fernando, P. (2012). Tempestite facies models for the epicontinental triassic carbonates of the betic cordillera (southern Spain). *Sedimentology* 59, 646–678. doi:10.1111/j.1365-3091.2011.01270.x

Allen, P. A. (1981). Wave-generated structures in the Devonian lacustrine sediments of southeast Shetland and ancient wave conditions. *Sedimentology* 28, 369–379. doi:10.1111/j.1365-3091.1981.tb01686.x

Arnott, R. W. C., and Southard, J. B. (1990). Exploratory flow experiments on combined flow bed configurations, and some implications for interpreting storm 2 event stratification. *J. Sediment. Petrology* 60, 211

Bourgeois, J. (1980). A transgressional shelf sequence exhibiting hummocky stratification: The Cape Sebastian Sandstone (Upper Cretaceous), southwestern Oregon. *J. Sediment. Res.* 50, 681–702. doi:10.1306/212f7ac2-2b24-11d7-8648000102c1865d

Chen, H., Tian, J. C., Jiang, Y. Q., YouZhang, L. W, X., and Kang, J. W. (2008). Sedimentary characteristics and significance of the storm deposits in the two and four stages of the Sichuan basinXinjiang. *Pet. Geol.* 29, 581–584. (in Chinese with English abstract)

Chen, Z. M., Zhang, S. K., and Wan, L. G. (1988). The formation of structural fissures in the mudstone in Qingshankou group in the northern part of Gulong Sag and a forecast of the distribution of oi and gas pools. *Acta Pet. Sin.* 9, 7–15. (in Chinese with English abstract).

Cui, J. W., Zhang, Z. Y., Liu, J. L., Liu, G. L., Huang, X., Qi, Y. L., et al. (2021). Hydrocarbon generation and expulsion quantification and contribution of multiple source rocks to hydrocarbon accumulation in yanchang formation, ordos basin, china. *J. Nat. Gas Geoscience* 6, 375–391. doi:10.1016/j.jnggs.2021.12.001

Dott, R. H., and Bourgeois, J. (1982). Hummocky stratification: Significance of its variable bedding sequences. *Geol. Soc. Am. Bull.* 93, 663–680. doi:10.1130/0016-7606(1982)93<663:hssoiv>2.0.co;2

Dumas, S., and Arnott, R. W. C. (2006). Origin of hummocky and swaley cross-stratification–The controlling influence of unidirectional current strength and aggradation rate. *Geol.* 34, 1073–1076. doi:10.1130/g22930a.1

Dumas, S., Arontt, R. W. C., and Southard, J. B. (2005). Experiments on oscillatory-flow and combined-flow bed forms: Implications for interpreting parts of the shallow-marine sedimentary record. *J. Sediment. Res.* 75, 501–513. doi:10.2110/jsr.2005.039

Fang, S. X., Hou, F. H., Yang, X. Y., He, J., Shen, Z. G., Qiao, L., et al. (2011). The tempestites in the two lower subsection of the middle triassic in the ordos basin. *Acta Sedimentol. Sin.* 29, 23–30. doi:10.14027/j.cnki.cjxb.2011.01.002

Feng, X. L., Ma, L. X., Deng, H. W., and Lin, H. X. (2011). Dawangbei subsag of lacustrine sedimentary characteristics of beach bar sand storm. *Xinjiang Geol.* 29, 80–85. (in Chinese with English abstract). doi:10.3969/j.issn.1000-8845.2011.01.017

Gao, R. Q. (1984). Characteristics of petroleum generation and expulsion in abnormal pressure shale zones and the formation of fractured shale reservoirs. *Petroleum Geol. Oilfield Dev. Daqing* 3, 160–167. (in Chinese with English abstract).

Gilbert, G. K. (1899). Ripple-marks and cross-bedding. *Geol. Soc. Am. Bull.* 10, 135–140. doi:10.1130/gsab-10-135

Greenwood, B., and Sherman, D. J. (1986). Hummocky cross-stratification in the surf zone: Flow parameters and bedding Genesis. *Sedimentology* 33, 33–45. doi:10.1111/j.1365-3091.1986.tb00743.x

Guo, F., and Guo, L. (2011). Lacustrine facies tempestites in the Western qaidam basin. *Xinjiang Geol.* 29, 125–129. (in Chinese with English abstract). doi:10.3969/j.issn.1000-8845.2011.02.002

He, W. Y., Cui, B. W., Wang, F. L., Wang, Y. Z., Meng, Q. A., Zhang, J. Y., et al. (2022b). Study on the shale fissures, shale calcite veins and oil-state of Qingshankou formation from Gulong Sag. *Geol. Rev.* 68, 693–741. (in Chinese with English abstract). doi:10.16509/j.georeview.2021.12.001

He, W. Y. (2022). Discovery of nm pores and nm fractures in Gulong shale oil reservoir and its significances. *Petroleum Geol. Oil develepment Daqing* 41, 1–15. (in Chinese with English abstract). doi:10.19597/J.ISSN.1000-3754.202112019

He, W. Y., Meng, Q. A., Feng, Z. H., Zhang, J. Y., and Wang, R. (2022a). *In-situ* accumulation theory and exploration and development practice of Gulong shale oil in Songliao Basin. *Acta Pet. Sin.* 43, 1–14. (in Chinese with English abstract). doi:10.7623/syxb202201001

He, W. Y., Meng, Q. A., and Zhang, J. Y. (2021). Controlling factors and their classification-evaluation of Gulong shale oil enrichment in Songliao Basin. *Petroleum Geol. Oil develepment Daqing* 40, 1–12. (in Chinese with English abstract). doi:10.19597/J.ISSN.1000-3754.202107045

Hunter, R. E., and Clifton, E. H. (1982). Cyclic deposits and hummocky cross-stratification of probable storm origin in upper cretaceous rocks of the cape sebastian area, southwestern Oregon. *J. Sediment. Petrology* 52, 027

Immenhauser, A. (2009). Estimating palaeo-water depth from the physical rock record. *Earth. Sci. Rev.* 96, 107–139. doi:10.1016/j.earscirev.2009.06.003

Jiang, Z. X., Zhao, C. L., Liu, M. H., and Yuan, Z. W. (1990). A preliminary study on the east sag web lacustrine storm deposits. *Acta Sedimentol. Sin.* 8, 107–114. (in Chinese with English abstract).

Kelling, G., and Mullin, P. R. (1975). Graded limestones and limestone-quartzite couplets: Possible storm-deposits from the Moroccan carboniferous. *Sediment. Geol.* 13, 161–190. doi:10.1016/0037-0738(75)90019-6

Klein, G. D., and Marsaglia, K. M. (1987). Hummocky cross-stratification, tropical hurricanes, and intense winter storms. *Sedimentology* 34, 333–337. doi:10.1111/j.1365-3091.1987.tb00781.x

Komar, P. D. (1998). *Beach processes and sedimentation*. Upper Saddle River, New Jersey: Prentice-Hall, 544.

Liu, Q. Y., Li, P., Jin, Z. J., Liang, X. P., Zhu, D. Y., Wu, X. Q., et al. (2021). Preservation of organic matter in shale linked to bacterial sulfate reduction (BSR) and volcanic activity under marine and lacustrine depositional environments. *Mar. Petroleum Geol.* 127, 104950. doi:10.1016/j.marpetgeo.2021.104950

Liu, Q. Y., Pi, P., Jin, Z. J., Sun, Y. W., Hu, G., Zhu, D. Y., et al. (2022). Organic-rich formation and hydrocarbon enrichment of lacustrine shale strata: A case study of chang 7 member. *Sci. China Earth Sci.* 65, 118–138. doi:10.1007/s11430-021-9819-y

Liu, X., Zhong, J. H., Rodney, G., Bian, S. H., and Liang, C. (2012). Late cretaceous tempestite in northern Songliao basin, China. *J. Asian Earth Sci.* 56, 33–41. doi:10.1016/j.jseaes.2012.02.007

Lowe, D. R. (1975). Water escape structures in coarse-grained sediments. *Sedimentology* 22, 157–204. doi:10.1111/j.1365-3091.1975.tb00290.x

Lu, C., Ma, L., Guo, J. C., Xiao, S. W., Zheng, Y. C., and Yin, C. B. (2020). Effect of acidizing treatment on microstructures and mechanical properties of shale. *Nat. Gas. Ind. B* 7, 254–261. doi:10.1016/j.ngib.2019.10.007

Macquaker, J. H. S., Bentley, S. J., and Bohacs, K. M. (2010). Wave-enhanced sediment-gravity flows and mud dispersal across continental shelves: Reappraising sediment transport processes operating in ancient mudstone successions. *Geology* 38, 947–950. doi:10.1130/g31093.1

Makoto, I., Asako, I., Toru, N., Takahiro, S., and Takahiro, S. (2001). Temporal variation in the wavelength of hummocky cross-stratification: Implications for storm intensity through Mesozoic and Cenozoic. *Geol.* 29, 87–89. doi:10.1130/0091-7613(2001)029<0087:tvitwo>2.0.co;2

Mohseni, H., and Al-Aasm, I. S. (2004). Tempestite deposits on a storm-influenced carbonate ramp: An example from the pabdeh formation (paleogene), zagros basin, swiran. *J. Pet. Geol.* 27, 163–178. doi:10.1111/j.1747-5457.2004.tb00051.x

Myrow, P. M., Lukens, C., Lamb, M. P., Houck, K., and Strauss, J. (2008). Dynamics of a Transgressive Prodeltaic System: Implications for Geography and Climate Within a Pennsylvanian Intracratonic Basin, Colorado, U.S.A. *J. Sediment. Res.* 78, 512–528. doi:10.2110/jsr.2008.061

Nie, H., Chen, Q., Zhang, G., Sun, C., Wang, P., Lu, Z., et al. (2021). An overview of the characteristic of typical Wufeng–Longmaxi shale gas fields in the Sichuan Basin, China. *Natural Gas Industry B.* 83 (3), 217–230. doi:10.1016/j.ngib.2021.04.001

Sun, L. D. (2020). Shale oil in Gulong Sag. *Petroleum Geol. Oilfield Dev. Daqing* 39, 1–7. (in Chinese with English abstract). doi:10.19597/J.ISSN.1000-3754.202005037

Tao, H. F., Xu, J., Zhang, Z. N., Wang, X. F., Liu, H. T., and Guo, W. H. (2021). Experimental studies on nanopore evolution in organic matter-rich shales. *J. Nat. Gas Geoscience* 6, 231–243. doi:10.1016/j.jnggs.2021.07.002

Wang, G. Y., Wang, F. L., Meng, Q. A., and Gu, S. F. (2020). Stratgic significance and research direction for Gulong shale oil. *Petroleum Geol. Oil develepment Daqing* 39, 8–19. (in Chinese with English abstract). doi:10.19597/J.ISSN.1000-3754.202005036

Xue, P., Zhang, L. X., Liang, Q. S., Sun, X. N., Zhao, Q. P., and Qi, P. W. (2020). Thermodynamic characteristics of CH4 adsorption by continental shale: A case study of the Upper Triassic Yanchang shale in the Yanchang Gasfield, Ordos Basin. *Nat. Gas. Ind. B* 7, 269–277. doi:10.1016/j.ngib.2019.10.009

Yang, W., Tian, J. C., Zhu, Y. T., and Wang, F. (2009). Two characteristics of Permian Shiqianfeng Formation in Dengfeng area of Henan storm deposits. *Sediment. Geol. Tethyan Geol.* 29, 55. doi:10.3969/j.issn.1009-3850.2009.01.011

Zalmai, Y., and Schieber, J. (2017). On the origin of silt laminae in laminated shales. *Sediment. Geol.* 360, 22–34. doi:10.1016/j.sedgeo.2017.09.001

Zhang, J. L., Shou, J. F., and Zhao, C. L. (1988). The storm deposits in Dongpu sag sand three section. *Acta Sedimentol. Sin.* 6, 50–57. (in Chinese with English abstract).

Zheng, N., Jiang, Z. X., Li, T. D., Geng, S. F., You, G. Q., and He, Y. B. (2010). The basic characteristics of sediments in Bohai Bay Basin in Gunan sag storm and its geological significance. *Geol. China* 37, 1191–1198. (in Chinese with English abstract).

Zhi, D. M., Tang, Y., He, W. J., Guo, X. G., Zheng, M. L., and Huang, L. L. (2021). Orderly coexistence and accumulation models of conventional and unconventional hydrocarbons in Lower Permian Fengcheng Formation, Mahu sag, Junggar Basin. *Petroleum Explor. Dev.* 48, 43–59. doi:10.1016/s1876-3804(21)60004-6

Zhong, J. H., Ni, L. T., Sun, N. L., Hao, B., Xue, C. Q., Shao, Z. F., et al. (2020a). Lacustrine storm and tempestite of Lower Cretaceous in the Lingshan Island, Qingdao, Shandong. *Acta Geol. Sin.* 94, 3036–3061. (in Chinese with English abstract). doi:10.19762/j.cnki.dizhixuebao.2020040

Zhong, J. H., Ni, L. T., Wang, L. D., Song, Q. Y., Sun, N. L., Song, G. X., et al. (2020b). Discovery of large sand dykes in the Lower Cretaceous of southern Beilaishi, Lingshan Island, Qingdao, and their formation dynamics. *Geol. Rev.* 66, 1457–1475. (in Chinese with English abstract). doi:10.16509/j.georeview.2020.06.001

Zhong, J. H., Song, G. X., Ni, L. T., Sun, N. L., Hao, B., Sim, Y. Z., et al. (2018). Modern non-seismically induced deformation bedding in the lower reaches of the Yellow river and Yellow river Delta. *Acta Sedimentol. Sin.* 37, 239–253. (in Chinese with English abstract). doi:10.14027/j.issn.1000-0550.2018.168

frontiers | Frontiers in Earth Science

TYPE Original Research
PUBLISHED 09 January 2023
DOI 10.3389/feart.2022.1031493

OPEN ACCESS

EDITED BY
Deyu Gong,
Research Institute of Petroleum Exploration and Development (RIPED), China

REVIEWED BY
Longyi Shao,
China University of Mining and Technology, China
Shuheng Tang,
China University of Geosciences, China

*CORRESPONDENCE
Yongshang Kang,
kangysh@sina.com

SPECIALTY SECTION
This article was submitted to Economic Geology,
a section of the journal
Frontiers in Earth Science

RECEIVED 30 August 2022
ACCEPTED 12 September 2022
PUBLISHED 09 January 2023

CITATION
Kang Y, Huangfu Y, Zhang B, He Z, Jiang S and Ma YZ (2023), Gas oversaturation in deep coals and its implications for coal bed methane development: A case study in Linxing Block, Ordos Basin, China.
Front. Earth Sci. 10:1031493.
doi: 10.3389/feart.2022.1031493

Gas oversaturation in deep coals and its implications for coal bed methane development: A case study in Linxing Block, Ordos Basin, China

Yongshang Kang[1,2]*, Yuhui Huangfu[3], Bing Zhang[4], Zhiping He[5], Shanyu Jiang[6] and Yuan Zee Ma[7]

[1]College of Geosciences, China University of Petroleum, Beijing, China, [2]State Key Laboratory of Petroleum Resources and Prospecting, China University of Petroleum, Beijing, China, [3]School of Earth and Space Sciences, Peking University, Beijing, China, [4]China United Coalbed Methane Corporation, Ltd, Beijing, China, [5]China Storage Energy, Beijing, China, [6]Consulting and Research Center of Ministry of Natural Resource, Beijing, China, [7]Schlumberger, Denver, CO, United States

Three coal bed methane (CBM) wells penetrating to coal seams 8+9# (Permian Taiyuan Formation), in deep coals (depth>1,500 m), show very differential production performance in Linxing Block, eastern margin of the Ordos Basin in China. The mechanism for the performance differentiation is analyzed through studies on coal permeability and gas saturation in deep coals, and specifically, the comparison of coal reservoir characteristics in the three wells. The mechanism for gas oversaturation is then discussed based on data from Linxing Block and spot but important exploration results relevant to deep coals in the Junggar Basin. This study demonstrates that: (1) Permeability values of coal seams 8+9# in deep coals are probably in the order of 10^{-2}mD from diverse sources including results of experimental permeability test simulating underground stress conditions. Studies on gas saturation distribution reveal that high gas rates (>3,000 m^3/d) can be achieved only from oversaturated coal reservoirs in Linxing Block. (2) Two types of oversaturation mechanism, including igneous intrusion-driven oversaturation and sorption capacity-driven oversaturation, exist in deep coals. The former is restricted to regions/blocks influenced by igneous intrusion, and characterized by secondary gas generation and supplementation to deep coals that have substantial similar Langmuir curves to that of shallow coals. The latter may play in deep coals that are not influenced by igneous intrusion, and is characterized by more free gas released from coals after adsorption saturation, due to reduced sorption capacity in deep coals; (3) Oversaturation may exist more frequently in deep coals (in comparison with shallow coals), due to mostly the sorption capacity-driven oversaturation mechanism, and the weaker tectonic deformation and uplifting experienced by deep coals in comparison with shallow coals, which favors gas preservation and oversaturation. (4) Generally, coal permeability in deep coals is low due to the increased effective stress, and exploring oversaturation areas should be a primary concern for CBM development. It appears that in most large, tectonically compressed coal basins, there is a critical depth beyond which

the oversaturation areas could occur, presenting opportunities and challlenges for CBM development.

KEYWORDS

CBM, gas oversaturation, Langmuir curve, production performance, permeability, deep coal

1 Introduction

Coals are mostly undersaturated with gas, because most coal basins have been variably uplifted from their maximum depth of burial (Bustin and Bustin, 2008; Seidle, 2011). Coal bed methane (CBM) production from undersaturated coals requires primary dewatering to induce desorption of adsorbed gas below the critical desorption pressure. Coal permeability and gas saturation are the two most vital parameters determining gas rate and CBM recovery (Moore, 2012).

Until now, the CBM development targets are mostly undersaturated shallow coals in China and also in other countries, although a large part of the world's coalbed methane resources is distributed in coal seams deeper than 1,500 m (Kuuskraa and Wyman, 1993; Johnson and Flores, 1998). A new round of CBM resource evaluation in China reported resources of about $30\times10^{12}m^3$, in the depth of 1,500–3,000 m (Li X. Z. et al., 2016). Notice that shallow coals and deep coals are divided with a burial depth of 1,500 m hereinafter.

Because of low permeability and low gas saturation, a large part of CBM blocks in shallow coals in China need long time primary dewatering (several months to more than 1 year), while produce at low gas rates then. Almost two-thirds of injection/falloff tested permeability values are inferior to 1 mD (Kang et al., 2017) and about half of tested samples are with saturation being lower than 60%, according to our recent statistical analysis. Low permeability and low gas saturation in shallow coals are due to complex tectonic evolution history and strong tectonic deformation and uplifting, specifically near the margins of compressional coal basins.

Although no much work has been done in deep CBM drilling and exploration due to the disadvantageous factors such as drilling cost and low permeability, several high gas rates from deep coals were reported. For example, tested gas rate in well Pinyon Ridge Federal A, in the Piceance basin, United States, was reported at 27,152 m^3/d (Kuuskraa and Wyman, 1993). In recent years, two CBM wells penetrating to deep coals in Linxing Block of the Ordos Basin in China have been found to produce gas directly, with almost zero water production and the gas rates are stable at a level of >3,000 m^3/d. However, one other nearby well penetrating to the same coal seams in deep coals has very low gas rate (<120 m^3/d). The production performance differentiation provides an opportunity to enhance the understandings on CBM in deep coals through discussion of coal permeability and gas saturation, and specifically, the comparison of coal reservoir characteristics in the three wells. Based on the understandings from Linxing Block, we will extend our discussion to a more general perspective on CBM in deep coals through integrating the spot but important exploration results relevant to deep coals in the Junggar Basin, where wells of similar performance were seen.

2 Backgrounds and CBM well production characteristics

2.1 Backgrounds

Linxing Block, with areal extent of 2,530 km^2, is located across the Yishan slope and the Jinxi flexural fold belt, in the eastern margin of the Ordos Basin (Figure 1A). The Zijinshan igneous rock outcrops are to the east of the Block (Figure 1B, Gu et al., 2016).

The coal seams 8+9$^{\#}$ and 4+5$^{\#}$, belonging to Permian Taiyuan Formation and Shanxi Formation respectively (Figure 2), are the main CBM targets. This study focuses on coal seams 8+9$^{\#}$ in Permian Taiyuan Formation, because three CBM wells in deep coals are producing from these coal seams. Figure 1B is the map showing the burial depth of coal seams 8+9$^{\#}$. They are buried from about 700 m to more than 2,000 m in the block. Shallow coals take a limited areal extent in the northeastern corner of block and deep coals (depth>1,500 m) are distributed in most part of the block. The coal seams 8+9$^{\#}$, deposited in peat-swamp facies of delta environments (Li Y. et al., 2016; Li et al., 2017b), are laterally continuous with the thickness range of 3.6–15.4 m, and an average of 7.9 m.

Most wells in Linxing Block are commingled production wells from coal seams 8+9$^{\#}$ and/or coal seams 4+5$^{\#}$, and overlying tight sandstones. The production performance of the commingled production wells will not be analyzed in this paper, due to the complexity from gas/water bearing tight sandstones. It is impossible to extract any valuable information about gas saturation states of coal seams of 8+9$^{\#}$ from these wells' production performance. Only three vertical wells penetrating to deep coals, including wells LX-29, LXX-23–2 and LXX-24 (see Figure 1B for well locations), are producing from coal seams 8+9$^{\#}$. The production performance of the three vertical wells will be compared in the following.

Laboratory tested porosity, maceral composition and proximate analysis on coal samples taken from coal seams 8+9$^{\#}$, are found in Supplementary Appendix S1. These data

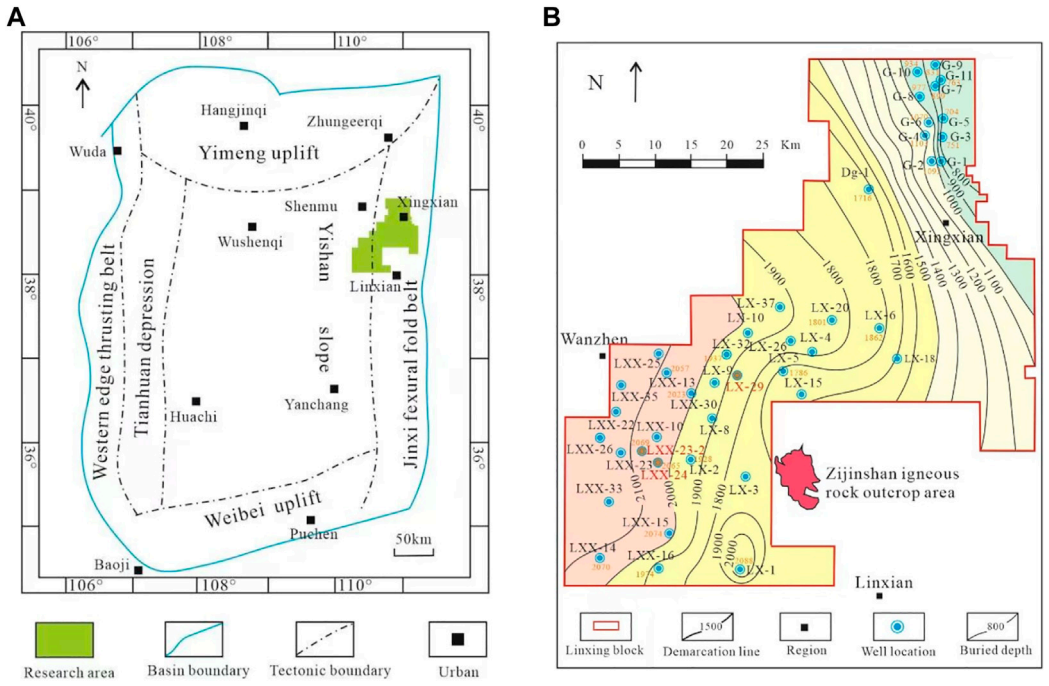

FIGURE 1
Location map **(A)**, burial depth of coal seams 8+9# **(B)**in Linxing Block.

will be used to analyze the influencing factors of coal sorption capacity.

In-situ gas content, methane compositional proportion (%), laboratory tested R_o (%), Langmuir parameters (air-dry basis) tested at formation temperature, on coal samples taken from coal seams 8+9#, are found in Supplementary Appendix S2. These data will be used to compare the Langmuir curves between shallow coals and deep coals, and to estimate gas saturation.

2.2 CBM well production characteristics

As mentioned above, three wells including LX-29, LXX-23–2 and LXX-24 (see Figure 1B for well locations), are producing from coal seams 8+9#. All the three wells were completed by hydrofracturing techniques with similar parameters. However, the wells have very different performance characteristics and can be lumped into two types (Figure 3).

1) Well LX-29 behaves as a normal CBM well that needs to pump out water before gas production. The coal seams 8+9# in well LX-29 are buried from 1,879.7 m to 1,907.7 m. Production began on 24 October 2017. The well was drained for up to 3 months before the onset of gas production (Figure 3A). Both the water production and gas production are very low, implying the permeability (no available data) is too low to produce any fluids in a significant amount.

2) Two wells, including LXX23-2 and LXX-24, have obtained high gas production without primary dewatering. These wells produced gas after hydraulic fracturing without installing any pump (Figures 3B,C).

Coal seams 8+9# in well LXX-23–2 are buried from 2,059.5m to 2,069.0 m. In April 2017, the coal seams 8+9# were hydro-fractured with slickwater. Gas production began after 3-day's flowing. The daily gas production from July 2017 to March 2018 was stable at 3,100–3,500 m^3 (Figure 3B), and the daily water production was less than 0.5 m^3 (water production curve is not shown in Figure 3B).

Coal seams 8+9# in well LXX-24, are buried from 2,013.4 m to 2,019.5 m. In November 2017, Coal seams 8+9# were hydro-fractured with slickwater and after only 2-day's flowing, gas began to produce. By September 2018, the daily gas production was stable at 3,200–3,600 m^3 (Figure 3C), and the daily water production was less than 1 m^3 (water production curve is not shown in Figure 3C).

The mechanism for the performance differentiation will be studied through discussion of permeability and saturation in deep coals (depth>1,500 m), and specifically, the comparison of coal reservoir characteristics in the three wells.

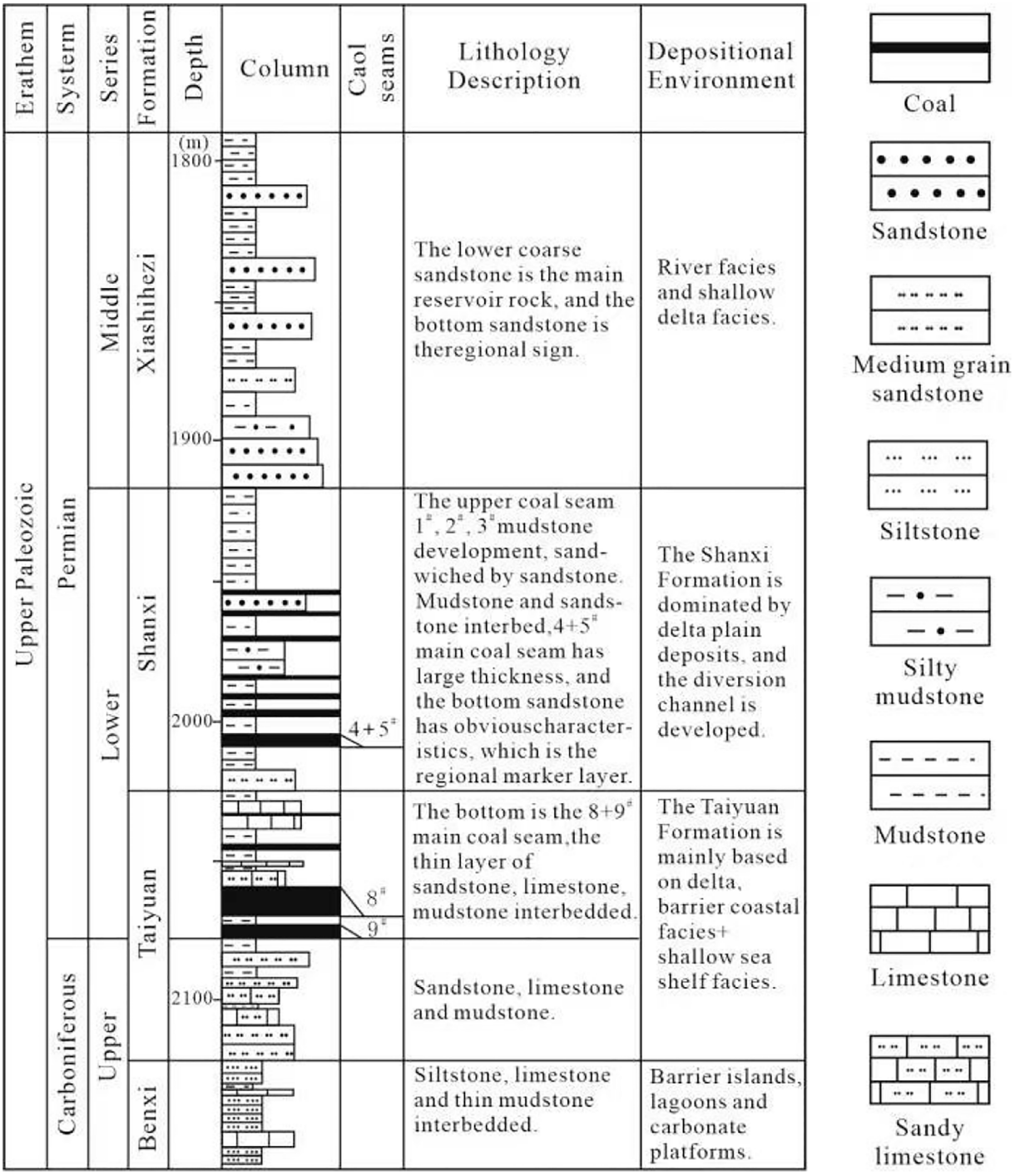

FIGURE 2
Stratigraphic column of coal measures (Li et al., 2017b; Shao et al., 2018) in Linxing Block.

3 Permeability in deep coals

Porosity data of coal samples taken from coal seams 8+9# are available in deep coals (see Supplementary Appendix S1). The location of wells used to collect samples can be found in Figure 1B. Figure 4A shows coal porosity variation with depth in deep coals. No obvious trend in porosity can be observed from 1,712.7 m to 2,088.1 m. The porosity values

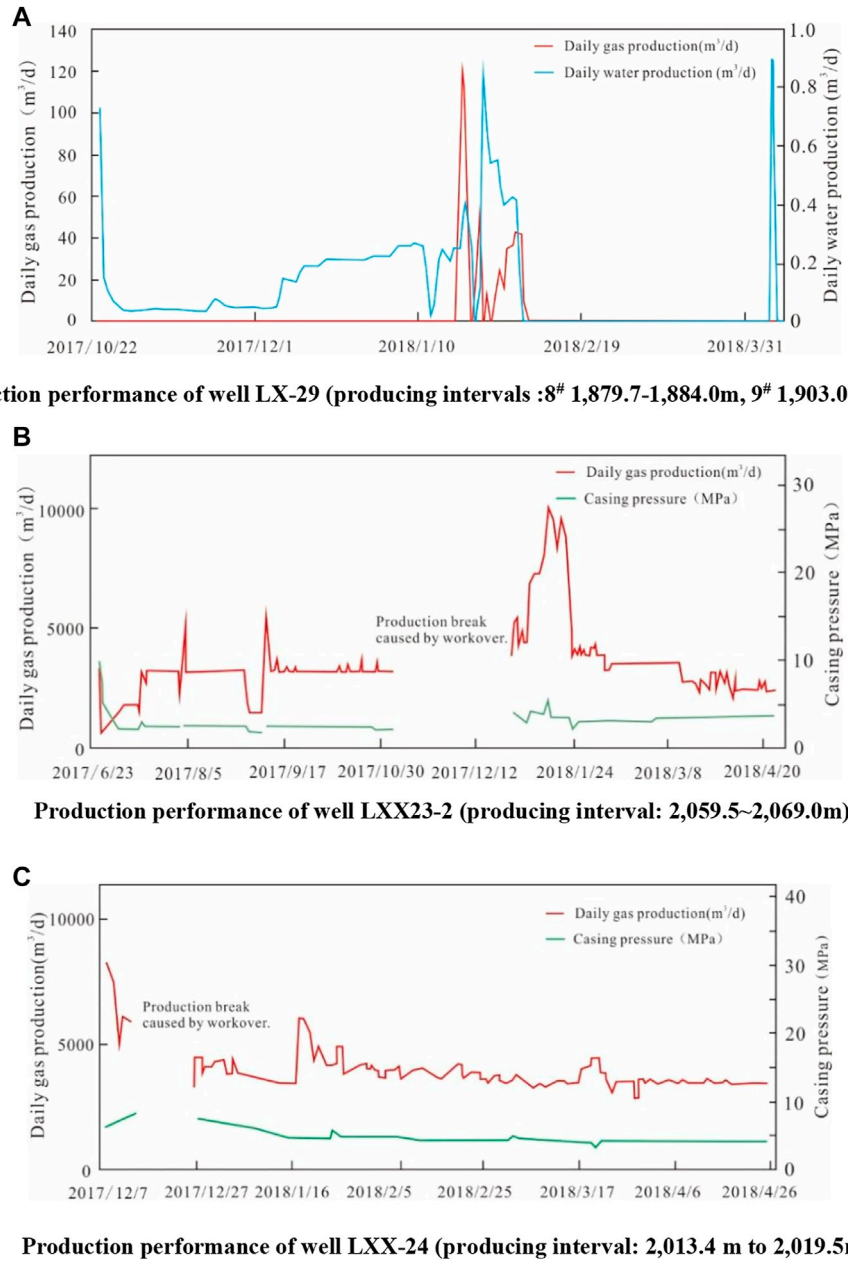

FIGURE 3
Production performance of CBM wells in Linxing CBM Block. **(A)** Production performance of well LX-29 (producing intervals :8# 1,879.7-1,884.0 m, 9# 1,903.0-1,907.7 m). **(B)** Production performance of well LXX23-2 (producing interval: 2,059.5~2,069.0 m). **(C)** Production performance of well LXX-24 (producing interval: 2,013.4 m to 2,019.5 m). (All the three wells are producing from coal seams 8+9# in Taiyuan Formation. Wells LXX23-2 and LXX24 had no water production. These wells were put on production after hydraulic fracturing without water pumping out).

range from 3.14 to 6.79%, with an average of 4.70% (Figure 4A).

The only one injection/falloff test of coal seams 8+9# in the block was done in well LXX-22 (see Figure 1B for well location). The interpretation indicates that the permeability of coal seams 8+9# is of 0.8×10^{-2}mD for the tested interval of 2,007.0–2,020.0 m.

Coal permeability is strongly stress-dependent. In laboratory studies, measured permeability of coal samples under different stress, in general, declined exponentially with increasing effective stress (Pomeroy and Robinson, 1966; Somerton et al., 1975; McKee et al., 1988a; Sparks et al., 1995; Bustin, 1997; Meng and Li, 2013; Bottomley et al., 2017). Due to the rising effective

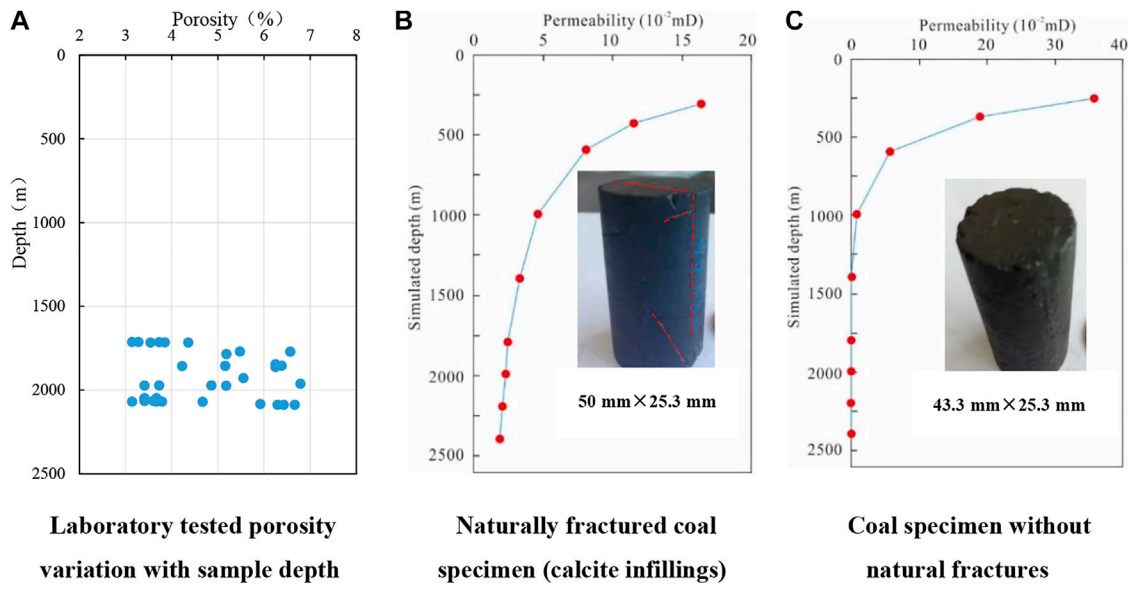

FIGURE 4
Laboratory tested porosity **(A)**, and results of experimental permeability test simulating underground stress conditions with simulated depth **(B)** and **(C)**. (Coal samples were taking from mines in or near Linxing Block)

stress with increasing depth, an exponential relation between coal permeability and depth was previously identified in the Piceance, San Juan, and Black Warrior basins, United States (McKee et al., 1988a; 1988b), in major coalbed methane (CBM) basins of Australia (Enever et al., 1994; Enever and Hennig, 1997; ScottMazumder and Gibson, 2013; Mukherjee and CopleyEsterle, 2017), as well as in some CBM blocks in Qinshui and Ordos basins, central China (Meng et al., 2011; Tao et al., 2014; Liu et al., 2016).

For simulating experimentally coal permeability values with increasing depth, eight blocky coal samples were taken from mines in or near Linxing Block, in eastern margin of the Ordos Basin, and prepared to cylindrical specimens. Among the eight specimens, only one is naturally fractured (fractures are infilled with calcite) and the measured permeability values in deep coals (simulated depth >1,500 m) are in the order of 10^{-2}mD (Figure 4B). No natural fractures or cleats were observed in all the other seven specimens, and the measured permeability values, in deep coals (simulated depth >1,500 m), are approaching to zero. Figure 4C presents the experimental results of one of these seven specimens. Comparing Figures 4B, C, difference in simulated permeability volume in depth is remarkable.

In the experimental permeability test simulating underground stress conditions, permeability values were measured using helium gas when axial pressure and confining pressure were loaded simultaneously on the tested specimen, with a lateral pressure ratio of 0.7. This ratio corresponds to the average lateral stress ratio in deep coals in eastern margin of the Ordos basin (Li et al., 2018; Wen et al., 2019). More concretely, the axial pressure and confining (lateral) pressure are determined by:

$$\sigma_v = \rho g h = 2.3{*}9.8h = 22.54h \quad (1)$$

$$\sigma_h = 0.7\sigma_v = 15.778h \quad (2)$$

where, $\sigma_v$and$\sigma_h$are axial pressure and confining (lateral) pressure, MPa, respectively; h is the simulated depth, 10^3 m.

For a simulated depth, for example, of 2000 m, in Figures 4B, C, an axial pressure of 45.08 MPa and a confining (lateral) pressure of 31.56 MPa are adapted for the tri-axial test.

Notice that our laboratory tested permeability values of the naturally fractured specimen (Figure 4B) are in agreement, from (simulated) depth 1,524 m (5,000 ft) to 1,829 m (6,000 ft), with the theoretically estimated values through Kozeney-Carman equation in Mckee et al. (1988a, their Figure 7), although the permeability values are very different in shallow (simulated) depths (<1,000 m) in the two comparative cases.

The experimental results shown in Figures 4B,C indicate that the permeability in deep coals is not only influenced by *in-situ* stress, but also by coal body structure. Coal-body structure, classified as normal, cataclastic, granular and mylonitic types in China's CBM applications (GB/T 30050, 2013), is an indicator of tectonic deformation degree that coals have been experienced. From normal to mylonitic types, the deformation gets stronger. Compared with normal type, cataclastic type contributes to permeability, while granular and mylonitic types destruct permeability (Kang et al., 2017).

TABLE 1 Statistical comparison of coal-body structure between shallow and deep coals in Linxing Block.

Shallow coals (depth<1,100 m)			Deep coals (depth>1,600 m)		
Structure type	Frequency (%)	Sum (%)	Structure type	Frequency (%)	Sum (%)
Normal	8.64	30.86	Normal	20.69	96.55
Cataclastic	22.22		Cataclastic	75.86	
Granular	32.10	69.14	Granular	1.15	3.45
Mylonitic	37.04		Mylonitic	2.30	

Notice: Totally 168 coal-body structure description records of cores in Linxing Block were collected. Among the 168 records, 81 records were assigned to shallow coals (<1100 m) and 87 records were assigned to deep coals (>1600 m).

TABLE 2 Logging Interpretation results for coal seams 8+9# and average daily gas production in wells LXX 23–2 and LXX-24.

Well	Top depth (m)	Bottom depth (m)	Thickness (m)	Porosity (%)	Permeability (10^{-2}mD)	Average daily gas production (m^3/d)
TB-23–2	2,059.5	2,069.0	9.5	4.3	1	3,181
TB-24	2,013.40	2,019.50	6.1	3.9	6	3,942

Due to the fact that cataclastic type is the predominant coal-body structure type (75.86%) in deep coals in Linxing Block (Table 1), it is believed that the permeability values in deep coals are probably in the order of 10^{-2}mD according to Figure 4B.

Logging interpretations show that the permeability values of coal seams 8+9# in wells LXX23-2 and LXX-24 are of 1×10^{-2}mD and 6×10^{-2} mD respectively (Table 2), which are in agreement with the experimental results from naturally fractured specimen (Figure 4B).

Permeability data from diverse sources presented above, including results from experimental permeability test simulating underground stress conditions, indicate that the permeability values of coal seams 8+9# in LXX23-2 and LXX-24 are probably in the order of 10^{-2}mD. The permeability value of coal seams 8+9# in well LX-29 is inferred to be in the same order or even a little higher, considering that the burial depth of coal seams 8+9# in this well is of 1,879.7–1,907.7 m, while the burial depths of coal seams 8+9# in wells LXX23-2 and LXX-24 are respectively of 2,059.5–2,069 m and 2,013.4–2,019.5 m. However, the production performance of wells LXX23-2 and LXX-24 is very different from that of well LX-29 (Figure 3). Besides permeability, gas saturation is another vital parameter to be considered.

Lacking test data of *in-situ* gas content and Langmuir parameters in the three wells, gas saturation values of coal seams 8+9# in these wells cannot be estimated directly. The gas saturation states of coal seams 8+9# in the three wells will be inferred from gas saturation distribution maps drawn from data in other wells in the block.

4 Gas saturation in deep coals

4.1 Comparison of Langmuir curves between shallow coals and deep coals

In-situ gas sorption capacity can be described by Langmuir equation (Langmuir, 1918):

$$V_t = V_L \times P/(P_L + P) \quad (3)$$

where, P is the formation pressure, MPa; V_L (m^3/t) and P_L (MPa) are the Langmuir volume and Langmuir pressure respectively, tested at formation temperature (°C); V_L (m^3/t) represents the maximum sorption capacity at formation temperature (°C) when pressure increases to infinite, which is called hereinafter sorption capacity.

Previous studies have demonstrated that the sorption capacity (V_L) decreases with increasing temperature, while P_L increases with increasing temperature (Ottiger et al., 2010). At a preset temperature, the sorption capacity increases with increasing vitrinite (Lamberson and Bustin, 1993; Clarkson and Bustin, 1996). Moisture is a competing factor to gas adsorption, which reduces the sorption capacity (Joubert et al., 1973; Yalçin and Durucan, 1991; Krooss et al., 2002). Mineral matter or ash is a diluent to the sorption capacity (Lamberson and Bustin, 1993; Crosdale et al., 1998). The sorption capacity increases with increasing rank (Levy et al., 1997; Bustin and Clarkson, 1998; Laxminarayana and Crosdale, 1999).

We initially focus on the differences, regarding the influencing factors of sorption capacity, between deep coals and shallow coals. Figure 5A demonstrates that deep coals

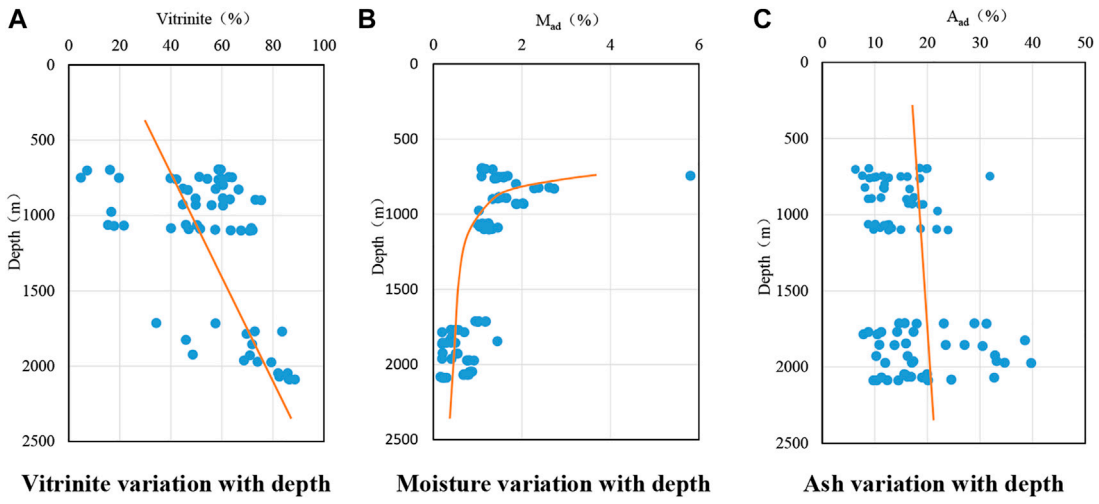

FIGURE 5
Diagram showing vitrinite **(A)**, moisture **(B)** and ash variations **(C)** with depth.

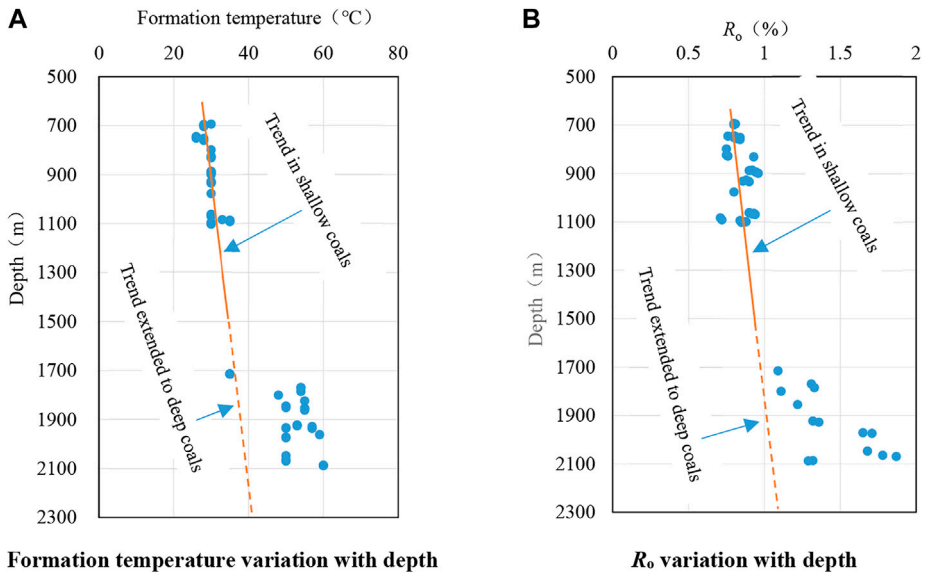

FIGURE 6
Diagram showing variations of formation temperature **(A)** and R_o **(B)**, with depth in Linxing Block.

have higher vitrinite than shallow coals. The difference may be caused by coal deposition environments and coal rank variation (Li et al., 2017a). Figure 5B demonstrates that moisture decreases with increasing depth. Deep coals generally have lower moisture than shallow coals. Figure 5C demonstrates that ash is almost random from shallow coals to deep coals.

Practically, formation temperature and coal rank both related to depth (Figure 6), can be considered as the two most important parameters determining Langmuir curves. In Langmuir curve comparison between shallow coals and deep coals, other influencing factors of sorption capacity are less important, since these factors either are related more or less to coal rank (such as vitrinite and moisture), or almost can be considered as random (such as ash) with increasing depth (Figure 5).

As can be seen, from Figure 6, that either the formation temperature (Figure 6A) or the coal rank (Figure 6B) in deep coals, deviate abnormally from the trend lines determined by shallow coals. The high-value anomalies in formation

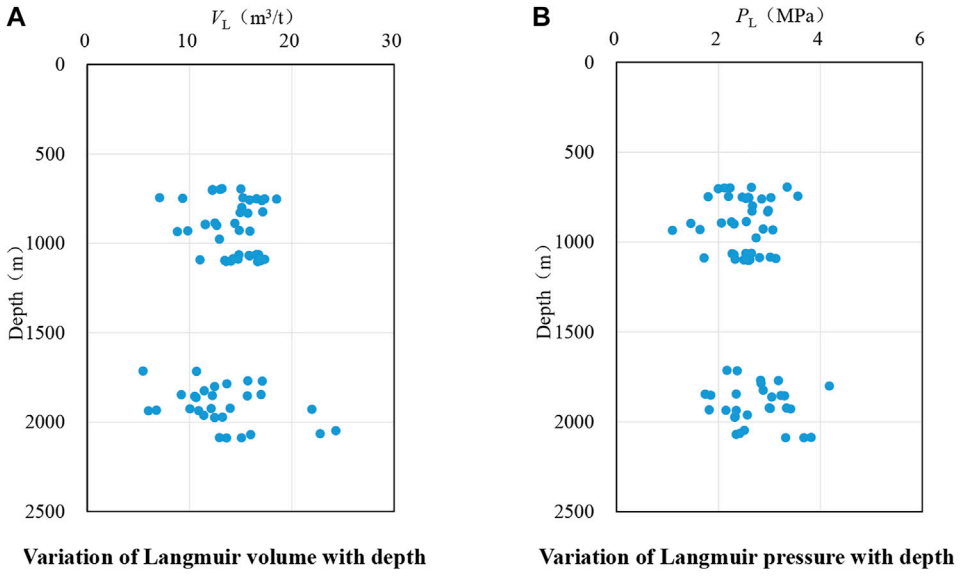

FIGURE 7
Diagram showing variations of Langmuir volume (sorption capacity) **(A)**, Langmuir pressure **(B)** with depth in Linxing Block.

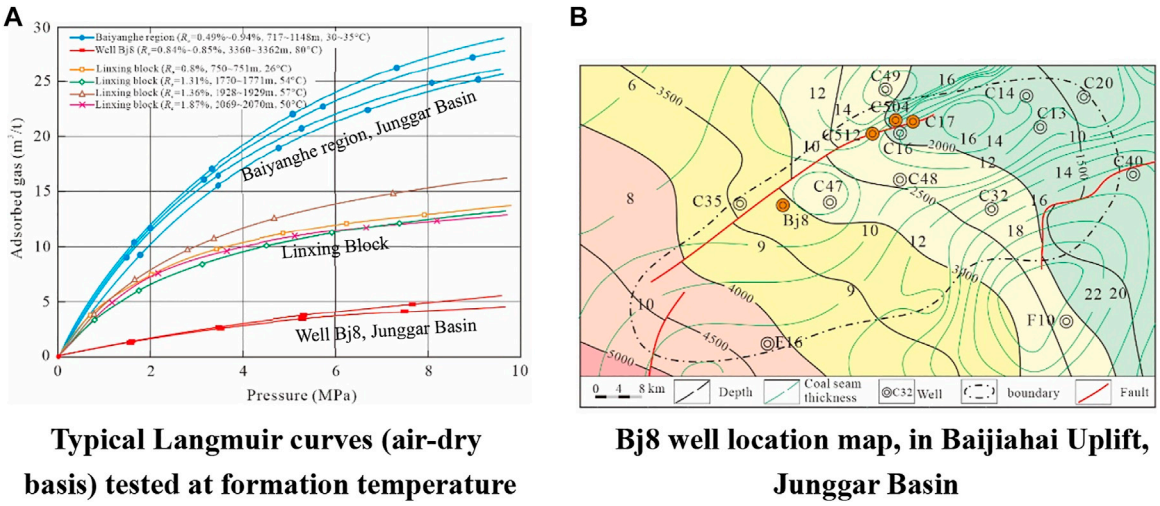

FIGURE 8
Typical Langmuir curves (air-dry basis) **(A)**, tested at formation temperature. In different depths in Linxing Block and in the Junggar Basin, and Bj8 well location **(B)**.

temperature and coal rank in deep coals are due to the Zijinshan igneous intrusion (Fu et al., 2016). Figure 6 indicates also that the shallow coals have not been influenced by the igneous intrusion. The sorption capacity relies on several factors such as vitrinite content, vitrinite reflection and temperature. The sorption capacity increases with vitrinite content and vitrinite reflection that increase with increasing depth (Figure 5A, Figure 6B), and decreases with temperature that increases with increasing depth (Figure 6A). Two opposite, increasing and decreasing factors of the sorption capacity make it almost stable with increasing depth (Figure 7A; Figure 8A).

The combined effect of abnormally increased temperature (reduction of sorption capacity), and increased rank and increased vitrinite content (increase of sorption capacity) in

deep coals, results in almost undifferentiated sorption capacity (Langmuir volume) and Langmuir pressure between deep coals and shallow coals, as shown in Figure 7.

Figure 8A shows that the Langmuir curves in deep coals are substantially similar to that in shallow coals in Linxing Block. Figure 8B shows the well location of Bj8.

However, according to our observations from several cases which are absent of influence of igneous intrusion, coal rank does not necessarily increase obviously with increasing depth, although the formation temperature does increase, following the geothermal gradient, with increasing depth. In these cases, the Langmuir curves in deep coals may be very different from that of shallow coals. As an example, Langmuir curves in shallow coals (Jurassic Badaowan Formation coals in Baiyanghe region) and in deep coals (Jurassic Xishanyao Formation coals in well Bj8, Figure 8B for well location) are very distinguishable in the Junggar Basin, western China (Figure 8A). In contrast to the case in Linxing Block, the sorption capacity (V_L) of deep coals, in the Junggar Basin, is highly reduced in comparison with that of shallow coals. The average sorption capacity (V_L) of four Jurassic Badaowan Formation coal samples, in shallow coals, is of about 26m^3/t (air-dry basis). The four samples ranked as sub-bituminous to high bituminous (R_o: 0.49–0.94%), were taken from wells in Baiyanghe region in depth interval of 717.0–1,148.0 m with formation temperature of 30°C–35°C. Remarkably, the average sorption capacity of two Jurassic Xishanyao Formation coal samples, in deep coals, is reduced to only of 6m^3/t (air-dry basis). The two samples ranked as high volatile bituminous (R_o: 0.84%–0.86%), were taken from well Bj8 in depth interval of 3,360.4–3,363.2 m with formation temperature of 80°C.

The implication of Langmuir curve differentiation between shallow coals and deep coals in the Junggar Basin will be discussed later.

4.2 Gas saturation distribution

Gas saturation is defined as:

$$S_g = 100\% \times V_r / V_t \quad (4)$$

where, V_r is the *in-situ* gas content, m^3/t, measured usually through canister desorption method; V_t is the *in-situ* gas sorption capacity (calculated at formation temperature and pressure), m^3/t. The *in-situ* gas sorption capacity (V_t), can be estimated by Langmuir Equation 3.

In reality, the *in-situ* gas content includes methane and other gases (such as carbon dioxide and nitrogen), whereas the Langmuir parameters are usually determined by using pure methane. Direct use of Equation 4 may induce over-estimation of gas saturation (Seidle, 2011). For precluding the multi-component impact on gas saturation estimation, the following equation is used for methane saturation estimation:

$$S_m = 100\% \times V_{rm} / V_{tm} \quad (5)$$

where, V_{rm} is the *in-situ* methane content (m^3/t) that can be estimated from *in-situ* gas content multiplied by the methane compositional proportion (%); V_{tm} is the *in-situ* methane sorption capacity (m^3/t) (calculated at formation temperature and pressure).

Notice that the methane saturation in Equation 5 is only a precise estimation for gas saturation. The term "gas saturation" is still used hereinafter as a general expression, except where the methane saturation is specifically referred.

By using Equation 5, the methane saturation was estimated for coal samples with *in-situ* gas content and Langmuir test data. For comparison, methane saturation estimation results and related parameters, in shallow coals (694.2–1,102.8 m depth interval, 43 coal samples) and in deep coals (1,716.2–2,088.3 m depth interval, 28 coal samples) in Linxing Block, are set forth in Supplementary Appendix S2. All the coal samples in Supplementary Appendix S2 were taken from coal seams 8+9#. The location of wells used to collect samples can be found in Figure 1B. The formation pressure (column 10 in Supplementary Appendix S2) for each coal sample is estimated as the product of the sample burial depth and the average pressure gradient of 0.9 MPa/100 in the block (Li et al., 2018). The formation pressure so estimated may bear some bias. This bias does not, however, influence the reliability of saturation estimation, since the formation pressure in deep coals (depth>1,500 m) is generally higher than 10 MPa beyond which the *in-situ* sorption capacity is almost stable with increasing formation pressure (Figure 8).

As can be seen, from column 12 in Supplementary Appendix S2, that shallow coals (694.2–1,102.8 m depth interval) are gas undersaturated with methane saturation from 11.72% to 64.48%, while the methane saturation in deep coals (1,716.2–2,088.3 m depth interval) is from 32.10% to 197.10%. By using the estimated methane saturation in column 12 in Supplementary Appendix S2, three alternative maps are drawn to show methane saturation distribution in coal seams 8+9# in Linxing Block (Figures 9A–C).

Since there are often two or more sample saturation values and the sample number is limited in individual wells, uncertainty exists in saturation assignment to the wells. Figures 9A–C are drawn by using the maximum sample saturation value, the average sample saturation value and the minimum sample saturation value in individual wells, respectively. Correspondingly, Figures 9A–C represent the optimistic, probable and pessimistic scenarios of methane saturation distribution respectively, based on available data. Figure 9D is the map of gas content that confirms the probable scenario (Figure 9B), considering that the Langmuir curves are

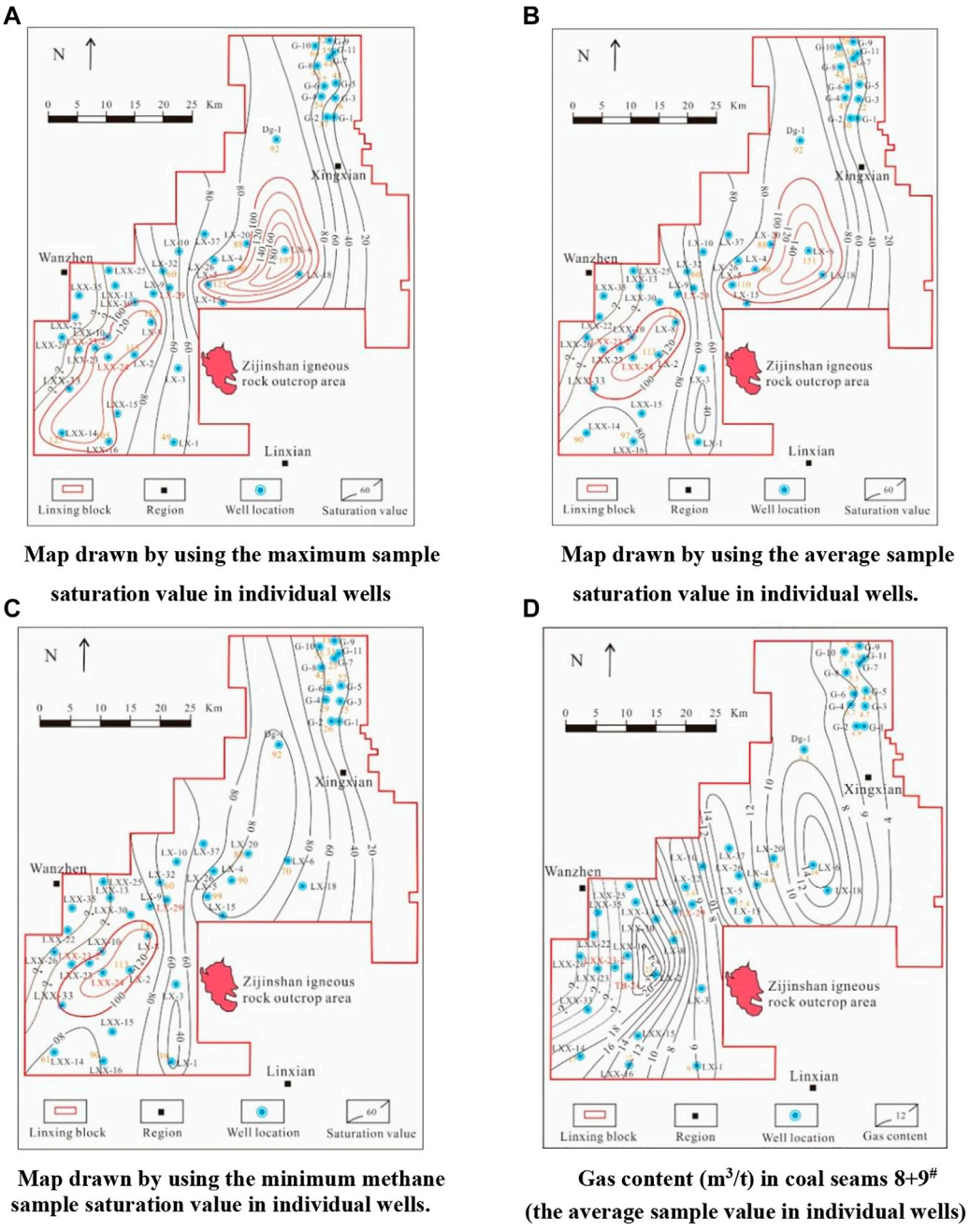

FIGURE 9
Alternative maps showing methane saturation in coal seams 8+9 # **(A–C)** and gas content **(D)** in Linxing Block (oversaturation zones are marked by red contour). (Note: A faulted zone along the line of well LX-10 and well LX-1, can be seen clearly in Li et al., 2018, their Figure 1, which corresponds to a low methane saturation zone in **(A–C)**.

substantially similar in different depths in Linxing Block (Figure 8).

Figures 9A–C demonstrate that oversaturation is not pervasive in deep coals. Rather, two oversaturation zones likely exist (Figure 9B), one in the center of the block and the other in the west of the block. Notice that the drilling cores from coal seams 8+9# in Well LXX-33 were observed with very intense and fast gas flow out when immerged in water, indicating that the coal seams 8+9# in this well bear *in-situ* free gas and the coal reservoirs are oversaturated. This well is contoured within the west oversaturation zone in Figures 9A–C, although no saturation value is estimated due to lack of coal sample test data in this well.

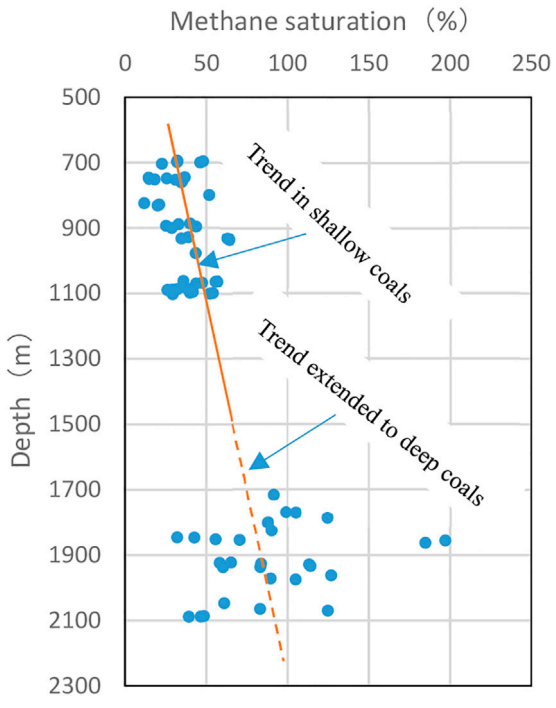

FIGURE 10
Diagram of methane saturation with depth, coal seams 8+9, Linxing Block.

Importantly, the two wells LXX23-2 and LXX-24 that produce gas directly without primary dewatering and have stable and high gas rates (>3,000m^3/d), can be both with great certainty delineated within the west oversaturation zone on any map in Figures 9A–C. While the well LX-29 that produce very low gas (<120 m^3/d) after about 3 months of dewatering, can be evidently contoured outside the oversaturation zones on any map in Figures 9A–C. Moreover, the diagram of gas (methane) saturation with depth shows clearly that there exist oversaturated and undersaturated coal reservoirs in deep coals (Figure 10). The mechanism for oversaturation will be discussed later.

5 Discussion

5.1 Mechanism for production performance differentiation

Well LX-29, producing gas from coal seams 8+9$^{\#}$ with a net coal thickness of 9m, is outside the methane oversaturation zones (Figures 9A–C). In undersaturated coals, the fluid phases are assumed to include irreducible water, free water, adsorbed gas, and possibly minor solution gas. Primary dewatering must be performed to reduce reservoir pressure to below the critical desorption pressure for gas desorption and production. Because of low permeability (in the order of 10^{-2}mD) and permeability sensitivity to increasing effective stress during dewatering, the depression cone cannot be extended far from the borehole, resulting in very low gas rates (<120 m^3/d) in this well.

It is very exciting that the two wells LXX23-2 and LXX-24 have reached high and stable gas rates (>3,000m^3/d), although the permeability values of coal seams 8+9$^{\#}$ are as low as in the order of 10^{-2}mD. Notice that the thickness of producing coal seams 8+9$^{\#}$, in wells LXX23-2 and LXX-24, is of 9.5 and 6.1 m respectively.

As shown above, coal seams 8+9$^{\#}$ in wells LXX23-2 and LXX-24 are almost certain to be gas oversaturated. In oversaturated coals, the fluid phases are assumed to include irreducible water, minor free water, adsorbed gas, minor solution gas and *in-situ* free gas. *In-situ* free gas is ready to migrate to the borehole, and the forerunner flow out of the *in-situ* free gas draws reservoir pressure down, resulting in the desorption of adsorbed gas (in saturated state) immediately. Water production is limited by high relative permeability of gas phase and low water content in deep coals (see Figure 5B). Gas is much easier to migrate than water, resulting in high gas production and very low or negligible water production.

The above interpretation is a simplified description of the real-world complex two-phase (water and gas) or even three-phase (water, gas and coal fines) flow in oversaturated coals. Works need to be done for better understanding the flowing phases at the beginning of production with different *in-situ* free gas saturation and in different coals. Different coals may have very differentiable relative permeability curves that are difficultly tested in laboratory with comparable results, although many scholars have done a lot of works for understanding coal relative permeability with the selected coals in their study cases (e.g., Conway et al., 1995; Meaney and Paterson, 1996; Shedid and Rahman, 2009). However, a conclusion can be drawn as that gas saturation states (undersaturation or oversaturation) are the most vital factor determining production performance of CBM wells in deep coals. High gas rates (>3,000m^3/d) can be achieved only from oversaturation zones in deep coals with permeability values being as low as in the order of 10^{-2}mD, in Linxing Block.

The term “oversaturated coals” used in this paper represents the coals which are gas oversaturated and bearing *in-situ* free gas, and can also bear minor free water in macroscopic pores (>50nm, according to IUPAC, 1982) and fractures. The term “dry coals” is frequently used by many scholars for representing no water CBM wells in shallow coals (Bastian et al., 2005; Hoch, 2005; Seidle, 2011). Shallow dry coals in Horseshoe Canyon, Alberta may also bear *in-situ* free gas (Bustin and Bustin, 2011). There may exist different mechanism for the occurrence of *in-situ* free gas between shallow coals and deep coals. The shallow dry coals in Horseshoe Canyon, Alberta, are characterized with extremely

low formation pressure (Bastian et al., 2005), this is evidently not the case in deep coals in Linxing Block.

5.2 Mechanism for oversaturation in deep coals

5.2.1 Igneous intrusion-driven oversaturation mechanism

Linxing Block is near the Zijinshan igneous rock outcrop area. The Zijinshan igneous intrusion took place mainly during late Jurassic to early Cretaceous (Tang et al., 2000; Chen et al., 2012), which had caused secondary gas generation (Tang et al., 2000). Gas supplied by the secondary gas generation might have increased the gas saturation to oversaturated state within the influence halo of the igneous intrusion in deep coals.

After crystallization and solidification of the intruded magma, two stages of uplift-cooling, including the early slow stage from 120 Ma (early Cretaceous) to 30 Ma (early Oligocene), and the later fast stage initiated at about 30 Ma, have happened (Chen et al., 2012). During the uplift-cooling stages, many small faults outgoing from the intrusion massif and a faulted zone along the western boundary of the intrusion massif, almost in N-S direction, have developed (Wu et al., 2018). This faulted zone, along the line of well LX-10 and well LX-1 in Figure 9, can be seen clearly in Li et al. (2018, their Figure 1). As conduits of gas escape and migration, the small outgoing faults and the faulted zone might have decreased gas saturation to an undersaturation state around the intrusion massif and along the faulted zone (for example, in Well LX-1). The previously-formed pervasive oversaturation area, within the influence halo of the igneous intrusion, might have been either separated into two oversaturation zones (Figures 9A,B) or reduced to the present-day west oversaturation zone (Figure 9C).

Figure 10 shows that gas saturation in shallow coals has a general increasing trend (solid line) with depth. Remind that the shallow coals have not been influenced by the igneous intrusion. With the increasing trend in shallow coals being extended to deep coals, it can be perceived that the saturation in deep coals consists of high oversaturation and deep undersaturation superimposed on an increasing saturation trend (dashed line) related to depth. The trend line is persistent from shallow coals, as if the igneous intrusion had not happened. This implies that beyond a certain depth, saying about 2200m, the coals could be yet oversaturated while the influence of igneous intrusion is absent. In fact, a persistent increasing saturation trend with depth was reported as well in Yanchuannan Block, eastern margin of the Ordos Basin, by Hou et al. (2016).

In Figure 10, the points characterized by high oversaturation to the extreme right of the trend line (dashed line) can be related to gas supplementation by the secondary gas generation mentioned above. While the points characterized by deep undersaturation to the extreme left of the trend line can be related to gas escape induced by the small outgoing faults and the faulted zone mentioned above.

The oversaturation mechanism in Linxing Block can be termed as igneous intrusion-driven oversaturation, which is characterized by secondary gas generation and supplementation to deep coals that have substantial similar Langmuir curves to that of shallow coals (Figure 8). Secondary gas generation necessary to supplement deep coals, superimposed on the persistent increasing saturation trend with depth, results in oversaturation (Figure 10). However, faults are destructive to oversaturation and may excite deep undersaturation in deep coals.

5.2.2 Sorption capacity-driven oversaturation mechanism

Importantly, the igneous intrusion-driven oversaturation mechanism is not the only mechanism in deep coals. Oversaturation may occur in deep coals due to the reduced sorption capacity shown above in the Junggar Basin (Figure 8A). Most coals have generated greater amounts of methane than they have the capacity to retain at some point in the high volatile bituminous rank range (if not earlier) (Levine, 1993). Due to the reduced sorption capacity in deep coals, more free gas may be released from coals after adsorption saturation, and kept completely or partially in coals as *in-situ* free gas compressed by increased pressure in deep coals, and coal reservoirs are thus oversaturated. For example, in well BJ8 in the Junggar Basin, the gas saturation in Jurassic coals (3,360.4–3,363.2 m) was estimated to be of 213.78–220.08% (Sun et al., 2017). Moreover, two nearby wells named Cai504 and Cai17, have been found to produce gas, without primary dewatering, from Jurassic coal seams buried in depth interval of 2,567.0–2,828.8 m. The stable gas rates from the two wells are of 2,300 m^3/d and 8,870 m^3/d, respectively (Zhi and Xue, 2013).

In the Junggar Basin, the oversaturation mechanism in deep coals can be termed as sorption capacity-driven oversaturation mechanism, which is characterized by more free gas released from coals after adsorption saturation, due to reduced sorption capacity in deep coals (Figure 8A). The reduction of sorption capacity is caused by the formation temperature-coal rank configuration in the Junggar Basin, which is characterized by a normal increase of formation temperature accompanied by a subtle coal rank increase with depth. Remind that in the Junggar Basin, from depth interval of 717–1148 m (in Baiyanghe region) to depth interval of 3,360.4–3,363.2 m (well Bj8), the formation temperature increases from 30–35°C–80°C, whereas coal rank (R_o) varies from 0.49–0.94% to 0.84–0.86%. The average sorption capacity (V_L) is dramatically reduced from about 26 m^3/t (air-dry basis) to about 6m^3/t (air-dry basis).

5.3 Perspective on CBM in deep coals

Oversaturation may exist more frequently in deep coals in comparison with in shallow coals, mostly due to the sorption

capacity-driven oversaturation mechanism. The formation temperature-coal rank configuration in the Junggar Basin, is not unique according to our preliminary observations elsewhere. This phenomenon has not been well documented and interpreted. Further works should be done in coal burial and thermal history studies. Notice that in the Aroma Basin, United States, the Hartshorne coal rank is interpreted as related to the maximum burial depth and accompanied heat flows in geological history and does not follow the present-day burial depths (Cardott, 2013).

Moreover, the weaker tectonic deformation and uplifting experienced by deep coals in comparison with shallow coals, favors gas preservation and oversaturation in deep coals. As can be seen from Table 1, more than half of coals are of granular and mylonitic types (69.14%) indicating a stronger tectonic deformation and related stronger uplifting in shallow coals. However, the coal-body structure is mostly of normal and cataclastic types (96%) in deep coals indicating a weaker tectonic deformation and related weaker uplifting. Although Table 1 is based on the coal-body structure data from Linxing Block, this observation may be generalized at least to most of the compressional basins. In fact, compressional tectonic force exerts on the margin of basins and attenuates to the center of the basins (Wang, 1992).

Our experimental permeability test simulating underground stress conditions demonstrates that the permeability values in deep coals are low (in the order of 10^{-2}mD or even lower). Kuuskraa and Wyman (1993) proposed a model predicting much higher permeability values in deep coals, specifically in low and moderate stress regions, but no supporting data from either experimental results or field were presented by them. In low permeability deep coals, exploring oversaturation areas should be a primary concern for CBM development in deep coals. It appears that in most large, tectonically compressed coal basins, there is a critical depth beyond which the oversaturation areas could occur. This critical depth is constrained by geothermal gradient, "coal rank gradient", formation pressure gradient and possibly along with other less important factors. The combined geothermal gradient and "coal rank gradient" may be the most predominant factors.

The oversaturation in deep coals provides opportunities and challenges for CBM development. Because of limited CBM drilling activities in deep coals, the understandings about the CBM in deep coals are limited. Many geological, geophysical and engineering issues related to CBM development in deep coals are to be studied while more data will be available through enhanced drilling in the future. These issues include, but not limited to: 1) The critical burial depth at which the oversaturation areas occur in different basins; 2) The conditions for basins in which coal rank has subtle increase from shallow coals to deep coals; 3) Geological conditions of oversaturation areas below the critical depth; 4) Geophysical technologies for identification and evaluation of oversaturated reservoirs in deep coals; 5) *In-situ* stress and permeability in deep coals; 6) Optimization of fracturing design and technologies; 7) Production regime control and technologies from deep coals.

6 Conclusion

From our study on the CBM field in Linxing Block, along with spot but important exploration results relevant to deep coals in the Junggar Basin, the following conclusions can be drawn:

1) Permeability data from diverse sources, including results of experimental permeability test simulating underground stress conditions, indicate that the permeability values of coal seams 8+9# in deep coals are probably in the order of 10^{-2}mD in Linxing Block.
2) Studies on gas saturation distribution reveal that high gas rates (>3,000 m^3/d) can be achieved only from oversaturated reservoirs with such low permeability in the order of 10^{-2}mD in Linxing Block.
3) Two types of oversaturation mechanism, including igneous intrusion-driven oversaturation and sorption capacity-driven oversaturation, exist in deep coals. The former is restricted to regions/blocks influenced by igneous intrusion such as in Linxing Block, and characterized by secondary gas generation and supplementation to deep coals that have substantial similar Langmuir curves to that of shallow coals. The latter may play in deep coals that are not influenced by igneous intrusion such as in the Junggar Basin and is characterized by more free gas released from coals after adsorption saturation, due to reduced sorption capacity in deep coals.
4) The reduction of sorption capacity in deep coals is caused by the formation temperature-coal rank configuration in the Junggar Basin, which is characterized by a normal increase of formation temperature accompanied by a subtle coal rank increase with depth. This configuration in the Junggar Basin is not unique. Oversaturation may exist more frequently in deep coals in comparison with in shallow coals, due to mostly the sorption capacity-driven oversaturation mechanism.
5) The weaker tectonic deformation and uplifting experienced by deep coals in comparison with shallow coals, is evidenced by statistical comparison of coal-body structure between shallow and deep coals in Linxing Block. This observation may be generalized at least to most of the compressional basins. The weaker tectonic deformation and uplifting favors gas preservation and oversaturation in deep coals.
6) Generally, the permeability is low in deep coals, due to the increased effective stress, and exploring oversaturation areas should be a primary concern for CBM development. It appears that in most large, tectonically compressed coal basins, there is a critical depth beyond which the oversaturation areas could occur, presenting opportunities and challenges for CBM development. Because of limited CBM drilling activities in deep coals, the understandings of

the CBM are limited. Many geological, geophysical and engineering issues related to CBM development in deep coals are to be studied while more data will be available through enhanced drilling in the future.

Data availability statement

The original contributions presented in the study are included in the article/Supplementary Material, further inquiries can be directed to the corresponding author.

Author contributions

YK offered a main idea to this research and accomplish this paper mainly. YH, BZ and ZH take part in some research and write this paper. SJ and YM help collect some data and put some useful advice for this paper.

Funding

This work was financially sponsored by National Science and Technology Major Projects of China (2016ZX05041-001 and 2016ZX05044-005). The authors would like to thank all the group members for providing valuable advice to accomplish this paper.

Conflict of interest

Author BZ was employed by the company China United Coalbed Methane Corporation, Ltd. Author YM was employed by the company Schlumberger.

The remaining authors declare that the research was conducted in the absence of any commercial or financial relationships that could be construed as a potential conflict of interest.

Publisher's note

Supplementary material

The Supplementary Material for this article can be found online at: https://www.frontiersin.org/articles/10.3389/feart.2022.1031493/full#supplementary-material.

References

Bastian, P. A., Wirth, O. F. R., Wang, L., and Voneiff, G. W. (2005). "Assessment and development of dry Horseshoe Canyon CBM play in Canada," in 2005 Annual Technical Conference and Exhibition, Dallas, Texas, U.S.A., October 2005, 9–12.

Bottomley, W., Furniss, J. P., Raza, S. S., Ge, L., and Rudolph, V. (2017). "Characterizing the dependence of coal permeability to methane adsorption, pore pressure and stress; laboratory testing of Walloon coals from the Surat basin," in SPE/ATMI Asia Pacific Oil & Gas conference and exhibition, Jakarta, Indonesia, 17-19 October, 2017.

Bustin, A. M. M., and Bustin, R. M. (2008). Coal reservoir saturation: Impact of temperature and pressure. *Am. Assoc. Pet. Geol. Bull.* 92 (1), 77–86. doi:10.1306/08270706133

Bustin, A. M. M., Bustin, R. M., and Russel-Houston, J. (2011). Horseshoe Canyon and belly river coal measures, south central Alberta: Part 2 - modeling reservoir properties and producible gas. *Bull. Can. Petroleum Geol.* 59 (3), 235–260. doi:10.2113/gscpgbull.59.3.235

Bustin, R. M., and Clarkson, C. R. (1998). Geological controls on coalbed methane reservoir capacity and gas content. *Int. J. Coal Geol.* 38, 3–26. doi:10.1016/s0166-5162(98)00030-5

Bustin, R. M. (1997). Importance of fabric and composition on the stress sensitivity of permeability in some coals, northern sydney basin, Australia: Relevance to coalbed methane exploitation. *AAPG Bull.* 81 (11), 1894–1908.

Cardott, B. J. (2013). Hartshorne coal rank applied to Arkoma Basin coalbed methane activity, Oklahoma, USA. *Int. J. Coal Geol.* 108, 35–46. doi:10.1016/j.coal.2011.07.002

Chen, G., Ding, C., Xu, L. M., Zhang, R. H., Hu, Y. X., Yang, F., et al. (2012). Analysis on the thermal history and uplift process of Zijinshan intrusive complex in the eastern Ordos basin. *Chin. J. Geophys.* 55 (11), 3731–3741.

Clarkson, C. R., and Bustin, R. M. (1996). Variation in micropore capacity and size distribution with composition in bituminous coal of the Western Canadian Sedimentary Basin: Implications for coalbed methane potential. *Fuel* 75, 1483–1498. doi:10.1016/0016-2361(96)00142-1

Conway, M. W., Mavor, M. J., Saulsberry, J., Barree, R. B., and Schraufnagel, R. A. (1995). "Multi-phase study flow properties for coalbed methane wells: A laboratory and field study," in 1995 Joint Rocky Mountain Regional Meeting and Low-Permeablity Reservoirs Symposium, Denver.

Crosdale, P. J., Beamish, B. B., and Valix, M. (1998). Coalbed methane sorption related to coal composition. *Int. J. Coal Geol.* 35, 147–158. doi:10.1016/s0166-5162(97)00015-3

Enever, J. R., and Hennig, A. (1997). "The relationship between permeability and effective stress for Australian coals and its implication with respect to coalbed methane exploration and reservoir modeling," in International Coalbed Methane Symposium Proceedings, the University of Alabama, Tuscaloosa, USA, 12~17 May.

Enever, J. R., Pattison, C. I., McWatters, R. H., and Clark, I. H. (1994). "The relationship between *in-situ* stress and reservoir permeability as a component in developing an exploration strategy for coalbed methane in Australia," in SPE/ISRM Rock Mechanics in Petroleum Engineering Conference, Delft, The Netherlands, 29~31 August.

Fu, N., Yang, S. C., He, Q., Xu, W., and Lin, Q. (2016). High-efficiency reservoir formation conditions of tight sandstone gas in Linxing-Shenfu Blocks on the east margin of Ordos Basin. *Acta Pet. Sin.* 37 (S1), 111–120.

GB/T 30050 (2013). *Classification of coal-body structure*. Beijing: Chinese Standards Press, 1–25.

Gu, J. Y., Zhang, B., and Guo, M. Q. (2016). Deep coalbed methane enrichment rules and its exploration and development prospect in Linxing Block. *J. China Coal Soc.* 41 (01), 72–79.

Hoch, O. (2005). "The dry coal anomaly-the Horseshoe Canyon formation of Alberta, Canada," in 2005 Annual Technical Conference and Exhibition, Dallas, Texas, U.S.A., 9-12 October 2005.

Hou, S. H., Wang, X. M., Wang, X. J., Yuan, Y., and Zhuang, X. (2016). Geological controls on gas saturation in the yanchuannan coalbed methane field, southeastern Ordos basin, China. *Mar. Petroleum Geol.* 78, 254–270. doi:10.1016/j.marpetgeo.2016.09.029

IUPAC (1982). Manual of symbols and terminology. Appendix 2, Part 1, Colloid and surface chemistry. *Pure Appl. Chem.* 52, 2201.

Johnson, R. C., and Flores, R. M. (1998). Developmental geology of coalbed methane from shallow to deep in Rocky Mountain basins and in Cook Inlet–Matanuska basin, Alaska, U.S.A. and Canada. *Int. J. Coal Geol.* 35, 241–282. doi:10.1016/s0166-5162(97)00016-5

Joubert, J. I., Grein, C. T., and Bienstock, D. (1973). Sorption of methane in moist coal. *Fuel* 52, 181–185. doi:10.1016/0016-2361(73)90076-8

Kang, Y. S., Sun, L. Z., Zhang, B., Gu, J. Y., Ye, J. P., Jiang, S. Y., et al. (2017). The controlling factors of coal bed reservoirs permeability and CBM development strategy in China. *Geol. Rev. (in Chinese with English abstract)* 63 (5), 1401–1418.

Krooss, B. M., van Bergen, F., Gensterblum, Y., Siemons, N., Pagnier, H. J. M., and David, P. (2002). High-pressure methane and carbon dioxide adsorption on dry and moisture-equilibrated Pennsylvanian coals. *International Journal of Coal Geology* 51, 69–92. doi:10.1016/s0166-5162(02)00078-2

Kuuskraa, V. A., and Wyman, R. E. (1993). "Deep coal seams: An overlooked source for long-term natural gas supplie," in The SPE Gas Technology Symposium, Calgary, Alberta, Canada, 26-30 June.

Lamberson, M. N., and Bustin, R. M. (1993). Coalbed methane characteristics of Gates Formation coals, northeastern British Columbia: effect of maceral composition. *American Association of Petroleum Geologists Bulletin* 77, 2062–2076.

Langmuir, I. (1918). The adsorption of gases on plane surfaces of glass, mica and platinum. *J. Am. Chem. Soc.* 40, 1361–1403. doi:10.1021/ja02242a004

Laxminarayana, C., and Crosdale, P. J. (1999). Role of coal type and rank on methane sorption characteristics of Bowen Basin Australia coals. *International Journal of Coal Geology* 40, 309–325. doi:10.1016/s0166-5162(99)00005-1

Levine, J. R. (1993). "Coalification: The evolution of coal as source rock and reservoir rock for oil and gas," in *Hydrocarbons from coal, AAPG studies in Geology*. Editors B. E. Law and D. D. Rice, 39–77.

Levy, J. H., Day, S. J., and Killingley, J. S. (1997). Methane capacities of Bowen Basin coals related to coal properties. *Fuel* 76 (9), 813–819. doi:10.1016/s0016-2361(97)00078-1

Li, S., Tang, D., Pan, Z., Xu, H., Tao, S., Liu, Y., et al. (2018). Geological conditions of deep coalbed methane in the eastern margin of the Ordos Basin, China: Implications for coalbed methane development. *J. Nat. Gas Sci. Eng.* 53, 394–402. doi:10.1016/j.jngse.2018.03.016

Li, X. Z., Wang, Y. H., Jiang, Z. C., Chen, Z. L., Wang, L. Z., and Wu, Q. (2016a). Progress and study on exploration and production for deep coalbed methane [J]. *Journal of China Coal Society* 41 (01), 24–31.

Li, Y., Cao, D., Wu, P., Niu, X., and Zhang, Y. (2017a). Variation in maceral composition and gas content with vitrinite reflectance in bituminous coal of the eastern Ordos basin, China. *Journal of Petroleum Science and Engineering* 149, 114–125. doi:10.1016/j.petrol.2016.10.018

Li, Y., Tang, D., Wu, P., Niu, X., Wang, K., Qiao, P., et al. (2016b). Continuous unconventional natural gas accumulations of Carboniferous-Permian coal-bearing strata in the Linxing area, northeastern Ordos basin, China. *Journal of Natural Gas Science and Engineering* 36, 314–327. doi:10.1016/j.jngse.2016.10.037

Li, Y., Tang, D. Z., and Niu, X. L. (2017b). Sedimentary features of C-P coal bearing strata controlled by variation of accommodation spaces in east margin of Ordos Basin. *Journal of China Coal Society* 42 (7), 1828–1838.

Liu, H. H., Sang, S. X., Xue, J. H., Wang, G., Xu, H., Ren, B., et al. (2016). Characteristics of an *in-situ* stress field and its control on coal fractures and coal permeability in the Gucheng Block, southern Qinshui basin, China. *Journal of Natural Gas Science and Engineering* 36, 1130–1139. doi:10.1016/j.jngse.2016.03.024

McKee, C. R., Bumb, A. C., and Koenig, A. (1988b). "Stress dependent permeability and porosity of coal and other geological formation," in 1984 SPE/DOC/GRI Unconventional Gas Recovery Symposium, Pittsburgh, 13~15, May.

McKee, C. R., Bumb, A. C., and Koenig, A. (1988a). Stress dependent permeability and porosity of Coal[J]. *Rocky Mountain Association of Geologist* 3 (1), 143–153.

Meaney, K., and Paterson, L. (1996). "Relative permeability in coal," in 1996 SPE Asia Pacific Oil&Gas Conference, Adelaide.

Meng, Z. P., and Li, G. Q. (2013). Experimental research on the permeability of high-rank coal under a varying stress and its influencing factors. *Engineering Geology* 162, 108–117. doi:10.1016/j.enggeo.2013.04.013

Meng, Z. P., Zhang, J. C., and Wang, R. (2011). *In-situ* stress, pore pressure and stress-dependent permeability in the southern Qinshui basin. *Int. J. Rock Mech. Min. Sci. (1997).* 48, 122–131. doi:10.1016/j.ijrmms.2010.10.003

Moore, T. A. (2012). Coalbed methane: A review. *International Journal of Coal Geology* 101, 36–81. doi:10.1016/j.coal.2012.05.011

Mukherjee, S., CopleyEsterle, J. J., et al. (2017). "*In-situ* stress and fracture controls on permeability distribution within Walloon Subgroup, Surat basin," in SPE/ATMI Asia Pacific Oil & Gas conference and exhibition, Jakarta, Indonesia, 17-19 October, 2017.

Ottiger, S., Pini, R., Storti, G., Mazzotti, M., Bencini, R., Quattrocchi, F., et al. (2010). Adsorption of pure carbon dioxide and methane on dry coal from the sulcis coal province (SW Sardinia, Italy). *Environ. Prog.* 25 (4), 355–364. doi:10.1002/ep.10169

Pomeroy, C. D., and Robinson, D. J. (1966). The effect of applied stress on the permeability of a middle rank coal to water. *International Journal of Rock Mechanism and Mining Science* 4, 329–343.

ScottMazumder, M. S., Gibson, M., et al. (2013). "Application of open-hole diagnostic fracture injection test results to regional stress interpretation in Bowen basin coals," in SPE Unconventional Resource Conference and Exhibition-Asia Pacific, Brisbane, Australia, 11-13 November 2013.

Seidle, J. (2011). *Fundamentals of coalbed methane reservoir engineering.*

Shao, L. Y., Zheng, M. Q., Hou, H. H., Dong, D. X., and Wang, H. S. (2018). Characteristics sequence–palaeogeography and coal accumulation of Permo–Carboniferous coal measures in Shanxi Province. *Coal Science and Technology* 46 (2), 1–8.

Shedid, S. A., and Rahman, K. (2009). "Experimental Investigations of Stress-Dependent Petrophysical Properties and Reservoir Characterization of Coalbed Methane (CBM)," in Asia Pacific Oil and Gas Conference & Exhibition, Jakarta.

Somerton, W. H., Söylemezoğlu, I. M., and Dudley, R. C. (1975). Effect of stress on permeability of coal. *International Journal of Rock Mechanics and Mining Sciences & Geomechanics Abstracts* 12, 129–145. doi:10.1016/0148-9062(75)91244-9

Sparks, D. P., Mclendon, T. H., Saulsberry, J. L., and Lambert, S. W. (1995). "The effects of stress on coalbed reservoir performance, Black Warrior basin, U.S.A. SPE30734," in SPE Annual Technical Conference and Exhibition, Dallas, TX, October 22–25.

Sun, B., Yang, M. F., Yang, Q., Tian, W. G., Sun, Q. P., and Xu, Y. G. (2017). Analysis on occurrence state of deep coalbed methane in Junggar basin. *J. China Coal Soc.* 42 (A1), 195–202.

Tang, D. Z., Wang, J. L., Zang, J. F., and Huang, W. H. (2000). Secondary hydrocarbon generation of coal and accumulation of coalbed methane in the east margin of the Ordos Basin. *Experimental Petroleum Geology* 22 (2), 140–145.

Tao, S., Tang, D., Xu, H., Gao, L., and Fang, Y. (2014). Factors controlling high-yield coalbed methane vertical wells in the Fanzhuang Block, southern Qinshui basin. *International Journal of Coal Geology* 134 (135), 38–45. doi:10.1016/j.coal.2014.10.002

Wang, P. (1992). A geomechanical technique—types and distribution of geostress under various tectonic forces. *Acta Petrolei Sinica* 13 (1), 1–12.

Wen, Z., Kang, Y. S., Ze, D., Sun, L. Z., Li, G. Z., and Wang, H. Y. (2019). Characteristics and distribution of current *in-situ* stress at shallow-medium-depth in coal-bearing basins in China. *Geological Review* 65 (3), 729–742.

Wu, J., Liu, X.J., Ma, Z.J., and Han, D. 2018. Tectonic genesis of Linxing Block and its influence on oil and gas accumulation. *National Coalbed Methane Symposium*. Beijing: Petroleum Industry Press:47–54.

Yalçin, E., and Durucan, A. 1991. Methane desorption characteristics of Zonguldak coals. *Min. Sci. Technol.* 13 (2), 207–214.

Zhi, D. M., and Xue, L. (2013). *Coalbed methane resources and exploration potential in Junggar Basin*. Bejing: Petroleum Industry Press, 167.

frontiers | Frontiers in Earth Science

TYPE Original Research
PUBLISHED 11 January 2023
DOI 10.3389/feart.2022.1007902

OPEN ACCESS

EDITED BY
Hao Zou,
Chengdu University of Technology, China

REVIEWED BY
Mao Luo,
State Key Laboratory of Palaeobiology and Stratigraphy (CAS), China
Xiaoqun Yang,
Institute of Geology and Geophysics (CAS), China

*CORRESPONDENCE
Xun Kang,
kangxunk@163.com

SPECIALTY SECTION
This article was submitted to Economic Geology, a section of the journal Frontiers in Earth Science

RECEIVED 31 July 2022
ACCEPTED 30 September 2022
PUBLISHED 11 January 2023

CITATION
Xu D, Qu Y, Huang L, Dai C, Hu R and Kang X (2023), Authigenic calcite as a record of geologic fluids in siliciclastic rocks: Evidences from the Upper Permian Wuerhe Formation, Junggar basin, NW China.
Front. Earth Sci. 10:1007902.
doi: 10.3389/feart.2022.1007902

Authigenic calcite as a record of geologic fluids in siliciclastic rocks: Evidences from the Upper Permian Wuerhe Formation, Junggar basin, NW China

Duonian Xu[1], Yongqiang Qu[1], Linjun Huang[1], Chao Dai[2,3], Ruipu Hu[2,3] and Xun Kang[2,3]*

[1]Research Institute of Petroleum Exploration and Development Northwest Branch, Lanzhou, China, [2]School of Geosciences and Info-Physics, Central South University, Changsha, China, [3]Key Laboratory of Metallogenic Prediction of Nonferrous Metals and Geological Environment Monitoring, Ministry of Education, Central South University, Changsha, China

The identification of geologic fluids and related fluid–rock interactions during diagenesis is the subject of much research in sedimentary petrology. Authigenic calcite potentially provides a record of geologic fluids and it occurs heterogeneously in the Upper Permian Wuerhe Formation (P_3w) in the Shawan Sag, Junggar Basin, which has a complex history of geologic fluid activity. This provides an ideal opportunity to study the effectiveness of authigenic calcite in tracing fluids. We conducted optical, cathodoluminescence (CL), and scanning electron microscopic observations, as well as the major and trace element and stable carbon and oxygen isotopes of authigenic calcite. The results show that three generations of calcite were precipitated in the P_3w Formation, and the diagenetic fluid was affected to varying degrees by paleo-meteoric water and hydrocarbon-bearing fluids. During early diagenesis, diagenetic fluid with low Mn contents precipitated the amorphous early-stage calcite (dark red in CL images, MnO <1.5%, $\delta^{13}C$ = −8.6‰ to 2.1‰, VPDB). Its carbon source was mainly meteoric CO_2. During mesodiagenesis, the limited hydrocarbon emplacement during the Middle Jurassic enriched the pore fluids in Mn and ^{13}C-depleted organic derived CO_2, subsequently precipitating the late-stage sparry calcite I (orange in CL images with MnO of 2.5%–4% and $\delta^{13}C$ of −14.5‰ to −8.1‰). The carbon in this calcite came from the dissolution of early-stage calcite and CO_2 generated by decarboxylation of organic acids. During the Early Cretaceous, large-scale hydrocarbon charging occurred and the pore fluids were further enriched in Mn and organic derived CO_2, eventually precipitating the late-stage sparry calcite II (bright yellow in CL images with MnO of >4% and $\delta^{13}C$ of −25.7‰ to −14.9‰). Its carbon source was mainly CO_2 produced by the decarboxylation of organic acids. The precipitation of abundant late-stage ^{s}C-depleted calcite suggests that the hydrocarbons were oxidized to organic acids in the reservoir. The two periods of hydrocarbon charging caused the dissolution of laumontite and the early-stage calcite, forming secondary minerals and dissolution pores, which increased the porosity and permeability of the rock. Therefore, authigenic calcite is a useful tracer of

fluid properties, fluid–rock interactions, and alteration processes in petroliferous basins.

KEYWORDS

authigenic calcite, geologic fluids, fluid-rock interaction, Upper Permian Wuerhe Formation, Junggar basin

Introduction

Siliciclastic petroleum reservoirs are distributed widely in petroliferous basins worldwide. For example, in China, the measured petroleum resources hosted in siliciclastic rocks account for >70% of total petroleum resources (Li, 2004; Ma et al., 2017). In petroliferous basins, meteoric water, hydrocarbon-bearing fluids, deep mantle-sourced fluids, and other external fluids can alter the diagenetic pathways of siliciclastic rocks by triggering fluid–rock interactions or by forming or destroying reservoir space (Jin et al., 2002; Seewald, 2003; Xie et al., 2009; Yuan et al., 2017; Huang et al., 2021; Zhi et al., 2022). Identifying these fluids is necessary for better understanding diagenesis and alteration in siliciclastic reservoirs and improving the evaluation of these reservoirs.

Typical authigenic minerals, such as calcite, pyrite, and quartz, can potentially record geologic fluids in altered sedimentary rocks. The precipitation of different generations of authigenic minerals can be identified using crystal morphology, cathodoluminescence (CL) images, and the relationships between minerals. The fluids that form authigenic calcite can then be identified from the chemical and stable carbon and oxygen isotopic compositions of the calcite, and the corresponding fluid–rock interactions can be further deciphered (Irwin et al., 1977; Spiro, 1977; Krouse et al., 1988; Zhu et al., 2006; Drake et al., 2015; Hu et al., 2018). In carbonate rocks, major element (e.g., iron and manganese), trace element (e.g., uranium), and carbon and oxygen isotopic compositions have been combined to identify different stages of calcite formation, alongside the source of their carbon and their formation processes (Irwin et al., 1977; Zhao et al., 2016; Xie et al., 2020; Sun et al., 2021). Thermochemical sulfate reduction accompanied by hydrocarbon oxidation has been identified using the relationships between authigenic minerals, the geochemical characteristics of H_2S-enriched natural gas, ^{13}C-enriched residual hydrocarbons, and the negative $\delta^{13}C$ values of authigenic calcite (Krouse et al., 1988; Zhu et al., 2006; Hao et al., 2008; Liu et al., 2020). In siliciclastic rocks, the precipitation of authigenic calcite with high MnO contents and extremely negative $\delta^{13}C$ values [down to −70‰ VPDB (Vienna Pee Dee Belemnite)] indicates hydrocarbon oxidation induced by high-valence Mn or Fe oxides (Hu et al., 2018; Kang et al., 2021). Therefore, authigenic calcite may record information implying the origin of geologic fluids and fluid–rock interactions in siliciclastic reservoirs.

The upper Permian Wuerhe (P_3w) Formation in the Shawan Sag is a coarse siliciclastic sedimentary sequence composed of gray sandy conglomerates and brown mudstones. During diagenetic stage, as well as diagenetic fluids, the rocks also affected by leaching by an external geologic fluid (e.g., meteoric water) and by hydrocarbon emplacement (Yuan et al., 2017; Zhi et al., 2022). Authigenic calcite with varying geochemical compositions was observed in the P_3w cores. This formation provides a good opportunity for testing the potential of using authigenic calcite to trace geological fluids in siliciclastic rocks; therefore, we conducted petrological and mineralogical studies of the P_3w Formation and used the *in situ* major element, trace element, and carbon and oxygen isotopic compositions of calcite formed in different stages to reveal the possible composition of geologic fluids that were present and the fluid–rock interactions and alteration of the reservoir that occurred during diagenesis.

Geologic setting

The study area is in the Shawan Sag in the west of the Junggar Basin, northwestern China, adjacent to the Zhongguai Uplift to the north, the Hongche Fault Zone to the west, the Homatu Anticline to the south, and the Western P1 Sag and Mosuowan Uplift to the east (Figure 1A). Since the late Carboniferous, the study area has been affected by subduction, accretion, and closure of the Darbute and northern Tianshan oceans, and several wedge-shaped fault depressions were developed in the sag (Han et al., 2006; Tang et al., 2010; Tao et al., 2021). At the end of the early Permian, the emergence of the structural wedge in the transition zone between the Shawan Sag and the Chepaizi Uplift caused the topography to slope gently from west to east (Liang et al., 2018). During the late Permian–Triassic, the strata were uplifted, exposed, and denuded, forming an unconformity. During the Cretaceous–Paleogene, the whole basin experienced steady subsidence. Since the Neogene, the large-scale thrusting adjacent to the Tianshan Mountains in response to the Himalayan Orogeny caused the sag to slope gradually southward, forming its current tectonic arrangement (Zhang et al., 1999; Zhang et al., 2006).

The late Permian Upper Wuerhe Formation (P_3w) unconformably overlies the middle Permian Lower Wuerhe Formation (P_2w) and also unconformably underlies the Lower Triassic Baikouquan (T_1b) Formation. The P_3w Formation is 150–210 m thick (Figure 1B) and was deposited in a coarse-grained fan delta system (Zou et al., 2007; Du et al., 2019). The formation is composed of coarse-grained gray and brown conglomerate with interbedded reddish-brown mudstone. The overall formation represents a fining upward sequence, and the

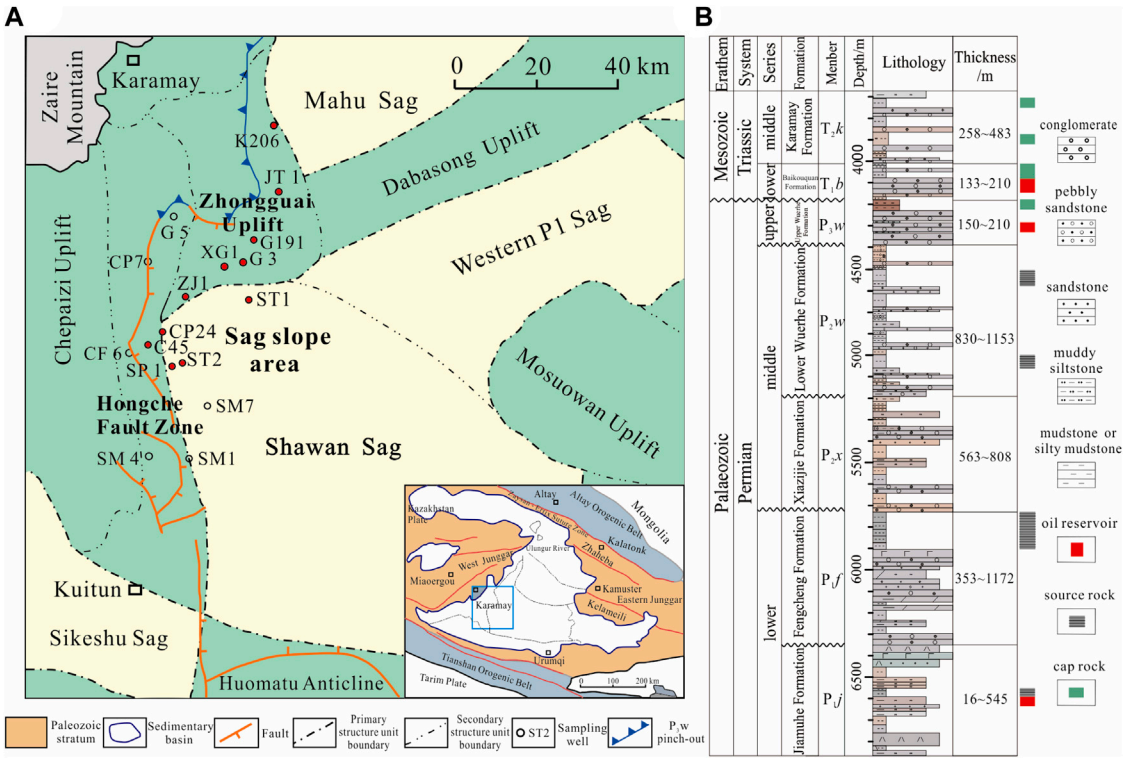

FIGURE 1
(A) Geologic map of the Shawan Sag and surrounding area. **(B)** Lithological column for the study area and typical geologic elements of the hydrocarbon reservoirs.

proportion of conglomerate decreases upward, reflecting a lake transgression systems tract.

Three mature to highly mature source rocks exist in the Shawan Sag—the Lower Wuerhe (P_2w), Fengcheng (P_1f), and Jiamuhe (P_1j) formations—leading to large-scale hydrocarbon production in the P_3w Formation (Zhang et al., 2015; Du et al., 2019; Xia et al., 2022). Two periods of oil and gas emplacement occurred (during the Middle Jurassic and Early Cretaceous) as the faults became active allowing migration (Wang, 2016; Pan et al., 2021). Since 2018, successful exploration has been carried out in the sandy conglomerate reservoir in the P_3w Formation. Daily oil and gas production from wildcat well ST1 reached 30.25 m^3 and 2.14 × 10^3 m^3, respectively, after hydraulic fracturing. High industrial oil and gas yields have also been obtained from well ST2, indicating that the reservoir shows a good prospect for future exploration and development (Kuang and Zhi, 2022).

TABLE 1 Core samples from the P_3w Formation.

well	samples	depth	Production test result
K206	6	3627.9–3642.5 m	Water layer
JT1	6	4453.5–4484.5 m	Water layer
	13	4502.5–4538.1 m	Water layer
CP24	6	4604.9–4610.8 m	Water layer containing oil
ST1	6	5281.9–5284.5 m	Water layer containing oil
	5	5309.3–5311.3 m	Water layer containing oil
G191	12	4333.2–4350.7 m	Heavy oil layer
ST2	8	4897.5–5168.6 m	Low-quality oil layer
	1	5171.0m	Dry layer
SP1	3	4828.5–4832.0 m	Dry layer
C45	7	4074.5–4220.3 m	Dry layer
XG1	3	4490.2–4491.9 m	Dry layer
G3	7	4610.5–4760.8 m	Gas layer
	6	4862.1–5260.5 m	Water layer

Sample descriptions and methods

Detailed core logging was conducted on 10 wells in the study area, and 89 core samples were collected systematically with vertical intervals of <1 m. Thin sections were studied under an optical microscope (Table 1). Thirty-two representative samples were analyzed using a scanning

electron microscope (SEM), and selected minerals were analyzed using energy dispersive spectroscopy (EDS). The SEM analyses were carried out on a TESCAN MIRA three using an accelerating voltage of 5 kV, 30 μm standard grating, and a counting time of 40 s, and the EDS analyses were carried out using an Oxford AZtec X-Max 150 detector with an accelerating voltage of 15 kV.

The different generations of authigenic calcite were identified using CL images, and the major element compositions of laumontite and each generation of calcite were measured using a JEOL JXA-8800 electron probe microanalyzer (EPMA). In addition, laser ablation–inductively coupled plasma–mass spectrometry (LA–ICP–MS) was used to analyze the trace element contents of authigenic calcite. We used a Jena PlasmaQuant MS Elite mass spectrometer with He as the carrier gas, a laser spot diameter of 40 μm, and an energy intensity of 3.5 J cm^{-2}. NIST SRM 610 was used as the external standard, and the Ca content obtained using the EPMA was used as the internal standard. The accuracy of the trace element analyses was <10%. Rare Earth element (REE) data were normalized to the composition of post-Archean Australian shale (PAAS) values.

The carbon and oxygen isotopic compositions of authigenic calcite from 29 samples were analyzed. Each sample aliquot of ca. 100–120 mg of rock powder (200 mesh) was cleaned in acetone for 2 h under ultrasound to remove adsorbed organic contaminants. After rinsing with deionized water, the aliquot was dried at 60°C. Half the aliquot was dissolved in a phosphate solution in a GasBench II system. The purified CO_2 gas was transferred to a Thermo Scientific MAT 253 isotope ratio mass spectrometer for analysis. The results were expressed relative to the VPDB standard using the Chinese standard GBW04416 ($\delta^{13}C$ = −6.06‰, $\delta^{18}O$ = −11.59‰) and expressed using δ notation. The accuracy of the C and O isotopic compositions is <0.10‰ and <0.08‰ (1 standard error), respectively.

To ascertain whether the crude oil in the study area has undergone microbial degradation, the composition of saturated hydrocarbons and biomarkers in the crude oil samples were also analyzed using a Shimadzu GC-2014 gas chromatograph and Shimadzu GCMS-QP2020 NX gas chromatography mass spectrometer, respectively.

Results

Petrology

The P_3w Formation contains mainly light gray and brown sandy conglomerate with interbedded brown mudstone. The clasts in the sandy conglomerate are dominated by lithic fragments (>90%; Figure 2A), with <10% quartz and feldspar grains (Figures 2C,D). The lithic fragments comprise mainly mafic–intermediate volcanic rock (Figure 2A), with low (<15%) metamorphic and sedimentary rock contents. The volcanic lithic fragments comprise mainly tuff (Figures 2A,B) with a small amount of basalt and andesite (Figure 2C). Poor sorting and subangular–subrounded clasts (Figure 2A) in the conglomerate demonstrate the low textural maturity of this formation and suggest that it was deposited close to provenance areas.

The reservoir rocks can be divided into oil-, gas-, and water-bearing and dry layers according to the fluid they host. Authigenic laumontite and calcite occur in oil-bearing layers alongside authigenic quartz and kaolinite (Figure 3B, D, E). Mixed-layer illite/smectite was observed in the intergranular pores (Figure 3C). Solid bitumen was also found in residual and secondary pores, indicating hydrocarbon emplacement (Figure 2E). Sparry laumontite and calcite with rare analcime are precipitated in the water-bearing layers (Figures 2C, 3F). Lithic clast surfaces are often coated with a mixed-layer illite/smectite. Dry layers have lower laumontite and calcite contents, and abundant mixed-layer illite/smectite coats the lithic grains and comprises the matrix in intergranular pores.

Diagenesis

During diagenesis, the P_3w Formation experienced mechanical compaction, mineral dissolution, cementation, and mineral replacement. Different diagenetic processes occurred in the different layers, particularly cementation and mineral dissolution. Because the studied strata have generally been buried to depths >4,000 m, all of the sandy conglomerates have undergone strong mechanical compaction. The grains have linear to concave and convex contacts (Figure 2A) and primary pores have been almost entirely destroyed (Figure 2B).

In the oil- and gas-bearing layers, laumontite and calcite occur as the primary cement (Figure 2F). Abundant secondary pores were generated by the extensive dissolution of laumontite and calcite cements and feldspar grains (Figures 2D,E, 3A). Bitumen often remains in the dissolution pores (Figure 2E). Late-stage calcite partially filled the pores formed by dissolution of laumontite and feldspar (Figure 2F, 4A, 5C). Authigenic quartz and vermicular kaolinite aggregates also occur in pores formed by dissolution of laumontite (Figures 3D,E). Leaf-like chlorite aggregates are often precipitated between grains (Figure 3C), and smectite has been gradually replaced by mixed-layer illite/smectite *via* illitization.

In the water-bearing layers, little dissolution has occurred and a small volume of dissolution porosity is found in only a few samples. Sparry laumontite and calcite form the primary cement (Figures 2B,C). Rare authigenic analcime occurs in several

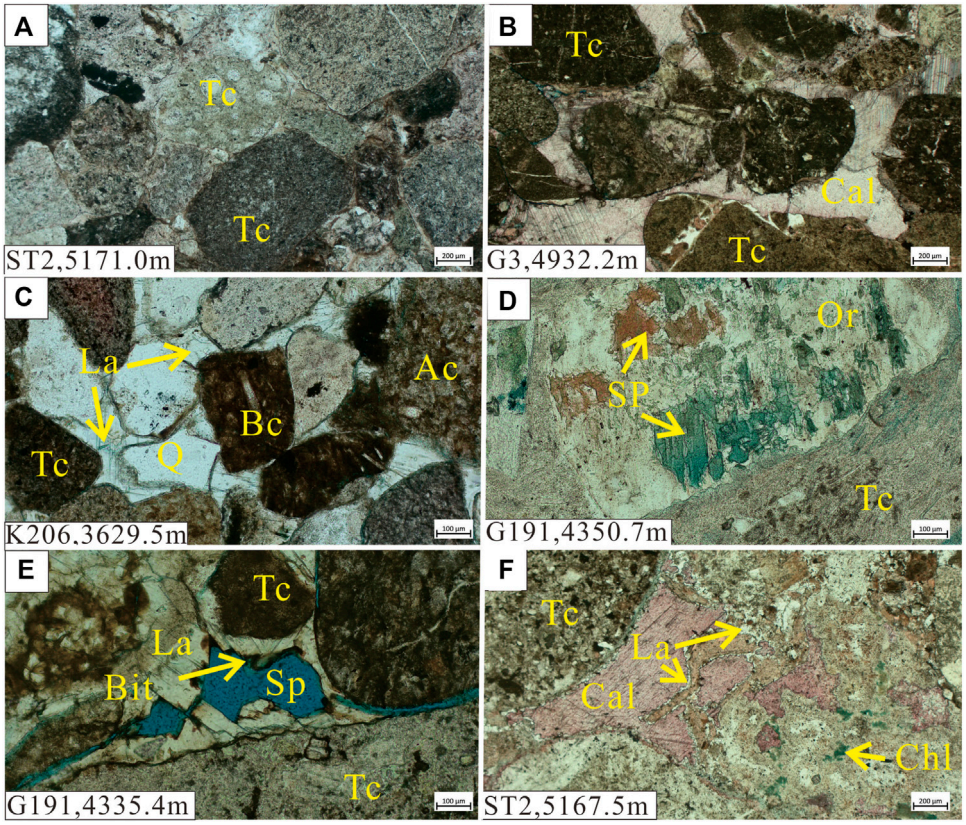

FIGURE 2
Photomicrographs of the Upper Wuerhe Formation. **(A)** Grayish white sandstone from a dry layer under plane-polarized light (PPL). **(B)** Water-bearing brown sandy conglomerate under PPL. **(C)** Water-bearing gray sandy conglomerate under PPL. **(D)** Brown gravelly conglomerate from a heavy oil-bearing layer under PPL. **(E)** Gray sandy conglomerate from a heavy oil-bearing layer under PPL. **(F)** Gray conglomerate from a low-quality oil-bearing layer under PPL. Tc: tuffaceous clast, Cal: calcite, Q: quartz, La: laumontite, Ac: andesite clast, Bc: basalt clast, Or: orthoclase, SP: secondary pores, Bit: bitumen, Chl: chlorite.

samples (Figure 3F). The dry layers have low zeolite and calcite contents and almost no dissolution has occurred. Smectite experienced extensive illitization, forming abundant mixed-layer illite/smectite (Figure 3C).

Calcite occurrence and geochemistry

In the oil-bearing layers, three generations of calcite can be identified by their dark red, orange, and bright yellow appearance in CL images (Figure 4). The dark red early-stage calcite occurs mainly as primary cement in primary pores and around the lithic grains (Figures 4C, 5A). The orange late-stage calcite I was precipitated mostly in primary pores through the recrystallization of early-stage calcite (Figure 4). The early-stage calcite in the oil- and gas-bearing layers has been partially dissolved then replaced by mixed-layer illite/smectite (Figure 5B). The bright yellow late-stage calcite II was precipitated in unconnected residual intergranular pores and pores formed by the dissolution of laumontite (Figures 4A, 5C,D). In the water-bearing layers, early-stage and late-stage calcite I commonly occurs with a small amount of late-stage calcite II in pores formed by the dissolution of laumontite (Figure 4A).

The authigenic calcite in the P_3w Formation has a wide range of MnO contents (Figure 6). Calcite in the oil-bearing layers yields MnO contents of 0.05%–5.06% (mean = 1.42%), the MnO contents of calcite in the water-bearing layers fall into two groups (0–1% and 2%–4%), and the MnO contents of calcite in the oil-bearing layers fall into three groups (<1.5%, 2.5%–4%, and 4%–6%; Figure 6). The FeO contents of calcite are generally <0.20%.

In situ LA–ICP–MS analyses were used to measure the REE contents of the calcite in the P_3w Formation and yielded light REE (LREE)/heavy REE (HREE) ratios of 2.20–7.80 (mean =

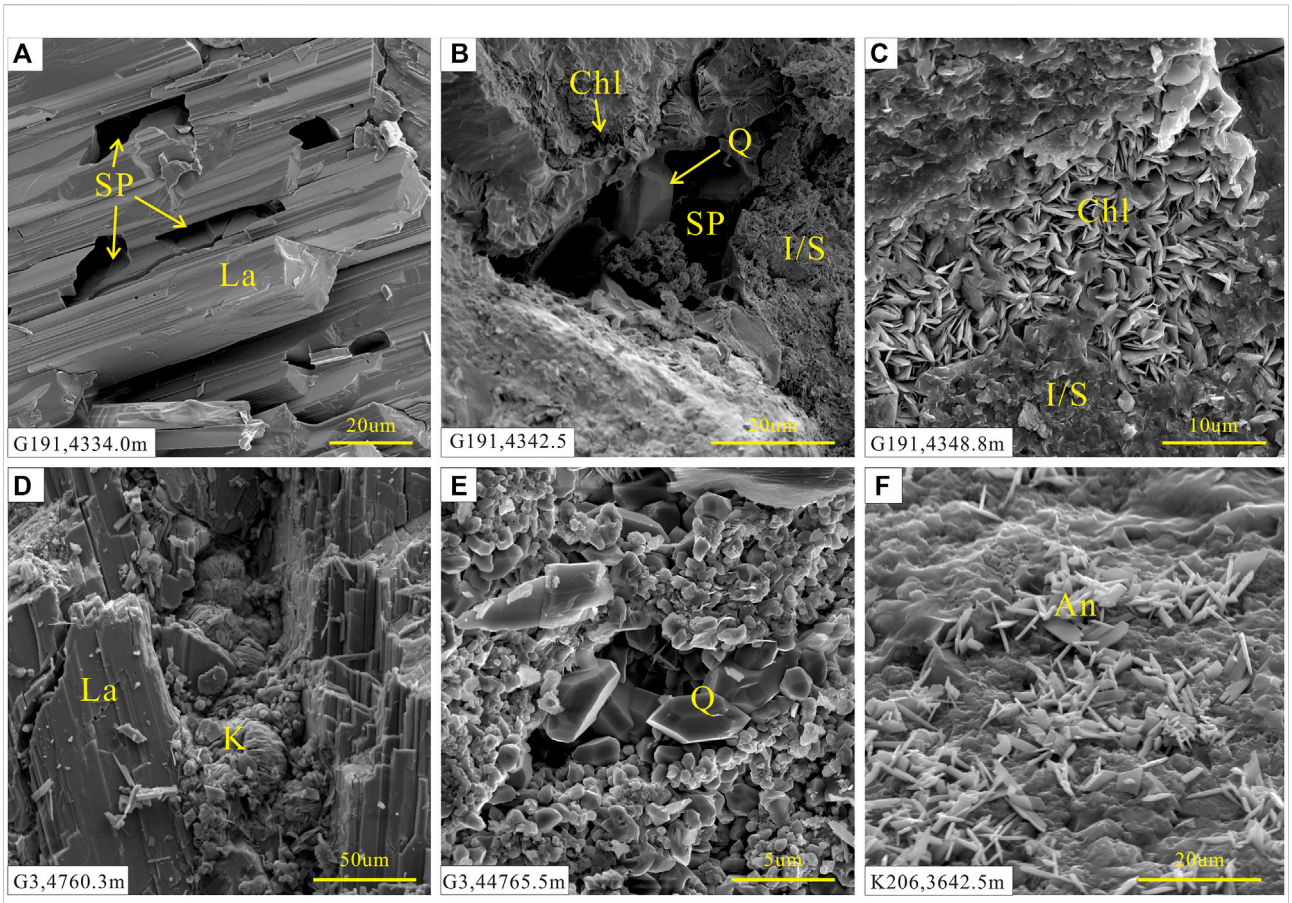

FIGURE 3
SEM images of intergranular minerals in the P_3w sandy conglomerates. **(A)** Gray sandy conglomerate from the heavy oil-bearing layer. **(B)** Gray sandstone from the heavy oil-bearing layer. **(C)** Gray–green sandy conglomerate from the heavy oil-bearing layer. **(D)** Gray sandy conglomerate from the gas-bearing layer. **(E)** Gray sandy conglomerate from the gas-bearing layer. **(F)** Gray gravelly conglomerate from the water-bearing layer. La: laumontite, SP: secondary pores, Chl: chlorite, Q: quartz, I/S: mixed-layer illite/smectite, **(K)** kaolinite, An: analcime.

5.17), showing LREE enrichment. The calcite yields Y/Ho ratios of 19.10–28.43 (mean = 21.77), negative Ce anomalies (δCe = 0.26–0.61; mean = 0.33), and positive Eu anomalies (δEu = 1.04–1.74; mean = 1.26).

Calcite carbon and oxygen isotopic compositions

The calcite in layers with different hydrocarbon charging intensities have different carbon isotopic compositions. The calcite in the oil-bearing layers is depleted in ^{13}C, with $\delta^{13}C$ values of −25.7‰ to −6.2‰ (mean = −14.1‰). The $\delta^{13}C$ values of calcite in the water-bearing layers is higher, at −12.4‰ to +1.2‰ (mean = −7.1‰). There are no clear differences in the oxygen isotopic compositions of the calcite among the different layers. The calcite in the oil-bearing layers yields $\delta^{18}O$ values of −20.9‰ to −13.6‰ (mean = −15.5‰), and the calcite in the water-bearing layers yields $\delta^{18}O$ values of −18.0‰ to −11.5‰ (mean = −15.6‰; Table 2).

Oil biomarkers

Previous studies have suggested that the crude oil hosted by the P_3w Formation may have been biodegraded near the fault zone (Pan et al., 2021); therefore, we analyzed crude oil biomarkers from the sampled layers. The total ion chromatogram from the crude oil from the study area shows a relatively complete sequence of *n*-alkanes, and typical biodegradation markers (e.g., 25-norhopanes) were not identified in the mass spectrum (Figure 7). Limited samples possibly underwent mild biodegradation as the existence of UCM (unidentified compound materials, Figure 7).

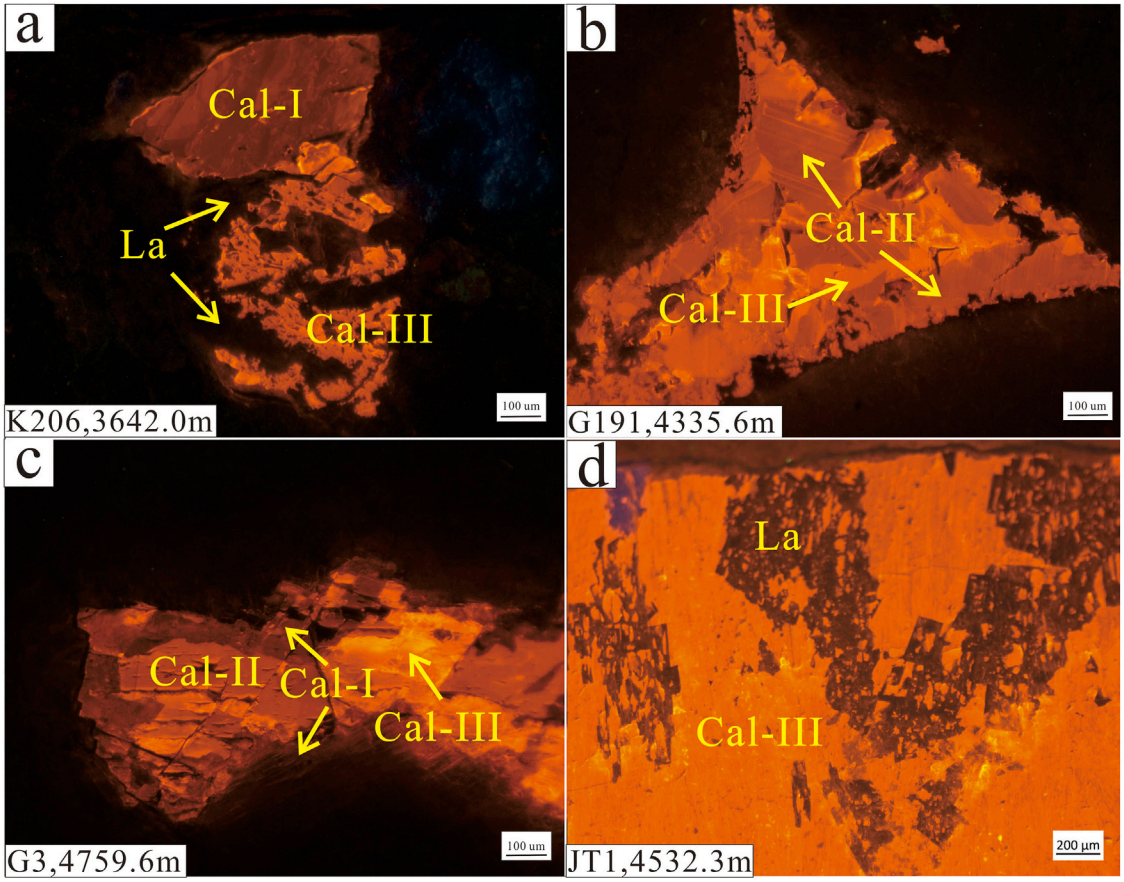

FIGURE 4
CL images of intergranular calcite cement in a sandy conglomerate from the P_3w Formation. **(A)** Gray fine-grained conglomerate from a water-bearing layer. **(B)** Gray sandy conglomerate from a heavy oil-bearing layer. **(C)** Gray conglomerate from a gas-bearing layer. **(D)** Gray sandstone from an oil-bearing layer. La: laumontite, Cal-I: early-stage calcite, Cal-II: late-stage calcite I, Cal-III: late-stage calcite II.

Discussion

Geologic fluid identification

The redox sensitive element (e.g., Mn and Fe) contents of calcite are closely related to the fluid from which it precipitated and can potentially indicate the geologic fluids present during diagenesis (Gregg and Shelton, 1989; Aggarwal et al., 2004; Liu et al., 2019). Previous studies have shown that hydrocarbon-bearing fluids in the Junggar Basin are enriched in Mn (Cao et al., 2007, 2020). In addition, in rocks containing red layers, the thermochemical oxidation of hydrocarbons by high-valence $Mn^{3+/4+}$ ions also releases Mn^{2+} ions into the pore water (Hu et al., 2018; Kang et al., 2021). Therefore, the MnO contents in calcite most likely reflect the intensity of hydrocarbon charging and subsequent hydrocarbon–water–rock interactions. Furthermore, the alteration of volcanic material may also lead to a slight increase in the Mn and Fe contents of pore water and a slight increase in its pH (Xi et al., 2015; Xie et al., 2020). In addition to elemental composition, the carbon isotopic compositions of calcite are also widely used to trace the sources of geological fluids, as calcite precipitated from meteoric water and calcite affected by ^{13}C-depleted organic carbon from hydrocarbons will have different carbon isotopic compositions (e.g., Irwin et al., 1977; Surdam et al., 1993; Seewald, 2003; Hu et al., 2018). The MnO contents in the three calcite stages and the lower $\delta^{13}C$ values of calcite in the hydrocarbon-bearing layers indicate that the diagenetic fluids were altered by hydrocarbon-bearing fluids during diagenesis (Irwin et al., 1977; Seewald, 2003; Cao et al., 2007; Zhi et al., 2022).

In the oil- and gas-bearing layers, some of the late-stage I calcite formed *via* recrystallization of early-stage calcite, and both of these generations of calcite are found mainly in the primary pores (Figures 4B,C). In contrast, the late-stage calcite II occurs mainly in secondary pores (Figure 5C), indicating that this calcite was precipitated after large-scale dissolution. As the MnO increase due to the alteration of volcanic material is limited,

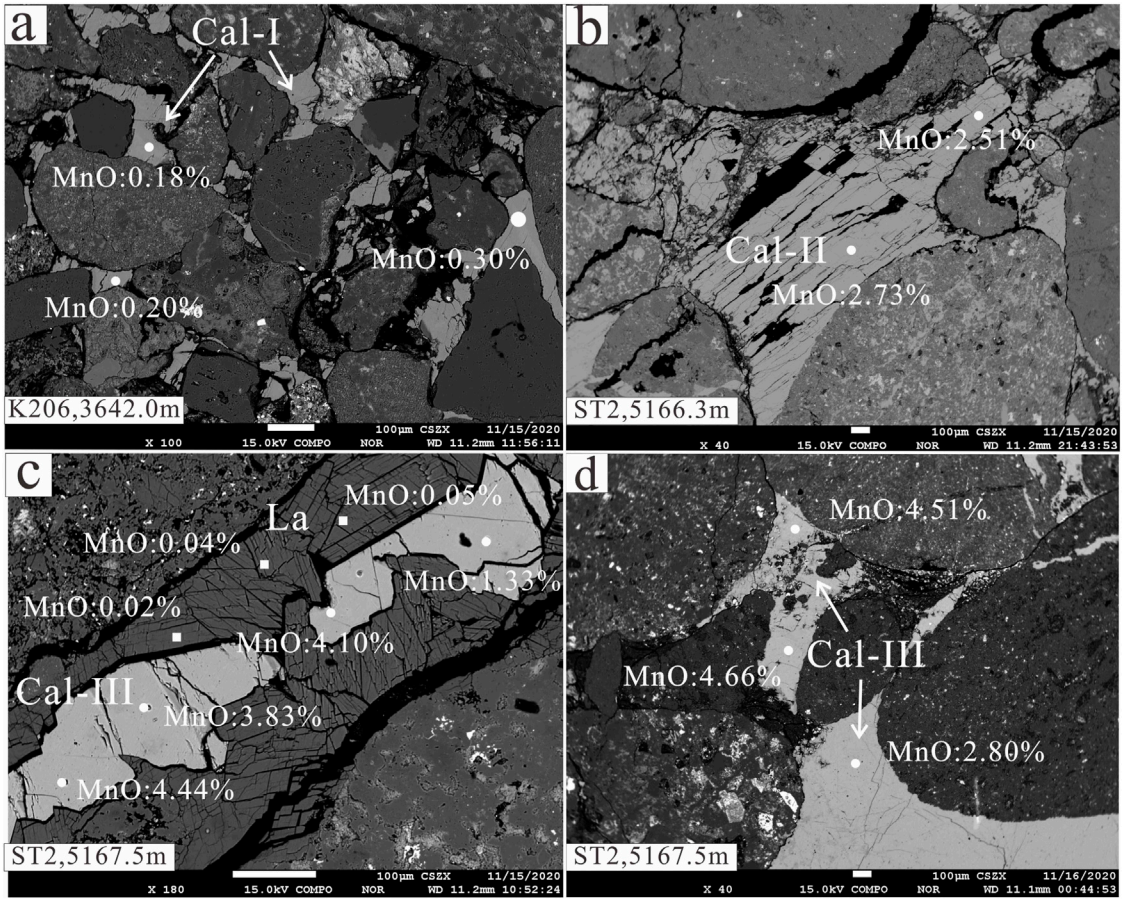

FIGURE 5
Backscattered electron images of laumontite and calcite in the P_3w Formation. **(A)** Gray sandstone from a water-bearing layer. **(B)** Gray sandy conglomerate from an oil-bearing layer. **(C)** Gray sandy conglomerate from an oil-bearing layer. **(D)** Gray sandy conglomerate from an oil-bearing layer. Cal-I: early-stage calcite, Cal-II: late-stage calcite I, Cal-III: late-stage calcite II, La: laumontite.

the higher MnO content of the late-stage calcite II reflects a change in the diagenetic fluid caused by hydrocarbon emplacement during diagenesis (Figure 6; Cao et al., 2007; Hu et al., 2018). The calcite in the oil- and gas-bearing layers yield a wide range of $\delta^{13}C$ values (−25.7‰ to −6.2‰), indicating that the source of the C in the calcite changed gradually during diagenesis from inorganic CO_2 in meteoric water to organic derived CO_2 from hydrocarbons (Irwin et al., 1977; Seewald, 2003). The early-stage calcite with low MnO contents (<1.5%) and high $\delta^{13}C$ and $\delta^{18}O$ values ($\delta^{13}C$ > −10.0‰; $\delta^{18}O$ > −15.0‰) was precipitated in the oil- and gas-bearing layers (Figures 6, 8), and the higher $\delta^{18}O$ values were inherited from meteoric water (Figure 8; Swart, 2015).

The first stage of hydrocarbon emplacement occurred during the Middle Jurassic (Wang, 2016; Pan et al., 2021); however little hydrocarbon charging occurred during this stage (Zhi et al., 2022). Organic acids and organic derived CO_2 in the hydrocarbon-bearing fluids led to a slight decrease in the pH and an increase in the Mn contents of the pore water (Cao et al., 2007; Hu et al., 2018) and provided organic carbon for the precipitation of the late-stage calcite (Seewald, 2003; Wu et al., 2017). This calcite generation is characterized by higher MnO contents (2.5%–4%) and slightly lower $\delta^{13}C$ values (−15.0‰ to −10.0‰). During the Early Cretaceous, a second, large-scale hydrocarbon charge further altered the diagenetic fluids, resulting in a series of hydrocarbon–water–rock interactions (Seewald, 2003; Swart, 2015; Kang et al., 2019; Sun et al., 2021). Organic acids and organic derived CO_2 dissolved in hydrocarbon-bearing fluids further reduced the pH of the pore water, and the decarboxylation of organic acids in moderately hot rocks also produced CO_2 (Irwin et al., 1977). Intense hydrocarbon charging led to further enrichment of the pore water in Mn and organic derived ^{13}C-depleted CO_2 (Cao et al., 2007; Zhi et al., 2022). Thermochemical oxidation of the hydrocarbons also likely occurred in some layers, forming organic acid intermediate, and even more ^{13}C-depleted CO_2 than

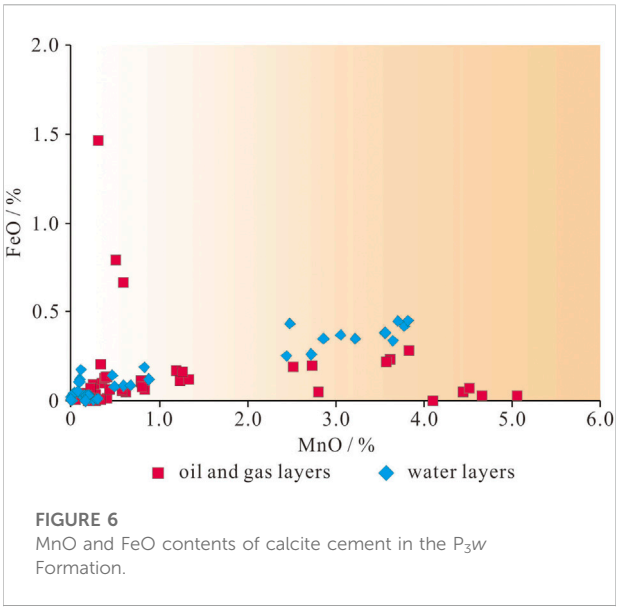

FIGURE 6
MnO and FeO contents of calcite cement in the P_3w Formation.

decarboxylation derived CO_2 (Seewald, 2003; Hu et al., 2018). The late-stage calcite that formed in this environment has high MnO contents (4%–6%) and low $\delta^{13}C$ values (less than −15.0‰; Figures 6, 8).

The water-bearing layers contain mainly early-stage and late-stage I calcite (Figure 5A), with a little late-stage II calcite precipitated in the pores formed during dissolution of laumontite (Figure 4A). The late-stage calcite in the water-bearing layers has low MnO contents (<1.0%; Figure 6), and their $\delta^{13}C$ values are generally lighter than −10.0‰ (Figure 8). This indicates that the diagenetic fluids in the water-bearing layers were not affected by large-scale hydrocarbon emplacement and inherited their compositions mainly from paleo-meteoric water (Zhi et al., 2022). However, in individual layers (e.g., at a depth of 3,629.5–3,642.0 m in well K206), the pore fluids might have been affected by water-soluble organic acids and CO_2 derived from hydrocarbons (Aggarwal et al., 2004; Minor et al., 2019). The late-stage calcite in these layers has high MnO contents (2.44%–3.82%) and negative $\delta^{13}C$ values (−12.4‰ to −10.7‰).

In the P_3w Formation, laumontite cement is abundant and widespread (Figure 2A) and is related to the alteration of volcanic lithic fragments in the rocks (Hay, 1966; Zhu et al., 2012). Laumontite can be observed in the water-, oil-, and gas-bearing layers (Figures 2C,E), indicating that the alteration of volcanic material was widespread. The moderately high MnO and FeO contents of early-stage calcite show that Mn^{2+} and Fe^{2+} ions were released into the pore water from the volcanic material during eodiagenesis, and the process slightly increased the pH of the pore water and promoted the precipitation of the early-stage calcite (Figure 6; Gieskes and Lawrence, 1981; Elderfield and Gieskes, 1982; Zhu et al., 2012).

Overall, the presence of calcite with low MnO contents (<1.5%) and moderately high $\delta^{13}C$ values (greater than −10.0‰) shows that the early diagenetic fluids in the study area were affected by meteoric water (Irwin et al., 1977; Aggarwal et al., 2004). The wide range of MnO contents (2.5%–6%) and lower $\delta^{13}C$ values (less than −10.0‰) of the authigenic calcite in the hydrocarbon-bearing layers indicate that during subsequent hydrocarbon charging the diagenetic fluid was altered by hydrocarbon-bearing fluids (Figures 6, 8). Individual water-bearing layers were also affected by water-soluble carboxylic acids and organic-matter derived CO_2. Moreover, in siliciclastic strata where oxidizing minerals occur, hydrocarbon–water–rock interactions promoted by high temperatures (>90°C) or microorganisms may cause hydrocarbon oxidation and generate organic acids and ^{13}C-depleted CO_2 (Surdam et al., 1993; Seewald, 2003; Hu et al., 2018; Wan et al., 2021). CO_2 generated *via* this process can lead to further precipitation of authigenic calcite with $\delta^{13}C$ values of less than −25‰ under alkaline conditions (Figure 8; Irwin et al., 1977; Hu et al., 2018).

Precipitation sequence of the authigenic minerals

Authigenic minerals are widespread in the P_3w Formation and characterized by multiple phases of precipitation (Figure 2). Multiple generations of authigenic minerals are products of changing geological fluids and complex fluid–rock interactions (Xie et al., 2020; Sun et al., 2021; Zhi et al., 2022). In the oil- and gas-bearing layers, hydrocarbon charging changed the diagenetic sequence, leading to the dissolution and re-precipitation of various secondary minerals (Walkden and Berry, 1984; Swart, 2015; Wu et al., 2017; Kang et al., 2019). During the early diagenetic stage, the pore water was transferred from the interbedded plastic mudstone layers to the clast-supported sandy conglomerate layers. As the burial depth increased, the temperature rose gradually, and the volcanic material experienced extensive alteration leading to the precipitation of authigenic laumontite as primary cement (Zhu et al., 2012). This process led to an increase in the pH of the pore water (Elderfield and Gieskes, 1982; Sample et al., 2017) and inorganic CO_2 and terrestrial Ca^{2+} concentrated gradually in the pore water, leading to precipitation of the early-stage calcite in residual intergranular pores (Figures 2B, 4C). There was a hiatus after the deposition of the P_3w Formation before the deposition of the overlying Early Triassic Baikouquan Formation, forming the Permian–Triassic unconformity around the sag (Figure 1B). This meant that the P_3w formation was affected by leaching by meteoric water during diagenesis (Yuan et al., 2017). The neutral to

10.3389/feart.2022.1007902

TABLE 2 $\delta^{13}C$ and $\delta^{18}O$ values of calcite in the P_3w Formation.

Sample well	Depth, m	Lithology	Calcite stages	Well test result	$\delta^{13}C_{VPDB}$, ‰	$\delta^{18}O_{VPDB}$, ‰
K206-1	3627.9	Gray sandy conglomerate	Early- and Late-stage	Water layers	−8.3	−16.9
K206-2	3629.5		Early- and Late-stage		−10.7	−15.5
K206-3	3635.1	Gray inequigranular sandstone Gray sandy conglomerate	Early- and Late-stage		−8.6	−17.1
K206-4	3640.1		Early- and Late-stage		−12.4	−18.0
K206-5	3642.0		Early- and Late-stage		−10.9	−14.8
K206-6*	3642.5		Early-stage		−2.1	−11.5
PD1-8	5262.6	Gray muddy siltstone	Early-stage		−4.2	−16.2
JT1-7*	4482.8	Gray inequigranular sandstone	Early- and Late-stage		−7.3	−15.1
JT1-14*	4530.1	Gray granule conglomerate	Early-stage		1.2	−16.6
JT1-16*	4532.3	Gray mudstone	Early- and Late-stage		−6.8	−14.5
G3-9v	4932.2	Grayish brown Medium-fine conglomerate	Early- and Late-stage		−7.6	−15.8
G191-2	4334.0	Gray sandy granule conglomerate	Early- and Late-stage	Heavy oil layers	−14.9	−15.1
G191-5	4334.8		Early- and Late-stage		−13.7	−17.7
G191-6	4335.0		Early- and Late-stage		−8.8	−14.0
G191-7*	4335.2		Early- and Late-stage		−13.9	−14.4
G191-8*	4335.4	Gray muddy sandstone	Late-stage		−14.3	−16.6
G191-9	4335.5	Gray sandy granule conglomerate	Early- and Late-stage		−14.9	−20.9
G191-10	4335.6		Early- and Late-stage		−12.9	−19.3
G191-12	4350.7	Gary muddy siltstone	Late-stage		−25.7	−15.0
ST1-2*	5282.3	Grayish white sandy conglomerate	Early- and Late-stage	Oil layers containing water	−11.0	−13.8
ST1-3*	5282.9		Early- and Late-stage		−14.5	−14.7
ST1-6*	5284.5		Late-stage		−18.9	−16.3
ST1-10*	5310.9	Gray mudstone	Late-stage		−19.5	−15.0
ST2-4*	5165.7	Gray sandy conglomerate	Early- and Late-stage	Low-quality oil layers	−8.3	−14.6
ST2-5*	5166.3		Early- and Late-stage		−18.5	−15.4
ST2-6	5167.5		Early- and Late-stage		−19.9	−13.7
ST2-8	5168.6	Gray sandy granule conglomerate	Early- and Late-stage		−8.1	−13.6
G3-4	4641.9	Gray medium-fine conglomerate	Early- and Late-stage	Gas layers	−6.2	−14.2
G3-5	4759.6		Early- and Late-stage		−6.8	−14.7

*indicates the $\delta^{13}C$ and $\delta^{18}O$ data was cited from Zhi et al., 2022.

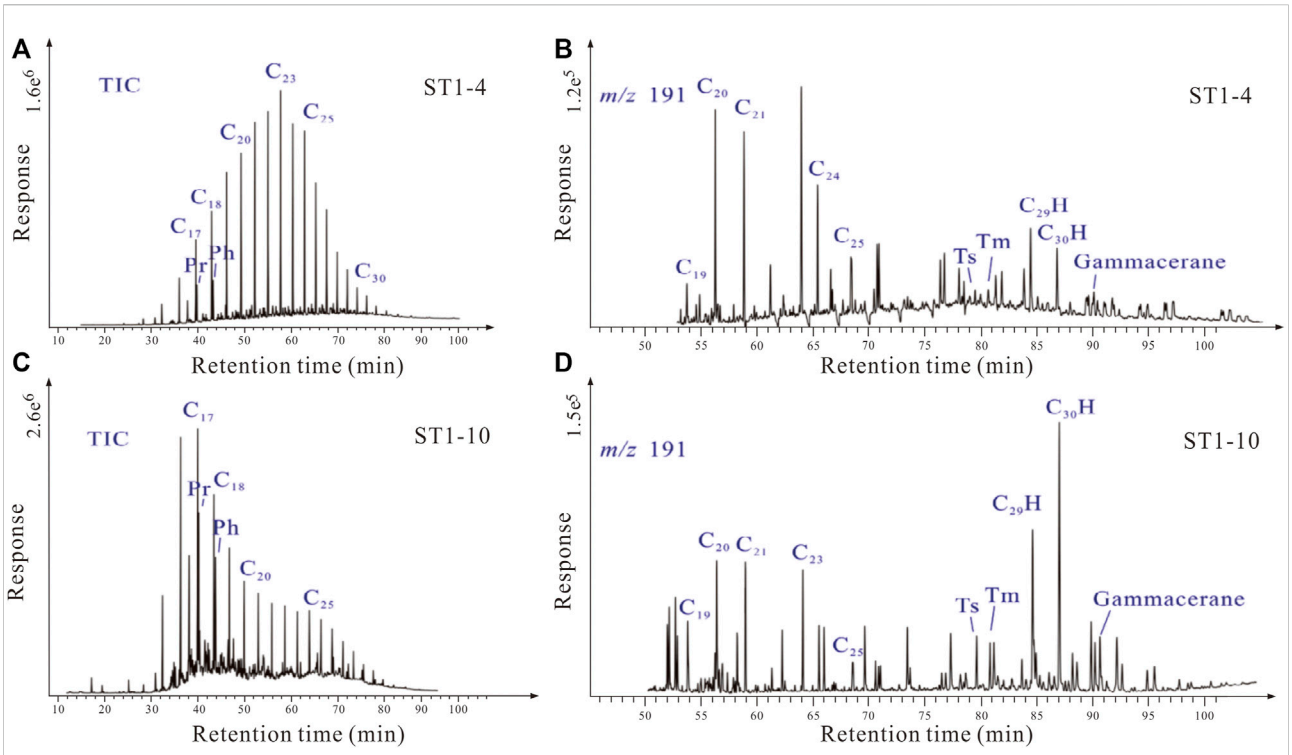

FIGURE 7
(A–C) Chromatograms and **(B–D)** mass spectrograms (with *m/z* ratio of 191) of crude oil samples from the P_3w Formation. Pr: pristane, Ph: phytane. **(A)** A complete sequence of *n*-alkanes in the total ion chromatogram (TIC) of ST1-4 oil sample. **(B–D)** 25-norhopanes were not found in *m/z* 191 mass spectrograms of ST1-4 and ST1-10 oil. **(C)** Limited unidentified compound materials occur in the total ion chromatogram of ST1-10 oil sample, indicating mild biodegradation.

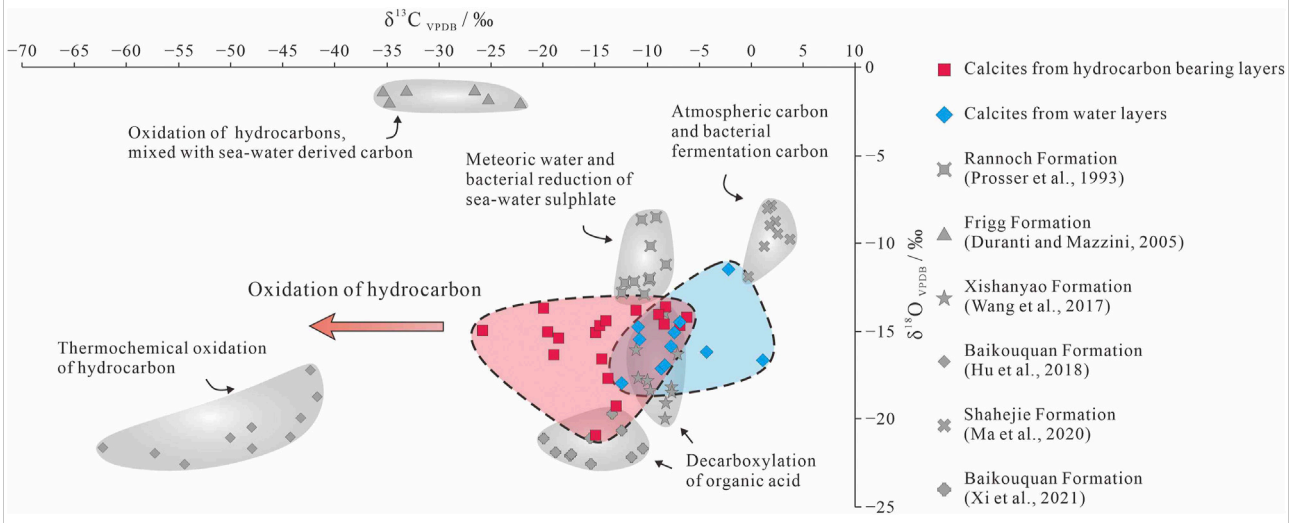

FIGURE 8
Carbon and oxygen isotopic compositions of the P_3w calcite compared with typical authigenic calcite in siliciclastic rocks.

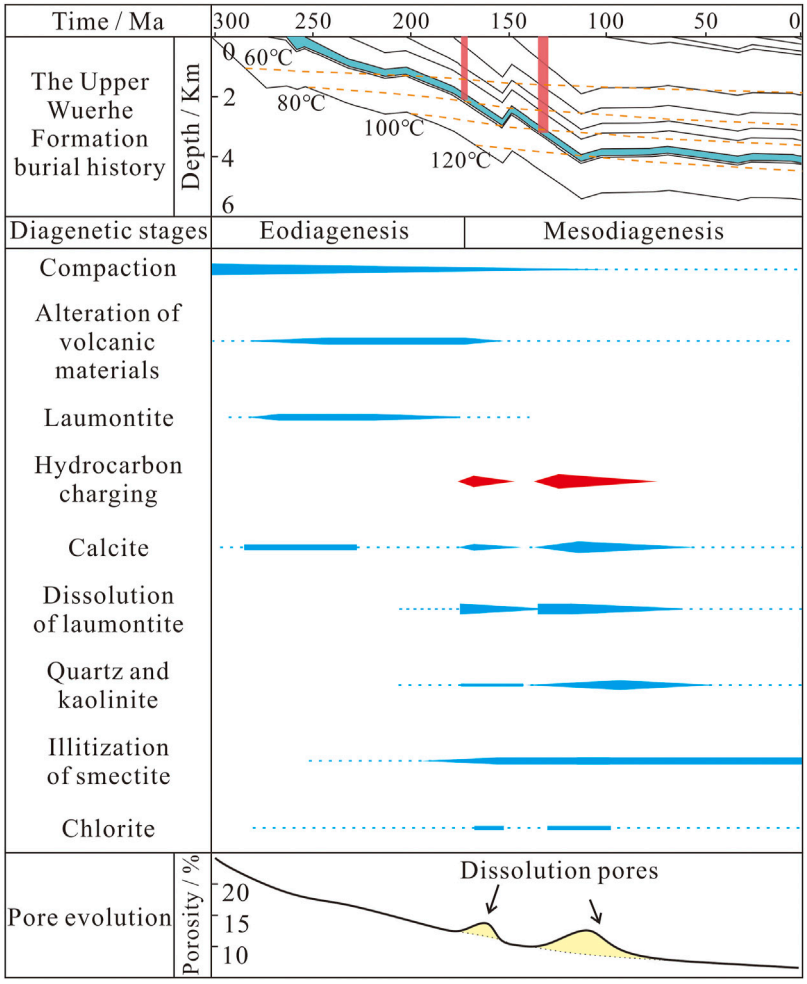

FIGURE 9
Integrated diagenetic evolution based on petrology and burial and thermal histories and their effect on the porosity of the P_3w sandy conglomerates. The burial history and thermal evolution of P_3w is taken from Well ZJ1. The stratigraphy is from Wang (2016), and the tectonic and geothermal evolution data are from Qiu et al. (2002).

acidic meteoric water changed the properties of the pore water and caused partial recrystallization of the early-stage calcite.

Limited hydrocarbon emplacement occurred during the Middle Jurassic (Figure 9; Pan et al., 2021). The acidic hydrocarbon-bearing fluids promoted the alteration of volcanic material and led to precipitation of the late-stage I calcite (Figure 5B). The second, large-scale hydrocarbon charging event during the Early Cretaceous introduced organic acids and organic derived CO_2 (Figure 9; Surdam et al., 1984, Surdam et al., 1989; Zhi et al., 2022), which further reduced the pH of the pore water, leading to extensive dissolution of laumontite and early-stage calcite (Figure 2E). These secondary pores became interconnected along cleavage fractures (Figure 3E) and retained small amounts of solid bitumen (Figure 2E). When the Ca^{2+}, Al^{3+}, and Si^{4+} ions released by the dissolution of laumontite and early-stage calcite reached saturation, secondary quartz and kaolinite precipitated in the pores (Figures 3D,E). Dissolution also buffered the pH of the pore water (Surdam et al., 1984, 1993), leading to the precipitation of late-stage calcite II in dissolution and residual intergranular pores (Figures 5C,D).

In the water-bearing and dry layers, alteration of volcanic lithic fragments and the pore water composition led to precipitation of laumontite and early-stage calcite during eodiagenesis. More sparry laumontite and calcite cements occur in the water-bearing layers than in the dry layers, as water aids ion transport (Figure 2C). Leaching by meteoric water also promoted recrystallization of early-stage calcite (Figures 2B, 5A). During mesodiagenesis, most minerals (including the laumontite cement) remained stable in the water-bearing layers, except for smectite, which was illitized.

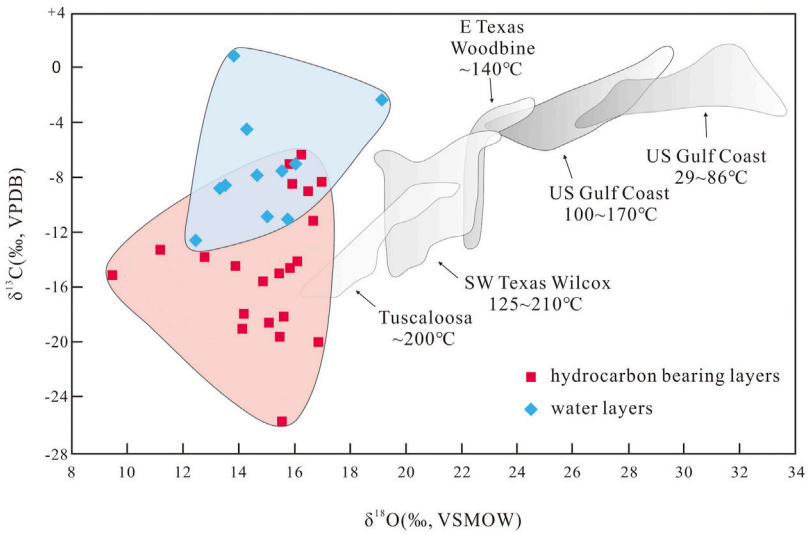

FIGURE 10
$\delta^{13}C$ and $\delta^{18}O$ values of calcite cement in the P_3w Formation compared with typical authigenic calcite in source rocks (modified from Franks and Forester, 1984).

Origin of organic acids in the reservoir

The late-stage calcite in the study area was affected by organic acids dissolved in the hydrocarbon-bearing fluids (Figure 8). A small amount of organic acid is dissolved in hydrocarbon-bearing fluids when they are extracted from source rocks (Irwin et al., 1977; Franks and Forester, 1984). The $\delta^{13}C$ values of the authigenic calcite in the oil- and gas-bearing layers of the P_3w Formation are lighter than those of calcite in typical source rocks (Figure 10), suggesting that insufficient organic acid was supplied from the source rocks to generate the ^{13}C-depleted late-stage calcite. Assuming that the maximum organic acid content in the in hydrocarbon-bearing fluids that migrated into the reservoirs in the P_3w Formation from the source rock was 10,000 mg L^{-1} (Shock, 1994), and that the porosity of the reservoir rock was 15% when the reservoir was charged by oil and gas, the organic acid in one cubic meter of rock could have generated 1,100 g of CO_2 through thermal decarboxylation. However, the calcite content of the formation is ~6%, which would have required 71,280 g of CO_2 per cubic meter of rock. As stable carbon isotopic fractionation is mass balanced, we can assume $\delta^{13}C$ values of −2‰ and −25‰ for the early-stage calcite and the calcite related to thermal decarboxylation of organic acids, respectively (Irwin et al., 1977; Hu et al., 2018). Using the carbon isotopic compositions of the calcite in the P_3w Formation, we can estimate that CO_2 from the thermal decarboxylation of organic acids accounts for 18%–100% (mean = 53%) of the calcite in the oil- and gas-bearing layers. In the water-bearing layers, this proportion reduces to 0%–45% (mean = 23%). Using these proportions, we still estimate that the authigenic calcite in one cubic meter of rock in the hydrocarbon- and water-bearing layers would have required 37,779 and 16,395 g, respectively, of CO_2 from the decarboxylation of organic acids. Both values are far higher than the 1,100 g supplied by the source rocks, which suggests that the supply of organic acids from source rocks was insufficient, and that additional organic acids were most likely produced in the reservoir rocks *via* interactions between organic hydrocarbons and inorganic minerals.

It has been suggested that hydrocarbons reacting with SO_4^{2-} or high-valance Fe and Mn oxides, induced by microorganisms or high temperatures, to generate organic acids after hydrocarbons are emplaced in a reservoir (Surdam et al., 1993; Seewald, 2003). The low $\delta^{13}C$ values (as low as −25.7‰) of the late-stage calcite confirm that hydrocarbon oxidation occurred in the P_3w reservoirs. The oxidation consisted of a series of intermediary reactions involving alkene, alcohol, ketone, and carboxylic acid, ultimately producing short-chained saturated hydrocarbons and CO_2 (Figure 11). The mineral oxidants provided a strong driving force for the reaction to proceed by consuming H_2 that would otherwise accumulate in pore fluids (Seewald, 2001). The rapid kinetics of the reactions that consume the alkene, alcohol, and ketone intermediaries resulted in very low concentrations of these species in solution during *n*-alkane oxidation, whereas the sluggish kinetics of the destruction of carboxylic acids by decarboxylation and oxidation would have allowed their certain concentrations in aqueous fluids (Seewald, 2001, 2003). The carboxylic acids most likely

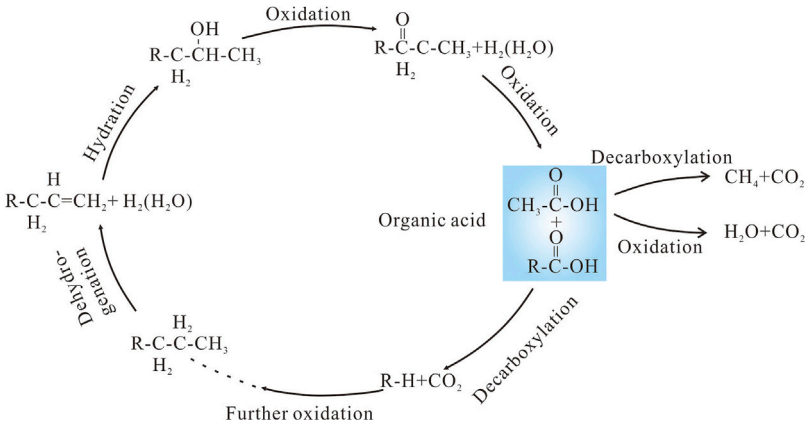

FIGURE 11
Reaction pathways for the oxidation of long-chain hydrocarbons alongside the reduction of high-valence Mn and Fe oxides. Modified after Seewald (2003).

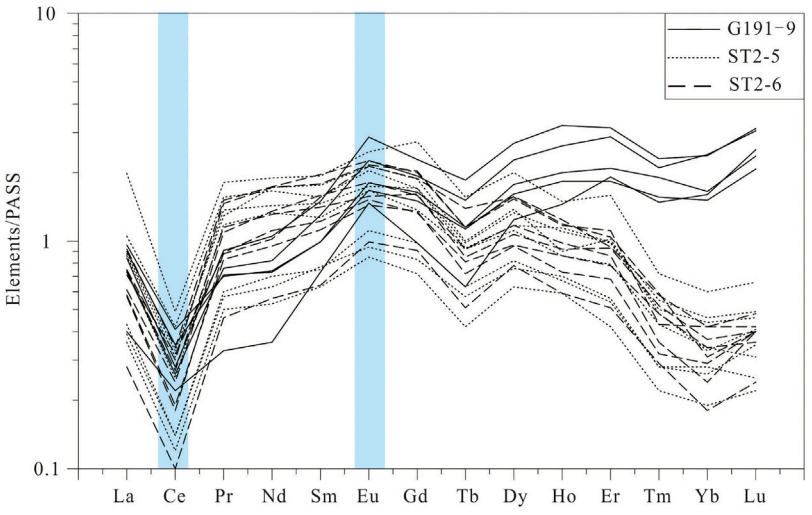

FIGURE 12
PAAS-normalized REE diagram for calcite in the P_3w Formation.

provided the excess organic derived CO_2 required to precipitate the calcite in the P_3w Formation.

The homogenization temperatures of fluid inclusions in the P_3w Formation indicate that they formed at temperatures of >80°C during hydrocarbon charging (Wang, 2016); such temperatures are not conducive to the metabolism and survival of bacteria (Peters et al., 2005). Moreover, the crude oil in the P_3w Formation contains a relatively complete n-alkane sequence, with no significant increase in typical microbial degradation biomarkers (e.g., 25-norhopanes; Figure 7), providing further evidence against the possibility that the organic acids were generated by microbial activity. In addition, no authigenic pyrite or H_2S were found in the samples, ruling out the possibility of thermochemical sulfate reduction (Krouse et al., 1988). Thus, some of the organic acids in the P_3w Formation were generated *via* the oxidation of hydrocarbons by high-valence Fe and Mn oxides at temperatures of >80°C.

The REE characteristics of the calcite also support an oxidized diagenetic environment during burial of the P_3w

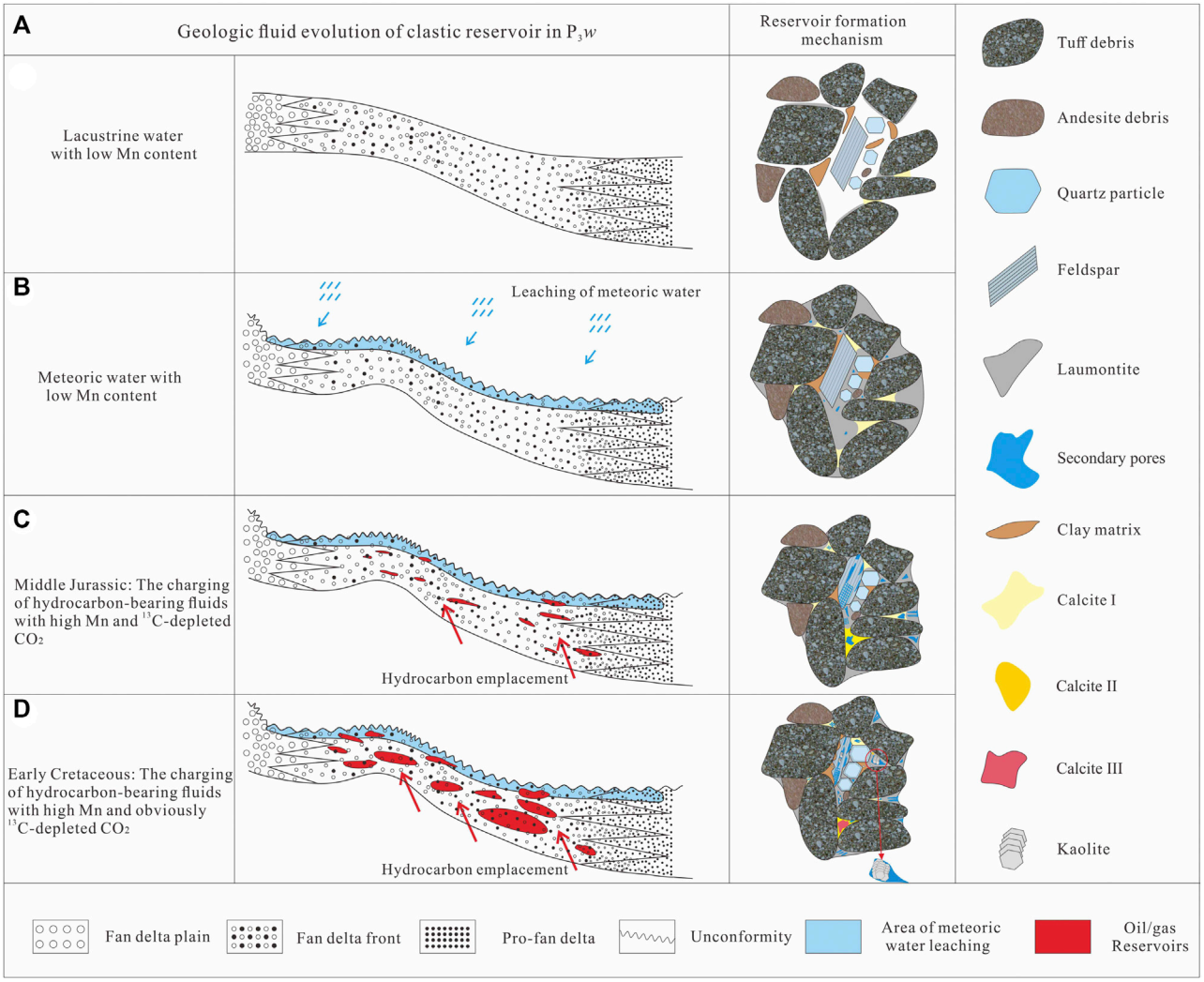

FIGURE 13
Evolution of the geologic fluid and formation of the P_3w reservoirs.

Formation. The calcite in this formation is enriched in LREEs relative to HREEs (Figure 12). Previous studies have shown that when crude oil or other organic matter is degraded, more LREEs than HREEs are released from hydrocarbon-bearing fluids into the pore water (Haley et al., 2004; Himmler et al., 2010). This process likely caused the LREE enrichment in the authigenic calcite. The calcite also yields negative Ce and positive Eu anomalies (Figure 12), indicating an oxidizing environment (Zhao, 1997). The calcite also yields high Y/Ho ratios (19.10–28.43). Bau and Dulski (1999) argued that Fe and Mn oxides and hydroxides preferentially adsorb Ho relative to Y in an oxidizing environment, thus increasing the Y/Ho ratios of diagenetic fluids. In addition, interbedded brown mudstone layers are found in the P_3w Formation, and hematite also exists in some conglomerate layers. These indicate an oxidizing diagenetic environment in this formation. It implies that organic acids were generated by the oxidation of long-chain hydrocarbons by oxidizing meterials when hydrocarbons migrated into reservoirs in the P_3w Formation.

Alteration of deeply buried siliciclastic reservoirs by fluid

Owing to the different volumes of meteoric water and hydrocarbon-bearing fluids, different fluid–rock interactions occurred in the hydrocarbon-bearing, water-bearing, and dry layers, which altered the diagenetic processes and affected reservoir quality. During the early stage of diagenesis, the P_3w Formation was only shallowly buried, leading to weak

compaction. Authigenic laumontite and early-stage calcite precipitated as primary cements, partially resisting compaction by the overlying strata (Figure 13A; Liu et al., 2019). As burial depth increased, increased compaction, the recrystallization of the early-stage calcite, and clay mineral precipitation reduced the residual primary porosity. During the depositional hiatus at the end of the Permian, the CO_2 supply from meteoric water caused slight dissolution of soluble components, including the laumontite cement and feldspar debris at the top of the formation, and these dissolution pores were filled mostly by recrystallized calcite. Thus, only limited secondary porosity formed close to the top of this formation owing to leaching by meteoric water (Figures 2, 13B).

During mesodiagenesis, a limited phase of hydrocarbon emplacement during the Middle Jurassic played an important role in alteration of the P_3w reservoirs. Owing to charging by acid hydrocarbon bearing fluids derived from the source rocks, the pH of the pore water in the reservoir decreased, preventing the precipitation of laumontite and calcite or promoting their dissolution and forming a small amount of secondary porosity. This period of hydrocarbon emplacement interrupted the decline in reservoir porosity caused by mechanical compaction, providing pore space for subsequent hydrocarbon accumulation and laying the foundation for further reservoir alteration (Figure 13C). After intense hydrocarbon charging during the Early Cretaceous, the high-temperature oxidation of hydrocarbons produced organic acids that added to those initially derived from the source rocks. The decrease in the pH of the pore fluids caused extensive dissolution of laumontite and early-stage calcite and produced abundant secondary pores. Overall, the two periods of hydrocarbon emplacement considerably increased the reservoir porosity and contributed to the formation of the P_3w reservoir beds (Figure 11D).

Conclusion

Multiple generations of calcite record the properties of and changes in diagenetic fluids and fluid–rock interactions in the P_3w Formation. In hydrocarbon-bearing layers, early diagenetic fluid mainly inherited its composition from paleo-meteoric water and precipitated early-stage calcite with low MnO contents (<1.5%) and normal $\delta^{13}C$ values (−10.0‰ to +2.0‰). During mesodiagenesis, limited hydrocarbon charging during the Middle Jurassic altered the diagenetic fluid, causing enrichment in Mn and ^{13}C-depleted organic derived CO_2, leading to precipitation of late-stage calcite I with high MnO contents (2.5%–4%) and negative $\delta^{13}C$ values (−10.0‰ to −15.0‰). Large-scale hydrocarbon emplacement during the Early Cretaceous produced diagenetic fluid that was more enriched in Mn and organic derived CO_2, thus forming late-stage calcite II, characterized by higher MnO contents (4%–6%) and more negative $\delta^{13}C$ values (less than −15.0‰). The emplacement of hydrocarbon-bearing fluids altered the diagenetic process substantially. The abundant volcanic lithic fragments in this formation were altered to form abundant authigenic laumontite during eodiagenesis, while hydrocarbon charging caused dissolution of laumontite and early-stage calcite and precipitation of other minerals, including kaolinite, quartz, and late-stage calcite. This process formed a network of dissolution pores, increasing the porosity and permeability of the rock. In contrast, in water-bearing and dry layers, most of the laumontite and calcite remained stable. In addition, in oxidizing rocks such as the P_3w formation, long-chain hydrocarbons can be oxidized to carboxylic acids that enhance diagenesis, as thermal decarboxylation forms ^{13}C-depleted CO_2. This study shows that authigenic calcite can record the properties of diagenetic fluids and the fluid–rock interactions that occur during diagenesis, and its composition can be used to identify diagenetic fluids in petroliferous basins.

Data availability statement

The raw data supporting the conclusions of this article will be made available by the authors, without undue reservation.

Author contributions

DX is the principal author and petrological interpreter, and also writes and edits the paper. YQ and LH contribute on the geological explanations, as well as writing/editing the paper. CD and RH conduct the geochemical analyses, and contribute on preparing the figures and writing the paper. XK provides the founding for this study and thoroughly edits the paper.

Funding

This work was financed by the National Natural Science Foundation of China (Grant Nos. 41902137), the China Hunan Provincial Science & Technology Department (2022WK 2004) and the Natural Science Foundation of Hunan Province (2020JJ5703). We extend our gratitude to Jeffery M. Dick for his helpful improving on the language.

Conflict of interest

The authors declare that the research was conducted in the absence of any commercial or financial relationships that could be construed as a potential conflict of interest.

Publisher's note

References

Aggarwal, P. K., Dillon, M. A., and Tanweer, A. (2004). Isotope fractionation at the soil-atmosphere interface and the ^{18}O budget of atmospheric oxygen. *Geophys. Res. Lett.* 31 (14), L14202. doi:10.1029/2004GL019945

Bau, M., and Dulski, P. (1999). Comparing yttrium and rare earths in hydrothermal fluids from the mid-atlantic ridge: implications for Y and REE behaviour during near-vent mixing and for the Y/Ho ratio of proterozoic seawater. *Chem. Geol.* 155 (1–2), 77–90. doi:10.1016/S0009-2541(98)00142-9

Cao, J., Hu, W. X., Yao, S. P., Zhang, Y. J., Wang, X. L., Zhang, Y. Q., et al. (2007). New inorganic geochemical indicators for tracing petroleum migration in Junggar Basin. *Sci. China Earth Sci.* 37 (10), 1358–1369. (in Chinese with English abstract). Available at: https://engine.scichina.com/doi/pdf/aeb4e4c0298d43348912d1e934726c32.

Cao, J., Xia, L., Wang, T., Zhi, D., Tang, Y., and Li, W. (2020). An alkaline lake in the late paleozoic ice age (lpia): A review and new insights into paleoenvironment and petroleum geology. *Earth. Sci. Rev.* 202 (2020), 103091. doi:10.1016/j.earscirev.2020.103091

Drake, H., Åström, M. E., Heim, C., Broman, C., Åström, J., Whitehouse, M., et al. (2015). Extreme ^{13}C depletion of carbonates formed during oxidation of biogenic methane in fractured granite. *Nat. Commun.* 6 (1), 7020–7029. doi:10.1038/ncomms8020

Du, J. H., Zhi, D. M., Tang, Y., Jia, C. M., and Xu, Y., (2019). Prospects in upper permian and strategic discovery in shawan sag, Junggar Basin. *China Pet. Explor* 24 (1), 24–35. doi:10.3969/j.issn.1672-7703.2019.01.004

Elderfield, H., and Gieskes, J. M. (1982). Sr isotopes in interstitial waters of marine sediments from Deep Sea Drilling Project cores. *Nature* 300 (5892), 493–497. doi:10.1038/300493a0

Franks, S. G., and Forester, R. W. (1984). Relationships among secondary porosity, pore-fluid chemistry and carbon dioxide, Texas gulf coast: Part 1. Concepts and principles. *AAPG Mem.* 37 (2), 63–80.

Gieskes, J. M., and Lawrence, J. R. (1981). Alteration of volcanic matter in deep sea sediments: Evidence from the chemical composition of interstitial waters from deep sea drilling cores. *Geochim. Cosmochim. Acta* 45 (10), 1687–1703. doi:10.1016/0016-7037(81)90004-1

Gregg, J. M., and Shelton, K. L. (1989). Minor-and trace-element distributions in the Bonneterre Dolomite (Cambrian), southeast Missouri: Evidence for possible multiple-basin fluid sources and pathways during lead-zinc mineralization. *Geol. Soc. Am. Bull.* 101 (2), 221–230. doi:10.1130/0016-7606(1989)101<0221:matedi>2.3.co;2

Haley, B. A., Klinkhammer, G. P., and McManus, J. (2004). Rare Earth elements in pore waters of marine sediments. *Geochim. Cosmochim. Acta* 68 (6), 1265–1279. doi:10.1016/j.gca.2003.09.012

Han, B. f., Ji, J. Q., and Song, B., (2006). Late paleozoic vertical growth of continental crust around the Junggar Basin, xinjiang, China (part: I): Timing of post-collisional plutonism. *Acta Pet. Sin.* 22 (5), 1077–1086.

Hao, F., Guo, T. L., Zhu, Y. M., Cai, X. Y., Zou, H. Y., and Li, P. P. (2008). Evidence for multiple stages of oil cracking and thermochemical sulfate reduction in the Puguang gas field, Sichuan Basin, China. *Am. Assoc. Pet. Geol. Bull.* 92 (5), 611–637. doi:10.1306/01210807090

Hay, R. L. (1966). Zeolites and zeolitic reactions in sedimentary rocks. *GSA Spec. Pap.* 85, 1–122. doi:10.1130/SPE85-p1

Himmler, T., Bach, W., Bohrmann, G., and Peckmann, J. (2010). Rare Earth elements in authigenic methane-seep carbonates as tracers for fluid composition during early diagenesis. *Chem. Geol.* 277 (1–2), 126–136. doi:10.1016/j.chemgeo.2010.07.015

Hu, W. X., Kang, X., Cao, J., Wang, X. L., Fu, B., and Wu, H. G. (2018). Thermochemical oxidation of methane induced by high-valence metal oxides in a sedimentary basin. *Nat. Commun.* 9 (5131), 1–10. doi:10.1038/s41467-018-07267-x

Huang, L., Liu, Y., Bian, B., Ma, Y., Liu, H., Guo, J., et al. (2021). Chemically active elements of reservoir quartz cement trace hydrocarbon migration in the Mahu Sag, Junggar Basin, NW China. *Geofluids* 2021, 6617945. doi:10.1155/2021/6617945

Irwin, H., Curtis, C., and Coleman, M. (1977). Isotopic evidence for source of diagenetic carbonates formed during burial of organic-rich sediments. *Nature* 269 (5625), 209–213. doi:10.1038/269209a0

Jin, Z. J., Zhang, L. P., Yang, L., and Hu, W. X. (2002). Primary study of geochemical features of deep fluids and their effectiveness on oil/gas reservoir formation in sedimental basins. *Earth Sci.* 27 (6), 659–665. Available at: http://www.earth-science.net/fileDQKX/journal/article/dqkxzx/2002/6/1182.pdf.

Kang, X., Hu, R. P., Hu, W. X., and Tan, J. Q. (2021). Oxidizing materials during thermochemical oxidation of hydrocarbons in the lower triassic Baikouquan Formation in the Junggar Basin. *Adv. Earth Sci.* 36 (10), 1004–1014. doi:10.11867/j.issn.1001-8166.2021.019

Kang, X., Hu, W., Cao, J., Wu, H., Xiang, B., and Wang, J. (2019). Controls on reservoir quality in fan-deltaic conglomerates: Insight from the lower triassic Baikouquan Formation, Junggar Basin, China. *Mar. Pet. Geol.* 103, 55–75. doi:10.1016/j.marpetgeo.2019.02.004

Krouse, H. R., Viau, C. A., Eliuk, L. S., Ueda, A., and Halas, S. (1988). Chemical and isotopic evidence of thermochemical sulphate reduction by light hydrocarbon gases in deep carbonate reservoirs. *Nature* 333 (6172), 415–419. doi:10.1038/333415a0

Kuang, Li. C., Zhi, D. M., et al. (2022). Hydrocarbon accumulation conditions and exploration directions of large-scale lithologic-stratigraphic oil and gas reservoirs in Upper Wuerhe Formation of Upper Permian in Junggar Basin. *Acta Pet. Sin.* 43 (3), 325–340. doi:10.7623/syxb202203001

Li, S. (2004). Basin geodynamics background of formation of huge petroleum systems. *Earth Sci.* 29 (5), 505–512. Available at: http://www.earth-science.net/fileDQKX/journal/article/dqkxzx/2004/5/1479.pdf.

Liang, Y. S., He, D. F., Zhen, Y., Zhang, L., and Tian, A. J. (2018). Tectono-stratigraphic sequence and basin evolution of shawan sag in the Junggar Basin. *Oil Gas. Geol.* 39 (5), 943–954. doi:10.11743/ogg20180509

Liu, Q., Peng, W., Meng, Q., Zhu, D., Jin, Z., and Wu, X. (2020). Fractionation of carbon and hydrogen isotopes of TSR-altered gas products under closed system pyrolysis. *Sci. Rep.* 10 (12921), 1–14. doi:10.1038/s41598-020-69580-0

Liu, Y., Hu, W., Cao, J., Wang, X., Zhu, F., Tang, Q., et al. (2019). Fluid–rock interaction and its effects on the upper triassic tight sandstones in the sichuan basin, China: Insights from petrographic and geochemical study of carbonate cements. *Sediment. Geol.* 383, 121–135. doi:10.1016/j.sedgeo.2019.01.012

Ma, Y. S., He, D. F., Cai, X. Y., and Liu, B. (2017). Distribution and fundamental science questions for petroleum geology of marine carbonate in China. *Acta Pet. Sin.* 33 (94), 1007–1020. Available at: http://html.rhhz.net/ysxb/20170401.htm.

Minor, E. C., Tennant, C. J., and Brown, E. T. (2019). A seasonal to interannual view of inorganic and organic carbon and pH in Western Lake Superior. *J. Geophys. Res. Biogeosci.* 124 (2), 405–419. doi:10.1029/2018JG004664

Pan, C., Wang, J., Yu, S., Wang, X., Xiang, B., Liao, J., et al. (2021). Oil origins, mixing and biodegradation in southwestern Junggar Basin, NW China. *J. Pet. Sci. Eng.* 196, 108017. doi:10.1016/j.petrol.2020.108017

Peters, K. E., Walters, C. C., and Moldowan, J. M. (2005). *The biomarker guide*. Cambridge, United Kingdom: Cambridge University Press.

Qiu, N. S., Yang, H. B., and Wang, X. L. (2002). Tectono-thermal evolution in the Junggar Basin. *Chin. J. Geol.* 37, 423–429. doi:10.3321/j.issn:0563-5020.2002.04.005

Sample, J. C., Torres, M. E., Fisher, A., Hong, W. L., Destrigneville, C., Defliese, W. F., et al. (2017). Geochemical constraints on the temperature and timing of carbonate formation and lithification in the Nankai Trough, NanTroSEIZE transect. *Geochim. Cosmochim. Acta* 198, 92–114. doi:10.1016/j.gca.2016.10.013

Seewald, J. S. (2001). Aqueous geochemistry of low molecular weight hydrocarbons at elevated temperatures and pressures: Constraints from mineral buffered laboratory experiments. *Geochim. Cosmochim. Acta* 65, 1641–1664. doi:10.1016/S0016-7037(01)00544-0

Seewald, J. S. (2003). Organic–inorganic interactions in petroleum-producing sedimentary basins. *Nature* 426 (6964), 327–333. doi:10.1038/nature02132

Shock, E. L. (1994). *Organic acids in geological processes*. Editors E. D. Pittman, and M. D. Lewan (New York: Springer), 270–318.

Spiro, B. (1977). Bacterial sulphate reduction and calcite precipitation in hypersaline deposition of bituminous shales. *Nature* 269 (5625), 235–237. doi:10.1038/269235a0

Sun, F., Hu, W., Wu, H., Fu, B., Wang, X., Tang, Y., et al. (2021). Two-stage mineral dissolution and precipitation related to organic matter degradation: Insights from *in situ* C-O isotopes of zoned carbonate cements. *Mar. Pet. Geol.* 124, 104812. doi:10.1016/j.marpetgeo.2020.104812

Surdam, R. C., Boese, S. W., and Crossey, L. J. (1984). The chemistry of secondary porosity: Part 2. Aspects of porosity modification. *AAPG Mem.* 37 (2), 127–161.

Surdam, R. C., Crossey, L. J., Hagen, E. S., and Heasler, H. P. (1989). Organic-inorganic interactions and sandstone diagenesis. *AAPG Bull.* 73 (1), 1–23.

Surdam, R. C., Jiao, Z. S., and MacGowan, D. B. (1993). Redox reactions involving hydrocarbons and mineral oxidants: A mechanism for significant porosity enhancement in sandstones. *Am. Assoc. Pet. Geol. Bull.* 77 (9), 1509–1518. doi:10.1306/BDFF8ED4-1718-11D7-8645000102C1865D

Swart, P. K. (2015). The geochemistry of carbonate diagenesis: The past, present and future. *Sedimentology* 62 (5), 1233–1304. doi:10.1111/sed.12205

Tang, G., Wang, Q., Wyman, D. A., Li, Z. X., Zhao, Z. H., Jia, X. H., et al. (2010). Ridge subduction and crustal growth in the central asian orogenic belt: Evidence from late carboniferous adakites and high-Mg diorites in the Western junggar region, northern xinjiang (west China). *Chem. Geol.* 277 (3–4), 281–300. doi:10.1016/j.chemgeo.2010.08.012

Tao, K., Cao, J., Hu, W., Zhi, D., Lei, D., Tang, Y., et al. (2021). Petroleum system for the continuous oil play in the lacustrine Lower Triassic, Junggar Basin, China. *Am. Assoc. Pet. Geol. Bull.* 105, 2349–2380. doi:10.1306/07022119211

Walkden, G. M., and Berry, J. R. (1984). Natural calcite in cathodoluminescence: Crystal growth during diagenesis. *Nature* 308 (5959), 525–527. doi:10.1038/308525a0

Wan, Y., Bourdet, J., Hu, W., Kang, X., Heath, C., Qiu, Y., et al. (2021). Experimental investigations on the thermochemical oxidation of n-alkane and alcohol compounds by MnO_2 and Fe_2O_3 at temperatures up to 325 °C. *Chem. Geol.* 559, 119982. doi:10.1016/j.chemgeo.2020.119982

Wang, Y. S. (2016). "The features of fluid inclusions and their contained information on hydrocarbon migration and accumulation among permian systems in Zhongguai area, northwestern Junggar Basin," (Xi'an, China: Northwest University), 47–60. Unpubl. Master Thesis.

Wu, H., Hu, W., Tang, Y., Cao, J., Wang, X., Wang, Y., et al. (2017). The impact of organic fluids on the carbon isotopic compositions of carbonate-rich reservoirs: Case study of the lucaogou Formation in the jimusaer sag, Junggar Basin, NW China. *Mar. Pet. Geol.* 85, 136–150. doi:10.1016/j.marpetgeo.2017.05.003

Xi, K., Cao, Y., Jahren, J., Zhu, R., Bjørlykke, K., Haile, B. G., et al. (2015). Diagenesis and reservoir quality of the lower cretaceous quantou formation tight sandstones in the southern songliao basin, China. *Sediment. Geol.* 330, 90–107. doi:10.1016/j.sedgeo.2015.10.007

Xia, L., Cao, J., Bian, L., Hu, W., Wang, T., Zhi, D., et al. (2022). Co-evolution of paleo-environment and bio-precursors in a Permian alkaline lake, Mahu mega-oil province, Junggar Basin: Implications for oil sources. *Sci. China Earth Sci.* 65 (3), 462–476. doi:10.1007/s11430-021-9861-4

Xie, D., Yao, S., Cao, J., Hu, W., and Qin, Y. (2020). Origin of calcite cements and their impact on reservoir heterogeneity in the triassic yanchang formation, ordos basin, China: A combined petrological and geochemical study. *Mar. Pet. Geol.* 117, 104376. doi:10.1016/j.marpetgeo.2020.104376

Xie, X. N., Cheng, J. M., and Meng, Y. L. (2009). Basin fluid flow and associated diagenetic processes. *Acta Sediment. Sin.* 27 (5), 863–871. doi:10.14027/j.cnki.cjxb.2009.05.016

Yuan, G., Cao, Y., Qiu, L., and Chen, Z. (2017). Genetic mechanism of high-quality reservoirs in Permian tight fan delta conglomerates at the northwestern margin of the Junggar Basin, northwestern China. *Am. Assoc. Pet. Geol. Bull.* 101 (12), 1995–2019. doi:10.1306/02071715214

Zhang, C. J., He, D. F., Wu, X. Z., Shi, X., and Luo, J. (2006). Formation and evolution of multicycle superimposed basins in Junggar Basin. *China Pet. explor.* 1, 47–58. doi:10.3969/j.issn.1672-7703.2006.01.008

Zhang, G. C., Chen, X. F., Liu, L., Yu, L. P., and Wang, Z. (1999). The tectonic evolution, architecture and petroleum distribution in the Junggar Basin in China. *Acta Pet. Sin.* 20 (1), 13–18. Available at: https://www.cnki.com.cn/Article/CJFDTOTAL-SYXB901.002.htm.

Zhang, L. F., Lei, D. W., and Tang, Y., (2015). Hydrocarbon fluid phase in the deep-buried strata of the MaHu sag in the Junggar Basin. *Acta Geol. Sin.* 89 (5), 957–969. Available at: http://www.geojournals.cn/dzxb/ch/reader/create_pdf.aspx?file_no=2014195&st=alljournals.

Zhao, M. Y., Zheng, Y. F., and Zhao, Y. Y. (2016). Seeking a geochemical identifier for authigenic carbonate. *Nat. Commun.* 7 (1), 10885–10887. doi:10.1038/ncomms10885

Zhao, Z. H. (1997). *Principles of trace element geochemistry*. Bei Jing: Science Press.

Zhi, D. M., Kang, X., Qin, Z. J., Tang, Y., Cao, J., and Hu, R. P. (2022). Fluid-rock interactions and porosity Genesis in deep clastic reservoirs: A perspective of differential oil charge intensity. *Mar. Pet. Geol.* 137, 105508. doi:10.1016/j.marpetgeo.2021.105508

Zhu, G. Y., Zhang, S. C., Liang, Y. b., Ma, Y. S., Dai, J. X., and Zhou, G. Y. (2006). Dissolution and alteration of the deep carbonate reservoirs by TSR: An important type of deep-buried high-quality carbonate reservoirs in sichuan basin. *Acta Pet. Sin.* 22 (8), 2182–2194. doi:10.3969/j.issn.1000-0569.2006.08.008

Zhu, S. F., Zhu, X. M., Wang, X. L., and Liu, Z. Y. (2012). Zeolite diagenesis and its control on petroleum reservoir quality of Permian in northwestern margin of Junggar Basin, China. *Sci. China Earth Sci.* 55 (3), 386–396. doi:10.1007/s11430-011-4314-y

Zou, C. N., Hou, L. H., Kuang, L. C., and Kuang, J. (2007). Genetic mechanism of diagenesis-reservoir facies of the fan-controlled Permo-Triassic in the Western marginal area, Junggar Basin. *China J. Geol.* 42 (3), 587–601. doi:10.1016/S1872-5791(07)60044-X

frontiers | Frontiers in Earth Science

TYPE Original Research
PUBLISHED 11 January 2023
DOI 10.3389/feart.2022.1018712

OPEN ACCESS

EDITED BY
Hao Zou,
Chengdu University of Technology, China

REVIEWED BY
Qingqiang Meng,
SINOPEC Petroleum Exploration and Production Research Institute, China
Bin Cheng,
China University of Petroleum, Qingdao, China
Hong Xiao,
China University of Petroleum, China

*CORRESPONDENCE
Zhijun Qin,
zhijunqin_karamay@126.com

SPECIALTY SECTION
This article was submitted to Economic Geology, a section of the journal Frontiers in Earth Science

RECEIVED 13 August 2022
ACCEPTED 30 September 2022
PUBLISHED 11 January 2023

CITATION
Qin Z, Qi H, Liang Z, Ma W, Wang R and Wu W (2023), Geochemical classification and secondary alteration of crude oil in the southern thrust belt of Junggar Basin.
Front. Earth Sci. 10:1018712.
doi: 10.3389/feart.2022.1018712

Geochemical classification and secondary alteration of crude oil in the southern thrust belt of Junggar Basin

Zhijun Qin[1]*, Hongyan Qi[1], Zeliang Liang[1], Wanyun Ma[2], Ruiju Wang[3] and Wei'an Wu[3]

[1]Research Institute of Petroleum Exploration and Development, Xinjiang Oil Company, PetroChina, Karamay, China, [2]Research Institute of Experiment and Testing, Xinjiang Oil Company, PetroChina, Karamay, China, [3]Research Institute of Petroleum Exploration and Development, PetroChina, Beijing, China

This study analyzed, 18 oil samples from four representative oil-bearing secondary tectonic units in the southern thrust belt of the Junggar Basin. The genetic types and the secondary alteration of oil were discussed based on the characteristics of light hydrocarbon compounds, adamantanes, sterane/terpene biomarkers, and stable carbon isotopic composition of the bulk oil. . The results show that the oil in the study area can be divided into five categories. Type I oil is characterized by ^{13}C-depleted carbon isotopes, a low pristane to phytane ratio, and high gammacerane and low diasterane content, whereas Type II oil exhibits the opposite characteristics. Type III is very similar to Type II oil but has a higher ^{13}C-depleted bulk carbon isotopic composition and a wider carbon number of tricyclic terpenes. Type IV and V oils are similar to Type I oils, except for relatively lower gammacerane content. Further, Type IV oils also have high αaα 20R regular sterane content, ^{13}C-enriched bulk oil carbon isotopes, and a higher pristane to phytane ratio than Type I oil. In contrast, the relative content of C_{27} regular steranes of Type V oils is considerably lower than that of Type I oils. The oil in the study area has not suffered from biodegradation. Maturity information indicated by regular biomarkers (i.e., steroid, terpene, and phenanthrene) and adamantane differs significantly, with the latter exhibiting a strong cracking characteristic. This reflects the charging and mixing of oils formed at different evolution stages. The other types of oils are in the normal oil-generating window and do not suffer from intense cracking. The oil in the study area is generally subjected to evaporative fractionation, but there are obvious differences in the degree of alteration between different oil-bearing structures and different reservoirs with the same structure. This study is of great significance for understanding the origin and accumulation process of oil and gas in a complex structural zone.

KEYWORDS

biomarker, carbon isotope, origin and genetic type, secondary alteration, southern thrust belt, Junggar Basin

1 Introduction

The southern thrust belt (STB) in the Junggar Basin is rich in oil and gas resources, and many oil and gas fields have been discovered since the discovery of the Dushanzi oilfield. In recent years, the successful breakthroughs of Wells Gaotan 1, Huotan 1, and Tianwan 1 have revealed broad oil and gas prospects in the STB (Du et al., 2019; He et al., 2019; Wang et al., 2021). Complex types of oil and gas have been found in the STB, including heavy oil, normal oil, light oil, condensates, and natural gas. The oil-producing strata are vertically distributed from Triassic to Neogene. Several sets of potential source rocks in this area overlap each other in the plane. Their maturity and hydrocarbon generation and expulsion history are significantly different. The geochemical characteristics of oil from different tectonic units or oil fields in the same tectonic unit are complex with several different origins (Guo et al., 2005; Chen et al., 2016a,b). Despite extensive research on the geochemical characteristics of source rocks, the geochemical characteristics and classification of oil, and the sources of oil and gas in the STB, there remains a lack of consensus (Zhang et al., 2003; Li et al., 2004; Guo et al., 2005; Wei D. et al., 2007; Cao et al., 2010; Chen et al., 2015a; Chen et al., 2016a). In addition, little attention has been paid to the secondary alteration of oil in this area and its implications for the petroleum accumulation process (Lu et al., 2019). Therefore, this study conducted a detailed geochemical anatomy of 18 oil samples collected from key oil-bearing structural units of the STB. Based on the characteristics of light hydrocarbons, adamantanes, biomarkers, and stable carbon isotopic composition of the bulk oil ($\delta^{13}C_{bulk}$), the geochemical classification and potential secondary alterations such as biodegradation, thermal cracking, and evaporative fractionation were discussed to better understand the genesis and accumulation process of multiple types of oil in this area.

2 Geological background

The STB spreads in an east-west direction and contains six second-order structural units from west to east, including the Sikeshu sag, Gaoquan tectonic belt, Aika anticline belt, Huomatu arc anticline belt, Qigu bruchfalten, and Fukang bruchfalten (Figure 1). The formation and evolution of the STB are closely related to the North Tianshan Orogenic Belt. The STB has experienced three tectonic evolution stages: the Permian foreland basin, the Triassic-Paleogene intracontinental depression, and the Neogene-Quaternary proterozoic continental basin (Gong et al., 2018; 2019). Many large anticlinal structures have been developed, and overlapping composite petroleum systems have been formed (He et al., 2019). The thrust nappe deformation is the main structural deformation mode in the thrust belt, and three rows of structural belts are formed from the piedmont basin of the orogenic belt in a nearly east-west direction, showing the typical characteristics of "north-south" zoning and "east-west" segmentation (Xiao et al., 2012; He et al., 2019). The strata of the STB have been continuously deposited since the Permian period, including Permian, Triassic, Jurassic, Cretaceous, Paleogene, and Quaternary, with a total thickness of 10–15 km (Chen et al., 2015a; Gong et al., 2018). Several sets of potential source rocks, such as Paleogene, Cretaceous, Jurassic, Triassic, and Permian, were developed with a considerable thickness (Figure 2). The lithology of the source rock is mainly dark mudstone, and the Jurassic and Triassic source rocks also developed carbonaceous mudstone and coal (Li et al., 2003; Chen et al., 2015a) (Figure 2). Exploration practice confirmed that the upper, middle, and lower reservoir and cap assemblages developed in the STB (Figure 2). The upper assemblage is composed of reservoirs in the Neogene

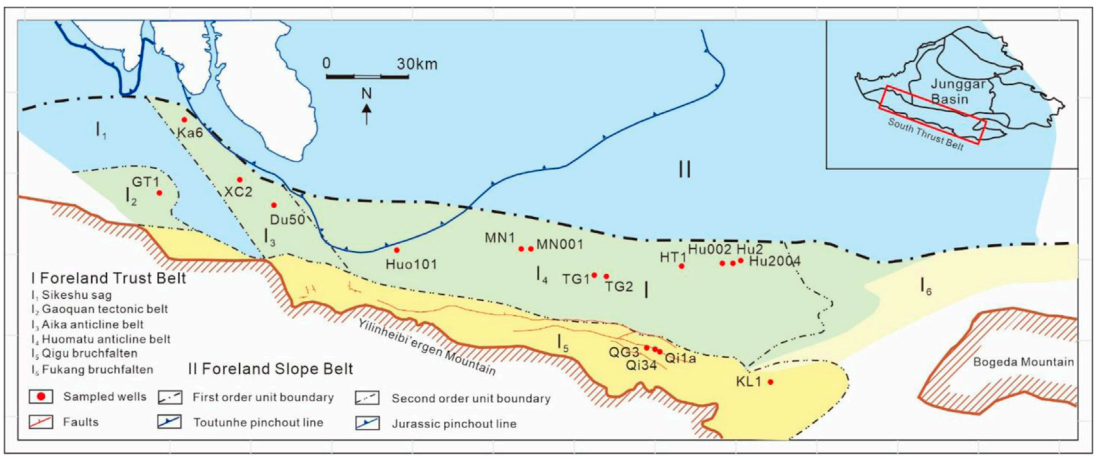

FIGURE 1
Map showing the structural units of STB and the location of sampled wells.

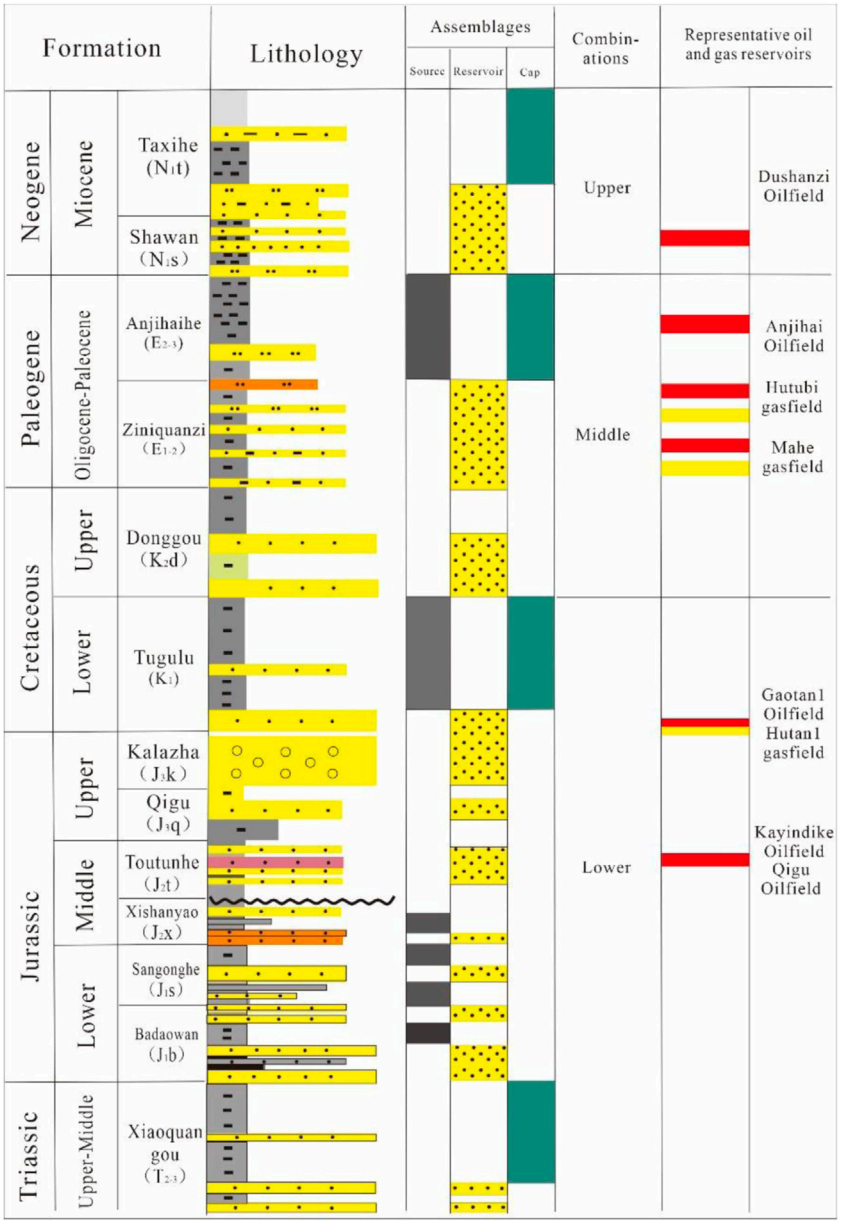

FIGURE 2
Stratigraphic chart and source-reservoir-cap assemblages in the STB of the Junggar Basin.

Dushanzi and Taxihe Formations and mudstone cap rocks of the Taxihe Formation; the middle assemblage is composed of reservoirs in the Anjihaihe and Ziniquanzi Formations and cap rocks in the Anjihaihe Formation; the lower assemblage consists of reservoirs in the Jurassic Badaowan, Sangonghe, Xishanyao, and Toutunhe Formations, Cretaceous Qingshuihe Formation, and mudstone caprocks in the Cretaceous Tugulu Group (Li et al., 2003; Du et al., 2019) (Figure 2). Several oil and gas resources have been found in different reservoir–cap assemblages (Gong et al., 2019).

3 Samples and methods

A total of 18 oil samples were collected from the Gaoquan tectonic belt, Aika anticline belt, Huomatu anticline belt, and Qigu bruchfalten in the STB. The oil-producing horizons include Triassic, Jurassic, Cretaceous, Paleogene, and Neogene. The well location is depicted in Figure 1.

After adding petroleum ether into a 50-mg oil sample to precipitate asphaltene, the sample was separated into saturated hydrocarbon, aromatic hydrocarbon, and non-

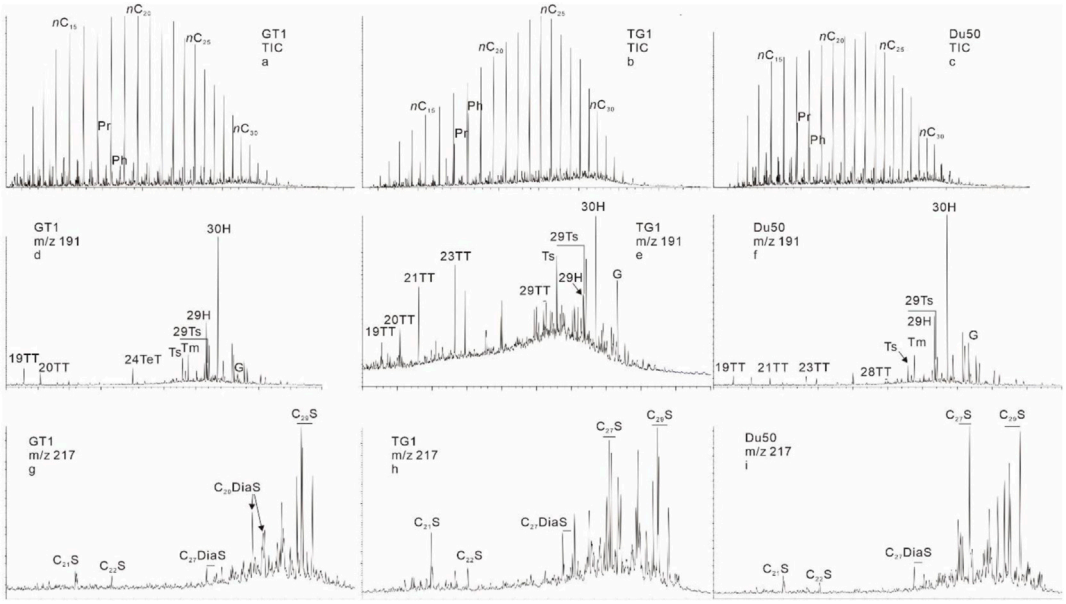

FIGURE 3
(A–C) TIC of saturated hydrocarbons showing distributions of *n*-alkanes and acyclic isoprenoids; **(D–F)** M/z 191 mass chromatograms showing distributions of terpanes; **(G–I)** M/z 217 mass chromatograms showing distributions of steranes. Pr: pristane; Ph: phytane; TT: tricyclic terpane, TeT: tetracyclic terpane, Ts: 18α (H)-trinorhopane; Tm: 17α (H)-trinorhopane; H: hopane, G: gammacerane; S: regular sterane; DiaS: diasterane.

hydrocarbon fractions by column chromatography filled with alumina and silica gel. The corresponding fractions were eluted by petroleum ether, a dichloromethane/petroleum ether mixture (2:1, V/V), and ethanol, respectively. The saturated and aromatic hydrocarbon fractions were analyzed by gas chromatography–mass spectrometry (GC–MS) using Agilent Intuvo 9000 GC and 5977BMS. Chromatography was performed on an HP–5MS capillary column (60 m × 0.25 mm × 0.25 μm) with helium as the carrier gas. The ion source of MS was electron bombardment (EI) with an ionization voltage of 70 eV, using two modes: full scan and selective ion scan. For the saturated hydrocarbon fraction, quantitative d_4-αααC_{29}20R sterane as an internal standard was added. The chromatograph furnace temperature was initially set at 50°C, 1 min after 20°C/min heating to 120°C, then 3°C/min heating to 310°C and constant temperature for 25 min. The d_8-dibenzothiophene was added to the aromatic hydrocarbon fraction as an internal standard. The furnace temperature was initially set at 80°C, a constant temperature for 1 min; then, the temperature was increased to 310°C at 3°C/min for 16 min. The saturated hydrocarbon fractions of representative samples were analyzed by metastable ion-monitoring GC–MS using Agilent 6890 GC, along with Quatro II MS. Chromatography was performed on a DB–5 capillary column (60 m × 0.25 mm × 0.25 μm) with helium as the carrier gas. The temperature of the chromatographic furnace was initially set at 100°C, then it was heated to 320°C at 4°C/min for 1 min, and the temperature remained constant for 20 min. EI was used as the ion source of MS, the ionization voltage was 70 eV, and the metastable reaction monitoring mode was employed.

In addition, an overall chromatographic analysis was performed on the oil samples using an Agilent 8,890 gas chromatograph, equipped with an HP–PONA capillary column (50 m × 0.2 mm × 0.5 μm), at an initial furnace temperature of 35°C, the constant temperature after 5 min at 3°C/min was increased to 70°C, and then the temperature was increased to 300°C at 4.5°C/min for 35 min. An Agilent Intuvo 9,000 gas chromatograph and a 5977B mass spectrometer were used to analyze the diamondoid series. The chromatogram was configured with HP–5MS capillary column (60 m × 0.25 mm × 0.25 μm), and the mass spectrum was selected through the ion scanning mode. The initial temperature of the chromatographic furnace was 50°C. After 1 min, the temperature was increased to 250°C at 3°C/min and then to 310°C at 20°C/min for 10 min d_{16}-adamantane was added to the oil sample as an internal standard to calculate the absolute content of the compound. Following PDB standards, the $\delta^{13}C_{bulk}$ ratios were determined using a FLASH 2000 EA–MAT 253 IRMS stable carbon isotope ratio mass spectrometer.

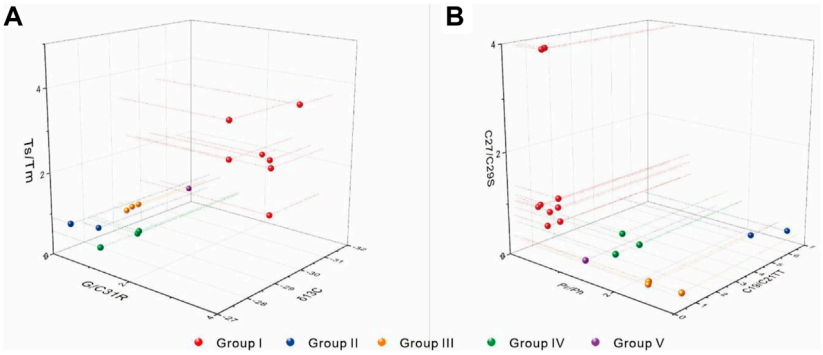

FIGURE 4
3-D scatter plots of **(A)** (x) $\delta^{13}C$, (y) Ts/Tm, and (z) $G/C_{31}R$ and **(B)** (x) C_{19}/C_{21} tricyclic terpane, (y) C_{27}/C_{29} steranes, and (z) pristane/phytane showing classification of genetic groups for studied oil samples.

4 Results

4.1 Group composition and stable carbon isotopes of bulk oil

The density of oil in the STB varies significantly from 0.76 to 0.90 g/cm^3. The composition of most oil groups is dominated by saturated hydrocarbons, and the content of non-hydrocarbon and asphaltene is low. Some oils do not contain asphaltene components. The percentages of saturated hydrocarbons, aromatic hydrocarbons, and non-hydrocarbon + asphaltene are 47.3%–88.7%, 2.81%–15.9%, and 4.94%–44.5%, respectively. There was a good negative correlation between the content of saturated hydrocarbons and non-hydrocarbon + asphaltene. The oil from Wells KL1 and Huo101 had the highest oil density, the lowest saturated hydrocarbon content, and the highest non-hydrocarbon + asphaltene content. The sample density correlated well with the chemical composition.

The $\delta^{13}C_{bulk}$ ratios also varied greatly, ranging from −31.4‰− to −27.0‰, reflecting the diversity of oil properties and the complex sources of the oil. Further, the $\delta^{13}C_{bulk}$ ratios from different tectonic units as well as the $\delta^{13}C_{bulk}$ ratios from different production layers of the same tectonic unit exhibit significant differences. On the other hand, oils from adjacent tectonic units have very similar $\delta^{13}C_{bulk}$ ratios. Based on the oil samples analyzed in this study, there are obvious differences in $\delta^{13}C_{bulk}$ ratios among the oils from different structural belts. The oil in the Aika anticline belt and its western tectonic units is more enriched in ^{13}C than in the eastern Huomatu anticline belt and Qigu bruchfalten.

4.2 C_5–C_7 light hydrocarbon compounds

Light hydrocarbons are important components of oil, especially for light oil and condensate, where light hydrocarbon compounds can account for up to 90% of the total oil mass (Wang, 2011). The relative light hydrocarbon content in oils in the STB varies greatly, ranging from 0% to 73.7%. Oil from Well HT1 exhibited the highest light hydrocarbon content, accounting for 73.7% of the total oil mass, whereas oil from Well KL1 exhibited the lowest light hydrocarbon content, almost losing all of them. In addition, the distribution of light hydrocarbon compounds varied significantly among samples, especially the relative abundance of toluene. For example, oil from Well Hu2004 exhibited very high toluene content, whereas that from Well GT1 exhibited relatively low abundance, with the Tol/nC_7 ratio ranging from 0.64 to 5.32.

4.3 Adamantanes

The oil samples contained varying amounts of adamantane series compounds, primarily monoadamantane, diamantine, and their alkyl-substituted isomers. Monoadamantane was the most abundant, and methyl adamantane was the absolute dominant compound. The total content of adamantanes varied significantly among the samples, ranging from 134.9 to 3,174.8 ppm (μg/g of total oil). The total content of monadamantanes and diamantanes was 88.4–2,779.8 ppm and 14.3–395.0 ppm, respectively. Both 3- and 4-methyldiamondotane were detected in the samples, but their abundance differs significantly, with their total content being 5.75–174.5 ppm.

TABLE 1 Summarized ranges and averages of biomarker parameters and whole oil/extracts carbon isotopes for sample groups.

Groups	$\delta^{13}C$/‰	Pr/Ph	C_{19}/C_{21} TT	$C_{24}TeT/C_{26}TT$	Ts/Tm	$C_{29}Ts/C_{29}H$	$C_{30}DiaH/C_{30}H$	G/$C_{31}R$	C_{27}/C_{29} S	C_{27}/C_{29} DiaS
I	−31.4 –−29.3 −30.1	0.45 – 0.90 0.67	0.24 – 0.65 0.38	0.18 – 0.52 0.30	1.11 – 3.66 2.45	0.55 – 1.39 0.82	0.17 – 0.92 0.49	2.26 – 4.81 3.21	0.74 – 3.96 1.67	0.78 – 3.70 1.87
II	−27.9 –−27 −27.5	2.55 – 2.74 2.65	5.29 – 6.83 6.06	8.95 – 12.1 10.5	0.52 – 0.91 0.72	0.19 – 0.29 0.24	0.16 – 0.25 0.20	0.46 – 0.52 0.49	0.24 – 0.34 0.29	0.18 – 0.20 0.19
III	−29.4 –−29 −29.2	2.40 – 2.91 2.58	0.42 – 0.62 0.52	1.61 – 2.24 1.9	0.65 – 0.72 0.69	0.24 – 0.27 0.26	0.13 – 0.15 0.14	0.37 – 0.40 0.39	0.21 – 0.25 0.23	0.28 – 0.31 0.30
IV	−28.2 –−27 −27.8	1.61 – 1.89 1.79	0.36 – 1.52 1.10	0.89 – 1.82 1.50	0.57 – 0.65 0.60	0.23 – 0.27 0.25	0.11 – 0.15 0.13	1.28 – 1.36 1.32	0.56 – 0.70 0.62	0.48 – 0.69 0.62
V	-30.7	1.42	0.18	0.58	0.91	0.24	0.11	0.81	0.34	0.47

Pr/Ph: pristane/phytane; TT: tricyclic terpane; TeT: tetracyclic terpane; Ts: 18α (H)-trinorneohopane; Tm: 17α (H)-trinorhopane; $C_{29}Ts/C_{29}H$: C_{29} norneohopane/C_{29} hopane; $C_{30}DiaH/C_{30}$ H: C_{30} diahopane/C_{30} hopane; G/$C_{31}R$: gammacerane/C_{31} hopanes 22R; S: regular sterane; DiaS: diasterane; Numerator: parameter range of minimum to maximum value, Denominator: average value.

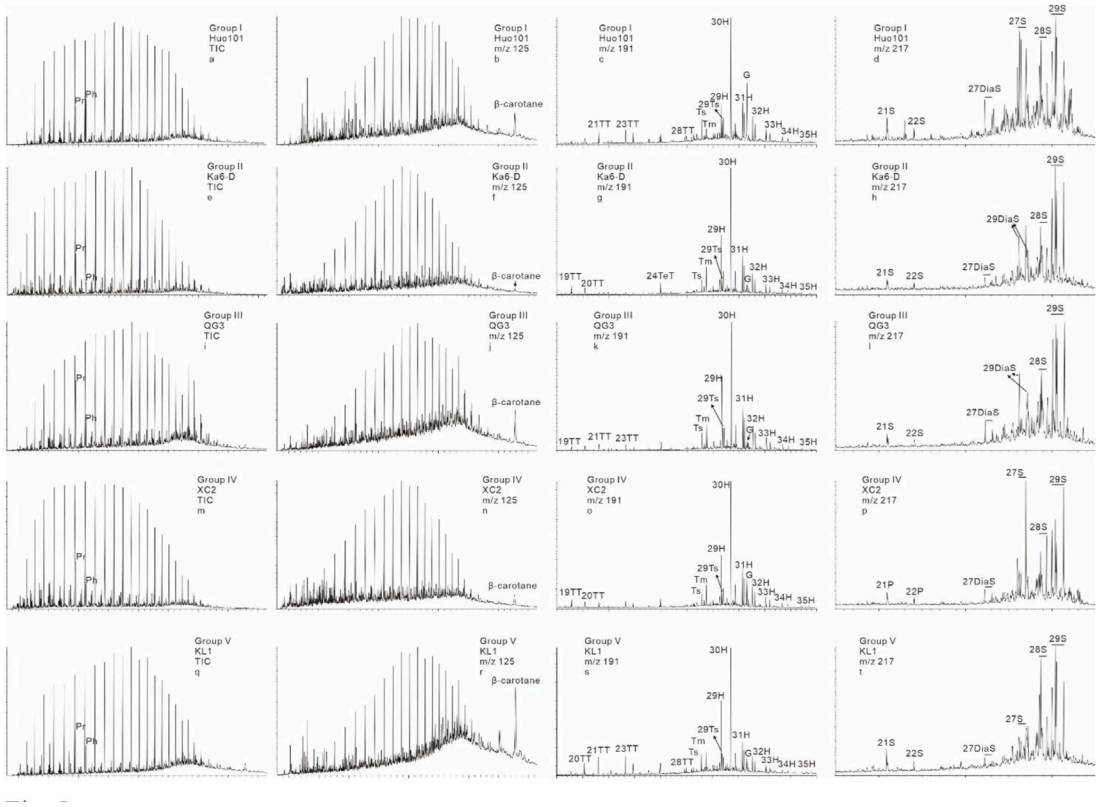

FIGURE 5
Summarized TIC, m/z 125, m/z 191, and m/z 217 mass chromatograms of saturated hydrocarbons showing distributions of *n*-alkanes and acyclic isoprenoids, β-carotane, terpanes, and steranes for **(A–D)** Group I oil; **(E–H)** Group II oil; **(I–L)** Group III oil; **(M–P)** Group IV oil; **(Q–T)** Group V oil. The abbreviations of compound names see Figure 3.

4.4 Biomarkers

4.4.1 n-alkanes and isoprenoids

The analyzed samples contain abundant *n*-alkanes, and the carbon number ranges from C_{11} to C_{36} (Figures 3A–C). The normal alkane series exhibits a unimodal distribution, with the main-peak-carbon number ranging from C_{17} to C_{25}, and the ratio of C_{21-}/C_{22+} varies significantly, ranging from 0.52 to 3.47. There is no odd and even carbon number advantage, and the OEP is close to 1. Pristane (Pr) and phytane (Ph) were the dominant

isoprenoids, and their relative abundance varied significantly among the samples, with Pr/Ph ratios ranging from 0.45 to 2.91. Some oils (e.g., oil from Well GT1) had high Pr/Ph ratios, typically greater than 2; some oils (e.g., oil from Well TG1) had low Pr/Ph ratios, mostly less than 1. Other oils have Pr/Ph ratios between the two groups s (e.g., oil from Well Du50). In addition, β-carotene was also detected in the oils with different abundances.

4.4.2 Terpene

The terpenes of the oil in the STB are primarily dicyclic sesquiterpenes, tricyclic terpenes, C_{24} tetracyclic terpenes, and pentacyclic triterpenes. 13β (H),14α (H)-tricyclic terpenes were detected in all samples, but the relative abundance and carbon number distribution range of tricyclic terpenes differed significantly among the samples. The relative content of tricyclic terpenes in some oil samples such as Well GT1 is significantly lower than that of hopanes. Among the tricyclic terpenes, C_{19} and C_{20} tricyclic terpenes dominate, and the content of high-carbon-number isomers is very low or even difficult to detect, whereas the relative content of C_{24} tetracyclic terpenes is very high. In contrast, in some oil samples such as Well TG1, the relative content of tricyclic terpenes is very high, consistent with hopanes. The carbon number of tricyclic terpenes is widely distributed, C_{19}–C_{29} tricyclic terpenes are detected, and C_{23} tricyclic terpenes are mostly the main peak. The relative content of C_{19}, C_{20}, and C_{24} tricyclic terpenes is very low. Some oil samples, such as oil from Well Du50, exhibit a relatively low content of tricyclic terpenes, but the carbon number distribution is wide. In these oils, C_{19}–C_{29} tricyclic terpenes are detected, and the relative content of C_{19}–C_{23} tricyclic terpenes does not differ, whereas the relative content of C_{24} tetracyclic terpenes is high (Figures 3D–F). Pentacyclic triterpenes such as C_{27} neohopanes (Tm), C_{27}-rearranged neohopanes (Ts), C_{29}–C_{35} hopanes, C_{30}-rearranged hopanes, and gammacerane were detected in the oil samples. The distribution characteristics of pentacyclic triterpenes significantly differed among the samples, primarily in the relative abundance of Ts, C_{29}-rearranged neohopane (C_{29}Ts), C_{30}-rearranged hopane, and gammacerane (Figures 3D–F), which can be used as powerful indicators to distinguish the oil samples.

4.4.3 Sterane

The steranes detected in oils in the STB included progesteranes, homoprogesteranes, C_{27}–C_{29} diasteranes, and regular steranes (Figures 3G–I). The distribution characteristics of steranes also differ significantly among the oils, primarily reflected in the relative content of C_{27} and C_{29} steranes (both rearranged and regular steranes). Some oil such as oil from Well GT1 exhibit low C_{27} regular sterane content but very high C_{29} diasterane content. On the contrary, oil such as that from Well TG1 has a very high content of C_{27} regular steranes but low content of C_{29} diasteranes. The difference between the two can be used as a typical index to distinguish the oil samples. In addition, the relative abundances of different configuration compounds of regular steranes also vary significantly. For example, oil from Well XC2 exhibits an extremely high ααα20R configuration of regular steranes.

5 Discussion

5.1 Geochemical classification of oil

Combining the biomarker fingerprints and the $\delta^{13}C_{bulk}$ ratios, the oil in the STB can be divided into five types (Figure 4).

5.1.1 Type I oil

Type I oil has the lightest stable carbon isotopic composition, with $\delta^{13}C_{bulk}$ values ranging from −31.4 to −29.3‰ (Table 1). Ph was dominant in isoprenoids, and the Pr/Ph ratio was low, indicating that the lacustrine algae organic matter or the oil-prone parent material was deposited in a reductive environment. β-carotene was found in high abundance in most Type oils (Figures 5A,B). Tricyclic terpenes tend to be relatively high in abundance and have a wide distribution of carbon numbers. C_{28}, C_{29}, and C_{29+} tricyclic terpenes are commonly found in Type I oil. C_{23} tricyclic terpenes typically dominated the distribution of tricyclic terpenes, C_{21} tricyclic terpenes were also high, and C_{19} and C_{20} tricyclic terpenes were very low (Figure 5C). Besides, the abundance of C_{24} tetracyclic terpenes was relatively low, with a C_{24} tetracyclic terpene/C_{26} tricyclic terpene ratio ranging from 0.18 to 0.52 (Table 1). Among the distribution of pentacyclic triterpenes, C_{30} hopane is the primary peak, whereas the abundance of the other hopanes is relatively low. The relative content of Ts is higher than that of Tm, and the relative content of gammacerane is very high, typically higher than that of C_{31} hopane. The gammacerane/C_{31}hopane22R ratio is between 2.19 and 3.55 (Table 1), which is significantly higher than that of the other types of oil. Gammacerane is a landmark biomarker in saline lakes or stratified water with high salinity. Along with its high carotenane abundance and low Pr/Ph ratio, Type I oil reflects the organic matter deposited in a brackish and reducing environment (Brassel et al., 1985; Moldowan et al., 1985; Grice et al., 1998). In the distribution of steranes, the relative content of progesteranes and homoprogesteranes was low, and regular steranes were dominated by C_{27} and C_{29} steranes, with low C_{28} sterane content. The configuration of ααα C_{27}–C_{29}20R regular steranes exhibited a "V"-shaped distribution (Figure 5D), and the relative diasterane content was significantly lower than that of regular steranes. Type I oil includes oils from Wells Huo101, MN1, Hu 2004, and TG1, primarily distributed in the Huomatu anticline belt.

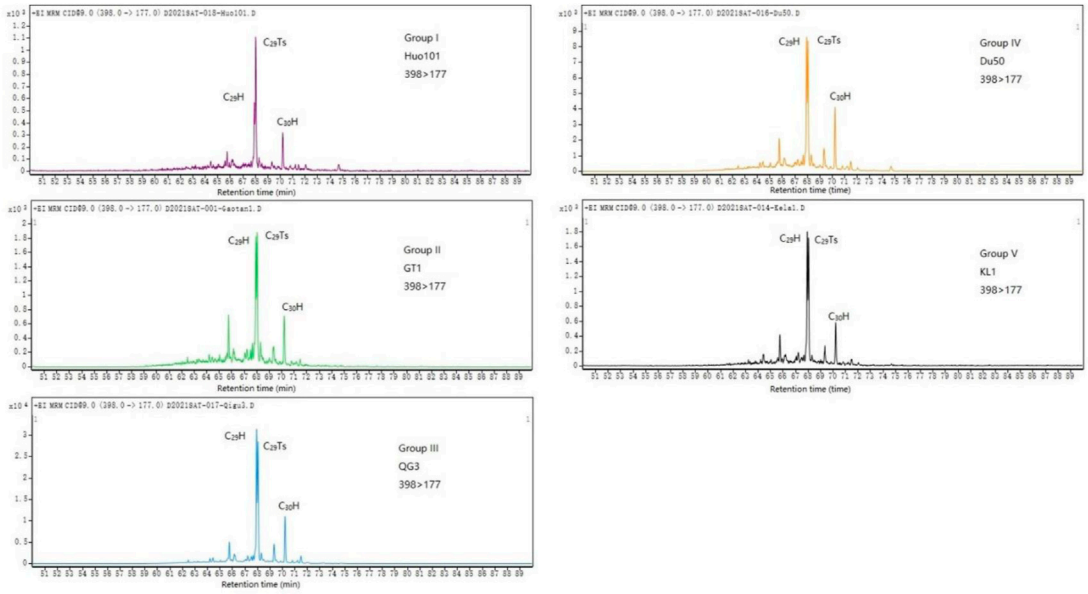

FIGURE 6
MRM chromatograms showing absence of 25-norhopanes in representative Group I–V oils. The abbreviations of compound names see Figure 3.

5.1.2 Type II oil

Type II oil has a more ^{13}C-enriched $\delta^{13}C_{bulk}$ ratio varying from −28.2 to −27.0‰ (Table 1) than Type I oil. The isoprenoid is dominated by Pr, and the Pr/Ph ratio is high, reflecting that their parent organic matter is dominated by terrigenous higher plants and deposited in an oxidation environment. It seldom contains β-carotene (Figures 5E,F). Generally, Type II oil exhibits relatively low tricyclic terpene content, whose distribution patterns are dominated by C_{19} and C_{20} tricyclic terpenes, with very low content of the other higher-carbon-number tricyclic terpenes (Figure 5G). This oil type has a high C_{19}/C_{21} tricyclic terpene ratio, ranging from 4.92 to 7.41 (Table 1). Owing to the low (or even undetected) C_{26} tricyclic terpene content, this oil type has a high C_{24}tetracyclic terpene/C_{26}tricyclic terpene ratio, ranging from 8.98 to 16.66 (Table 1). In pentacyclic triterpenes, the relative abundance of Ts was lower than that of Tm, and the Ts/Tm ratios were all less than 1; the primary peak of C_{30} hopanes is obvious, and the abundance of C_{29} and C_{31} hopanes was higher than that of C_{30} hopanes. In addition, the relative gammacerane content of Type II oil is generally low, with the gammacerane/C_{31}22Rhopane ratios mostly below 0.5 (Table 1). In the distribution of steranes, the content of C_{27} and C_{28} steranes was lower than that of C_{29}, dominating the distribution of steranes. Diasteranes were relatively abundant, with a high abundance in C_{29} diasteranes and low abundance in C_{27} diasteranes (Figure 5H). Type II oil includes Jurassic reservoir oil from Wells GT1 and Ka6, which is distributed in the western section of the study area.

5.1.3 Type III oil

Types III and II oils exhibited very similar distribution characteristics of isoprenoids, tetracyclic terpenes, gammacerane, and steranes but exhibited different $\delta^{13}C_{bulk}$ ratios, tricyclic terpenes distribution patterns, and β-cartane abundance (Figure 5I–L). Types III oil has relatively ^{13}C-depleted $\delta^{13}C_{bulk}$ ratios varying from −29.4 to −29.0‰ (Table 1). The relative content of tricyclic terpenes is very low, but the carbon number distribution is broad, from C_{19} to C_{26}. Extremely low content of C_{28} and C_{29} tricyclic terpenes may also exist. Among the C_{19}–C_{26} tricyclic terpenes, C_{21} and C_{23} tricyclic terpenes were dominant, whereas the abundance of the other tricyclic terpenes was slightly low (Figure 5K). The C_{19}/C_{21}tricyclic terpene ratios were 0.42–0.62 (Table 1). Type III oil includes Jurassic reservoir oil from Wells QG3, Qi34, and Qi1 in the Qigu bruchfalten.

5.1.4 Type IV oil

The distribution characteristics of hopanes and steranes in Type IV oil are generally similar to those of Type I oil. However, Type IV oil has relatively low gammacerane/C_{31}hopane22R ratios and high ααα20Rsteranes abundance in C_{27}–C_{29} regular steranes (Figures 5O and P). In addition, Type IV oil has relatively ^{13}C-enriched $\delta^{13}C_{bulk}$ ratios and a higher Pr/Ph ratio (Table 1) than Type I oil. Although the content of tricyclic terpenes is generally low, the carbon number distribution is wide, ranging from C_{19} to C_{29}. The abundance of C_{28} and C_{29} tricyclic terpenes is low, and the ratio of C_{19}/C_{21} tricyclic terpenes

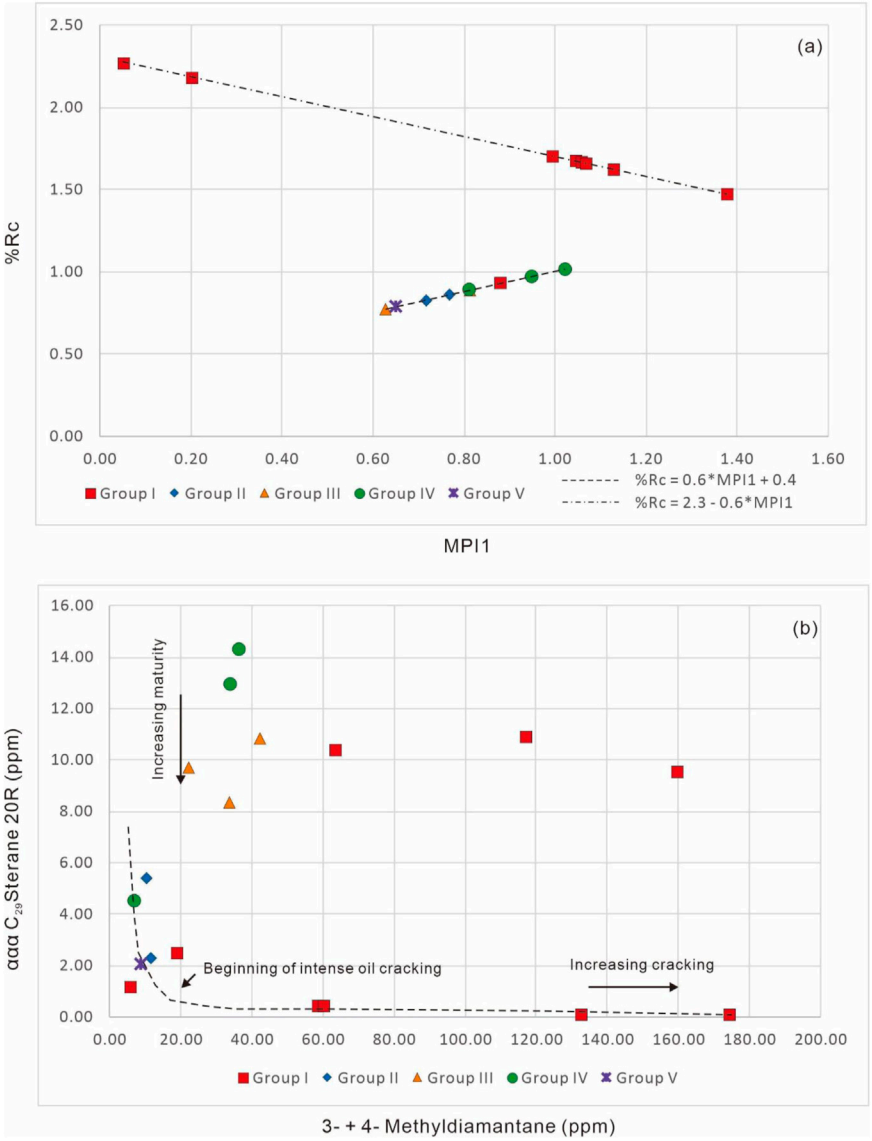

FIGURE 7
Crossplot of **(A)** MPI1 *versus* %Rc; **(B)** concentrations of 3- + 4-methyldiamantane *versus* those of ααα C_{29} sterane 20R.

varies greatly, ranging from 0.36 to 1.52 (Table 1). The content of C_{24} tetracyclic terpenes in Type IV oil was high, with the C_{24} tetracyclic terpene/C_{26} tricyclic terpene ratios ranging from 0.89 to 1.82 (Table 1). Type IV oil includes Neogene reservoir oil from Wells XC2, Du50, and Ka6, collected from the shallow strata of the Aika anticline belt.

5.1.5 Type V oil

Type V oil is collected from Well KL1, exhibiting Pr dominance with relatively high β-carotene content (Figures 5Q,R). The tricyclic terpenes, C_{24} tetracyclic terpenes, hopanes, and gammacerane of this oil sample are similar to those of Type I oil (Figure 5S). The relative gammacerane content of the KL1 oil was slightly lower than that of Type I oil (Table 1). In addition, the relative content of C_{27} regular steranes in C_{27}–C_{29} regular steranes is much lower than that of Type I oil, and the configuration of C_{27}–C_{29} ααα20R regular steranes in Type V oil show an inverse "L" shape distribution (Figure 5T).

5.2 Maturity and cracking of oil

With the increase in the burial depth, the increase in reservoir temperature will lead to the cracking of compounds in oil. Oil

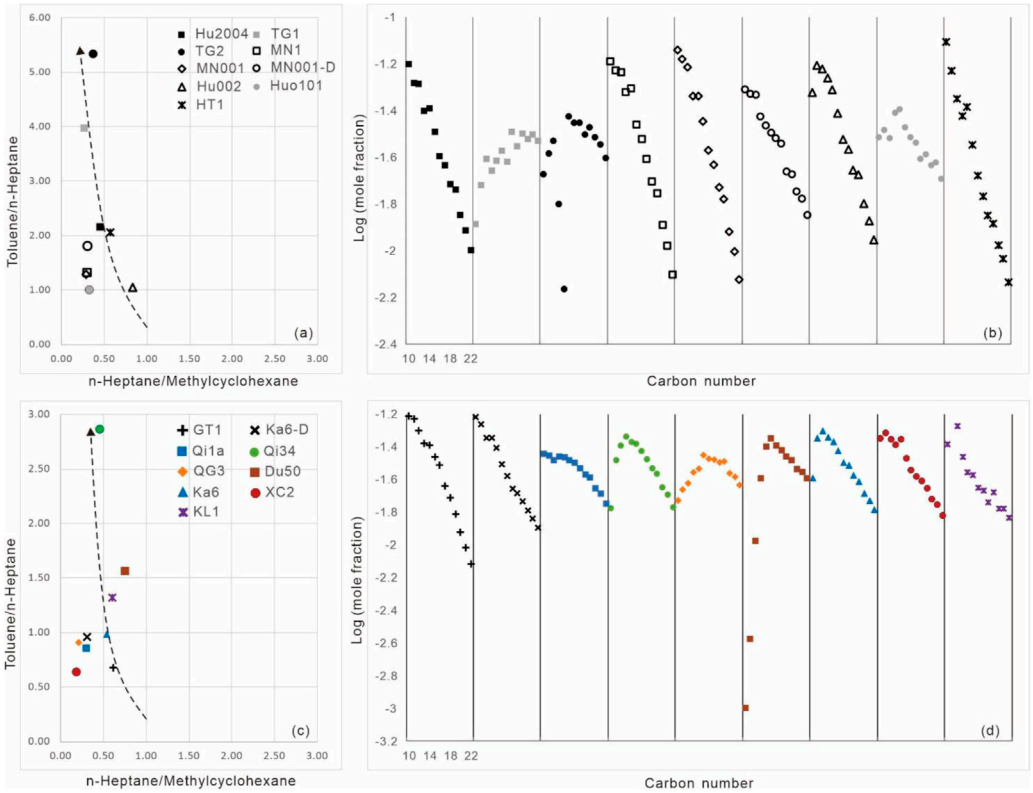

FIGURE 8
Crossplots of **(A)** the toluene/*n*-heptane *versus* *n*-heptane/methylcyclohexane and **(B)** carbon number *versus* the log of mole fraction for the C_{10}–C_{22} *n*-alkanes for Group I oils; **(C)** the toluene/*n*-heptane *versus* *n*-heptane/methylcyclohexane and **(D)** carbon number *versus* the log of mole fraction for the C_{10}–C_{22} *n*-alkanes for Group II–V oils.

maturity is an important index to judge whether it has reached the cracking stage. In this study, the isomerization maturity parameters 22S/(22S + 22R) of C_{31} and C_{32}hopane of Types I–V oils are between 0.81–0.58 and 0.52–0.58, respectively, indicating that the oil entered the oil-generating window (Peters et al., 2005). C_{29}22S/(22S + 22R) and ββ/(ββ + αα) regular sterane ratios did not evolve to the equilibrium endpoint, indicating that most of the oils have not exceeded the oil-generating window (Peters et al., 2005). Among them, Type I oil exhibited the highest parameter value, corresponding to the vitrinite reflectance (%Ro) value in the range of 0.82–0.86, whereas Type IV oil exhibited the lowest parameter value, corresponding to the %Ro value in the range of 0.68–0.72, and the parameter values of the other three oil types were between those of Types I and IV oils. The corresponding %Ro value is 0.78–0.80 (Huang et al., 1990). Phenanthrene and its alkyl isomers have been used in previous studies to construct several maturity parameters, such as the methylphenanthrene index (MPI1) and methylphenanthrene ratio (2-/1-MP). An empirical correspondence between such maturity parameters in oil and the reflectance of source rock vitrinite has also been established (Radke and Welte, 1983; Cassani et al., 1988; Radke, 1988). The evaluation of oil and source rock maturity based on phenicylates-related parameters has been extensively performed, and most of them have achieved good application results (Budzinski et al., 1995; Luo et al., 2016; Cheng et al., 2020). The correlation between the methylphenanthrene index and vitrinite reflectance shows a "two-stage pattern," that is, with increasing maturity, the MPI1 value of the sample increases first and then decreases (Figure 6A). The formula used to calculate vitrinite reflectance can be effectively judged using 2-/1-methylphenanthrene and 1-methylphenanthrene/phenanthrene ratios (Radke, 1988). Therefore, the equivalent R_o based on the methylphenanthrene ratio and methylphenanthrene index indicates that Types II–V oils are mature oils within the oil-generating window, which is consistent with the maturities from C_{29} regular sterane isomers. However, most of Type I oil has entered the condensate–wet gas-generating stage, which is significantly higher than the maturities indicated by the maturity parameters of steranes, indicating that there may be a mixing of early normal mature oil and later highly mature oil or natural gas in Type I oil.

Adamantanes are a series of compounds with high thermal stability in oil. Previous studies have demonstrated that an increasing degree of oil cracking would enrich adamantanes. Based on this conception, the correlation chart of the absolute content of $\alpha\alpha\alpha C_{29}$ regular sterane and 3- + 4-methyldiamantanes (Dahl et al., 1999) was used to judge the degree of thermal evolution and oil cracking (Figure 6B). Normal mature oil (oil without intense cracking) has high $\alpha\alpha\alpha C_{29}$ regular steranes20R content and low 3- + 4-methyldiamontadane content. With increasing maturity, $\alpha\alpha\alpha C_{29}$ regular steranes20R content decreases gradually, whereas methyldiamontadane content increases gradually. When the former content drops to the detection limit, this indicates that the oil is at the start of strong cracking, that is, high-molecular-weight compounds in the oil, such as steroidal and terpenes biomarkers, are entirely cracked. At that time, the relevant content of adamantanes continues to increase with an increasing cracking degree because of their extremely high thermal stability. As shown in Figure 6, relatively high $\alpha\alpha\alpha C_{29}$ regular sterane20R content was observed in Types II–V oils. Although their maturities vary slightly, no severe cracking process occurred. Most of Type I oil exhibited high maturities. The $\alpha\alpha\alpha C_{29}$ regular sterane20R content of oils from Wells Hu002, Hu 2004, MN1, and MN001 was close to zero, and the content of 3- + 4-methyldiamondoadamane was high, exhibiting strong cracking characteristics. Progesteranes and progesteranes dominated the distribution characteristics of steranes with low carbon numbers. In addition, the oil samples from Wells MN001–D, TG1, and TG2 exhibit the characteristics of "mixed oil" (Dahl et al., 1999) with high content of both $\alpha\alpha\alpha C_{29}$ regular sterane20R and 3- + 4-methyldiamondoadamane, reflecting the complexity of oil origin in the Huomatu anticline belt.

5.3 Biodegradation

The biodegradation of oil refers to the alteration of oil by microorganisms (Peters et al., 2005; Gong et al., 2017a). It is mainly a hydrocarbon oxidation process, which produces carbon dioxide and partially oxidized substances, such as organic acids. Because microorganisms typically consume oil compounds selectively, degraded oil is enriched in heteroatomic compounds that are difficult to modify (Huang et al., 2003, 2004; Peters et al., 2005; Wei Z. B. et al., 2007; Ross et al., 2010). Biodegraded oil will generally form an unresolved complex mixture (UCM) bulge in saturated hydrocarbon chromatography or total ion current pattern of saturated hydrocarbon chromatography–MS (Peters et al., 2005; Wei D. et al., 2007; Gong et al., 2017a). In the case of intense degradation, hopanes undergo bacterial modification to form 25-norhopanes, which are typically used as indicators of intense biodegradation (Huang et al., 2003, 2004; Peters et al., 2005; Wei Z. B. et al., 2007; Ross et al., 2010). Different oil components have different resistance to biodegradation. *N*-alkanes, as the most vulnerable series of compounds to bacterial modification, typically suffer a severe loss due to biodegradation, and their abundance is also an important index for discriminating biodegradation (Peters et al., 2005). 25-norhopanes (Figure 7) and a UCM bulge were not detected in the oil in this study, and *n*-alkanes were also abundant (Figure 5), so the oils were not modified for biodegradation.

5.4 Evaporative fractionation

After the accumulation of oil, the tectonic movement or the injection of a large amount of natural gas will redistribute the oil and gas phase in a reservoir (Gong et al., 2014, 2016; 2017b). Compounds of low-molecular-weight fractions will be dissolved in natural gas and separated from the original liquid hydrocarbon phase (Gong et al., 2014, 2016; 2017b). In a petroleum reservoir with favorable preservation conditions, subsequently charged natural gas will dilute the original hydrocarbon, making the density of petroleum lighter. In contrast, when the preservation conditions of a petroleum reservoir are poor, low-molecular-weight compounds of the original oil will dissolve in subsequently charged natural gas and migrate to a shallower reservoir to form a new gas pool or be lost (Gong et al., 2014, 2016; 2017b). Numerous geological examples of evaporative fractionation have been reported in previous studies (Matyasik et al., 2000; Zhang et al., 2011; Gong et al., 2017b). Evaporative fractionation is most likely to affect light hydrocarbon fractions in oil. Using simulation experiments and geological case studies, previous studies constructed a map plate for identifying evaporative fractionation based on the *n*-heptane/methylcyclohexane and toluene/*n*-heptane ratios (Thompson, 1987) (Figure 8A). Oil unmodified by evaporative fractionation typically has a normal range of the two ratios, whereas modified oil has relatively high toluene/*n*-heptane and low *n*-heptane/methylcyclohexane ratios due to the enrichment of aromatic and naphthene light hydrocarbon compounds (Thompson, 1987; Gong et al., 2014, 2016, 2017b). Strong evaporative fractionation can also change the distribution of *n*-alkanes (Kissin, 1987; Meulbroek et al., 1998; Losh et al., 2002). Thus, the evaporative fractionation-based modification was identified using the correlation between the carbon number distribution of n-alkanes and their molar mass (Figure 8B).

The carbon number of n-alkanes and the molar mass of oil without evaporative fractionation has a good linear relationship, whereas an inversion will be observed in evaporative fractionation-modified oil. Generally, a carbon number of inversion greater than 10 indicates strong evaporative fractionation (Losh et al., 2002; Gong et al., 2014). In this study, potential evaporative fractionation in Types I–V oils was discussed.

Type I oil, located in the Huomatu anticline belt, was subjected to evaporative fractionation of different degrees (Figures 8A,B). Oils from Wells TG1 and TG2 had the strongest modification effect, and the gas chromatographic analysis showed that the light hydrocarbon compounds in these oils had been lost. Furthermore, low-molecular-weight *n*-alkanes also suffered a strong loss. Thus, it could be concluded that the preservation conditions in the Huomatu anticline belt are poor, and a large amount of natural gas filled in the late period migrated with low-molecular-weight compounds of the original oil. In other words, the current oil reservoirs are residual. The current oil densities of the oils from Wells TG1 and TG2 are 0.86 and 0.84 g/cm^3, respectively, which is consistent with the poor reservoir preservation conditions. In contrast, oils from Wells Hu 2004, HT1, MN1, and MN001, were only weakly modified by evaporative fractionation. Only the light hydrocarbon fraction was modified, increasing the toluene/*n*-heptane ratio (Figure 8A). The low-molecular-weight *n*-alkanes of these oils are well preserved, indicating that the oil reservoirs have superior preservation conditions. When subsequently charged natural gas mixed with the original oil, the condensate oil and gas did not lose and thus heavily diluted the oil, making the oil lighter, which is supported by the current reservoir's relatively low oil densities (0.76–0.81 g/cm^3).

The light hydrocarbon fractions and *n*-alkanes of oils from GT1 and Ka6–D (Type II oil) were not subjected to intense evaporative fractionation and remained intact. Type III oil was intensively altered by evaporation fractionation. This process is most evident in oils from Wells Qi34 and QG3. The light hydrocarbon fractions and two reservoirs of low-carbon-number alkanes were severely lost, reflecting a poor preservation condition. Such a fractionation process could also be inferred from the heavy oils in these reservoirs, which are difficult to flow. Type IV oil also exhibited evaporative fractionation characteristics (Figures 8C,D). Among them, oils from Well Du50 exhibited the most intense alteration, whose light hydrocarbon fraction and low-carbon-number *n*-alkanes suffered strong losses, reflecting a poor preservation condition. The light hydrocarbon fraction in oils from Well KL1 (Type V oil) is depleted.

5.5 Comprehensive identification of oil origin and its implications for petroleum accumulation

Several oil-bearing anticlines, including Horgos, Manas, Tugulu, and Hutubi anticlines, have been formed in the Huomatu anticline belt. Light oil, condensate, and natural gas are the main types discovered in this area. The origin of oil and gas in this structural belt is the most debated (Chen et al., 2004; Kong, 2007; Liao et al., 2011; Wang et al., 2013; Chen et al., 2016c). Nevertheless, this study showed that oils in this area belong to the same genetic type because of their similar $\delta^{13}C_{bulk}$ ratios and biomarker fingerprints, which is consistent with previous studies (Chen et al., 2015b). There is a significant difference in maturity indicated by the maturity parameters of sterohopanes and phenanthrene/adamantanes in this area. In this area, there is a significant difference in the maturity parameters of sterohopanes and phenanthrene/adamantanes, indicating the charging and mixing of hydrocarbons with different maturities (Dahl et al., 1999). Oils in this study widely suffered from evaporation fractionation. However, the degree of evaporation fractionation in different anticline structures differs. The differences in reservoir preservation conditions are likely the direct cause of the current differences in the physical properties of these oils. For example, Himalayan orogeny tectonic activities form several large-scale thrust faults, resulting in poor petroleum preservation conditions in the Tugulu anticline (Tian et al., 2017). The light oil charged in the late stage was heavily lost, deteriorating the physical properties of the oil (Tian et al., 2017).

Well GT1 is located in the Gao Quan tectonic belt in the western part of the STB, and a high oil flow is produced in the Lower Cretaceous Qingshuihe Formation (Du et al., 2019). The $\delta^{13}C_{bulk}$ values and biomarker fingerprints of oils from Well GT1 were similar to those from Well Ka6 in the Aika anticline belt and other Jurassic-originated oils in the Junggar Basin (Chen et al., 2016a; Jin et al., 2019). Oils from Wells GT1 (Cretaceous reservoir) and Ka6 (Jurassic reservoir) were generated within the main oil-generating window and did not undergo intense cracking. These oils did not suffer from biodegradation during migration and accumulation. They were not subjected to obvious evaporative fractionation, indicating that the superior sealing ability of the caprocks prevented the reservoirs from a large-scale loss of oil and gas.

The accumulation process of Jurassic reservoirs in the Qigu bruchfalten is very complex and controversial (Hu et al., 2019; Lu et al., 2019). Previous studies have shown that Jurassic reservoir oils are mixed oils generated from the Permian and Jurassic source rocks (Wang et al., 2013; Chen et al., 2016b). The samples in this study also demonstrated a "mixing" characteristic based on the biomarker fingerprints and $\delta^{13}C_{bulk}$ values. The Jurassic reservoir oils in the Qigu Oilfield are all normal oils within the oil-generating window. They contain high-molecular-weight biomarkers and low methyl diadamantane content, indicating that they have not been buried to oil-cracking depths following a series of tectonic activities. These oils did not suffer from biodegradation during migration and accumulation. Evaporative fractionation is common, and poor cap preservation conditions lead to different degrees of oil and gas loss in reservoirs, resulting in high current density and waxy oils (Lu et al., 2019).

Several oil-bearing anticlines are found in the Aika anticline belt, including the Kayindike, Xihu, and Dushanzi anticlines, and shallow oil and gas reservoirs are primarily distributed in the

Neogene Shawan and the Paleogene Anjihaihe Formations (Wang et al., 2013). The origin of these oils remains controversial. Nevertheless, they have very similar biomarker fingerprints and $\delta^{13}C_{bulk}$ ratios, indicating that they belong to the same genetic type, consistent with previous studies (Chen et al., 2015b). These oils were primarily generated within the main oil-generating window and have not suffered oil cracking. Evaporative fractionation is very common and is associated with shallow burial depths and relatively poor preservation conditions. Oils from Well KL1 are also products within the oil-generating window and have not yet been cracked. The light oil components have been lost because of evaporative fractionation, reflecting poor reservoir preservation conditions. This is consistent with the tectonic background of the study area (Chen et al., 2007; Guo et al., 2011).

6 Conclusion

Five types of oils have been identified in the STB of the Junggar Basin. Type I oil is distributed in the Huomatu anticline belt, characterized by ^{13}C-depleted $\delta^{13}C_{bulk}$ ratios, low Pr/Ph ratios, high gammacerane abundance, and low diasterane content. Type II oil is distributed in the Jurassic reservoir in the Gaoquan tectonic belt and Aika anticline belt, characterized by ^{13}C-enriched $\delta^{13}C_{bulk}$ ratios, high Pr/Ph ratios, low gammacerane abundance, and high diasterane content. Type III oil is distributed in the Jurassic reservoir of Qigu bruchfalten and has similar geochemical characteristics to Type II oil despite its relatively ^{13}C-depleted $\delta^{13}C_{bulk}$ ratios and tricyclic terpene distribution pattern. TType IV oil is distributed in the shallow strata of the Aika anticline belt and has similar geochemical characteristics to Type I oil despite its relatively ^{13}C-enriched $\delta^{13}C_{bulk}$ ratios, low gammacerane content, and high Pr/Ph ratio. ype V oil is geochemically similar to Type I oil despite its relatively low C_{27} regular sterane and gammacerane content. These oils have not been subjected to biodegradation. Notable differences were observed in the evolution of maturity parameters from steroterpenes and phenanthrene/adamantanes. The former inferred normal mature oil, whereas the latter inferred strong oil cracking. Thus, a mixing process occurred in this area. The other four types of oils have normal maturities and have not suffered intense cracking. All oil types, except Type II oils, were altered by evaporative fractionation, with different alteration degrees. For Type I oils, different oil-bearing structures exhibit different evaporative fractionation, with the most severe fractionation occurring in the Tugulu anticline.

Data availability statement

The original contributions presented in the study are included in the article/Supplementary Material, further inquiries can be directed to the corresponding author.

Author contributions

ZQ: Conceptualization, Resources, Project administration HQ: Writing Original Draft, Formal analysis ZL: Writing Original Draft, Formal analysis, Methodology WM: Investigation, Data Curation RW: Investigation, Data Curation WW: Investigation, Data Curation.

Conflict of interest

All authors were employed by PetroChina.

Publisher's note

References

Brassel, S. C., Fglinton, G., and Fu, J. (1985). Biological marker compounds as indicators of the depositional history of the Maoming oil shale. *Org. Geochem.* 10, 927–941.

Budzinski, H., Garrigues, P., Connan, J., Devillers, J., Domine, D., Radke, M., et al. (1995). Alkylated phenanthrene distributions as maturity and origin indicators in crude oils and rock extracts. *Geochimica Cosmochimica Acta* 59, 2043–2056. doi:10.1016/0016-7037(95)00125-5

Cao, J., Wang, X., Wei, D., Sun, P., Hu, W., Jia, D., et al. (2010). Complex petroleum migration and accumulation in central region of southern Junggar basin, Northwest China. *J. Earth Sci.* 21, 83–93. doi:10.1007/s12583-010-0004-5

Cassani, F., Gallango, O., Talukdar, S., Vallejos, C., and Ehrmann, U. (1988). Methylphenanthrene maturity index of marine source rock extracts and crude oils from the Maracaibo Basin. *Org. Geochem.* 13, 73–80. doi:10.1016/b978-0-08-037236-5.50013-0

Chen, J., Deng, C., and Wang, X. (2016c). Source of condensate oil in the middle of southern margin, Junggar Basin, NW China. *Petroleum Explor. Dev.* 43 (5), 830–840. doi:10.1016/s1876-3804(16)30108-2

Chen, J., Wang, X., and Deng, C. (2015b). Geochemcial features and classification of crude oil the southern margin of Junggar Basin, Northwestern China. *Acta Pet. Sin.* 36, 1316–1331. doi:10.7623/syxb201511001

Chen, J., Wang, X., and Deng, C. (2015a). Geochemcial features of source rocks in the southern margin, Junggar Basin, Northwestern China. *Acta Pet. Sin.* 36 (7), 768–780. doi:10.7623/syxb201507001

Chen, J., Wang, X., and Deng, C. (2016a). Investigation of typical reservoirs and occurrence regularity of crude oils in the southern margin of Junggar Basin, Northwestern China. *Acta Pet. Sin.* 37 (4), 415–429.

Chen, J., Wang, X., and Deng, C. (2016b). Oil-source correlation of typical crude oils in the southern margin, Junggar Basin, Northwestern China. *Acta Pet. Sin.* 37 (2), 160–171.

Chen, S., Qi, J., and Yu, F. (2007). Deformation characteristics in the southern margin of the Junggar Basin and their controlling factors. *Acta Geol. Sincia* 81 (2), 151–157.

Chen, S., Wang, X., and Yang, A, B. (2004). Geochemical study of forming gas reservoir in Hutubi field in zhunge'er basin. *Nat. Gas. Ind.* 24 (3), 16–18.

Cheng, B., Liu, H., Cao, Z., Wu, X., and Chen, Z. (2020). Origin of deep oil accumulations in carbonate reservoirs within the north Tarim Basin: Insights from molecular and isotopic compositions. *Org. Geochem.* 139, 103931. doi:10.1016/j.orggeochem.2019.103931

Dahl, J. E., Moldowan, J. M., Peters, K. E., Claypool, G. E., Rooney, M. A., Michael, G. E., et al. (1999). Diamondoid hydrocarbons as indicators of natural oil cracking. *Nature* 399, 54–57. doi:10.1038/19953

Du, J., Zhi, D., and Li, J. (2019). Major breakthrough of Well Gaotan 1 and exploration prospects of lower assemblage in southern margin of Junggar Basin, NW China. *Petroleum Explor. Dev.* 46, 205–215. doi:10.1016/s1876-3804(19)60003-0

Gong, D. Y., Cao, Z. L., Ni, Y. Y., Jiao, L. X., Yang, B., and Zhao, L. L. (2016). Origins of Jurassic oil reserves in the Turpan-Hami Basin, northwest China: Evidence of admixture from source and thermal maturity. *J. Petroleum Sci. Eng.* 146, 788–802. doi:10.1016/j.petrol.2016.07.025

Gong, D. Y., Li, J. Z., Ablimit, I., He, W. J., Lu, S., Liu, D. G., et al. (2018). Geochemical characteristics of natural gases related to Late Paleozoic coal measures in China. *Mar. Petroleum Geol.* 96, 474–500. doi:10.1016/j.marpetgeo.2018.06.017

Gong, D. Y., Ma, R. L., Chen, G., Ma, W. Y., Liao, L. X., Fang, C., et al. (2017a). Geochemical characteristics of biodegraded natural gas and its associated low molecular weight hydrocarbons. *J. Nat. Gas Sci. Eng.* 46, 338–349. doi:10.1016/j.jngse.2017.07.027

Gong, D. Y., Song, Y., Wei, Y. Z., Liu, C. W., Wu, Y. W., Zhang, L. J., et al. (2019). Geochemical characteristics of Carboniferous coaly source rocks and natural gases in the Southeastern Junggar Basin, NW China: Implications for new hydrocarbon explorations. *Int. J. Coal Geol.* 202, 171–189. doi:10.1016/j.coal.2018.12.006

Gong, D. Y., Wang, Z. Y., Liu, G., Chen, G., Fang, C. C., and Xiao, Z. Y. (2017b). Re-examination of the oil and gas origins in the kekeya gas condensate field, northwest China-A case study of hydrocarbon-source correlation using sophisticated geochemical methods. *Acta Geol. Sin. - Engl. Ed.* 91 (1), 186–203. doi:10.1111/1755-6724.13071

Gong, D. Y., Yu, C., Yang, X., Tao, X. W., Wu, W., and Liao, F. R. (2014). Geochemical characteristics of the condensates and their evaporative fractionation in kuqa depression of tarim basin, NW China. *Energy Explor. Exploitation* 32 (1), 191–210. doi:10.1260/0144-5987.32.1.191

Grice, K., Schouten, S., Peters, K. E., and Sinninghe Damsté, J. S. (1998). Molecular isotopic characterisation of hydrocarbon biomarkers in Palaeocene-Eocene evaporitic, lacustrine source rocks from the Jianghan Basin, China. *Org. Geochem.* 29, 1745–1764. doi:10.1016/s0146-6380(98)00075-8

Guo, C., Shen, Z., and Zhang, L. (2005). Biogenic origin characteristics of hydrocarbonsource rocks and classification of oils inthe south part of Junggar Basin, China. *J. Chengdu Univ. Technol.* 32 (3), 257–262.

Guo, Z., Wu, C., and Zhang, Z. (2011). Tectonic control on hydrocarbon accumulation and prospect for large oil-gas field exploration in the southern Junggar Basin. *Geol. J. China Univ.* 17 (2), 185–195. doi:10.16108/j.issn1006-7493.2011.02.005

He, H., Zhi, D., and Lei, D. (2019). Strategic breakthrough in Gaoquan anticline and exploration assessment on lower assemblage in the southern margin of Junggar Basin. *China Pet. Explor.* 24 (2), 137–146. doi:10.3969/j.issn.1672-7703.2019.02.001

Hu, H., Zhang, Y., and Zhuo, Q. (2019). Hydrocarbon charging history of the lower petroleum system in the southern Junggar Basin: Case study of the Qigu Oil Field. *Nat. Gas. Geosci.* 30 (4), 456–467. doi:10.11764/j.issn.1672-1926.2019.03.003

Huang, D., Li, J., and Zhang, D. (1990). Maturation sequence of continental crude oils in hydrocarbon basins in China and its signigicance. *Org. Geochem.* 16, 521–529.

Huang, H. P., Bowler, B. F. J., Oldenburg, T. B. P., and Larter, S. R. (2004). The effect of biodegradation on polycyclic aromatic hydrocarbons in reservoired oils from the Liaohe basin, NE China. *Org. Geochem.* 35, 1619–1634. doi:10.1016/j.orggeochem.2004.05.009

Huang, H. P., Bowler, B. F. J., Zhang, Z. W., Oldenburg, T. B. P., and Larter, S. R. (2003). Influence of biodegradation on carbazole and benzocarbazole distributions in oil columns from the Liaohe basin, NE China. *Org. Geochem.* 34, 951–969. doi:10.1016/s0146-6380(03)00033-0

Jin, J., Wang, F., Ren, J., Feng, W., Ma, W., and Li, S. (2019). Genesis of high-yield oil and gas in well Gaotan-1 and characteristics of source rocks in Sikeshu Sag, Junggar Basin. *Xinjiang Petrol. Geol.* 40 (2), 145–151. doi:10.7657/XJPG20190203

Kissin, Y. V. (1987). Catagenesis and composition of petroleum: Origin of *n*-alkanes and isoalkanes in petroleum crudes. *Geochimica Cosmochimica Acta* 51, 2445–2457. doi:10.1016/0016-7037(87)90296-1

Kong, X. (2007). Oil source of foothill fault-fold structural belt in Western part of the southern margin, Junggar Basin. *Petroleum Explor. Dev.* 34, 413–418.

Li, X., Shao, Y., and Li, T. (2003). Three oil-reservoir combinations in south marginal of Junggar Basin, Northwest China. *Petroleum Explor. Dev.* 30 (6), 32–34.

Li, Y., Wang, T., and Zhang, Y. (2004). Natural gas genesis and formationof gas pools in the south margin of Junggar Basin. *Acta Sedimentol. Sin.* 22 (3), 530–534.

Liao, J., Zhao, C., and Ma, W. (2011). Analysis on oil-gas origin and accumulation hydrocarbons in Hutubi gas field, Junggar Basin. *Xinjiang Geol.* 29 (4), 454–456.

Losh, S., Cathles, L., and Meulbroek, P. (2002). Gas washing of oil along a regional transect, offshore Louisiana. *Org. Geochem.* 33, 655–663. doi:10.1016/s0146-6380(02)00025-6

Lu, X., Zhao, M., Chen, Z., Li, X., Hu, H., and Zhuo, Q. (2019). Recognition of hydrocarbon accumulation in Qigu oilfield and implications for exploration in the southern margin of Junggar Basin. *Acta Petrolei Sinica* 40 (9), 1045–1058. doi:10.7623/syxb201909003

Luo, Q., George, S. C., Xu, Y., and Zhong, N. (2016). Organic geochemical characteristics of the Mesoproterozoic Hongshuizhuang Formation from northern China: Implications for thermal maturity and biological sources. *Org. Geochem.* 99, 23–37. doi:10.1016/j.orggeochem.2016.05.004

Matyasik, I., Steczko, A., and Philp, R. P. (2000). Biodegradation and migrational fractionation of oils from the Eastern Carpathians, Poland. *Org. Geochem.* 31, 1509–1523. doi:10.1016/s0146-6380(00)00103-0

Meulbroek, P., Cathles, L., III, and Whelan, J. (1998). Phase fractionation at south eugene island block 330. *Org. Geochem.* 29, 223–239. doi:10.1016/s0146-6380(98)00180-6

Moldowan, J. M., Seifert, W. K., and Gallegos, E. J. (1985). Relationship between petroleum composition and depositional environment of petroleum source rock. *AAPG Bull.* 69, 1255–1268.

Peters, K. E., Waters, C. C., and Moldowan, J. M. (2005). "The biomarker guide," in *II. Biomarkers and isotopes in petroleum system and Earth history* (New York: Cambridge University Press).

Radke, M. (1988). Application of aromatic compounds as maturity indicators in source rocks and crude oils. *Mar. Petroleum Geol.* 5, 224–236. doi:10.1016/0264-8172(88)90003-7

Radke, M., and Welte, D. H. (1983). "The methylphenanthrene index (MPI): A maturity parameter based on aromatic hydrocarbons," in *Advances in organic geochemistry*. Editor M. Bjoroy (Chichester: Wiley), 504–512.

Ross, A. S., Farrimond, P., Erdmann, M., and Larter, S. R. (2010). Geochemical compositional gradients in a mixed oil reservoir indicative of ongoing biodegradation. *Org. Geochem.* 41, 307–320. doi:10.1016/j.orggeochem.2009.09.005

Thompson, K. F. M. (1987). Fractionated aromatic petroleums and the generation of gas-condensates. *Org. Geochem.* 11, 573–590. doi:10.1016/0146-6380(87)90011-8

Tian, X., Zhuo, Q., and Zhang, J. (2017). Sealing capacity of the Tugulu Group and its significance for hydrocarbon accumulation in the lower play in the southern Junggar Basin, northwest China. *Oil Gas Geol.* 38 (2), 334–344. 10.11743/ogg20170213

Wang, P. (2011). *Analysis and geochemical application of light hydrocarbon fractionation in crude oil and source rock*. Beijing: Petroleum Industry Press.

Wang, Q., Liang, B., and Liu, X. (2021). Fluid phases and gas reservoirs of Qingshuihe Formation in well Hutan-1. *Xinjiang Pet. Geol.* 42 (6), 709–713. doi:10.7657/XJPG20220511

Wang, X., Zhi, D., and Wang, Y. (2013). *Source rocks and oil-gas geochemistry in Junggar Basin*. Beijing: Petroleum Industry Press.

Wei, D., Jia, D., and Zhao, Y. (2007a). Geochemical behaviors of crude oil in the southern margin of Junggar basin. *Oil Gas Geol.* 28 (4), 434–440.

Wei, Z. B., Moldowan, J. M., Peters, K. E., Wang, Y., and Xiang, W. (2007b). The abundance and distribution of diamondoids in biodegraded oils from the San Joaquin Valley: Implications for biodegradation of diamondoids in petroleum reservoirs. *Org. Geochem.* 38, 1910–1926. doi:10.1016/j.orggeochem.2007.07.009

Xiao, L., Lei, D., and Wei, L. (2012). Structural types and features in the west of south margin in the Junggar Basin. *Nat. Gas. Ind.* 32 (11), 36–39. 10.3787/j/issn.1000-0976.2012.11.08

Zhang, S., Su, J., Wang, X., Zhu, G., Yang, H., Liu, K., et al. (2011). Geochemistry of palaeozoic marine petroleum from the tarim basin, NW China: Part 3. Thermal cracking of liquid hydrocarbons and gas washing as the major mechanisms for deep gas condensate accumulations. *Org. Geochem.* 42, 1394–1410. doi:10.1016/j.orggeochem.2011.08.013

Zhang, W., Zhang, S., and Wang, S. (2003). Geochemical characteristics of oil and correlation of oil to resource rock in the southern edge of Junggar Basin. *J. Chengdu Univ. Technol.* 30 (4), 374–377.

frontiers | Frontiers in Earth Science

TYPE Original Research
PUBLISHED 13 January 2023
DOI 10.3389/feart.2022.1031799

OPEN ACCESS

EDITED BY
Hao Zou,
Chengdu University of Technology, China

REVIEWED BY
Bin Cheng,
China University of Petroleum, Qingdao, China
Zeyang Liu,
Chengdu University of Technology, China

*CORRESPONDENCE
Chenchen Fang,
fangchenchen@petrochina.com.cn

SPECIALTY SECTION
This article was submitted to Economic Geology, a section of the journal Frontiers in Earth Science

RECEIVED 30 August 2022
ACCEPTED 31 October 2022
PUBLISHED 13 January 2023

CITATION
Zhai J, Cao Z, Fang C, Yuan Y, Wu W and Liu J (2023), The evolution characteristics of diamondoids in coal measures and their potential application in maturity evaluation.
Front. Earth Sci. 10:1031799.
doi: 10.3389/feart.2022.1031799

The evolution characteristics of diamondoids in coal measures and their potential application in maturity evaluation

Jia Zhai[1,2], Zhenglin Cao[2], Chenchen Fang[2]*, Yilin Yuan[2], Wei Wu[3] and Jinzhong Liu[4]

[1]China University of Mining & Technology, Beijing, China, [2]PetroChina Research Institute of Petroleum Exploration and Development, Beijing, China, [3]Shale Gas Research Institute, Petro China Southwest Oil & Gasfield Company, Chengdu, Sichuan, China, [4]State Key Laboratory of Organic Geochemistry (SKLOG), Guangzhou Institute of Geochemistry, Chinese Academy of Sciences, Guangzhou, China

In this study, gold tube thermal simulation experiments were carried out on the soluble components (extracts) and insoluble components (extracted coal-measure mudstones) of coal-measure mudstones, and diamondoid compounds in the pyrolysis products were quantitatively analyzed. The results showed that diamondoid compounds in the extracts and the extracted coal-measure mudstones had undergone the process of formation and decomposition during thermal evolution. Based on the quantitative composition of the extracts and the extracted coal-measure mudstones, the calculated evolution characteristics of the diamondoid compounds in the coal-measure mudstones were mainly consistent with the results of thermal simulation experiments, indicating that the formation of diamondoid compounds was primarily controlled by the original material source. Some diamondoid maturity parameters (MAI, EAI, TMAI-1) in coal-measure mudstones were consistent with the parameters of the evolution characteristics in marine shale. Therefore, the relationship between these parameters and vitrinite reflectance can be established, to calculate the maturity of marine source rocks. In addition, the evolution characteristics and some diamondoid maturity parameters in the extracts and the extracted coal- measure mudstones showed a good linear relationship, but the specific characteristics were different, which may enable the identification of kerogen cracking and secondary cracking of crude oil.

KEYWORDS

diamondoids, pyrolysis simulation experiment, coal measures, diamondoid parameters, thermal maturity

1 Introduction

Diamondoids, named with reference to their diamond-like structure, are highly resistant to thermal degradation and biodegradation. Thus, they are preserved and enriched during the long and complex geological process, and carry geological information. Therefore, diamondoids have wide applications in petroleum geochemistry, such as oil maturity ascertain (Chen et al., 1996; Li et al., 2000; Zhang et al., 2005; Jiang et al., 2019), oil cracking extent assessment (Dahl et al., 1999), lithofacies discern (Schulz et al., 2001; Chai et al., 2020), secondary change assessment (Jiang et al., 2020), thermochemical sulfate reduction research (Wei et al., 2011), oil spill source identification in accident (Stout and Douglas, 2004; Wang et al., 2006), and so on.

Owing to their presence in immature and sub-mature peat and sedimentary rocks and absence in modern sediments, diamondoids are inferred to be formed in the early diagenesis stage and to be non-biogenic (Schultz et al., 2001; Wei et al., 2006a; Wei et al., 2006b; Wei et al., 2007). According to previous research, there are two main mechanisms for lower diamondoid formation. First, lower diamondoids (adamantanes and diamantanes) are created through Lewis acid-catalyzed rearrangements of polycyclic hydrocarbons (Petrov et al., 1974; Wingert, 1992; Lin and Wilk, 1995). Second, simulation experiments have shown that diamondoids can be produced from high molecular-mass fractions (Giruts et al., 2006; Giruts and Gordadze, 2007), such as kerogen (Wei et al., 2006b), source rocks (Wei et al., 2007b; Fang et al., 2015a; Fang et al., 2015b), crude oils (Fang et al., 2012) and their different group components (Giruts et al., 2006; Giruts and Gordadze, 2007; Fang et al., 2013), and light hydrocarbon component (Fang et al., 2016), C_{16}, C_{19}, C_{22}, C_{34}, C_{36} n-alkanes (Gordadze and Giruts, 2008) and b-ionone (Berwick et al., 2011).

By means of simulation experiments (Fang et al., 2015a), diamondoids can be generated in coal-measure mudstones. However, little work has been done to determine the yield and distribution of diamondoids in coal measure mudstone extracts and extracted mudstones during pyrolysis under non catalytic conditions and their possible interactions. Therefore, in this work, we aimed to investigate these questionsto broaden the potential applications of diamondoids.

2 Materials and methods

2.1 Samples

Coal-measures, are mainly composed of coal, black mudstone and carbonaceous shales (Gong et al., 2018). A sample of coal- measure mudstones from the Xujiahe Formation, Sichuan Basin (used in Fang et al., 2015a), was used in this work, with TOC value of 13.3% and vitrinite reflectance (Ro) of 0.96%. The sample was first ground to pass through 100 mesh and then extracted using the Soxhlet method with a mixed solvent of dichloromethane (DCM) and methanol (MeOH) at a volume ratio of 93:7 for 72 h. The extracts were gently evaporated using a rotary evaporator and dried to a constant weight. The soluble components of the extracts are referred to as mudstone extracts, while the insoluble components, which were further dried in a fume hood, are referred to as extracted coal-measure mudstones in this work. The concentrations of the final extracts and extracted coal-measure mudstones were 6.18 mg/g and 993.82 mg/g in the coal-measure mudstones, respectively.

Gas chromatography–triple quadrupole mass spectrometry (GC–MS–MS) was used to determine the diamondoid concentration (178.77 μg/g) in the mudstone extracts, which was comprised of 155.89 μg/g adamantanes and 22.88 μg/g diamantanes. The target compounds are displayed in Table 1, and in this paper, diamondoids refers to adamantanes and diamantanes combined.

2.2 Simulation experiments

Closed-system pyrolysis experiments were conducted in gold tubes under high-temperature and high-pressure conditions. The detailed pyrolysis method was described previously by Xiong et al. (2004). In the experiments discussed in this work, one end of the gold tubes was sealed by welding, while samples (25–90 mg of extracted mudstone samples or 5–40 mg of extracts) were loaded into the tubes from the other end. The loaded tubes were flushed slowly with argon until the air was completely removed. The other ends of the tubes were then sealed under argon. The sealed gold tubes were mounted in a series of stainless steel autoclaves. Two heating rates (2°C/h and 20°C/h) were used in these autoclaves for the pyrolysis experiments. Between 336 and 600°C, twelve different temperature points were set. At each temperature point, one autoclave was taken out of the oven to air-cool. The gold tubes were then taken out of the cooled autoclave for analysis.

2.3 Quantification of diamondoids

The gold tubes were cleaned with DCM and placed in liquid nitrogen to cool for about 25 min. The tubes were then rapidly cut in half and immersed in a 4 ml sample vial filled with isooctane. A certain amount of isooctane, with n-dodecane-d_{26} as internal standard, was spiked into each vial. To improve the dissolution of pyrolysates, the vials were ultrasonically treated for 10min, and then allowed to stand for 12 h to precipitate the ashphaltenes. An aliquot of the supernatant was placed in a 2 ml vial for the GC-MS-MS analysis of diamondoids. The quantification method was as described by Liang et al. (2012).

TABLE 1 Diamondoids (adamantanes and diamantanes) identified in this work.

Category	Number	Assignment	Abbreviation
Adamantanes	1	Adamantane	A
	2	1-Methyladamantane	1-MA
	3	1,3-Dimethyladamantane	1,3-DMA
	4	1,3,5-Trimethyladamantane	1,3,5-TMA
	5	1,3,5,7-Tetramethyladamantane	1,3,5,7-TeMA
	6	2-Methyladamantane	2-MA
	7	1,4-Dimethyladamantane(*cis*)	1,4-DMA(*cis*)
	8	1,4-Dimethyladamantane(*trans*)	1,4-D MA(*trans*)
	9	1,3,6-Trimethyladamantane	1,3,6-TMA
	10	1,2-Dimethyladamantane	1,2-DMA
	11	1,3,4-Trimethyladamantane(*cis*)	1,3,4-TMA(*cis*)
	12	1,3,4-Trimethyladamantane(*trans*)	1,3,4-TMA(*trans*)
	13	1,2,5,7-Tetramethyladamantane	1,2,5,7-TeMA
	14	1-Ethyladamantane	1-EA
	15	2,6-+2,4-Dimethyladamantane	2,6-+2,4-DMA
	16	1-Ethyl-3-methyladamantane	1-E-3-MA
	17	1,2,3-Trimethyladamantane	1,2,3-TMA
	18	1-Ethyl-3,5-dimethyladamantane	1-E-3,5-DMA
	19	2-Ethyladamantane	2-EA
	20	1,3,5,6-Tetramethyladamantane	1,3,5,6-TeMA
	21	1,2,3,5-Tetramethyladamantane	1,2,3,5-TeMA
	22	1-Ethyl-3,5,7-trimethyladamantane	1-E-3,5,7-TMA
Diamantanes	23	Diamantane	D
	24	4-Methyldiamantane	4-MD
	25	4,9-Dimethyldiamantane	4,9-DMD
	26	1-Methyldiamantane	1-MD
	27	1,4-+2,4-Dimethyldiamantane	1,4-+2,4-DMD
	28	4,8-Dimethyldiamantane	4,8-DMD
	29	1,4,9-Trimethyldiamantane	1,4,9-TMD
	30	3-Methyldiamantane	3-MD
	31	3,4-Dimethyldiamantane	3,4-DMD
	32	3,4,9-Trimethyldiamantane	3,4,9-TMD

3 Results and discussion

3.1 Yields of diamondoids

To apply the results of the simulation experiments carried out under high temperature and fast reaction conditions to explain the actual geological phenomena under low temperature and slow reaction conditions, and to compare them with results obtained in the lab, we used equivalent Ro (EasyRo) (Sweeney and Burnham, 1990) to characterize the thermal maturation (temperature) in the simulation experiments (Figure 1).

In this study, the total contents of 32 diamondoids (22 adamantanes and 10 diamantanes, Table 1) in the pyrolysates were quantitatively analyzed, and the diamondoid yields were used to indicate the changes in the quantities of diamondoids generated during the pyrolysis simulation experiments. The yield of gold tube i, Y_i (μg/g), was defined as the mass of diamondoids in the gold tube, M_i (μg), divided by the mass of sample (extracts or extracted mudstones) in the corresponding gold tube before the pyrolysis simulation experiment, M_0 (g), namely Y_i (μg/g) = M_i (μg)/M_0 (g). Figure 2 shows that the yields of adamantanes and diamantanes, and the total (adamantanes and diamantanes) yield, increased at first, during the slow and rapid generation stages, and then, after peaking, decreased during the destruction stage.

As shown in Figure 2A, during the pyrolysis of the extracts, the yield of diamondoids was 178.36 μg/g (162.86 μg/g of adamantanes and 15.50 μg/g of diamantanes) at the initial

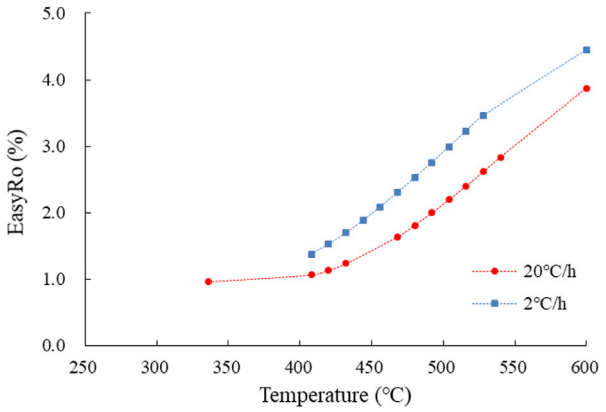

FIGURE 1
Relationship between pyrolysis temperature (°C) and equivalent vitrinite reflectance (EasyRo, %).

point (EasyRo = 0.96%), and reacheed 199.00 μg/g (178.54 μg/g of adamantanes and 20.47 μg/g of diamantanes) at EasyRo 1.14%, indicating that diamondoids were generated slowly below EasyRo 1.14%, in a slow generation stage. With the increase in thermal maturity, the yield increased until it reached a peak value of 303.01 μg/g (270.73 μg/g of adamantanes and 32.27 μg/g of diamantanes) at EasyRo 1.38%, indicating that diamondoids were generated rapidly between EasyRo 1.14% and 1.38%, in a rapid generation stage. The yield then gradually decreased in a fluctuating way to EasyRo 3.23% when the diamondoids were almost all destroyed, in a destruction stage between EasyRo 1.38% and 3.23%. During the pyrolysis process, adamantanes were the major components and had the same evolutionary trend as the diamondoids. The diamantanes were the minor contributors and evolvd more slowly slower than the adamantanes, i.e., the yield of diamantanes reaches a peak value of 45.16 μg/g at EasyRo 2.30%.

During the pyrolysis experiments of the extracted mudstones (Figure 2B), the yield of diamondoids increased slowly from 0.17 μg/g (0.16 μg/g of adamantanes and 0.01 μg/g of diamantanes) at the initial stage (EasyRo 0.96%) to 0.28 μg/g (0.26 μg/g of adamantanes and 0.02 μg/g of diamantanes) at EasyRo 1.07%. After this slow generation stage, the yield of diamondoids began to increase rapidly until EasyRo = 1.38% with a yield of 1.94 μg/g (1.72 μg/g of adamantanes and 0.22 μg/g of diamantanes). Then, the diamondoids entered the destruction stage until almost all were destroyed at EasyRo 2.52%. The adamantanes provided the major contribution to the overall yield. The yield of diamantanes reached a maximum of 0.28 μg/g at EasyRo 1.70%, which was later than the peak of adamantane production.

As shown in Figure 2, the overall evolutionary trends in diamondoid production during extract and extracted mudstone pyrolysis displayed the similar characteristics, which were similar to those for adamantanes, as the main contributors to total diamondoids. However, the trends for diamantanes did not display these similar characteristics.

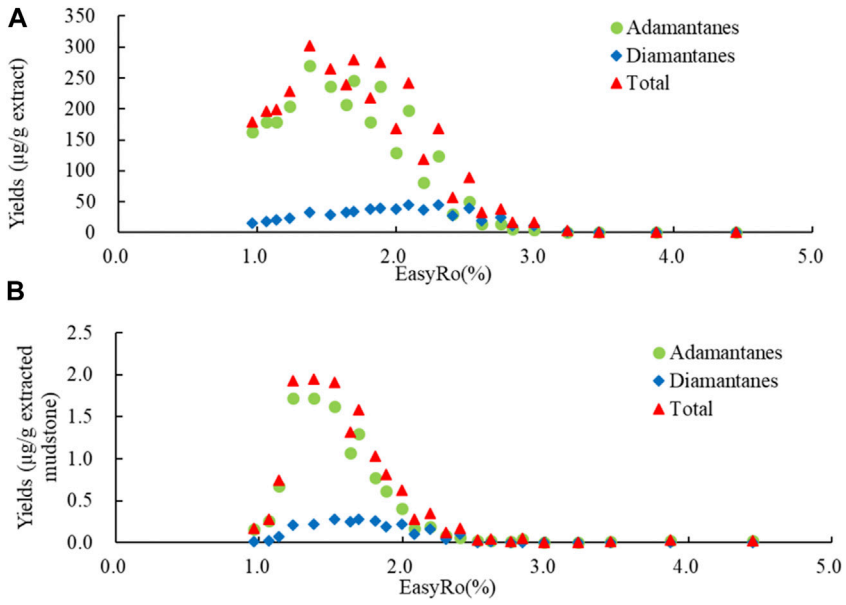

FIGURE 2
Variation in the diamondoid yields (μg/g) with EasyRo (%) during **(A)** extracts and **(B)** extracted mudstones pyrolysis. Total represents all adamantanes and diamantanes in Table 1.

10.3389/feart.2022.1031799

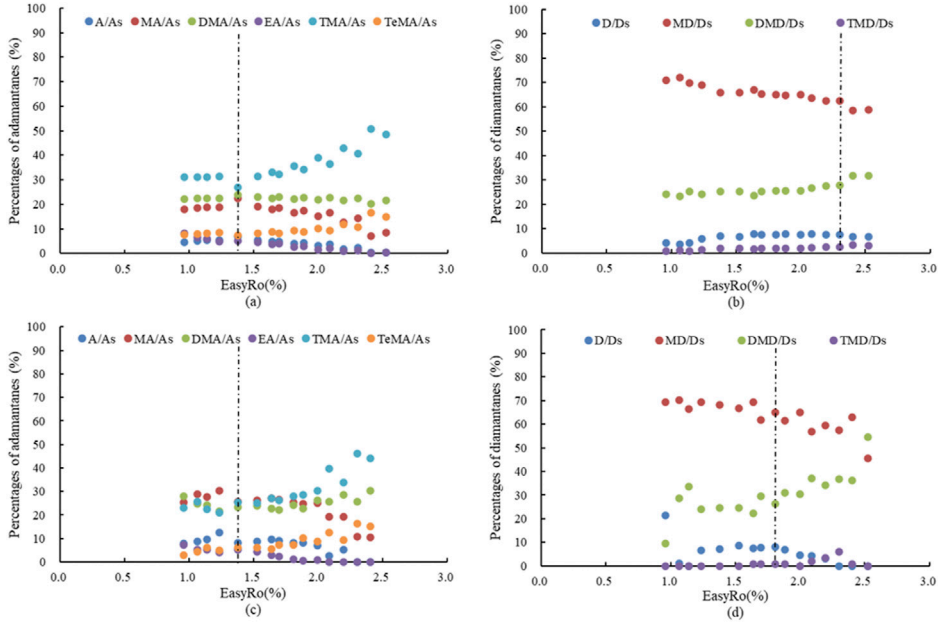

FIGURE 3
The percentage variation of the different alkyl-substituted adamantanes **(A,C)** and diamantanes **(B,D)** of the total adamantanes and diamantanes with extract **(A,B)** and extracted mudstone pyrolysis **(C,D)**, respectively. (A, adamantane; MA, all methyladamantanes; DMA, all dimethyladamantanes; EA,all ethyladamantanes; TMA,all trimethyladamantanes; TeMA, all tetramethyladamantanes; As, all adamantanes; D, diamantine; MD, all methyldiamantanes; DMD, all dimethyldiamantanes; TMD, all trimethyldiamantanes).

Although the diamantanes experienced generation and destruction during both extract and extracted mudstone pyrolysis, the diamantine yield reached a maximum during the extract pyrolysis, which was later than during the extracted mudstone pyrolysis. These results indicated that the mechanism of diamantane formation may be different to that of adamantanes, and the precursor is probably the main controlling factor for diamantane formation. In addition, the maturity of diamantanes corresponding to the maximum yield was higher than that of adamantanes, indicating that the sources or the generation mechanisms of diamantanes differed from those of adamantanes, and the thermal stability of diamantanes higher than that of adamantanes.

3.2 Compositions of diamondoids

To better understand the differences between the extract pyrolysates and the extracted mudstone pyrolysates, the percentage values for the yields of different alkyl-substituted adamantanes and diamantanes generated from extract pyrolysis (Figures 3A,B) and extracted mudstone pyrolysis (Figures 3C,D) were calculated.

During the extract pyrolysis, at the initial point (EasyRo 0.96%), the percentage values for the yields of the different alkyl-substituted adamantanes within the total adamantanes [adamantanes/adamantanes (A/As), methyladamantanes/adamantanes (MA/As), dimethyladamantanes/adamantanes (DMA/As), ethyladamantanes/adamantanes (EA/As), trimethyladamantanes/adamantanes (TMA/As), and tetramethyladamantanes/adamantanes (TeMA/As)] were 4.44%, 17.89%, 22.32%, 8.14%, 31.10%, 7.67%, respectively. These generally remained stable until EasyRo 1.38%, namely, the generation stage, including the slow generation and rapid generation stage, indicating that these compounds (A, MA, DMA, EA, TMA, TeMA) had similar generation rates and formation mechanisms. At this stage, the dominant adamantane compounds were TMA, followed by DMA and MA, and finally TeMA, A and EA. Above EasyRo 1.38%, at the destruction stage, the percentage values for the yields of different alkyl-substituted adamantanes in the total adamantanes began to change. As shown in Figure 3, the percentage values of TMA/As and TeMA/As increased, while the percentage values of MA/As, EA/As and A/As decrease, and the percentage values of DMA/As generally remained stable. These results indicated that these compounds (A, MA, DMA, EA, TMA, TeMA) had different destruction rates at this stage. The adamantanes with a higher carbon number (such as TMA and TeMA) had slower cracking speeds than the adamantanes with a lower carbon number (such as MA, EA, and A). Although DMA and EA have the same carbon number, their destruction characteristics were different, indicating that the different chemical structures

determined the various pyrolysis properties. In other words, these adamantanes had different destruction mechanisms, and TMA and TeMA were relatively more stable than MA, EA, and A.

The percentage values for the yield of different alkyl-substituted diamantanes within the total diamantanes [diamantine/diamantanes (D/Ds), methyldiamantanes/diamantanes (MD/Ds), dimethyldiamantanes/diamantanes (DMD/Ds), and trimethyldiamantanes/diamantanes (TMD/Ds)] were 4.26%, 70.88%, 24.08%, 0.78% at the initial point (EasyRo 0.96%). They generally changed slowly, almost constantly, at the generation stage (EasyRo 0.96%–2.30%), including the slow generation stage and rapid generation stage, indicating that these compounds (D, MD, DMD, TMD) had similar generation rates and formation mechanisms. At this stage, the dominant diamantane compounds were MD, followed by DMD, and finally D and TMD. At the destruction stage, the percentage values began to change rapidly, with DMD/Ds and TMD/Ds increasing and D/Ds and MD/Ds decreasing, indicating that these compounds (D, MD, DMD, TMD) had different destruction rates at this stage. The diamantanes with a higher carbon number (such as DMD and TMD) had slower cracking speed than the diamantanes with a lower carbon number (such as D and MD). In summary, these diamantanes had different cracking mechanisms, and DMD and TMD were relatively more stable than D and MD.

During the extracted mudstone pyrolysis, the percentage values for the yield of different alkyl-substituted adamantanes within the total adamantanes (A/As, MA/As, DMA/As, EA/As, TMA/As, TeMA/As) were 7.98%, 25.45%, 27.88%, 7.36%, 23.09%, 2.88%, respectively, at EasyRo 0.96%. Their fluctuations were very small at the generation stage (EasyRo 0.96%–1.38%), with the dominant adamantane compounds being DMA, MA, and TMA, followed by TeMA, A and EA. At the destruction stage (EasyRo > 1.38%), the percentage values of TMA/As and TeMA/As increased, and the percentage values of MA/As, A/As and EA/As decreased, while the DMA/As values showed small fluctuations within a certain range, indicating faster cracking speeds for A, MA, and EA than TMA and TeMA, and greater relative stability of TMA and TeMA than MA, EA, and A. Similar to the results obtained during the extract pyrolysis, these findings indicated that these adamantanes (A, MA, DMA, EA, TMA, TeMA) had similar generation rates and formation mechanism at the generation stage, but different destruction rates and destruction mechanisms at the destruction stage.

For diamantanes, the percentage values for the yields of different alkyl-substituted diamantanes within the total diamantanes (D/Ds, MD/Ds, DMD/Ds, TMD/Ds) generally showed small changes at the generation stage (lower than EasyRo 1.70%). Then, at the destruction stage, the changes became somewhat larger, with DMD/Ds and TMD/Ds increasing, and MD/Ds and D/Ds decreasing. Similar to the results obtained during the extract pyrolysis, these findings indicated that these adamantanes (D, MD, DMD, TMD) had similar generation rates and formation mechanisms at the generation stage, and different destruction rates and destrution mechanisms at the destruction stage.

Comparing the evolutionary characteristics between the extract pyrolysis and the extracted mudstone pyrolysis, as shown in Figure 3, there was no significant change in the percentage values for either adamantanes or diamantanes at the generation stage. Hence, differences at the initial point may be decided by the precursors in the organic matter. As, there was no significant difference among the different alkyl-substituted compounds, at the destruction stage, the evolutionary characteristics may therefore be decided by the pyrolysis. Moreover, the higher the carbon number, the better the thermal stability, as in TMA/As, TeMA/As, DMD/Ds, and TMD/Ds with increasing EasyRo caused by the high thermal stability and low cracking rate of TMA, TeMA, DMD, and TMD.

3.3 Possible interaction between extracts and extracted mudstones

In the study by Fang et al. (2015a), the generation and evolution of diamondoids in coal measures was discussed. In addition, previous studies have shown that the extract along with kerogen from marine source rocks, can produce diamondoids during the maturing process (Fang et al., 2015b). To properly understand the source and origin of diamondoids in coal measures, pyrolysis experiments were undertaken on both the extracts and extracted mudstones. It is also valuable to determine whether there is a mutual effect between the soluble and insoluble components of coal-measure mudstones.

We calculated the yields of diamondoids during the mudstone pyrolysis, extract pyrolysis and extracted mudstone pyrolysis, as well as the contents of extracts and extracted mudstones within the source rock, to obtain the yields of calculated diamondoids (extracts and extracted mudstones) (Figure 4). We then compared the yields of measured diamondoids during the mudstone pyrolysis (Fang et al., 2015a) to obtained the measured diamondoids, as shown in Figure 4. In general, the diamondoids were shown to undergo generation and destruction during the coal mudstone pyrolysis.

The calculated diamondoids (extracts and extracted mudstones) reached a maximum value, 3.80 μg/g coal measures, at EasyRo 1.38% as shown in Figure 4, while the calculated diamondoids reached a maximum value, 3.66 μg/g coal measures, at EasyRo 1.53% (Fang et al., 2015a). Both the calculated and measured diamondoids during the mudstone pyrolysis reached similar maximum yields of diamondoids, and also their levels of maturity similarly corresponded to the maximum yields of diamondoids. These results, therefore, indicated that the main controlling factor of yield was the

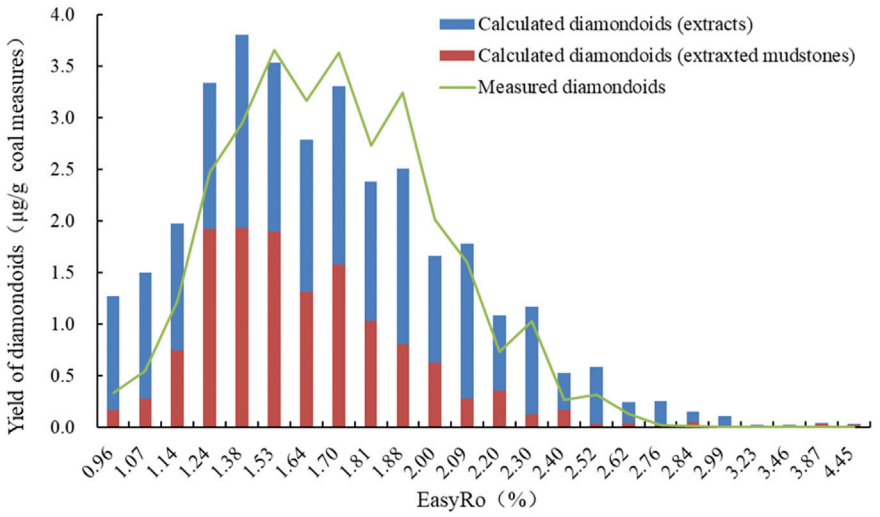

FIGURE 4
Variation in the yields (μg/g) of calculated diamondoids (extracts), calculated diamondoids (extracted mudstones), and measured diamondoids (Fang et al., 2015a) with EasyRo (%).

source matter and not the interaction between the extracts and extracted mudstones.

The overall calculated evolutionary trend of diamondoids was consistent with the measurements of the calculated yields (Fang et al., 2015a). There were no obvious interactions or mutual effects between the soluble and insoluble components. However, at the low yield stages (EasyRo ≤ 1.14% and EasyRo ≥ 2.40%), there was a big difference between the measured and calculated yields, as shown in Figure 4, probably caused by measurement error when the yield was very low. Moreover, the inhibitory effect of the minerals in the coal-measure mudstones on the generation of diamondoids (Wei et al., 2006c) was another possible reason, but this requires further analysis.

The major contributors to the diamondoid generation were the extracts (Figure 4), which accounted for 42.3%–96.1% of the overall yield. At the initial thermal evolution (EasyRo 0.96%), 86.8% of the generated diamondoids were attributed to the extracts. However, with the increase in maturity, the contribution from the extracts gradually decreased and the minimum yield was 42.3% at EasyRo 1.24%. In the subsequent destruction stage, the contribution from the extracts increased again until it reached a maximum of 96.1% at EasyRo 2.99%. Meanwhile, the contribution from the extracted coal mudstones, displayed the opposite evolutionary trend, with the contribution varying from 3.9 to 57.7%. This indicated that, at the generation stage, the overall generation rate of diamondoid compounds in the extracted coal-measure mudstones was faster than that in the soluble organic matter, which may be related to the source of the parent material. This was consistent with the results from research on marine shale, which indicated that the major source of diamondoids in marine shales is the soluble extracts, with a ratio of 59.7%–100% (Fang et al., 2015b).

In summary, the major source of diamondoids was the extracts, which accounted for 42.6%–96.1% of the total yield. The rest was contributed by the extracted mudstones and there were no obvious mutual effects of the soluble and insoluble components on each other. Both the adamantanes and diamantanes had the same major source as the overall diamondoids. The changes in contributions of the extracts, along with the insoluble components, shared the same trends for the adamantanes and diamantanes.

3.4 Diamondoid parameters

A lot of work has been carried out on diamondoid maturity parameters (Chen et al., 1996; Grice et al., 2000; Schulz et al., 2001; Zhang et al., 2005; Wei et al., 2007b), including methyladamantane index [MAI, 1-MA/(1-MA+2-MA)], dimethyladamantane index-1 [DMAI-1,1,3-DMA/(1,2-DMA+1,3-DMA)], dimethyladamantane index-2 [DMAI-2, 1,3-DMA/(1,3-DMA+1,4-DMA)], ethyladamantane index [EAI, 1-EA/(1-EA+2-EA)], trimethyladamantane index-1 [TMAI-1, 1,3,5-TMA/(1,3,5-TMA+1,3,4-TMA)], trimethyladamantane index-2 [TMAI-2, 1,3,5-TMA/(1,3,5-TMA+1,3,6-TMA)], methyldiamantane index [MDI, 4-MD/(4-MD+1-MD+3-MD)], dimethyldiamantane index-1 [DMDI-1,

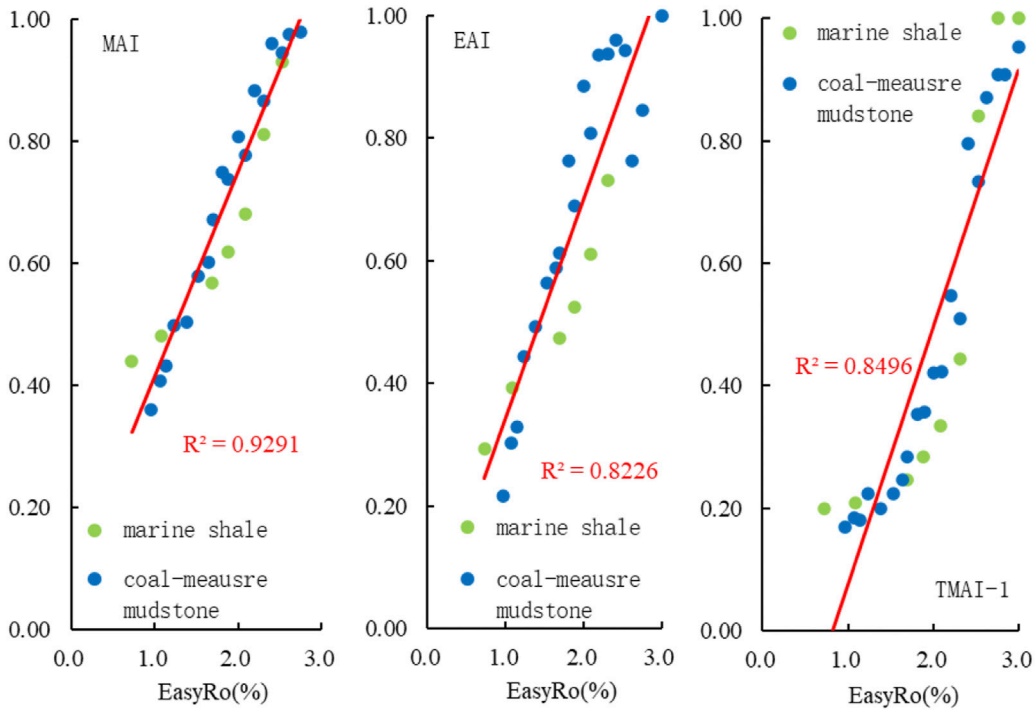

FIGURE 5
Change diagram of diamondoid parameters (MAI, EAI, TMAI-1) during marine shale (Fang et al., 2015b) and coal-measure mudstone pyrolysis.

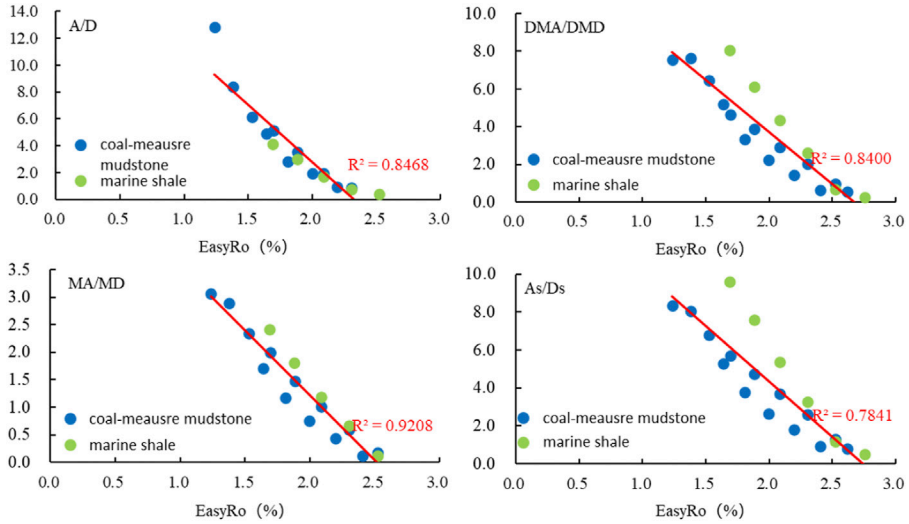

FIGURE 6
Change diagram of diamondoid yield ratios (A/D, MA/MD, DMA/DMD, As/Ds) during marine shale (Fang et al., 2015b) and coal-measure mudstone pyrolysis.

4,9-DMD/(4,9-DMD+3,4-DMD)], and dimethyldiamantane index-2 [DMDI-2, 4,9-DMD/(4,9-DMD+4,8-DMD)].

As pointed out in Figure 5, MAI, EAI, and TMAI-1 are well correlated with maturity (EasyRo, %) in the evolution of coal-measure mudstones. Comparing these parameters (MAI, EAI, and TMAI-1) during marine source rock pyrolysis (Fang et al., 2015b), MAI, EAI, and TMAI-1 were found to have the same evolutionary trend, with increasing EasyRo (%), between marine source rock pyrolysis (Fang et al., 2015b) and coal-measure mudstone pyrolysis. In other words, the source of organic matter had no significant effect on the maturity parameters of diamondoid compounds during the pyrolysis of source rocks, and the evolutionary characteristics of diamondoid maturity parameters in different types of source rocks are very similar, within the EasyRo range of 1.0–3.0%, with the correlation coefficients ranging from 0.8226 to 0.9291.

It is also pointed out in Figure 6 that there was a strong correlation between thermal maturity and the following yield (concentration) ratios: A/D, MA/MD, DMA/DMD and As/Ds (adamantanes/diamantanes) within certain EasyRo ranges. Comparing with these parameters (A/D, MA/MD, DMA/DMD and As/Ds) during the marine source rock pyrolysis (Fang et al., 2015b), we also found that A/D, MA/MD, DMA/DMD and As/Ds have the same evolution trend with EasyRo (%) increasing between marine source rock pyrolysis (Fang et al., 2015b) and coal-measure mudstone pyrolysis, within the EasyRo range of 1.2%–2.5%, with correlation coefficients ranging from 0.7841 to 0.9208.

In summary, both the isomerization indices (MAI, EAI and TMAI-1) and the yield indices (A/D, MA/MD, DMA/DMD and As/Ds) during coal-measure mudstone pyrolysis were shown to have strong correlations with thermal maturity. Similar correlations were also found in highly cracked marine shales (Fang et al., 2015b). This indicated that these parameters were not dependent on the source of organic matter. Therefore, it is possible that the isomerization and yield indices can be more broadly applied for maturity assessment in different samples.

3.4.1 Maturity evaluation of marine source rocks

The maturity of coal-measure source rocks can be measured by the Ro, as a commonly used maturity measure. Whereas due to the lack of vitrinite in marine source rocks, the maturity evaluation of source rocks and crude oil has always been difficult.

Oil and gas exploration in the Tarim and Ordos basins has confirmed the important role of lower Paleozoic marine sedimentary source rocks in China. There are two notable characteristics of the lower Paleozoic marine sediments: high maturity (generally high- and over-mature stages, Ro in the range 1.0%–2.0%) and little organic matter. Thus, assessing the maturity of these lower Paleozoic hydrocarbon source rocks is difficult. There may be two reasons for this. First, vitrinite reflectance cannot be detected to assess maturity, for vitrinite derived from higher plants is absent in marine sediments. Second, conventional molecular organic geochemical maturity parameters, such as biomarker parameters (Song et al., 2016; Song et al., 2017; Xu et al., 2021; Xu et al., 2022, etc), may be invalid at the high- to over-mature stage.

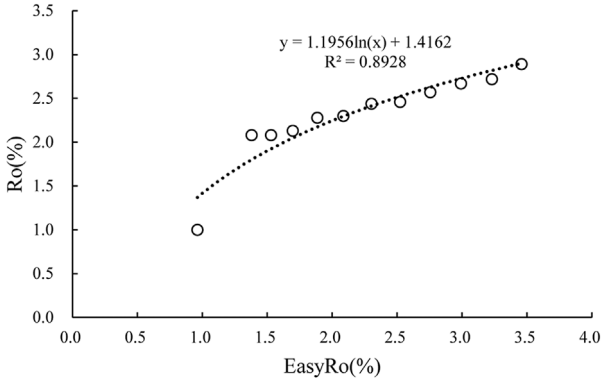

FIGURE 7
Relationship between vitrinite reflectance (Ro) and equivalent vitrinite reflectance (EasyRo).

There is abundant vitrinite in coal-measure mudstones, and maturity can be characterized by measuring Ro. From the relationship between the diamondoid indics and maturity values seen in Figures 5, 6, the relationship between Ro and EasyRo can be established by using the measurement of Ro in coal-measure mudstones, as shown in Figure 7. Therefore, the diamondoid parameters can be used to calculate the maturity parameter Ro, so as to further expand the scope for application of the diamondoid maturity parameter and the comparability of the obtained maturity value.

3.4.2 Kerogen cracking and crude oil secondary cracking

During the separate pyrolysis of the soluble and insoluble organic matter components in the coal-measure mudstones, the evolutionary characteristics of yield were similar, but there were certain differences in the diamondoid parameters. Under the same maturity conditions, the diamondoid parameters (MAI, EAI, TAI-1) in the thermal evolution of the extracts were lower than the diamondoid parameters in the evolution of the extracted coal-measure mudstones (Figure 8). Therefore, it can be assumed that early hydrocarbon expulsion causes the difference in the diamondoid parameters of the reservoir and source rock, and is the reason why the diamondoid parameters from crude oil secondary cracking are lower than those from kerogen cracking.

This indicates that, the evolutionary characteristics of total diamondoid yields in soluble and insoluble organic matter may be different, but the main controlling factor is the original organic matter. Meanwhile, the difference in the original

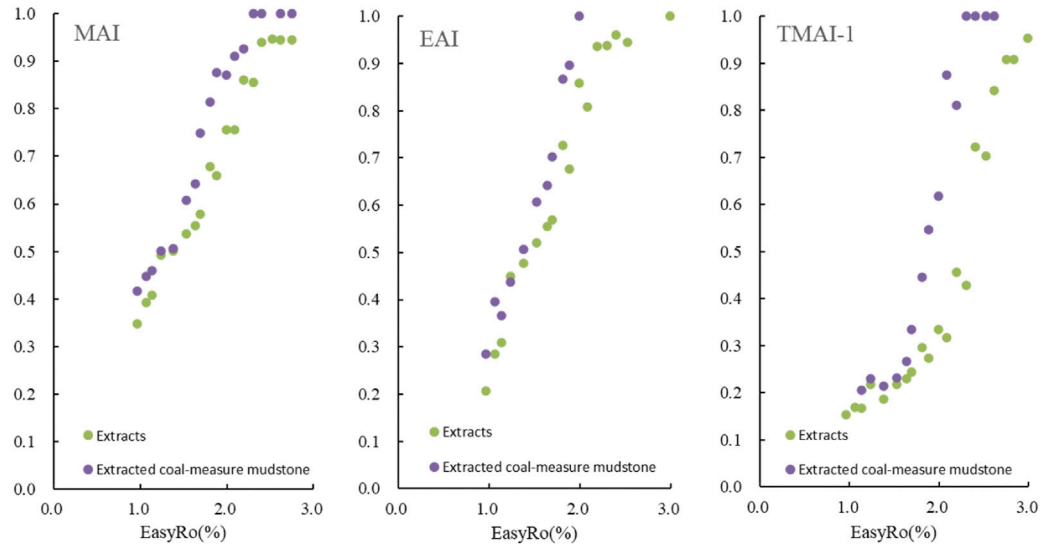

FIGURE 8
Change diagram of diamondoid parameters (MAI, EAI, TMAI-1) during extract and extracted coal-measure mudstone pyrolysis.

organic matter may also lead to the differences in diamondoid parameters, which may distinguish kerogen cracking and crude oil secondary cracking.

Therefore, the diamondoid parameters (MAI, EAI, TAI-1) in late hydrocarbon expulsion may be similar to those of the source rocks, while the diamondoid parameters formed by geological processes after hydrocarbon expulsion in the early stage may be different from those of the source rocks.

4 Summary

(1) We conducted pyrolysis simulation experiments on both the extracts and the extracted mudstones from coal-measure mudstones and quantified the amount of diamondoids in the pyrolysates. The results showed that both the extracts and the extracted mudstones generated diamondoids and that both experienced two-stage pyrolysis (generation and destruction).

(2) Based on the measured diamondoid yields in the extracts and the extracted mudstones along with the composition of the coal-measure mudstone samples (the percentage of the extracts and the extracted mudstones), the results showed that the extracts formed the majority of the total diamondoid yield (42.3%–96.1%). In addition, by comparing the calculated and measured yields, the diamondoid yields depend on the original matter source. This indicated that there was no obvious mutual effects of the extracts and the extracted mudstones on each other in terms of diamondoid generation.

(3) In the comparison of the diamondoid parameters during pyrolysis between coal-measure mudstones and marine shales, it was found that some parameters (MAI, EAI, and TAMI-1), had a strong linear relationship with maturity within the range of EasyRo 1.0%–3.0% and correlation coefficients of 0.8226–0.9291. Another example was taken from the yield ratios including A/D, MA/MD, DMA/DMD as well as As/Ds. These yield ratios were strongly correlated with maturity within the EasyRo 1.2%–2.5% range and the correlation coefficients varied from 0.7841 to 0.9208. All of the strong correlations mentioned above suggested that these parameters can be widely used as proxies for maturity in broader geological conditions.

(4) Through the measurement of Ro in coal-measure mudstones, the diamondoid parameters could be converted directly into Ro, which is convenient for comparison with maturity in other studies. In addition, the difference in diamondoid parameters between the extracts and extracted kerogen could reflect the difference between kerogen cracking and crude oil secondary cracking.

Data availability statement

The raw data supporting the conclusion of this article will be made available by the authors, without undue reservation.

Author contributions

JZ: data curation, writing—original draft preparation, validation. ZC: investigation, supervision. CF: conceptualization, writing-

reviewing and editing, validation. YY: methodology, data curation. WW: investigation, formal analysis. JL: methodology.

Funding

This work was financially supported by the National Natural Science Foundation of China (Grant Nos. 42172184 and 41503044), and the Scientific Research and Technological Development Project of China National Petroleum Corporation (Grant No. 2021DJ0601).

Acknowledgments

We are grateful to Zhang W. B. for his assistance with the GC-MS-MS analysis, and Xu A., Li Y., and Yang X. for their help with the pyrolysis experiments.

Conflict of interest

The authors JZ, ZC, CF and YY were employed by PetroChina Research Institute of Petroleum Exploration and Development. The author WW was employed by PetroChina Southwest Oil & Gasfield Company.

The remaining authors declare that the research was conducted in the absence of any commercial or financial relationships that could be construed as a potential conflict of interest.

Publisher's note

References

Berwick, L., Alexander, R., and Pierce, K. (2011). Formation and reactions of alkyl adamantanes in sediments: Carbon surface reactions. *Org. Geochem.* 42, 752–761. doi:10.1016/j.orggeochem.2011.05.008

Chai, Z., Chen, Z. H., Liu, H., Cao, Z. C., Cheng, B., Wu, Z. P., et al. (2020). Light hydrocarbons and diamondoids of light oils in deep reservoirs of Shuntuoguole Low Uplift, Tarim Basin: Implication for the evaluation on thermal maturity, secondary alteration and source characteristics. *Mar. Pet. Geol.* 117, 104388–388. doi:10.1016/j.marpetgeo.2020.104388

Chen, J. H., Fu, J. M., Sheng, G. Y., Liu, D. H., and Zhang, J. J. (1996). Diamondoid hydrocarbon ratios: Novel maturity indices for highly mature crude oils. *Org. Geochem.* 25, 179–190. doi:10.1016/S0146-6380(96)00125-8

Dahl, J. E., Moldowan, J. M., Peters, K. E., Claypool, G. E., Rooney, M. A., Michael, G. E., et al. (1999). Diamondoid hydrocarbons as indicators of natural oil cracking. *Nature* 399, 54–57. doi:10.1038/19953

Fang, C. C., Wu, W., Liu, D., and Liu, J. Z. (2015a). Evolution characteristics and application of diamondoids in coal measures. *J. Nat. Gas Geoscience* 26 (1), 93–99. doi:10.1016/j.jnggs.2016.02.001

Fang, C. C., Xiong, Y. Q., Li, Y., Chen, Y., and Tang, Y. J. (2015b). Generation and evolution of diamondoids in source rock. *Mar. Pet. Geol.* 67, 197–203. doi:10.1016/j.marpetgeo.2015.05.018

Fang, C. C., Xiong, Y. Q., Li, Y., Liang, Q. Y., Wang, T. S., and Li, Y. X. (2016). The effect of volatile components in oil on evolutionary characteristics of diamondoids during oil thermal pyrolysis. *Sci. China Earth Sci.* 59, 362–370. doi:10.1007/s11430-015-5163-x

Fang, C. C., Xiong, Y. Q., Liang, Q. Y., and Li, Y. (2012). Variation in abundance and distribution of diamondoids during oil cracking. *Org. Geochem.* 47, 1–8. doi:10.1016/j.orggeochem.2012.03.003

Fang, C., Xiong, Y., Li, Y., Chen, Y., Liu, J., Zhang, H., et al. (2013). The origin and evolution of adamantanes and diamantanes in petroleum. *Geochim. Cosmochim. Acta* 120, 109–120. doi:10.1016/j.gca.2013.06.027

Giruts, M. V., and Gordadze, G. N. (2007). Generation of adamantanes and diamantanes by thermal cracking of polar components of crude oils of different genotypes. *Pet. Chem.* 47, 12–22. doi:10.1134/s0965544107010021

Giruts, M. V., Rusinova, G. V., and Gordadze, G. N. (2006). Generation of adamantanes and diamantanes by thermal cracking of high-molecular-mass saturated fractions of crude oils of different genotypes. *Pet. Chem.* 46, 225–236. doi:10.1134/S0965544106040025

Gong, D. Y., Li, J. Z., Ablimit, I., He, W. J., Lu, S., Liu, D. G., et al. (2018). Geochemical characteristics of natural gases related to Late Paleozoic coal measures in China. *Mar. Petroleum Geol.* 96, 474–500. doi:10.1016/j.marpetgeo.2018.06.017

Gordadze, G. N., and Giruts, M. V. (2008). Synthesis of adamantane and diamantane hydrocarbons by high-temperature cracking of higher n-alkanes. *Pet. Chem.* 48, 414–419. doi:10.1134/S0965544108060029

Grice, K., Alexander, R., and Kagi, R. I. (2000). Diamondoid hydrocarbon ratios as indicators of biodegradation in Australian crude oils. *Org. Geochem.* 31, 67–73. doi:10.1016/s0146-6380(99)00137-0

Jiang, W. M., Li, Y., and Xiong, Y. Q. (2020). Reservoir alteration of crude oils in the Junggar Basin, northwest China: Insights from diamondoid indices. *Mar. Pet. Geol.* 119, 104451. doi:10.1016/j.marpetgeo.2020.104451

Jiang, W. M., Li, Y., and Xiong, Y. Q. (2019). Source and thermal maturity of crude oils in the Junggar Basin in northwest China determined from the concentration and distribution of diamondoids. *Org. Geochem.* 128, 148–160. doi:10.1016/j.orggeochem.2019.01.004

Li, J. G., Philp, P., and Cui, M. Z. (2000). Methyl Diamantane index (MDI) as a maturity parameter for Lower Palaeozoic carbonate rocks at high maturity and overmaturity. *Org. Geochem.* 31, 267–272. doi:10.1016/s0146-6380(00)00016-4

Liang, Q. Y., Xiong, Y. Q., Fang, C. C., and Li, Y. (2012). Quantitative analysis of diamondoids in crude oils using gas chromatography-triple quadrupole mass spectrometry. *Org. Geochem.* 43, 83–91. doi:10.1016/j.orggeochem.2011.10.008

Lin, R., and Wilk, Z. A. (1995). Natural occurrence of tetramantane ($C_{22}H_{28}$), pentamantane ($C_{26}H_{32}$) and hexamantane ($C_{30}H_{36}$) in a deep petroleum reservoir. *Fuel* 74, 1512–1521. doi:10.1016/0016-2361(95)00116-m

Petrov, A., Arefjev, D. A., Yakubson, Z. V., Tissot, B., Bienner, F., Schneider, A., et al. (1974). *Advances in organic geochemistry*, 31. Paris: Editions Technip, 1617–1625. doi:10.1021/jo01343a070Hydrocarbons of adamantane series as indices of petroleum catagenesisFormation of perhydrophenalenes and polyalkyladamantanes by isomerization of tricyclic perhydroaromatics*J. Org. Chem.*

Schulz, L. K., Wilhelms, A., Rein, E., and Steen, A. S. (2001). Application of diamondoids to distinguish source rock facies. *Org. Geochem.* 32, 365–375. doi:10.1016/S0146-6380(01)00003-1

Song, D. F., Simoneit, B. R., and He, D. F. (2017). Abundant tetracyclic terpenoids in a Middle Devonian foliated cuticular liptobiolite coal from northwestern China. *Org. Geochem.* 107, 9–20. doi:10.1016/j.orggeochem.2017.02.010

Song, D. F., Wang, T. G., and Li, M. J. (2016). Geochemistry and possible origin of the hydrocarbons from wells Zhongshen1 and Zhongshen1C, tazhong uplift. *Sci. China Earth Sci.* 59, 840–850. doi:10.1007/s11430-015-5226-z

Stout, S. A., and Douglas, G. S. (2004). Diamondoid hydrocarbons – application in the chemical fingerprinting of natural gas condensate and gasoline. *Environ. Forensics* 5, 225–235. doi:10.1080/15275920490886734

Sweeney, J. J., and Burnham, A. K. (1990). Evaluation of a simple-model of vitrinite reflectance based on chemical-kinetics. *Am. Assoc. Pet. Geol. Bull.* 74, 1559–1570. doi:10.1306/0C9B251F-1710-11D7-8645000102C1865D

Wang, Z. D., Yang, C., Hollebone, B., and Fingas, M. (2006). Forensic fingerprinting of diamondoids for correlation and differentiation of spilled oil and petroleum products. *Environ. Sci. Technol.* 40, 5636–5646. doi:10.1021/es060675n

Wei, Z. B., Mankiewicz, P., Walters, C., Qian, K. N., Phan, N. T., Madincea, M. E., et al. (2011). Natural occurrence of higher thiadiamondoids and diamondoidthiols in a deep petroleum reservoir in the Mobile Bay gas field. *Org. Geochem.* 42, 121–133. doi:10.1016/j.orggeochem.2010.12.002

Wei, Z. B., Moldowan, J. M., Dahl, J., Goldstein, T. P., and Jarvie, D. M. (2006a). Diamondoids and molecular biomarkers generated from modern sediments in the absence and presence of minerals during hydrous pyrolysis. *Org. Geochem.* 37, 891–911. doi:10.1016/j.orggeochem.2006.04.008

Wei, Z. B., Moldowan, J. M., Dahl, J., Goldstein, T. P., and Jarvie, D. M. (2006b). The catalytic effects of minerals on the formation of diamondoids from kerogen macromolecules. *Org. Geochem.* 37, 1421–1436. doi:10.1016/j.orggeochem.2006.07.006

Wei, Z. B., Moldowan, J. M., Jarvie, D. M., and Hill, R. (2006c). The fate of diamondoids in coals and sedimentary rocks. *Geol.* 34, 1013–1016. doi:10.1130/G22840A.1

Wei, Z. B., Moldowan, J. M., Peters, K. E., Wang, Y., and Xiang, W. (2007b). The abundance and distribution of diamondoids in biodegraded oils from the San Joaquin Valley: Implications for biodegradation of diamondoids in petroleum reservoirs. *Org. Geochem.* 38, 1910–1926. doi:10.1016/j.orggeochem.2007.07.009

Wei, Z. B., Moldowan, J. M., Zhang, S. C., Hill, R., Jarvie, D. M., Wang, H. T., et al. (2007). Diamondoid hydrocarbons as a molecular proxy for thermal maturity and oil cracking: Geochemical models from hydrous pyrolysis. *Org. Geochem.* 38, 227–249. doi:10.1016/j.orggeochem.2006.09.011

Wingert, W. S. (1992). Gc-ms analysis of diamondoid hydrocarbons in Smackover Petroleums. *Fuel* 71, 37–43. doi:10.1016/0016-2361(92)90190-Y

Xiong, Y. Q., Geng, A. S., and Liu, J. Z. (2004). Kinetic-simulating experiment combined with GC-IRMS analysis: Application to identification and assessment of coal-derived methane from zhongba gas field (Sichuan Basin, China). *Chem. Geol.* 213, 325–338. doi:10.1016/j.chemgeo.2004.07.007

Xu, H. Y., Liu, Q. Y., Zhu, D. Y., Meng, Q. Q., Jin, Z. J., Fu, Q., et al. (2021). Hydrothermal catalytic conversion and metastable equilibrium of organic compounds in the Jinding Zn/Pb ore deposit. *Geochimica Cosmochimica Acta* 307, 133–150. doi:10.1016/j.gca.2021.05.049

Xu, H. Y., Liu, Q. Y., Zhu, D. Y., Peng, W. L., Meng, Q. Q., Wang, J. B., et al. (2022). Molecular evidence reveals the presence of hydrothermal effect on ultra-deep-preserved organic compounds. *Chem. Geol.* 608, 121045. doi:10.1016/j.chemgeo.2022.121045

Zhang, S. C., Huang, H. P., Xiao, Z. Y., and Liang, D. G. (2005). Geochemistry of palaeozoic marine petroleum from the Tarim basin, NW China. Part 2: Maturity assessment. *Org. Geochem.* 36, 1215–1225. doi:10.1016/j.orggeochem.2005.01.014

frontiers | Frontiers in Earth Science

TYPE Original Research
PUBLISHED 17 January 2023
DOI 10.3389/feart.2022.1057313

OPEN ACCESS

EDITED BY
Hao Zou,
Chengdu University of Technology, China
EDITED BY
Zhiye Gao,
China University of Petroleum, Beijing, China
Xiaoqi Wu,
Sinopec Petroleum Exploration and Production Research Institute, China

*CORRESPONDENCE
Zhijun Qin,
zhijunqin_karamay@126.com

SPECIALTY SECTION
This article was submitted to Economic Geology, a section of the journal Frontiers in Earth Science

RECEIVED 29 September 2022
ACCEPTED 31 October 2022
PUBLISHED 17 January 2023

CITATION
Qin Z, Tang Y, Chang Q, Liu C and Ren H (2023), The characteristics and genetic mechanisms of the Upper Permian Shangwuerhe clastic reservoir in the eastern Junggar Basin, Northwest China.
Front. Earth Sci. 10:1057313.
doi: 10.3389/feart.2022.1057313

The characteristics and genetic mechanisms of the Upper Permian Shangwuerhe clastic reservoir in the eastern Junggar Basin, Northwest China

Zhijun Qin[1,2]*, Yong Tang[2], Qiusheng Chang[2], Chaowei Liu[2] and Haijiao Ren[2]

[1]China University of Petroleum (East China), Shandong, China, [2]Research Institute of Exploration and Development, Xinjiang Oil Company, PetroChina, China

In this paper, the lithology, pore type, throat structure, and physical characteristics of the sandstone and conglomerate reservoirs of the Upper Permian Shangwuerhe Formation in the Fukang Sag of the Junggar Basin were analyzed through rock cast thin section, scanning electron microscopy, fluid inclusions, piezometric mercury, and porosity–permeability analysis. In addition, the reservoir densification mechanism and the genesis of deep effective reservoirs were discussed. The results show that the reservoir is dominated by lithic sandstone (or lithic sandstone conglomerate). The lithic fragments primarily comprise tuffaceous volcanic rocks, supported by grains and cemented by clay, carbonate, authigenic quartz, and laumontite. The reservoir properties are characterized by extra-low porosity and permeability, and the pore type is dominated by inter- and intragrain dissolved pores of lithic fragments, feldspar, and quartz. The pore connectivity is poor due to poorly sorted extra-fine throat channels. The tightness of the reservoir.is due to the strong cementation of calcite, chlorite, montmorillonite, illite-montmorillonite mixed layer, authigenic quartz, and laumontite. Furthermore, the large amount of Ca^{2+} released by the hydration of tuff rock debris and intermediate–basic volcanic rock debris and the CO_2-rich thermal fluid from the deep layers cause the development of several calcites. The formation of several montmorillonites is mainly related to the alteration of filled volcanic ash, and the hydration of volcanic tuff material primarily causes the development of laumontite cementation. The dissolution of feldspar and various volcanic lithic fragments by acidic fluids triggers the physical improvement of the reservoir in the local section.

KEYWORDS

reservoir characteristics, genesis mechanism, Shangwuerhe formation, Fukang Sag, Junggar Basin

1 Introduction

Due to the rise in oil and gas exploration in the basin uplift areas and shallow layers, and the rapid advancement of drilling and development technologies, the petroleum exploration field shifted from tectonic reservoirs in uplift areas to lithologic reservoirs in the depression areas. Moreover, it moved from conventional petroleum systems to unconventional systems (i.e., tight and shale petroleum systems) and from shallow to deep petroleum reservoirs (Jia et al., 2007, 2016; He and Li, 2014; Du et al., 2016; Hou et al., 2021; Liu et al., 2021; Zhang et al., 2021; Li et al., 2022).

Entering deep depressions for "near-source petroleum exploration" has become an important direction for current oil and gas exploration. Therefore, depression areas are becoming important for current oil and gas exploration (Zhou, 2005; Zou et al., 2009; Zhi et al., 2012; Du et al., 2014; Gong et al., 2018; Yang and Zou, 2019). Based on this, significant breakthroughs were made in depression areas in the Junggar Basin, such as the Mahu and Shawan sags located in the western part of the basin (Figure 1) (Zhi et al., 2012; Du et al., 2019; Tang et al., 2019; Song et al., 2022; Yu et al., 2022; Zhang et al., 2022). However, as the largest proliferous depression in the Junggar Basin, the hydrocarbon

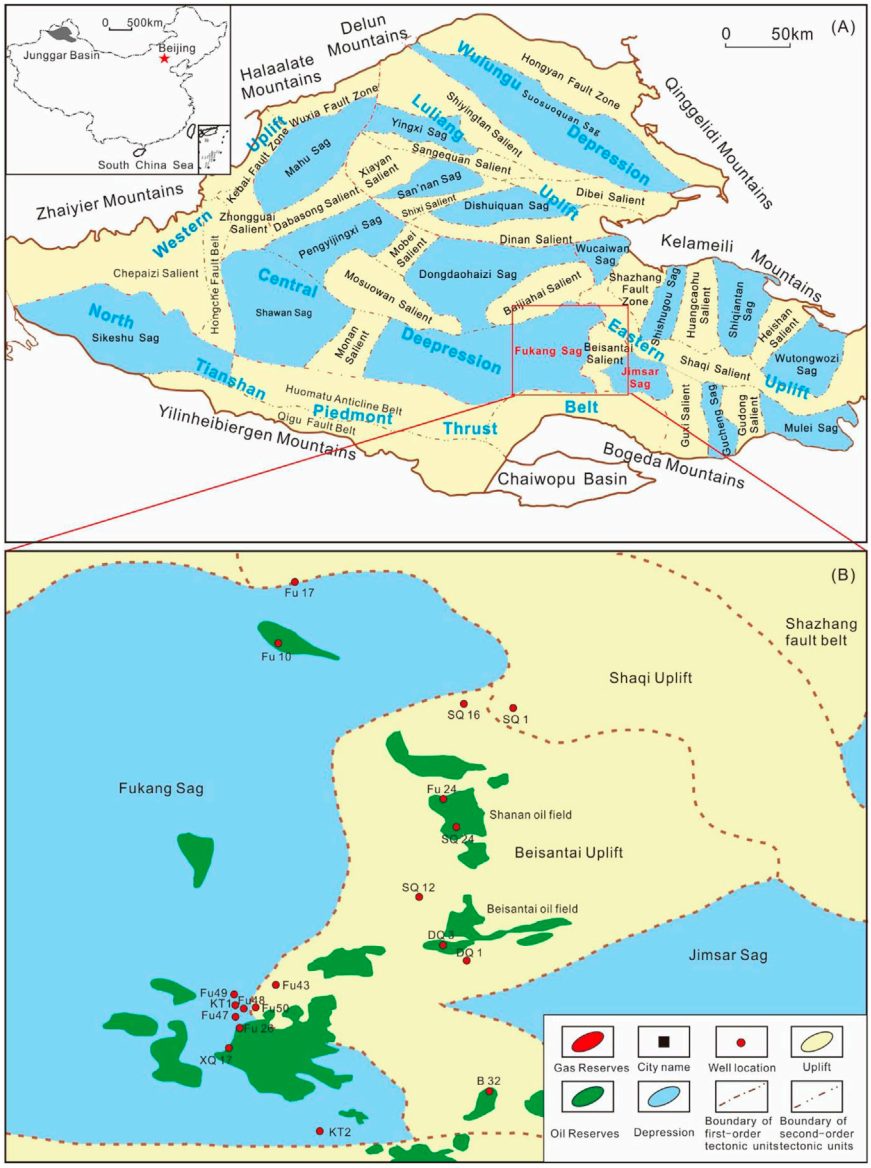

FIGURE 1
Tectonic units in the Junggar Basin and the location of Fukang Sag (after Lian et al., 2011; Gong et al., 2019).

exploration in the Fukang Sag has not yielded any significant discoveries. This may be because previous hydrocarbon exploration in the area centered on the bulge around the perimeter of the sag (Zhang, 2011; Wang et al., 2013; Sun et al., 2016; Gong et al., 2017, 2019; Hu et al., 2020; Wu et al., 2020). The important discovery of "near-source exploration" in the proliferous Mahu and Shawan sags demands that exploration targets change from uplift to depression areas in the Fukang Sag.

In 2020, Well KT1 in the Fukang Sag drilled a highly productive oil formation in the Upper Permian Shangwuerhe Formation (P_3w), revealing that the Fukang Sag has favorable potential for hydrocarbon exploration in deep reservoirs (He et al., 2021). However, as a new exploration area, the reservoir characteristics and formation mechanisms of the effective P_3w reservoir in the Fukang Sag are still unclear. Based on rock cast thin section, scanning electron microscopy (SEM), fluid inclusions, piezometric mercury analysis, and porosity–permeability analysis of the latest drilled cores in the Fukang Sag, the characteristics and genesis mechanism of the P_3w reservoir were discussed. The results provided a basis for the preferential selection of promising targets and sweet-spot areas in the Fukang Sag.

2 Geological setting

The Junggar Basin is an important component of the Central Asian Orogenic Belt, which is located at the intersection of the Siberian Plate, the Kazakhstan Plate, and the Tarim Plate. It is bordered by the Junggar Mountains to the north and the Tien Shan Mountains to the south, and multiple secondary depressions are developed in the basin (Guo et al., 2020; Tang et al., 2021; Wu et al., 2021).

The Junggar Basin is a complex superimposed basin with deposits from the Late Carboniferous to Quaternary periods (Zhao et al., 2014; Tang et al., 2019; Tang et al., 2021; Wu et al., 2021). During the Late Carboniferous to early Permian periods, a foreland basin was formed under Hercynian compressional tectonics (Guo et al., 2020; Zhang et al., 2020). Simultaneously, the orogenic belt was rapidly elevated and denuded during the land–continental collision process, which provided sufficient provenance for the later stratigraphic deposition (Zhao et al., 2014; Xu et al., 2019; Wu et al., 2021). The orogeny weakened, and the basin evolution entered the whole depression stage of the inland basin during the Middle and late Permian periods. Due to the subsidence of the basin, the sedimentary range gradually increased, and the Middle–Upper Permian strata were deposited, overlying the uplift area that separates the depressions. The Triassic has been characterized by lacustrine deposits formed by inherited unified depressions (Wu et al., 2012; Zhao et al., 2014; Xu et al., 2019; Zhao et al., 2020; Wu et al., 2021). Summarily, the Middle and late Permian were transitional periods from fault depression to depression. During those periods, the sediment provenance sufficiently provided much sedimentary debris for the depression area, with a large deposition thickness and wide distribution (Zhao et al., 2014; Xu et al., 2019; Hu et al., 2020; Zhao et al., 2020; Wu et al., 2021).

The Fukang Sag (a secondary-order structural unit) is located in the southeastern part of the Central Depression (a first-order structural unit). It is adjacent to the Beisantai Bulge to the east, the Monan Bulge to the west, the southern thrust belt to the south, and the Baijiahai and Mosowan bulges to the north (Figure 1). Its tectonic evolutionary features are closely related to the formation and evolution of peripheral bulge zones, with multiphase stratigraphic overburden developing toward the bulge zone (Xu et al., 2019). Figure 2 shows the Fukang Sag stratigraphic system, including the entire strata from the Carboniferous basement to Quaternary sediments. The target strata of this study are located in the middle and upper Permian, including the Pingdiquan Formation (P_2p) and the Shangwuerhe Formation (P_3w).

The Shangwuerhe Formation, which is the fill-in deposition during the transition from "foreland" to "depression," is the study's focus. A large regional unconformity developed beneath the Shangwuerhe Formation, indicating that it represented the beginning of the unified depressional lacustrine basin. The earliest broadly overlying fan-deltaic deposits were developed in this formation, making it one of the most critical exploration intervals for finding large-scale oil reserves (Xu et al., 2019; Hu et al., 2020).

3 Samples and methods

3.1 Materials and sampling

This paper details the observations on the cores of nine wells drilled in Fukang Sag of Junggar Basin in the last 2 years, with a total length of over 200 m. A total of 150 P_3w core samples were collected. Ordinary thin section observation was performed on 70 representative samples, based on which the content of quartz, feldspar, and lithic fragments was classified; the types of lithic fragments were classified; and the structural characteristics (e.g., grain size, sortability, and roundness) and the mode of cementation were analyzed. Approximately 80 samples were prepared into cast thin sections to observe the pore type, morphology, and size and to analyze their relationship with fractures. SEM was applied to 105 samples to observe the filling characteristics of the fillings and pore morphology. Eighteen samples were prepared into thin sections for fluid inclusion analysis.

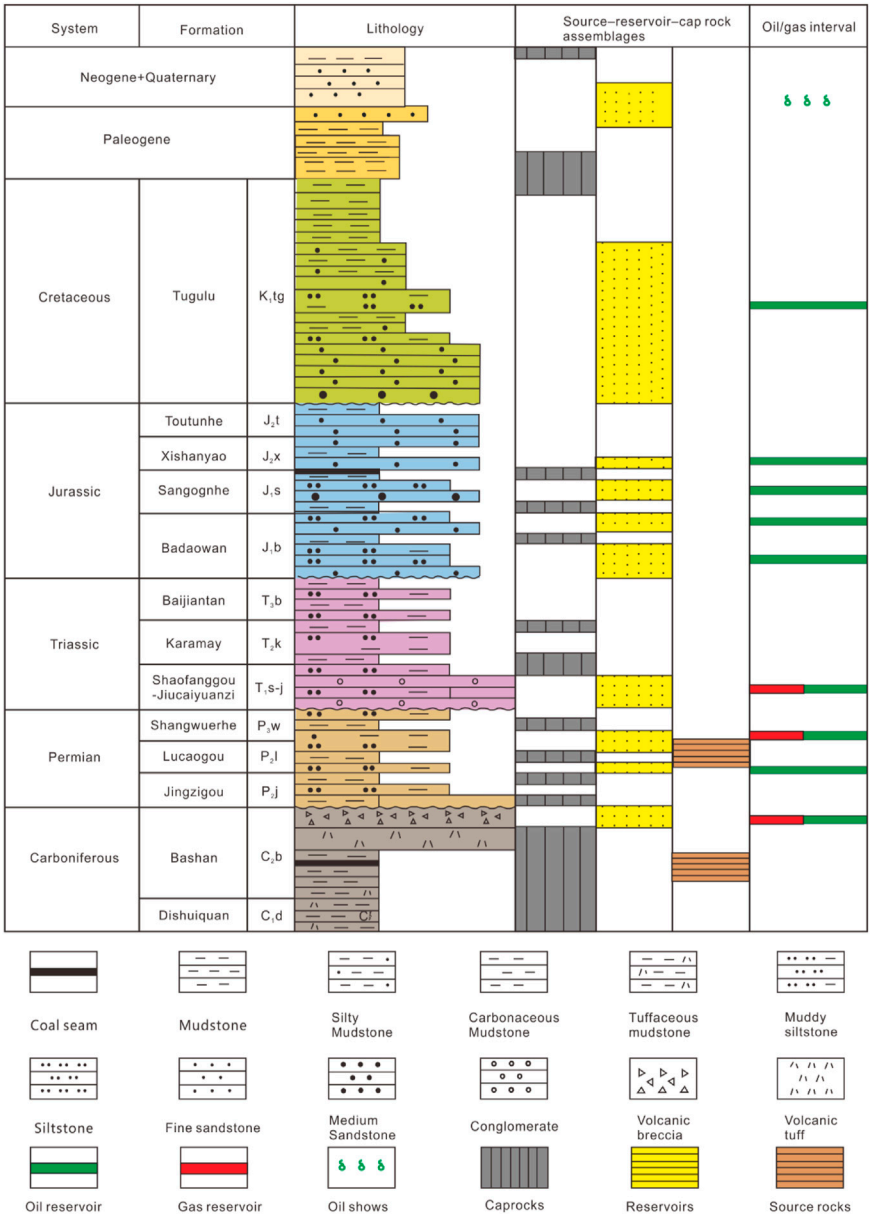

FIGURE 2
Synthetic column of strata, lithology, source rocks, reservoirs, cap rocks, and oil or gas intervals of the Fukang Sag, Junggar Basin (after Gong et al., 2019).

3.2 Mineralogical composition

In this study, the mineralogical composition was obtained following quantitative evaluation of minerals by scanning electron microscopy (QEMSCAN) analysis of cut-out minilet samples (~2 cm^2) or random subsamples of each pseudo-cutting interval. Due to the high repeatability of its measurements, QEMSCAN is heavily used in micromineralogy studies, and repeated measurements of the same samples often have more than 98% similarity (Power and Burns, 2013).

3.3 Scanning electron microscopy

In this study, optical microscopy and SEM were combined to observe the morphology and distribution of pores in Fukang samples. Before imaging, both polished and non-polished (freshly crushed) samples were coated with carbon or gold. A smooth surface was obtained by mechanical polishing and, subsequently, ion milling. SEM and energy dispersive X-ray spectroscopy analysis were performed on field-emission scanning electron microscopy (FE-SEM) with an accelerating voltage of 20 kV.

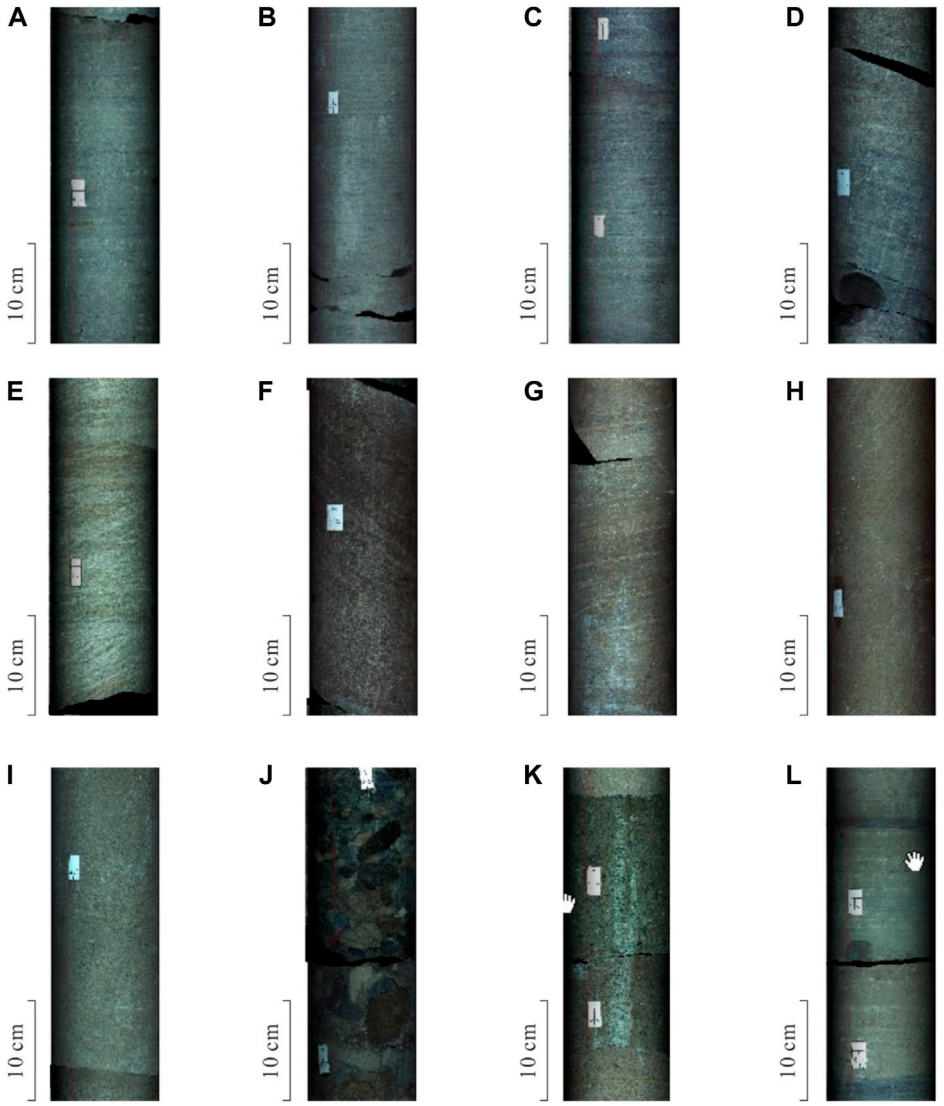

FIGURE 3
Typical core photographs of the Shangwuerhe Formation in the Fukang Sag Junggar Basin. **(A)** Argillaceous siltstone, Fu48, 4489.5–4489.8 m, and P_3w; **(B)** Silty fine sandstone, Fu47, 5035.6–5035.9 m, and P_3w; **(C)** Sandy mudstone and silty fine sandstone, Fu47, 5035.2–5035.5 m, and P_3w; **(D)** Silty mudstone, KT2, 4849.7–4850.0 m, and P_3w; **(E)** Fine sandstone, KT1, 5086.6–5086.9 m, and P_3w; **(F)** Medium-grained sandstone, KT2, 4601.6–4601.9 m, and P_3w; **(G)** Gravelly fine sandstone, KT5, 5969.1–5969.5 m, and P_3w; **(H)** Fine sandstone, Fu48, 4531.1–4531.4 m, and P_3w; **(I)** Gravelly coarse sandstone, Fu47, 5038.0–5038.3 m, and P_3w; **(J)** Conglomerate, Fu47, 5140.7–5141.0 m, and P_3w; **(K)** Glutenite, Fu48, 4533.7–4534.0 m, and P_3w; and **(L)** Silty fine sandstone and mudstone, Fu48, 4493.2–4493.5 m, and P_3w.

Mercury injection capillary pressure method

High-pressure mercury pore size analysis is a common reservoir pore throat distribution method at the core scale, where liquid mercury (Hg) is injected into the sample. Following the Young-Duper equation, the work required to force mercury into the pores by applied pressure equals the work required to submerge the powder surface (Roberts et al., 1991). Hence, the specific surface area is obtained, and the average pore radius can be estimated from the pore volume and the specific surface. A high-pressure mercury pore size analysis analyzed pores in the macropore range. The samples must be dried at 110°C for 2 h of free and adsorbed water and vacuumed at low pressure.

All the analytical tests were completed at the Analysis and Testing Center of Xinjiang Oilfield Company, PetroChina.

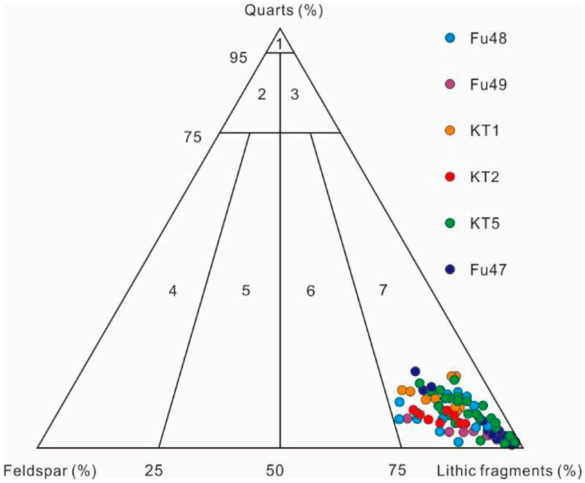

FIGURE 4
Petrological classification of the P_3w reservoirs in Fukang Sag.

4 Results

4.1 Reservoir petrology

The P_3w clastic reservoirs in the Fukang Sag lithologically comprise argillaceous siltstone, fine sandstone, silty fine sandstone, gravelly fine sandstone, medium-grained sandstone, gravelly coarse sandstone, glutenite, conglomerate, sandy mudstone, and mudstone (Figure 3). Fine sandstone, silty fine sandstone, gravelly fine sandstone, medium-grained sandstone, gravelly coarse sandstone, glutenite, and conglomerate are developed in the distributary channel, underwater distributary channel, and estuary bar sedimentary microfacies. However, argillaceous siltstone and siltstone are developed in distal sand and beach bar microfacies, while sandy mudstone and mudstone are developed in interdistributary bay microfacies and shallow and deep lake subfacies.

Following lithological classification, they are mainly lithic sandstone (or conglomerate) (Figure 4). The quartz content ranges from 1% to 18%, with an average of 6.9%; the feldspar content ranges from 1% to 22%, with an average of 7.6%; and the content of lithic fragments ranges from 68% to 100%, with an average of 85.5%. The quartz particles are not only single-crystal quartz from parent granite rock but also polycrystaline quartz from metamorphic rock. The lithic fragments are dominated by tuffaceous volcanic rocks, whose content accounts for above 70% of the lithic fraction, followed by andesite, fayalite, and a few granite lithic fragments (Figure 5). The main types of reservoir fillings are mud, carbonate minerals, silica, and laumontite. Among them, mud is the primary cement, the content is 2%–12%, and the mud composition is mainly chlorite, illite, kaolinite, and illite-montmorillonite mixed layer. The genesis of mud cement relates to the alteration of volcanic ash fillings. Carbonate minerals are the secondary cement, with approximately 1%–9% content, mainly calcite and a few rhodochrosites. There are two major forms of siliceous cementation. One is a secondary increase in quartz, and the other is filled with microcrystalline quartz in the pores. The laumontite content ranges from 0% to 3%, with low overall content, and its genesis is related to the hydrolytic alteration of volcanic ash (Figure 5). Generally, the reservoir's compositional and textural maturities are low. The lithic particles are often coarse-grained and have poor–medium sorting. The rounding of lithic particles is often angular and sub-angular. Point–line contact was widely observed between particles, indicating that support mode is frequently particle support, followed by few suspension contacts. Calcite is characterized by basal-type cementation, and clay minerals are characterized by porous cementation.

4.2 Types of reservoir space

The common pore P_3w clastic reservoirs in the Fukang Sag include residual primary intergranular pores, intergranular dissolved pores of different degrees, intragrain dissolved pores of lithic fragments, feldspar, and quartz, as well as intergranular pores of cement and fractures (Figure 6). The surface porosity of the secondary dissolved pores in this set of clastic reservoirs accounts for over 90% of the total pores. Intergranular dissolved pores are formed by the dissolution of carbonate cement and rigid grain edges based on primary intergranular pores. Therefore, it is difficult to distinguish between residual primary and secondary intergranular dissolved pores. The pores in the study area were categorized into four types, characterized as follows:

(1) Residual primary intergranular pores

Here, the residual primary intergranular pores in the P_3w reservoirs are the pores remaining after mechanical compaction, pressure dissolution, and authigenic mineral filling. Such pores are often distributed in the Well Fu43 area, where the primary pores of the P3w Formation reservoir are preserved by the absence of large-scale carbonate and clay cementation between the clastic particles (Figure 6A). Conversely, the primary intergranular pores were poorly developed in the other area due to strong cementation.

(2) Intergranular dissolved pores

This is a unique P_3w reservoir pore type in the Fukang Sag, formed by partial or total dissolution of the outer edges of various volcanic rock fragments and feldspar grains and early-

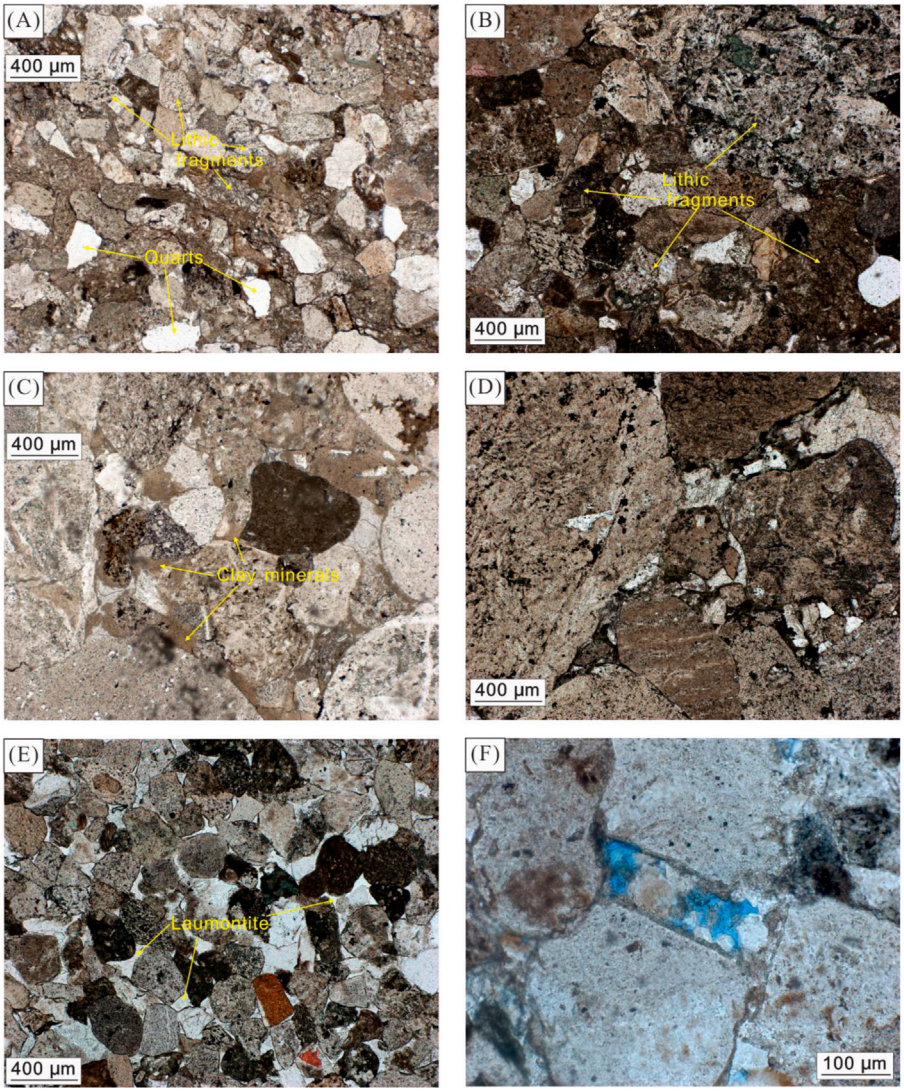

FIGURE 5
Petrological and mineral characteristics of the P_3w reservoirs in Fukang Sag **(A)** Well Fu48, 4596.1 m, P_3w, fine and medium-grained clastic sandstone, siliceous 3%, and illite-montmorillonite mixed layer 1%; **(B)** Well Fu47, 5111.3 m, P_3w, gravelly medium-grained clastic sandstone, illite-montmorillonite mixed layer 6%; the reservoir is tight, and the pores are invisible; **(C)** Well Fu49, 5402.98 m, P_3w, unequal grained sandstone, calcite 2%, and illite-montmorillonite mixed layer 6%; **(D)** Well KT1, 5161.0 m, P_3w, sandy conglomerate; **(E)** Well Fu48, 4511.0 m, P_3w, fine-to medium-grained clastic sandstone, laumontite 6%, and a few muddy shrinkage pores were observed; and **(F)** Well Fu50, 4291.46 m, P_3w, and gravelly medium to coarse-grained clastic sandstone with the intergrain filling of laumontite minerals.

formed carbonate cement. The pore morphology was highly irregular, and harbor-shaped intergranular dissolved pores were observed (Figures 6B,C,E–L). The P_3w reservoir in the study area is tight, and the development of some intergranular dissolved pores is often accompanied by fractures. This indicates that dissolved fluids can only move along the fractures and improve the reservoir around the fractures locally but fail to improve them on a larger scale by penetrating deep into the tight reservoir. During diagenesis, geological fluid enters the reservoir along the fracture. The surface of soluble mineral particles near the fracture and the calcite cement filled between particles were dissolved first. This dissolution on the surface of particles often cannot completely dissolve minerals. Although the main body of undissolved mineral particles exists in the form of debris, the existence of dissolution distinguishes between intergranular dissolved pores and residual primary intergranular pores.

(3) Intragranular dissolved pores

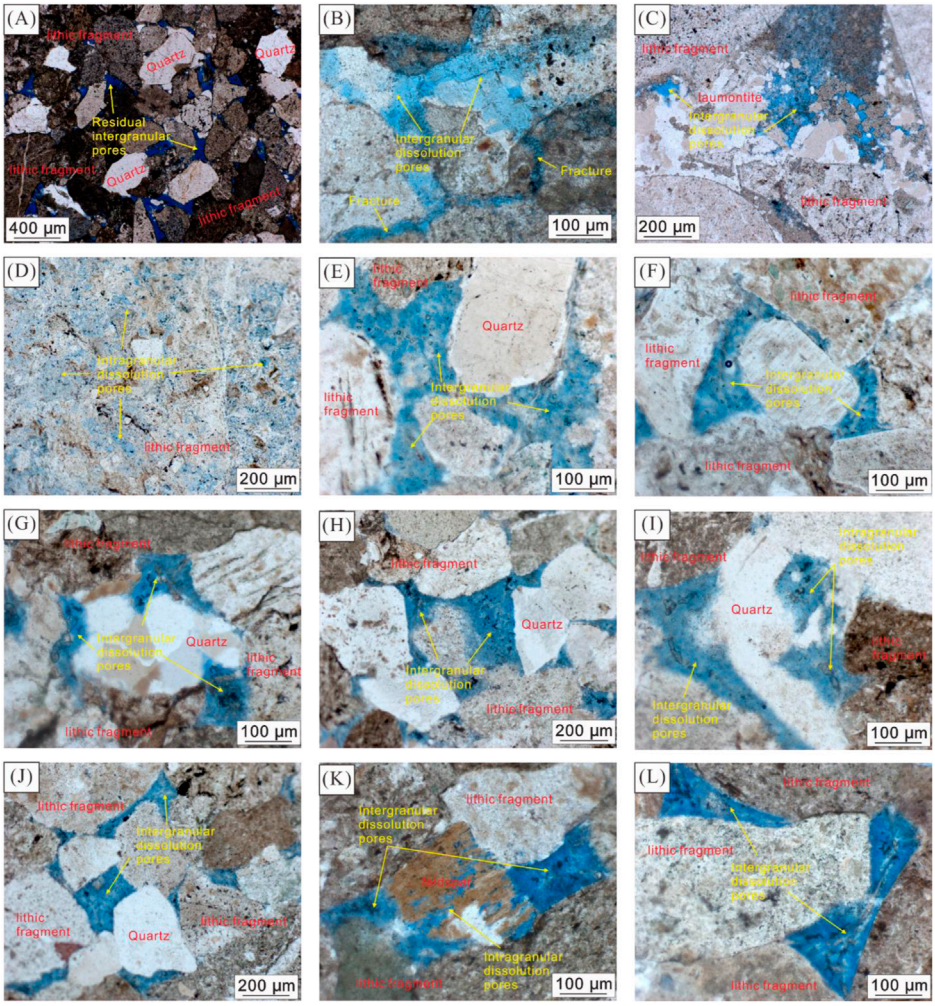

FIGURE 6
Pore characteristics of the P_3w reservoir in Fukang Sag under the thin section **(A)** Well Fu43, 3136.7 m, P_3w, and residual intergranular pores; **(B)** Well KT5, 5944.00 m, P_3w, and intergranular pores formed by dissolution of lithic fragments and cement; **(C)** Well Fu50, 4289.81 m, P_3w, and intergranular pores formed by cement dissolution; **(D)** Well Fu50, 4292.81 m, P_3w, and intragranular microporosity formed by dissolution of lithic fragments; **(E)** Well Fu48, 4541.47 m, P_3w, and intergranular pores formed by cement dissolution; **(F)** Well Fu48, 4541.47 m, P_3w, and intergranular pores formed by cement dissolution; **(G)** Well Fu48, 4541.47 m, P_3w, intergranular pore formed by dissolution of polycrystalline quartz, and lithic fragments; **(H)** Well Fu48, 4541.47 m, P_3w, and intergranular pore formed by dissolution of lithic fragments; **(I)** Well Fu48, 4540.71 m, P_3w, and intragranular pores formed by quartz dissolution; **(J)** Well Fu48 well, 4540.71 m, P_3w, and intergranular pores formed by cement dissolution; **(K)** Well Fu48, 4538.76 m, P_3w, intragranular and intergranular pores formed by dissolution of the feldspar and cement; and **(L)** Well Fu48, 4538.76 m, P_3w, and intergranular pores formed by the cement dissolution.

Intragranular dissolved pores are another primary pore type in the P_3w reservoirs, formed through the internal dissolution of various rock fragments and feldspar grains (Figures 6D,I,K). Intragrain pore shapes vary from particle to particle, with various types. The lithic fragments could form either intragrain micropores or large pores in continuous distribution. Conversely, the intragrain feldspar pores tend to develop along the decomposition and thus have good connectivity with intergrain pores. The main difference between intragranular dissolved pores and intergranular dissolved pores is that dissolution occurs inside the mineral particles rather than on the surface, so the pores formed by dissolution are inside mineral particles, and the external contour of mineral particles is unchanged. The formation of intergranular dissolved pores requires minerals to provide a channel for geological fluids to enter inside the particles. Volcanic lithic fragments with a reticular pore structure and feldspar particles with cleavage meet this condition. Thus, they are the main minerals for developing intergranular dissolved pores in the study area.

(4) Fractures

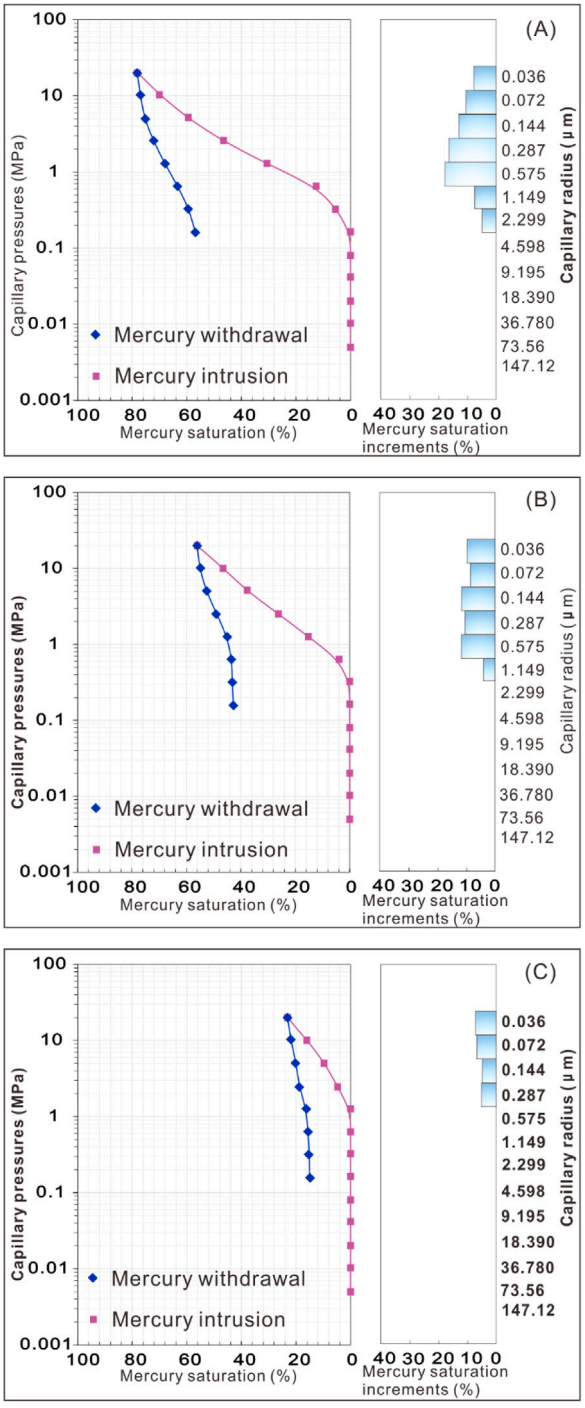

FIGURE 7
Capillary pressure profile of P_3w reservoir in the Fukang Sag **(A)** Medium-throated type, **(B)** Thin-throated type, and **(C)** extra-fine throat type.

Fractures are moderately developed in the P_3w reservoir (Figure 6B), and both tectonic and diagenetic seams can be observed. The pore space of the fractures contributes less to the reservoir pore space. However, it provides a channel for moving the dissolved fluids, improving the reservoir pore space and significantly enhancing the reservoir permeability in the study area.

4.3 Structural characteristics of the pore throat

The pore structure characteristics refer to the geometry, size, distribution, connectivity, configuration relationship, and evolutionary characteristics of the pores and the throat connected. Pores and throats determine the reservoir space of clastic rocks. Pores affect porosity, and throats affect permeability. Therefore, studying the spatial distribution characteristics and collocation relationship between pores and throats is crucial. The capillary pressure curve pattern and the related parameters of the P_3w reservoir in the Fukang Sag were analyzed to discuss the pore throat diameter, connectivity, distribution, and inter-configuration relationship of the reservoir. The pore structure is divided into three types.

(1) Mid-throat type.

This pore structure accounts for a low proportion in the P_3w reservoir in Fukang Sag and is mainly distributed in a few sections in the Wells KT1, KT2, and Fu48 (Figure 7A). A slightly developed platform characterizes its capillary pressure profile and medium pore throat sorting with an average throat radius, median mercury saturation radius, throat sorting coefficient, pore discharge pressure, median mercury saturation pressure, maximum incoming mercury saturation, and mercury withdrawal efficiency of 0.63 μm, 0.23 μm, 2.03, 0.32 Mpa, 6.26 Mpa, 77.88%, and 26.79%, respectively (Figure 7A). The corresponding ranges of porosity and permeability are 13.9–15.5% and 0.69–3.15 mD.

(2) Fine throat type

This is the second type of pore structure in the P_3w reservoirs distributed in some sections of the Wells KT1, KT2, Fu47, Fu48, Fu49, and Fu50 (Figure 7B). Its capillary pressure curve is characterized by an inconspicuous plateau and poor pore throat sorting, with an average throat radius, median mercury saturation radius, throat sorting coefficient, pore discharge drive pressure, median mercury saturation pressure, maximum incoming mercury saturation, and mercury withdrawal efficiency of 0.31 μm, 0.05 μm, 1.82, 0.69 Mpa, 13.97 Mpa, 56.15%, and 23.45%, respectively. The corresponding ranges of porosity and permeability are 5.8%–13.3% and 0.04–0.62 mD.

(3) Extra-fine throat type

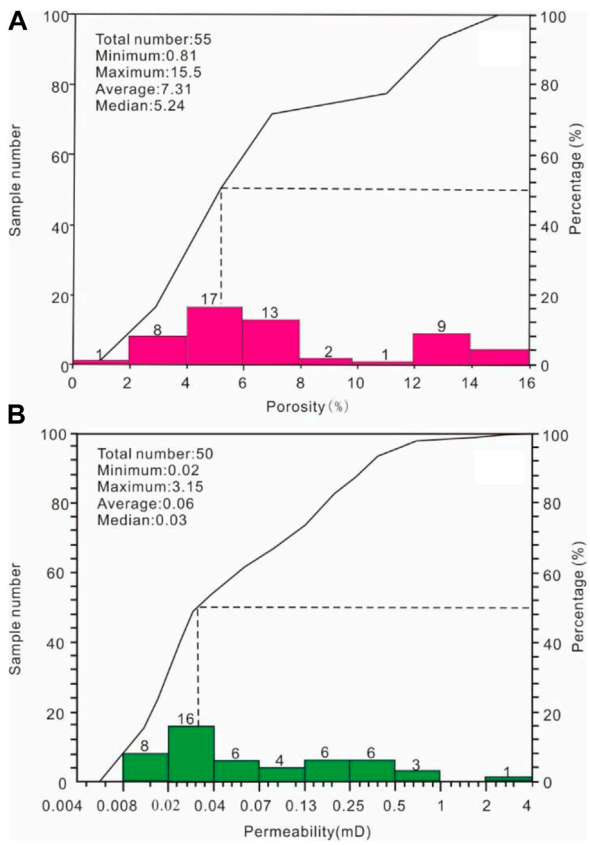

FIGURE 8
Histogram of **(A)** porosity and **(B)** permeability of the P_3w reservoir in Fukang Sag.

This is the most dominant pore structure in the P_3w reservoir in the Fukang Sag and is widely developed all over the P_3w reservoirs in Wells KT1, KT2, KT5, Fu47, Fu48, Fu49, and Fu50 (Figure 7C). The features of its capillary pressure curve are zero platforms, extremely poor pore throat sorting, an average throat radius of approximately 0.1 μm, and a throat sorting coefficient of 0.94. The features also include pore discharge drive pressure greater than 1.0 Mpa, maximum incoming mercury saturation of approximately 23.39%, and mercury withdrawal efficiency of 35.41%. The corresponding range of porosity and permeability are 0.8%–10.4% and 0.01–0.27 mD.

4.4 Physical characteristics of the reservoir

The porosity of the P_3w reservoir in Fukang Sag ranges from 0.81% to 15.5%, with average and median values of 7.31% and 5.24%, respectively. The permeability of the P_3w reservoir ranges from 0.02 to 3.15 mD, with average and median values of 0.06 and 0.03 mD, respectively (Figure 8). In the plane, the physical properties of the P_3w reservoir of Well KT2 in the southern Fukang subsag are relatively good, with average porosity and permeability of 12% and 0.26 mD, respectively. Conversely, those of Wells Fu47, Fu48, Fu47, and KT2 in the middle Fukang subsag are relatively poor, with average porosity and permeability of 6.02% and 0.07 mD, respectively.

5 Discussion

5.1 Mechanisms of reservoir densification

5.1.1 Carbonate cementation

Carbonate cement is developed in the P_3w reservoir in Fukang Sag (Figures 9A,B,H–J). Calcite is the primary type of carbonate cement in the study area, and several Ca^{2+} and CO_3^{2-} are required for calcite formation. The P_3w reservoir in Fukang Sag is rich in volcanic lithic fragments. The hydration of tuffaceous and intermediate–basic volcanic lithic fragments could release many Ca^{2+}, accounting for the primary calcite source in the P_3w reservoir. The analysis of the correlation between the content of tuffaceous/intermediate–basic volcanic lithic fragments and that of carbonate cement showed that the content of carbonate cement increases first and then decreases with the increase of the content of tuffaceous/intermediate–basic volcanic lithic fragments (Figure 10). From the viewpoint of the cementation type, when the content of tuffaceous/intermediate–basic volcanic lithic fragments is below 55%, the cementation is primarily pore type. Moreover, when they are higher than 55%, the cementation is a compression-embedded type (Figure 10). Due to the high plasticity of tuffaceous/intermediate–basic volcanic lithic fragments, an increase in the content of plastic lithic fragments tended to result in an increase in particle compaction and a larger reduction in original pore space, which causes a decrease in cement content.

The carbon source of calcite cement in the P_3w reservoir is deep CO_2-rich hydrothermal fluids. The homogenization temperature of fluid inclusions in the P_3w reservoir is concentrated in the range of 120°C–130°C and also has a certain distribution in the temperature range of 110°C–120°C and 120°C–130°C. However, according to the burial history and geothermal gradient evolution in the study area, such a high temperature could not be reached at a depth of 1591.38 m during the normal burial evolution, indicating a tectono-thermal event.

Additionally, the illite content in the study area was significantly higher in wells and sections near the fault where the carbonate cement was well developed than in wells and sections far from the fault where the carbonate cement was poorly developed. Most illites were produced in wispy form,

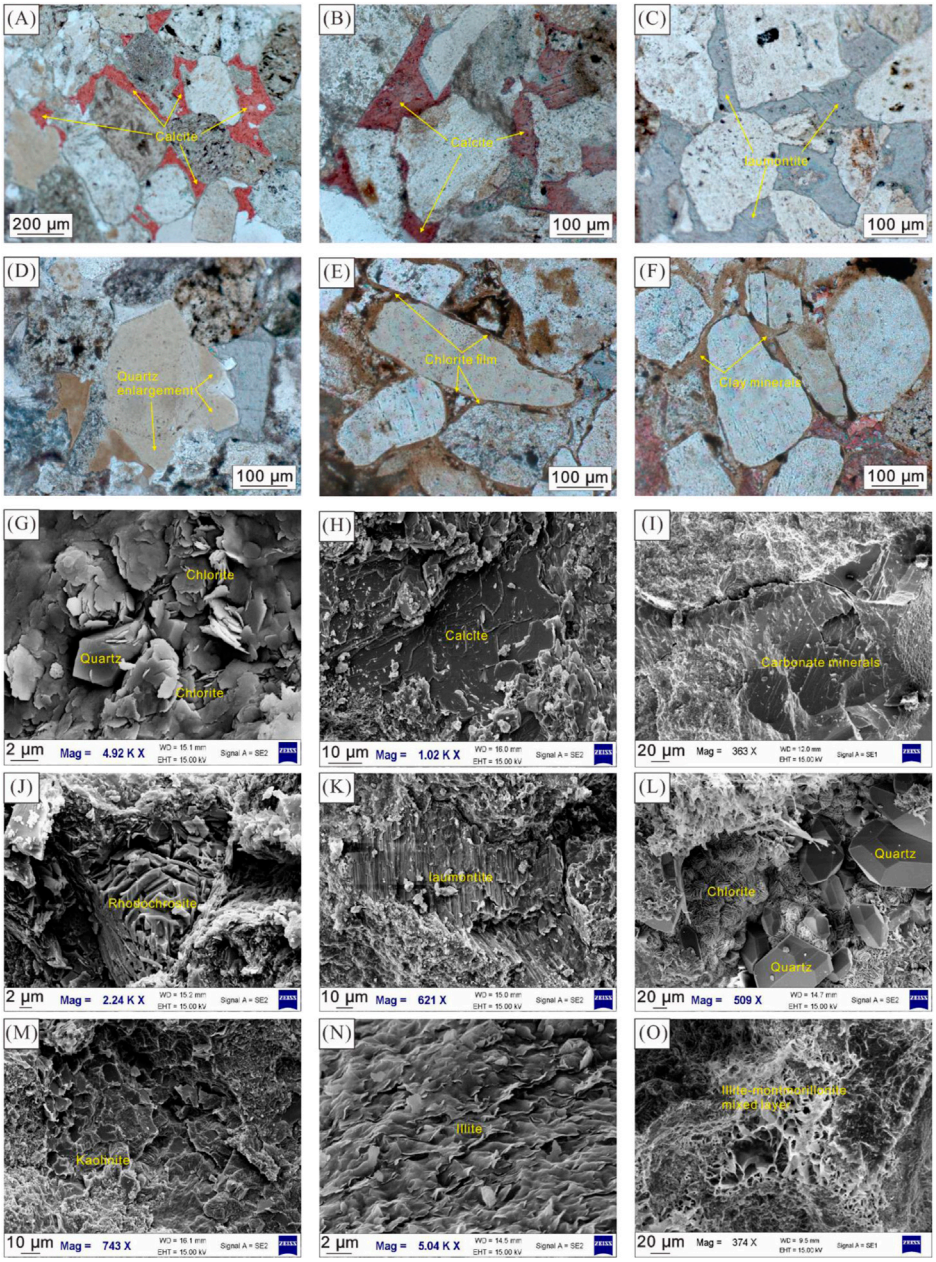

FIGURE 9
Cementation characteristics of the P_3w reservoirs in Fukang Sag **(A)** Well Fu48, 4492.66 m, P_3w, and calcite cementation; **(B)** Well Fu49, 5402.69 m, P_3w, and calcite cementation; **(C)** Well Fu48, 4537.95 m, P_3w, laumontite cementation; **(D)** Well Fu48, 4471.00 m, P_3w, and secondary enlargement of quartz; **(E)** Well Fu49, 5384.00 m, P_3w, and clay cementation; **(F)** Well Fu49, 5384.00 m, P_3w, and intergranular clay-filled; **(G)** Well Fu47, 5143.60 m, P_3w, intergranular developed granular quartz crystals, and bladed chlorite; **(H)** Well Fu47, 5038.10 m, P_3w, and intergranularly filled calcite cementation of embedded crystalline; **(I)** Well Fu49, 5402.69 m, P_3w, and intergranularly filled carbonate minerals; **(J)** Well Fu48, 4492.36 m, P_3w, and intergranularly filled rhodochrosite cement; **(K)** Well Fu47, 5135.65 m, P_3w, and intergranularly filled laumontite cement; **(L)** Well Fu50, 4289.81 m, P_3w, intergranularly filled fluffy chlorite, quartz crystals, and filamentous illite; **(M)** Well Fu48, 4538.09 m, P_3w, and intergranularly filled book-structure kaolinite; **(N)** Well KT1, 5085.78 m, P_3w, and intergranularly filled granular illite; and **(O)** Well KT2, 4602.03 m, P_3w, and intergranularly filled honeycomb-like illite-montmorillonite mixed layer.

and metasomatism of kaolinite was observed (Figures 7O, 9L). The temperature threshold for the conversion of kaolinite to illite is 120°C–140°C. When the temperature exceeds this threshold, kaolinite converts to illite in large quantities and can form wiry illite (Blanc et al., 2021; Asaad et al., 2022). However, there was an abrupt segment in the study area's

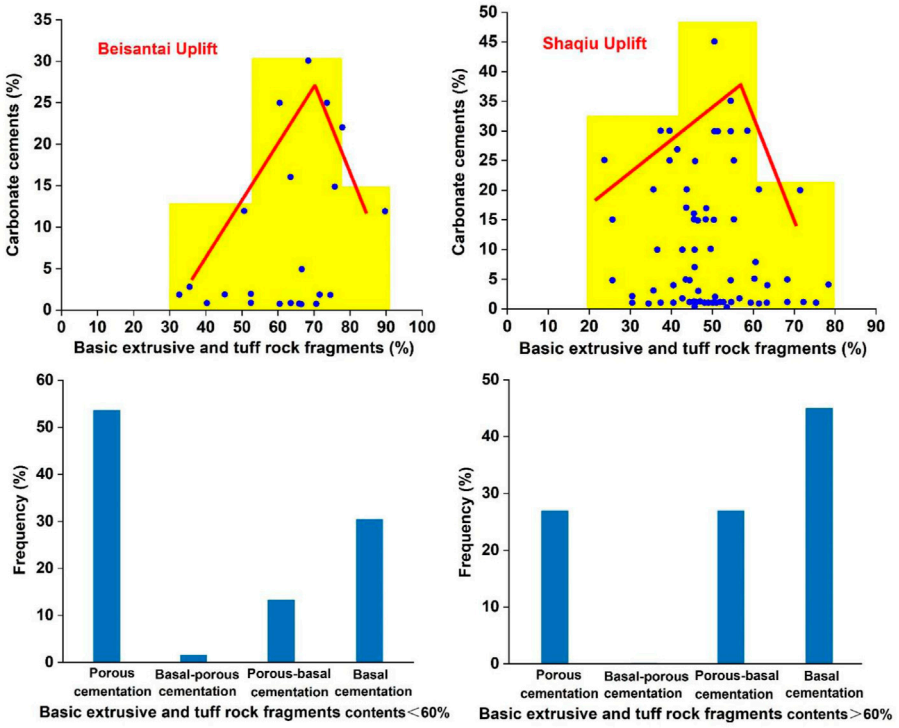

FIGURE 10
Relationships between the content of carbonate cement, the content of volcanic lithic fragments, and the types of cementation in Fukang Sag.

vitrinite reflectance (Ro) profile (Figure 11). Under the consistent tectonic properties of the samples in this area, the intrusion activity of hydrothermal fluid may be the reason for the abrupt change in the R_o profile.

Thus, calcite cement in the P_3w reservoir of Fukang Sag has a deep hydrothermal genesis. The deep hydrothermal fluid moves to the shallow part through the vertical fracture. During this process, the hydrothermal fluid will laterally move along the dominant transport channel (i.e., a highly porous sand body) and react with the rocks. The CO_2-rich hydrothermal fluid gradually dissolves the feldspar to form the secondary pores during transport and provides several carbon sources, which generate carbonate minerals.

The distribution of calcite in the Fukang Sag is controlled by the content of tuff rock debris and intermediate–basic volcanic rock debris and the distance from the active hydrothermal fault. The average content of calcite corresponds to the distance from the fault and the content of volcanic rock debris. From the perspective of sedimentary facies and lithology, calcite is mainly distributed in fine sandstone, pebbly sandstone, and the conglomerate of those developed at the bottom of underwater distributary channels.

5.1.2 The cementation of chlorite, montmorillonite, and illite

Clay minerals dominate the pore fillings of the P_3w reservoir in the Fukang Sag. This is one of the most critical factors causing the reduction of pore space in deeply buried reservoirs. The main clay mineral types are chlorite, montmorillonite, and illite (Figures 9E–G,L–N). Chlorite is mainly characterized by clay film that develops on the surface of mineral particles. The montmorillonite is honeycomb-like, with many intergranular pores under electron microscopy. However, while the illite demonstrates a lamellar geometry, the intergranular pores are undeveloped.

The montmorillonite in the study area is presumably related to the alteration of pore fillings derived from volcanic ash during the sedimentary period. Several tuffaceous lithic fragments in the sandstone indicate that the source area was rich in volcanic debris during the sedimentary period. The conversion of montmorillonite to illite is an important reaction with two possible mechanisms. In the first mechanism, the Al^{3+} is an active component, while in the second mechanism, the Al^{3+} is inactive. Both reactions require a source of K^+, obtained from the destruction of clastic potassium feldspar.

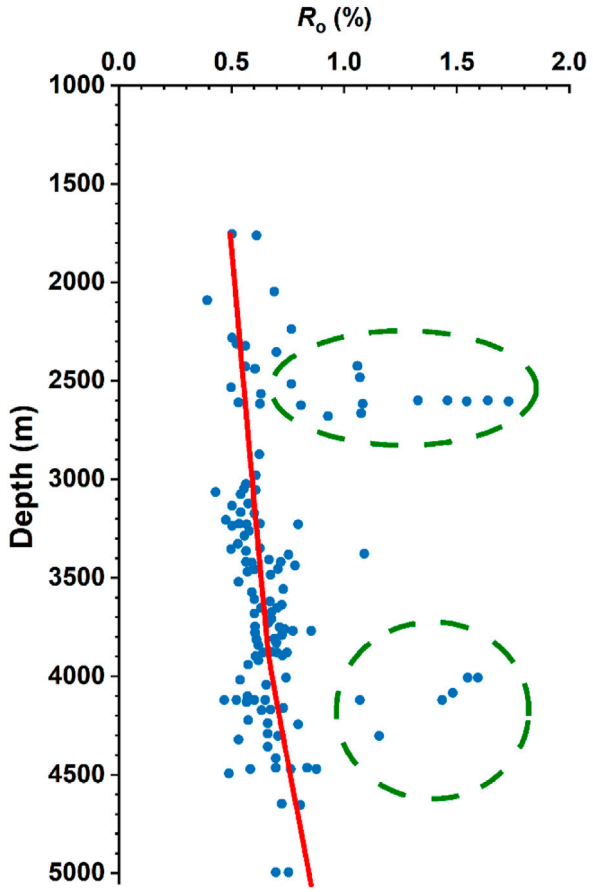

FIGURE 11
The R_o profile in the study area.

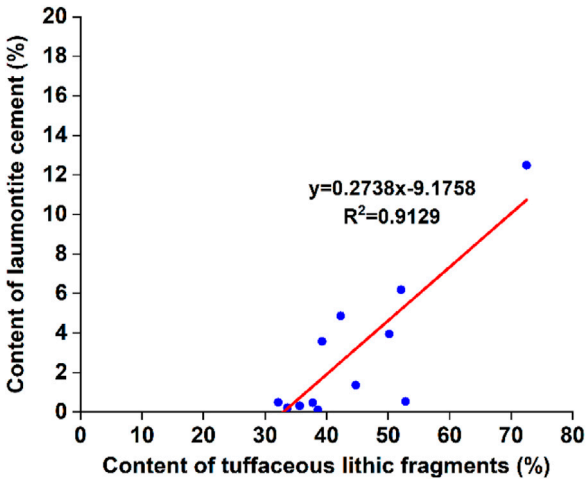

FIGURE 12
Relationship between contents of tuffaceous lithic fragments and laumontite cement in the P_3w reservoir in Fukang Sag.

$$4.5K^+ + 8Al^{3+} + \text{Montmorillonite} = \text{Illite} + \text{illite}\,Na^+\ \text{illite} + \text{illite}\,2Ca^{2+}\ \text{illite} + \text{illite}\,2.5Fe^{3+}\ \text{illite} + \text{illite}\,2Mg^{2+}\ \text{illite} + \text{illite}\,3Si^{4+}\ \text{illite} + \text{illite}\,10H_2O\ (\text{reaction 1}) \quad (1)$$

$$3.9K^+\ \text{illite} + \text{illite}\,1.57\ \text{Montmorillonite} = \text{Illite} + 1.57Na^+ + 3.14Ca^{2+} + 4.78Fe^{3+} + 4.28Mg^{2+} + 24.66Si^{4+} + 57O^{2-} + 11.4H^- + 15.7H_2O\ (\text{reaction 2}) \quad (2)$$

For sandstone cementation, the key to the above reaction is the release of various components while converting montmorillonite to illite. These components are found in the diagenetic phase of the P_3w reservoir, that is, silica precipitation (Figures 9D,G). The transition from montmorillonite to illite provides significant cement to the reservoir, resulting in great damage.

Particularly, the Si^{4+} released in Reaction two is approximately five times greater than that in Reaction 1, causing the severe quartz cementation observed in the P_3w sandstones in the study area. The temperature at which montmorillonite starts to convert to illite is more remarkable at around 60°C (Blanc et al., 2021; Asaad et al., 2022; Hueck et al., 2022). However, when the temperature exceeds 60°C–100°C, the silica released from the transitional reaction will be produced in the form of a quartz secondary increase (French and Worden, 2013; Oye et al., 2018; Fiedrich et al., 2020). A secondary enlargement of quartz is developed, and microcrystalline quartz is filled in the pores, combined with several calcite cementations. This indicates that Reaction 2 may be the dominant mechanism of transforming montmorillonite to illite in Fukang Sag.

5.1.3 The cementation of laumontite

The P_3w reservoir in Fukang Sag contains some laumontite cement (Figures 9C,K), whose formation mechanisms have two explanations. On the one hand, the formation of laumontite cement relates closely to the development of plagioclase, and laumontite can be formed during the sodic feldsparization of plagioclase. On the other hand, the hydration of tuff material is an important way of forming laumontite. Volcanic tuff contains many unstable minerals at low temperatures, which are rapidly decomposed by hydration and release several K^+, Na^+, Ca^{2+}, and Mg^{2+}. This favors the formation of laumontite.

The primary type of clastic rocks in the P_3w reservoir is sandstone and conglomerate, with a high content of volcanic lithic fragments and low feldspar content. Thus, the hydration of volcanic tuff material should be the leading cause of the formation of laumontite cement compared with the sodium feldsparization of plagioclase. Using the relationship between the contents of tuffaceous lithic fragments and laumontite cement, a significant positive correlation is observed, indicating that the laumontite starts to appear when the content of the tuffaceous lithic fragments is >30% (Figure 12).

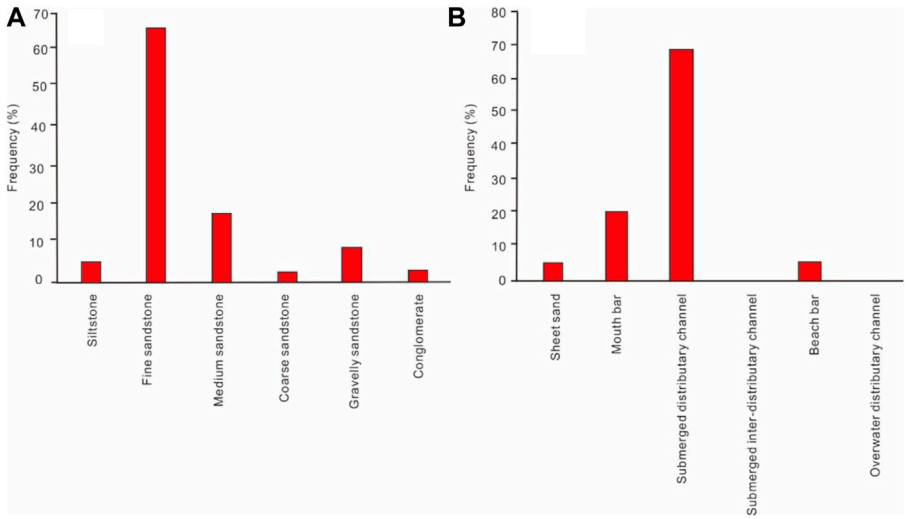

FIGURE 13
(A) Lithology and **(B)** sedimentary phase of contents of laumontite in the P_3w reservoir in Fukang Sag.

Combined with the analysis of single well sedimentary facies, the vertical distribution of laumontite in the study area is discussed. Laumontite cement was distributed mainly in fine sandstone and less in middle sandstone (Figure 13). As for the sedimentary phase, the laumontite is more distributed in the submerged distributary channel microphase and partly in the mouth bar microphase (Figure 13). The depth calibration of laumontite cement from a single well concluded that laumontite cement is mainly formed in the middle and lower parts of the sand body of the submerged distributary channel, with less content at the top (Figure 13).

5.2 The main control factors in forming high-quality reservoirs

The middle-grained sandstone of the Shangwuerhe Formation in Fukang Sag has the highest porosity of 7%–16% and permeability of 0.2–3 mD, followed by siltstone with porosity and permeability of 6%–13% and 0.1–0.2 mD, and fine sandstone with porosity and permeability of 3%–14% and 0.01–0.2 mD. The conglomerate reservoir has the lowest physical properties, with porosity and permeability of 0.5%–7.7% and 0.01–0.05 mD. The higher porosity and permeability of medium sandstone, fine sandstone, and siltstone are mainly related to the higher textural and compositional maturity. Additionally, these rocks contain many soluble mineral components, and the dissolution of soluble minerals by acidic fluids controls the formation of high-quality reservoirs in the study area.

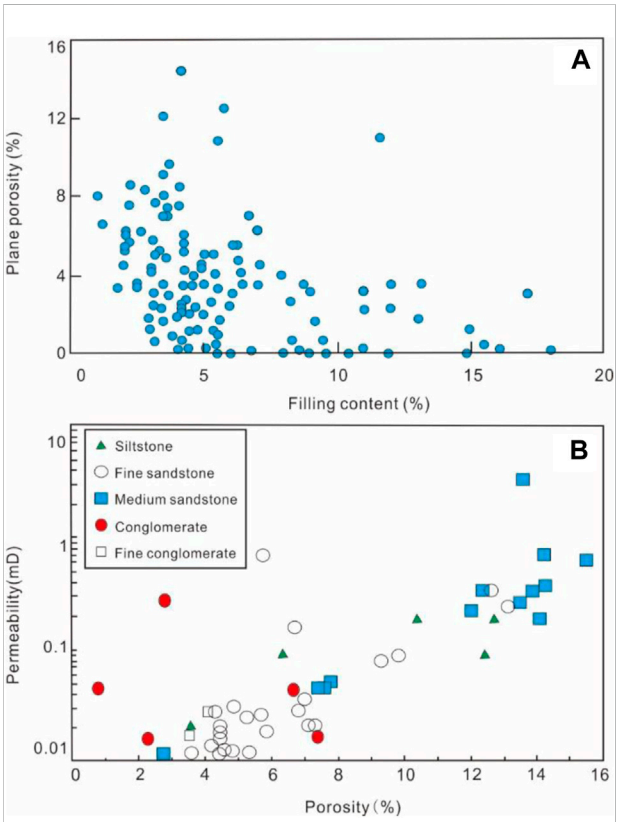

FIGURE 14
The cross plots of **(A)** plane porosity vs. filling content and **(B)** porosity vs. permeability of the P_3w reservoir in Fukang Sag.

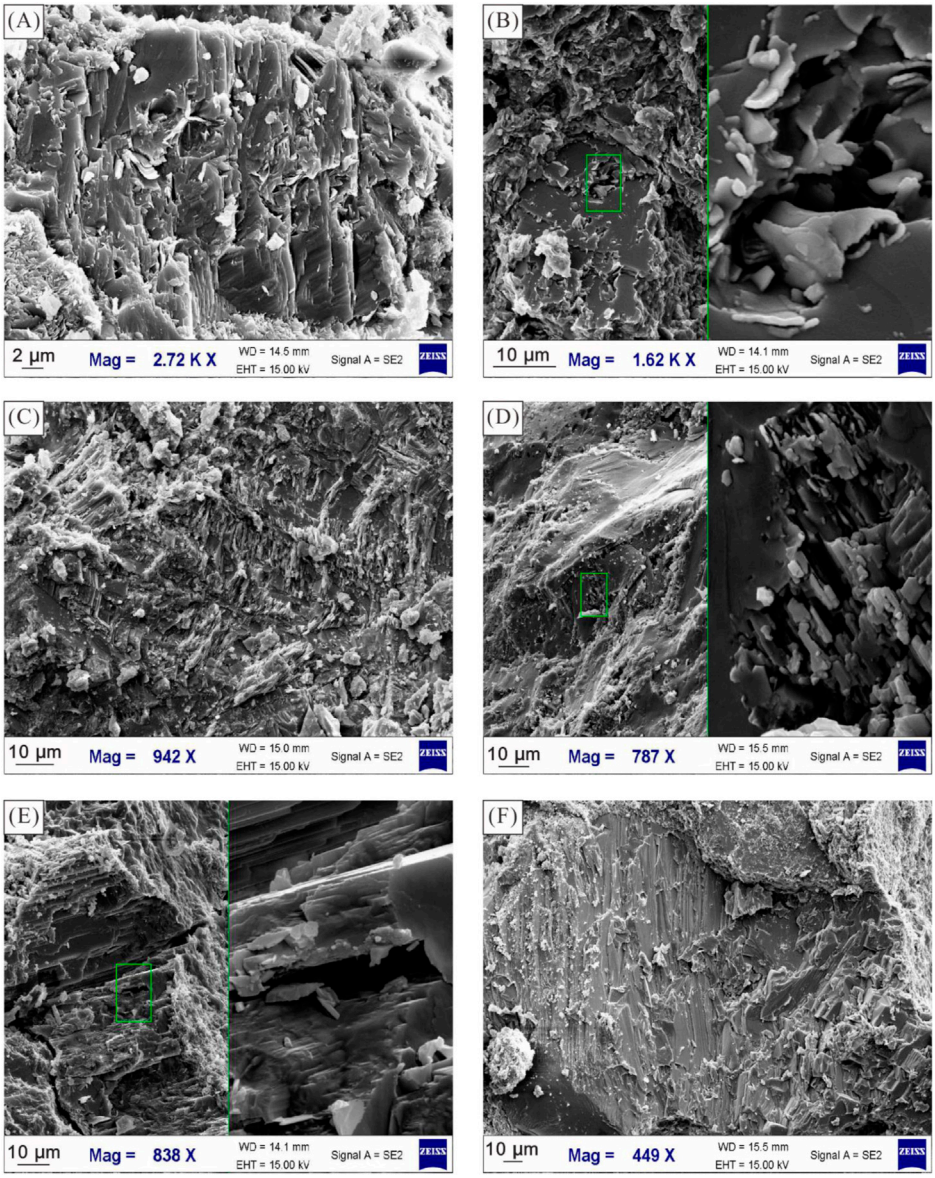

FIGURE 15
Dissolution characteristics of P_3w reservoir in the Fukang Sag **(A)** Well Fu47, 5128.80 m, P_3w, and grain surface dissolution of feldspar; **(B)** Well Fu48, 4542.36 m, P_3w, intragrain dissolution of feldspar; **(C)** Well Fu50, 4179.94 m, P_3w, and intragrain dissolution of lithic fragments; **(D)** Well Fu47, 5125.2 m, P_3w, and intragrain dissolution of lithic fragments; **(E)** Well Fu47, 5137.40 m, P_3w, dissolution of laumontite; and **(F)** Well Fu48, 4540.87 m, P_3w, and dissolution of intergranular calcite.

5.2.1 Influence of rock structure on physical properties

The nature of the parent rock, transport distance, and hydrodynamic conditions determine the composition and structure of the lithic fragments. Sandstones with low matrix content and good sorting have high primary porosity and a slow decay rate of pores and pore throats during diagenesis. In sandstone with high plastic particles and matrix content, the plastic deformation of lithic particles caused by mechanical compaction can destroy the pore space between particles. The sedimentary environment of the P_3w Formation in Fukang Sag is gradually transitioned from the fan-delta plain to the fan-delta front from the east to the west, and the P_3w reservoirs are mainly sand bodies of distributary channels, submerged distributary channels, and mouth bar. The short transport distances experienced by the sediments result in clastic particles with relatively low compositional and textural maturities but high mud-filling

content. Therefore, the properties of the P_3w clastic reservoir in Fukang Sag are influenced by both filling content and lithology (grain size). From the correlation diagram of surface porosity and filling content, it is observed that surface porosity and filling content are negatively correlated. An increase in the filling content reduces the surface porosity and worsens the reservoir properties (Figure 14). The porosity and grain size correlation plots show that the medium sandstone has better physical properties, while the sand conglomerate has relatively poor physical properties (Figure 14). Summarily, the reservoir's physical properties suit medium sandstone with low clay content and fine sandstone.

Generally, the P_3w reservoir in Fukang Sag is characterized by extra-low pore and extra-low permeability, which corresponds to the depositional environment of the fan-delta. The sandstone reservoir has considerable variation in grain size, poor sorting, and high mud content. Consequently, several muddy matrices were filled between the rock grains, and more intergrain porosity was lost under cementation during the rock formation process, resulting in low permeability and throat radius of the reservoir.

5.2.2 Improvement of reservoir physical properties by dissolution

A comprehensive analysis of the pore type, pore structure, and the relationship between rock-forming minerals and pores illustrated that dissolution is the most significant diagenesis for improving the physical properties of the P_3w reservoir. The surface porosity of dissolution pores accounted for over 90% of the total pores. Dissolution increases the porosity of the reservoir by about 5%–8%. According to the rock thin section, cast thin section, and scanning electron microscope observation, the dissolution phenomenon was observed in several sections of the P_3w reservoir in the study area, mainly characterized by the dissolution of feldspar, lithic fragments, and laumontite (Figure 15). The boundary of the feldspar was dissolved into a harbor shape. Some of the intergranular cement of laumontite showed substantial dissolution, and some showed no dissolution. These nondissolution laumontites are the second phase of laumontite cement formed after the dissolution of early laumontite. Additionally, a few calcite cements were dissolved in the study area. However, it is not widespread and is only seen in some sections of individual wells. The physical properties of these deep reservoirs where the dissolution of calcite cement has occurred have improved, with increased porosity and permeability. No dissolution was seen in most of the core samples drilled in the study area, probably because the reservoir had undergone strong cementation of carbonate, clay, siliceous, and laumontite, and no fractures were developed for acidic fluids to enter into the tight reservoir, thus preventing extensive dissolution of soluble components. Consequently, the P_3w reservoir in this area is characterized by extremely low porosity and permeability.

6 Conclusion

(1) The rock type of the clastic P_3w reservoir in Fukang Sag is mainly lithic sandstone and lithic conglomerate. There are two quartz types in the rock component (i.e., single-crystal quartz and polycrystalline quartz). The lithic fragments were derived from tuffaceous volcanic rock and the pore fillings and are composed of clay, carbonate minerals, silica, and laumontite, among others. The reservoir's compositional and textural maturities were poor–medium-sorted, with a roundness of angularity–sub-angularity.

(2) The physical properties of the P_3w reservoir are characterized by extra-low porosity and extra-low permeability. The P_3w reservoir's porosity ranges from 0.81% to 15.5%, while its permeability mainly ranges from 0.02 to 3.15 mD. The pore types are mainly intergrain dissolved pores and intragrain dissolved pores of lithic fragments, feldspar, and quartz to different degrees. The throat channel is of extra-fine throat type, and the characteristics of the capillary pressure curve are non-platform-type, extremely poor pore throat sorting with an average throat radius of approximately 0.1 μm, and pore discharge pressure of over 1.0 Mpa.

(3) Calcite, chlorite, montmorillonite, illite-montmorillonite mixed layer, siliceous, and laumontite cementation cause the tight P_3w reservoir in the Fukang Sag. Several Ca^{2+} released by the hydration of tuffaceous lithic fragments and intermediate–basic volcanic lithic fragments in the reservoir and the hydrothermal fluid from deep CO_2-rich layers trigger the massive development of leucogranite calcite. The formation of several montmorillonites in the fillings is related to the alteration of volcanic tuff fillings during the deposition period in the study area. The hydration of volcanic tuff material triggers laumontite in the P_3w reservoir.

(4) The properties of the P_3w reservoir are influenced by filling content and lithology, and a negative relationship was observed between surface porosity and filling content. Medium sandstone with low mud content and some fine sandstone reservoirs have the best physical properties. Therefore, the reservoir's physical properties improved the study area due to the dissolution and alteration of calcite, feldspar, and various lithic fragments by acidic fluids.

Data availability statement

The raw data supporting the conclusion of this article will be made available by the authors, without undue reservation.

Author contributions

ZQ: Conceptualization, resources, project administration YT: Writing original draft, formal analysis QC: Investigation, data curation CL: Investigation, data curationm, figure preparation HR: Investigation, data curation, figure preparation.

Funding

This research is supported by the Prospective and Fundamental Project of PetroChina (2021DJ0405).

Conflict of interest

The authors declare that the research was conducted in the absence of any commercial or financial relationships that could be construed as a potential conflict of interest.

Publisher's note

All claims expressed in this article are solely those of the authors and do not necessarily represent those of their affiliated organizations, or those of the publisher, the editors and the reviewers. Any product that may be evaluated in this article, or claim that may be made by its manufacturer, is not guaranteed or endorsed by the publisher.

References

Asaad, A., Hubert, F., Dazas, B., Razafitianamaharavo, A., Brunet, J., Glaus, M. A., et al. (2022). A baseline study of mineralogical and morphological properties of different size fractions of illite du Puy. *Appl. Clay Sci.* 224, 106517. doi:10.1016/j.clay.2022.106517

Blanc, P., Gherardi, F., Vieillard, P., Marty, N. C. M., Gailhanou, H., Gaboreau, S., et al. (2021). Thermodynamics for clay minerals: Calculation tools and application to the case of illite/smectite interstratified minerals. *Appl. Geochem.* 130, 104986. doi:10.1016/j.apgeochem.2021.104986

Du, J. H., He, H. Q., Yang, T., Li, J. Z., Huang, F. X., Guo, B. C., et al. (2014). Progress in China's tight oil exploration and challenges. *China Pet. Explor.* 19 (1), 1–9. (in Chinese with English abstract). doi:10.3969/j.issn.1672-7703.2014.01.001

Du, J. H., Yang, T., Li, X., Amp, P., and Company, P. (2016). Oil and gas exploration and discovery of PetroChina Company limited during the 12th FiveYear plan and the prospect during the 13th five-year plan. *China Pet. Explor.* 21 (2), 1–15. (in Chinese with English abstract). doi:10.3969/j.issn.1672-7703.2016.02.001

Du, J. H., Zhi, D. M., Tang, Y., Jia, C. M., Xu, Y., Abulimity, Y. M., et al. (2019). Prospects in upper permian and strategic discovery in shawan sag, Junggar Basin. *China Pet. Explor.* 24 (1), 24–35. (in Chinese with English abstract).

Fiedrich, A. M., Heinrich, C. A., and Bachmann, O. (2020). Evolution from magmatic to hydrothermal activity beneath the Cerro Escorial volcano (NW Argentina) as sampled by erupted quartz and brines. *Lithos* 374–375, 105706. doi:10.1016/j.lithos.2020.105706

French, M. W., and Worden, R. H. (2013). Orientation of microcrystalline quartz in the Fontainebleau Formation, Paris Basin and why it preserves porosity. *Sediment. Geol.* 284–285, 149–158. doi:10.1016/j.sedgeo.2012.12.004

Gong, D. Y., Li, J. Z., Ablimit, I., He, W. J., Lu, S., Liu, D. G., et al. (2018). Geochemical characteristics of natural gases related to Late Paleozoic coal measures in China. *Mar. Petroleum Geol.* 96, 474–500. doi:10.1016/j.marpetgeo.2018.06.017

Gong, D. Y., Song, Y., Wei, Y. Z., Liu, C. W., Wu, Y. W., Zhang, L. J., et al. (2019). Geochemical characteristics of Carboniferous coaly source rocks and natural gases in the Southeastern Junggar Basin, NW China: Implications for new hydrocarbon explorations. *Int. J. Coal Geol.* 202, 171–189. doi:10.1016/j.coal.2018.12.006

Gong, D. Y., Wang, Y., Yuan, M., Liu, C. W., Mi, J. L., Lu, S., et al. (2017). Genetic types and origins of natural gases from eastern Fukang Sub-depression of the Junggar Basin, NW China: Implication for low-mature coal-derived gases. *J. Nat. Gas Geoscience* 2, 179–189. doi:10.1016/j.jnggs.2017.07.002

Guo, J. M., Fan, H. L., Zhang, S. Y., Liu, X., Wu, T., Ma, W. Y., et al. (2020). Petrological, He-Ne-Ar and Sr-Nd-Pb geochemical of volcanic rocks constraint on tectonic settings and geodynamic process of the Carboniferous, East Junggar. *J. Nat. Gas Geoscience* 5 (2), 91–104. doi:10.1016/j.jnggs.2020.02.002

He, H. Q., and Li, J. Z. (2014). PetroChina's oil and gas exploration results, new geological theories and technological achievements since 11th Five-Year Plan period. *China Pet. Explor.* 19 (6), 1–13. (in Chinese with English abstract). doi:10.3969/j.issn.1672-7703.2014.06.001

He, H. Q., Zhi, D. M., Tang, Y., Liu, C. W., Chen, H., Guo, X. G., et al. (2021). A great discovery of well kangtan 1 in the Fukang sag in the Junggar Basin and its significance. *China Pet. Explor.* 26 (2), 1–11. (in Chinese with English abstract). doi:10.3969/j.issn.1672-7703.2021.02.001

Hou, M. G., Zha, M., Ding, X. J., Yin, H., Bian, B. L., Liu, H. L., et al. (2021). Source and accumulation process of jurassic biodegraded oil in the eastern Junggar Basin, NW China. *Petroleum Sci.* 18, 1033–1046. doi:10.1016/j.petsci.2021.07.010

Hu, S. Y., Wang, X. J., Cao, Z. L., Li, J. Z., Gong, D. Y., and Xu, Y. (2020). Formation conditions and exploration direction of large and medium gas reservoirs in the Junggar Basin, NW China. *Petroleum Explor. Dev.* 47 (2), 266–279. doi:10.1016/s1876-3804(20)60045-3

Hueck, M., Wemmer, K., Ksienzyk, A. K., Kuehn, R., and Vogel, N. (2022). Potential, premises, and pitfalls of interpreting illite argon dates - a case study from the German Variscides. *Earth-Science Rev.* 232, 104133. doi:10.1016/j.earscirev.2022.104133

Jia, C. Z., Pang, X. Q., and Jiang, F. J. (2016). Research status and development directions of hydrocarbon resources in China. *Petroleum Sci. Bull.* 1 (1), 2–23. doi:10.3969/j.issn.2096-1693.2016.01.001

Jia, C. Z., Zhao, W. Z., Zou, C. N., Feng, Z. Q., Yuan, X. J., Chi, Y. L., et al. (2007). Formation and distribution of volcanic hydrocarbon reservoirs in sedimentary basins of China. *Petroleum Explor. Dev.* 34 (3), 257–271. doi:10.1016/s1876-3804(08)60071-3

Li, C., Chen, G. J., Li, X. T., Zhou, Q. S., and Sun, Z. T. (2022). The occurrence of tight oil in the Chang 8 lacustrine sandstone of the Huaqing area, Ordos Basin, China: Insights into the content of adsorbed oil and its controlling factors. *J. Nat. Gas Geoscience* 7, 27–37. doi:10.1016/j.jnggs.2021.11.001

Lian, X. C., Wang, Z. Q., Ye, C., Liu, Z. Q., and Li, S. T. (2011). Pore structure and influencing factors of reservoir of Sangonghe Formation in Baijiahai area. Junggar Basin. *Lithol. Reserv.* 23, 35–39.

Liu, X. Y., Wei, L. B., Liu, B. X., Zhang, L., Guo, W., Zhang, J. W., et al. (2021). Characteristics of natural gas accumulation in the Cambrian weathered crust in southwestern Ordos Basin. *Nat. Gas. Ind. B* 8 (5), 421–430. doi:10.1016/j.ngib.2021.08.001

Oye, O. J., Aplin, A. C., Jones, S. J., Gluyas, J. G., Bowen, L., Orland, I. J., et al. (2018). Vertical effective stress as a control on quartz cementation in sandstones. *Mar. Petroleum Geol.* 98, 640–652. doi:10.1016/j.marpetgeo.2018.09.017

Power, M., and Burns, S. (2013). "The comparison of WEMSCAN and XRD analysis in the mineralogical characterization of unconventional reservoirs: the benefits of an integrated approach," in *Geoconvention. CSPG CSEG CWLS* (Calgary, AB, Canada.

Roberts, R. J., Rowe, R. C., and York, P. (1991). The relationship between Young's modulus of elasticity of organic solids and their molecular structure. *Powder Technol.* 65 (1), 139–146. doi:10.1016/0032-5910(91)80176-j

Song, J. Y., Chen, T., and Zhang, J. L. (2022). Permian and triassic hydrocarbon migration and accumulation in the cainan area, Junggar Basin, China. *J. Petroleum Sci. Eng.* 210, 109965. doi:10.1016/j.petrol.2021.109965

Sun, P. A., Wang, Y. C., Leng, K., Hui, W. Y., and Cao, J. (2016). Geochemistry and origin of natural gas in the eastern Junggar Basin, NW China. *Mar. Petroleum Geol.* 75, 240–251. doi:10.1016/j.marpetgeo.2016.04.018

Tang, W. B., Zhang, Y. Y., Pe-piper, G., Piper, D. J. W., Guo, Z., and Li, W. (2021). Permian rifting processes in the NW Junggar Basin, China: Implications for the post-accretionary successor basins. *Gondwana Res.* 98, 107–124. doi:10.1016/j.gr.2021.06.005

Tang, Y., Guo, W. J., Wang, X. T., Bao, H. J., and Wu, H. S. (2019). A new breakthrough in exploration of large conglomerate oil province in Mahu Sag and its implications. *Xinjiang Pet. Geol.* 40 (2), 127–137. (in Chinese with English abstract). doi:10.7657/XJPG20190201

Wang, X. L., Zhi, D. M., Wang, Y. T., Chen, J. P., Qin, Z. J., Liu, D. G., et al. (2013). *Geochemistry of source rock and petroleum in the Junggar Basin*. Beijing: Petroleum Industry Press. (in Chinese).

Wu, C. J., Zhang, M. F., Xiong, D. M., Tuo, J. C., Ma, W. Y., and Qian, Y. (2020). Gas generation from Jurassic coal measures at low mature stage and potential gas accumulation in the eastern Junggar Basin, China. *J. Nat. Gas Sci. Eng.* 84, 103692. doi:10.1016/j.jngse.2020.103692

Wu, X. Z., Zhou, L., Yang, D. S., Qi, X. F., and Li, B. H. (2012). Structure evolution and hydrocarbon accumulation the Beisantai uplift in Junggar Basin. *Chin. J. Geol. Sci. Geol. Sinica)* 47 (3), 653–668. (in Chinese with English abstract).

Wu, Z. J., Han, X. Z., Ji, H., Cai, Y. F., Xue, L., and Sun, S. J. (2021). Mesozoic-Cenozoic tectonic events of eastern Junggar Basin, NW China and their significance for uranium mineralization: Insights from seismic profiling and AFT dating analysis. *Ore Geol. Rev.* 139, 104488. doi:10.1016/j.oregeorev.2021.104488

Xu, Q. S., Wang, J., Cao, Y. C., Wang, X. T., Xiao, J., and Kashif, M. (2019). Characteristics and evolution of the late Permian "source-to-sink" system of the Beisantai area in the eastern Junggar Basin, NW China. *J. Asian Earth Sci.* 181, 103907. doi:10.1016/j.jseaes.2019.103907

Yang, Z., and Zou, C. N. (2019). Exploring petroleum inside source kitchen: Connotation and prospects of source rock oil and gas. *Petroleum Explor. Dev.* 46 (1), 181–193. doi:10.1016/s1876-3804(19)30018-7

Yu, Z. C., Wang, Z. Z., Wang, J., and Li, Z. Y. (2022). Subtle reservoirs and implications for hydrocarbon exploration in terrestrial lacustrine fan-delta deposits: Insights from the triassic baikouquan formation, Mahu sag, Junggar Basin, Western China. *Mar. Petroleum Geol.* 142, 105730. doi:10.1016/j.marpetgeo.2022.105730

Zhang, L. L. (2011). *Sedimentary facies of wutonggou formation in Beisantai area in Junggar Basin*. Qingdao: China University of Petroleum. (East China) (in Chinese with English abstract).

Zhang, M. J., Gong, Z., Tan, Z. H., Liu, H., and Yang, M. X. (2021). Study on heat adsorption based on the experiment of coal adsorption of methane by using the weight method. *J. Nat. Gas Geoscience* 6 (4), 245–253. doi:10.1016/j.jnggs.2021.08.002

Zhang, S. C., Zhang, S. Y., Fang, L. H., Lu, X. C., Guo, H., and Shi, J. A. (2020). Petrological and geochemical constraints on tectonic settings of the late carboniferous-early permian, central junggar, China. *J. Nat. Gas Geoscience* 5 (1), 1–10. doi:10.1016/j.jnggs.2019.12.002

Zhang, Z. D., Gu, Y. L., Jin, J., Li, E. T., Yu, S., and Pan, C. C. (2022). Assessing source and maturity of oils in the Mahu sag, Junggar Basin: Molecular concentrations, compositions and carbon isotopes. *Mar. Petroleum Geol.* 141, 105724. doi:10.1016/j.marpetgeo.2022.105724

Zhao, R., Zhang, J. Y., Zhou, C. M., Zhang, Z. J., Chen, S., Stocklic, D. F., et al. (2020). Tectonic evolution of Tianshan-Bogda-Kelameili mountains, clastic wedge basin infill and chronostratigraphic divisions in the source-to-sink systems of Permian-Jurassic, southern Junggar Basin. *Mar. Petroleum Geol.* 114, 104200. doi:10.1016/j.marpetgeo.2019.104200

Zhao, S. J., Li, S. Z., Liu, X., Suo, Y. H., Dai, L. M., Lou, D., et al. (2014). Intracontinental orogenic transition: Insights from structures of the eastern Junggar Basin between the altay and tianshan orogens. *J. Asian Earth Sci.* 88, 137–148. doi:10.1016/j.jseaes.2014.03.008

Zhi, D. M., Song, Y., Zheng, M. L., Qin, Z. J., and Gong, D. Y. (2012). Genetic types, origins, and accumulation process of natural gas from the southwestern Junggar Basin: New implications for natural gas exploration potential. *Mar. Petroleum Geol.* 123, 104727. doi:10.1016/j.marpetgeo.2020.104727

Zhou, X. X. (2005). Time-space structure of reservoiring elements and hydrocarbon enrichment-concurrently discussing near-source reservoiring. *Oil Gas Geol.* (6), 711–716. (in Chinese with English abstract).

Zou, C. N., Xu, C. C., Song, J. R., Li, G. H., Tao, S. Z., Zhu, R. K., et al. (2009). formation and distribution of "continuous" gas reservoirs nd their giant gas province: A case from the upper riassic xujiahe formation giant gas province, sichuan basin. *Petroleum Explor. Dev.* 36 (3), 307–319. doi:10.1016/s1876-3804(09)60128-2

frontiers | Frontiers in Earth Science

TYPE Original Research
PUBLISHED 17 January 2023
DOI 10.3389/feart.2022.1002581

OPEN ACCESS

EDITED BY
Deyu Gong,
Research Institute of Petroleum Exploration and Development (RIPED), China

REVIEWED BY
Zhiye Gao,
China University of Petroleum, China
GuoSheng Xu,
Chengdu University of Technology, China

*CORRESPONDENCE
Yongan Xue,
x200504020104@126.com

SPECIALTY SECTION
This article was submitted to Economic Geology, a section of the journal Frontiers in Earth Science

RECEIVED 25 July 2022
ACCEPTED 12 September 2022
PUBLISHED 17 January 2023

CITATION
Xue Y, Yang H, Xu P and Xiao S (2023), Formation conditions of natural gas fields in the lacustrine basin in eastern China: Insights into the first discovery within the Bohai Bay Basin.
Front. Earth Sci. 10:1002581.
doi: 10.3389/feart.2022.1002581

Formation conditions of natural gas fields in the lacustrine basin in eastern China: Insights into the first discovery within the Bohai Bay Basin

Yongan Xue*, Haifeng Yang, Peng Xu and Shuguang Xiao

CNOOC Co., Ltd., Tianjin, China

The hydrocarbon source of Bohai Bay Basin is dominated by oil-prone kerogens of type II_2-II_1 within semi-deep and deep lacustrine facies. In the Neogene period, faults were well-developed via significant structural activity. The Bohai Sea is generally considered to have no geological basis for the formation of large natural gas fields. Through analogous analysis of domestic and international gas fields, the key geological factors that restrict formation in continental rift lacustrine basins were studied, including gas source, preservation conditions, and reservoirs. A natural gas enrichment and accumulation model within a petroliferous basin is presented. The model indicates that rapid subsidence and high-intensity gas generation within petroliferous sags during the late stages were main contributors to natural gas field formation. Archean metamorphic buried hill reservoirs and thick, overpressure mudstone with strong vertical sealing ability provided favorable storage space and preservation, respectively. Using the model, an integrated Archaean metamorphic buried hill condensate gas reservoir, Bozhong 19–6, was discovered in the Bohai Bay Basin. The natural gas reserves are about 450×10^9 m^3, equivalent to oil production of 800 $\times10^6$ m^3, and signify a breakthrough in natural gas exploration of continental rift lacustrine basins in China.

KEYWORDS

continental rift lacustrine basin, large natural gas field, high intensity generation of natural gas, metamorphic rock buried hill, Bozhong 19–6

Introduction

The Bohai Bay Basin includes the Bohai Sea and coastal areas in eastern China. The Cenozoic continental lacustrine basin was developed on the North China Craton, which is one of the two super-basins in China. Through more than 60 years of exploration and development, a series of oil fields have been discovered using "Continental Oil Generation Theory" (Shi, 1981). Seven major oil regions, namely Shengli, Liaohe, Dagang, North China, Jidong, Zhongyuan, and Bohai have been built

in the Bohai Bay Basin. These oil fields account for more than one-third of China's reserves and production (Hu and Zhou, 2006; Wang and Xi, 2009). So far, no large natural gas field has been discovered within this basin. Only the Banqiao and Qianmiqiao gas fields have reserves exceeding 200×10^8 m^3. In addition, the distribution of natural gas is limited and found only in a few depressions (Wang, 1997; Wang, 2005).

Xue (2002) and Xue et al. (2007) proposed the theory of "gas formation in lacustrine basins" and believed that natural gas enrichment areas exist in the Bohai Bay Basin. Based on the gas potential of more than 60 sags and sub-sags in the Bohai Bay Basin, combined with the dynamics of natural gas accumulation, gas field potential was hypothesized. The geological factors, such as structure and deposition, suggested that the Bohai Bay Basin can form natural gas fields under conditions that include the presence of a regional overpressure mudstone "quilt", strong sealing, and high-intensity gas generation in the late stage of source rock maturation (Xue, 2018; Xue and Li, 2018; Xu et al., 2019; Xue, 2019). By integrating enrichment geological theory with natural gas reservoir technologies and practices, the condensate gas field Bozhong 19–6 was discovered in the southwest of Bozhong sag. The field has gas reserves of about 450×10^9 m^3, which equals the oil production of 800×10^6 m^3, representing a breakthrough in natural gas exploration within continental lacustrine basins in eastern China.

Geological setting of the Bohai Bay Basin

The Bohai Bay Basin is bordered by the Jiaodong uplift and the Liaodong uplift to the east, the Taihang Mountain uplift to the west, the Luxi uplift to the south, and the Yanshan fold belt to the north (Figure 1) (Li, 1980; Qi et al., 1995). The Cenozoic basin developed as a result of Indosinian and Yanshanian movements in the China-Korea paraplatform after Paleozoic deposition (Jiang, 1999). Since the Cenozoic period, multiple episodes of rifting have occurred in the Bohai Bay Basin, and the filling structure shows the characteristics of two sets of structural units, the rifting unit in the Paleogene and the depression unit in the Neogene (Hou et al., 2001; Li et al., 2010). The Cenozoic strata, revealed by drilling wells from bottom to top, consist of the Kongdian and Shahejie Formations in the Paleogene and the Guantao and Minghuazhen Formations in the Neogene (Figure 1). The Paleogene basin shows obvious "basin-ridge" structure during the rifting stage, and primarily developed half-graben and graben internal depressions with pervasive vulcanism (Wang, 1998). In the Neogene, the basin mainly experienced post-rifting thermal subsidence (Gong, 2004; Wang et al., 2012). From the perspective of the whole basin, the strata distribution in sags were stable during the depositional periods of the Kongdian and Shahejie Formations. Nevertheless, the basin showed characteristics of differential subsidence in various sags. From the deposition period of the Dongying Formation, the subsidence

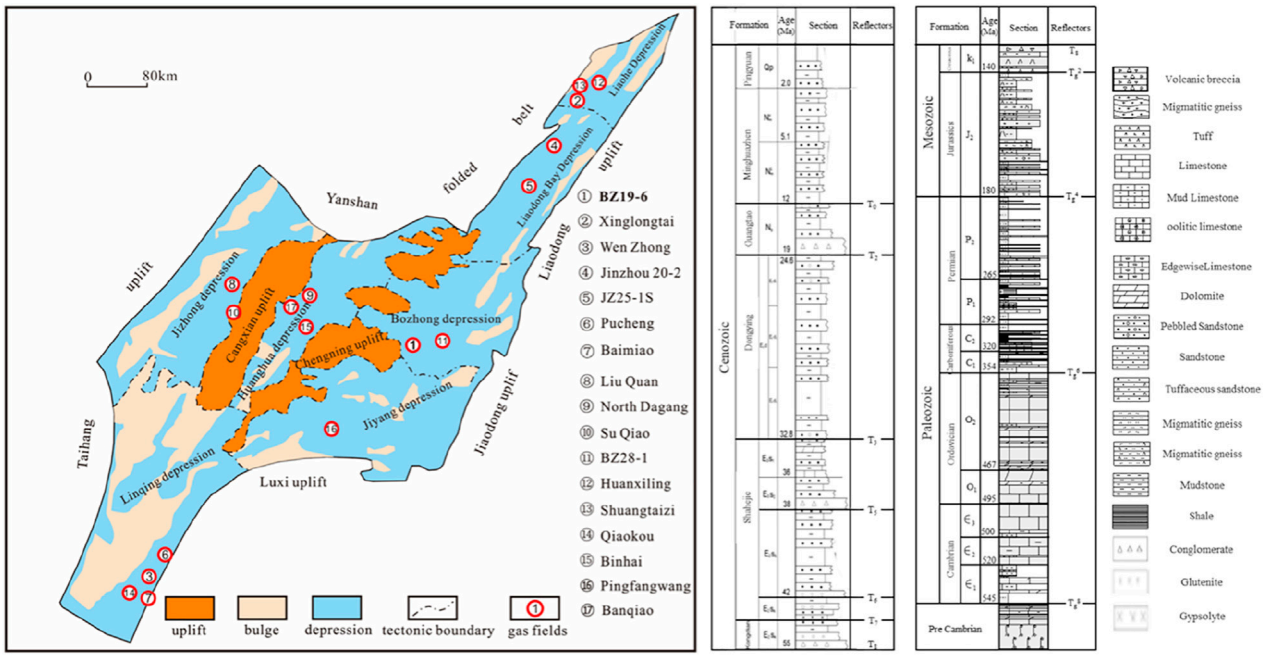

FIGURE 1
Schematic diagram of structural units in the Bohai Bay Basin and comprehensive stratigraphic column.

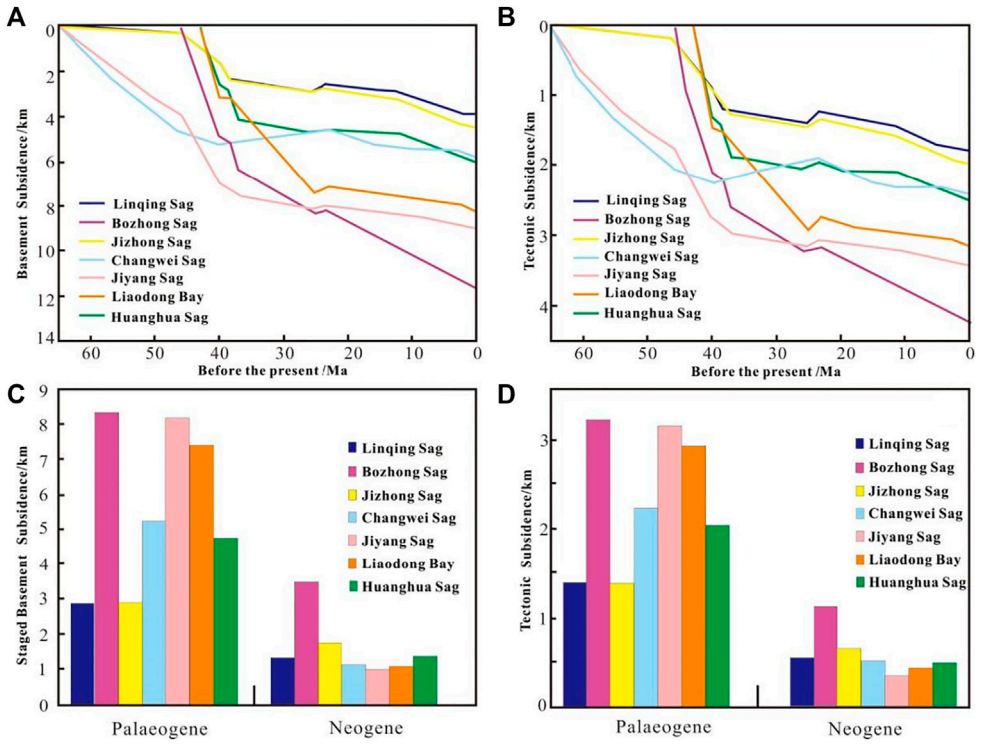

FIGURE 2
Basement/tectonic subsidence history and subsidence comparison of each depression in the Bohai Bay Basin. **(A)** Basement subsidence of various sags in the Bohai Bay Basin; **(B)** tectonic subsidence of various sags in the Bohai Bay Basin; **(C)** staged basement subsidence of various sags in the Bohai Bay Basin; **(D)** tectonic subsidence of various sags in the Bohai Bay Basin.

center of the basin gradually moved toward the sea. The Bozhong Depression became the depocenter of this basin in the Quaternary. During the Paleogene, several sets of hydrocarbon source rock were developed, including the Kongdian, Shahejie, and Dongying Formations. The Shahejie and Dongying Formations were major hydrocarbon-supplying strata, which commonly comprise organic matter of Type I, Type II_1, and Type II_2 kerogen, with total organic carbon (TOC) ranging from 2% to 4%.

Most of the depressions in the Bohai Bay Basin are located on land, except the Bozhong, Liaodong Bay, Huanghua, and Jiyang Depressions, which are fully or partially located in the sea. The Bozhong Depression exhibits the largest Cenozoic subsidence, reaching 11,000–12,000 m. However, the Jizhong, Linqing, Changwei, and Huanghua Depressions show the smallest subsidence, ranging from 4,000 to 6,000 m. In between are the Liaodong Bay and Jiyang Depressions, with about 9,000–10,000 m of subsidence (Figure 2A). The structural subsidence of each depression has similar characteristics to the base subsidence (Figures 2A,B). During the Paleogene rifting period, the Bozhong, Jiyang, and Liaodongwan Depressions had the largest total and structural subsidence, followed by the Changwei and Huanghua Depressions. The total and structural subsidence of the Linqing and Jizhong Depressions were the smallest (Figure 2C). In the Neogene post-rifting stage, the total and tectonic subsidence of the Bozhong Depression were the largest, while other depressions were smaller (Figure 2D). In general, the subsidence center of this basin migrated along the Tan-Lu fault zone during the Paleogene rifting period, showing a tendency to migrate from south to north and from west to east (Figure 2C). From the Guantao to the lower member of the Minghuazhen Formation, the subsidence centers were in the Bozhong and Huanghua Depressions in the middle of the Bohai Bay Basin, migrating from the land toward the sea. The subsidence center from the deposition period of the upper member of the Minghuazhen Formation to present has been completely immobilized within the sea, especially in the Bozhong sag near the Tan-Lu fault zone (Figure 2D). There have been many hydrocarbon discoveries within the Paleogene lacustrine deltaic sand bodies and Neogene fluvial sand bodies in the Bohai Bay Basin. In the onshore oilfields, the Paleogene Shahejie and Dongying Formations are the main oil-bearing formations, accounting for more than 60% of the discovered oil and gas reserves, followed by the Neogene strata, accounting for about 30%. In

the offshore oilfields, the hydrocarbon reserves are predominately in the Neogene strata, accounting for about 60% (Jiang et al., 2021).

The pre-Cenozoic basement revealed by drilled wells in the Bohai Bay Basin is composed of five structural layers from bottom to top: the Precambrian metamorphic rocks; the Lower Paleozoic Cambrian-Middle Ordovician (Є-O) neritic platform carbonate interbedded with shale and clastic deposits; the Upper Paleozoic Carboniferous-Permian (C-P) carbonate, coal-bearing, and red clastic deposits developed in marine-terrestrial interaction areas; the Mesozoic Middle Jurassic (J_2) grey tuffaceous clastic, coal beds, and volcanic breccia deposits; and the Mesozoic Lower Cretaceous (K_1) volcanic rocks and variegated clastic deposits. Nevertheless, the Middle and Upper Proterozoic, the Upper Ordovician-Lower Carboniferous in the Paleozoic, and the Triassic, Lower Jurassic, Upper Jurassic, and Upper Cretaceous in the Mesozoic were generally absent in this area (Hou et al., 2001; Li et al., 2010). The discovery of buried hill oil and gas reservoirs in the Renqiu Oilfield in 1975 set off a flurry of buried hill exploration (Zhao and Zhang, 1991; Jiang and Cha, 2010). However, since 1995, the discovery of buried hill oil and gas in the Bohai Bay Basin has gradually decreased. In recent years, the pre-Cenozoic buried hill exploration has led to discovery of oil and gas (Kang, 2000; Dai et al., 2002; Jia et al., 2002). In 2005, hydrocarbon reservoirs of the Archean metamorphic rocks in the buried hill below the sedimentary rocks were discovered at a depth of 2500 m in the Xinglongtai area of the western Liaohe sag (Xue, 2010). In 2010, the ultra-deep carbonate buried hill at a depth of more than 6000 m in the Baxian sag was found to harbor hydrocarbon reservoirs. In 2012, the Mesozoic granite buried hill hydrocarbon reservoir, with reserves of 100×10^6 tons, was discovered in the central Bohai Sea. The above discoveries were primarily oil, like the Cenozoic hydrocarbon discoveries. No large natural gas fields were discovered. Thus far, the buried hill reservoirs have been the source of minor discoveries in this basin, with uneven distribution. The Jizhong Depression is the site of the most abundant hydrocarbon source yet discovered, with proven oil of about 540×10^6 tons in place and accounting for about 60% of the oil in the Bohai Bay Basin. The next largest source is the Xialiaohe Depression, with proven oil of about 400×10^6 tons in place and accounting for about 20% of oil in the basin. There were fewer hydrocarbon discoveries in buried hills in the Bohai Sea, accounting for only about 5% of the oil in the region.

Conditions for the formation of natural gas fields

The distribution of natural gas fields throughout the world is characterized by marine sedimentary basins with humic source kerogen (Jiang et al., 2017; Lan et al., 2017). These natural gas fields are mainly located in structurally stable areas with regional gypsum formations (Gong and Wang, 2001). The discoveries in lacustrine sedimentary basins are dominated by crude oil, with minor amounts of natural gas (Dang et al., 2001). The Bohai Bay Basin is a rifted lacustrine formation developed in the Cenozoic period and characterized by initial sedimentation, subsequent well-developed faults, lack of regional gypsum strata, and lacustrine sapropelic kerogen as source rock. Based on these geological conditions, the differences between the Bohai Bay Basin and other domestic or foreign gas-prone basins were compared. The formation conditions of gas reservoirs in more than 60 sags/sub-sags within the Bohai Bay Basin were also studied. Requirement of "one core and two key elements" for the formation of natural gas fields in the continental lacustrine basin of the Bohai Bay is proposed and the core element is interpreted as strong sealing by the overpressure mudstone cap rock. The two key elements are high-intensity gas generation of source rocks in the late stage and the storage space of buried hills.

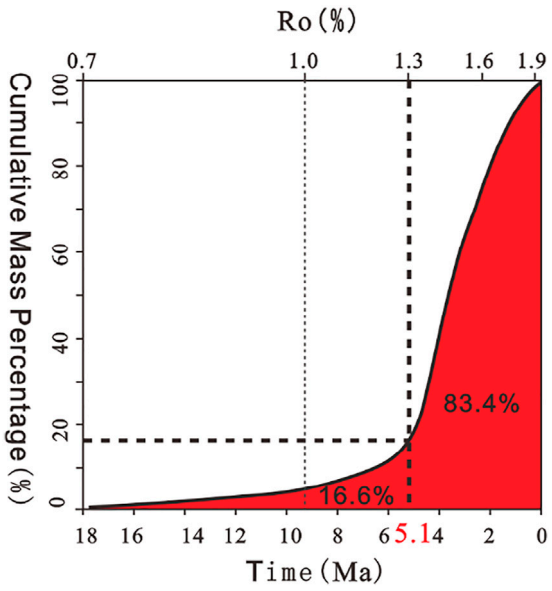

FIGURE 3
Subsidence rate, maturation rate, and gas generation pattern of source rocks in the Bozhong sag.

Production of natural gas from source rocks

Natural gas molecules are small and diffuse easily (Hao, 1994). The formation of natural gas reservoirs demands a continuous and sufficient supply of gas sources (Dai et al., 1997; Dai et al., 2003), requiring source rocks with gas generation intensity exceeding 20×10^8 m^3/km^2. The later the peak, the greater the intensity of gas generation, and the more favorable for the formation of gas fields.

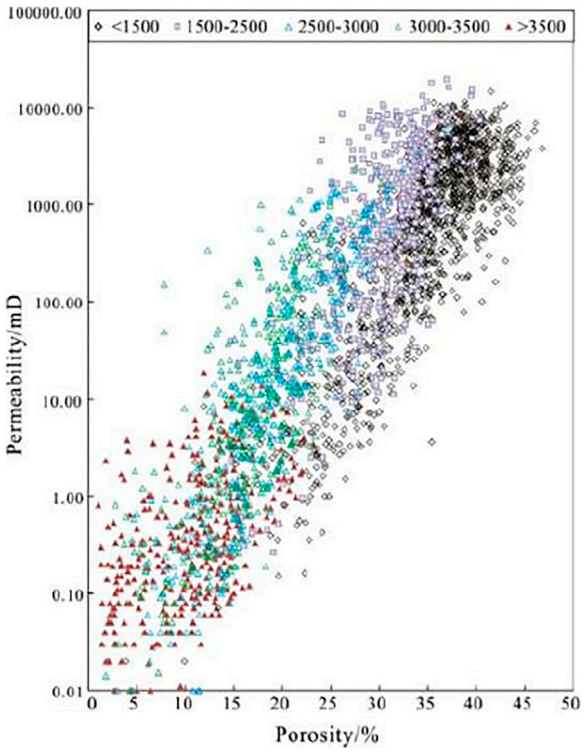

FIGURE 4
Physical characteristics of clastic rock reservoirs at different depths in the Bohai Sea.

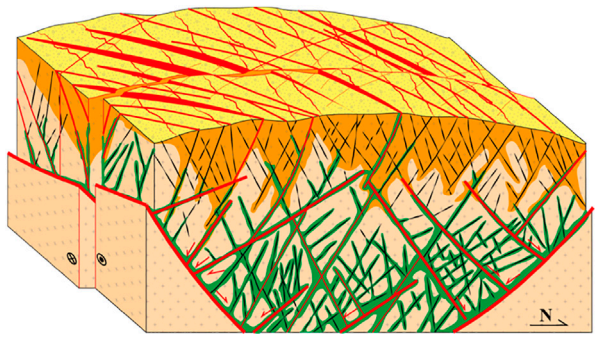

FIGURE 5
Genetic model of large metamorphic buried hill reservoir in the Bozhong sag.

The main hydrocarbon source rock in the Bohai Sea is type II_2-II_1 kerogen in the Shahejie Formation (Zhu, 2009). Over time, multi-stage structural movements and thermal evolution through numerous sags lowers the generation of gas. However, in the Late Neogene, subsidence rates of the Bozhong, Qinnan, and Qikou sags increased significantly, generally exceeding 200 m/Ma (Gong and Wang, 2001). Especially in the Bozhong sag, the subsidence rate was up to 320 m/Ma from 5.1 Ma to present (Xue and Li, 2018). The rapid subsidence of the sags increased the burial depth of the source rock and accelerated thermal evolution. The change rate of the main source rocks in the Shahejie Formation in the Bozhong, Qikou, and Qinnan sags exceeded 0.25% per million years. Among these formations, the change rate of source rock maturity in the Bozhong sag reached 0.41% per million years. The results of a new source rock evaluation in the Bohai Sea showed that the gas generation intensity of the Bozhong, Liaozhong, Qikou, and Huanghekou sags were greater than 20×10^8 m^3 in the Late Neogene (Gong et al., 2000). Among them, the natural gas resources in the Bozhong sag were the largest, with gas generation intensity up to $(50–200)\times10^8$ m^3/km^2 (Cai et al., 2001). The natural gas resource in this sag has changed from 0.3×10^{12} m^3 to 1.9×10^{12} m^3 from 5.1 Ma to present, which is a more than 5 times increase in this natural gas resource (Figure 3). These data indicate that the continental lacustrine basin in the Bohai Sea had favorable conditions for late-stage, large-scale gas generation.

Storage volume of buried hill reservoirs

A number of clastic rock reservoirs were developed in the Bohai Sea during the Cenozoic, consisting mainly of conglomerate, sandy conglomerate, gravelly coarse sandstone, and tuffaceous glutenite, with a small amount of coarse sandstone and fine sandstone. Mudstone was less developed in the glutenite, which was primarily distributed from 1,500 to 3,500 m in depth. The sand bodies below the mudstone of the Dongying Formation were generally more than 3,500 m deep. Based on the sedimentary characteristics of continental lacustrine basins, fan delta facies were dominant reservoirs, commonly with area of less than 50 km^2. The statistics of the physical properties of nearly 383 core and wall core samples of the glutenite reservoirs drop sharply when the reservoir depth exceeds 3,500 m. Reservoir porosity was generally less than 10%, and the permeability was less than 1 mD, indicating ultra-low porosity and permeability (Figure 4). Therefore, the clastic sedimentary rocks cannot provide enough storage space for large natural gas reservoirs.

Buried hills tended to develop reservoirs of more than 1,000 km^2 with various lithologies, including metamorphic rocks, granites, igneous rocks, carbonate, and clastic rocks. The Archean buried hills mostly comprised felsic-rich brittle minerals, such as plagioclase gneiss, mixed granite, mixed gneiss, and granulite. The Bohai Bay Basin has experienced multi-stage tectonic movements since the Indosinian period, resulting in many multi-stage structural fractures. The fractures developed at distinct stages were superimposed to form complex and intersecting fractures. Early fractures often experienced multi-stage uplifting and denudation, atmospheric

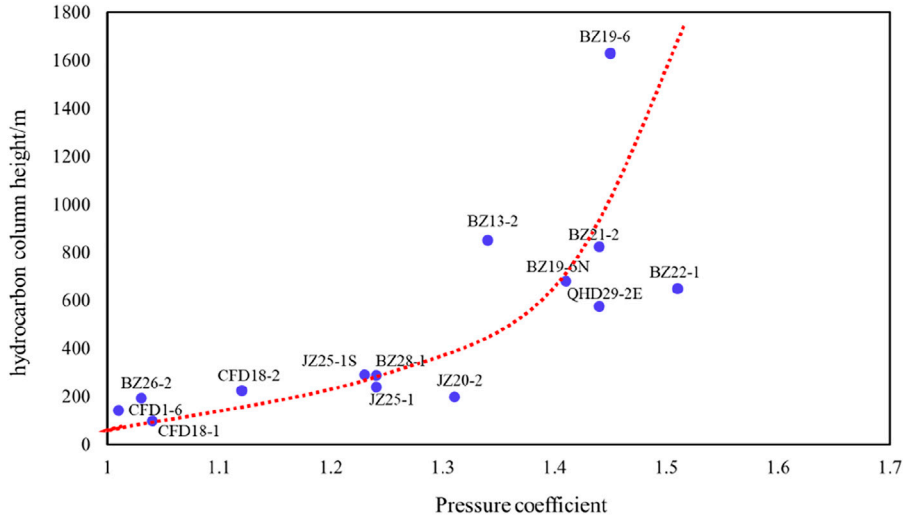

FIGURE 6
Relationship between hydrocarbon column height and cap rock pressure coefficient of the large and medium-sized oil and gas reservoirs in the Bohai Sea.

freshwater leaching, and dissolution of mantle-derived CO_2, hydrocarbon, and magmatic hydrothermal fluids (Xue and Wang, 2020). The storage space was modified by dissolution expansion pores along the fractures. The physical properties of the inner reservoir 1,000 m below the weathering crust were improved, forming three sets of structural fracture zones from bottom to top: the lower dissolution fracture zone, the middle fracture zone, and the upper weathering crust fracture zone (Figure 5). Many fractures developed in the weathering crust, and the inner part of the buried hill strengthened the storage capacity of the buried hill for natural gas. The discovery of the Bozhong 19–6 gas field has confirmed the development of large-scale reservoirs in buried hills. The thickness of drilled buried hill reservoirs exceeds 1,600 m, with average net-to-gross ratio of 42%, which is much higher than that of glutenite.

Preservation conditions of large gas fields

Later-stage preservation conditions were important for gas field formation (Bradley and Powley, 1994; Otroleva, 1994). Large natural gas fields are mainly formed under thick gypsum caps or in structurally stable areas (Lv et al., 2002; Liu et al., 2005). As a Cenozoic continental basin, Bohai Bay has undergone multiple intense tectonic activities. The Tan-Lu fault developed through the basin, and is made up of large, deep faults.

Exploration suggested that the pressure coefficient of the overlying cap of the gas reservoirs in the Bohai oilfield was significantly correlated with the height of the hydrocarbon column. The height of the hydrocarbon columns shows positive correlation with the pressure coefficients (Figure 6). The Paleogene Dongying Formation was developed in the Bohai Bay Basin during the periods of transition from rifting to depression. The depositional environment was deep lake in the early stage and semi-deep lake in the late stage, forming thick mudstone with an average thickness of more than 500 m. Due to late rapid subsidence, the mudstone generally shows under-compaction. Meanwhile, the hydrocarbon source rock in the Dongying Formation was accompanied by strong late hydrocarbon generation in the subsidence process and abnormal overpressure. The average displacement pressure was up to 10.24 MPa, and the pressure coefficient of mudstone cap was up to 1.2–2.0, which provided superior conditions for preservation of natural gas.

Although the Bohai Bay Basin experienced multi-stage tectonic movements in the Cenozoic, two sets of independent fault systems were formed in the Bozhong sag and other regions. Both the upper and lower fault systems disappeared in the thick mudstone of the Dongying Formation, which enabled the formation of regional overpressure mudstone caprocks in the Paleogene. However, there were differences in the fault systems of different sags, resulting in huge variations in the preservation conditions of different sags. Faults were well-developed in the Qikou and Huanghekou sags in the late stage, with most cutting through the Paleogene mudstone and destroying the regional mudstone cap rock conditions. The natural gas was often lost along the faults as the Cenozoic subsidence center of the Bohai Bay Basin, the Bozhong sag, developed the major source rocks in the Shahejie Formation, consisting of partially sapropelic kerogen dominated by oil generation, with less natural gas than crude oil generated in the early stage. Since 5.1 Ma, the large-area rapid subsidence in the sag

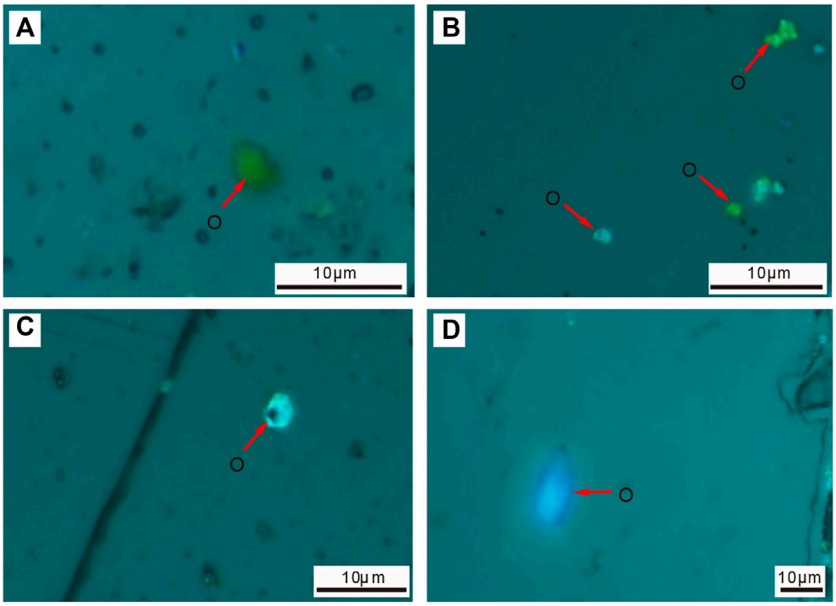

FIGURE 7
Microscopic characteristics of different fluorescent crude oil inclusions and gas inclusions. **(A)** BZ19-6-8, 4498.5 m, yellow-brown fluorescence of crude oil inclusions; **(B)** BZ19-6-1, 4428.5 m, yellow-green fluorescence of crude oil inclusions; **(C)** BZ19-6-10, 4435.16 m, light blue fluorescence of crude oil inclusions; **(D)** BZ19-6-7, 4600.2 m, bright blue fluorescence of crude oil inclusions.

area resulted in under-compaction, and the overpressure of the mudstone in the lower Dongying Formation was rapidly established and increased, providing the overpressure dynamic sealing conditions for the preservation of buried hill natural gas (Xue and Wang, 2020). At that time, the overpressure mudstone of the Dongying Formation began to form, which ensured that the natural gas generated was strongly downward charged and forced into reservoirs in the short term under control by the overpressure mudstone (similar to the action of gypsum rock in a gas-type basin), effectively reducing the loss of natural gas. Although faults were developed in the late stage, they did not penetrate the thick mudstone of the Dongying and Shahejie Formations. The sealing capacity of the regional overpressure mudstone adjacent to the natural gas was not compromised, which provided the necessary conditions for the formation of large gas fields.

Accumulation and depletion-enrichment model of natural gas in the Bohai Bay Basin

Accumulation model of natural gas reservoirs in buried hills of the Bohai Bay Basin

The main cause of the development of large gas fields in buried hills in the Bohai Bay basin was the thick overpressure mudstone overlying the Dongying Formation, with a thickness of more than 300 m and pressure coefficient of more than 1.4. The natural gas that was generated along with the crude oil migrated laterally under the set of overpressure capping layers and accumulated in the buried hill, forming a natural gas reservoir (Ma and Cheng, 2000). The condensate gas reservoir of Bozhong 19–6 in the Bozhong sag of the Bohai Sea followed the typical enrichment model, with overpressure mudstone undergoing the continuous gas-invasion accumulation process after the oil accumulated in the trap. The gas originated from kerogen cracking in the mudstone of the Paleogene Shahejie Formation in the Bozhong sag. Yellow-green and blue-white fluorescent oil inclusions were observed under the microscope (Figures 7A–D), and the homogenization temperatures of the associated saline inclusions were 90–160°C (Figure 8A). According to the burial history, the recovered crude oil charging period is generally 12.0–5.1 Ma (Figure 8B), reflecting the long-term continuous charging of crude oil with low maturity (yellow-green fluorescence) (Figures 7A,B) and high maturity (blue-white fluorescence) (Figures 7C,D). Many gas inclusions were also observed, with the homogenization temperature ranging from 140°C to 180°C. The natural gas filling occurred predominately from 5.1 Ma to the present (Figure 8B).

Oily asphalt, with vitrinite reflectance ranging from 1.3% to 1.6%, was found on the top of the buried hill, suggesting the cause of gas invasion. These observations indicate that the Bozhong

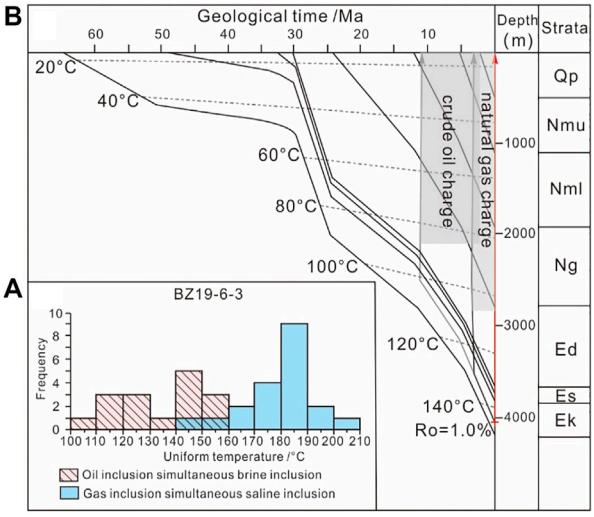

FIGURE 8
Homogeneous Temperature Histogram **(A)** and Thermal History of Oil and Gas **(B)** Inclusion in Well BZ19-6-3.

19–6 condensate gas reservoir experienced gas accumulation after oil accumulation. In the Middle Miocene to Early Pleistocene (12.0–5.1 Ma), the source rocks in the Shahejie Formation generated oil extensively, thereby generating overpressure. The pressure coefficient was routinely over 1.6, which was the main cause of hydrocarbon migration. The large amount of discharged crude oil filled the Archaeozoic buried hills and sand-conglomerate reservoirs in the Kongdian Formation, forming oil fields. Due to the neotectonics (5.1 Ma), some of the deep-buried crude oil migrated along the faults to the shallow Neogene reservoirs and formed the medium-sized BZ19-4 oilfield. The early filled oil was deeply buried with cracking (i.e., regular cracking to light oil). Based on the evolution of the Dongying Formation, the overpressure increased after the period of neotectonics, providing dynamic sealing conditions for the hydrocarbon in deeply buried hills. Since the Pleistocene (5.1 Ma), natural gas has been produced from highly to overmature source rocks. Fault activities brought more CO_2, which has caused gas invasion in the previously deep oil reservoirs. In addition, light oil was easily soluble in natural gas and converted into condensate gas. Under the cover of the "quilt-like" overpressure mudstone cap, the invasion process has continued to the present. The oil reservoirs gradually transformed into large-scale condensate gas reservoirs. According to data from simulation of temperature and pressure conditions, the fluid phase state of the Bozhong 19–6 condensate gas field has changed gradually, from 12 Ma to the present, from pure liquid to the critical state and the pure condensate gas phase. Based on the above discussion, the Bozhong 19–6 condensate gas field experienced a natural gas reservoir forming mode characterized by oil before gas, shallow formation and deep burial, and local adjustment and transformation. The preservation of the Paleogene "quilt-like" overpressure mudstone was the controlling factor in the enrichment and preservation of the deep atmospheric field in buried hills of the Bohai Bay Basin.

The gas field was well-developed and sheltered from dissipation by the mudstone cap. However, in different parts of the depression, limited by the overpressure mudstone in the Dongying Formation, the cap was poorly developed in the sand-rich area or the overpressure was destroyed by fractures or faults, leading to the development of oil or heavy oil fields, or even small-scale gas fields (Luo, 2003; Ma et al., 2019). Generally, the natural gas accumulated within the low buried hills; the small gas and the oil and gas fields within the buried hills are of medium depth, whereas the large-scale oilfields are structurally high (Figure 9). These features caused the circular distribution of the natural gas, middle-light oil, and heavy oil fields surrounding the source rocks.

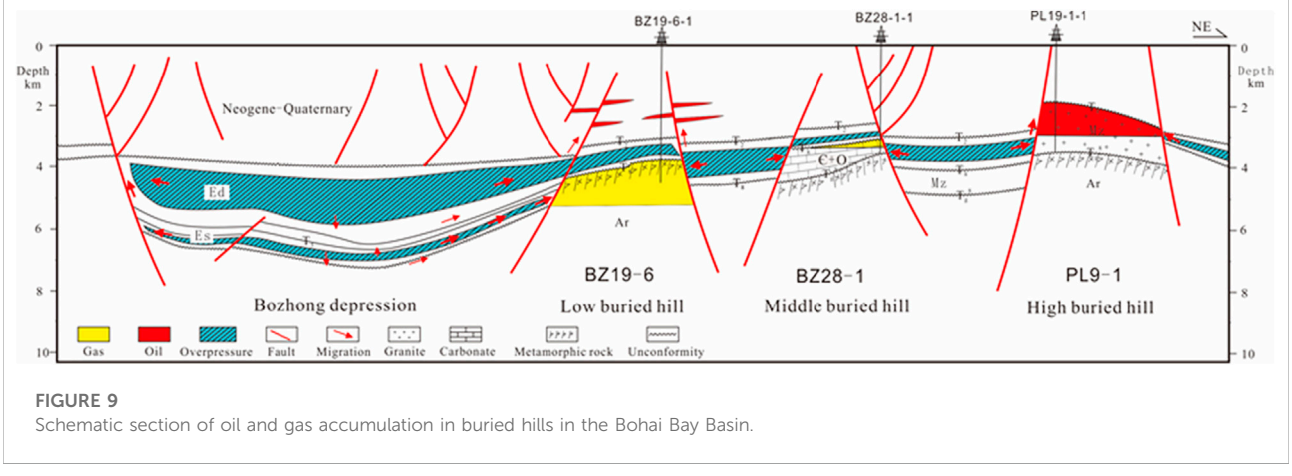

FIGURE 9
Schematic section of oil and gas accumulation in buried hills in the Bohai Bay Basin.

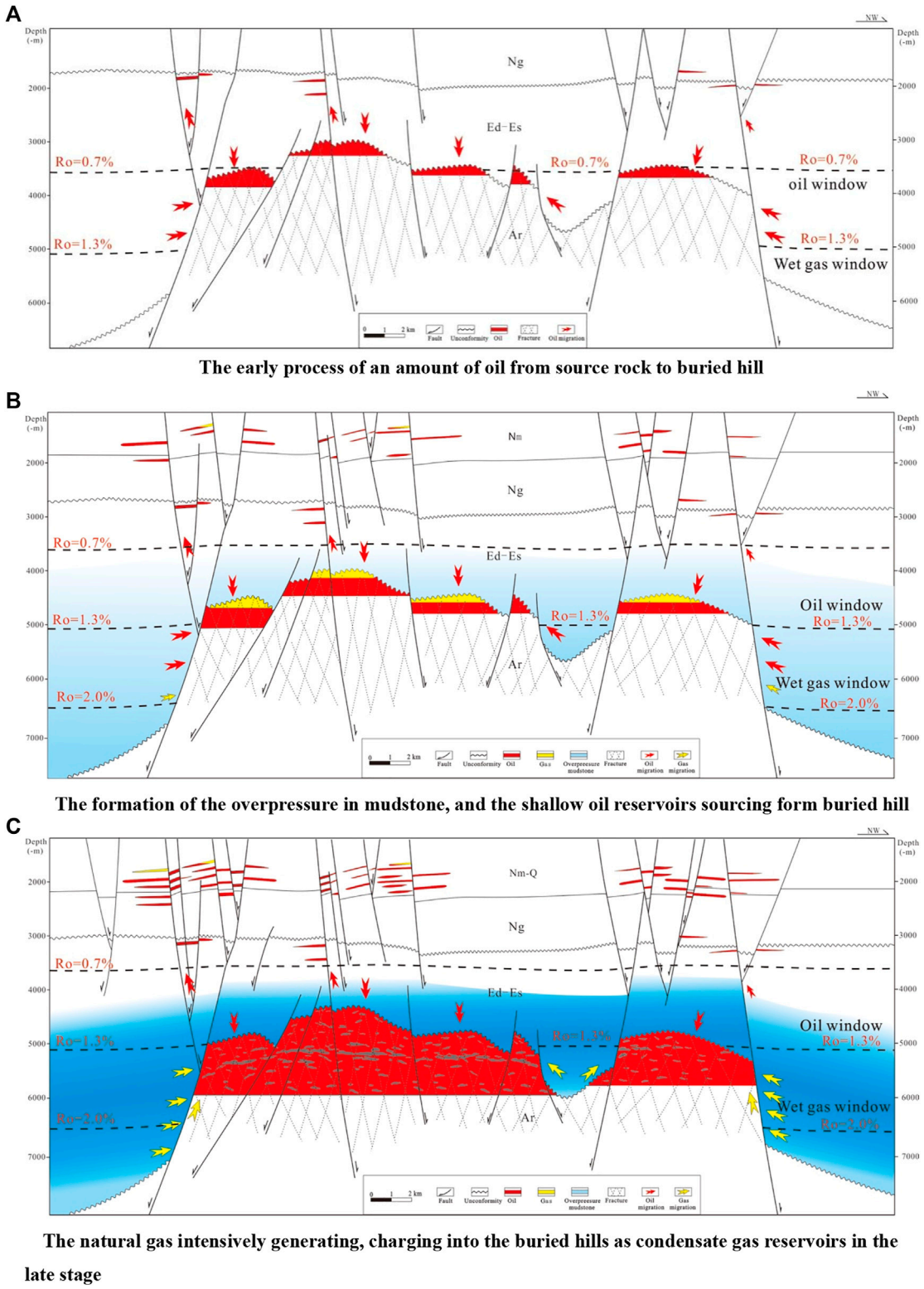

FIGURE 10
Enrichment and accumulation models of the Bozhong 19–6 large-scale natural gas field. **(A)** The early process of transition of an amount of oil from source rock to buried hill. **(B)** The formation of overpressure in mudstone and the shallow oil reservoirs sourced from buried hills. **(C)** Intensively generated natural gas charging into buried hills to form condensate gas reservoirs in the late stage.

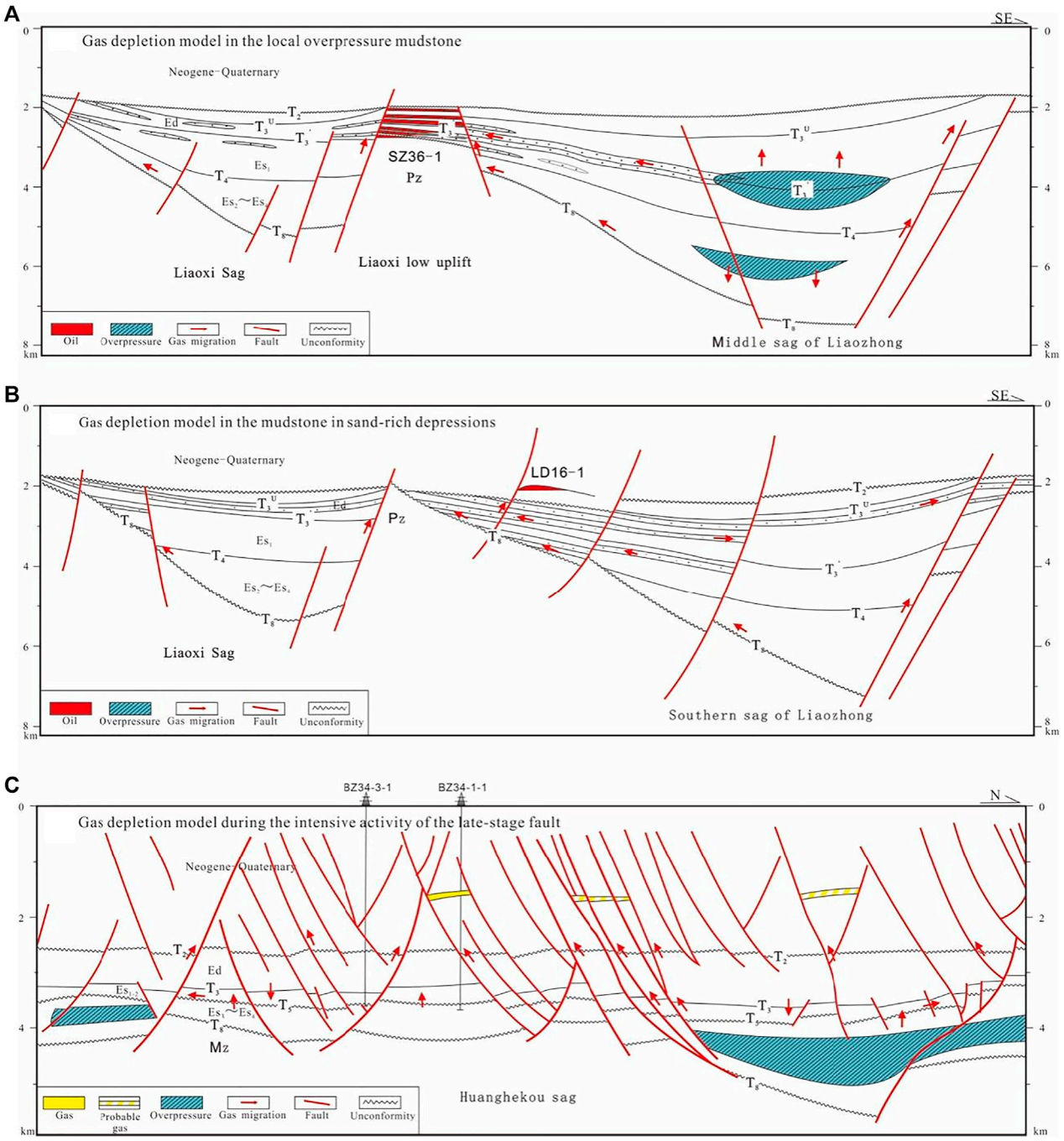

FIGURE 11
Large-scale natural gas depletion model in the Bohai Bay Basin.**(A)** Gas depletion model inthe local overpressure mudstone; **(B)** Gas depletion model inthe mudstone in sand-rich depressions; **(C)** Gas depletion model during the intensive activity of the late-stage fault.

Natural gas depletion-enrichment models

There are more than 60 sags distributed in the Bohai Bay Basin. According to the formation conditions mentioned above, combined with exploration practice, depletion-enrichment models for natural gas can be divided into four models.

Gas enrichment under regional overpressure mudstone

In gas-producing depressions and surrounding areas with humus-type or high-mature saprolite-type kerogen, the huge and "quilt-like" overpressure mudstone cap was deposited in the Dongying Formation (Shahejie Formation) above the source

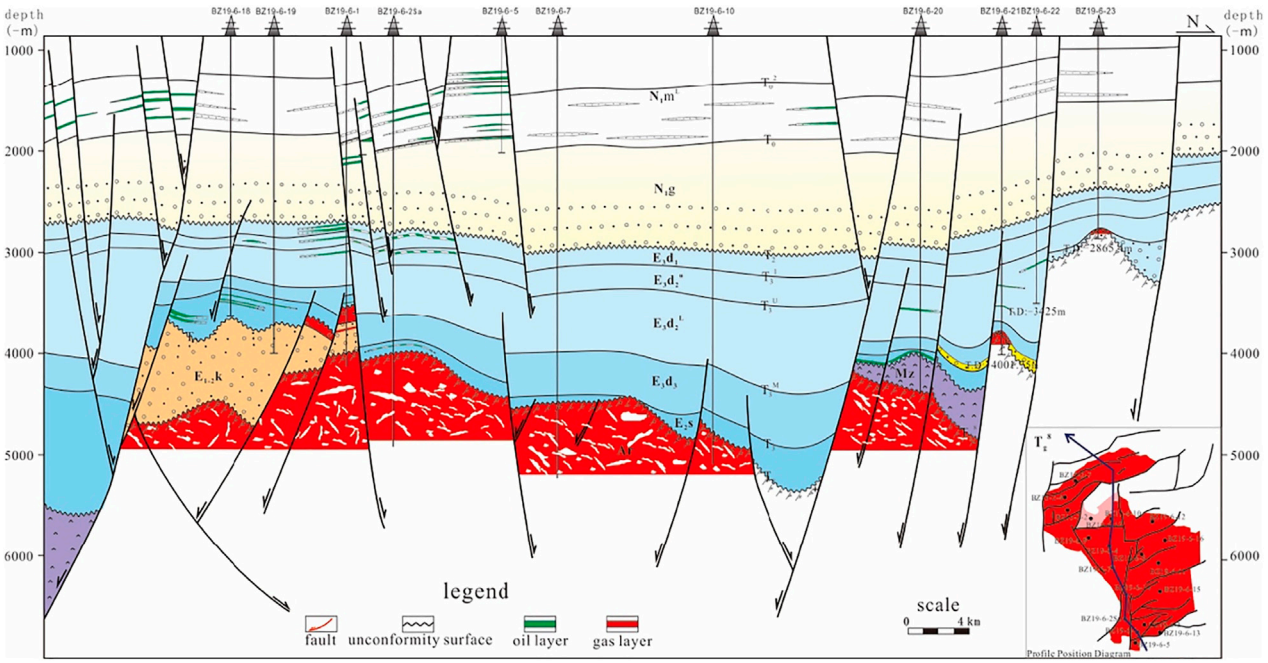

FIGURE 12
Oil and gas accumulation model of the Bozhong 19–6 condensate gas field.

rock. The cap was not damaged by the late-stage faults and contributed to the progressive development of the overpressure (Hao et al., 2004). Prevented from dissipating by the mudstone cap, the natural gas from the Paleogene migrated laterally and was trapped in the Dongying Formation. Particularly within the low buried hill of the sag, the gas field formed when the overpressure mudstone expelled the natural gas to form a strongly filled reservoir (Figure 10). This field is at the northern area of Liaodong Bay and the Bozhong sag.

Gas depletion in local overpressure mudstone

Although mudstone was widely deposited in the Dongying Formation of the Bohai Bay Basin, the sandstone-mudstone interlayers developed by river systems were dominant on the slopes of the sag. The fluids were discharged in a timely manner during sedimentation and compaction due to the conduction of sandstone on slopes. The mud-rich formation that generated the overpressure only formed in the central sag. As a result, the sealed cap was absent and the natural gas dissipated vertically through the cap. This type of mudstone in the Dongying Formation did not provide a seal for natural gas but did seal in crude oil, thereby forming the large and medium-sized oil fields in the central part of Liaodong Bay (Figure 11A).

Gas depletion in sand-rich sags

During the sedimentary period of the Dongying Formation, the depression entered the deposition stage. Due to the sufficient supply of external sources, sandstone and glutenite were widely deposited in the depression. The distribution range and thickness of mudstone decreased and its sealing capacity was significantly weakened. Most of the natural gas was lost and it was difficult to form a large-scale gas reservoir (Lv et al., 2005). Exploration and discovery are often dominated by reservoirs, as demonstrated in the southern area of Liaodong Bay (Figure 11B).

Gas depletion via intensive activity of the late-stage fault

Thick mudstone in the Dongying Formation (Shahejie Formation) was developed, yet late-stage faults penetrated the mudstone cap in the center and surrounding areas of the gas-producing sag. Under this condition, the natural gas dissipated instead of migrating along the pathways and being preserved by the cap. Some of the dissipated gas accumulated in the shallow-buried Neogene reservoirs. Due to gas dissipation, a large natural gas field was not formed, as observed in the Yellow River Mouth Sag (Figure 11C).

Exploration cases

Exploration cases

Exploration guided by an understanding of natural gas formation conditions allowed Bozhong 19–6 to be discovered

as the first large gas field in the old oil region in eastern China. The open-hole test of the Archaean buried hill obtained high yield, with a daily gas production of 11.35×10^4 m^3~33.18×10^4 m^3 and a daily oil production of 111.06 m^3~338.76 m^3. The third-order natural gas reserves are about 450×10^9 m^3, and the oil equivalent reaches 800×10^6 m^3.

The Bozhong 19–6 gas field is in the southwest of the Bozhong sag, on a near-SN-trending structural ridge between the Bozhong Southwest Sub-sag and the Bozhong Main Sub-sag. The field was an anticline structural area cut by near-SW-NE-trending and near-EW-trending faults. This area has experienced multiple episodes of rifting and superimposed composite structural evolution of neotectonic movements, resulting in the superimposed structural characteristics of faulting and depressing. The Bozhong 19–6 structure was surrounded by the Bozhong, Shanan, and Huanghekou sags. The basement, with burial depth of 4,000–5,500 m, comprises mainly Archaean metamorphic rocks with regional distribution characteristics and is the metamorphic buried hill reservoir with the largest burial depth in the Bohai Bay Basin (Figure 12). The discovery of the Bozhong 19–6 large condensate gas field confirmed that the Archean metamorphic rocks had great exploration potential. Different from other metamorphic rock reservoirs, the Archean metamorphic rock reservoir in the Bozhong 19–6 structure showed the characteristics of large burial depth and high diagenetic strength. The development of high-quality reservoirs is closely related to the development of internal fractures in buried hills. The regional Tan-Lu fault activity and the coupling of high-quality lithology in buried hills have formed large-scale high-quality natural gas reservoirs. The deep-buried Archean metamorphic rocks in the Bozhong sag have a huge distribution area. The high-quality hydrocarbon source rocks in the center of the sag provided a sufficient resource base for the formation of natural gas. Coupled with multi-stage tectonic movements, the natural gas accumulation conditions were favorable, and the deep-buried hills in the Bozhong sag had great potential for natural gas exploration.

The Bozhong sag and the northern part of the Liaozhong sag are favorable for natural gas exploration

The Bozhong sag has the largest Cenozoic sedimentary thickness in the Bozhong Depression. Mudstone in the Shahejie and Dongying Formations were widely distributed, with thickness of more than 200 m. Since 5.1 Ma, the rapid subsidence of a large area in the Bozhong sag has led to under-compaction and rapid formation of mudstone overpressure (Ge and Zhu, 2001). Today, the pressure coefficient generally exceeds 1.6, which can seal most of the natural gas in deep layers and provide good sealing conditions for natural gas preservation. Three sets of high-quality source rock series were developed in the third member of the Shahejie Formation, the first and second members of Shahejie Formation, and the third member of the Dongying Formation in the Bozhong sag. The type of organic matter was mainly type II_1-II_2 kerogen. The hydrocarbon source rock of the third member of the Shahejie Formation had the largest burial depth and the highest thermal evolution degree of organic matter, with R_o exceeding 2.0%, indicating the dry gas stage. The thermal evolution degree of organic matter in the first and second members of the Shahejie Formation was up to 2.0%. The maturity of hydrocarbon source rocks in the third member of the Dongying Formation ranged from 0.7% to 0.9% in most areas. Only near the center of the Bozhong sag did the maturity reach 1.0%. Therefore, the large-scale development of high-quality, matured source rocks in the Shahejie Formation in the hydrocarbon generation center provided the foundation for the mass production of natural gas. The lithology of buried hills in the Bozhong sag consists mainly of igneous, carbonate, and metamorphic rocks. These three lithologies were affected by multi-stage tectonic movements including the Indosinian, Yanshan, and Himalayan movements, leading to fractures that developed into three-dimensional reticulation reservoirs that provided large-scale storage space for natural gas. Overall, the thick overpressure mudstone "quilts" in the Bozhong sag, the area that generated the largest gas volume, were distributed continuously in the region. The scale of natural gas resources was predicted to reach trillions of cubic meters in the low-buried hills of the central Bohai Sea. Therefore, in addition to the large-scale condensate gas field of Bozhong 19–6, other areas in the Bozhong sag are favorable targets in the exploration of natural gas fields.

The Liaozhong sag is in the Liaodongwan Depression in the northern part of the Bohai Sea. The Jinzhou 20–2 gas field was discovered in the northern part of the Liaozhong sag and is currently the largest natural gas producing area in the Bohai Sea. The degrees of development of Paleogene mudstone in the southern and northern Liaozhong sag were different. The Paleogene in the southern area mainly comprises interbedded sand and mudstone, and the degree of overpressure is low, making it difficult to preserve a large volume of natural gas effectively. The northern Paleogene is dominated by thick mudstone, with a pressure coefficient up to 1.8, providing sealing conditions for large-scale natural gas preservation. The Shahejie Formation in the Liaozhong sag developed high-quality hydrocarbon source rocks with type II_1-II_2 kerogen at a high degree of thermal evolution, providing a good source rock foundation for the generation of a large amount of natural gas. The buried hill reservoirs in the sag, slope, and adjacent uplift areas had good conditions to support the formation of large-scale reservoirs, which also formed the conditions for large-scale natural gas preservation. Together, the thick overpressure mudstone "quilts" developed by the Paleogene in the northern part of the Liaozhong sag and the Shahejie Formation source rock

with a relatively large burial depth that can generate a large amount of gas for the reservoirs in buried hills indicate a favorable area for natural gas field exploration.

Conclusions

1) The Bohai Bay Basin is a typical Cenozoic continental rift basin that has the following characteristics that commonly support the formation of gas reservoirs: 1) rapid maturation and high-intensity gas generation in the late stage; 2) a buried hill reservoir that is less affected by burial depth but rather by multi-stage structural uplift, deep fluids, atmospheric fresh water, weathering crust, and inner fractures; and 3) an overpressure mudstone "quilt" in the developed area that replaces the gypsum layer to promote sealing.
2) Enrichment and depletion models for natural gas accumulation in the Bohai Bay Basin were established and divided into the following types: regional overpressure mudstone enrichment, local overpressure mudstone depletion, sand-rich sedimentary depression depletion, and late fault strong development depletion.
3) The areas with high-quality reservoirs and the thick Paleogene overpressure mudstone "quilts" were closed to hydrocarbon generation in both center and buried hills, such as in the surrounding zone of the Bozhong sag and the northern part of the Liaozhong sag.

Data availability statement

The original contributions presented in the study are included in the article/Supplementary material; further inquiries can be directed to the corresponding author.

Author contributions

In this study, YX contributed to the key geological conditions for the formation of large natural gas fields in the continental lacustrine basin of the Bohai Bay; HY contributed to natural gas accumulation law and depletion and enrichment modeling in continental lacustrine basins of Bohai Bay; PX contributed to exploration cases and favorable exploration directions; and SX contributed to discussion of how buried hill large-scale reservoirs provide large storage space.

Acknowledgments

The authors would like to express their gratitude to EditSprings (https://www.editsprings.cn) for the expert's linguistic services provided.

Conflict of interest

YX, HY, PX, and SX were employed by the company CNOOC Co., Ltd.

Publisher's note

All claims expressed in this article are solely those of the authors and do not necessarily represent those of their affiliated organizations, or those of the publisher, the editors and the reviewers. Any product that may be evaluated in this article, or claim that may be made by its manufacturer, is not guaranteed or endorsed by the publisher.

References

Bradley, J. S., and Powley, D. E. (1994). Pressure compartment in sedimeatary basin a review, basin compartment and seal. *AAPG Mem.* 61, 3–25.

Cai, D. S., Luo, Y. H., Wu, W. L., and Yao, C. (2001). Shallow tectonic deformation and its relationship to hydrocarbon enrichment in Bozhong depression and anjacent area, Bohai Bay Basin. *China Offshore Oil Gas* 15 (1), 35–43.

Dai, J. X., Cheng, J. F., and Zhong, N. N. (2003). *Atmospheric fields and their gas sources in China*. Beijin: Science Press.

Dai, J. X., Wang, T. B., Song, Y., Zhang, H., Xu, Y. C., and Zhang, Q. M. (1997). *Formation conditions and distribution rules of large gas fields in China*. Beijing: geological publishing house.

Dai, J. X., Xia, X. Y., and Hong, F. (2002). Natural gas geology accelerated the growth of natural gas reserve in largr scale in China. *Xinjiang Pet. Geol.* 23 (5), 357–365. doi:10.3969/j.issn.1001-3873.2002.05.002

Dang, Z. R., Liu, Y. D., Wang, X., Zhang, R. F., and Liu, H. P. (2001). Discussion on the source rock in Suqiao buried hill hydrocarbon reservoirs. *Acta Pet. Sin.* 22 (6), 18–23. doi:10.7623/syxb200106004

Ge, J. D., and Zhu, W. L. (2001). An analysis of offshore gas exploration potential in terms of comparison between offshore and onshore areas in Bohai Bay Basin. *China Offshore Oil Gas* 15 (2), 93–98.

Gong, Z. S. (2004). Neotectonics and petroleum accumulation in offshoreChinese basins. *Earth Sci.* 29 (5), 513–517. doi:10.3321/j.issn:1000-2383.2004.05.002

Gong, Z. S., Wang, G. C., and He, Q. (2000). The upper tertiary is the main field of oil and gas exploration in bozhong depression and its surrounding areas. *China Offshore Oil Gas* 14 (3), 148–149.

Gong, Z. S., and Wang, G. C. (2001). Neotectonism and late hydrocarbon accumulation in bohai sea. *Acta Pet. Sin.* 22 (2), 1. doi:10.3321/j.issn:0253-2697.2001.02.001

Hao, F., Cai, D. S., Zhou, H. Y., Fang, Y., and Zeng, Z. P. (2004). Overpressure-tectonic activity controlled fluid flow and rapid petroleum accumulation in bozhong depression, bohai Bay basin. *Earth Sci.* 29 (5), 518–524. doi:10.3321/j.issn:1000-2383.2004.05.003

Hao, S. S. (1994). *Natural gas transport dynamic equilibrium and its application*. Beijing: Petroleum Industry Press.

Hou, G. T., Qian, X. L., and Cai, D. S. (2001). The tectonic evolutionof bohai basin in mesozoic and cenozoic time. *ActaScicentiarum Nat. Univ. Pekinesis* 37 (6), 845–851. doi:10.3321/j.issn:0479-8023.2001.06.016

Hu, A. P., and Zhou, Q. H. (2006). The largest gas field in the world--north-south Pars gas field. *Nat. Gas. Geosci.* 17 (6), 753–759. doi:10.3969/j.issn.1672-1926.2006.06.003

Jia, C. Z., Zhao, W. Z., and Wei, G. Q. (2002). The recent progress and developing tendency in natural gas exploration and its studies seen at abroad. *Nat. Gas. Ind.* 22 (4), 5–9. doi:10.3321/j.issn:1000-0976.2002.04.002

Jiang, Y. L. (1999). Geological characteristics and formation conditions of the natural gas accumulation belts in Bohai Bay Basin. *J. Univ. Petroleum, China (Edition Nat. Sci.* 23 (5), 9–13.

Jiang, Y. L., and Cha, M. (2010). *Petroleum and natural gas geology and exploration*. Beijing: Petroleum Industry Press.

Jiang, Y. L., Hu, H. J., and Tan, Y. M. (2017). Genesis and distribution of Paleogene oil type gases in the northern Dongpu depression. *J. China Univ. Pet. (Ed. Nat. Sci.)* 41 (3), 42–48.

Jiang, Y. L., Su, S. M., Liu, H., and Zhao, H. H. (2021). Differences in oil and gas accumulation periods and their main controlling factors in Bohai Bay Basin. *Petroleum Nat. gas Geol.* 42 (6), 1255–1264. doi:10.11743/ogg20210602

Kang, Z. L. (2000). *Introduction to large and medium-sized gas fields in China*. Beijing: Petroleum Industry Press.

Lan, L., Sun, Y. M., and Wang, K. (2017). Genetic types and sources of natural gas in deep water areas in South Gabon Sub-basin. *China Pet. Explor.* 22 (2), 63–67. doi:10.3969/j.issn.1672-7703.2017.02.008

Li, D. S. (1980). The Geology and structural characteristics of BohaiBay, China. *Acta Pet. Sin.* 1 (1), 6–20.

Li, S. Z., Suo, Y. H., Dai, L. M., Liu, L. P., Jin, C., Liu, X., et al. (2010). Development of the bohai Bay basin and destruction of the north China Craton. *Earth Sci. Front.* 17 (4), 64–89. doi:10.16562/j.cnki.0256-1492.2017.04.006

Liu, G. D., Li, J., Li, J. M., Zhu, X. M., Wang, Z. L., Wang, Y. X., et al. (2005). The controls and the assessment method for the effectiveness of natural gas migration and accumulation process. *Nat. Gas. Geosci.* 16 (1), 1–6. doi:10.3969/j.issn.1672-1926.2005.01.001

Luo, X. R. (2003). Review of hydrocarbon migration and accumulation dynamics. *Nat. Gas. Geosci.* 14 (5), 337–346. doi:10.3969/j.issn.1672-1926.2003.05.002

Lv, S. F., Fu, G., and Wang, P. Y. (2002). *Quantitative study on main controlling factors of natural gas enrichment*. Beijing: Petroleum Industry Press.

Lv, Y. F., Fu, G., and Yu, D. (2005). Comprehensive evaluation of sealing ability of cap rock in China's large and medium gas fieldsand their contribution to gas accumulation. *Oil Gas Geol.* 26 (6), 742–753. doi:10.3321/j.issn:0253-9985.2005.06.007

Ma, Q. F., and Cheng, S. S. (2000). *Overpressure basins and hydrocarbon distribution*. Beijing: Geological Publishing House.

Ma, X. H., Yang, Y., Wen, L., and Luo, B. (2019). Distribution and exploration direction of medium-and large-sized marine carbonate gas fields in Sichuan Basin, SW China. *Petroleum Explor. Dev.* 46 (1), 1–15. doi:10.1016/s1876-3804(19)30001-1

Otroleva, P. J. (1994). Basin compartmenttasion: Difinition and mechanisms, basin compartments and seals. *AAPG, Mem.* 61, 39–52.

Qi, J. F., Zhang, Y. W., Lu, K. Z., Yang, Q., and Chen, F. J. (1995). Cenozoic tectonicevolution in bohai Bay basin province. *J. Univ. Petroleum, China (Edition Nat. Sci.* 19 (S1), 1–6.

Shi, B. H. (1981). Origin and development of continental oil theory (II). *Petroleum Explor. Dev.* 8 (4), 40–46.

Wang, D. Y., Yu, H. Z., Yu, H. B., and Chui, Y. Y. (2012). An analysis and refined depiction of lithologic trap development under the framework of Neogene sequence stratigraphy in bohai water: A case of lower member of Minghuazhen Formation in shijiutuo rise. *China Offshore Oil Gas* 24, 23–27. doi:10.3969/j.issn.1673-1506.2012.z1.006

Wang, G. C. (1998). Tanlu fault and reverse structure and flower structure in bohai sea. *China Offshore Oil Gas* 12 (5), 289–295.

Wang, G. Z., and Xi, Q. L. (2009). Natural gas distribution, main controls over accumulation and exploration targets in Bohai sea. *China Offshore Oil Gas* 21 (1), 15–18. doi:10.3969/j.issn.1673-1506.2009.01.003

Wang, T. (1997). *Theoretical basis and practice of natural gas geology in China*. Beijing: Petroleum Industry Press.

Wang, T. B. (2005). Distribution of large-middle sized gas fields in China: Geological characteristics and key controlling factors. *Petroleum Explor. Dev.* 32 (4), 1–8. doi:10.3321/j.issn:1000-0747.2005.04.001

Xu, C. G., Yu, H. B., Wang, J., and Liu, X. (2019). Formation conditions and accumulation characteristics of Bozhong 19-6 large condensate gas field in offshore Bohai Bay Basin. *Petroleum Explor. Dev.* 46 (1), 27–40. doi:10.1016/s1876-3804(19)30003-5

Xue, Y. A., and Li, H. Y. (2018). Large condensate gas field in deep archean metamorphic buried hill in Bohai Sea: Discovery and geological significance. *China Offshore Oil Gas* 30 (3), 1–9. doi:10.11935/j.issn.1673-1506.2018.03.001

Xue, Y. A., Liu, T. H., Wang, Y. B., Zhang, G. L., and Wei, Z. H. (2007). Main controlling factors and mode of natural gas accumulation in Bohai Bay area. *Petroleum Explor. Dev.* 34 (5), 521–533. doi:10.3321/j.issn:1000-0747.2007.05.002

Xue, Y. A. (2018). New breakthroughs in hydrocarbon exploration in the Bohai Sea area driven by understanding innovation: A review of major exploration progresses of Bohai Sea area in recent years. *China Offshore Oil Gas* 30 (2), 1–8. doi:10.11935/j.issn.1673-1506.2018.02.001

Xue, Y. A. (2002). *Selection of natural gas exploration fields and exploration suggestions in the Bohai Sea*. Internal material.

Xue, Y. A. (2010). *Study on gas accumulation characteristics and exploration direction of large and medium-sized gas fields in bohai sea*. Qingdao: China university of petroleum press.

Xue, Y. A. (2019). The breakthrough of the deep-buried gas exploration in the Bohai Sea area andits enlightenment [J. *Natur. Gas. ind.* 39 (1), 11–20. doi:10.3787/j.issn.1000-0976.2019.01.002

Xue, Y. A., and Wang, D. Y. (2020). Formation conditions and exploration direction of large natural gas reservoirs in the oil-prone Bohai Bay Basin, East China. *Petroleum Explor. Dev.* 47 (2), 280–291. doi:10.1016/s1876-3804(20)60046-5

Zhao, X. Z., and Zhang, W. X. (1991). Types, distribution sequence model and enrichment of natural gas pools in Bohai GulfBasin. *J. Univ. Petroleum, China (Editionof Nat. Sci.* 15 (2), 1–9.

Zhu, W. L. (2009). *Paleolimnology and hydrocarbon source conditions of Cenozoic oil-bearing basins in offshore China*. Beijing: Geological Publishing House.

Frontiers in Earth Science

Investigates the processes operating within the major spheres of our planet

Advances our understanding across the earth sciences, providing a theoretical background for better use of our planet's resources and equipping us to face major environmental challenges.

Discover the latest Research Topics

See more →

Frontiers

Avenue du Tribunal-Fédéral 34
1005 Lausanne, Switzerland
frontiersin.org

Contact us

+41 (0)21 510 17 00
frontiersin.org/about/contact